GRAPHENE ELECTROCHEMISTRY: FUNDAMENTALS THROUGH TO ELECTROANALYTICAL APPLICATIONS

D. A. C. BROWNSON

PhD 2013

GRAPHENE ELECTROCHEMISTRY: FUNDAMENTALS THROUGH TO ELECTROANALYTICAL APPLICATIONS

Dale Anthony Christopher Brownson

Submitted in partial fulfilment of the requirements of Manchester Metropolitan University for the degree of Doctor of Philosophy

2013

School of Science and the Environment
Division of Chemistry and Environmental Science
Manchester Metropolitan University

Graphene is reported to possess a range of unique and highly desired properties and consequently has potential to revolutionise the field of electrochemistry if diligently employed as a new-generation electrode material. Graphene potentially represents the world's thinnest electrode material, but there are experimental parameters to be overcome: the first problem is how to electrically wire/connect to the graphene sample(s) as to obtain the reported benefits; the second issue is how to reduce aggregation of graphene sheets back to their lowest energy conformation, that is, graphite, due to the strong π–π interactions between the graphene sheets; the third and final limitation is that various fabrication routes produce graphene to differing qualities, a factor that must be considered when exploring its fundamental electrochemical properties and electroanalytical implementation.

This thesis reports on the fundamental electrochemical characterisation and resultant electroanalytical applicability of utilising graphene as a novel electrode material. The thesis consists of four key contributions, each developing on the knowledge gained from the previous.

Chapters 1 through to 3 give an overview of the relevant fundamental electrochemical concepts with which this thesis is concerned. Chapter 4 provides a 'snap-shot' of the state of the graphene literature from 2010 (upon the commencement of this work), from which successive chapters follow the chronological development and investigation of graphene as produced through a variety of synthesis methods, gradually building a complete picture and understanding of the electrochemistry of graphene and the implications of its properties towards the fabrication and implementation of graphene as an electroanalytical sensor substrate.

Chapter 5 details the relevant experimental information and the full physicochemical characterisation of the various graphene materials utilised within this work.

Chapters 6 and 7 utilise graphenes that are fabricated *via* a 'top-down' approach, which is most commonly employed in the literature, where in order to 'connect to' the graphene a liquid suspension is immobilised onto a suitable electrode surface. Chapter 6 uses surfactant-modified graphene and investigates, for the first time, the influence that such surfactants have on the observed electrochemistry. Chapter 7 uses pristine graphene in solution and considers; the aspects of various 'coverages' of graphene, the supporting electrode substrate, and how the formation of few and multiple layered graphene structures can influence the observed response. These parameters are overlooked within the current literature.

Chapter 8 utilises graphene that is fabricated *via* a 'bottom-up' Chemical Vapour Deposition approach, which gives rise to high quality single layer graphene domains that, once efficiently 'housed' in order to connect to the graphene, allow the electrochemical exploration of monolayer graphene to be realised and be compared to *quasi*-graphene and defect abundant graphene structures for the first time. This approach allows the structure of graphene to be correlated with that of the electrochemical response for the first time. Critically, this work unambiguously demonstrates that the electrochemical response is edge plane like defect dependent.

The final part of this thesis (Chapter 9) utilises a range of modified graphenes including novel three-dimensional (3D) structures (a graphene foam and graphene paste) and functionalised graphene (graphene/graphitic oxide), with the effects of said modifications explored towards the fundamental electrochemical and electroanalytical properties obtained. The first part of this chapter reports the electrochemistry of a novel freestanding 3D graphene

foam and, for the first time, critically compares this to a freestanding 3D carbon foam alternative. It is demonstrated that the graphene foam gives rise to beneficial voltammetric responses in non-aqueous media, namely ionic liquids. This chapter also explores the use of a graphene paste electrode and demonstrates that the voltammetric response is no better than that of a graphite based paste electrode. Last, the use of graphene/graphitic oxide as an electrode material is explored and shown to give rise to unique voltammetric signatures, which are coverage dependant and can be utilised as a means of characterising the successful production of graphene through the reduction of graphene/graphitic oxide (as commonly utilised within the current electrochemical literature). Furthermore, it is shown that the unique voltammetry observed at graphene/graphitic oxide modified electrodes can be used beneficially for electrocatalytic processes.

This thesis demonstrates that, within the graphene electrochemical literature, control experiments are often an overlooked comparison, which are needed for the electrochemical response of graphene to be understood and before the benefits of graphene can be claimed in such instances where superiority is ‘demonstrated’.

The primary focus of this thesis is to investigate and evaluate the fundamental electrochemical properties of graphene as a novel electrode material and as a foundation for the development and integration of its inclusion in next-generation electroanalytical sensing platforms. The objectives of this work are described in greater detail below.

Objectives:

1) Establish the impact and effects that surfactants have on the electrochemical performance of graphene given that they are used routinely in its fabrication (and preservation) to reduce π-π stacking, *i.e.* the formation of graphite.

2) Compare the electrochemical properties of graphenes fabricated through various 'top-down' and 'bottom-up' approaches (resulting in graphenes of various 'qualities', such as possessing a fewer or greater degree of structural defects). Establish the effects that such alterations in the fabrication process can impart onto the observed electrochemistry.

3) Explore the role of graphene's structure on its electron transfer properties. Establish through the comparison of graphene to other graphitic structures the role of edge plane sites (their reactivity) and determine the relationship between electron transfer and material composition (at carbon based electrodes).

4) Utilise the knowledge gained through the completion of prior objectives to successfully implement, fabricate and evaluate graphene modified components for sensing related devices. Determine the impact and outcomes (whether beneficial or detrimental) of said devices towards the electroanalytical sensing of a range of target analytes.

ACKNOWLEDGMENTS

First and foremost I would like to thank Prof. Craig Banks, primarily for gifting me this opportunity but also for the unprecedented knowledge, sustained support and enthusiastic encouragement (including useful critiques) he has afforded me over the past few years. Furthermore, I would like to offer a special thank you to Dr. Jonathan Metters and Dr. Dimitrios Kampouris who have joined me on this long and perilous journey from the very beginning. All three persons noted above have helped me stay on course throughout my studies and have truly made this period of my life one that I will fondly remember.

I would also like to extend my gratitude to all members of the Banks research group (past and present), without whom this experience would not have been as enjoyable and I would not have developed such strong and lasting relationships. I would like to thank those particularly whom I have had the pleasure of supervising during my studies, namely Alexandre Lacombe, Christopher Foster and Luiz Figueiredo-Filho. The opportunity to supervise said students provided me with an invaluable experience, within which I learnt both academically and professionally but also on a personal level in terms of self-discovery and I can only hope that those noted above have taken in equal measure from the experience.

Finally, I would not have been able to complete my studies without the selfless sacrifices made by my grandmother Norma Roberts, father Graham Brownson and mother Lisa Brownson, in addition to the love and support offered by my entire family, for which I am forever grateful. It is unto them, as only proper, I dedicate this thesis.

"*Arise, awake and stop not till the goal is reached.*"

Swami Vivekananda, 1863–1902

values shown should be considered representative, yet approximate. *: Pristine graphene; commercially available from 'Graphene Supermarket', produced *via* a substrate-free gas-phase synthesis method. ‡: Chemically exfoliated graphene; commercially available from 'NanoIntegris', produced *via* a surfactant intercalation process – note that this range is also representative of graphene produced through other chemical exfoliation routes such as the reduction of GO. †: Mechanically exfoliated graphene was fabricated through the so-called 'scotch tape method'. Note that graphene synthesised *via* CVD has been excluded given that crystal size and quality are large variables through this route, however single graphene crystals with dimensions of up to 0.5 mm have been reported. A schematic representation of the *La* and *Lc* microcrystalline characteristics of graphene and HOPG is also shown.

50. Figure 2.4 (A) Schematic representation of an electrochemical reaction occurring on the same electrode surface with different Butler-Volmer characteristics; and a top-down perspective (B).
51. Figure 2.5 Cyclic voltammograms recorded at 1 Vs^{-1} for the oxidation of 1 mM ferrocyanide in 1 M KCl at a basal plane HOPG electrode and an EPPG electrode. The dashed line voltammogram is the simulated fit using linear diffusion only.
52. Figure 2.6 Schematic diagrams showing: (a), (i) the overhead view of a section of the basal plane HOPG surface and (ii) the approximation of each island/band combination as a partially covered circular disc of the same area; (b) the resulting diffusion domain from the approximation in (a) (ii) and the cylindrical coordinate system employed.
53. Figure 2.7 Solid curves are simulated dimensionless current cyclic voltammograms for diffusion domains where D = 6.1 x 10^{-6} cm^2 s^{-1}, $k_1^o = k_{edge}^o$ = 0.022 cm s^{-1}, $k_2^o = k_{basal}^o$ = 10^{-9} cm s^{-1}, υ = 1 V s^{-1}, the band thickness is 1.005 nm and the domain radius is (a) 0.01 µm, (b) 0.1 µm, (c) 1 µm and (d) 10 µm. Overlaid in each section are the simulated inert equivalents (dotted curves), *i.e.*, $k_2^o = k_{basal}^o$ = 0 cm s^{-1}.
54. Figure 2.8 (A) The surface is split into a series of identical domains (unit cells), namely band islands. (B) Schematic difference between diffusion to macro- (i) and micro- (ii) scale electrode systems. The darker area represents the island (r_{band}) with the faster kinetics.
55. Figure 2.9 (A) Voltammetry of a one-electron transfer process at an electrochemically heterogeneous electrode consisting of an array of microbands (k^o = 10 cm s^{-1})

ΔE_P	Peak-to-peak separation
2D	Two-dimensional
3D	Three-dimensional
AA	*L*-ascorbic acid
AFM	Atomic force microscopy
AP	Acetaminophen
ASV	Anodic stripping voltammetry
BDD	Boron-doped diamond
BPPG	Basal plane pyrolytic graphite
BQ	*p*-Benzoquinone
CNT	Carbon nanotube
CV	Cyclic voltammogram
CVD	Chemical vapour deposition
DA	Dopamine hydrochloride
DFT	Density-functional theory
DMF	Dimethylformamide
DMPC	Dimyristoyl phosphatidylcholine
DOS	Density of electronic states
DPV	Differential pulse voltammetry
EDX	Energy-dispersive X-ray spectroscopy
E_P	Peak potential
EPPG	Edge plane pyrolytic graphite
FWHM	Full width at half maximum
GC	Glassy carbon
GNR	Graphene nano ribbon
GNS	Graphene nano sheet
GO	Graphene oxide

Hb	Haemoglobin
HET	Heterogeneous electron transfer
HOMO	Highest occupied molecular orbital
HOPG	Highly ordered pyrolytic graphite
IHP	Inner Helmholtz plane
I_P	Peak current
IUPAC	International union of pure and applied chemistry
k^o	Electrochemical rate constant
LOD	Limit of detection
LUMO	Lowest unoccupied molecular orbital
MWCNT	Multi-walled carbon nanotube
NADH	β-Nicotinamide adenine dinucleotide
OHP	Outer Helmholtz plane
PBS	Phosphate buffer solution
PG	Pyrolytic graphite
PMMA	Poly-methyl methacrylate
PTFE	Polytetrafluoroethylene
RGS	Reduced graphene sheet
RMS	Root-mean-square
RSD	Relative standard deviation
RTIL	Room temperature ionic liquid
RVC	Reticulated vitreous carbon
SCCM	Standard cubic centimetres per minute
SCE	Saturated calomel electrode
SECM	Scanning electrochemical cell microscopy
SEM	Scanning electron microscope
SHE	Standard hydrogen electrode
SPE	Screen-printed electrode

STM	Scanning tunnelling microscopy
SWCNT	Single-walled carbon nanotube
SWV	Square wave voltammetry
TEM	Transmission electron microscope
TMPD	N,N,N’,N’-tetramethyl-*para*-phenylenediamine
UA	Uric acid
XPS	X-ray photoelectron spectroscopy

3D carbon foam	Freestanding, three-dimensional RVC foam (see Chapter 5.4.6).
3D graphene foam	Freestanding, three-dimensional graphene foam (see Chapter 5.4.6).
CVD-graphene	CVD grown graphene on nickel substrate/underlying-support (see Chapter 5.4.4).
D-graphene	Double-layered defect-graphene on silicon dioxide (electrochemically inert) supporting substrate; the two-layer graphene is grown *via* CVD and transferred onto the supporting substrate using a PMMA method (see Chapter 5.4.5).
GO	Graphene oxide sheets suspended in aqueous solution (see Chapter 5.4.8).
M-graphene	Monolayer graphene on silicon dioxide (electrochemically inert) substrate; single-layer graphene grown *via* CVD and transferred onto the supporting substrate using a PMMA method (see Chapter 5.4.5).
P-graphene	Pristine (surfactant free) graphene sheets suspended in ethanol (see Chapter 5.4.2).
Q-graphene	Few-/multi- layered (*quasi*-) graphene on silicon dioxide (electrochemically inert) supporting substrate; the graphene, which has an average of 4 layers, is grown *via* CVD and transferred onto the supporting substrate using a PMMA method (see Chapter 5.4.5).
S-graphene	Graphene sheets with adsorbed surfactant (sodium cholate) suspended in aqueous solution (see Chapter 5.4.1).
S-graphite	Graphite dispersed in aqueous solution containing sodium cholate (same concentration as present in S-graphene, *i.e.* to mimic the surfactant content) (see Chapters 5.4.3 and 5.5).

Please see Chapter 5.4 for full details regarding the various graphene fabrication approaches and for the appropriate characterisation.

CHAPTER 1: INTERPRETING ELECTROCHEMISTRY

This chapter introduces the important aspects of electrochemistry which allow a greater understanding and appreciation of the subject, which are then applied in subsequent chapters where graphene and related structures are explored as potential electrode materials.

1.1. INTRODUCTION TO ELECTROCHEMISTRY AND ELECTROANALYSIS

Electrochemical and electroanalytical techniques are concerned with the interaction between electricity and chemistry. More specifically, electrochemistry concerns the measurements of electrical quantities such as current, potential, or charge, and their relationship to chemical parameters. [1] There are two principle types of electrochemical techniques that can be used in electroanalysis; potentiometric and potentiostatic measurements, differentiated *via* the electrical signal used for quantification. In contrast to many chemical measurements that involve bulk solutions, electrochemical processes take place at the electrode | solution interface. Controlled-potential techniques deal with the study of charge transfer processes at the electrode | solution interface based on dynamic (non-zero current) situations (*vide infra*). In this situation, the electrode potential is used to drive an electron transfer reaction, where the resulting current is measured. This is effectively 'electron pressure', forcing a chemical species to either gain or lose an electron (undergo reduction or oxidation respectively). The advantages of using controlled-potential techniques include high sensitivity and selectivity towards electroactive species where extremely low limits of detection (nanomolar, nM) can be achieved with very small sample volumes (5–20 µL). Note, it is the electrode material utilised that defines the resultant performance, hence the purpose of this work is to investigate the electrochemical properties/usefulness of graphene as a potential 'next generation' electrode material.

1.1.1. FARADAIC PROCESSES

1.1.1.1. EQUILIBRIUM ELECTROCHEMISTRY

Electrochemical reactions involve charged species whose energy depends on the potential of the phase that such species are contained within. Consider the following simple electrochemically reversible redox reaction:

$$O(aq) + ne^{-}(m) \underset{k_{ox}}{\overset{k_{red}}{\rightleftharpoons}} R^{n-}(aq) \qquad (1.1)$$

where *O* and *R* are the oxidised and reduced forms of a redox couple. The electrochemical process as expressed in equation (1.1) involves the transfer of charge across the interfacial region of a metallic electrode, termed *(m)* to indicate the source of electrons, and a solution phase *(aq)* species. The electrochemical reaction described in equation (1.1) only proceeds once a suitable electrode is placed into the solution phase, which acts as a source or sink of electrons. It is important to realise that this reaction involves the transfer of charged species, *viz* electrons, between the electrode surface, *(m)*, and the solution phase species, *(aq)*, hence the electrode reaction is an interfacial process. As the electron transfer moves towards equilibrium a net charge separation must develop between the electrode and the solution, which creates a potential difference at the solution | electrode interface which is expressed as ϕ_s and ϕ_m respectively, such that the potential drop across the interface is thus:

$$\Delta\phi = \phi_m - \phi_s \qquad (1.2)$$

In order to measure such a value a complete conducting circuit is required. However, if another electrode is placed into the solution then one would have two electrodes, both monitoring the change of the potential difference at the two electrode | solution interfaces, resulting in

meaningless information. The solution is to use one electrode | solution interface and a reference electrode which maintains a fixed potential difference, thus leads to the following being realised:

$$E = (\phi_m - \phi_s) + X \tag{1.3}$$

where E is the potential difference being measured, the term $E = (\phi_m - \phi_s) + X$ refers to the electrode of interest and X is the role of the reference electrode, which is constant. Such measurements are undertaken at equilibrium such that no current is drawn through the cell. The potential E reaches a steady value, E_e which now depends on the relative concentrations of O and R, which can be expressed as:

$$E_e = \Delta\phi_{m/s}(O/R) - \Delta\phi_{m/s}(X) = \Delta\phi_{m/s}(O/R) - 0 \tag{1.4}$$

where X is a reference electrode such as the Standard Hydrogen Electrode (SHE) or the more commonly utilised Saturated Calomel Electrode (SCE). Conventionally the SHE is defined as exhibiting a potential of zero, allowing one to report the potential of half-cells, such as the *O/R* couple, relative to the SHE.

For the process defined in equation (1.1), the *Nernst equation* is given by:

$$E_e = E_f^0(O/R) + \left(\frac{RT}{nF}\right) Ln\left(\frac{[O]}{[R]}\right) \tag{1.5}$$

for the potential established at the electrode under equilibrium, where E_e is the equilibrium potential of the formal potential E_f^0 and the concentrations of the species O and R at the electrode surface, which, under conditions of equilibrium, are the same as their bulk solution values. Above, R is the universal gas constant (8.314 J K^{-1} mol^{-1}), T is the temperature

(in Kelvin), n is the number of electrons transferred in the reaction and F is the Faraday constant (96,485.33 C mol^{-1}). Note that in equation (1.5) the formal potential is defined as:

$$E_f^0 = E^0 + \left(\frac{RT}{nF}\right) Ln\left(\frac{\gamma_O^v}{\gamma_R^v}\right) \tag{1.6}$$

where E^0 is the standard electrode potential and γ is the relevant activity coefficients. The formal potentials depend on temperature and pressure, as do the standard potentials, but will also have a dependence on electrolyte concentrations, not only of the species involved in the potential determining equilibrium but also on other electrolytes that will be present in the solution, since these influence ion activities. The formal potential loses the thermodynamic generality of the standard potentials which are only applicable under specific conditions but enables experimentalists to proceed with meaningful voltammetric measurements.

Equilibrium electrochemistry, while being of fundamental importance, since it allows thermodynamic parameters to be readily obtained (such as reaction free energies, entropies and equilibrium constants and solution pH), it is not as extensively used as dynamic electrochemistry which is the main thrust of electrochemistry that is used commercially in numerous areas (such as in determining the electron transfer properties of various potential electrode materials and for electroanalytical applications) and indeed is the main focus of electrochemistry utilised in this work.

1.1.1.2. DYNAMIC ELECTROCHEMISTRY

In dynamic electrochemistry the intention of controlled-potential electroanalytical experiments is to obtain a current response that is interrelated to the concentration of the target

analyte. This is achieved by recording the transfer of electron(s) during the redox process of the target analyte. Consider the following electrochemical process:

$$O(aq) + ne^{-}(m) \longrightarrow R^{n-}(aq) \tag{1.7}$$

at an electrode which is brought about through the application of a suitability negative potential to the electrode. Note that a second electrode will be needed somewhere in the solution to facilitate the passage of the required electrical current through the solution and a reference electrode will also be required as identified above. The process, as described in Figure 1.1, occurs in the following general steps. First, the reactant diffuses from the bulk solution to the electrode interface, termed mass transport. Next, a potential is applied into the cell which is different to E_e, the current induces the exchange of electrons between the electrode surface and the species in solution and as such, electrolysis occurs where the magnitude of the current, i, is related to the flux of the species in solution, j, by the following:

$$i = nAFj \tag{1.8}$$

where F is the Faraday constant, n is the number of electrons per molecule involved in the electrochemical process and A is the electrode area. The electron transfer process between the electrode and the *O (aq)* species takes place *via* quantum mechanical tunnelling between the electrode and reactant close to the electrode, typically *ca*. 10–20 Å, as the rate of tunnelling falls off strongly with separation since it requires overlap of quantum mechanical wave-functions which describes the electron in the electrode and the electroactive species. Note that the above process is complicated by the reactivity of the electro-active species, the nature (type, geometry) of the electrode surface, the applied voltage and the structure of the interfacial region over which the electron transfer process occurs.

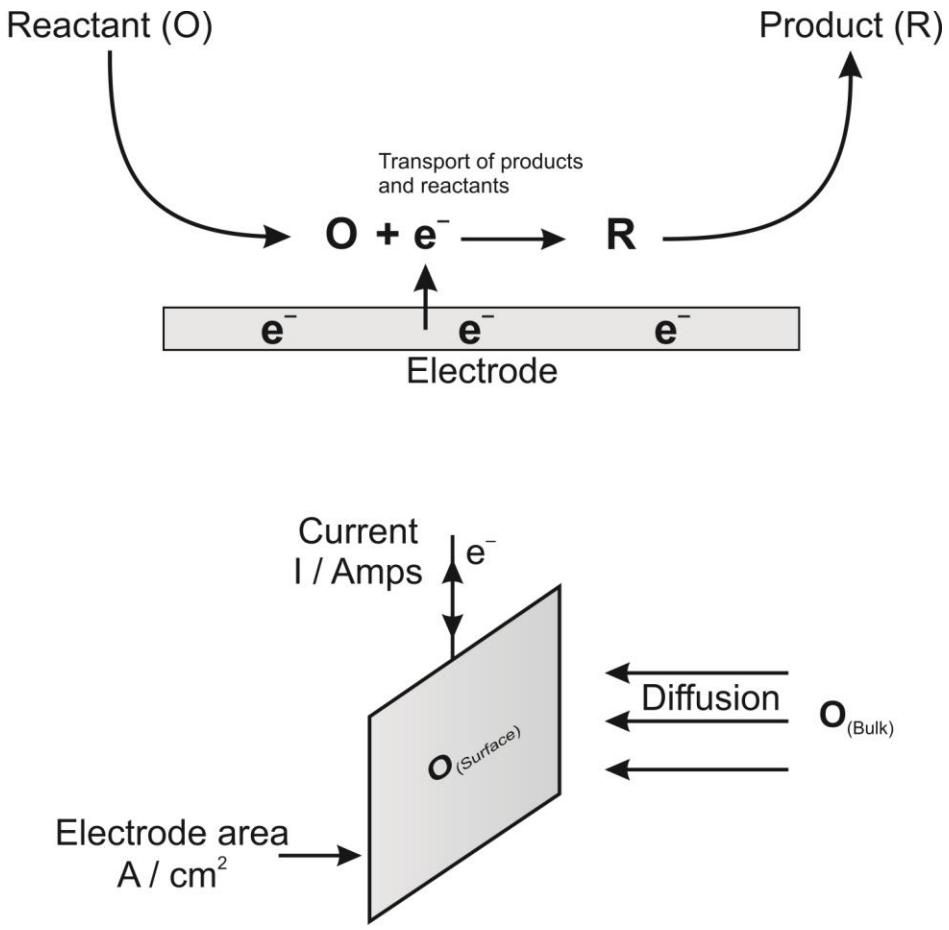

Figure 1.1 *Schematic representation of a simple electrochemical reaction, occurring at an electrode surface of electrode area (A).*

In equation (1.8) the units of flux are: mol cm^{-2} s^{-1}, which effectively reflects the quantity of material reaching the electrode surface per second. The rate law can be described by:

$$j = k^0[A]_0 \tag{1.9}$$

assuming the rate of reaction (in this case) is first order, where k^0 is the heterogeneous rate constant for the electron transfer reaction and $[A]_0$ is the concentration of species A at the electrode surface (and not the bulk).

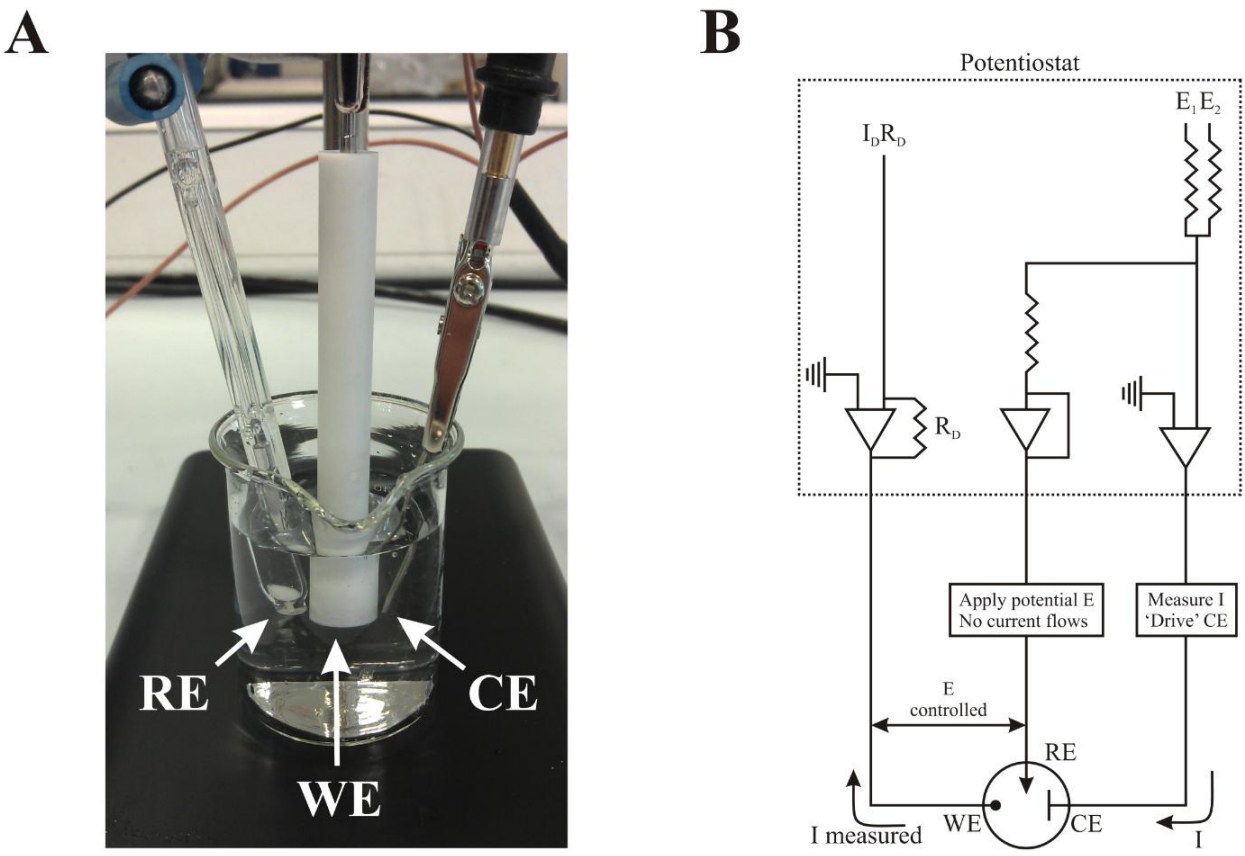

Figure 1.2 *A typical experimental set-up showing the reference electrode (RE, saturated calomel electrode), the working electrode (WE) and the counter electrode (CE, a platinum rod) immersed into an electrolyte solution (**A**). A simple electronic scheme equivalent to the electrochemical cell (**B**).*
A potentiostat is required for running electrochemical experiments. Note, all the resistances are equal except R_D which is variable.

The most common configuration for running dynamic electrochemical experiments involves the use of three electrodes, the working electrode, a counter (auxiliary) electrode and a reference electrode, all connected to a commercially available potentiostat which allows the potential difference between the reference and working electrode to be controlled with minimal interference from ohmic (*IR*) drop. The current flowing through the reference electrode is minimised, avoiding polarisation of the reference electrode, which keeps the applied potential between the working and reference electrode stable. Depicted in Figure 1.2 is a typical

experimental set-up where the three electrode system is being utilised. The reference electrode can be a Ag/AgCl or a SCE which can either be commercially obtained or fabricated within the laboratory. The counter electrode should be a non-reactive high surface area electrode such as platinum or carbon and the working electrode can be a plethora of configurations and compositions, indeed, the purpose of this work is to utilise graphene as a working electrode.

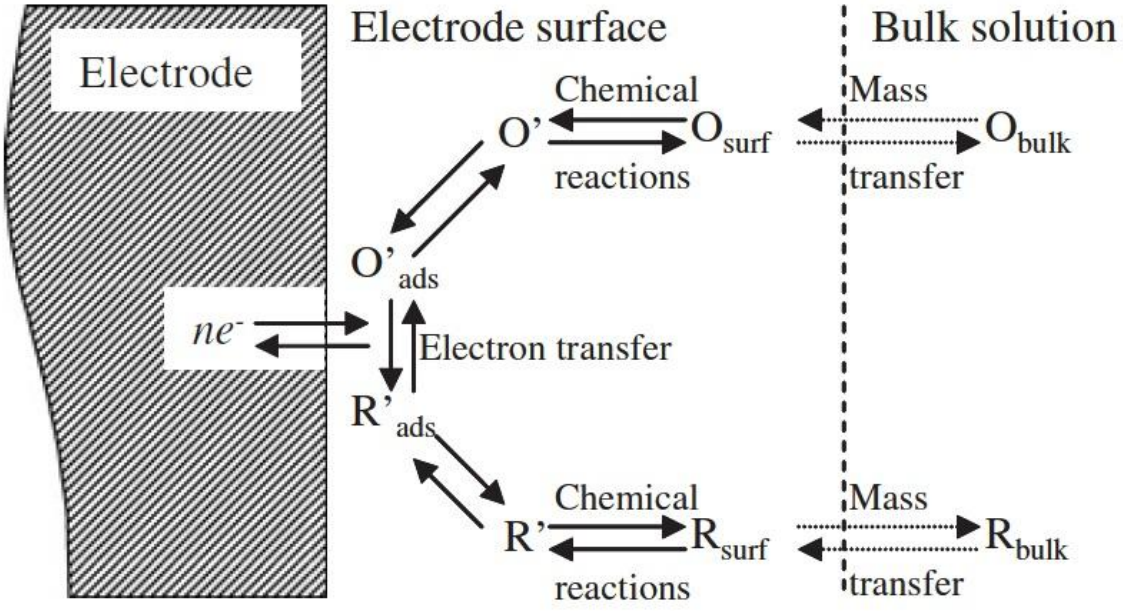

Figure 1.3 *The general electrochemical reaction pathway. Reproduced from Ref. [2].*

If one concerns themselves with only the working electrode, since it is where all the significant processes occur, a general overview of an electrode reaction is depicted in Figure 1.3 which builds on that shown in Figure 1.1. This general electrochemical process shows that the observed electrode current is dependent on mass transport; which usually occurs in series with other processes, such as chemical reactions, adsorption/desorption and also the heterogeneous rate constant for the electron transfer reaction. The working electrode is immersed into an electrolyte, usually containing the electroactive species under investigation and a supporting

electrolyte salt, to achieve the required conductivity and to minimise the IR_u drop. The electric double layer at the working electrode occurs over a distance of *ca*. 1 nm. Figure 1.4 shows a schematic representation of the composition of the solution phase close to the (working) electrode surface where the compact layer is also termed the "Inner Helmholtz" layer which is closest to the surface in which the distribution of charge, and hence potential, changes linearly with the distance from the electrode surface and the diffuse layer, known as the "Gouy-Chapman" layer, in which the potential changes exponentially. Also shown in Figure 1.4 is a zoomed in perspective of the compact layer showing the Inner and Outer Helmholtz Plane (IHP and OHP) where specifically adsorbed anions and solvated cations can reside.

Under typical experimental conditions, the magnitude of the diffusion layer is several orders of magnitude larger than the diffuse layer. In dynamic electrochemistry the potential is always being changed and hence the surface organisation will change and a concentration perturbation travels away from the electrode surface into the solution, where the diffusion layer (δ) is related to the diffusion coefficient of the electroactive species being perturbed as a function of time (t): this is covered in greater detail when discussing cyclic voltammetry (*vide infra*).

As discussed above with reference to Figure 1.1, the application of a voltage is key for electrochemical reactions to proceed. The application of a potential, that is, a voltage, *V = Joule / Coulombs*, such that the voltage is simply the energy (Joule) required to move charge (Coulomb). The application of such a voltage supplies electrical energy and can be thought of as an electrochemical 'pressure'.

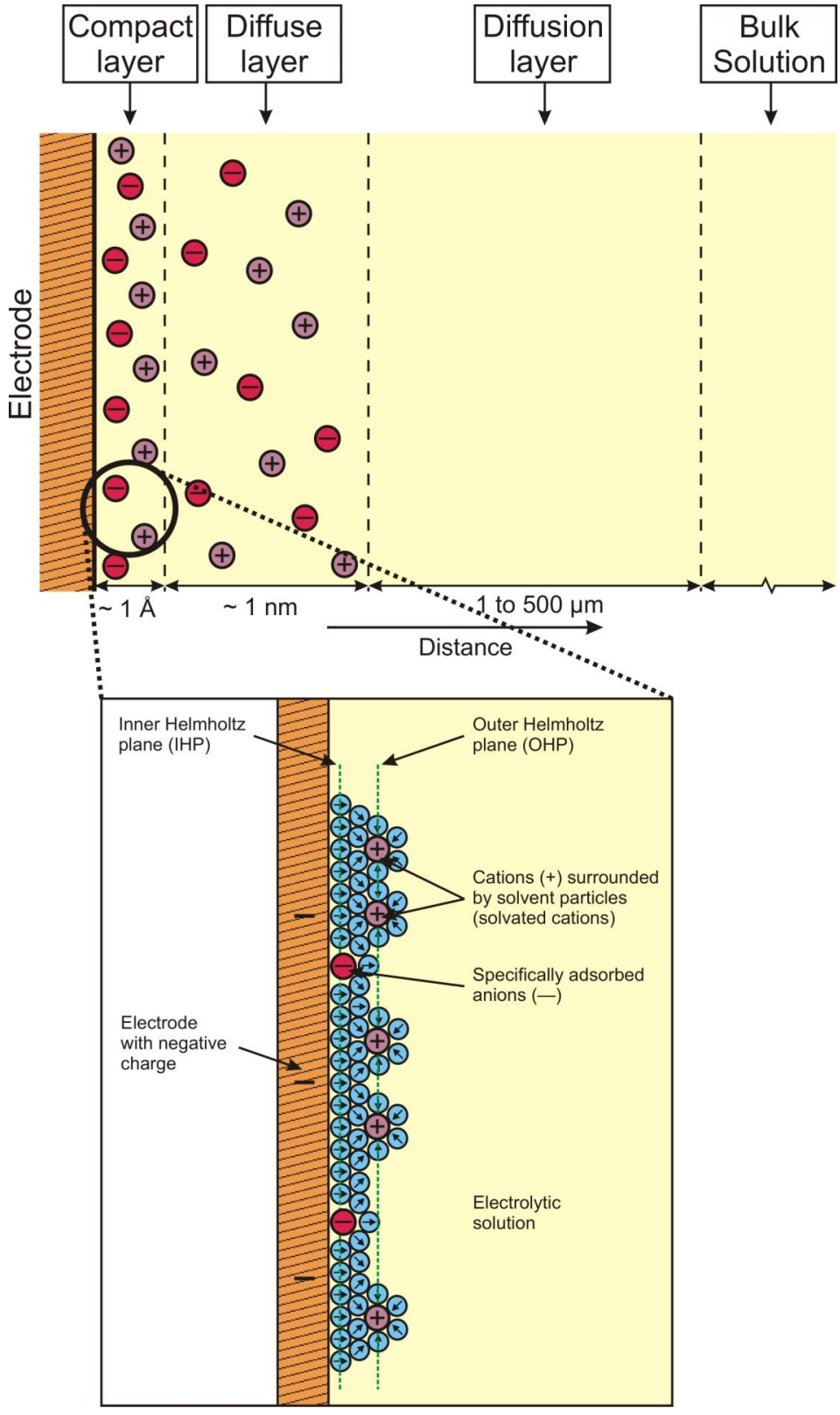

Figure 1.4 *Schematic representation of the composition of the electrode | solution interface (not to scale).*

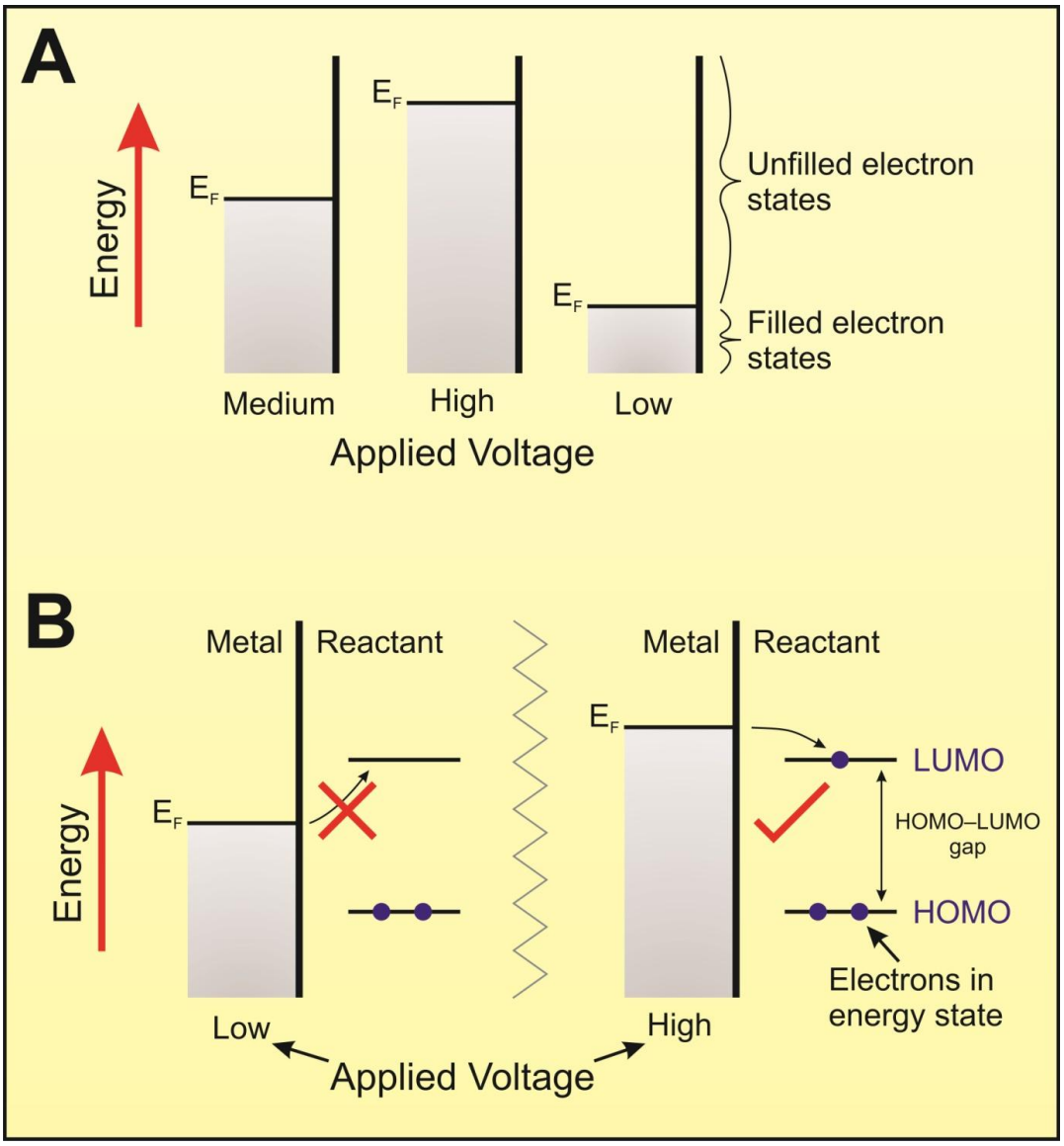

Figure 1.5 *An overview of 'driving' an electrochemical reaction.* ***A****: Band diagram showing the effect of low, medium and high applied voltages.* ***B****: Effect of applied voltage on the Fermi level.*

The electronic structure of a metal involves electronic conduction bands in which electrons are free to move throughout the metal, which binds the (metal) cations together. The energy levels in these bands form an effective continuum of levels, which are filled-up to an energy maximum (Fermi level). Such levels can be altered by supplying electrical energy in the form of applying or driving a voltage, as shown in Figure 1.5A. In Figure 1.5B (left image), the

Fermi level energy is lower than that of the Lowest Unoccupied Molecular Orbital (LUMO) of the reactant and as such it is *thermodynamically unfavourable* for an electron to jump/transfer from the electrode to the molecule. However, as shown in Figure 1.5B (right image), when the Fermi level of the electrode is above the LUMO of the reactant it is then *thermodynamically favourable* for the electron transfer process to occur, that is, the electrochemical reduction of the reactant can proceed. This concept is explored further in Chapter 1.2 as the process depends on the kinetics of the electrochemical transfer reaction.

1.2. ELECTRODE KINETICS

Consider the reduction of iron(III) and the oxidation of iron(II):

$$Fe^{3+}(aq) + e^{-}(m) \underset{k_{ox}}{\overset{k_{red}}{\rightleftharpoons}} Fe^{2+}(aq) \tag{1.10}$$

where the rate constants k_{red} and k_{ox} describe the reduction and oxidation respectively. Note that a cathodic process is one at an electrode (a 'cathode') supplying electrons causing a reduction whilst an anodic process is one at an electrode (an 'anode') which removes electrons and causes an oxidation process. The rate law for this net process can be described by the following:

$$j = k_{red}[Fe^{3+}]_0 - k_{ox}[Fe^{2+}]_0 \tag{1.11}$$

where the rate constants k_{red} and k_{ox} are potential dependent with the cathodic reduction dominating at applied negative electrode potentials whilst the anodic oxidation would be the dominant term at applied positive potentials.

Figure 1.6 depicts a reaction profile for the electrochemical process (equation (1.10)) of interest. The dashed line depicts the energy barrier when no potential has been applied, where it

can be seen that the process is thermodynamically uphill. When a potential is applied, the free energy of reactants is raised since the Gibbs free energy for the reduction is related to the formal potential by: $\Delta G^0 = -nF(E - E_f^0)$ where $E - E_f^0$ measures the potential applied to the working electrode relative to the formal potential of the Fe^{3+}/Fe^{2+}couple, with *both* potentials measured relative to the same reference electrode. The reaction coordinate changes to that represented by the solid line where it can be seen that the energy required to reach the transition state is lowered and the process is 'downhill' and is thus thermodynamically driven.

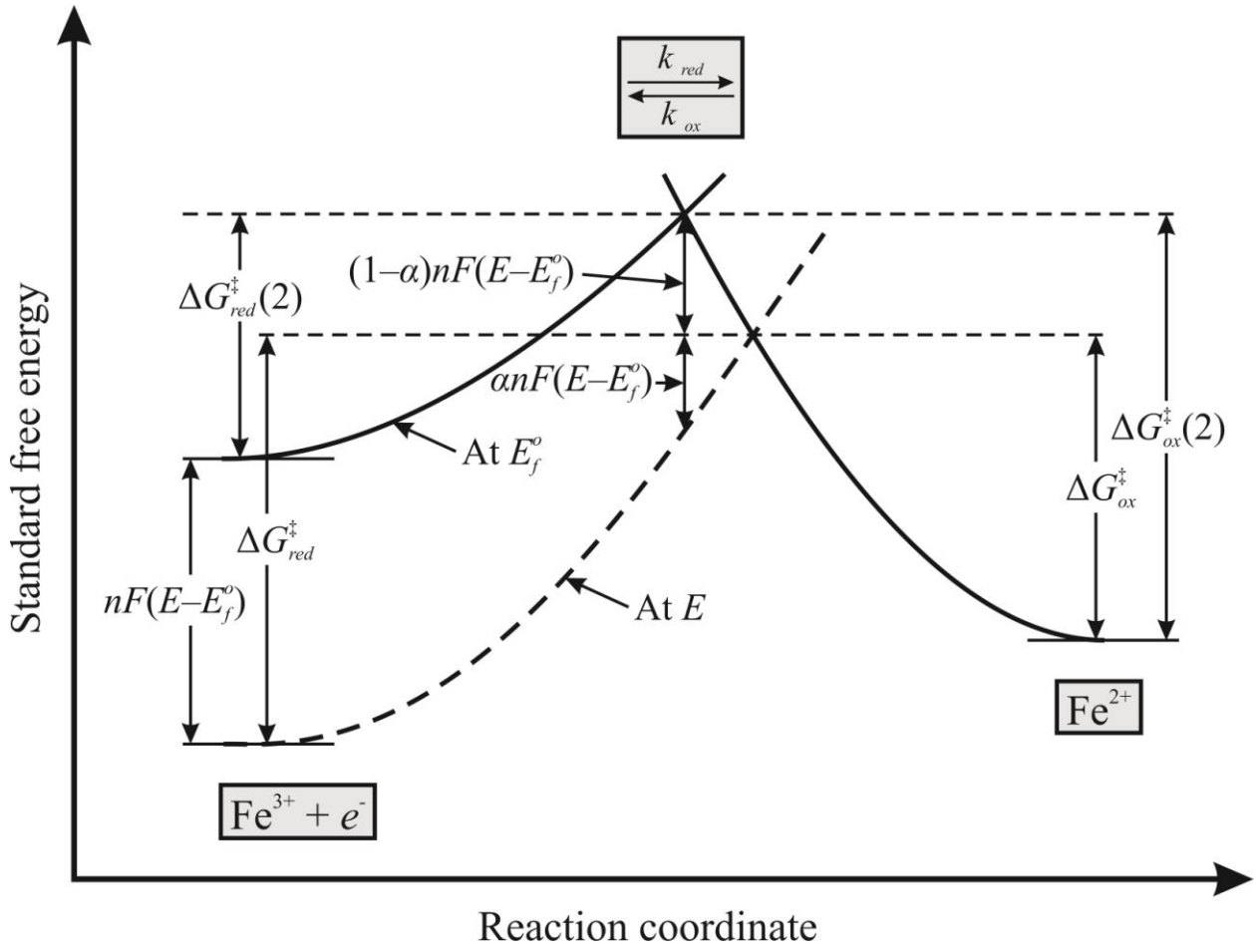

Figure 1.6 *Schematic drawing of the energy profiles along the reaction coordinate for a heterogeneous electron transfer.*

From inspection of Figure 1.6, one can write:

$$\Delta G_{red}^{\pm}(2) = \Delta G_{red}^{\pm} + \alpha nF(E - E_f^0) \tag{1.12}$$

and

$$\Delta G_{ox}^{\pm}(2) = \Delta G_{ox}^{\pm} - (1-\alpha)nF(E - E_f^0) \tag{1.13}$$

where the parameter α is known as the transfer coefficient, which provides physical insights into how the transition state is influenced by the application of voltage and typically is found to have a value of 0.5. A value of one half means that the transition state behaves mid-way between the reactants and products response to applied voltage. Figure 1.7 shows the effect of changing the potential on the free energy curve. In most systems this lies between 0.7 and 0.3 and usually a value of 0.5 is assumed.

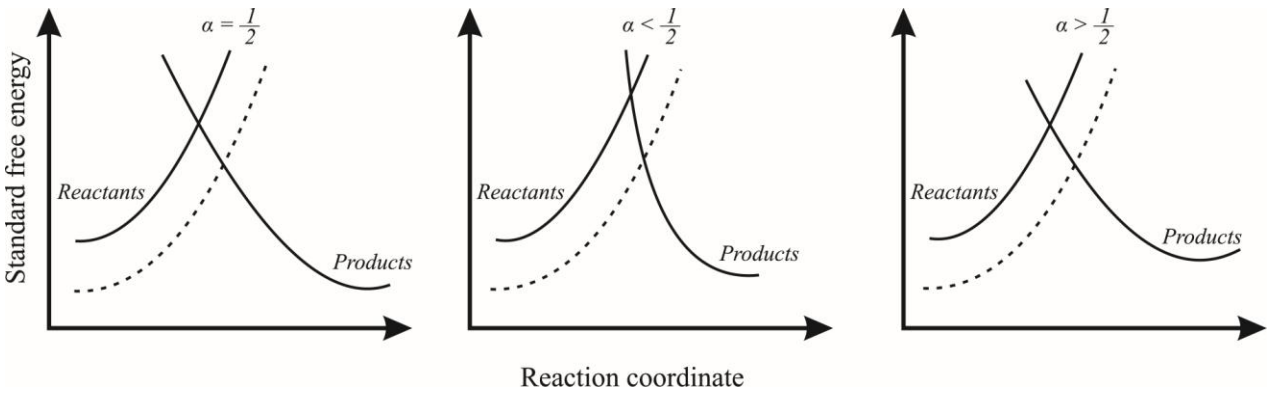

Figure 1.7 *Schematic representation showing the transfer coefficient as an indicator of the symmetry of free energy curve. The dotted line indicates the shift for* $Fe^{3+}(aq) + e^{-}(m) \underset{k_{ox}}{\overset{k_{red}}{\rightleftharpoons}} Fe^{2+}(aq)$ *as the potential is altered to more positive potentials.*

Assuming the rate constants, k_{red} and k_{ox} behave in an Arrhenius form:

$$k_{red} = A_{red} \exp\left(\Delta G_{red}^{\pm} / RT\right) \tag{1.14}$$

$$k_{ox} = A_{ox} \exp\left(\Delta G_{ox}^{\pm} / RT\right) \tag{1.15}$$

Inserting the activation energies (1.12) and (1.13) gives rise to:

$$k_{red} = A_{red} \exp\left(\Delta G_{red}^{\pm}(2) / RT\right) \exp\left(-\alpha nF(E - E_f^0) / RT\right) \tag{1.16}$$

$$k_{ox} = A_{ox} \exp\left(\Delta G_{ox}^{\pm}(2) / RT\right) \exp\left((1-\alpha) nF(E - E_f^0) / RT\right) \tag{1.17}$$

since the first part of equations (1.16) and (1.17) are potential independent one can write:

$$k_{red} = k_{red}^0 \exp\left(-\alpha nF(E - E_f^0) / RT\right) \tag{1.18}$$

$$k_{ox} = k_{ox}^0 \exp\left((1-\alpha) nF(E - E_f^0) / RT\right) \tag{1.19}$$

This shows that the electrochemical rate constants for the one electron oxidation of $Fe^{2+}(k_{ox})$ and for the reduction of $Fe^{3+}(k_{red})$ depend exponentially on the electrode potential: k_{ox} increases as the electrode is made more positive relative to the solution whilst k_{red} increases as the electrode is made more negative relative to the solution. It is clear that changing the voltage affects the rate constants. However, the kinetics of the electron transfer is not the sole process which can control the electrochemical reaction; in many circumstances it is the rate of mass transport to the electrode which controls the overall reaction, which is diligently explored later.

Given that the net rate (flux) of reaction is specified by: $j = k_{red}[Fe^{3+}]_0 - k_{ox}[Fe^{2+}]_0$, using equations (1.18) and (1.19) one can write:

$$j = k_{red}^{0} \exp\left[\frac{-\alpha F(E - E_f^0)}{RT}\right]\left[Fe^{3+}\right]_0 - k_{ox}^{0} \exp\left[\frac{(1-\alpha)F(E - E_f^0)}{RT}\right]\left[Fe^{2+}\right]_0 \quad (1.20)$$

If the case of a dynamic equilibrium is considered at the working electrode, such that the oxidation and reduction currents exactly balance each other, then (since no net current flows) $j = 0$ and given the fact that $\alpha = 0.5$:

$$E = E_f^0 + \frac{RT}{F} Ln\left(\frac{[Fe^{2+}]}{[Fe^{3+}]}\right) + \frac{RT}{F} Ln\left(\frac{k_{ox}^{0}}{k_{red}^{0}}\right) \quad (1.21)$$

From the discussion earlier it is clear that when no net current flows the potential is given by:

$$E = E_f^0 + \frac{RT}{F} Ln\left(\frac{[Fe^{2+}]}{[Fe^{3+}]}\right) \quad (1.22)$$

so that $k_{ox}^0 = k_{red}^0 = k^0$ which is the *Nernst equation*. Therefore one can write:

$$k_{red} = k^0 \exp\left[\frac{-\alpha F(E - E_f^0)}{RT}\right] \quad (1.23)$$

$$k_{ox} = k^0 \exp\left[\frac{(1-\alpha)F(E - E_f^0)}{RT}\right] \quad (1.24)$$

Equations (1.23) and (1.24) are the most convenient forms of the *Butler-Volmer expression* for the electrochemical rate constants k_{red}^0 and k_{ox}^0. The quantity k^0, with units of cm s^{-1}, is the *standard electrochemical rate constant*.

Mass transport of the analyte under investigation is governed by the *Nernst-Planck equation* defined by:

$$J_i(x) = -D_i \frac{\partial C_i(x)}{\partial x} - \frac{z_i F}{RT} D_i C_i \frac{\partial \phi(x)}{\partial x} + C_i V(x) \tag{1.25}$$

where $J_i(x)$ is the flux of the electroactive species i (mol s^{-1} cm^{-2}) at a distance x from the electrode surface, D_i is the diffusion coefficient (cm^2 s^{-1}), $\frac{\partial C_i(x)}{\partial x}$ is the concentration gradient at distance x, $\frac{\partial \phi(x)}{\partial x}$ is the potential gradient, z_i and C_i are the charge (dimensionless) and concentration (mol cm^{-3}) of species i respectively and $V(x)$ is the velocity (cm s^{-1}) with which a volume element in solution moves along the axis. These three key terms comprising equation (1.25) represent the contributions to the flux of species i, that is, diffusion, migration and convection respectively.

If an electrochemical experiment is considered which is conducted in a solution that has supporting electrolyte and in stagnant solutions (non-hydrodynamic conditions, see later) such that migration and convection can be neglected from equation (1.25), this is thus reduced to consider the only relevant mode of mass transport to the electrode surface on the experimental time scale, which is diffusion. The diffusion of species i, from bulk solution to the electrode is described by Fick's first and second laws of diffusion:

$$J_i(x) = -D_i \frac{\partial C_i(x)}{\partial x} \tag{1.26}$$

and

$$\frac{\partial C_i}{\partial t} = D_i \frac{\partial^2 C_i(x)}{\partial x^2} \tag{1.27}$$

where j is the flux in mol cm^2 s^{-1}, D the diffusion coefficient in cm^2 s^{-1} and C is the concentration of the electro-active species in mol cm^{-3}. In order to obtain the concentrations of the electro-active species at a location x and time t, the partial differential equation should be solved which is possible if the initial (values at $t = 0$) and boundary conditions (values at certain location x) are known.

If one considers a simple redox process involving the transfer of one-electron between the electrode and species A in solution to form the product B in solution, as shown below;

$$A + e^- \underset{k_{ox}}{\overset{k_{red}}{\rightleftharpoons}} B \tag{1.28}$$

where the rate of electron transfer is fast compared to the rate of mass transport, *i.e.* an electrochemically and chemically reversible redox process. Assuming that the electron transfer follows Butler-Volmer kinetics,

$$k_{red} = k_{red}^0 \exp\left(\frac{-\alpha F}{RT}\eta\right) \tag{1.29}$$

and

$$k_{ox} = k_{ox}^0 \exp\left(\frac{\beta F}{RT}\eta\right) \tag{1.30}$$

where k^o is the standard electrochemical rate constant, α and β are transfer coefficients such that $\alpha + \beta = 1$, and η is the over-potential defined as:

$$\eta = E - E_{A/B}^{0'} \tag{1.31}$$

where E is the electrode potential and $E_{A/B}^{o'}$ the formal potential for the A/B couple. As the electrolysis of A progresses, all of the species A at the electrode surface will be consumed,

resulting in a depletion of the concentration of *A* in the vicinity of the electrode surface and setting up a concentration gradient down which fresh *A* must diffuse from the bulk solution to support further electrolysis; see Figure 1.4 which depicts the structure of the electrode surface. This depletion zone is known as the diffusion layer, the thickness of which, δ, increases in size as a function of time, *t*, such that (in one-dimension):

$$\delta = \sqrt{2Dt} \tag{1.32}$$

Figure 1.8 depicts the Nernst diffusion layer model which shows that beyond the critical distance, δ, the solution is well mixed such that the concentration of the electroactive species is maintained at a constant bulk value. In this vicinity, the mixing of the solution to even out inhomogeneities is due to 'natural convection' induced by density differences. Additionally, if the electrochemical arrangement is not sufficiently thermostated, slight variation throughout the bulk of the solution can provide a driving force for natural convection.

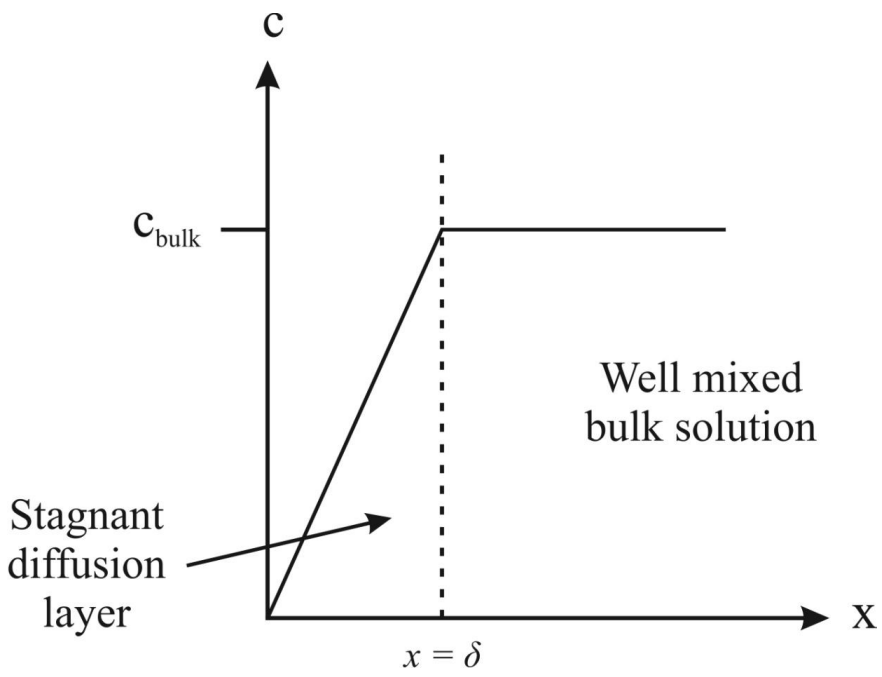

Figure 1.8 *The Nernst diffusion layer model.*

Departing from the bulk solution towards the electrode surface, natural convection dies away due to the rigidity of the electrode surface and frictional forces, this is the diffusion layer, and since only concentration changes occur in this zone, diffusional transport is in operation. Note that in reality there is no real defined zones and these merge into one another, but it is a useful concept. Under experimental conditions, the diffusion layer is in the order of tens to hundreds of micrometres in size.

1.4. VOLTAMMETRIC TECHNIQUES: CYCLIC VOLTAMMETRY

Cyclic voltammetry is the most extensively used technique for acquiring qualitative information about electrochemical reactions. It tenders the rapid identification of *redox* potentials distinctive to the electroactive species, providing considerable information about the thermodynamics of a redox process, kinetics of heterogeneous electron transfer reactions, and analysis of coupled electrochemical reactions or adsorption processes. Cyclic voltammetry consists of scanning (linearly) the potential of the working electrode using a triangular potential wave form (Figure 1.9).

The potential is swept from E_1 to E_2 and the rate at which this is achieved is the voltammetric scan rate (or the gradient of the line) typically measured in V/s, as shown in Figure 1.9. In this case, if the potential is stopped, this is known as a linear sweep experiment. If the scan is returned back to E_1, a full potential cycle, this is known as cyclic voltammetry. Depending on the information sought, either single or multiple cycles can be performed. For the duration of the potential sweep, the potentiostat measures the resulting current that arises *via* the applied voltage (potential). The plot of current *versus* potential (voltage) is termed a

'cyclic voltammogram', CV. A Cyclic voltammogram is complex and dependent on time along with many other physical and chemical properties.

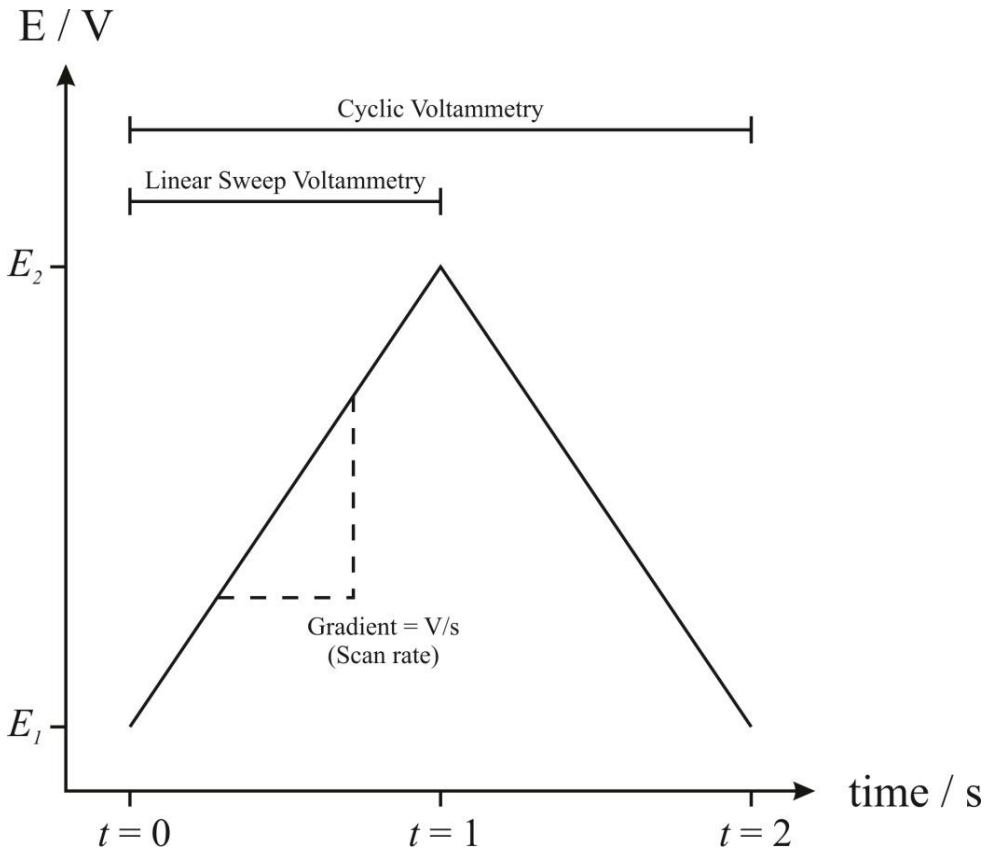

Figure 1.9 *Potential–time profiles used to perform linear sweep and cyclic voltammetry.*

The *cyclic voltammetric* response can be discovered by solving the transport equations (in three-dimensions, *x*, *y* and *x*): [3]

$$\frac{\partial[A]}{\partial t} = D_A \nabla^2 [A] \tag{1.33}$$

and

$$\frac{\partial[B]}{\partial t} = D_B \nabla^2 [B] \tag{1.34}$$

and applying equations (1.29), (1.30) and (1.31) as boundary conditions where the equations: [3]

$$E = E_{start} + \upsilon t \qquad 0 < t < \frac{E_{end} - E_{start}}{\upsilon} \tag{1.35}$$

and

$$E = E_{end} - \upsilon\left[t - \frac{E_{end} - E_{start}}{\upsilon} \right] \tag{1.36}$$

define the potential sweep between E_{start} and E_{end} with a voltage sweep rate of, υ, Vs^{-1} and D_A and D_B are the diffusion coefficients of *A* and *B*, respectively.

1.4.1. INTERPRETATION OF DATA

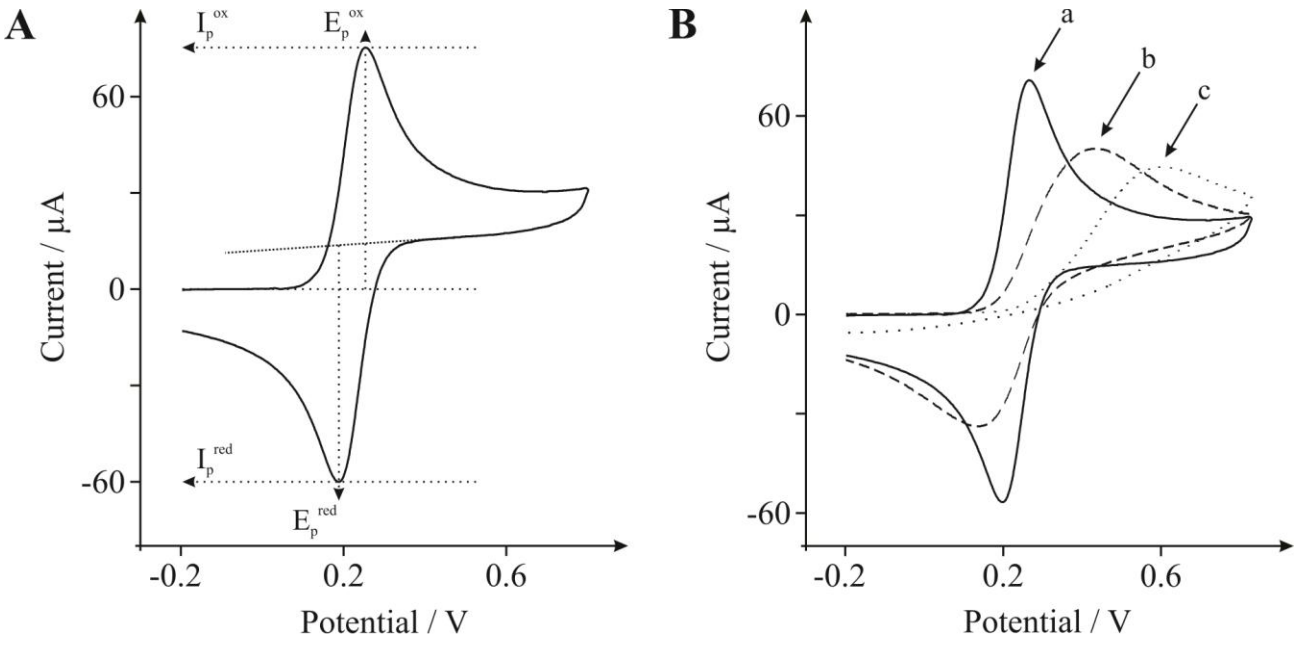

Figure 1.10 A*: Typical cyclic voltammogram depicting the peak position E_P and peak height I_P.*
B*: Cyclic voltammograms for reversible (a), quasi-reversible (b) and irreversible (c) electron transfer.*

Figure 1.10 shows a typical cyclic voltammetric curve (or CV) for the case of the electrochemical process as described in equation (1.28) where a voltammetric potential is applied and the current monitored which gives rise to the unique profile presented in Figure 1.10A.

Characteristics of the voltammogram (CV) which are routinely monitored and reported are the peak height (I_P) and the potential at which the peak occurs (E_P).

Shown in Figure 1.10B is the case of different heterogeneous electron transfer rates, that is, reversible, quasi-reversible and irreversible, each giving rise to unique voltammetric profiles. The physical processes responsible for the characteristic shape of a 'reversible' voltammogram, for the process, $A + ne^- \longrightarrow B$ are based on i) Fick's laws and ii) Nernst's laws:

$$\frac{\partial [A]}{\partial t} = D\frac{\partial^2 [A]}{\partial x^2}; \quad \frac{[A]_0}{[B]_0} = e^{\frac{nF\eta}{RT}} \tag{1.37}$$

where the Nernst law is written in the exponential form. It is insightful to consider the diffusion layer at each point in a cyclic voltammetric experiment, which gives rise to the characteristic peak shape observed. Consider the case of electrochemically reversible behaviour. Figure 1.11 shows a typical cyclic voltammogram for $k^o = 1\ cm/s$ highlighting concentration–distance plots at six different parts on the voltammetric wave.

In the 'reversible' limit the electrode kinetics are so 'fast' (relative to the rate of mass transport – see later) that Nernstian equilibrium is attained at the electrode surface throughout the voltammogram with concentrations of *A* and *B* at the electrode surface governed by the Nernst equation:

$$E = E^0_{red}(A/B) + \frac{RT}{F} Ln \frac{[B]_0}{[A]_0} \tag{1.38}$$

where *E* is now the applied potential which defines the ratio of the surface concentrations $[A]_0$ and $[B]_0$ once $E^0_f(A/B)$ is specified.

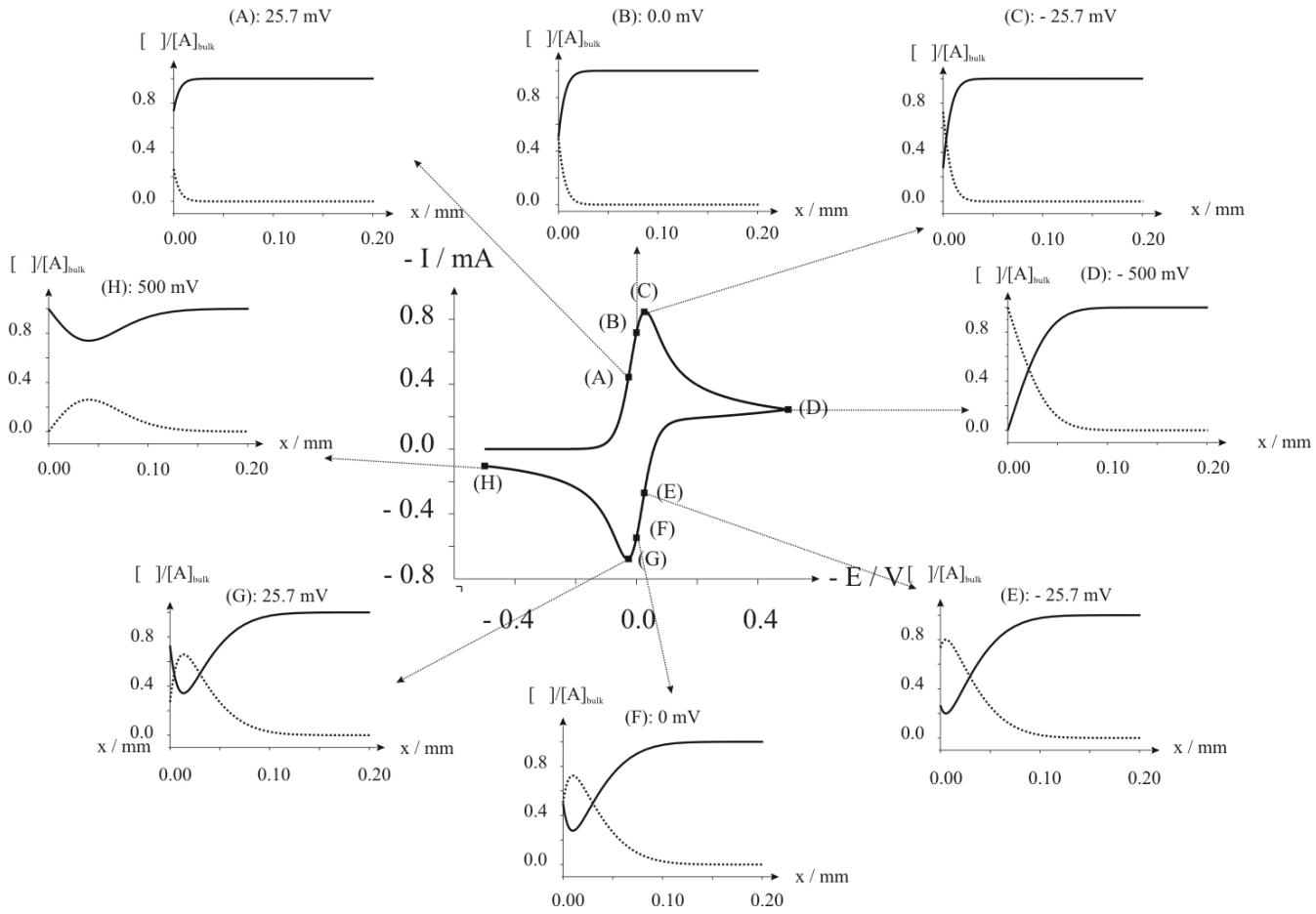

Figure 1.11 *Cyclic voltammogram for the reversible reduction of A to B. Parameters: $E^0 = 0$ V; $\alpha = 0.5$; $k^0 = 1$ cm s^{-1}; $\upsilon = 1$ Vs^{-1}; $A = 1$ cm^2; $[A]_0 = 1$mM; $D_A = D_B = 10^{-5}$ cm^2 s^{-1}. The concentration profiles show the distributions of A (solid line) and B (dashed line) at eight locations, A-H, on the voltammogram. Reproduced from Ref. [4].*

Figure 1.11 depicts how the concentration profiles and the surface concentrations change during the voltammogram. Point A on the graph corresponds to the formal potential ($E = E_f^0$). At point A, prior to the start of the peak corresponding to the reduction of *A*, only a small amount of *A* has been consumed at the electrode surface and only a small layer of *B* has consequently built up. This diffusion layer is relatively small, typically in the order of *ca*. 10 μm. At point C the maximum reduction current in the voltammetric wave is evident and the diffusion layer has

increased in thickness. At point D the current is decreasing with increasing potential and the concentration profile plot shows the concentration of *A* at the electrode surface to be close to zero so that this part of the voltammogram is under diffusion control whereas at (A) it was the electrode kinetics which controlled the response. The diffusion layer at this point has reached a thickness of *ca*. 40 μm. At point D, the direction of the voltammetric scan is reversed. At point E the working electrode potential has the value of 0 V corresponding to the formal potential of the *A/B* couple. At this point the electrode potential is insufficient to noticeably reduce *A* or oxidise *B*. Point G corresponds to the peak in the reverse scan due to the re-conversion of *B* to *A*. The concentration profiles show the build-up of *A* and depletion of *B*. Point H corresponds to a point on the reverse peak beyond the maximum G and shows that the concentration of *B* is very close to zero at the electrode surface whilst that of *A* has returned to almost its original value, nearly that in the bulk solution.

In the case of an electrochemically reversible process *with* fast electron transfer, the peak-to-peak separation $\Delta E_p = (E_p^{ox} - E_p^{red})$ is relatively small at the reversible limit, where $\Delta E_p = 2.218RT / nF$, corresponding to a value of *ca.* 57 mV (at 298K where *n* = 1). For the case of *n* electrons, the wave-shape of the voltammogram can be characterised by:

$$E_p - E_{1/2} = 2.218\frac{RT}{nF} \qquad (1.39)$$

where $E_{1/2}$ corresponds to the potential at which half the peak current is observed.

The magnitude of the voltammetric current (I_p^{rev}) observed at a macroelectrode is governed by the following Randles–Ševćik equation:

$$I_p^{rev} = \pm 0.446 nFAC(nFD\upsilon / RT)^{1/2} \qquad (1.40)$$

where the $\pm$ sign is used to indicate an oxidation or reductive process respectively, though the equation is usually devoid of such sign. The voltammetric diagnosis that the electrochemical process is undergoing a reversible heterogeneous charge transfer process is given by equation (1.39) where ΔEp is independent of the applied voltammetric scan rate and: $I_p^{ox} / I_p^{red} = 1$.

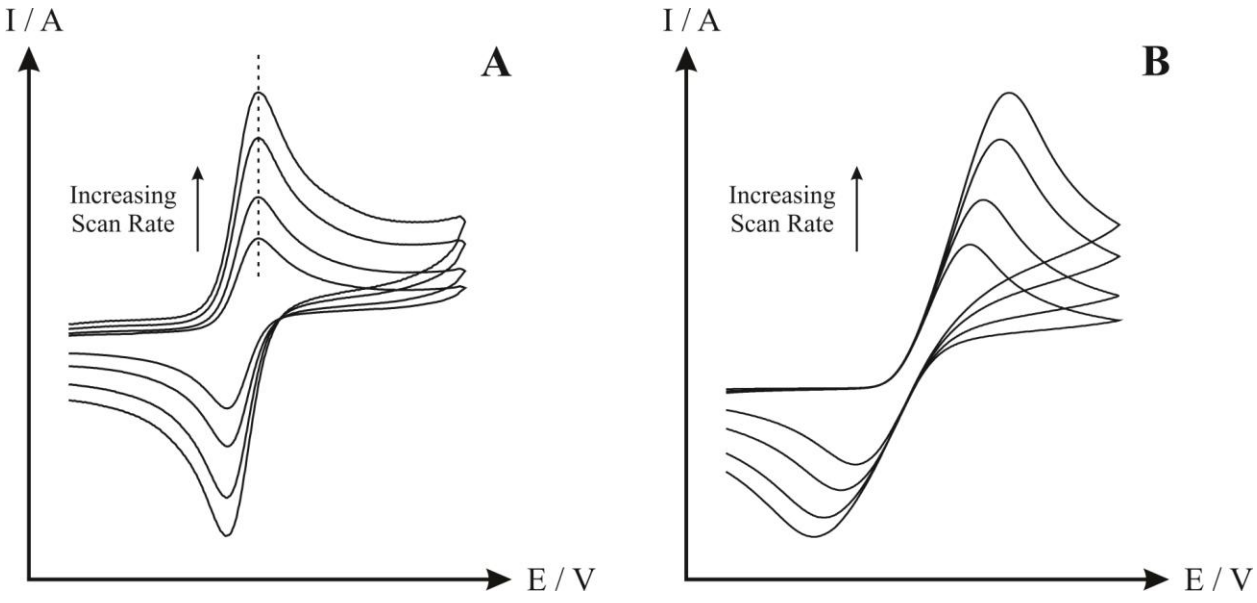

Figure 1.12 *Reversible (**A**) and irreversible (**B**) cyclic voltammetric responses. Note the shift of the peak maxima with scan rate.*

The question is; *how can one determine if the observed voltammetry corresponds to this range?* A key diagnostic is a scan rate study. As shown in equation (1.40), the peak height (I_P) is proportional to the applied voltammetric scan rate and a plot of I_p^{Rev} against $\upsilon^{1/2}$ should be linear. Figure 1.12 depicts typical voltammetric profiles resulting from applying a range of scan rates. It is evident that each voltammetric signature is the same but that the current increases with

increasing scan rate as predicted by equation (1.40). It is important to note that when the position of the current maximum occurs at the same potential; this peak maximum, which does *not* shift in potential with scan rate, is characteristic of electrode reactions which exhibit rapid electron transfer kinetics, usually termed reversible electron transfer reactions. In such cases the formal potential can be found at mid-way between the two voltammetric peaks comprising the voltammogram:

$$E_f^0 = \left(E_p^{ox} + E_p^{red} \right) / 2 \qquad (1.41)$$

assuming that the diffusion coefficients of the reactant and product are equal.

Also shown in Figure 1.10B is the cyclic voltammetric response for an irreversible electrochemical couple (in which the ΔE_P is larger than that observed for the reversible and quasi-reversible case) where appreciable over-potentials are required to drive the reaction, as evidenced by the peak height (maxima) occurring at a greater potential than that seen for the reversible case.

In Figure 1.10 it is evident that as the standard electrochemical rate constant, k^o, is either fast or slow, termed 'electrochemically reversible' or 'electrochemically irreversible' respectively, changes in the observed voltammetry are striking. It is important to note that these are relative terms and that they are in relation to the rate of mass transport to the electrode surface. The mass transport coefficient, m_T, is given by:

$$m_T = \sqrt{D / (RT / F\upsilon)} \qquad (1.42)$$

The distinction between fast and slow electrode kinetics relates to the prevailing rate of mass transport given by '$k^o >> m_T$' indicating electrochemical reversibility or '$k^o << m_T$' indicating electrochemical irreversibility. Matsuda and Ayabe [5] introduce the parameter, ζ, given by:

$$\zeta = k^o / \left(FD\upsilon / RT \right)^{1/2} \tag{1.43}$$

where the following ranges are identified at a stationary macroelectrode: '$\zeta \geq 15$' corresponds to the reversible limit, '$15 > \zeta > 10^{-3}$' corresponds to the quasi-reversible limit and '$\zeta \leq 10^{-3}$' corresponds to the irreversible limit. Thus returning to Figure 1.10B, three cases are evident, reversible, quasi-reversible and irreversible, which are all related to the rate of mass transport. In reversible reactions the electron transfer rate is, at all potentials, greater than the rate of mass transport and the peak potential is independent of the applied voltammetric scan rate (Figure 1.12A). In the case of quasi-reversible reactions the rate of electron transfer becomes comparable to the mass transport rate. In this regime, the peak potentials increase with the applied scan rate. Last, it is obvious that for the irreversible case the electron transfer rates are smaller than the rate of mass transport; the summary by Matsuda and Ayabe is extremely useful in Ref. [5].

The above conditions given by Matsuda and Ayabe show that the observed electrochemical behaviour depends on the applied voltammetric scan rate. In applying various scan rates the diffusion layer thickness dramatically changes, in the case of slow scan rates, the diffusion layer is very thick while at faster scan rates the diffusion layer is relatively thinner. Since the electrochemical process, that is, reversible or irreversible, reflects the competition between the electrode kinetics and mass transport, faster scan rates will encourage greater electrochemical irreversibility. This is shown in Figure 1.13 where upon the application of faster

scan rates, there is a clear transition (solid line, Figure 1.13) from that of reversible towards irreversible behaviour.

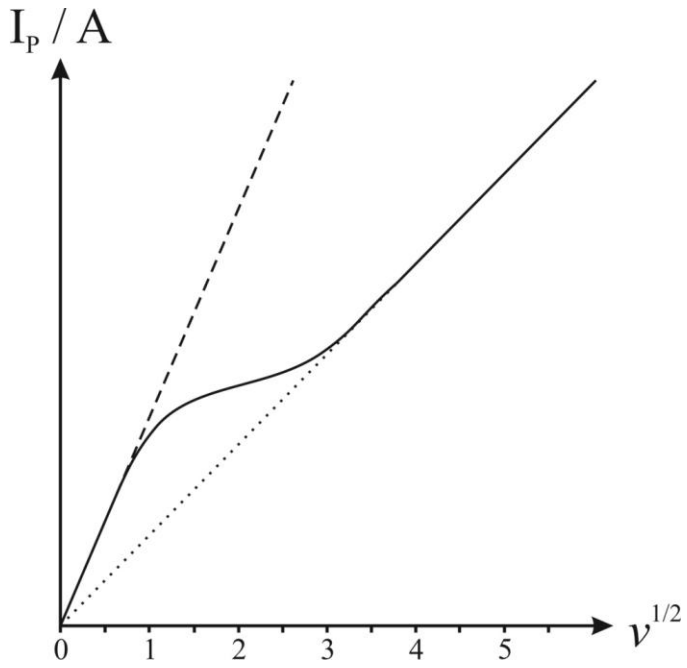

Figure 1.13 *Transition from a reversible to an irreversible process with increasing scan rate (solid line). The dashed line indicates a reversible process, while the dotted line is that of an irreversible process.*

At macroelectrodes the Nicholson method is routinely used to estimate the observed *standard heterogeneous electron transfer rate constant* (k^o, cm s^{-1}) for quasi-reversible systems using the following equation; [6]

$$\psi = k^o[\pi D n \upsilon F / (RT)]^{-1/2} \qquad (1.44)$$

where ψ is the kinetic parameter and is tabulated (see Table 1.1) at a set temperature for a one-step, one electron process as a function of the peak-to-peak separation (ΔE_P); where one determines the variation of ΔE_P with υ and from this, the variation in the ψ. Table 1.1 shows the variation of ΔE_P with ψ for a one-step, one electron process at 25 °C and where α = 0.5. A plot

of ψ against $[\pi Dn\upsilon F/(RT)]^{-1/2}$ allows the standard heterogeneous rate transfer constant, k^o to be readily deduced.

Table 1.1 *Variation of ΔE_p with ψ at 25 °C. Reproduced from Ref. [6].*

ψ	ΔE_p / mV
20	61
7	63
6	64
5	65
4	66
3	68
2	72
1	84
0.75	92
0.50	105
0.35	121
0.25	141
0.10	212

Note that there are some restrictions, in that the above method is based on the assumption that electron transfer kinetics are described by the Butler-Volmer formalism, that α is 0.5, the switching potential is 141 mV past the reversible $E_{1/2}$, and the temperature is 298 K. Lack of strict adherence to most of these factors will lead to only minor errors. However, there is one experimental problem that can be severe: incomplete compensation of solution resistance.

As such, measurement error will be low at slow scan rates where currents and *IR* errors are low, generally however, potentiostats help overcome this problem.

Lavagnini *et al.* [7] proposed the following function of $\psi(\Delta E_P)$, which fits Nicholson's data, for practical usage (rather than producing a working curve):

$$\psi = (-0.6288 + 0.021X)/(1 - 0.017X) \tag{1.45}$$

where $X = \Delta E_P$. Note however, for more accurate results in determining k^o, recourse to electrochemical simulation packages is usually advised.

Last, the Randles–Ševćik equation for a quasi-reversible system (at 298 K) is given by:

$$I_P^{quasi} = \pm(2.65 \times 10^5) n^{3/2} A C D^{1/2} v^{1/2} \tag{1.46}$$

For an irreversible system (those with slow electron exchange), the individual peaks are reduced in magnitude and widely separated. Figure 1.12 shows a characteristic response where the peak maximum clearly shifts with the applied voltammetric scan rate. Totally irreversible systems are quantitatively characterised by a shift in the peak potential with scan rate as given by:

$$E_{p,c} = E_f^0 - \frac{RT}{\alpha n' F}\left[0.780 + Ln\frac{D^{1/2}}{k^0} + 0.5Ln\left(\frac{\alpha n' F \upsilon}{RT}\right)\right] \tag{1.47}$$

where α is the transfer coefficient, *n'* is the number of electrons transferred per mole before the rate determining step and where E_f^0 is the formal potential. Hence, E_P occurs at potentials higher than E_f^0, with the over-potential related to k^o and α (the voltammogram becomes increasingly 'drawn out' as αn decreases).

For the case of a fully irreversible electron transfer process, the Randles–Ševćik equation is:

$$I_p^{irrev} = \pm 0.496(\alpha n')^{1/2} nFAC(FD\upsilon / RT)^{1/2} \qquad (1.48)$$

where A is the geometric area of the electrode (cm^2), α is the transfer coefficient (usually assumed to be close to 0.5), n is the total number of electrons transferred per molecule in the electrochemical process and n' is the number of electrons transferred per moles before the rate determining step.

It is useful to know the generic Randles–Ševćik equation (for stagnant solutions):

$$I_p = -\Upsilon(p)\sqrt{\frac{n^3F^3\upsilon D}{RT}}A[C] \qquad (1.49)$$
$$where: p = r\sqrt{\frac{nF\upsilon}{RTD}}$$

for the case of different electrode geometries:

(1) Planar disc electrode: r = radius, $\Upsilon(p) = 0.446$

(2) Spherical or hemispherical electrode: r = radius, $\Upsilon(p) = 0.446 + 0.752p^{-1}$

(3) For a small disk electrode: r = radius, $\Upsilon(p) = 0.446 + (0.840 + 0.433e^{-0.66p} - 0.166e^{-11/p})p^{-1} \sim 0.446 + 4/\pi p^{-1}$

(4) For a cylinder or hemi-cylinder: r = radius, $\Upsilon(p) = 0.446 + 0.344p^{-0.852}$

(5) For a band electrode: $2r$ = width, $\Upsilon(p) = 0.446 + 0.614\ (1 + 43.6p^2)^{-1} + 1.323p^{0.892} \sim 0.446 + 3.131p^{-0.892}$

The wave-shape for an irreversible reduction is given by: $E_p - E_{1/2} = 1.857\frac{RT}{\alpha F}$, while for an irreversible oxidation it is given by: $E_p - E_{1/2} = 1.857\frac{RT}{(1-\alpha)F}$.

1.4.2. CHANGING THE ELECTRODE GEOMETRY: MACRO TO MICRO

At a macroelectrode, electrolysis of *A* occurs across the entire electrode surface such that the diffusion of *A* to the electrode or *B* from the electrode surface is termed planar, and the current response is typically described as 'diffusion limited', giving rise to an asymmetric peak as shown in Figure 1.14A. At the edge of the macroelectrode, where the electrode substrate meets the insulting material defining the electrode area, diffusion to or from the edge of the electrode is effectively to a point. Therefore, the flux, *j*, and the rate of mass transport are larger at the edge and as such diffusion becomes convergent. This is termed an 'edge effect' which is negligible at a macroelectrode since the contribution of convergent diffusion to the edges of the macroelectrode is inundated by that of planar diffusion to the entire electrode area.

As the electrode size is reduced from macro to micro, or even smaller to that of nano, convergent diffusion to the edges of the electrode becomes significant. In this regime a change in the observed voltammetric profile is observed which results in the loss of the peak shaped response, as evident in Figure 1.14B with that of a sigmoidal voltammogram. The effect of convergent diffusion has the benefit of improvements in mass transport such that the current density is greater than at a macroelectrode under planar diffusion.

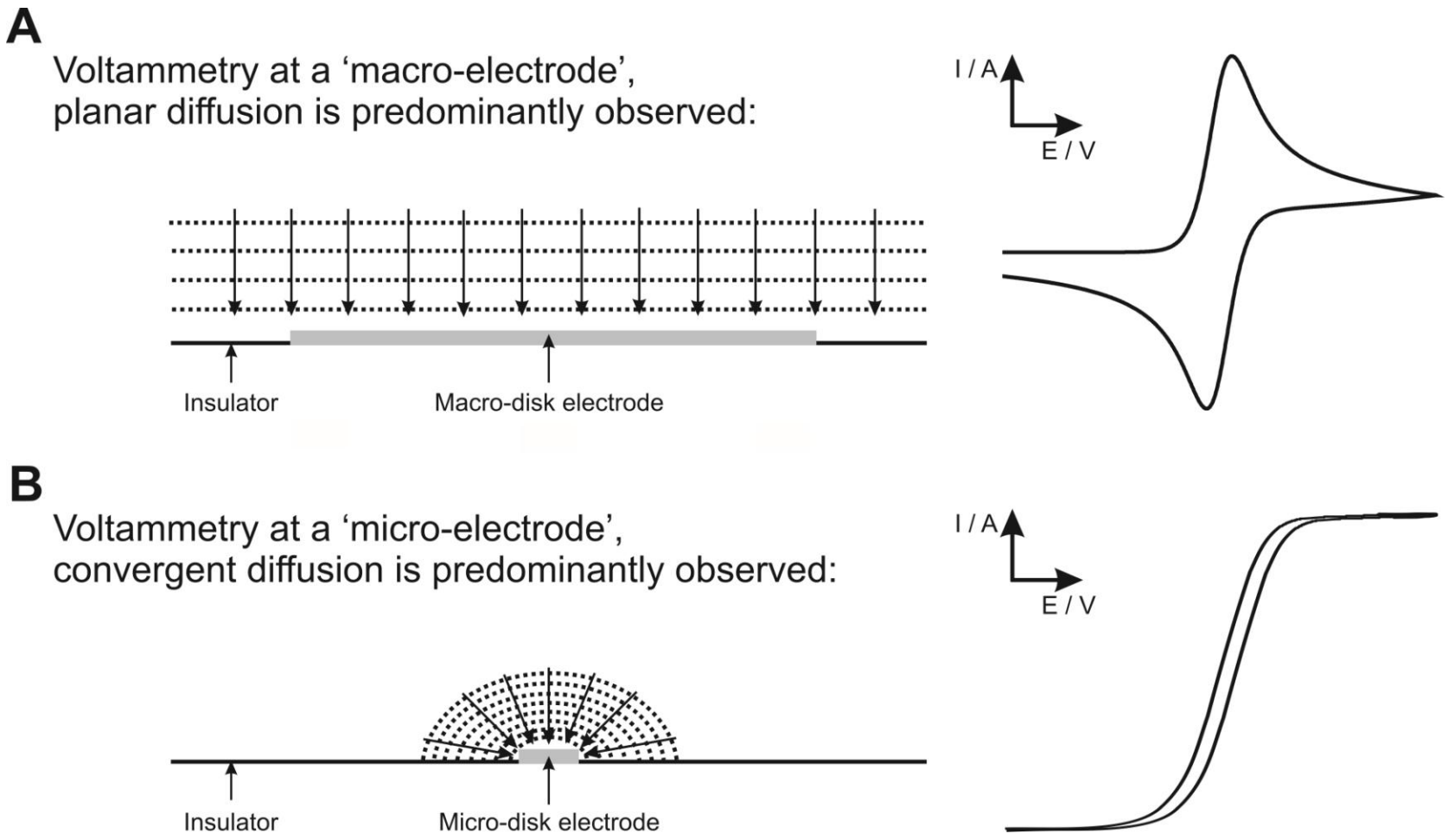

Figure 1.14 *The unique differences between the cyclic voltammetric signatures observed at a macroelectrode (**A**) compared to a microelectrode (**B**).*

1.4.3. ELECTROCHEMICAL REACTION MECHANISMS

Above has exclusively considered an *E* reaction where the (electrochemical) process involves the transfer of an electron. This chapter now considers that this process is perturbed by a subsequent chemical reaction, as described by:

$$\begin{aligned} O + ne^- &\rightleftharpoons R \\ R &\longrightarrow Z \end{aligned} \qquad (1.50)$$

using the notation of Testa and Reinmuth [8] this is described as an *EC* reaction. The cyclic voltammogram will display a smaller reverse peak (because the product *R* is chemically removed from the surface). The peak ratio of the forward and reverse peaks will thus be less than 1 (not equal); the exact value can be used to estimate the rate constant of the chemical step. In some (extreme) cases, the chemical reaction may progress so rapidly that all of *R* is converted to *Z*, resulting in no reverse wave being observed. Note that by varying the scan rate, further information on the rates of these coupled reactions can be obtained.

Table 1.2 overviews the different electrochemical mechanisms involving coupled chemical reactions that can be encountered.

A specific example worth exploring is the *EC'* reaction. Such an example of this process is the modification of a glassy carbon electrode with an osmium polymer, $[Os(bpy)_2(PVP)_{10}Cl]Cl$ and Nafion^{TM} prepared by drop-coating, producing a double-layer membrane modified electrode. [9] In this case the modified electrode was explored towards the sensing of the neurotransmitter epinephrine. [9] Figure 1.15 shows the voltammetric response of the electroactive polymer (curves A and B in Figure 1.15) where upon contact with epinephrine,

(curve C in Figure 1.15) a reduction in the back peak coupled with an increase in the forward wave is evident. The process can be described as:

$$[Os-(PVP)_{10}]^{+} \rightleftharpoons [Os-(PVP)_{10}]^{2+} + e^{-} \tag{1.51}$$

$$2[Os-(PVP)_{10}]^{2+} + EP_{RED} \longrightarrow 2[Os-(PVP)_{10}]^{+} + EP_{OX} \tag{1.52}$$

The first step in the above equations (1.51 and 1.52) is the *E* step due to it being a purely electrochemical process, while the process in equation (1.52) is noted as a *C* step due to it being a chemical process. As shown in Figure 1.15, the magnitude of curve *C* is dependent on the chemical rate constant for the process as governed by equation (1.52).

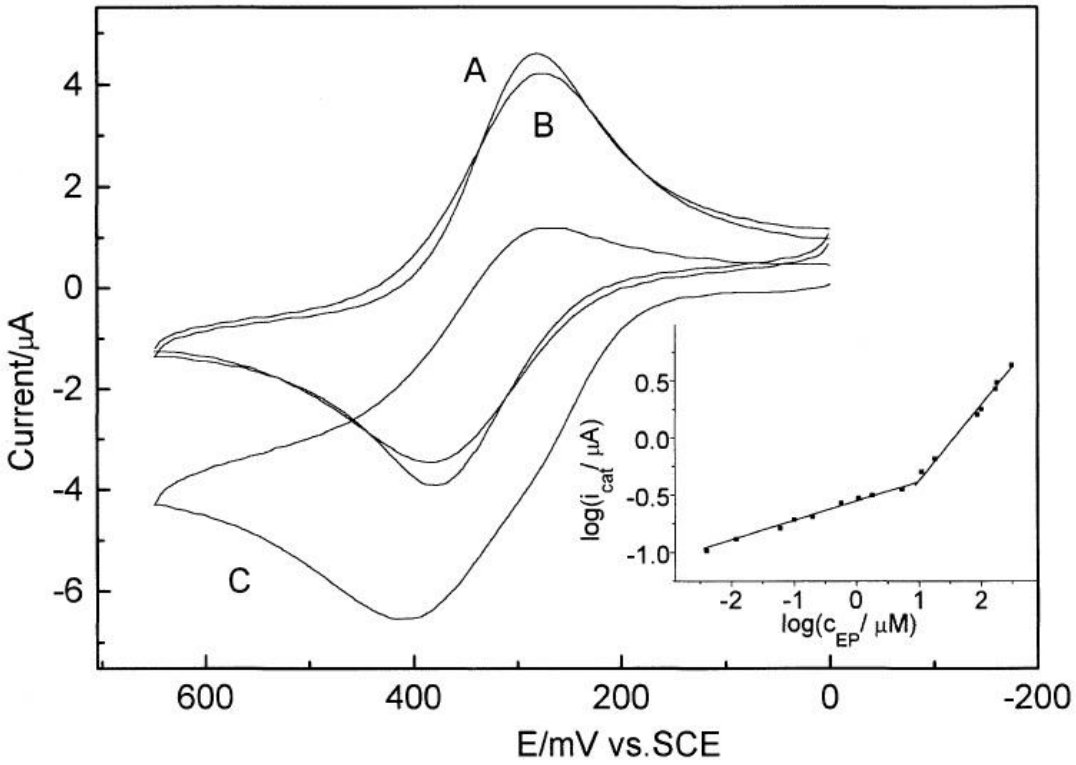

Figure 1.15 *Cyclic voltammograms of Os-$(PVP)_{10}$* (***A***) *and Os-$(PVP)_{10}$/Nafion* (***B***, ***C***) *modified electrodes in pH 6.9 PBS* (***A***, ***B***) *and* (***B***), *+ 1.0×10^{-4} M epinephrine* (***C***) *at a scan rate of 40 mV s^{-1}.*
Inset: plot of logarithm of catalytic current vs. epinephrine concentration.
Reproduced from Ref. [9].

Table 1.2 *Electrochemical mechanisms involving coupled chemical reactions.*

Reversible electron transfer process, no follow-up chemistry; an E_r step:

$$O + ne^- \rightleftharpoons R$$

Reversible electron transfer process followed by a reversible chemical reaction; E_rC_r:

$$O + ne^- \rightleftharpoons R$$

$$R \underset{k_1 -1}{\overset{k_1}{\rightleftharpoons}} Z$$

Reversible electron transfer profess followed by an irreversible chemical reaction; E_rC_i:

$$O + ne^- \rightleftharpoons R$$

$$R \xrightarrow{k_1} Z$$

Reversible chemical reaction preceding a reversible electron transfer process; C_rE_r:

$$Z \underset{k_1 -1}{\overset{k_1}{\rightleftharpoons}} O$$

$$O + ne^- \rightleftharpoons R$$

Reversible electron transfer processes followed by an irreversible regeneration of starting materials; E_rC_i'

$$O + ne^- \rightleftharpoons R$$

$$R \xrightarrow{k} Z + O$$

Multiple electron transfer processes with an intervening reversible chemical reaction; $E_rC_rE_r$:

$$O + ne^- \rightleftharpoons R$$

$$R \underset{k_1 -1}{\overset{k_1}{\rightleftharpoons}} Z$$

$$Z + ne^- \rightleftharpoons Y$$

Multiple electron transfer processes with an intervening irreversible chemical reaction; $E_rC_iE_r$:

$$O + ne^- \rightleftharpoons R$$

$$R \xrightarrow{k_1} Z$$

$$Z + ne^- \rightleftharpoons Y$$

Another electrochemical process worth highlighting, which demonstrates how cyclic voltammetry can be used to yield mechanistic information, is an *EE* process. Here the example considered is of TMPD (N,N,N',N'-tetramethyl-*para*-phenylenediamine), the structure of which is shown in Figure 1.16.

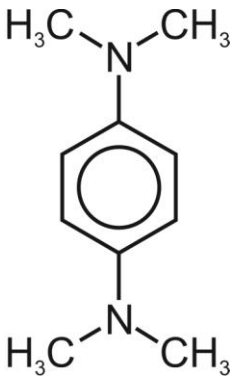

Figure 1.16 *The structure of TMPD.*

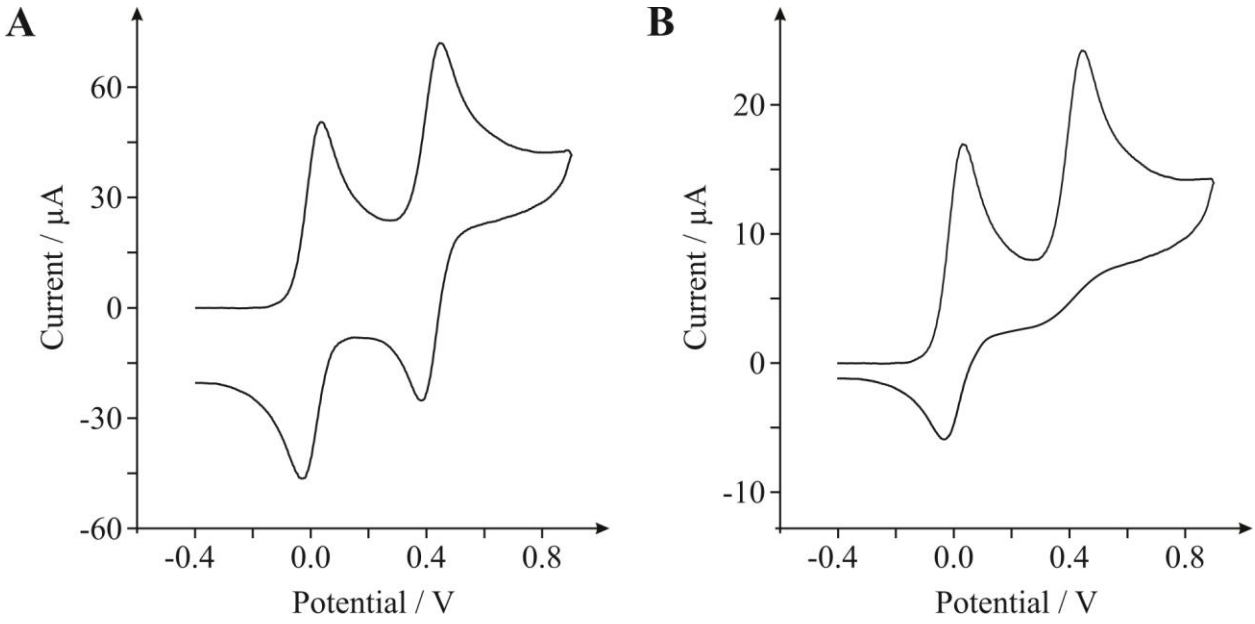

Figure 1.17 *Cyclic voltammograms obtained from the electrochemical oxidation of TMPD at a scan rate of (**A**) 100 mVs^{-1} and (**B**) 10 mVs^{-1}.*

Figure 1.17 shows a typical cyclic voltammogram recorded for the oxidation of TMPD in an aqueous solution (pH 7 phosphate buffer solution, PBS) utilising an edge plane pyrolytic graphite (EPPG) electrode. The two voltammetric peaks, as shown in Figure 1.17A, represent the following electrochemical process:

$$\begin{aligned} TMPD - e^{-} &\longrightarrow TMPD^{\bullet+} \\ TMPD^{\bullet+} - e &\longrightarrow TMPD^{2+} \end{aligned} \qquad (1.53)$$

where the cation radical and the dication are shown in Figure 1.18.

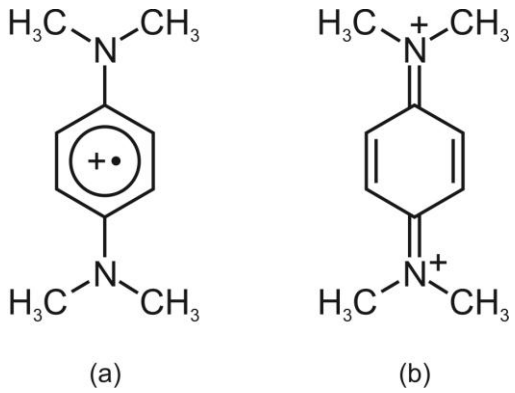

Figure 1.18 *The structures of (a) the cation radical $TMPD^{\bullet+}$ and (b) the dication $TMPD^{2+}$.*

On the reverse scan, the corresponding reduction takes place;

$$\begin{aligned} TMPD^{2+} + e^{-} &\longrightarrow TMPD^{\bullet+} \\ TMPD^{\bullet+} + e &\longrightarrow TMPD \end{aligned} \qquad (1.54)$$

The voltammetric response, as shown in Figure 1.17B is recorded at a slower scan rate than that used in Figure 1.17A and it is evident that the second reduction peak, corresponding to the reduction of $TMPD^{2+}$, has significantly changed. This is because in the case of Figure 1.17B the time taken to scan the voltammetric window is long in comparison with the lifetime of the electro-generated species (formed on the forward scan). In fact, $TMPD^{2+}$ reacts with water with

the displacement of dimethylamine, as shown in Figure 1.19 and hence on the timescale of the voltammetric experiment the electro-generated species undergoes a chemical reaction such that the initially formed product cannot be electrochemically reduced on the return voltammetric scan. Note that this is not the case when using fast scan rates where the time take to scan the voltammetric window is fast in comparison to the lifetime of the electro-generated species such that the chemical process is outrun.

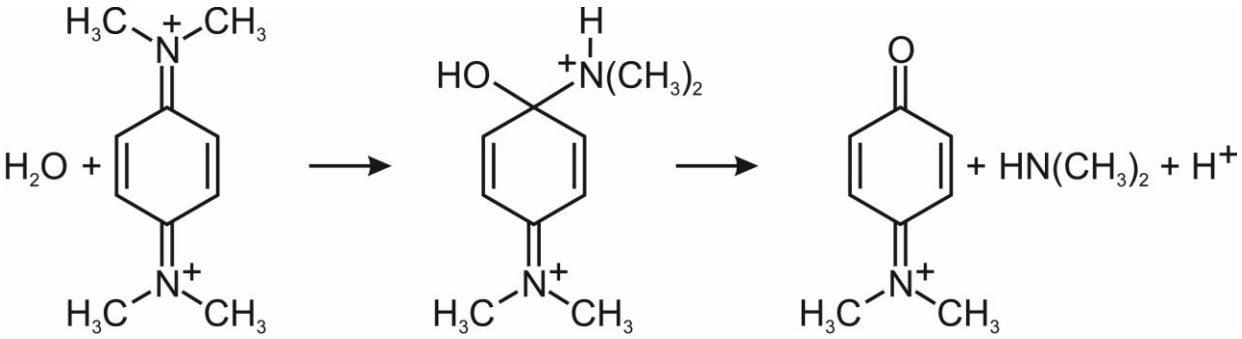

Figure 1.19 *$TMPD^{2+}$ reacts with water with the displacement of dimethylamine.*

Hence, given the above insights, it is clear that cyclic voltammetry can be used to provide a facile methodology to study unstable and exotic species.

1.4.4. EFFECT OF PH

Considering the following process involving the uptake of *m*-protons and consumption of *n*-electrons:

$$A + mH^+ + ne^- \rightleftarrows B \tag{1.55}$$

The limiting cases correspond to those of electrochemical reversibility and irreversibility. Considering the electrode process as being fully electrochemically reversible, the relevant Nernst equation can be written as: [4]

$$E^0_{f,eff} = E^0_f(A/B) - 2.303\frac{mRT}{nF}\,pH \qquad (1.56)$$

which is in essence a formal potential. Provided D_A = D_B the potential midway between the peaks for the reduction of *A* and the oxidation of *B* corresponds to $E^0_{f,eff}$ with the shape of the voltammogram being otherwise unaffected. Accordingly the midpoint potential varies by an amount of $2.303\frac{mRT}{nF}$ per pH unit. In the commonly seen case where *m* = *n*, this corresponds to *ca.* 59 mV per pH unit at 25 °C as in the following case.

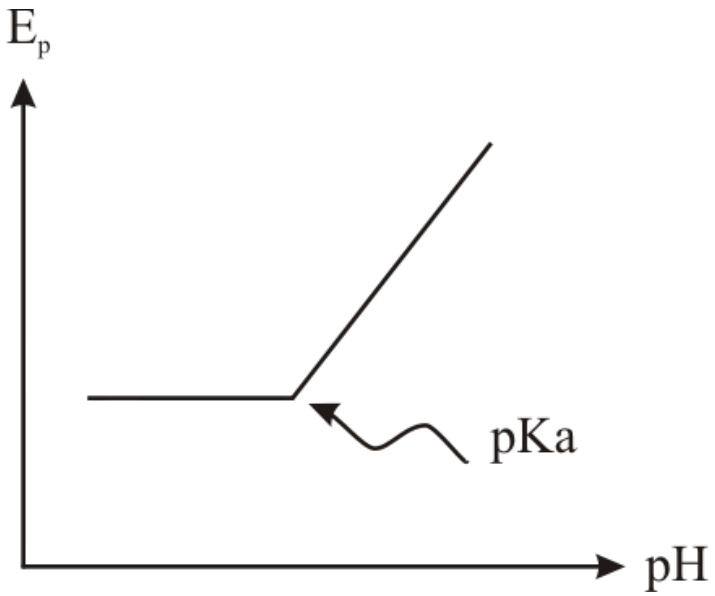

Figure 1.20 *A typical plot of E_P versus pH.*

Experimentally, the cyclic voltammetric response is recorded over a range of pH's with the $E^0_{f,eff}$ plotted as a function of pH. Figure 1.20 shows a typical response where the deviation from linearity is due to the *pKa* of the target analyte and the gradient from the linear part allows information on the number of electrons and protons transferred in the electrochemical process. Clearly, the use of pH measurements can provide insights into electrochemical mechanisms.

1.4.5. ADSORPTION PROCESSES

In some instances, rather than having the analyte under investigation undergoing simply diffusional processes, the species of interest might adsorb onto the electrode surface and will give rise to different voltammetry. Figure 1.21 shows a typical voltammetric profile where a unique shape is observed, for the case where an adsorbed species exhibits ideal Nernstian behaviour of non-reacting species (in a reversible system only) where $\Delta E_P = 0$. Since the adsorbed species does not have to diffuse to the electrode surface, the observed voltammogram is symmetrical.

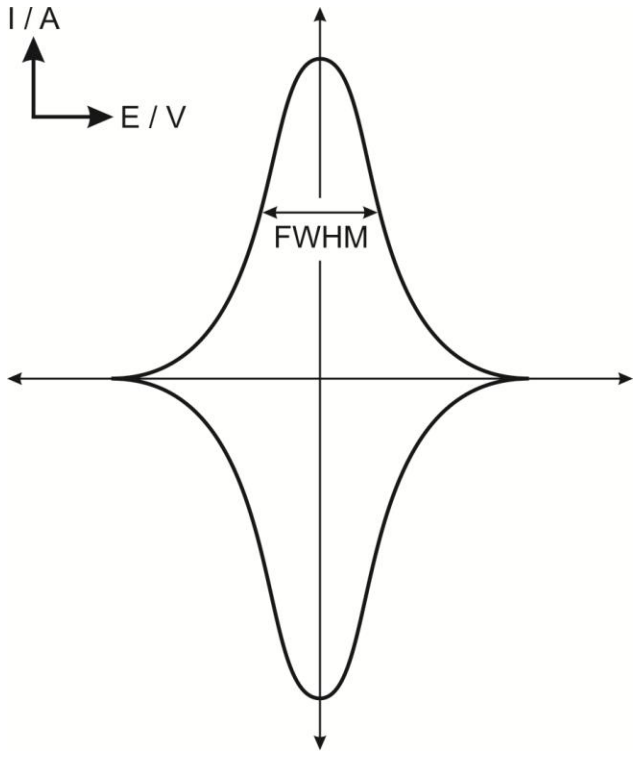

Figure 1.21 *Cyclic voltammetric response for the reversible reaction of an adsorbed species.*

The peak current can be related directly to the surface coverage (Γ) and potential scan rate for a reversible process:

$$I_p = \frac{n^2 F^2 \Gamma A \upsilon}{4RT} \tag{1.57}$$

with integration of the peak(s) shown in Figure 1.21, allows the charge (*Q*) to be deduced, which is related to the surface coverage by the following expression:

$$Q = nFA\Gamma \tag{1.58}$$

As shown in Figure 1.21, the full width at half of the peak maximum height (FWHM) is given by:

$$FWHM = 3.53RT / nF \tag{1.59}$$

The diagnosis of an adsorbed species is to explore the effect of scan rate on the voltammetric response, which should yield a linear response for the case of I_p *versus* scan rate υ. A practical example is shown in Figure 1.22 where Haemoglobin (Hb) – Dimyristoyl phosphatidylcholine (DMPC) films are immobilised upon a BPPG surface. The modified electrode was then explored with the voltammetric response evident in Figure 1.22A, with a plot of peak current against scan rate also provided. Near symmetric cyclic voltammetric profiles are observed with approximately equal reduction and oxidation peak heights, characteristic of *thin layer* electrochemical behaviour. As shown in Figure 1.22, both cathodic and anodic peak potentials remain almost unchanged over the chosen scan rate range. A plot of $\log_{10}$ (peak current) against $\log_{10}$ (scan rate) was found to linear with a slope of 0.98

(correlation coefficient of 0.999), which is very close to the expected theoretical slope of 1 for thin layer voltammetry, as predicted by equation (1.57). [10]

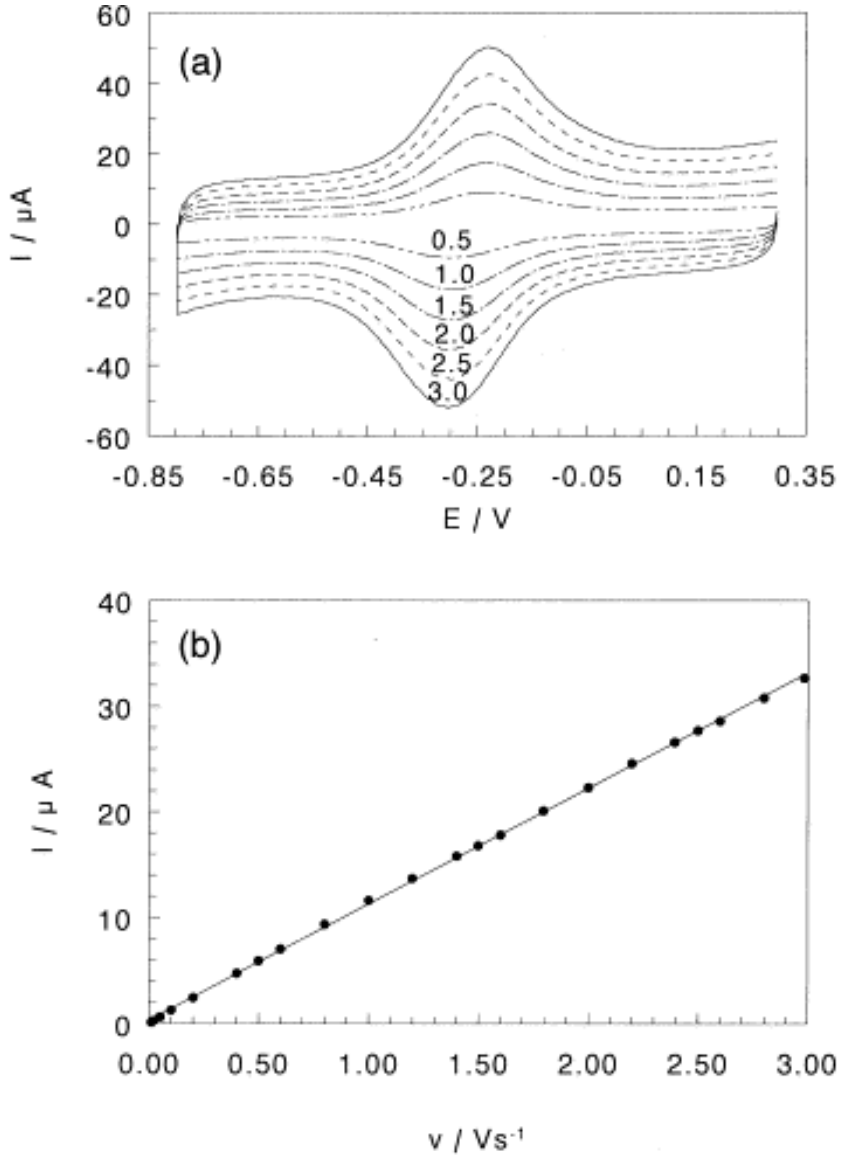

Figure 1.22 *Cyclic voltammograms (a) for Hb-DMPC films in pH 5.5 buffer at different scan rates (V s^{-1}); (b) influence of scan rate on reduction peak current. Reproduced from Ref. [*[10]*].*

In real situations, the absorbed species may be weakly or strongly absorbed. In these contexts, one usually refers to the reactants that are adsorbed, but four scenarios can be encountered, as shown in Figure 1.23, each giving rise to unique and intriguing voltammetry.

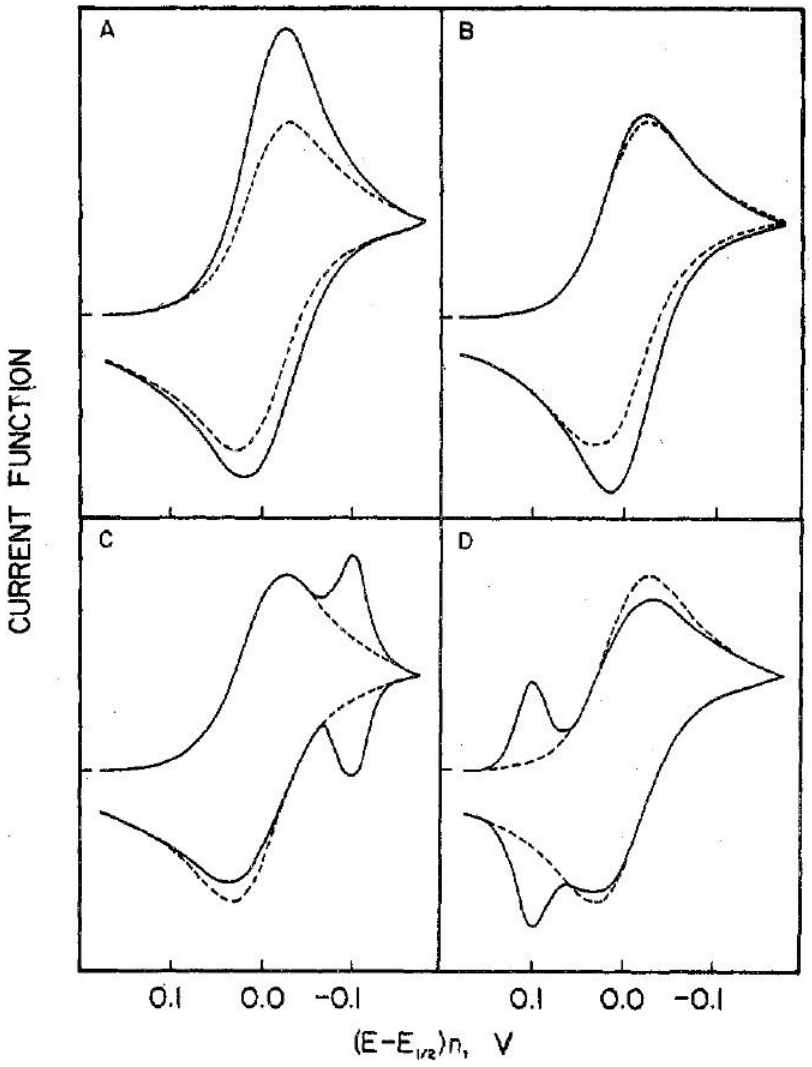

Figure 1.23 *Voltammetry with adsorption of reactants and products.* ***A****: reactant adsorbed weakly;* ***B****: product adsorbed weakly;* ***C****: reactant adsorbed strongly;* ***D****: product adsorbed strongly. Dashed lines are for response in the absence of adsorption. Reproduced from Ref. [*[11]*].*

Of note is that in the case of a strongly absorbed product (Figure 1.23D) there is a pre-peak before the solution phase voltammetric peak while in the case that the reactant is strongly adsorbed, the adsorption wave is seen following the solution phase peak (Figure 1.23C). The effect of varying the voltammetric scan rate can be highly illuminating, as shown in Figure 1.24, where at slow scan rates (curve A) the adsorption pre-wave is small relative to the second diffusional peak. As the scan rate is increased, the current of the adsorption peak

increases in magnitude while the diffusional peak current decreases. At very high scan rates the adsorption pre-wave reaches its diffusion controlled maximum and the second diffusional peak is absent (curve D). [11]

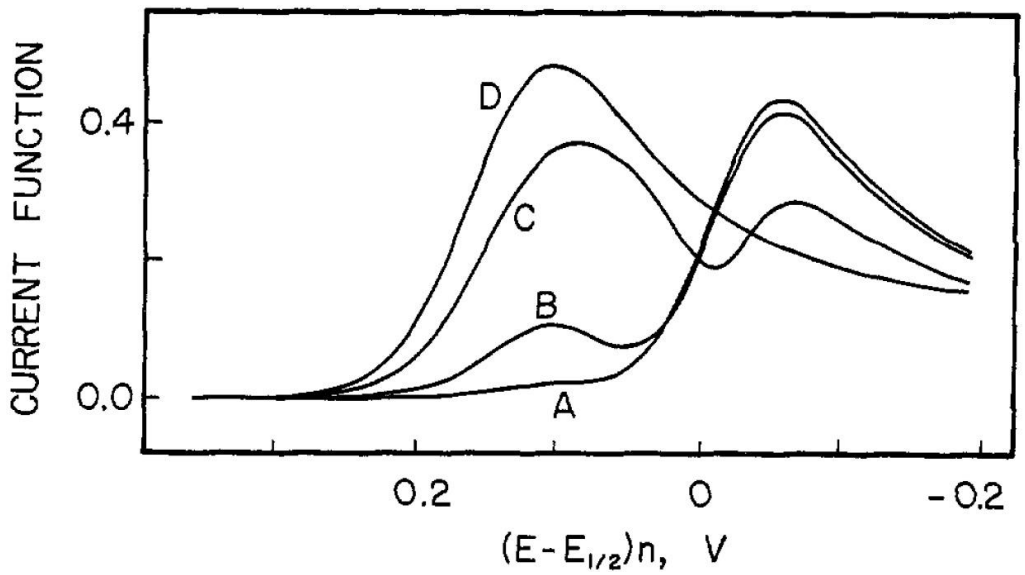

Figure 1.24 *Voltammetric response at scan rates of 1 (A), 25 (B), 625 (C) and 2500 (D) mVs^{-1} for a product strongly adsorbed. Reproduced from Ref. [11].*

1.4.5.1. THIN LAYER EFFECTS

There is also another scenario which can give rise to unique voltammetry. In the context of studying new materials, such as carbon nanotubes (and indeed graphene, which is the focus of this thesis), researchers usually disperse their chosen nanotubes into a non-aqueous solvent and put aliquots onto the working electrode of their choice. This modified surface is allowed to dry to enable the solvent to evaporate, leaving the nanotubes immobilised on the electrode surface, which is now ready to be electrochemically explored (the so called drop-coating method). This modified nanotube electrode surface is shown in Figure 1.25. It has been shown that the nanotube modified electrode exhibits a porous surface where 'pockets' of the electroactive species are trapped in-between multiple layers of nanotubes and the trapped species act akin to

that of a *thin layer* cell. [12] The porous nanotube layer has a large surface area and the electrode is thought to be in contact with a finite, '*thin layer*' of solution (the species is trapped within the nanotube structure). In this case a mixture of diffusional regimes exists.

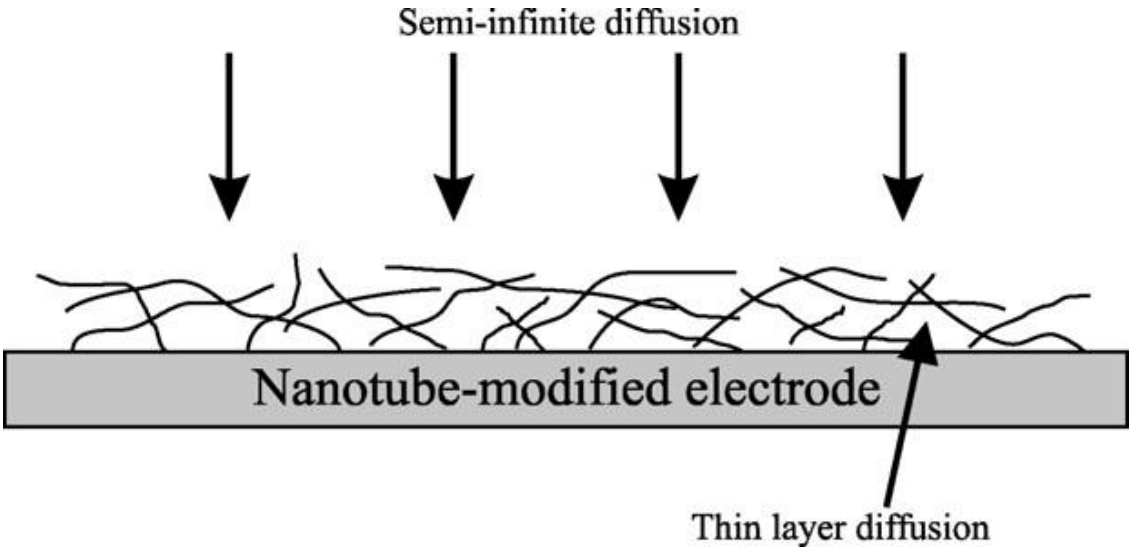

Figure 1.25 *Schematic representation of the two types of diffusion that contribute to the observed current at a highly porous CNT modified electrode. Reproduced from Ref. [12].*

Figure 1.26 shows the voltammetry that will be observed as more nanotube material is immobilised onto the electrode surface, where there is an apparent improvement in the voltammetric peak height and a reduction in the potentials to lower values. Such a response is usually (mistakenly) assumed to be due to the electro-catalytic nature of the nanotubes themselves rather than a simple change in mass transport. Such a response can be expected at porous macrostructures, such as at three-dimensional freestanding graphitic structures (see Chapter 9.1).

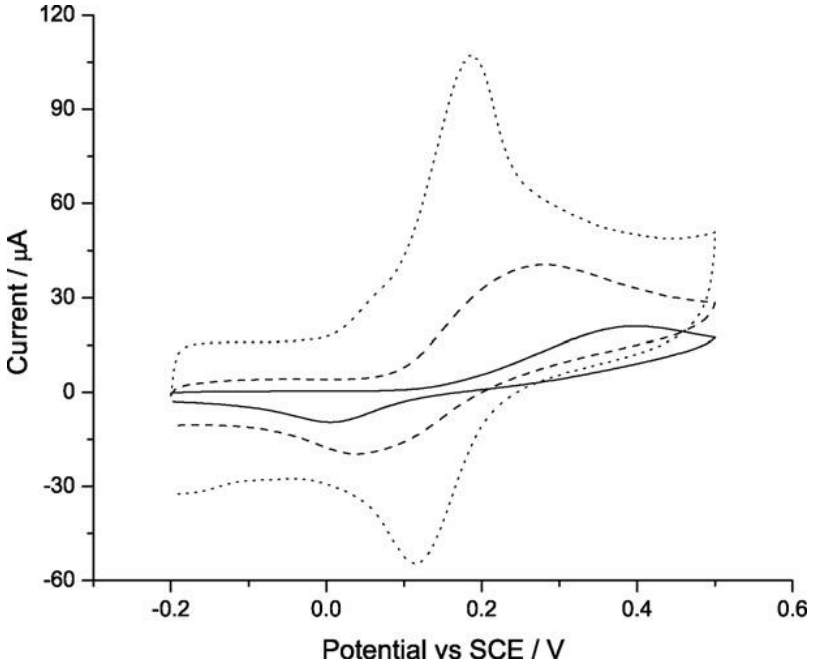

Figure 1.26 *Overlaid voltammograms recorded at 100mVs^{-1} of 1mM dopamine at a glassy carbon electrode modified with 0 µg (solid line), 0.4 µg (dashed line) and 2.0 µg (dotted line) MWCNTs. Reproduced from Ref. [12].*

As thin-layer dominates, the ΔE_P changes from diffusional to that of thin-layer such that the peak separation decreases giving the misleading impression that a material with fast electron transfer properties is giving rise to the response and hence misinterpretation can arise. Care also needs to be taken when adsorbing species are being explored as this will also give rise to thin layer type voltammetry. [13] Indeed the distinction between thin-layer diffusion and adsorption effects is not easy to make, especially in cases where the adsorption is rapidly reversible. Where there is slow adsorption (and desorption) kinetics then the presence or absence of "memory effects" can be useful. If it is possible to transfer the electrode, after exposure to the target solution, to a fresh electrolyte containing no analyte, then adsorption effects can be inferred if voltammetric signals are retained or if signals increase steadily over a period of time. [13]

Another technique that can be used to study graphene is chronoamperometry. The electrochemical technique of chronoamperometry involves stepping the potential applied to the working electrode, where initially it is held at a value at which no Faradaic reactions occur before jumping to a potential at which the surface concentration of the electroactive species is zero (Figure 1.27A), where the resulting current-time dependence is recorded (Figure 1.27C).

The mass transport process throughout this process is solely governed by diffusion, and as such the current-time curve reflects the change in concentration at the electrodes surface. This involves the continuing growth of the diffusion layer associated with the depletion of reactant, thus a decrease in the concentration gradient is observed as time progresses (Figure 1.27B). This technique is known as *single potential step chronoamperometry*, an example of which is shown in Figure 1.28 for the case of an osmium complex modified electrode and also shown in the inserts are the effect of concentration of epinephrine which is electro-catalysed undergoing an *EC*' process (see Chapter 1.4.3).

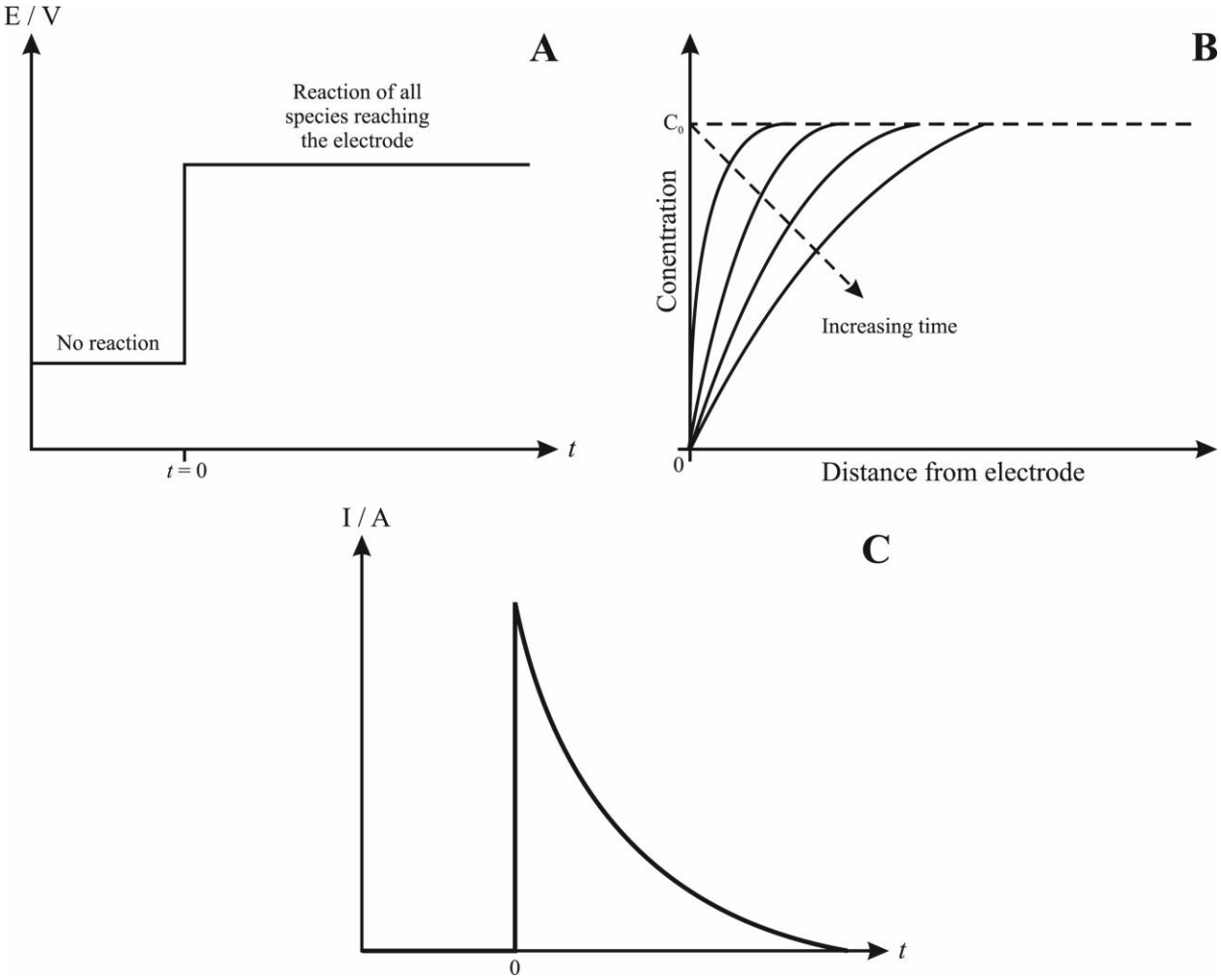

Figure 1.27 *Chronoamperometric experiment:* ***A****) potential-time waveform;* ***B****) change of concentration gradient;* ***C****) resulting current-time response.*

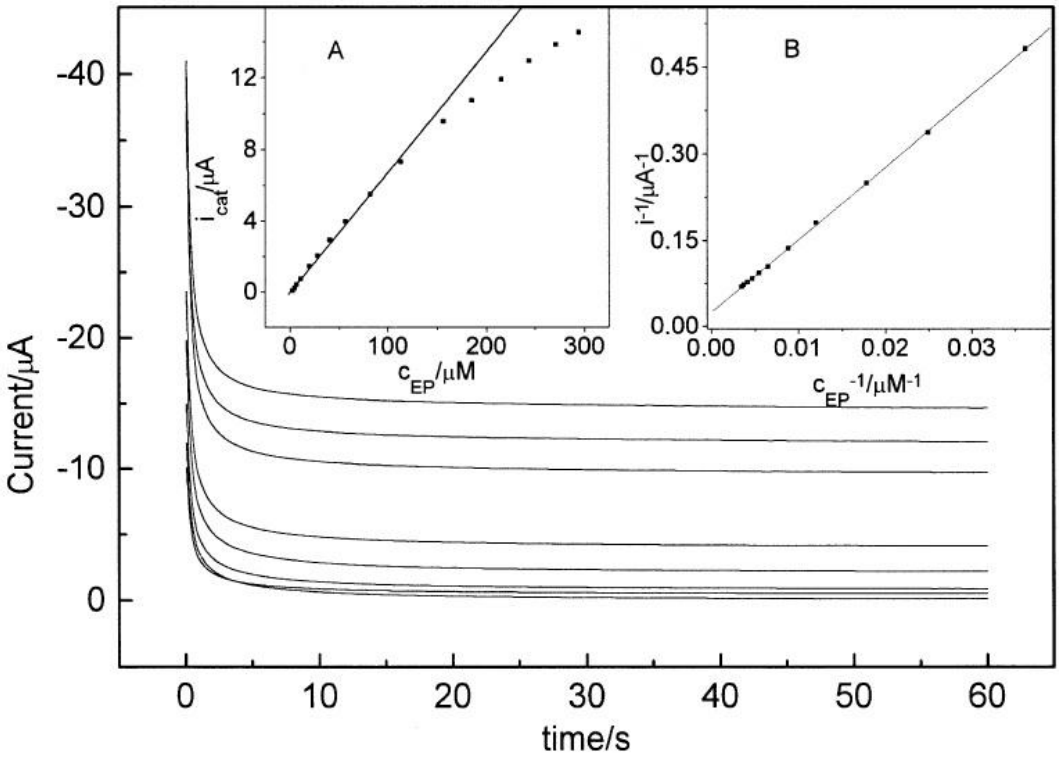

Figure 1.28 *Chronoamperometric curves with a potential step from 0 to + 0.4 V at Os-$(PVP)_{10}$/Nafion modified electrode in pH 6.9 PBS containing 0, 6.5, 11, 28, 56, 156, 215 and 294 μM (from bottom to top). Inset: (**A**) plot of catalytic current vs. epinephrine concentration; (**B**) data analysis of catalytic current vs. epinephrine concentration. Reproduced from Ref. [9].*

The most useful equation in chronoamperometry is the Cottrell equation, which describes the observed current (planar electrode of infinite size) at any time following a large forward potential step in a reversible redox reaction (or to large over-potential) as a function of $t^{-1/2}$.

$$I_L(t) = nFAD^{1/2}C(\pi t)^{-1/2} \qquad (1.60)$$

where n = stoichiometric number of electrons involved in the reaction, F is the Faraday's constant, A is the electrode area, C is the concentration of electroactive species and D is the diffusion coefficient. The current due to double layer charging also contributes following a

potential step but decays as a function of 1/*t* and is only significant during the initial period, typically a few milliseconds following the potential step.

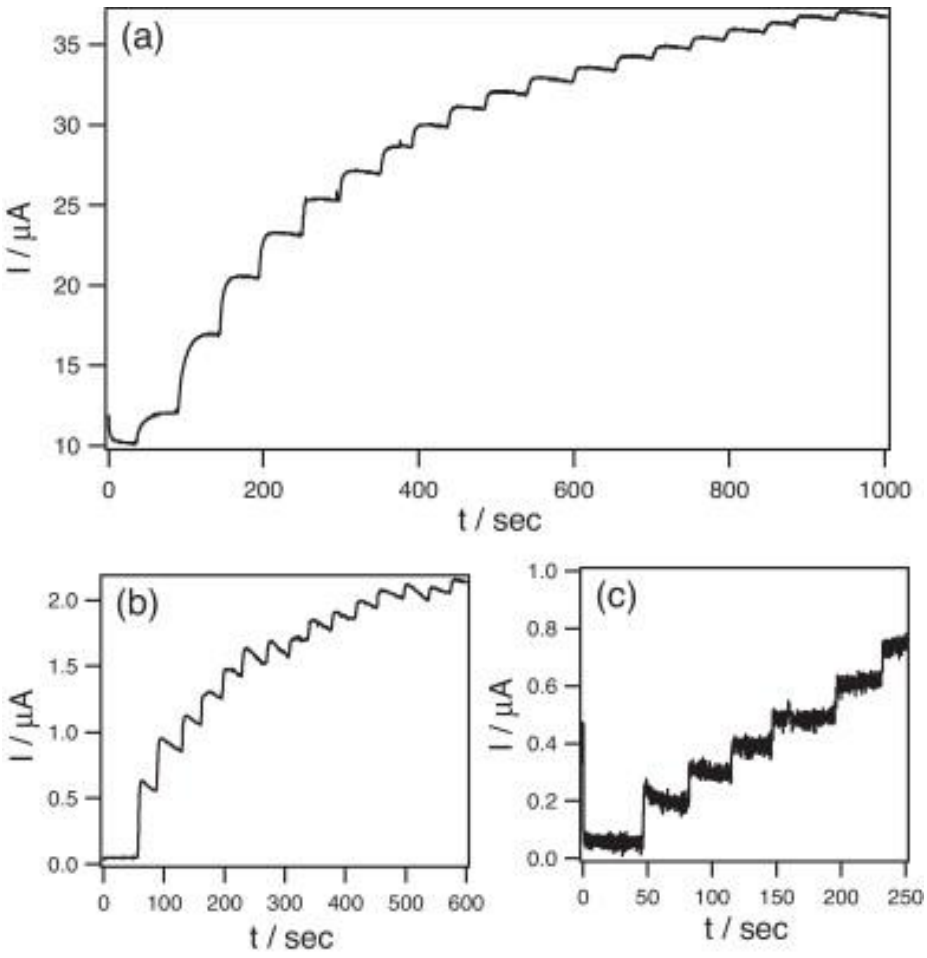

Figure 1.29 *Current–time curve obtained for ITO/AuNP/CYT C electrode upon successive addition of 20 μL aliquots of 200 mM H_2O_2 to 5 mL stirred 10 mM HEPES buffer at pH 7 with an applied potential of −0.1 V under nitrogen atmosphere; chronoamperometric curve obtained for (b) CYT C/ITO and (c) AuNP/ITO obtained by the addition of 20 μL aliquots of 200 mM H_2O_2 in 5 mL stirred solution of 10 mM HEPES buffer at the potential of −0.1 V under nitrogen atmosphere. Reproduced from Ref. [14].*

A variant on the chronoamperometry as discussed in Figure 1.28 is that presented in Figure 1.29 which is where hybrid biointerface electrodes, consisting of a gold nanoparticle (AuNP) and cytochrome C (CYT C) on indium tin oxide (ITO) platform, is explored towards the

sensing of hydrogen peroxide. In this example, the potential is held at a value, which induces the desired electrochemical reaction, and the solution is stirred such that a convective flow is induced. Aliquots of the analyte under investigation are made and at each time, the convective flow ensures that the species is transported to the electrode surface and is electrochemically transformed; this is recognised in Figure 1.29 by a 'step' in the current which then plateaus or reduces as all the electroactive species are consumed. Analysis of the 'steps', as evident in Figure 1.29, yields the corresponding calibration plot. Such an approach, where convection is used to enhance the rate of mass transport to the electrode surface is known as hydrodynamic electrochemistry and offers improvements in the analytical sensitivity in comparison to measurements performed in stagnant solution (Figure 1.28).

1.6. VOLTAMMETRIC TECHNIQUES: DIFFERENTIAL PULSE VOLTAMMETRY (DPV)

As introduced above, voltammetry so far has been concerned with applying a potential step where the response is a pulse of current which decays with time as the electroactive species near the vicinity of the electrode surface are consumed. This Faradaic process (I_F) is superimposed with a capacitative contribution (I_C) due to double layer charging which dies away much more quickly, typically within microseconds (see Figure 1.30). The current (for a reversible system) is in the form of the Cottrell Equation where $I \propto t^{-1/2}$ and charge, Q, is $Q \propto t^{-1/2}$. When a step in potential is applied the current is sampled when the capacitative current (I_C) decays away. To achieve this, pulse widths are chosen that meet this condition.

In pulse techniques such as differential pulse and square wave voltammetry, the capacitative contribution is eliminated *via* subtraction. Differential pulse voltammetry (DPV) measures the difference between two currents just before the end of the pulse and just before its application. Figure 1.31 shows the waveform of pulse utilised which is superimposed on a staircase.

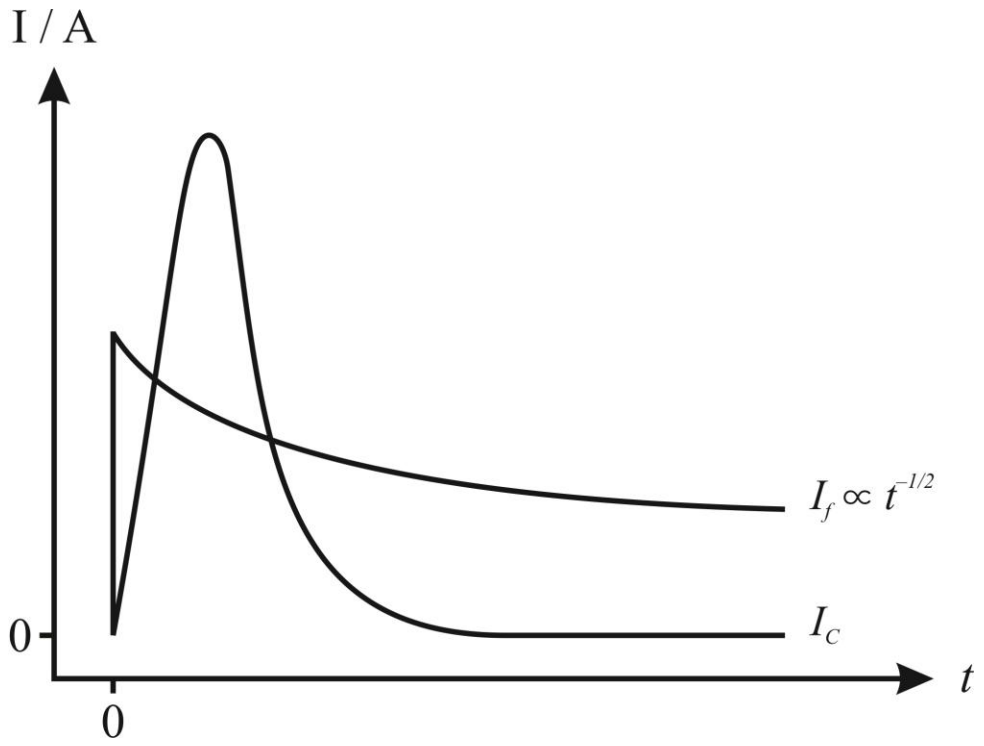

Figure 1.30 *Effect of capacitative and Faradaic current following the application of a potential step.*

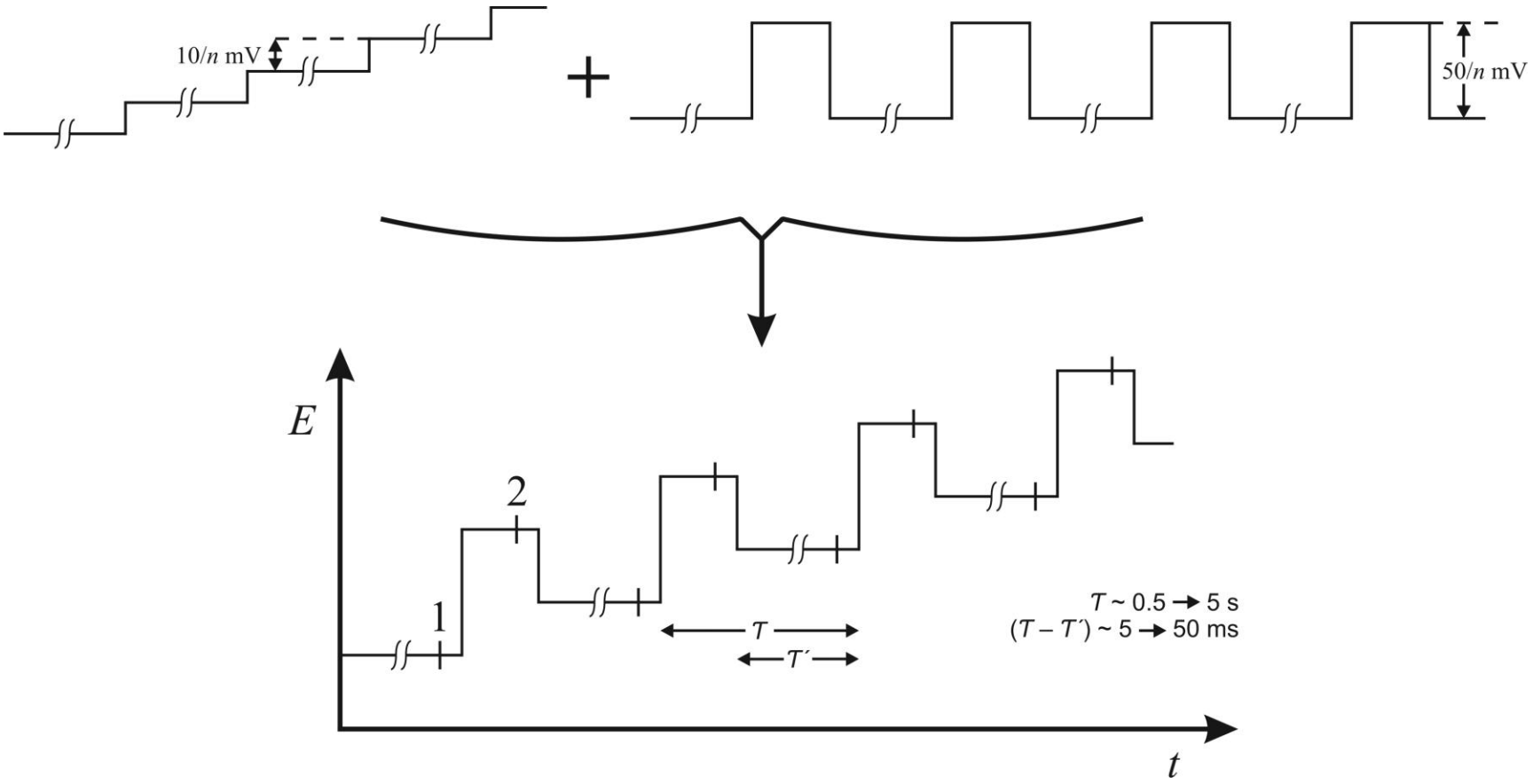

Figure 1.31 *Differential pulse voltammetry waveform of pulses superimposed on a staircase*.

The base potential is implemented in a staircase and the pulse is a factor of 10 (or more) shorter than the pulse of the staircase waveform. The difference between the two sampled currents is plotted against the staircase potential leading to a peak shaped waveform as shown in Figure 1.32.

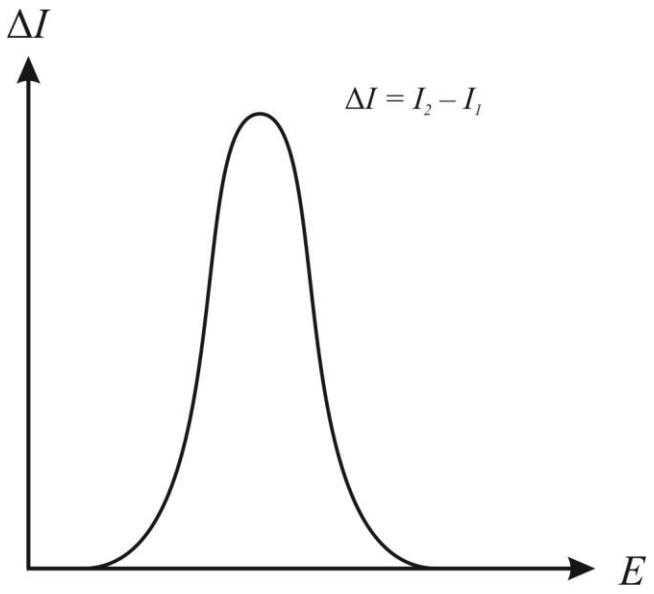

Figure 1.32 *Differential pulse voltammetry; voltammetric profiles of ΔI versus staircase potential.*

For a reversible system the peak occurs at a potential: $E_p = E_{1/2} - \Delta E/2$ where ΔE is the pulse amplitude. The current is given by:

$$I_p = \frac{nFAD^{1/2}C}{\pi^{1/2}t^{1/2}}\left(\frac{1-\alpha}{1+\alpha}\right) \tag{1.61}$$

$$\text{where} \quad \alpha = \exp(nF\Delta E/2RT) \tag{1.62}$$

DPV is useful due to eliminations in the contribution of non-Faradaic (capactitative) processes, which are effectively subtracted out. The power of DPV is evident from inspection of Figure 1.33 for the super-coiled plasmid DNA where poor electrochemical signals obtained

using linear sweep voltammetry are transformed into quantifiable and beautiful voltammetric signatures.

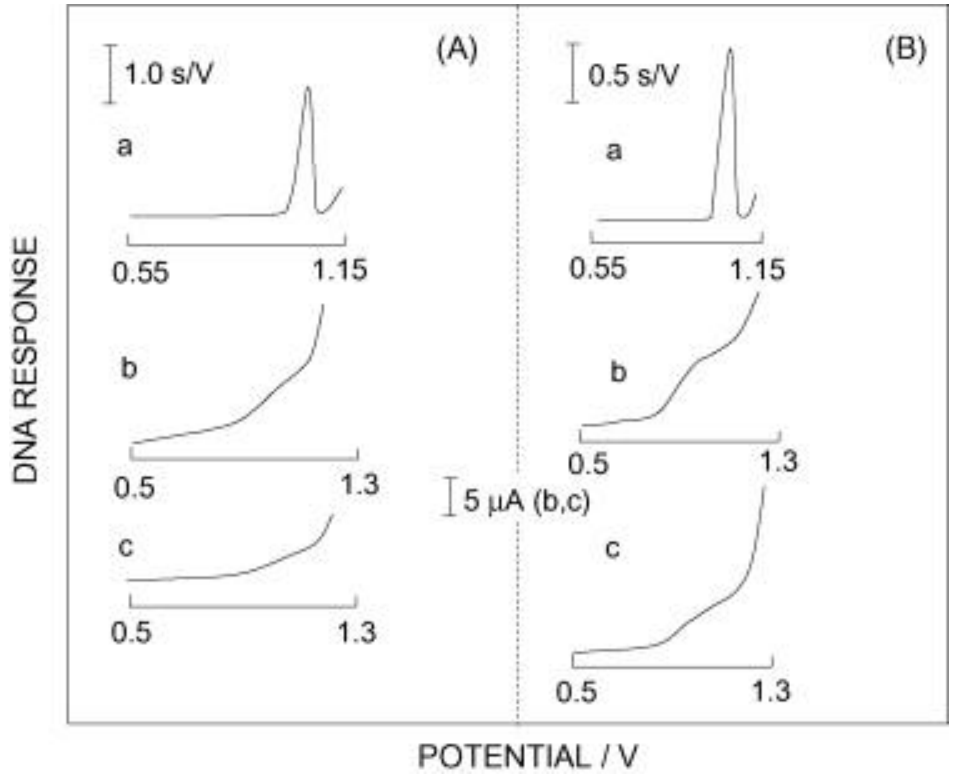

Figure 1.33 *Differential pulse (a) and linear scan (b, c) voltammograms for 15 µg mL^{-1} super-coiled plasmid DNA (**A**) and 15 µg mL^{-1} linearised DNA (**B**) at carbon paste electrodes. The anodic signal corresponds to the electrochemical oxidation of DNA–G residues. Reproduced from Ref. [15].*

Additionally, DPV is useful for resolving the voltammetric signals due to two species with close half-wave potentials, producing easily quantifiable peak shaped responses. This is exemplified in Figure 1.34 for the simultaneous sensing of ascorbic acid and acetaminophen which are well known to cause problems due to their overlapping voltammetric responses.

Figure 1.34 compares cyclic and differential pulse voltammetry using a range of modified electrodes. In all cases, two sharp and well-resolved peaks are observed when DPV is utilised; in this analytical case, the resulted separation in the two peak potentials is sufficient enough to

achieve the accurate simultaneous determination of ascorbic acid and acetaminophen in real samples. [16]

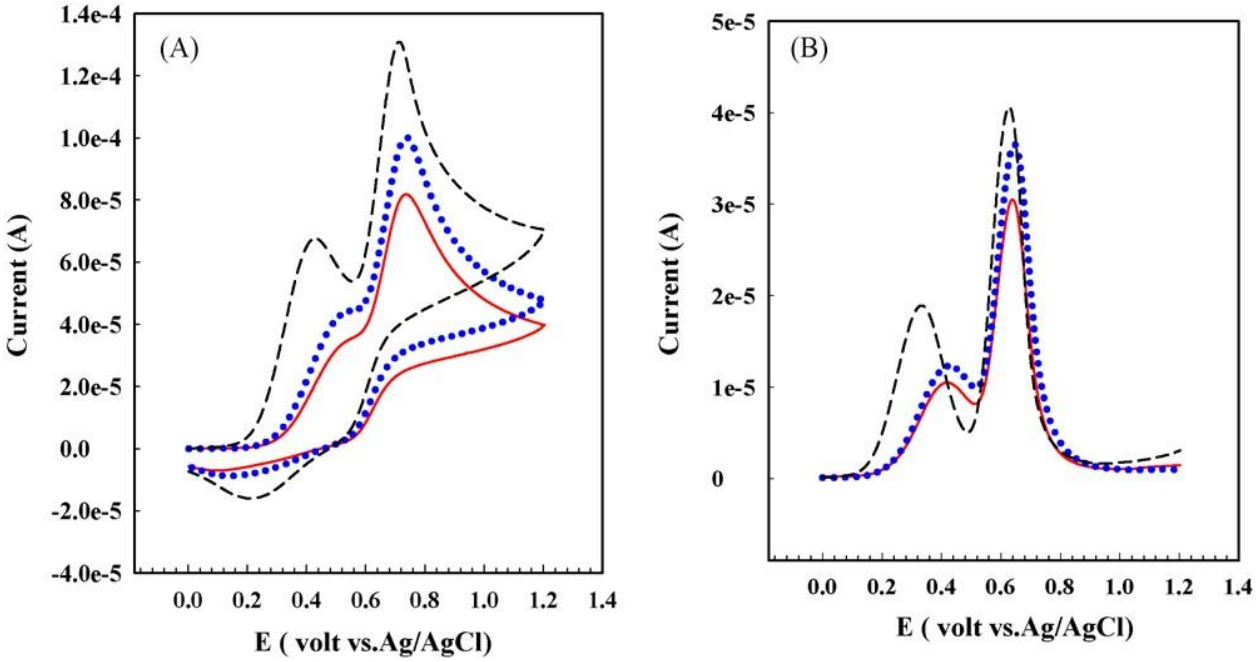

Figure 1.34 *(**A**) Cyclic and (**B**) differential pulse voltammograms of 0.1 mM ascorbic acid and 0.1 mM acetaminophen in acetate buffer solution (0.1 M, pH 4.0) on the surface of various electrodes; unmodified carbon paste electrode (solid line), CNT–carbon paste electrode (dotted line) and multi-walled carbon nanotube/thionine modified electrode (dashed line). Sweep rate was 100 mV* s^{-1}*. Reproduced from Ref. [*[16]*].*

Note that such a response is obtained through increasing the pulse amplitude, but in doing so the peak width also increases, meaning that in practice, ΔE values of more than 100 mV are not viable; careful optimisation of the electrochemical parameters is clearly required. The expression for the half-width at half-height, $W_{1/2}$; where $W_{1/2} = 3.52RT/nF$ leads to a value of 90.4 mV for n = 1 at 298 K, showing that peaks separated by 50 mV may often be resolved. Detection limits of DPV can be realised at *ca.* 10^{-7} M. [4]

1.7. VOLTAMMETRIC TECHNIQUES: SQUARE WAVE VOLTAMMETRY (SWV)

The square wave voltammetric waveform consists of a square wave superimposed on a staircase, as shown in Figure 1.35. The currents at the end of the forward and reverse pulses are both registered as a function of staircase potential. The difference between them, the net current, is larger than either of its two component parts in the region of the peak which is centred on the half-wave potential (see Figure 1.36). Capacitative contributions can be effectively discriminated against before they die away, since, over a small potential range between forward and reverse pulses, the capacity is constant and is thus annulled by subtraction. In this way the pulses can be shorter than in DPV and the square wave frequency can be higher. Instead of the effective sweep rates of 1–10 mVs^{-1} of DPV, scan rates of 1 Vs^{-1} can be employed. [1] Detection limits of *ca*. 10^{-8} M or lower are readily achievable under optimum conditions. The advantages over cyclic voltammetry are as follows: faster scan rates are possible (faster reactions can be studied), higher sensitivity (lower concentrations can be used) and a higher dynamic range (a larger range of concentrations can be investigated). Usually in electrochemistry, solutions are vigorously degassed (with, for example nitrogen) to remove oxygen which can be electrochemically reduced and may interfere with the voltammetric measurement under investigation. A different way of greatly diminishing or eliminating the interference of oxygen, with no need for its removal, is by the use of the high frequencies employed in SWV. In fact, due to the irreversibility of oxygen reduction, the increase of its signal with frequency is small at high frequencies, and becomes negligible eventually, when compared with the response of the determinant. [17]

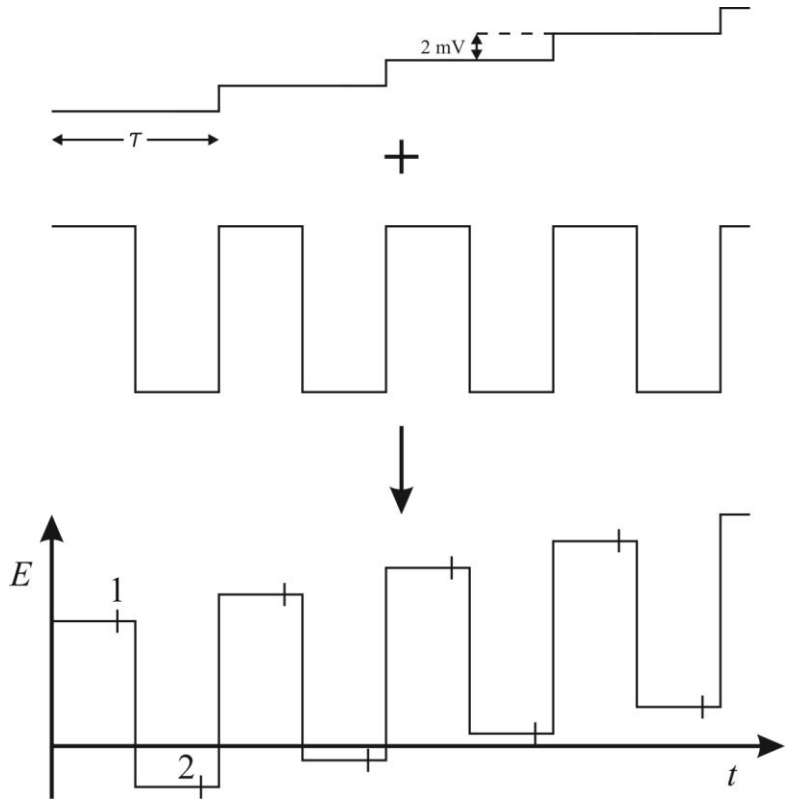

Figure 1.35 *SWV: waveform showing the summation of a staircase and a square wave.*

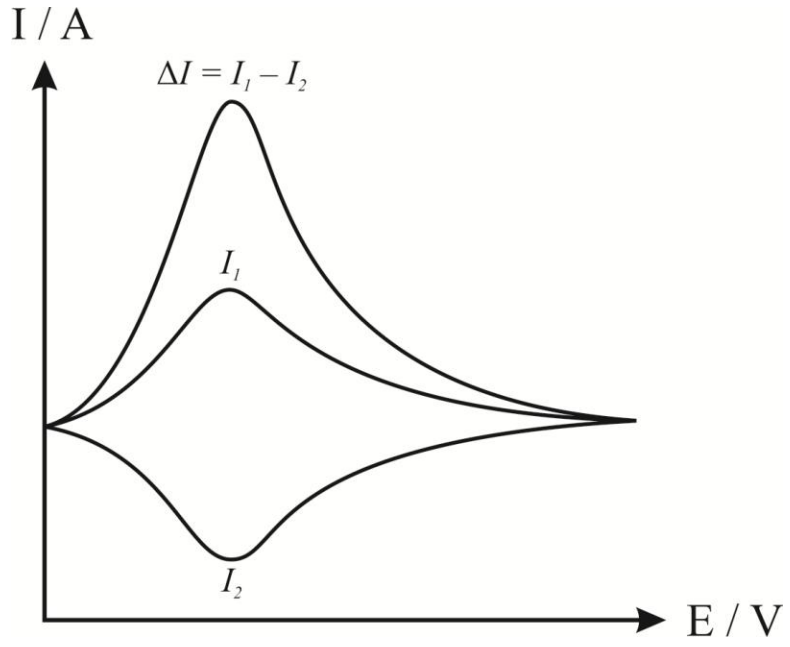

Figure 1.36 *SWV: voltammetric profile of current vs. staircase potential.*

I_1 represents the forward and I_2 the reverse sweep where ΔI is the resultant voltammogram.

Anodic Stripping Voltammetry (ASV) is an extremely sensitive electroanalytical technique that can determine trace quantities of certain metals at the parts-per-billion level, or even lower. The first phase of an ASV experiment involves a pre-concentration step, in which the analyte is deposited (*i.e.* in the case of metal analysis, reduced to its elemental form) at the working electrode by controlled potential electrolysis in a stirred solution at a suitable reduction potential as shown in Figure 1.37. The process can be written as:

$$M^{n+}(aq) + ne^{-} \rightarrow M(electrode) \tag{1.63}$$

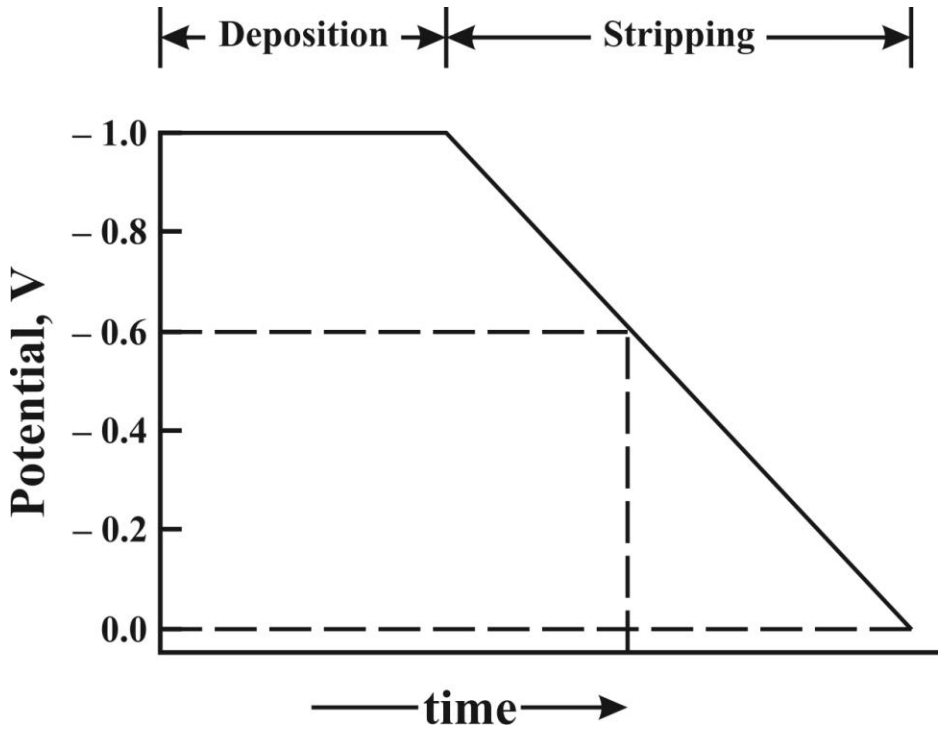

Figure 1.37 *A potential vs. time profile showing the stages in ASV.*

In the second phase, the potential of the working electrode is scanned so that the deposited metal is oxidised back to its ionic form, *i.e.* is anodically stripped from the electrode (see Figure 1.37) by scanning the potential to a value where the following process occurs:

$$M(electrode) \rightarrow M^{n+}(aq) + ne^{-} \tag{1.64}$$

Figure 1.38 shows a schematic representation of this process for the case of lead and copper.

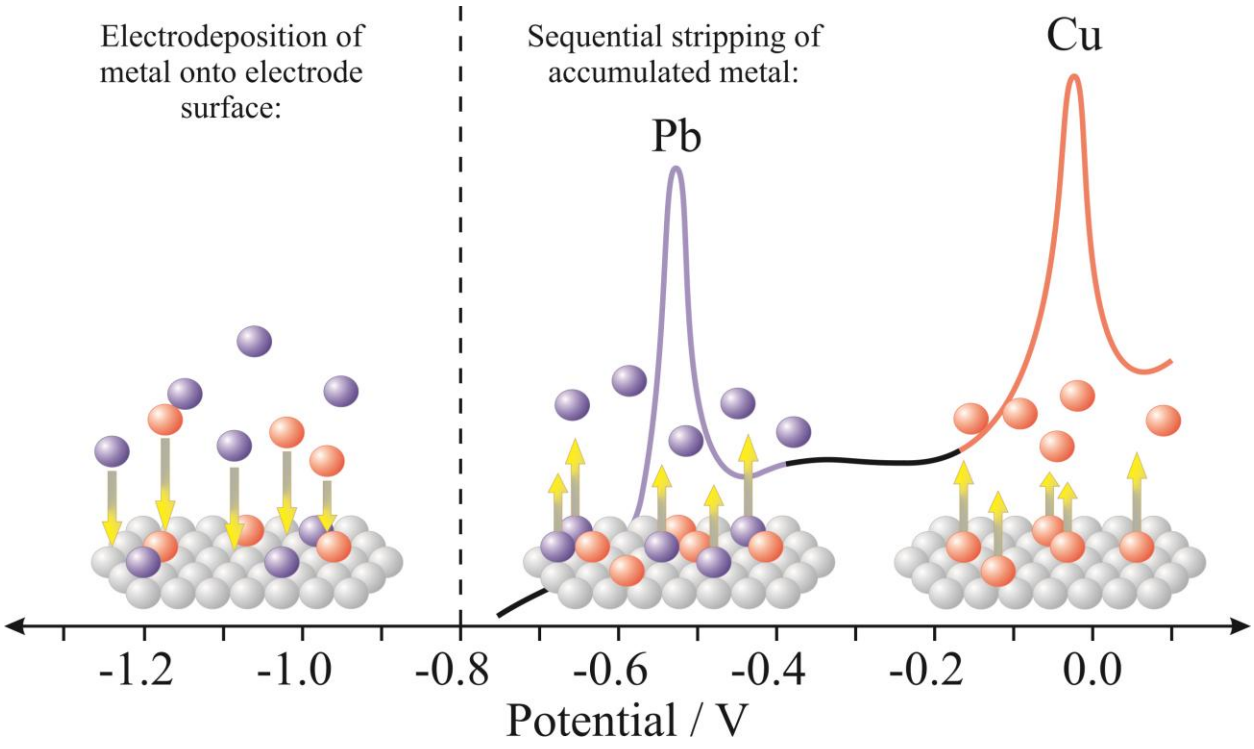

Figure 1.38 *A schematic representation of anodic stripping voltammetry showing the two key steps: electro-deposition and stripping.*

Additionally, as shown in Figure 1.39, the potential–time profile can be used in ASV with a cleaning step (*step A*). This is usually applied in-between measurements to ensure that the deposited metal is fully stripped from the electrode surface, so as to improve the reproducibility of the analytical measurement.

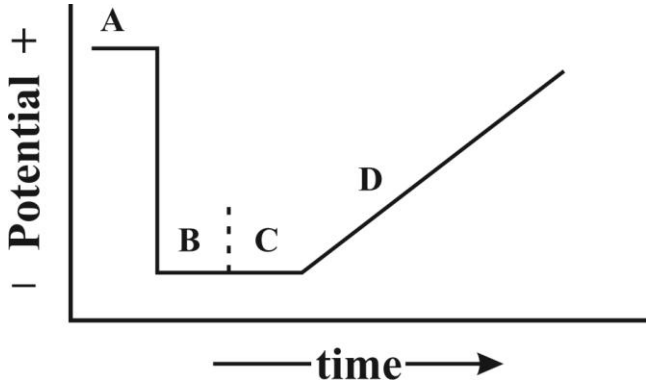

Figure 1.39 *A typical experimental potential–time profile used in ASV. Step A is the 'Cleaning step', B: 'electro-deposition, C: 'Equilibration step', D: 'Stripping step'.*

Figure 1.40 shows the response of a range of metals which occur at different stripping potentials, allowing a multitude of metals to be readily analysed at once. The peak area and/or peak height of each stripping signal is proportional to concentration, allowing the voltammetric signal to be used analytically.

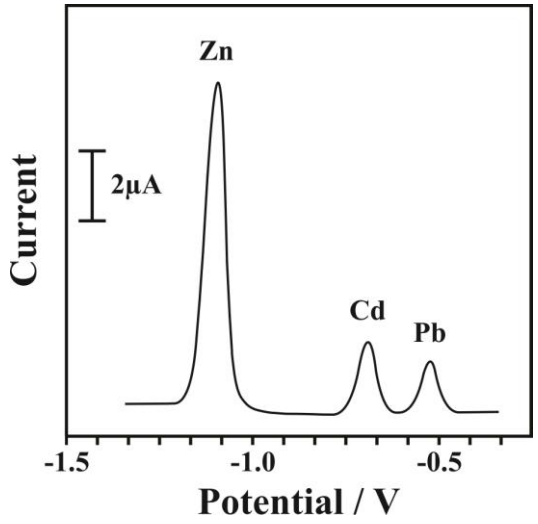

Figure 1.40 *Stripping voltammetry of zinc, cadmium and lead all in the same aqueous solution.*

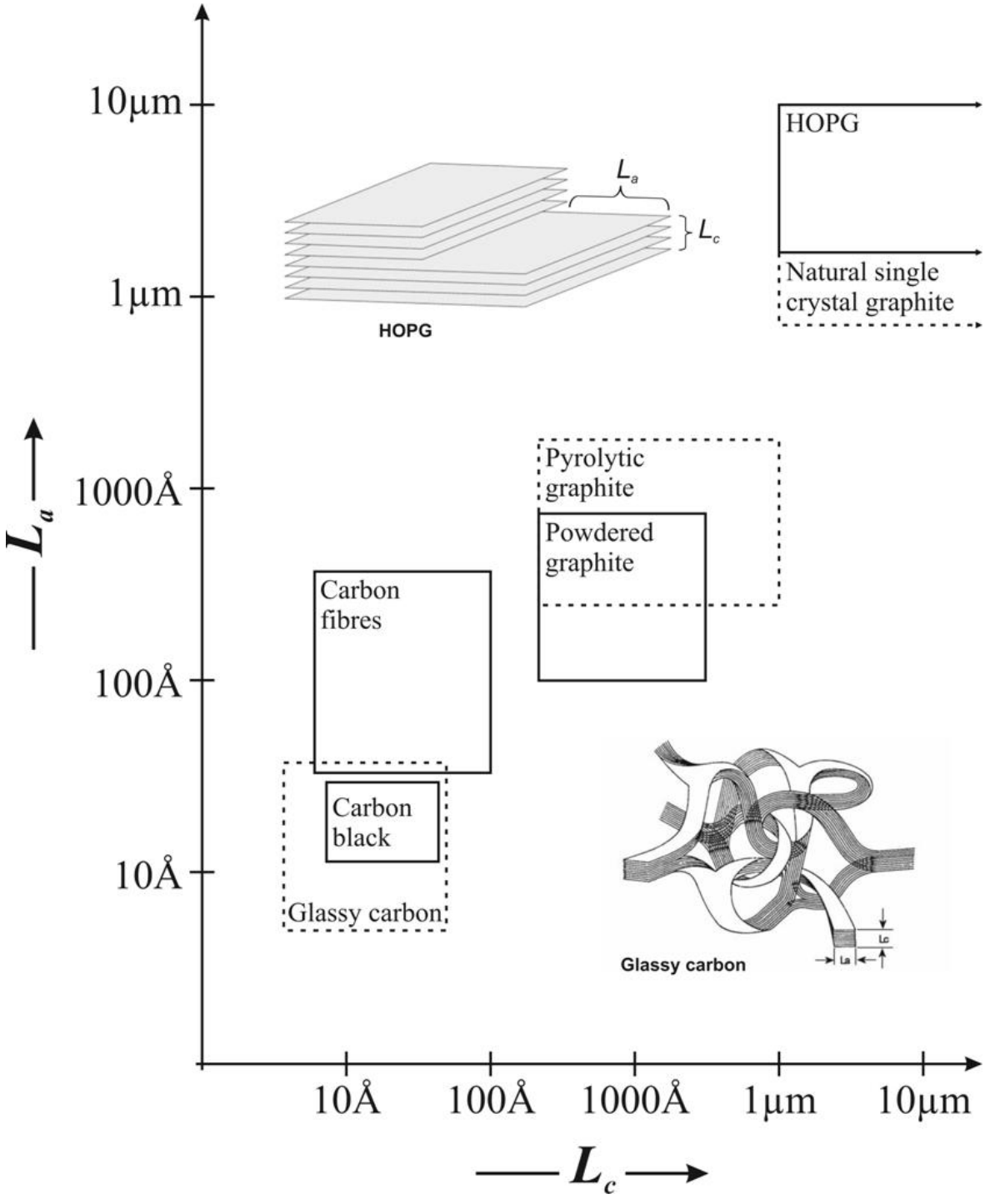

Figure 1.41 *The approximate ranges of L_a and L_c values for various sp^2 carbon materials. Note, there is large variation of L_a and L_c with sample history and thus the values shown should be considered representative, yet approximate. A schematic representation of the L_a and L_c microcrystalline characteristics of HOPG and glassy carbon is also shown.*

1.9. ELECTRODE MATERIALS

The development of electrochemical cells intended for electroanalytical applications rely heavily on the working electrode. The material selected can enhance or hinder the desirable characteristics sought by researchers since all the electrochemical processes of interest take place at the working electrode surface.

The choice of material used for the working electrode depends heavily on the system being electrochemically investigated. A wide variety of noble metal electrodes are available, the most common utilised being gold and platinum as they offer favourable electron rate kinetics and a large potential range. However, elemental metals can be highly reactive, undergoing electrochemical processes, forming oxides which limit their electrical conductivity and results in the appearance of high background currents; such metal-oxide films strongly affect the rate kinetics of the electrode reaction, resulting in irreproducible data. Additionally, the high cost of noble metal electrodes makes them unfavourable for use as disposable electrodes.

1.9.1. CARBON-BASED ELECTRODE MATERIALS

As is discussed in greater detail in Chapter 2 and 3.3.1, carbon based electrodes are widely utilised due to them being readily available, cheap (depending on its form), easily modified and relatively chemically inert. There is a large range of carbon based forms available for use as an electrode material, with various allotropic forms exhibiting distinct properties. Of particular note and interest for this thesis, there are a whole host of commercially available working electrodes which utilise a large variety of graphite/carbon products, such as amorphous carbon, glassy carbon (GC), carbon black, carbon fibres, powdered graphite, pyrolytic graphite (PG) and highly ordered pyrolytic graphite (HOPG), each with different

chemical and physical properties. The key structural factor that leads to such an assortment of different materials is the average graphite microcrystallite size (also known as the lateral grain size), L_a, which is effectively the average size of the hexagonal lattices that make up the macro structure. In principle, this can range from being infinitely large, as in the case of a macro single crystal of graphite, to the size of a benzene molecule; approximately 3 Å. In practice, the smallest L_a values are found in amorphous carbon, GC and carbon black and can be as low as 10 Å. Carbon fibres and pyrolytic graphite are intermediates in the range, with L_a values of *ca*. 100 Å and 1000 Å respectively. The assortment of carbon based materials are compared in Figure 1.41 which reveals that the largest graphite monocrystals are found in high quality (ZYA and SPI–1 grade) HOPG, which can be 1–10 μm in size.

Regions where individual graphite monocrystals meet each other (*i.e.* grain boundaries) are poorly defined and when exposed result in surface defects. In the case of pyrolytic graphite, the individual graphite crystallites lie along the same axis making it possible to obtain carbon surfaces with significantly less defects. This is especially true for HOPG where the large lateral grain size can result in a well-defined surface with values of defect coverage as low as 0.2 %. [18]

1.9.2. GRAPHITE

The low cost and ease of manipulation of graphite has established its use as an electrode material in electrochemistry. Note that the next chapter considers the electrochemistry and in-depth characterisation of graphite (particularly HOPG).

The structural conformation and thus the degree of hybridisation strongly influences the physical, chemical and electronic characteristics of carbon based nanomaterials. The orbital configuration of carbon's six electrons (in its ground-state) is $1s^2$, $2s^2$, $2p^2$. The small energy gap

between the 2s and 2p electron orbitals aids in the promotion of one s orbital electron to the higher energy p orbital that is unoccupied in this ground state. Conditional to the bonding interactions with adjacent atoms, the promotion credits carbon with the ability to hybridize its electron orbitals into a sp, sp^2 or sp^3 configuration. Covalent bonding with adjacent atoms tenders increased stability, compensating for the higher energy state of this electronic configuration. This return is approximately equal for the sp^2 and sp^3 hybridization states after the out-of-plane π bonding among un-hybridised p orbitals is considered.

Hybridisation of the carbon atom changes the crystal structure of the material. In the case of sp^2 hybridisation, the carbon atom remains with one free electron in the 2p orbital. Each of the sp^2 hybridised orbitals then combines with other hybridised atoms/orbitals to form a series of planar hexagonal structures (Figure 1.42). The free delocalised orbital is orientated perpendicular to this plane. Thus the electron can move easily from one side of the carbon atom layer to the other but cannot easily move from one layer to the other. This phenomenon makes the material anisotropic.

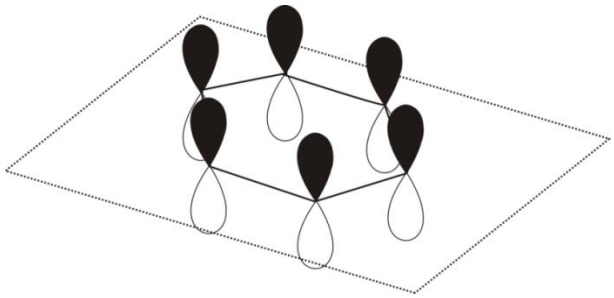

Figure 1.42 *Schematic representation of the sp^2 hybridised structure of graphite (free 2p orbitals shown).*

Graphite is comprised of a series of parallel planar layers, termed basal-planes. Graphite has a perfect (defect free) hexagonal, crystallographic structure (shown below) and should not be confused with other graphitic materials. The stacking of the basal-plane occurs in two ordered

structures, hexagonal or rhombohedral. The most commonly found stacking order is hexagonal (or alpha) with a –ABABAB– sequence, superimposing the carbon atoms of alternating basal-planes as shown in Figure 1.43.

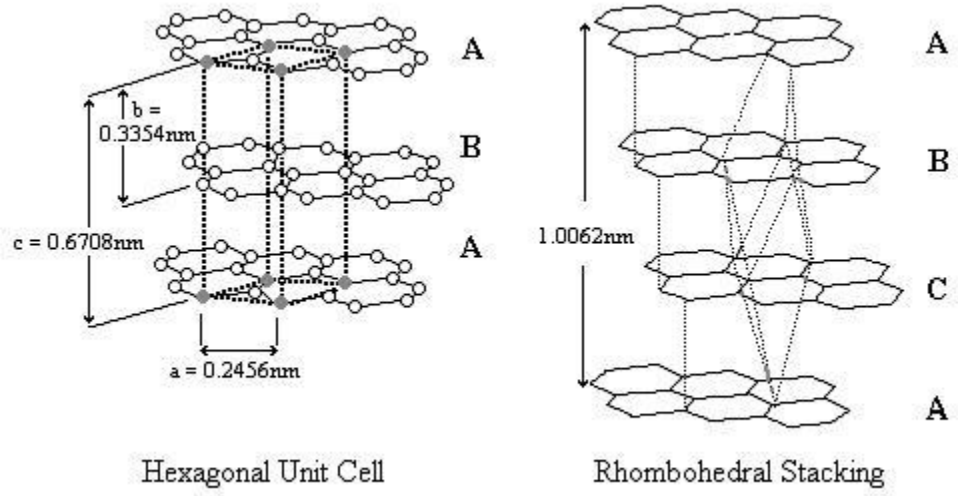

Figure 1.43 *Schematics of hexagonal and rhombohedral graphite stacking arrangements.*

A rhombohedral structure (Figure 1.43) displays a –ABCABC– stacking order, thus the carbon atoms of every third basal layer are superimposed. This type of structure is not found in a pure form but in a blend with the hexagonal arrangement. The rhombohedral configuration converts to the hexagonal form, which is thermodynamically more stable, after heat treatment (over 1300 °C). The significant difference between the two structures is found in the distance between the basal layers (C_o), *ca*. 0.6708 and 1.0062 nm for hexagonal and rhombohedral systems respectively. No direct overlap of carbon atoms between adjacent layers is found in either structure.

The graphitic crystal (basal) layer has two faces (zig-zag or arm-chair) originating at its termination, depending on the orientation of the basal layer (Figure 1.44); these two configurations are reported to display different electron conductivities (see Chapter 2.2).

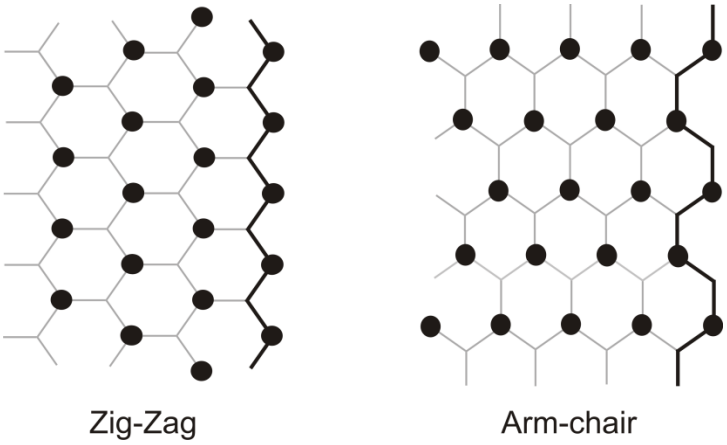

Figure 1.44 *Schematic representation of zig-zag (left) and arm-chair (right) graphitic crystal formations.*

In line with the basal-plane is what researchers term the 'edge-plane'. The edge-plane is formed *via* the termination sites found around the perimeter of the basal-plane layers. Basal and edge-plane sites (*of graphite*) are reported to exhibit significantly different surface energies (0.11 J/m^2 and 5 J/m^2 respectively). Thus, the reaction rate at the edge-plane sites is believed to be considerably faster than that found at the basal-plane. This parameter is important when constructing or tailoring a *graphite electrode* for a specific system. Evidently, for processes that require fast electro-catalytic reactions, the working surface area should contain an elevated percentage of edge-plane-like sites/defects. Concurrently, the reverse is true for systems favourable to slow electro-catalytic processes. Edge-plane and basal-plane pyrolytic graphite electrodes (EPPG and BPPG respectively) are fashioned from HOPG. The HOPG surface consists of islands of basal-plane graphite, surrounded by nano bands of edge-plane sites, which lie parallel to the surface. Defects along the surface occur in the form of steps exposing the edges of the graphite layers. Graphite's layered structure tenders low resistivity along the plane (*ca*. 2.5 to 5 × 10^{-6} Ω·m), conversely through (perpendicular to) the plane, resistivity values approach close to *ca*. 3000 × 10^{-6} Ω·m. This consequently results in electrodes, consisting

entirely of edge-plane *viz* an EPPG electrode, displaying a near reversible voltammogram, while an electrode consisting mostly of basal-planes will show irreversible behaviour.

The electrochemistry and indeed the properties and structural configuration of HOPG is explored in greater detail in Chapter 2; where one can acquire an understanding of the electrochemistry of graphite prior to investigating the electrochemistry of graphene for the first time.

1.9.3. BORON-DOPED DIAMOND

The boron-doped diamond (BDD) electrode is a commonly employed tool within electrochemistry. BDD does not interact or bind with organic compounds, such that by-products are not absorbed onto its surface during a redox reaction occurring at its surface, leaving it unpolluted and available for further redox reactions of further electroactive species present in solution. BDD is a tough, stable (does not form oxides) material, resistant to most chemicals. The reason for these distinctive characteristics lies in the BDD structure.

Carbon atoms have a $1s^2$, $2s^2$, $2p^2$ electron configuration at the ground state. Once these atoms bond together in a diamond structure (similar to methane), the following electron configuration is present: $1s^2$ and four $2sp^3$ (hybrid orbitals). This raises the energy state of the electrons in the carbon atom, stabilised *via* the bonds found in the structure. The resulting hybridisation is the formation of four strong covalent bonds with an additional four carbon atoms (each sharing two electrons). The arrangement of the carbon atoms is a regular tetrahedron (see Figure 1.45).

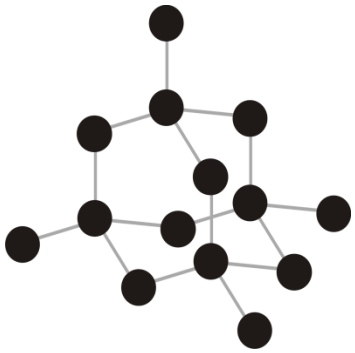

Figure 1.45 *Schematic representation of a sp^3 hybridised (tetrahedral) 'diamond' structure.*

The four sp^3 valence electrons of the hybrid carbon atoms, in conjunction with a small atom size results in a strong covalent bond. This is enhanced as four of the six electrons found at the carbon atom formulate bonds.

Diamond is one of the best known electrical insulators, making it a poor candidate as an electrode material. Conversely its high strength, stability and chemical resistance make it ideal. This only occurs when the diamond is a pure crystal. The presence of impurities or defects diminishes these optimum properties. Thus doping diamond with metal impurities alters its electrical properties (increasing conductivity). Boron has a similar atom size to carbon and is a known electron acceptor, due to electron deficiencies found in its outer shell. To provide adequate conductivity, doping of the diamond electrode ranges from 1019 to 1021 atoms/cm^3. The resulting electrode, a BDD electrode, has a wide operating potential window (*ca*. –1.35 to +2.3 V *versus* a normal hydrogen electrode), low background currents and stability in aggressive media.

1.9.4. GLASSY (VITREOUS) CARBON

Glassy carbon (GC) offers unique properties compared to other types of carbon materials. Essentially non-porous, it offers low permeability, while free from surface defects and containing

little or no impurities. These characteristics are attributed to the organic precursor (polymer) from which it is produced. The crystallite arrangement is random (no long-range order) making the material isotropic and produces a 'ribbon' like structure (Figure 1.46). The aromatic rings are twisted and cross linked with covalent bonds, producing variable bond energies and thus the existence of sp^2 and sp^3 structures. The partial diamond structure (sp^3) is believed to give the GC its high strength and hardness. It is for this reason that this material is not easily graphitised (converted to graphite under high temperatures) and is highly resistant to chemical attack.

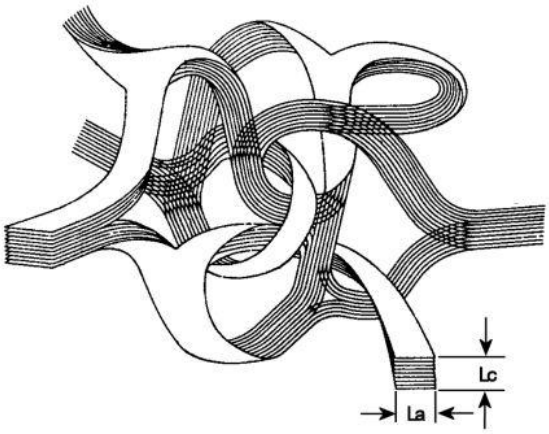

Figure 1.46 *GC 'ribbon' network where L_a and L_c microcrystalline sizes are highlighted. Reproduced from Ref. [19].*

The next chapter considers the electrochemistry of graphite (EPPG and BPPG electrodes constructed from HOPG) before attempts are made in later chapters to characterise and understand the electrochemistry of graphene.

1.10. REFERENCES

1. A. J. Bard and L. R. Faulkner, *Electrochemical methods: fundamentals and applications*, 2nd edn., John Wiley & Sons, Inc., United States of America, 2001.
2. C. G. Zoski, *Handbook of Electrochemistry*, Elsevier, Oxford, 2007.
3. T. J. Davies, C. E. Banks and R. G. Compton, *J. Solid State Electrochem.*, 2005, **9**, 797.

4. R. G. Compton and C. E. Banks, *Understanding Voltammetry*, World Scientific, Singapore, 2007.
5. H. Matsuda and Y. Ayabe, *Z. Elektrochem.*, 1955, **59**, 494.
6. R. S. Nicholson, *Anal. Chem.*, 1965, **37**, 1351.
7. I. Lavagnini, R. Antiochia and F. Magno, *Electroanalysis*, 2004, **16**, 505.
8. A. C. Testa and W. H. Reinmuth, *Anal. Chem.*, 1961, **33**, 1320.
9. J.-A. Ni, H.-X. Ju, H.-Y. Chen and D. Leech, *Anal. Chim. Acta*, 1999, **378**, 151.
10. J. Yang and N. Hu, *Bioelectrochem. Bioenerg.*, 1999, **48**, 117.
11. R. H. Wopschall and I. Shain, *Anal. Chem.*, 1967, **39**, 1514.
12. I. Streeter, G. G. Wildgoose, L. Shao and R. G. Compton, *Sens. Actuators, B*, 2008, **133**, 462.
13. M. C. Henstridge, E. J. F. Dickinson, M. Aslanoglu, C. Batchelor-McAuley and R. G. Compton, *Sens. Actuators, B*, 2010, **145**, 417.
14. A. K. Yagati, T. Lee, J. Min and J.-W. Choi, *Colloids Surf., B*, 2012, **92**, 161.
15. X. Cai, G. Rivas, P. A. M. Farias, H. Shiraishi, J. Wang, M. Fojta and E. Paleček, *Bioelectrochem. Bioenerg.*, 1996, **40**, 41.
16. S. Shahrokhian and E. Asadian, *Electrochim. Acta*, 2010, **55**, 666.
17. A. A. Barros, J. A. Rodrigues, P. J. Almeida, P. G. Rodrigues and A. G. Fogg, *Anal. Chim. Acta*, 1999, **385**, 315.
18. C. E. Banks, T. J. Davies, G. G. Wildgoose and R. G. Compton, *Chem. Commun.*, 2005, 829.
19. G. M. Jenkins and K. Kawamura, *Nature*, 1971, **231**, 175.

CHAPTER 2: FUNDAMENTAL ELECTROCHEMISTRY OF GRAPHITE

In order to understand and characterise the fundamental electrochemical properties of graphene, this chapter explores what has already been established in the literature with respect to comprehending the electrochemical performance of graphite. Given that graphite is effectively multiple layers of stacked graphene, this offers a worthy starting point for the journey of graphene exploration.

2.1. AN INTRODUCTION TO GRAPHITE

Graphite surfaces are heterogeneous (anisotropic) in nature, with the overall chemical and electrochemical reactivity differing greatly between two distinct structural contributions which are fundamental to the behaviour of graphitic electrodes, namely the edge and basal planes. [1, 2] As mentioned in Chapter 1.9, the intraplanar (L_a, or *basal plane*) and interplanar (L_c, or *edge plane*) microcrystallic values define distinct structural characteristics of carbon materials (see for example Figure 2.3), with Highly Ordered Pyrolytic Graphite (HOPG) exhibiting the largest graphite monocrystals; which are found in high quality (ZYA and SPI-1 grade) HOPG. Pyrolytic graphite is a graphitic material with a high degree of preferred crystallographic orientation of the ***c***-axes perpendicular to the surface of the substrate (see Figure 2.1) and is obtained by graphitisation heat treatment of pyrolytic carbon or by Chemical Vapour Deposition (CVD) at extremely high temperatures (*ca*. 2500 °K). The hot working of pyrolytic graphite by annealing under compressive stress at high temperatures produces HOPG. The crystal structure of HOPG is shown in Figure 2.1, which is characterised by an arrangement of carbon atoms in stacked parallel layers and the graphite structure is described by the alternate succession of these identical staked planes where carbon atoms within a single plane have a stronger interaction than

with those from adjacent planes (which explains the cleaving behaviour of graphite). Note that a single-atom thick form of carbon is known as *graphene*, where the lattice consists of two equivalent interpenetrating triangular carbon sub-lattices denoted A and B (see Figure 2.1) where each one contains a half of the carbon atoms. Each atom within a single plane has three nearest neighbours: the sites of one sub-lattice (A – marked by the red layer in Figure 2.1) are at the centres of triangles defined by tree nearest neighbours of the other one (B – marked by the blue layer). The lattice of graphene has two carbon atoms, designated A and B, per unit cell, and is invariant under 120° rotation around any lattice site.

The term "mosaic spread" is used to characterise the quality of HOPG which is performed *via* X-ray crystallography with CuKα radiation by measuring (in degrees) a Full Width at Half Maximum (FWHM) of the rocking curve. Disorder in the HOPG produces broadening of the (002) diffraction peak where the more disorder, the wider the peak becomes. The measured value of the mosaic spread depends not only on crystal quality, but also on the energy and the cross section of the reflected beam. Figure 2.2A depicts a picture of a commercially obtainable HOPG ‘slab’ which in this case is ‘Grade SPI-1’, which has the tightest mosaic spread of 0.4° (± 0.1°) demonstrating outstanding crystalline perfection. Note that the ZYB, ZYD and ZYH grade HOPG results in mosaic spread values of 0.8° (± 0.2°), 1.5° (± 0.3°) and 3.5° (± 0.5°) respectively.

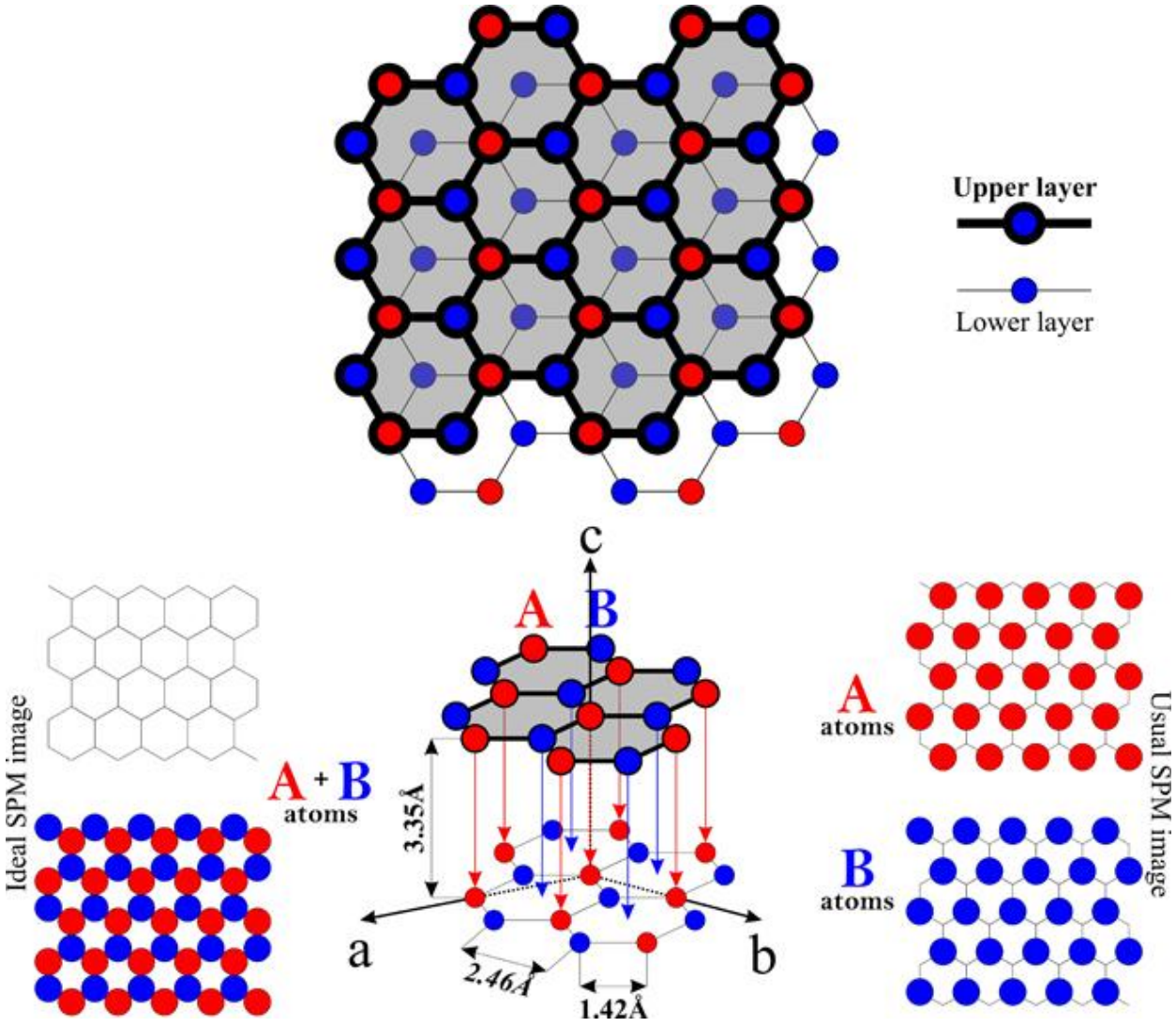

Figure 2.1 *A schematic representation of the structure of a bulk hexagonal graphite crystal. The dashed lines show the axes of bulk unit cell. Side insets: top view of the basal plane of graphite and a schematic representation of the surface structure (carbon atoms) of graphite, where every other atom is enhanced (right-side inset) and viewed under ideal conditions, and where every single atom is seen (left-side inset). Reproduced from Ref. [3].*

Shown in Figure 2.2 is a top-down schematic representation of the HOPG surface, which depicts the discrete edge plane and basal plane islands, and a side on view highlighting the edge plane and basal plane like- sites/defects which are defined by the quality of the chosen HOPG.

Also shown in Figure 2.2D is a scanning tunnelling microscopy (STM) image of a HOPG surface, highlighting the hexagonal crystal structure. Note that in terms of the electrochemical performance of graphitic materials, it has been deduced (see Chapter 2.3) that the electrochemical activity of edge and basal planes is distinct such that electrochemical reactions on the edge plane like- sites/defects are anomalously faster (exhibit greater reactivity) over that of the basal planes. [4-6] In terms of relating this to other carbon allotropes, Figure 2.3 shows the range of L_a and L_c values for a collection of other graphitic forms where it is evident that HOPG has L_a and L_c values exceeding 1 μm while polycrystalline graphite has values from 10 to 100 nm and carbon from 1 to 10 nm. Graphene, which is readily obtainable from a range of commercial suppliers is also included, highlighting the variation in structure that can be obtained, which is of course dependant on the fabrication methodology; with L_a values for graphene ranging from below 50 up to 3000 nm and larger, and of course true (monolayer) graphene possess an L_c value of 0.34 nm.

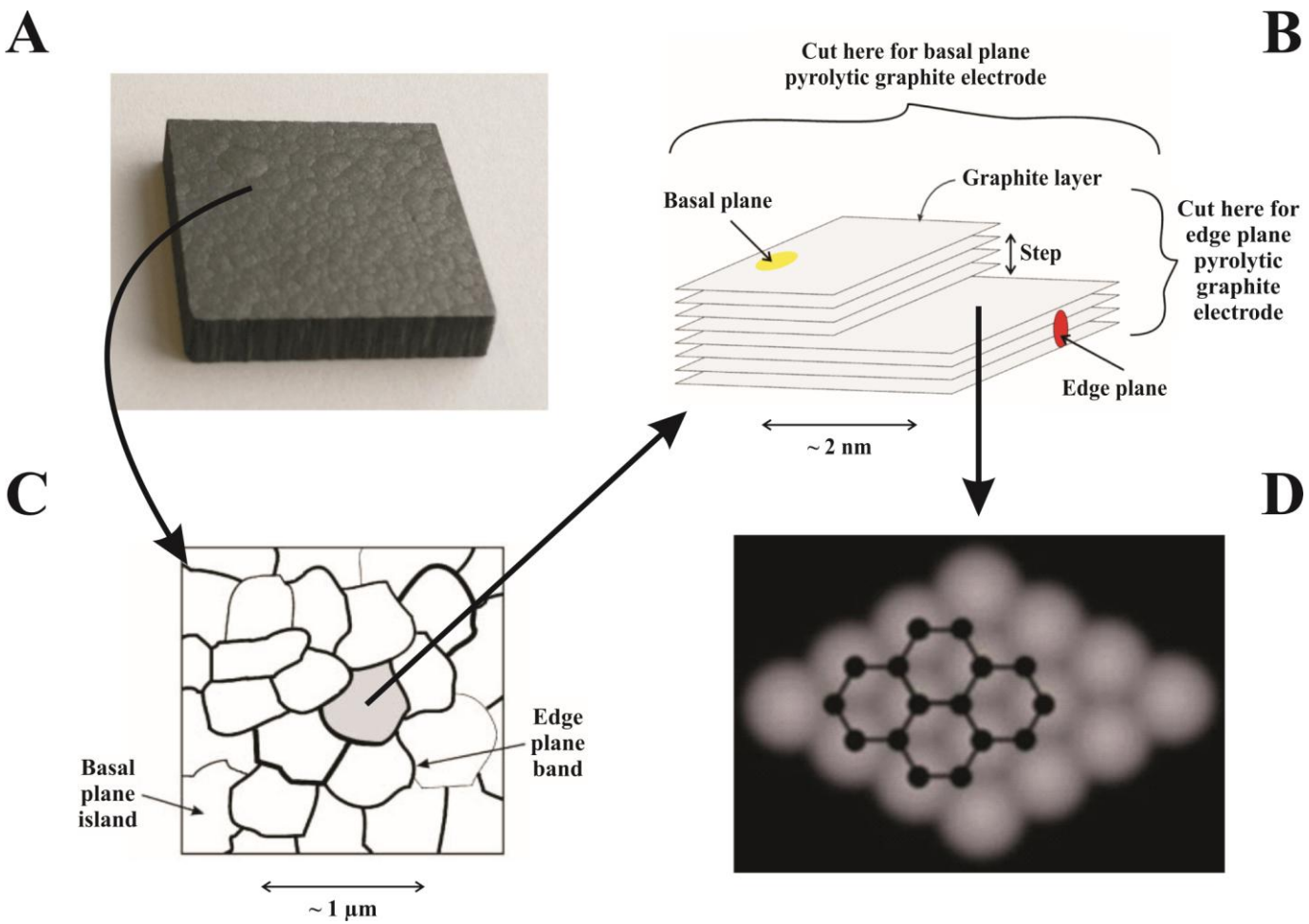

Figure 2.2 *(**A**) Image of a commercially available slab of HOPG. (**B**) Schematic representation of the side on view of a HOPG surface, highlighting its basal plane and edge plane like- sites/defects which exhibit contrasting behaviours in terms of electrochemical activity, where electron transfer kinetics of the latter are overwhelmingly dominant over that of the former which in comparison are relatively (electrochemically) inert. (**C**) A schematic representation of a HOPG surface showing the discrete basal plane and edge plane islands. (**D**) A typical STM image of a HOPG surface with the corresponding fragment of the graphene structure is superimposed.*

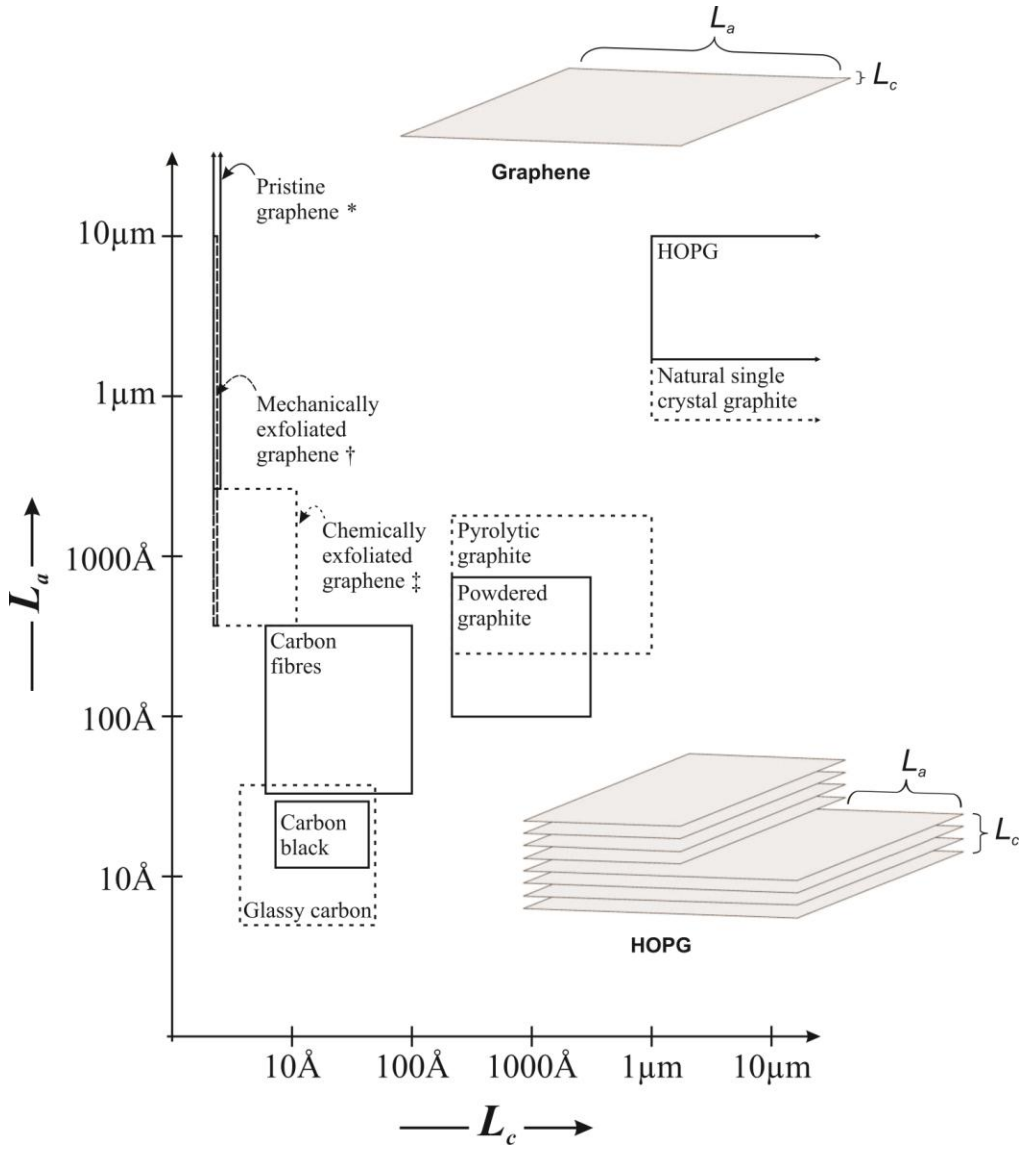

Figure 2.3 *The approximate ranges of L_a and L_c values for various sp^2 carbon materials. Note, there is large variation of L_a and L_c with sample history and thus the values shown should be considered representative, yet approximate.* *******: Pristine graphene; commercially available from 'Graphene Supermarket', produced via a substrate-free gas-phase synthesis method.* [7, 8] *‡: Chemically exfoliated graphene; commercially available from 'NanoIntegris', produced via a surfactant intercalation process – note that this range is also representative of graphene produced through other chemical exfoliation routes such as the reduction of GO.* [9, 10] *†: Mechanically exfoliated graphene was fabricated through the so-called 'scotch tape method'. Note that graphene synthesised via CVD has been excluded given that crystal size and quality are large variables through this route, however single graphene crystals with dimensions of up to 0.5 mm have been reported.* [11, 12] *A schematic representation of the L_a and L_c microcrystalline characteristics of graphene and HOPG is also shown. Reproduced from Ref. [*[13]*].*

2.2. THE ELECTRONIC PROPERTIES (DOS) OF GRAPHITIC MATERIALS

An important parameter of an electrode material is its electronic properties, namely, the density of electronic states (DOS) which varies greatly on the different forms of graphite. Gold typically has a DOS of 0.28 states $atom^{-1}$ eV^{-1} with the high conductivity of gold arising from the combination of a high proportion of atomic orbitals to form bands with a high density of electronic states. [2] For a given electrode material, a higher DOS increases the possibility that an electron of the correct energy is available for the electrode to transfer to an electroactive species; the heterogeneous electron transfer rate is thus dependent on the DOS of the electrode material. [2] HOPG has a DOS which overall is lower than that of metal, but is particularly low near the Fermi level and has been reported to have a minimum DOS of *ca*. 0.0022 states $atom^{-1}$ eV^{-1}, which is *ca*. 0.8 % that of gold. [2]

The DOS at graphitic materials can be increased through disorder such that electroactive species exhibit increasing electron transfer rates but by varying amounts. In terms of outer-sphere electron transfer systems, disorder increases the rate by modifying the electronic structure of the carbon while for inner-sphere systems, specific surface interactions also contribute (see Appendix A.1). [14] A perfect/pristine basal surface of HOPG has no edge plane (in theory), no location for surface functional groups and there are no dangling bonds since the carbon atoms have satisfied valances. [2] When disorder is introduced, such as through mechanical roughening of the electrode surface, the surface is disturbed such that surface defects are introduced, *viz* edge plane sites, which increase the DOS. [2] A further extreme is the complete change of a graphitic surface to a different structural composition (L_a and L_c; see Figure 2.2 and 2.3) towards that of edge plane pyrolytic graphite (EPPG) which has a high proportion of edge plane sites and thus improvements in electron transfer are observed. [2, 13]

Electronic properties of graphitic materials are thus highly relevant and critical, where the energy-dependant densities of electronic states have major effects on electron transfer. Note that graphitic materials differ greatly in their surface chemistry which is also critical when understanding electrochemical processes at these materials. [2] Such insights from graphitic materials can be applied for the case of *graphene*. In terms of the DOS for graphene, insights from HOPG (multiple layers of graphene) can be illuminating to understand its electrochemical reactivity. For example, it is well established that there is a direct relationship between the DOS and the standard electrochemical rate constant (k^o) at HOPG, with recent work demonstrating that, for graphite, the DOS varies significantly as a function of energy with a minimum at the Fermi level. [15] It has also been shown that electron transfer is non-adiabatic and that the rate of electron transfer varies as a function of the applied potential for outer-sphere redox systems. [15]

It has been reported that the basal plane of pristine graphene has a DOS of 0 at the Fermi level, which was shown to increase with edge plane defects. [16-18] Conversely the edge plane sites on graphene nanoribbon's zigzag edge have been reported to possess a high DOS. [18] Other work has shown that depending on how the edge of graphene terminates, [19] a variable DOS is observed. [20] Thus, graphene, a single layer comprising HOPG, should in theory act similar in terms of its DOS to that observed for HOPG (*vide supra*); that is, pristine graphene with no defects *should* exhibit poor electrochemical behaviour and on the contrary graphene possessing a high degree of defects *should* exhibit improvements in the observed electrochemical rate constant (given the geometric structure of pristine graphene contrasted to graphene with a high level of surface defects).

There is a wealth of literature on graphene which reports that the edge of graphene is particularly more reactive than its side (basal plane). For example, using Raman spectroscopy

Strano and co-workers [21] have reported the reactivity of graphene, that being single-, double-, few- and multi-layer towards electron transfer chemistries with 4-nitrobenzenediazonium tetrafluoroborate. Strano *et al.* [21] interpret their observations with consideration to the Gerischer−Marcus theory which states that the charge transfer depends on the electronic DOS of the reacting species and is not restricted to their Fermi levels only. Calculations presented by Strano *et al.* suggest that double layer graphene is almost 1.6 times more reactive than single layer graphene. [21] Thus based on the DOS, it is clear that double layer graphene (or further graphitic structures consisting of multiple graphene layers) is more reactive than single layer graphene. This has clear implications for graphene as an electrode material; which is the concept that is explored in greater depth throughout this thesis.

2.3. ELECTROCHEMISTRY OF HETEROGENEOUS GRAPHITIC SURFACES

The electrochemical characteristics and reactivity of HOPG has been fully understood by Compton and co-workers, [5] who have shown convincing evidence that edge plane sites/defects are the predominant origin of electrochemical activity. Figure 2.4A shows a schematic representation of the heterogeneous HOPG surface (see Figure 2.2B and C) which has the two distinctive structural contributions, namely edge plane and basal plane sites, each with their own electrochemical activity and thus differing Butler-Volmer terms, k^o and α.

Using a simple redox couple, Figure 2.5 depicts the voltammetry obtained when using either a basal plane pyrolytic graphite (BPPG) (i) or (ii) an EPPG electrode of HOPG, and the responses are compared with numerical simulations (iii) assuming linear diffusion only, in that, all parts of the electrode surface are uniformly (incorrectly) electrochemically active. Two features of Figure 2.5 are to be noted: 1) there is a significant increase in the peak-to-peak

separation, ΔE_P, observed for (iii) over the EPPG voltammetric response (ii); 2) the fit to the 'linear diffusion' only (iii) simulation is not fully satisfactory, especially in the return scan where a significantly lower back peak (current) is observed than expected. [22] It has been shown that the observed voltammetric signature (i) can be correctly and quantitatively simulated through considering the HOPG surface (as shown in Figure 2.2 and 2.4) to be a heterogeneous surface consisting of edge plane nano bands which have been concluded to be exclusively the sites of electro-catalysis whereas the basal plane 'islands' are electro-catalytically inert. [5]

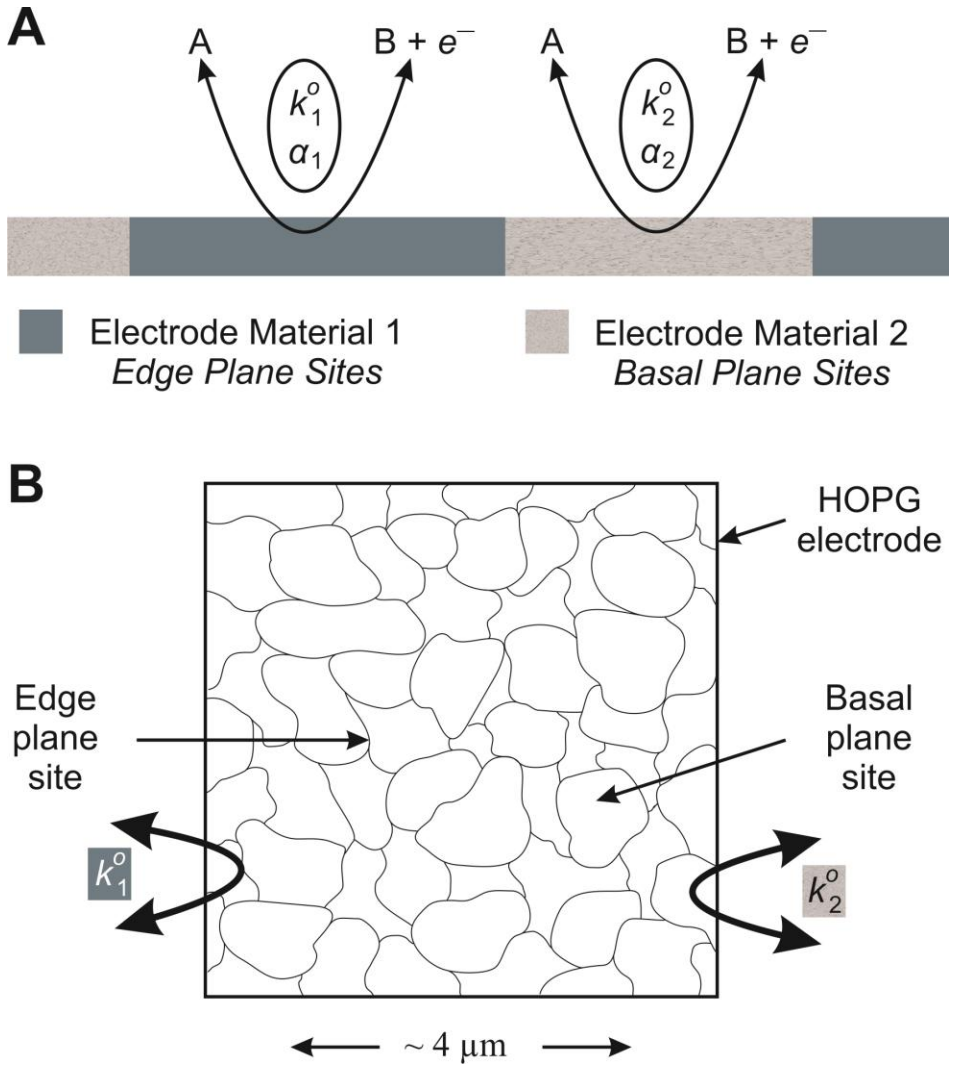

Figure 2.4 *(**A**) Schematic representation of an electrochemical reaction occurring on the same electrode surface with different Butler-Volmer characteristics; and a top-down perspective (**B**).*

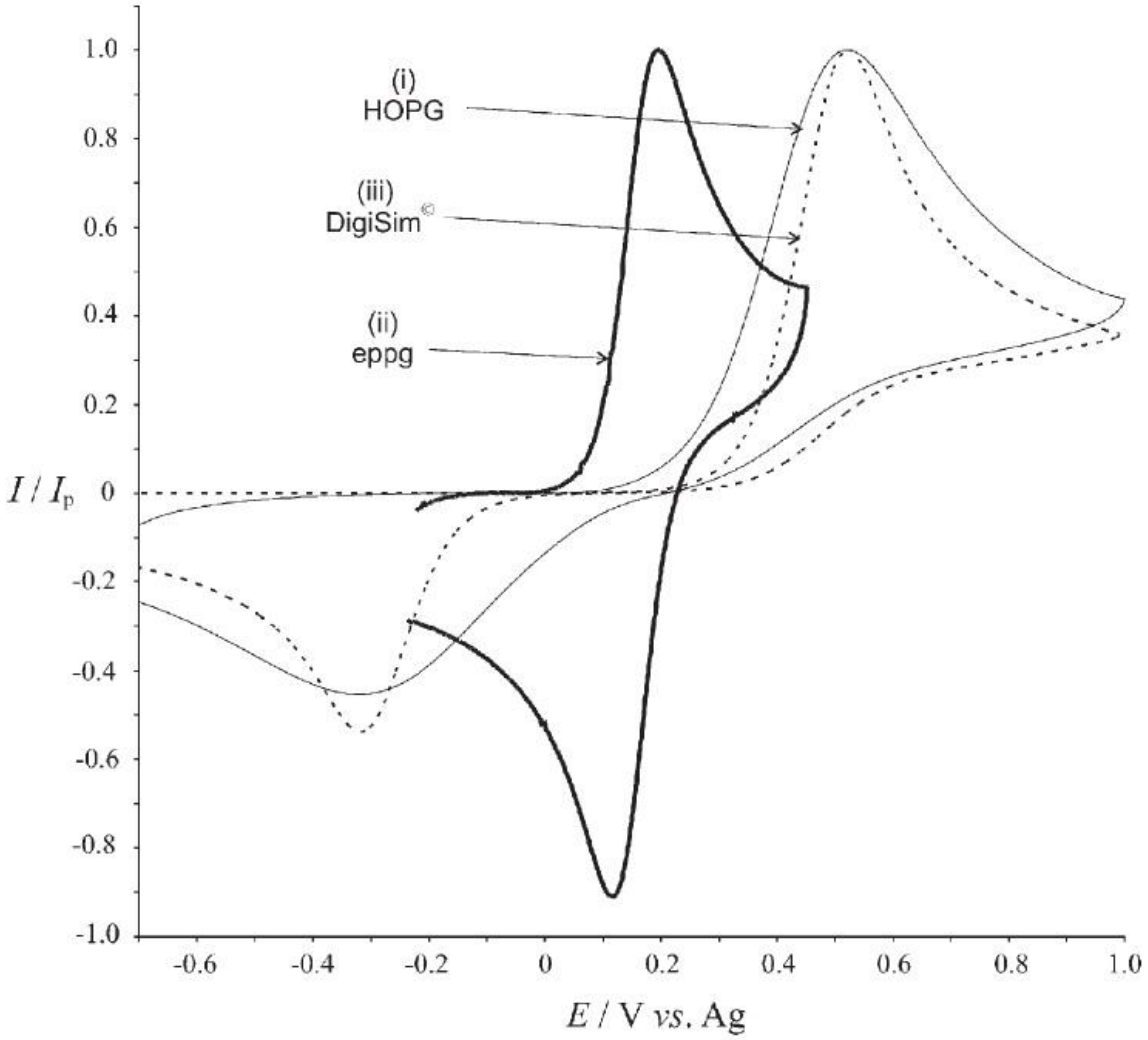

Figure 2.5 *Cyclic voltammograms recorded at 1 Vs^{-1} for the oxidation of 1 mM ferrocyanide in 1 M KCl at a basal plane HOPG electrode and an EPPG electrode. The dashed line voltammogram is the simulated fit using linear diffusion only. Reproduced from Ref. [22].*

Figure 2.6 depicts how the HOPG surface has been simulated using numerical simulation *via* the diffusion domain approach, where each basal plane island and the surrounding edge-plane band is considered as a circular disc of edge-plane graphite partially (or almost completely) covered with basal plane graphite, such that the areas of edge and basal plane are consistent. Since the island and band are surrounded by other island/band combinations, little or zero net flux of electroactive species will pass from one island to its neighbour. [5, 22]

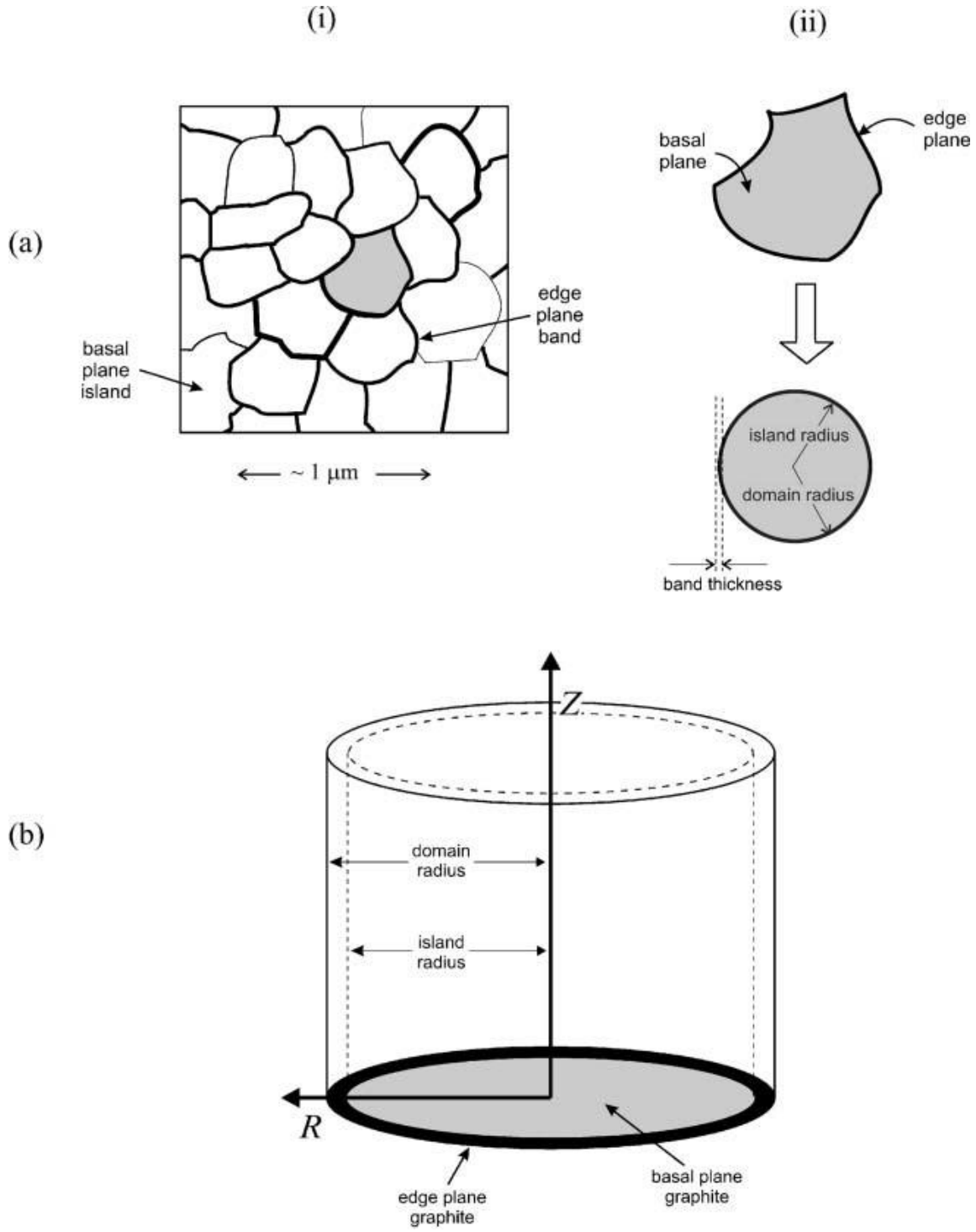

Figure 2.6 *Schematic diagrams showing: (a), (i) the overhead view of a section of the basal plane HOPG surface and (ii) the approximation of each island/band combination as a partially covered circular disc of the same area; (b) the resulting diffusion domain from the approximation in (a) (ii) and the cylindrical coordinate system employed. Reproduced from Ref. [22]. Note that the island radius is termed* R_b *and the domain radius is* R_0.

The circular discs are treated as independent entities with cylindrical walls through which no net flux can pass. These unit cells are better known as diffusion domains and are illustrated in Figure 2.6 where the two electrode materials (edge plane and basal plane) are highlighted. The voltammetric response of the whole HOPG electrode is therefore the sum of that for every domain on the electrode surface. Also shown is a single diffusion domain unit cell and the cylindrical polar coordinate system employed where interacting cylindrical units of radius R_0 are centred around a circular block of radius R_b, where the fractional coverage of the domain, $\theta = R_b^2/R_0^2$ such that the surface areas of the basal sites and edge sites are given by $(1-\theta)\pi R_0^2$ and $\theta\pi R_0^2$ respectively, allowing the effect of varying the edge sites while keeping the surface coverage constant. The island radius is termed as R_b and R_0 is the domain radius which includes the width of the edge plane site/band. As is evident from Figure 2.7, the ΔE_P of the edge plane nano band signal depends strongly on the edge plane coverage, and the domain size has little or no influence on the observed voltammetry of the three smaller domains due to the depleting effect of non-linear diffusion which becomes less relevant as the domain sizes increase. Note that the maximum lateral grain size of HOPG is 1 – 10 μm resulting in a maximum R_0 of *ca*. 0.5 – 5 μm, the edge plane coverage is such that the basal plane is effectively inert [22] and the HOPG response can be assigned to nano bands of edge plane graphite with the basal plane islands having no contribution.

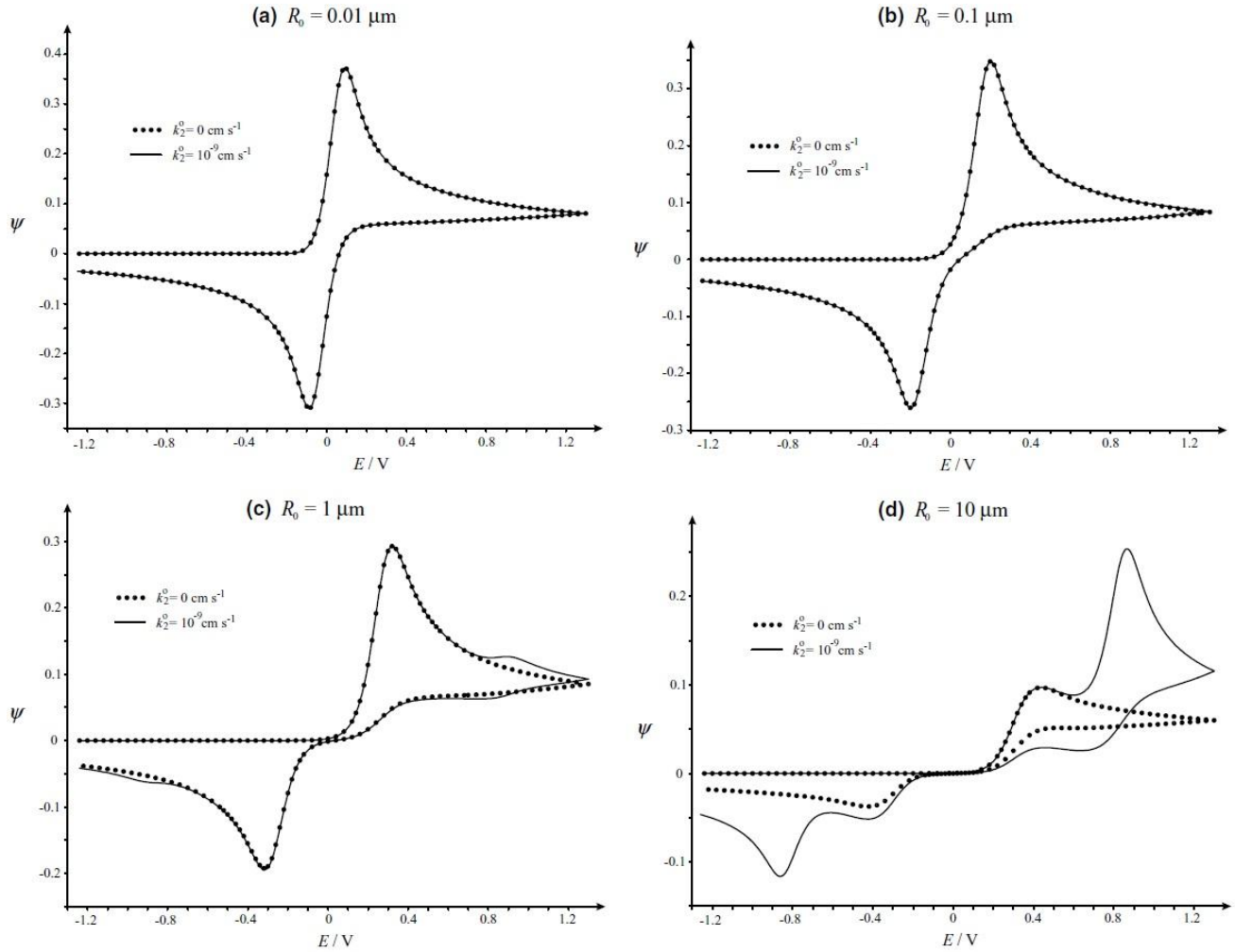

Figure 2.7 *Solid curves are simulated dimensionless current cyclic voltammograms for diffusion domains where D = 6.1 x 10^{-6} cm^2 s^{-1}, $k_1^o = k_{edge}^o$ = 0.022 cm s^{-1}, $k_2^o = k_{basal}^o$ = 10^{-9} cm s^{-1}, υ = 1 V s^{-1}, the band thickness is 1.005 nm and the domain radius is (a) 0.01 µm, (b) 0.1 µm, (c) 1 µm and (d) 10 µm. Overlaid in each section are the simulated inert equivalents (dotted curves), i.e., $k_2^o = k_{basal}^o$ = 0 cm s^{-1}. Reproduced from Ref. [5].*

Further work from the Compton group has explored the 'double peak concept', [1] modelling a HOPG surface as an array of microbands; the unit cell is shown in Figure 2.8A while Figure 2.9 depicts the response of an electrochemically heterogeneous surface, highlighting the effect of microband width along with the domain coordinates utilised where the fractional coverage of the surface covered is given by: $\theta_{band} = r_{band}/r_{domain}$. Figure 2.9A shows that as the width of the band is increased the diffusion profile changes from being largely

convergent, as shown schematically in Figure 2.8B, to that of linear – which is seen as one peak becoming two and a decrease in the peak current is also evident; note that Chapter 1.3 considered the case of mass transport. The depletion of the electroactive species above the electrochemically slower substrate proceeds to a greater extent so the substrate has less of an influence on the diffusion of the electroactive species and thus less of an influence on the observed voltammetry. [1] The depletion, known as the diffusion layer, is given by equation (1.32) where for voltammetry t is replaced by: '$\Delta E/\upsilon$' where ΔE is the potential range over which electrolysis occurs and t (referred to as t_{peak}: below) is the time taken to sweep the potential from its initial value to the point where the current reaches a maxima. It has been shown that: [1]

$$\sqrt{2Dt_{peak}} \gg r_{sep} \tag{2.1}$$

where $$r_{sep} = \frac{1}{2}(r_{domain} - r_{band})$$

where r_{band} is the width of the edge plane site and r_{domain} accounts for the edge plane site *plus* the basal plane site (see Figure 2.8A). In this case, the inter-band separation is small compared to the extent of diffusion parallel to the electrode surface and only one peak will be observed in the voltammetry. Figure 2.9B shows the effect of the band width upon k^o_{subs} and in which region split peaks will be observed. In the case that there is a large domain width, $\sqrt{2Dt_{peak}} \ll r_{sep}$, such that the voltammetry will be a superposition of the voltammetry of the band and substrate in isolation where diffusion to each will be linear in nature.

If the heterogeneous rate constants on the two electrode surfaces are similar, two peaks will be observed arising at similar potentials which will merge into one larger peak. If $k^o_{band} \gg k^o_{subs}$ (*i.e.* $k^o_{edge} \gg k^o_{basal}$) two peaks will be observed if the k^o_{subs} has measurable

activity; however it has been shown that this is not the case and only the k^o_{band} is active, or sometimes reported as anomalously faster over that of k^o_{subs}. [4]

The rate of electron transfer for basal plane sites has been reported to correspond to *ca*. 10^{-9} cm s^{-1} for the oxidation of ferrocyanide and is considered to be possibly even zero. [4-6] *How does one know that this is actually correct?* As shown in Figure 2.9A, a strangely distorted voltammogram would be observed in the limit of very low defect density. [22] Due to the fact that two peaks have never been observed experimentally, it is generally accepted that edge plane electron transfer kinetics are anomalously faster over that of basal plane; the latter is sometimes referred to as being inert. [5, 6, 22]

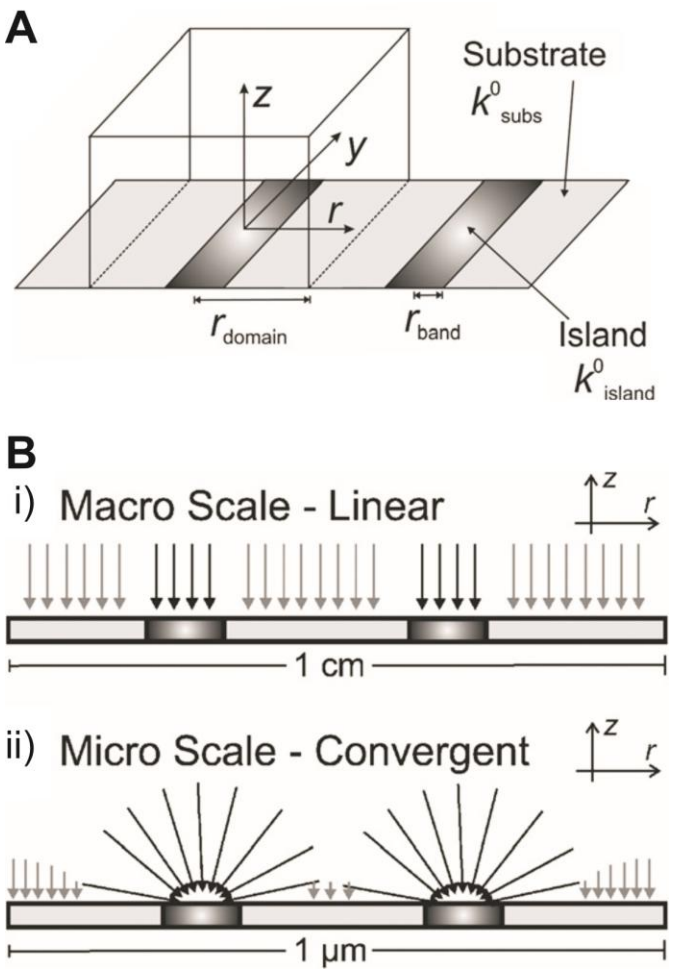

Figure 2.8 *(**A**) The surface is split into a series of identical domains (unit cells), namely band islands. (**B**) Schematic difference between diffusion to macro- (i) and micro- (ii) scale electrode systems. The darker area represents the island (r_{band}) with the faster kinetics. Reproduced from Ref. [1].*

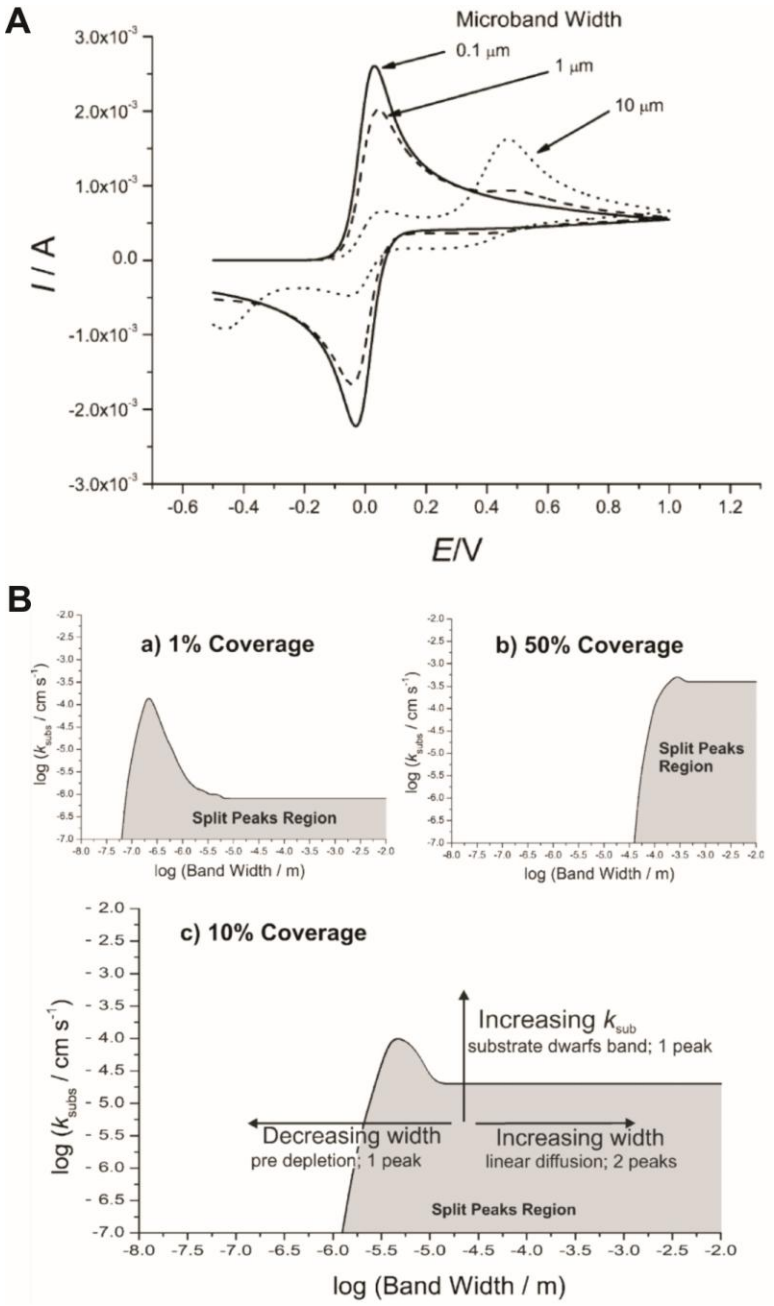

Figure 2.9 *(**A**) Voltammetry of a one-electron transfer process at an electrochemically heterogeneous electrode consisting of an array of microbands (k^o = 10 cm s^{-1}) distributed over a substrate material (k^o = 10^{-6} cm s^{-1}) of area 1 mm^2 and a surface coverage of the bands of 10 % at a scan rate of 0.1 Vs^{-1}. The diffusion coefficient of all species is 10^{-5} cm^2 s^{-1} with an initial concentration of 10 mM. The voltammetry transitions from 1 peak to 2 peaks as the width of the band (labelled) is increased.*
*(**B**) Schematics showing the region of the 'Band Width'-'Substrate rate constant' space for which there are two peaks in the forward sweep of a cyclic voltammogram at band surface coverages of (a) 1 %, (b) 50 % and (c) 10 %. Scan rate = 0.1 Vs^{-1}; diffusion coefficient = 10^{-5} cm^2 s^{-1}; island rate constant k^o_{band} = 10 cm s^{-1}. Reproduced from Ref. [1].*

Further evidence on the role of edge plane sites *versus* basal plane sites has been reported [4] by the selective blocking of the basal plane sites of HOPG with a polymer whilst the edge plane sites were left exposed. Identical voltammetric behaviour was observed with this modified surface when compared to that of the initial bare electrode and with numerical simulations, confirming the edge planes to be the sites of electrochemical activity; Figure 2.10 depicts how this was achieved.

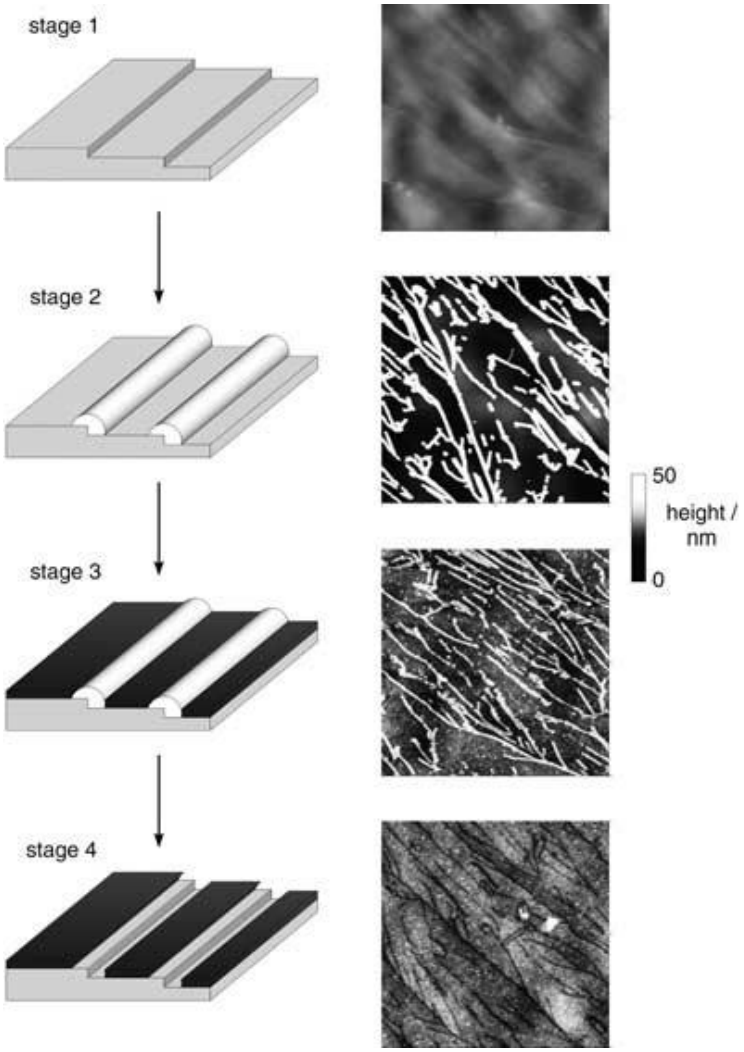

Figure 2.10 *Initially a HOPG surface is cleaved to produce a fresh surface (stage 1). In stage 2, MoO_2 nanowires are formed exclusively along the edge plane sites. In stage 3, the basal plane sites are covered by the electrochemical reduction of 4-nitrobenzenediazonium cations. Stage 4 then involves exposing the edge plane sites by dissolution of MoO_2 in HCl. Reproduced from Ref. [4].*

During each stage (as shown in Figure 2.10) each surface was voltammetrically examined and the corresponding voltammograms are depicted in Figure 2.11. As shown in Figure 2.11 it is evident that the final stage is nearly identical with that of stage 1 (a freshly produced HOPG surface) despite the basal plane sites being covered. The small deviation is reported to be due to the treatments that the electrode has undergone and a slight loss in activity of the edge plan sites. In the case of the modified electrode, Figure 2.11d, only the edge-plane steps located along the bottom of the nanotrenches are exposed to the solution such that an array of nanobands have been created. This work demonstrates that the cyclic voltammetric response of a basal-plane HOPG electrode (BPPG) is solely due to the edge-plane defects present, no matter how small their coverage may be, and that the basal-plane graphite terraces have no influence on the voltammetry and are effectively inert; hence blocking the basal-plane sites results in no overall change to the observed voltammetry.

Last, it is important to note that researchers will (and have already done so) dispute the extensive literature reported above. As such it has been reported that under certain (limited) conditions the basal plane sites have measurable electrochemical activity. [23-25] Using elaborate scanning electrochemical cell microscopy (SECM) it has been reported that the basal plane sites of *freshly exposed* HOPG display considerable electro-activity which, interestingly, is time dependent, in that exposure to air for less than one hour after cleaving leads to a decrease in the observed electron transfer rates at the basal surface. [25] Such work is highly fascinating and studies into this time-dependent surface effect are, at the time of writing this *thesis*, underway. [25] However, ultimately this means that over the lifetime of an experiment the observed electro-activity of the freshly cleaved basal plane sites of HOPG becomes negligible as previously reported. [4-6] Furthermore, an important challenge that has not been realised in

Ref. [25] is the correlation of this local microscopic result to that of the well documented macroscopic response of a HOPG electrode; [26] *i.e.* if such 'pristine' HOPG surfaces, as used within Ref. [25], are used in a conventional cyclic voltammetric experiment do the voltammograms appear fully reversible or not? If so can the pristine surfaces be reproduced by other groups? If not, then why not? [26]

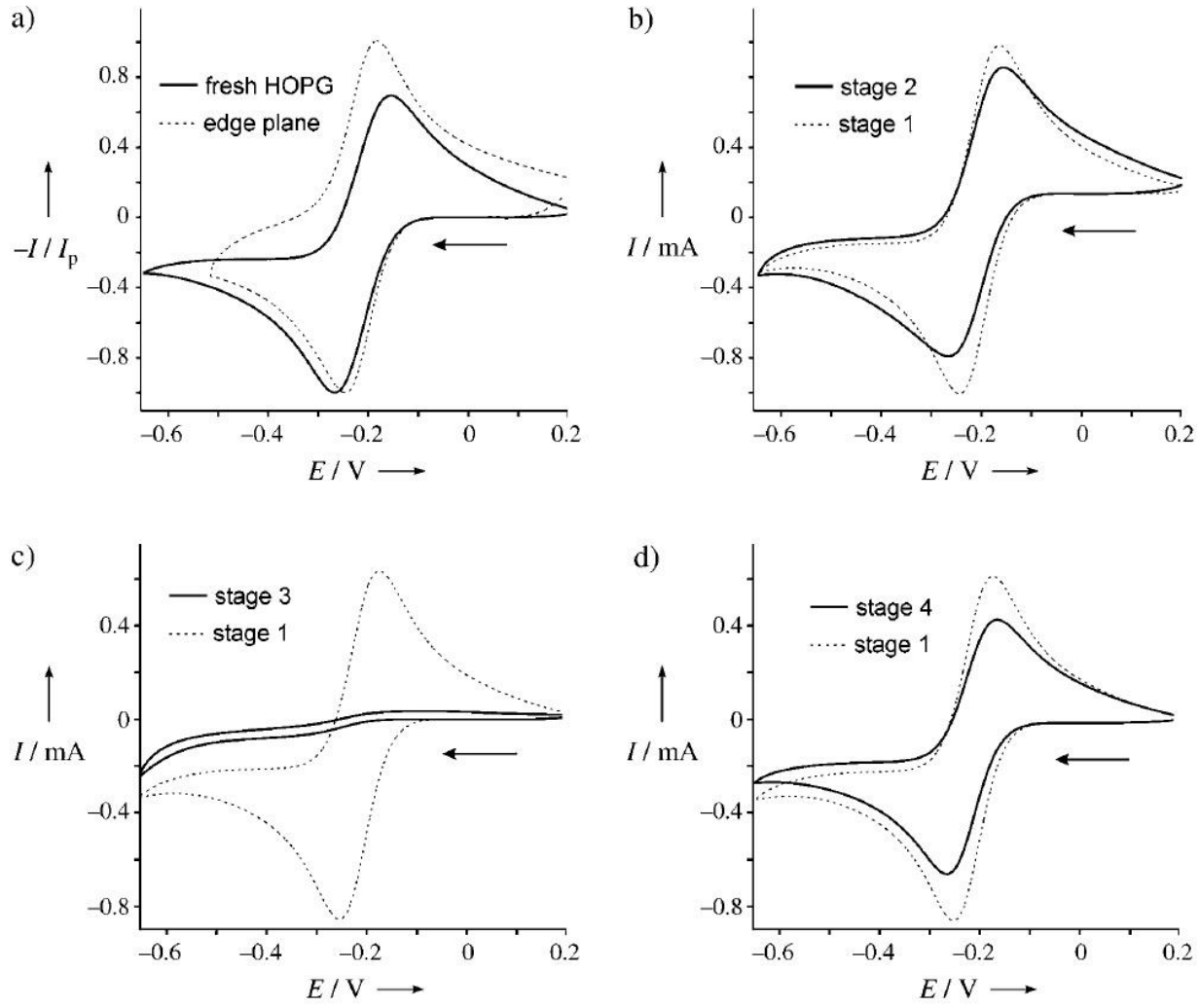

Figure 2.11 *Cyclic voltammograms for the reduction of 1.1 mM $[Ru(NH3)_6]^{3+}$ at a HOPG electrode (vs. SCE) after each stage of nanotrench fabrication (Figure 2.10): a) stage 1, b) stage 2, c) stage 3, d) stage 4. The voltammograms in a) were obtained from the same experiment with an EPPG electrode. Voltammograms in b) through to d) were obtained after stage 1 of nanotrench fabrication. Reproduced from Ref. [4].*

1. K. R. Ward, N. S. Lawrence, R. S. Hartshorne and R. G. Compton, *Phys. Chem. Chem. Phys.*, 2012, **14**, 7264.
2. R. L. McCreery, *Chem. Rev.*, 2008, **108**, 2646.
3. Internet-Resource, Accessed: 18/01/2013; http://www.nanoprobes.aist-nt.com/apps/HOPG%2020info.htm.
4. T. J. Davies, M. E. Hyde and R. G. Compton, *Angew. Chem. Int. Ed.*, 2005, **44**, 5121.
5. T. J. Davies, R. R. Moore, C. E. Banks and R. G. Compton, *J. Electroanal. Chem.*, 2004, **574**, 123.
6. C. E. Banks and R. G. Compton, *Analyst*, 2006, **131**, 15.
7. Internet-Resource, *Graphene Supermarket Ltd.*, Accessed: 28/02/2012; http://www.graphene-supermarke.com.
8. A. Dato, V. Radmilovic, Z. Lee, J. Phillips and M. Frenklach, *Nano Lett.*, 2008, **8**, 2012.
9. M. Lotya, P. J. King, U. Khan, S. De and J. N. Coleman, *ACS Nano*, 2010, **4**, 3155.
10. Internet-Resource, *Nano Integris Ltd.*, Accessed: 28/02/2012; http://www.nanointegris.com.
11. X. Li, C. W. Magnuson, A. Venugopal, R. M. Tromp, J. B. Hannon, E. M. Vogel, L. Colombo and R. S. Ruoff, *J. Am. Chem. Soc.*, 2011, **133**, 2816.
12. D. A. C. Brownson and C. E. Banks, *Phys. Chem. Chem. Phys.*, 2012, **14**, 8264.
13. D. A. C. Brownson, D. K. Kampouris and C. E. Banks, *Chem. Soc. Rev.*, 2012, **41**, 6944.
14. K. K. Cline, M. T. McDermott and R. L. McCreery, *J. Phys. Chem.*, 1994, **98**, 5314.
15. R. Nissim, C. Batchelor-McAuley, M. C. Henstridge and R. G. Compton, *Chem. Commun.*, 2012, **48**, 3294.
16. R. L. McCreery and M. T. McDermott, *Anal. Chem.*, 2012, **84**, 2602.
17. N. M. R. Peres, L. Yang and S.-W. Tsai, *New J. Phys.*, 2009, **11**, 095007.
18. D. Jiang, B. G. Sumpter and S. Dai, *J. Chem. Phys.*, 2007, **126**, 134701.
19. M. Pumera, *Chem. Soc. Rev.*, 2010, **39**, 4146.
20. Y. Shimomura, Y. Takane and K. Wakabayashi, *J. Phys. Soc. Jpn.*, 2011, **80**, 054710.
21. R. Sharma, J. H. Baik, C. J. Perera and M. S. Strano, *Nano Lett.*, 2010, **10**, 398.
22. C. E. Banks, T. J. Davies, G. G. Wildgoose and R. G. Compton, *Chem. Commun.*, 2005, 829.
23. M. A. Edwards, P. Bertoncello and P. R. Unwin, *J. Phys. Chem. C*, 2009, **113**, 9218.
24. C. G. Williams, M. A. Edwards, A. L. Colley, J. V. Macpherson and P. R. Unwin, *Anal. Chem.*, 2009, **81**, 2486.

25. S. C. S. Lai, A. N. Patel, K. McKelvey and P. R. Unwin, *Angew. Chem., Int. Ed.*, 2012, **51**, 5405.

26. C. Batchelor-McAuley, E. Laborda, M. C. Henstridge, R. Nissim and R. G. Compton, *Electrochim. Acta*, 2013, **88**, 895.

CHAPTER 3: INTRODUCTION TO GRAPHENE

This chapter first explores the fascinating story behind graphene's emergence onto the scientific horizon, thereafter focusing on the various methodologies for fabricating graphene before finally depicting the truly outstanding and exceptional properties of graphene to be reported in the literature, which have captured the imagination of scientists in a plethora of disciplines.

3.1. THE ORIGINS OF GRAPHENE

According to IUPAC, the suggested definition of graphene is: "*a single carbon layer of the graphite structure, describing its nature by analogy to a polycyclic aromatic hydrocarbon of quasi infinite size*". [1] It is then noted by IUPAC that "*previously, descriptions such as graphite layers, carbon layers or carbon sheets have been used for the term graphene. Because graphite designates that modification of the chemical element carbon, in which planar sheets of carbon atoms, each atom bound to three neighbours in a honeycomb-like structure, are stacked in a three-dimensional regular order, it is not correct to use for a single layer a term which includes the term graphite, which would imply a three-dimensional structure. The term graphene should be used only when the reactions, structural relations or other properties of individual layers are discussed*"; [1] a conceptual depiction along with scanning electron microscope (SEM) and transmission electron microscope (TEM) images of the graphene structure are shown in Figure 3.1.

3.1.1. GRAPHENE: A BRIEF HISTORY

The exact history of graphene and how it appeared on the scientific horizon is fascinating. In theory, as an integral part of various three-dimensional materials, graphene has

been studied since the 1940s. [2, 3] In 1947 Philip Wallace wrote a pioneering paper concerning the electronic behaviour of graphite that sparked interest into the exploration of graphene, [3] however it was not until the recent work of Novoselov *et al.* [4, 5] and Zhang *et al.* [6] that interest in graphene escalated due to reports of its unique properties. [7]

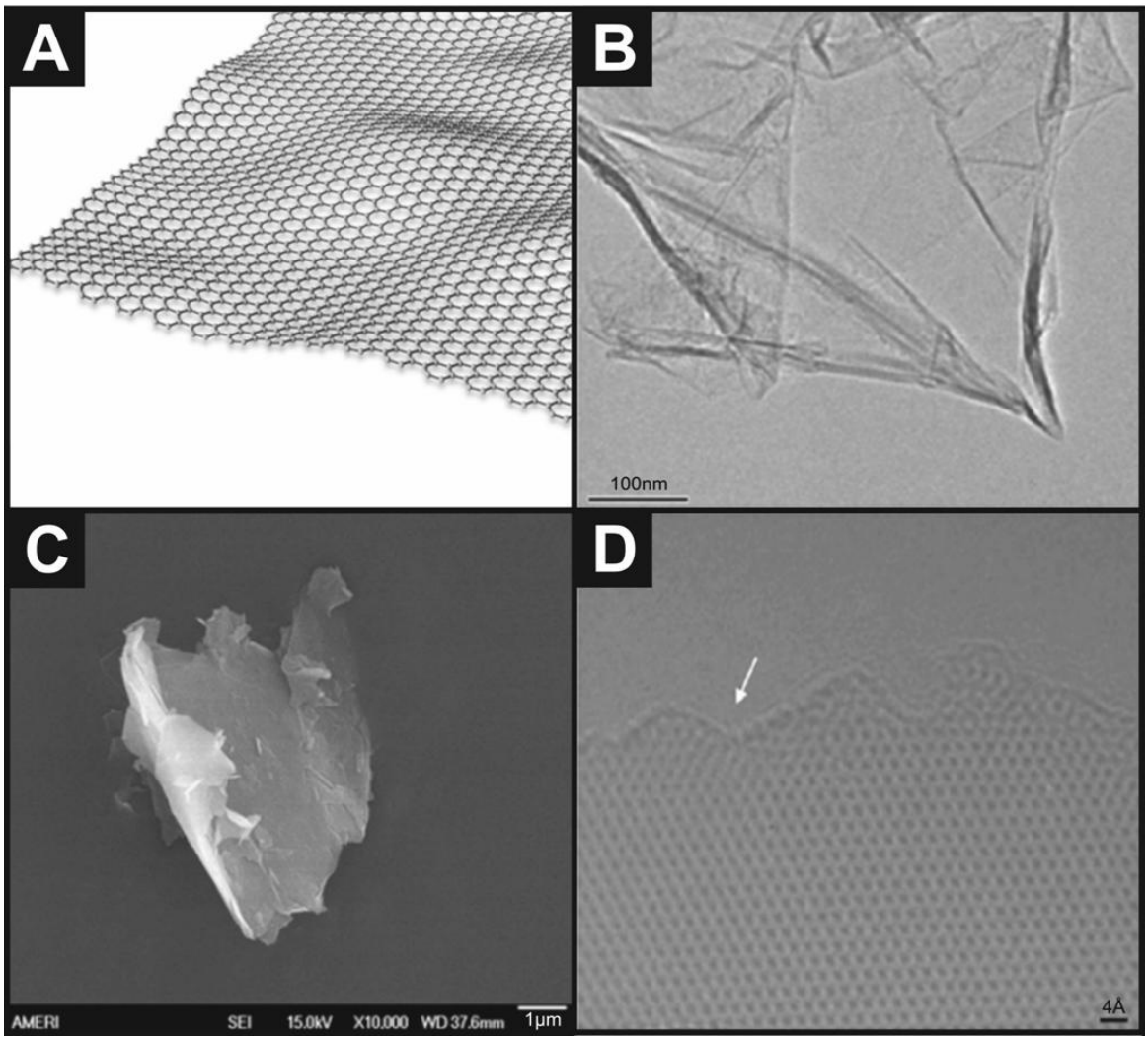

Figure 3.1 *A conceptual model depicting the structure of graphene (**A**) and TEM (**B**) / SEM (**C**) images of a single atomic layer of graphite, known as graphene. A high-resolution TEM (**D**) image is also shown, where the white arrow indicates the edge of the graphene sheet. Note, in reality the graphene utilised in the majority of work is 1 – 4+ layers thick. **B** and **D** are reproduced from Ref. [8] and **C** is reproduced from Ref. [9].*

In 2004 Novoselov and co-workers reported the development of a simple, yet time consuming methodology in which one could produce and observe microscopic few-layer graphene crystals on silicon wafers (silicon dioxide on silicon). [4] Subsequently, this technique has been copied globally as a protocol to produce large area single layer graphene samples, allowing two-dimensional transport studies to be performed. [10] In 2010 the Nobel Prize in Physics was awarded jointly to Geim and Novoselov for ground breaking experiments regarding the two-dimensional material graphene. [11] However, as highlighted by de Heer, [10] there is a common misconception regarding the 2004 paper by Novoselov and Geim. In his letter to the Nobel Committee addressing such issues (a copy of which can be found at Appendix A.2), de Heer noted that the majority of scientific publications incorrectly cite the 2004 report as the paper that presented both the 'scotch tape method' and graphene's unique electronic properties to the world. [10] In fact such findings were not reported with regards to individual single layer graphene in 2004, [4] but actually in a 2005 paper by Novoselov and Geim. [5, 10] Furthermore, in reality, graphene had been identified and characterised as a two-dimensional-crystalline material in many reports prior to 2004 where ultra-thin graphitic films were observed and occasionally even monolayer graphene (see for example Ref. [7] and [12] for pertinent reviews). [10, 13]

Dryer and co-workers [12] have elegantly produced a detailed account of the synthesis and characterisation of graphene; Figure 3.2 shows a timeline representing the history of the preparation, isolation and characterisation of graphene as given in Ref. [12]. Of note is that in 1962, H-P. Boehm, who coined the name graphene in 1986, [14-16] reported his observations of graphene and demonstrated beyond reasonable doubt the existence of freestanding graphene. [14-16] Dryer and co-workers point out that in the 1962 report, Boehm *et al.* isolated reduced graphene oxide with heteroatomic contamination rather than pristine graphene, [17] where ultimately as a

result of this the electrical conductance is significantly lower for this material than for pristine graphene prepared by the 'scotch tape method'. [16-19] Of historical significance is that, excluding the work of Boehm *et al.*, reports of graphene prior to 2004 were merely observational and failed to describe any of graphene's distinguishing properties. [7, 12] Thus, the 2005 report by Novoselov and Geim can be considered as the first to report both the isolation of 'pristine' graphene (*i.e.* single layer graphene without heteroatomic contamination) and its unique properties to the world; which in doing so sparked the graphene gold rush and brought new and exciting physics to light. [7, 12]

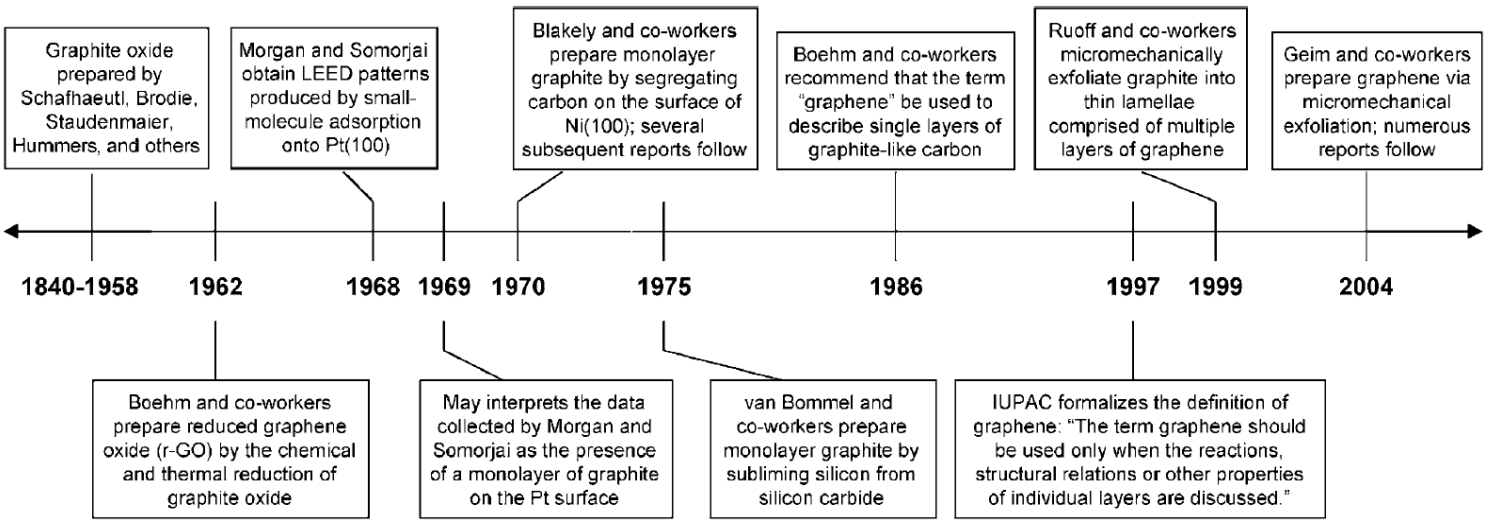

Figure 3.2 *A timeline of selected events in the history of graphene for its preparation, isolation and characterisation. Reproduced from Ref. [[12]].*

Since the pioneering reports of 2004/5 many other unique properties have been assigned to graphene (see Chapter 3.3) and a significant array of other methodologies has been reported regarding its fabrication (see Chapter 3.2). [20-28] Graphene has truly captured the imagination of scientists from around the globe and is now an extensive and vibrant area of research, where its

utilisation has resulted in an improved understanding of fundamental factors in addition to significantly enhanced device performance in a wide range of scientific fields.

3.1.2. GRAPHENE: MEET THE FAMILY

Pristine graphene is a two-dimensional sp^2 bonded carbon nanostructure. [2, 29] Most significantly however, graphene is a key derivative of carbon and originates from a large family of fullerene nanomaterials where it is the essential 'building block' for many of the allotropic dimensionalities that have significant and widespread use as electrode materials. [2, 29]

The constituent atoms of graphite, fullerenes and graphene share the same basic structural arrangement in that each structure begins with six carbon atoms which are tightly bound together (chemically, with a separation of *ca*. 0.142 nm) in the shape of a regular hexagonal lattice. [30] At the next level of organisation graphene is widely considered as the 'mother of all graphitic forms', where, as depicted in Figure 3.3, in addition to existing in its planar state a singular graphene sheet can be 'wrapped' into a zero-dimensional spherical C_{60} buckyball, 'rolled' into a one-dimensional carbon nanotube (CNT) (further categorised into single- or multi- walled depending on the number of graphene layers present (SWCNTs/MWCNTs respectively)), or multiple graphene sheets can be 'stacked' into three-dimensional graphite (generally consisting of $\geq$ 8 graphene layers, *vide infra* for more details); the stacked graphene sheets/planes in graphite are separated by a distance of 0.335 nm and are held together by weak, attractive intermolecular forces. [30]

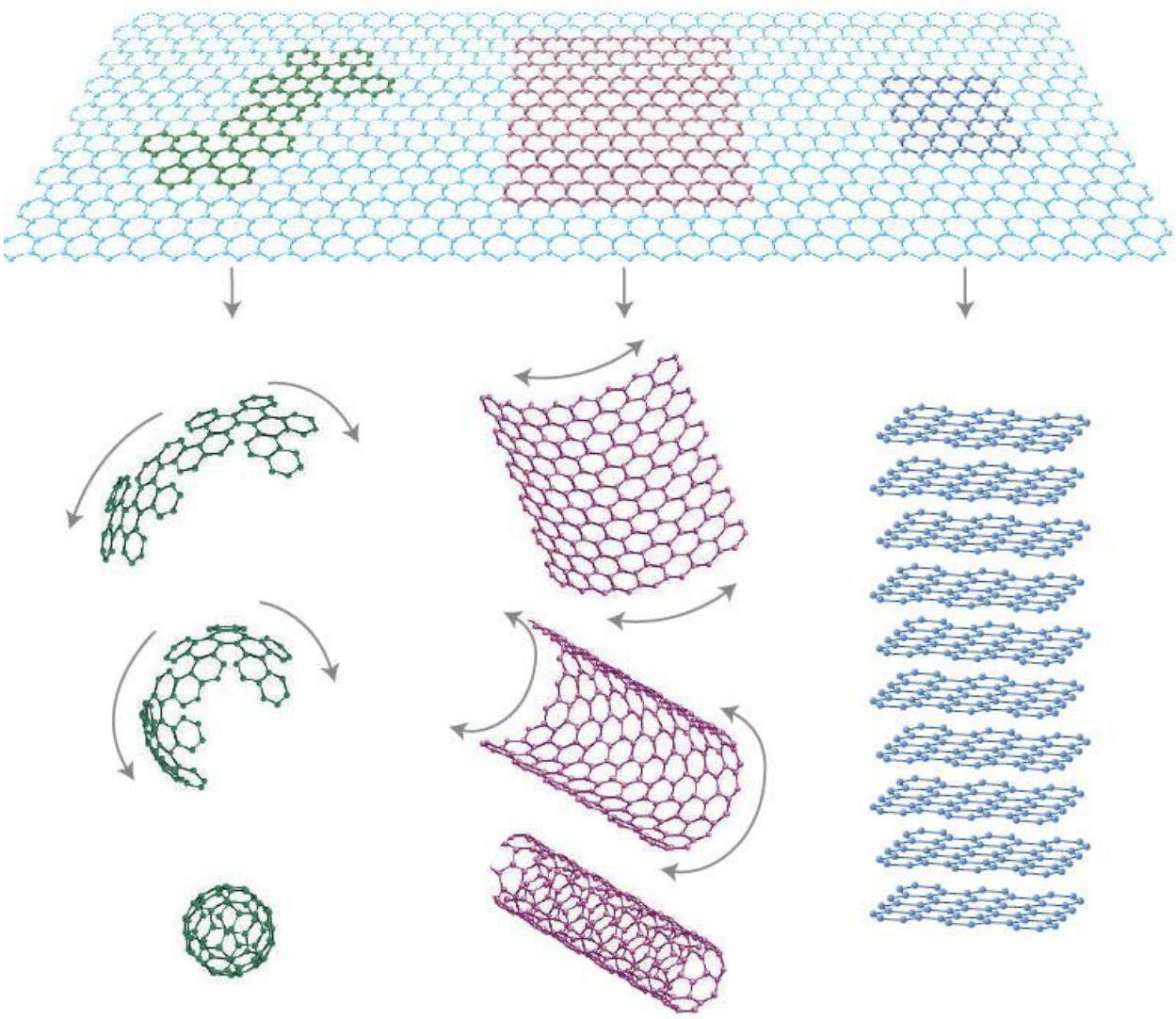

Figure 3.3 *The "mother of all graphitic forms". Schematic representation of graphene, which is the fundamental starting material for a variety of fullerene materials; C_{60} (buckyballs) (bottom row at the left), CNTs (bottom row in the centre), and graphite (bottom row at the right). Reproduced from Ref. [2].*

It is important to note that the graphene structure itself (that is, in its standard pristine form, a single layer/sheet of the carbon structure) is often referred to as a graphene nano sheet (GNS) which implies a large, scalable graphene sheet of 'quasi-infinite size'; however, variations in the graphene structure do exist. Graphene nano ribbons (GNRs) are strips of graphene that

possess an ultra-thin width (< 50 nm) (note that other various shapes also exist), [31] whereas graphene nano-platelets are a further variation (often referred to as double-, few-, or multi-layered graphene sheets) which are characterised by stacks consisting of between two and seven graphene sheets and thus should not be considered as graphene (which implies one individual carbon layer) or graphite (which implies a structure of eight or more graphene layers) but as an intermediate phase with distinct properties that vary accordingly with increasing layer numbers until the graphite structure is achieved; [32-35] this intermediate phase of graphene/graphite is known as *quasi*-graphene, [36] however given the varying properties it is wise to state the number of graphene layers when working within this subgroup. Increasing the number of graphene layers past eight results in negligible alterations in terms of the evolution of the electronic structure and various other properties of graphene and such structures are thus to be considered as graphite (as determined by Raman spectroscopy and SECM). [32-35]

Finally, another form of graphene that is commonly employed across the literature is that of graphene oxide (GO). GO consists of graphene that has been oxidised within the employed fabrication process or spontaneously by contact with air, however, this form is usually chemically or electrochemically reduced before use (see Chapter 3.2.3). [37] Depending on the fabrication approach utilised to synthesise GO its structure varies significantly in terms of the presence of specific oxygenated species and their given quantities; Figure 3.4 depicts the proposed structure of GO as produced through varied methodologies. It is important to bear in mind that different oxygenated species present on various GOs will significantly influence the observed electrochemical response.

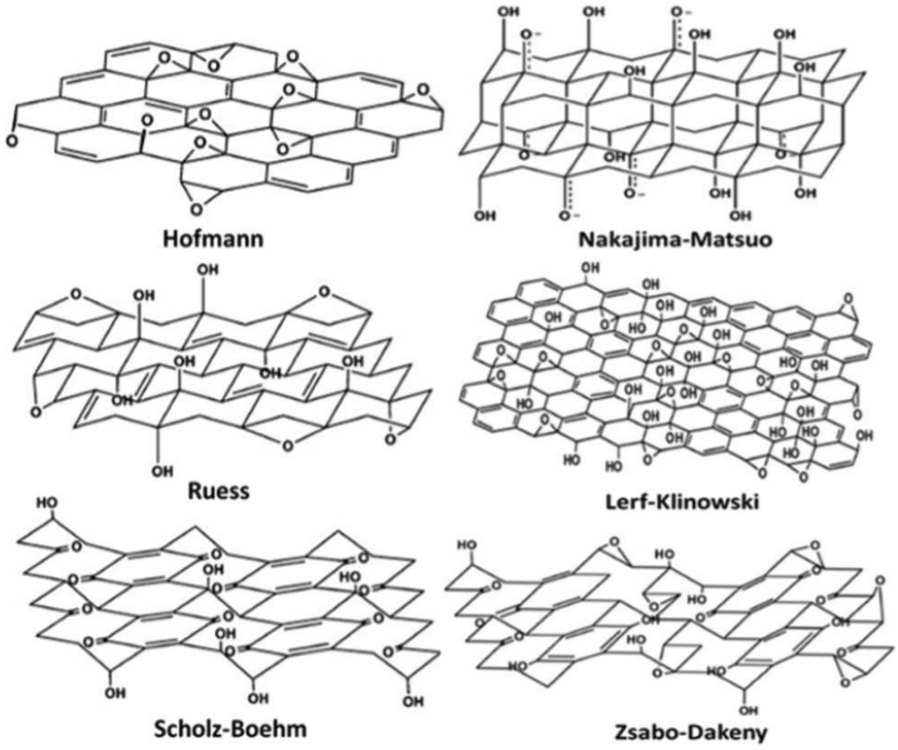

Figure 3.4 *Proposed configurations for GO when synthesised via varying routes. Reproduced from Ref. [38, 39].*

3.2. FABRICATING GRAPHENE

Preparative methods of graphene are currently a heavily researched and important issue. The search for a methodology that can reproducibly generate high quality monolayer graphene sheets with large surface areas and large production volumes is greatly sought-after. Consequently, several physical and chemical methods exist for the production of graphene, which include the mechanical or chemical exfoliation of graphite, unrolling of CNTs (either through electrochemical, chemical or physical methods), chemical vapour deposition (CVD) or epitaxial growth, reduction of GO and many other organic synthetic protocols. [17, 29, 40-42] It is important to note however that each method has innate advantages and disadvantages in terms of the resultant quality (properties), quantity and thus electrochemical applicability of the graphene

produced and that there is presently no single method that exists for the production of graphene sheets that are suitable for all potential applications. [29, 42] Table 3.1 gives a direct comparison of selected graphene fabrication methodologies with their inherent advantages and disadvantages.

3.2.1. MECHANICAL EXFOLIATION

Among the methods stated above, dry mechanical exfoliation remains one of the most popular and successful methods for producing single- or few- layers of graphene. [43] This approach is known as the so-called "scotch tape method". As highlighted in Figure 3.5, D.I.Y. graphene is possible given that this method is relatively simple. The process involves cleaving a sample of graphite (usually HOPG) with a cellophane-based adhesive tape. [4] The number of graphene layers formed can be controlled to a limited degree *via* the number of repeated peeling steps performed prior to the flakes then being transferred to appropriate surfaces for further study; however, as depicted in Figure 3.5 and 3.6A, when present, single layer graphene crystals are usually integrated with few- and multi- layer graphene crystals and it is a difficult process to separate out these individual graphene sheets. Nonetheless, this method is ideally suited for the investigation of graphene's physical properties given that it does allow the low cost isolation of single graphene sheets that are of high quality. [4, 41] However, disadvantages including poor reproducibility, low-yield and the labour intensive processes required result in it being difficult to scale this process to mass production and have thus lead to this method being used predominantly only for fundamental studies. [41] Moreover, this process generally yields graphene flakes of small sizes, although graphene flakes with sizes of up to 1 mm have been obtained; see Figure 3.6B. A further disadvantage of this process is the possible damage (disrupting the basal surface, *viz* the generation of edge plane like- sites/defects) and

Table 3.1 *Comparison of various graphene fabrication methodologies commonly utilised to obtain graphene for electrochemical studies. Reproduced from Ref. [44].*

Fabrication method	Graphene precursor	Operating conditions	Advantages	Disadvantages	Application implications	Ref.
Mechanical exfoliation	HOPG	Scotch-tape	Direct, simple, high structural and electronic quality, low cost	Delicate and time-consuming (hours), low yields, poor reproducibility, possible contamination of sample from the adhesive tape utilised	Fundamental research. High quality single layer graphene sheets obtained with little lattice defect density and domain sizes ranging from 500 Å up to 10 µm	4, 41, 43
Chemical exfoliation	Graphite	Dispersion and exfoliation of graphite in organic solvents or through the use of surfactant complexes	Direct, simple, large-scale production, low-cost, high yield, practicability of sample handling (liquid suspension)	Time-consuming (hours), impure, possible contamination of sample from surfactant or solvents utilised	General graphene research for modified substrates. Often multiple layered graphene incorporated with structural defects originating from the fabrication process with domain size ranging from 500 Å up to 1500 Å	41-43, 45, 46
Reduction of GO	Graphite	Graphite exfoliation and oxidation, subsequent reduction of exfoliated graphite oxide	Facile scalability, high yields, low cost, excellent processability, practicability of sample handling (liquid suspension)	Indirect, large number of structural defects, disruption of the electronic structure of graphene owing to impurities, reduction to graphene is often not complete	General graphene research for modified substrates. Often multiple layered graphene incorporated with structural defects originating from the fabrication process with domain size ranging from 500 Å up to 1500 Å	29, 41-43
CVD	Hydrocarbon gas (primarily)	CVD under variable temperatures and pressures (see Table 3.2)	Large-scale production, high qualities, uniform films, tailoring of graphene quality possible (see Table 3.2)	High temperature requirements, high cost, complicated process, variable yields	Fundamental and basic research. High quality single layer graphene sheets obtained with little lattice defect density, however, graphene can be tailored to contain specific defects and impurities where these are required for beneficial implementation in given devices. Layer thickness and domain sizes are thus variable (see Table 3.2)	43, 47, 48

Abbreviations; CVD: chemical vapour deposition; GO: graphene oxide; HOPG: highly ordered pyrolytic graphite.

D.I.Y. Graphene

1 Work in a clean environment; stray dirt or hair plays havoc with graphene samples.

2 Prepare a wafer of oxidized silicon, which helps you see graphene layers under a microscope. To smooth out the surface to accept the graphene and to clean it thoroughly, apply a mix of hydrochloric acid and hydrogen peroxide.

3 Attach a graphite flake to about six inches of plastic sticky tape with tweezers. Fold the tape at a 45-degree angle right next to the flake, so that you sandwich it between the sticky sides. Press it down gingerly and peel the tape apart slowly enough so that you can watch the graphite cleaving smoothly in two.

4 Repeat the third step about 10 times. This procedure gets harder to do the more folds you make.

5 Carefully lay the cleaved graphite sample that remains stuck to the tape onto the silicon. Using plastic tongs, gently press out any air between the tape and sample. Pass the tongs lightly but firmly over the sample for 10 minutes. With the tongs, keep the wafer planted on the surface while slowly peeling off the tape. This step should take 30 to 60 seconds to minimize shredding of any graphene you have created.

6 Place the wafer under a microscope fitted with a 50× or 100× objective lens. You should see plenty of graphite debris: large, shiny chunks of all kinds of shapes and colors (*upper image*) and, if you're lucky, graphene: highly transparent, crystalline shapes having little color compared with the rest of the wafer (*lower image*). The upper sample is magnified 115×; the lower 200×.

—JR Minkel, online news reporter

Figure 3.5 *"D.I.Y. graphene: how to make one-atom-thick carbon layers with sticky tape". Reproduced from Ref. [30].*

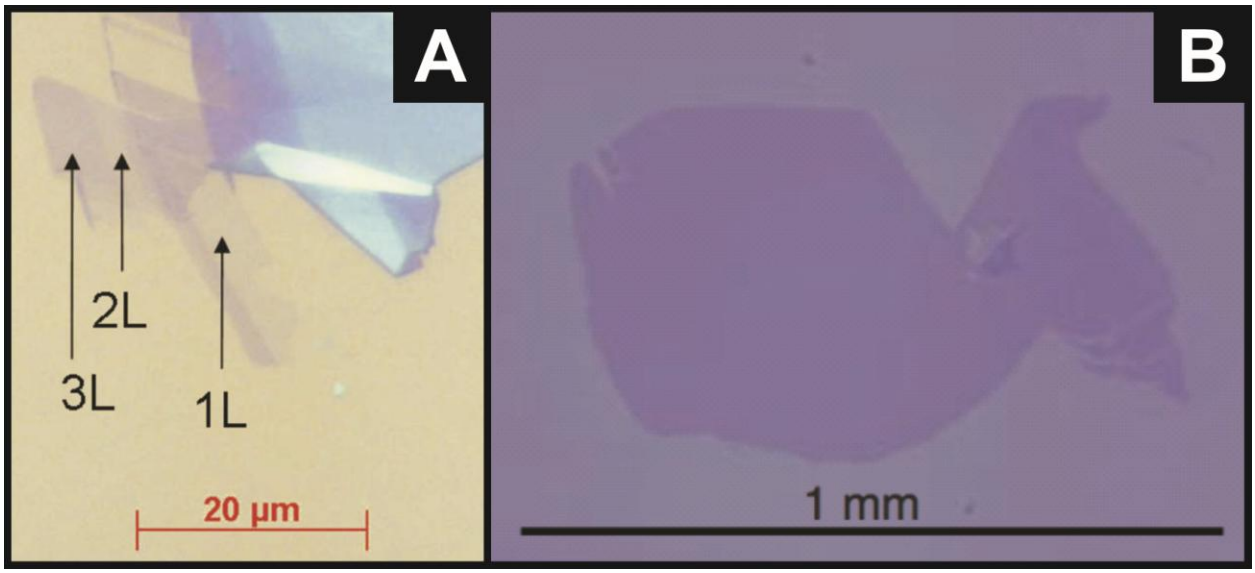

Figure 3.6 *(**A**) Optical microscopy image of single-, double- and triple- layer graphene (labelled as 1L, 2L and 3L respectively) on Si with a 300 nm SiO_2 over-layer. Reproduced from Ref. [49]. (**B**) Monolayer graphene, produced by mechanical exfoliation, on a Si/SiO_2 wafer. This is a large sample with a length of 1 mm. Reproduced from Ref. [50].*

contamination of the graphene samples, particularly from the adhesive utilised in the cellophane-based tape, which renders this method less appealing for the electrochemical investigation of pristine graphene.

3.2.2. CHEMICAL EXFOLIATION

An alternative preparative method that is commonly utilised owing to the ease of production, high-yield and relative low cost is the chemical exfoliation of graphite. [41] This includes ultrasound in both solution and intercalation steps, usually prior to the implementation of a centrifugation technique. For example, one ultrasonication route entails the use of a water-surfactant solution, sodium cholate, [46] which forms stable encapsulation layers on each side of the graphene sheets; graphite flakes are dispersed in the aqueous surfactant solution and transformed into monolayer graphene by the application of ultrasound, resulting in

graphene-surfactant complexes having buoyant densities that vary with graphene thickness. [46, 51] Following sonication the obtained solutions undergo centrifugation, which results in a 'sorting' of the graphene and hence different fractions are observed meaning that graphite and multi-layer graphene are not inadvertently incorporated into the graphene samples; after which the upper part of the resultant supernatant contains single layers of graphene floating in the solution which are then transferred using a pipette and dropped onto the surface of choice for further study. [46] Note that graphene fabricated *via* this route is readily commercially available. [51, 52] This procedure is also possible without additives in many organic solvents that have a high affinity for graphite where ultrasonic agitation is used to supply the energy to cleave the graphene precursor. [23] The success of ultrasonic cleavage depends on the correct choice of solvents and surfactants as well as the sonication frequency, amplitude and time. [45] Note that as with mechanical exfoliation, the quality of the obtained graphene is not always sufficient (structural damage to the graphene can occur during preparation owing to ultrasonication, which may result in the graphene possessing a high defect density) and additionally homogeneity of the number of graphene layers is often poor, [41] thus graphitic impurities may remain. Note also that material produced *via* such means often contains remains from the exfoliating agents utilised. These impurities can possibly have a significant effect on the observed electrochemical characteristics and performance of the graphene sample.

3.2.3. REDUCTION OF GRAPHENE OXIDE (GO)

Another popular aqueous based synthetic route for the production of graphene utilises GO. [29, 41] GO is produced *via* '*graphite oxide*' which itself can be fabricated *via* various different routes. The Hummers method for example involves soaking graphite in a solution of sulphuric acid and potassium permanganate to produce graphite oxide. [41, 53] Stirring or sonication of the

graphite oxide is then performed to obtain single layers of GO – this is achieved given that GO's functional groups render it hydrophilic, allowing it to be dispersed in water based solutions. Finally, GO is chemically, thermally or electrochemically reduced to yield graphene. [40, 41] Note that the majority of graphene used in electrochemistry is produced through the reduction of GO (often referred to as 'reduced GO' or 'chemically modified graphene'). It is important to note that graphene produced in this manner usually has abundant structural defects (edge plane like-sites/defects) [17, 54] and remaining functional groups which results in partially functionalised graphene and thus is not pristine graphene: this may therefore have implications with regards to contributory factors influencing the observed electrochemistry. This method has the advantages of being scalable, rapid and cost effective in addition to the beneficial handling versatility of the liquid suspension; [42] however, (as stated above) reduction to graphene is often only partial, lattice defects and graphitic impurities can also remain after reduction and additional interferences may arise in this case from the presence of reducing agents.

3.2.4. MISCELLANEOUS FABRICATION

Note that recent developments have led to the commercial availability of 'pristine' graphene that is produced *via* a substrate-free gas-phase synthesis method. [8, 26, 55] This single-step technique involves sending an aerosol consisting of liquid ethanol droplets and argon gas directly into a microwave-generated argon plasma (at atmospheric-pressure), where over a time scale in the order of 10^{-1} s, ethanol droplets evaporate and dissociate in the plasma forming solid matter that through characterisation by transmission electron microscopy (TEM) and Raman spectroscopy is confirmed to be clean and highly ordered graphene sheets that are similar in quality to the graphene obtained through the mechanical exfoliation of HOPG. [8, 26, 55] When commercially available, the fabricated graphene sheets are sonicated in ethanol to form a

homogeneous suspension before being distributed by the supplier. [55] Production in this manner has proven that graphene can be created without the use of three-dimensional materials as precursors or supporting substrates, and has demonstrated the viability of the large-scale synthesis of graphene.

3.2.5. CHEMICAL VAPOUR DEPOSITION (CVD) FABRICATION

One of the most interesting fabrication approaches is the CVD growth of graphene. This method appears ideally suited for applications within electrochemistry with regards to the prevalence of uniform graphene sheets with high crystal quality and large surface areas, which are readily transferable and can be obtained at large manufacturing volumes. [56, 57] Additionally, CVD fabricated graphene is often supported on a (desirable and suitable) solid substrate and as such the positioning and orientation of the graphene can be precisely manipulated for specific purposes, alleviating issues with regards to the controlled placement of solution based graphene sheets and in terms of the natural formation of graphite once the solvent is removed, as has been reported in some cases. [44] The underlying principle of CVD is to decompose a carbon feedstock with the help of heat in order to provide a source of carbon which can then rearrange to form sp^2 carbon species. This is usually accomplished over a catalyst; [41] for the growth of graphene, hydrocarbon gases are generally utilised as precursors and the most successful catalysts thus far are transition metal surfaces (namely nickel and copper). [47] Figure 3.7 illustrates the three main stages of graphene growth over a copper catalyst *via* a CVD process.

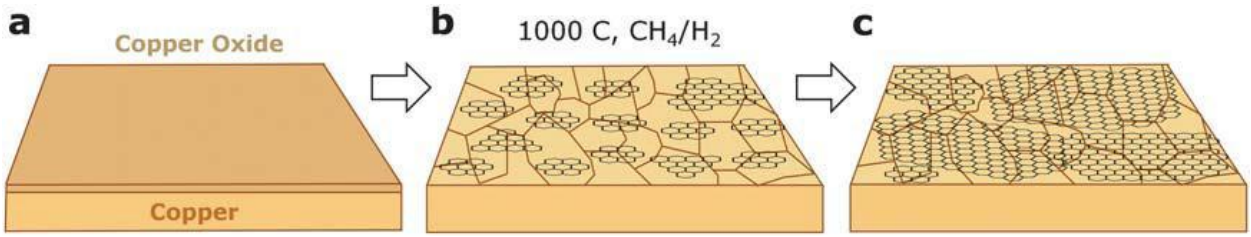

Figure 3.7 *Schematic illustrating the three main stages of graphene growth on copper by CVD: (a) copper foil with native oxide; (b) the exposure of the copper foil to CH_4/H_2 atmosphere at 1000 °C leading to the nucleation of graphene islands; (c) enlargement of the graphene flakes with different lattice orientations. Reproduced from Ref. [58].*

Since the discovery of a uniform deposition of high-quality single layered graphene on copper there has been significant interest in the exploration of copper as a catalyst for the CVD growth of graphene. [58] It has been established that the most suitable catalysts for graphitic carbon formation are those transition metals that have a low affinity towards carbon but that are still able to stabilise carbon on their surfaces by forming weak bonds. [58] Interestingly, when compared to the alternative transition metals utilised in the CVD fabrication of graphene, copper has the lowest affinity to carbon (as reflected by the fact that it does not form any carbide phases) and has very low carbon solubility compared to Co and Ni (0.001 – 0.008 weight % at 1084 °C for Cu, 0.6 weight % for Ni at 1326 °C and 0.9 weight % for Co at 1320 °C). [58] Copper's low reactivity with carbon can be attributed to the fact that it has a filled 3d-electron shell {[Ar]$3d^{10}4s^1$}, the most stable configuration (along with the half filling, $3d^5$) because the electron distribution is symmetrical which minimises reciprocal repulsions. [58] As a result, Cu can form only soft bonds with carbon *via* charge transfer from the π electrons in the sp^2 hybridised carbon to the empty 4s states of copper. [58] Hence this peculiar combination of very low affinity between carbon and copper along with the ability to form intermediate soft bonds makes copper a true catalyst, as defined by textbooks, for graphitic carbon formation (whereas the $3d^7$ and $3d^8$

orbitals of Co and Ni are between the most unstable electronic configuration (Fe) and the most stable one (Cu)). [58] Furthermore, note that often in the pursuit of obtaining large graphene domains upon transition metal catalysts, the pre-treatment of the said foils (*i.e.* annealing) has been found to be of vital importance. [44, 58]

In recent work, single graphene crystals with dimensions of up to 0.5 mm were grown by low-pressure CVD in copper-foil enclosures using methane as a precursor. [59] Low-energy electron microscopy analysis showed that the large graphene domains had a single crystallographic orientation, with an occasional domain having two orientations. [59] The authors report that Raman spectroscopy revealed the graphene crystals to be uniform monolayers with a low D-band intensity. [59] SEM images of the fabricated graphene are presented in Figure 3.8 – this work was the first to report the growth of high quality large-grain-size *single* graphene crystals. However, bear in mind that recent studies of graphene produced by CVD on copper (and particularly on nickel) [44] showed that the majority of graphene produced is few- and multi-layered, in addition to being polycrystalline where its resultant mechanical strength is weakened (and its electronic properties altered) at the grain boundaries of the underlying substrate. Such sites are reported to be the origin of surface defects in graphene (graphitic impurities) and thus in an electrochemical sense the degree of defect coverage is likely to strongly influence the electrochemical properties of the graphene film. [44] Note that one of the major advantages when utilising CVD in the fabrication of graphene is the variability in the graphene structure obtained at various conditions and hence the CVD process allows one to tailor the surface composition/structure, [44] which will likely have inherent implications on its electrochemical performance – see Figure 3.9 and Table 3.2 for example.

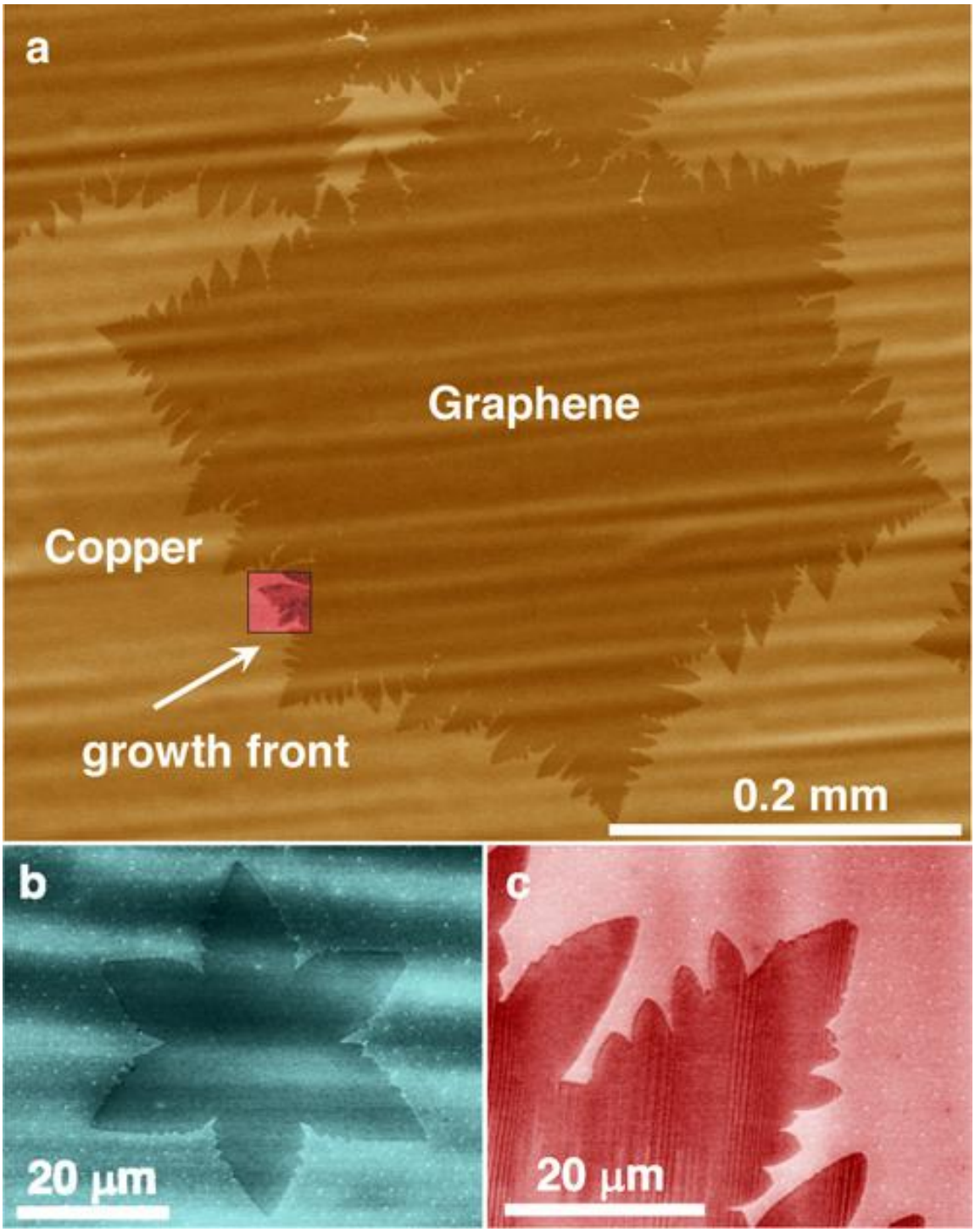

Figure 3.8 *SEM images of graphene on copper grown by CVD. (a) Graphene domain grown at 1035 °C on copper at an average growth rate of ca. 6 µm/min. (b) Graphene nuclei formed during the initial stage of growth. (c) High-surface-energy graphene growth front shown by the arrow in (a). Reproduced from Ref. [59].*

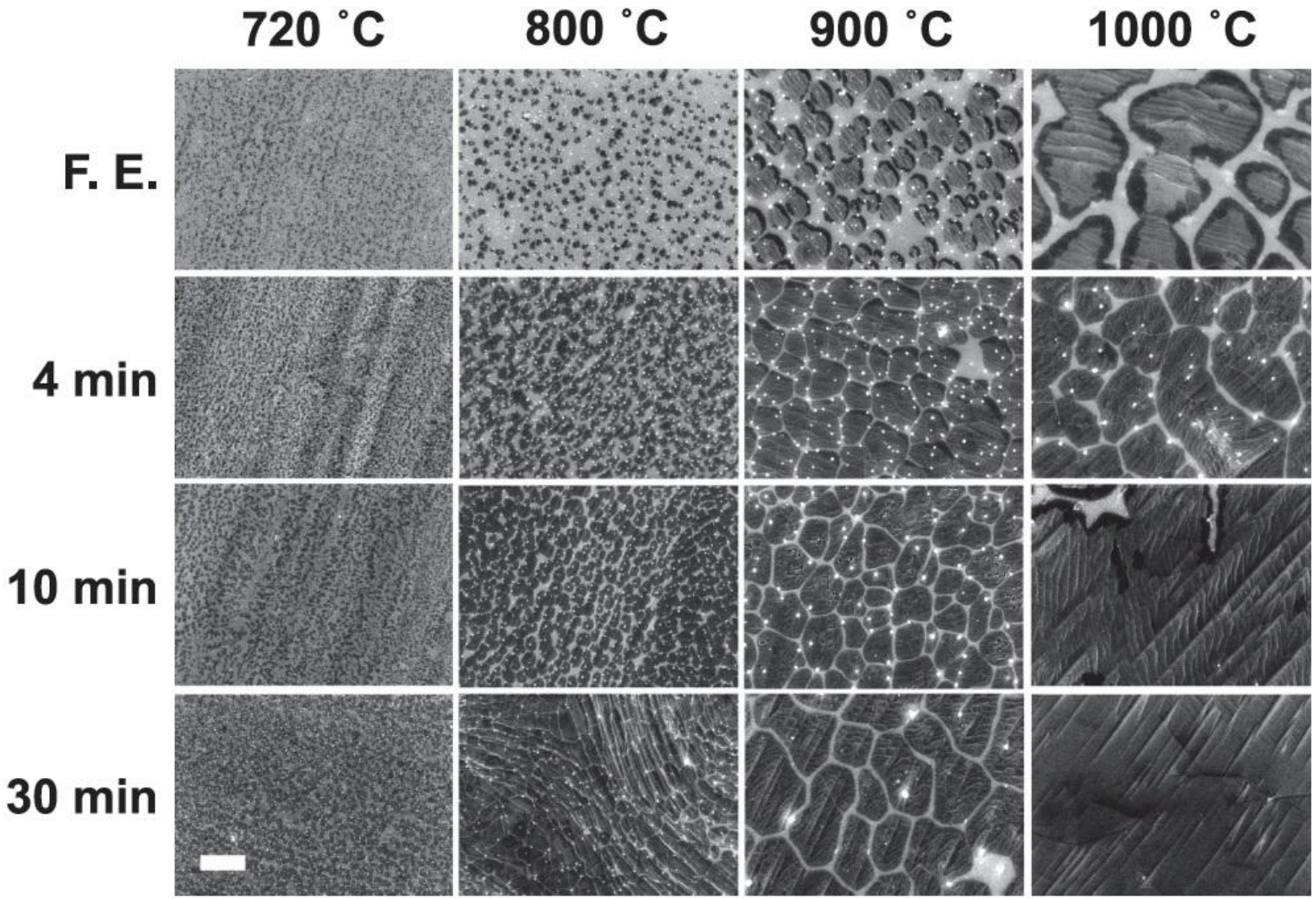

Figure 3.9 *High-resolution SEM images of graphene nuclei grown on Cu for different growth temperatures and times. These are identifiable as areas darker than the exposed Cu surface, which quickly oxidise in air after being taken out from the CVD growth system. Scale bar: 1 µm. Reproduced from Ref. [*[60]*].*

Table 3.2 *Comparison of variable CVD fabrication protocol/conditions utilised and the resultant variability in graphene quality obtained. Reproduced from Ref. [44].*

Substrate /catalyst	Temperature / °C	Gas reaction mixtures (precursors)	Growth time	Special conditions	Graphene grain size	Thickness of graphene layer	Graphene quality	Ref.
Nickel	1000, cooling rate *ca*. 10 °C s^{-1}	CH_4 : H_2 : Ar at 50 : 65 : 200 standard cubic centimetres per minute (sccm). Ambient pressure	7 minutes	Nickel thickness less than 300 nm deposited on Si/SiO_2 substrate. Prior annealing of nickel substrate	≤ 20 µm	*ca*. 1 to 12 layers	Highly polycrystalline surface, small grain sizes and multilayered regions of graphene result in an extremely large degree of edge plane surface defects in the graphene film	61
Nickel	1000, cooling rate of 100 °C min^{-1}	CH_4 at 10 sccm, H_2 at 1400 sccm. Ambient pressure	5 minutes	Nickel thickness *ca*. 500 nm deposited on Si/SiO_2 substrate. Prior annealing of nickel substrate	3–20 µm	1, 2 and multi-layered graphene regions occupy up to 87 % of the film area and single-layer coverage accounts for *ca*. 5–11 % of the overall film	Highly polycrystalline surface, small grain sizes and areas of few layered graphene islands result in a large degree of edge plane surface defects in the graphene film	62
Copper	800, cooling rate not specified	H_2/CH_4 at 5 sccm and partial pressure 0.39 Torr (Ar at 80 sccm, 1 Torr)	10 minutes	Copper foil (206 nm thick)	*ca*. 10 µm	1, 2 and 3 layers	Few crystallographic orientations and edge plane defects present at the grain boundaries and at variable multiple layer graphene areas	63
Copper	1000, cooling rate 40 – 300 °C min^{-1}	H_2/CH_4 at 0.06 sccm and partial pressure 0.5 Torr	< 3 minutes	Copper foil (25 µm thick)	10 µm	*ca*. 95 % 1 monolayer	Few crystallographic orientations and few defects present at the grain boundaries with *ca*. 5 % being multiple layer graphene	47
Copper	*ca*. 1035, cooling rate not specified	CH_4 at a flow rate and partial pressure less than 1 sccm and 50 mTorr respectively	> 1 hour	Copper foil (25 µm thick), enclosure utilised	0.5 mm	1 monolayer	Single crystallographic orientation, high purity defect free single graphene crystals	59

Furthermore, note that for the case of the CVD fabrication of CNTs, metallic impurities are commonly reported as the 'hidden' origin of electrochemical activity for many analytes. [64] This is inherent to the CVD fabrication process for the case of CNTs, where the amount of metallic impurities varies greatly between batches and hinders exploitation, for example in the fabrication of reliable CNT based sensor and energy devices. [64] It is clear that where graphene is fabricated *via* CVD appropriate control experiments will need to be performed in order to confirm the absence of such metallic impurities. Additionally, given the possible contribution of the underlying metal support/catalyst towards the observed electrochemistry at CVD grown graphene (where incomplete coverage of the graphene layer occurs), investigation towards the utilisation of non-metallic catalysts for graphene's CVD synthesis has the potential to overcome this possible issue. Note that alternatively, transfer of the fabricated graphene onto a more suitable insulating substrate is often necessary and is possible. [44, 57]

3.2.6. FABRICATION FOR ELECTROCHEMICAL APPLICATIONS

Most of the interesting applications of graphene require growth of single-layer graphene onto a suitable substrate in addition to controllable coverage and favourable manipulation/positioning of the graphene, which is very difficult to control.

The more 'practical' solution-chemistry based approaches towards the fabrication of graphene are currently favoured for electrochemical applications because of their high yields and the flexibility of handing the graphene obtained from these processes. [43] In these cases the graphene is usually dispersed into a solvent which is then cast onto a suitable surface, where following evaporation the graphene left immobilised can then be used experimentally. This process, while facile, has inherent disadvantages such as surface instability, reproducibility and

uncertainty issues in terms of the coverage and quality of the graphene remaining, where deviation from true single layer 'pristine graphene' may exist (*viz* graphitic impurities). Consequently, in these instances post-application characterisation of the graphene is required for clarity. [42] Yet it is an effective way to explore the electrochemical properties of graphene.

More recent work in this field has focused on the use of CVD grown graphene. Through careful control of the experimental conditions utilising CVD, it is possible to obtain high quality, contaminant free, single layered graphene films of bespoke sizes (or alternatively selectively impure graphene with customised properties). [44] Such variability is beneficial for the electrochemical utilisation of graphene. It is however important to note; given that the structural characteristics and/or composition of graphene are likely to vary significantly depending on the fabrication route utilised, it is essential that any such fabricated graphene nanomaterial is thoroughly characterised prior to its implementation within electrochemistry to avoid potential misinterpretation of the experimental data.

3.3. THE UNIQUE PROPERTIES OF GRAPHENE

Since the isolation of graphene and the reporting of its exceptional electronic properties in 2005 there has been substantial interest in terms of exploring the full range of properties it has to offer. Table 3.3 summarises some of the reported astonishing properties of graphene that have been determined to date. Note that graphene is reported in the media to be the "thinnest, most flexible and strongest material known".

Table 3.3 *Some reported properties of graphene.*

Property	Details	Ref.
Optical transparency	97.7 %	[40, 65]
Electron mobility	200,000 $cm^2 V^{-1} s^{-1}$	[40, 65]
Thermal conductivity	5000 $Wm^{-1} K^{-1}$	[40, 65]
Specific surface area	2630 $m^2 g^{-1}$	[40, 65]
Breaking strength	42 N m^{-1}	[40, 65]
Elastic modulus	0.25 TPa	[40]

Clearly graphene has captured the imagination of scientists and is now a hugely active area of research in a plethora of fields, none more so than in the field of electrochemistry which has reported many benefits in the areas of sensing through to energy storage and conversion. [29, 66]

3.3.1. ELECTROCHEMICALLY IMPORTANT PROPERTIES

Carbon materials have been widely utilised in both analytical and industrial electrochemistry, where in many areas they have out-performed the traditional noble metals. This diversity and success stems largely from carbons structural polymorphism, chemical stability, low cost, wide potential windows, relatively inert electrochemistry, rich surface chemistry and electro-catalytic activities for a variety of redox reactions. [29, 67]

When reviewing the essential characteristics of an electrode material for widespread applicability within electrochemistry, graphene's 'theoretical advantage' becomes apparent. An essential characteristic of an electrode material is its surface area, which is important in

applications such as energy storage, biocatalytic devices and sensors. Graphene has a theoretical surface area of 2630 m^2 g^{-1}, surpassing that of graphite (*ca.* 10 m^2 g^{-1}), and is two times larger than that of CNTs (1315 m^2 g^{-1}). [68] Of further significance for electrochemical applications is the electrical conductivity of graphene, which has been calculated to be *ca*. 64 mS cm^{-1} and is approximately 60 times greater than that of SWCNTs. [9, 69] Note that graphene's conductivity has been shown to remain stable over a vast range of temperatures and such stability is essential for reliability within a plethora of applications. [2] More interestingly, graphene is distinguished from its counterparts by its unusual band structure, rendering the quasiparticles in it formally identical to the massless Dirac Fermions. [29] A further indication of graphene's extreme electronic quality is that it displays the half-integer quantum Hall effect, with the effective speed of light as its Fermi velocity, $v_F \approx 10^6$ m s^{-1}, which can be observed in graphene even at room temperature. [70-72] Ultra high electron mobility has been achieved in graphene, [73] with mobilities in excess of 200,000 cm^2 V^{-1} s^{-1} reported at room temperature. In comparison, the mobility of an electron in silicon is at its maximum at *ca*. 1,000 cm^2 V^{-1} s^{-1}; meaning the electron mobility is 200 times higher in graphene. [29] Graphene's quality clearly reveals itself with a pronounced ambipolar electric field effect; charge carriers can be tuned continuously between electrons and holes where electron mobility remains high even at high concentrations in both electrically and chemically doped devices, which translates to ballistic transport on the sub-micrometre scale. [72]

Due to graphene's unique properties it has been speculated that a GNS can carry a super-current [72] and it is clear that its theoretical electron transfer rates are superior when contrasted to graphite and CNTs. Furthermore, the fast charge carrier properties of graphene (and other two-dimensional materials) were found not only to be continuous, but to exhibit high crystal quality, where importantly for graphene, charge carriers can travel thousands of

inter-atomic distances without scattering. [2] These isolated graphene crystallites demonstrate exceptional electronic qualities and graphene has exhibited the fastest electron mobilities when compared to all other potential materials, 'theoretically' meaning that in many applications graphene based electrodes react much faster.

As highlighted above, graphene holds inimitable properties that are superior in comparison to other carbon allotropes of various dimensions and from any other electrode material for that matter, thus 'theoretically' suggesting that graphene is an ideal electrode material that could yield significant benefits in many electrochemical applications; it is this concept that is explored in greater detail throughout this thesis.

3.4. REFERENCES

1. E. Fitzer, K.-H. Kochling, H.-P. Boehm and H. Marsh, *Pure Appl. Chem.*, 1995, **67**, 473.
2. A. K. Geim and K. S. Novoselov, *Nat. Mater.*, 2007, **6**, 183.
3. P. R. Wallace, *Phys. Rev.*, 1947, **71**, 622.
4. K. S. Novoselov, A. K. Geim, S. V. Morozov, D. Jiang, Y. Zhang, S. V. Dubonos, I. V. Grigorieva and A. A. Firsov, *Science*, 2004, **306**, 666.
5. K. S. Novoselov, D. Jiang, F. Schedin, T. J. Booth, V. V. Khotkevich, S. V. Morozov and A. K. Geim, *Proc. Natl. Acad. Sci. U. S. A.*, 2005, **102**, 10451.
6. Y. Zhang, Y.-W. Tan, H. L. Stormer and P. Kim, *Nature*, 2005, **438**, 201.
7. A. K. Geim, *Phys. Scr.*, 2012, **2012**, 014003.
8. A. Dato, Z. Lee, K.-J. Jeon, R. Erni, V. Radmilovic, T. J. Richardson and M. Frenklach, *Chem. Commun.*, 2009, 6095.
9. C. Liu, S. Alwarappan, Z. Chen, X. Kong and C.-Z. Li, *Biosens. Bioelectron.*, 2010, **25**, 1829.
10. See summary by: E. S. Reich, *Nature*, 2010, **468**, 486.
11. Internet-Resource, *Nobelprize.org.*, Accessed: 28/02/2012; http://www.nobelprize.org/nobel_prizes/physics/laureates/2010/press.html.
12. D. R. Dreyer, R. S. Ruoff and C. W. Bielawski, *Angew. Chem., Int. Ed.*, 2010, **49**, 9336.
13. N. R. Gall, E. V. Rutkov and A. Y. Tontegode, *Int. J. Mod. Phys. B*, 1997, **11**, 1865.

14. H.-P. Boehm, A. Clauss, G. O. Fischer and U. Hofmann, *Z. Naturforsch., B: Anorg. Chem. Org. Chem. Biochem. Biophys. Biol.*, 1962, **17**, 150.

15. H.-P. Boehm, R. Setton and E. Stumpp, *Carbon*, 1986, **24**, 241.

16. H.-P. Boehm, *Angew. Chem., Int. Ed.*, 2010, **49**, 9332.

17. S. Park and R. S. Ruoff, *Nat. Nanotechnol.*, 2009, **4**, 217.

18. S. Stankovich, R. D. Piner, X. Chen, N. Wu, S. T. Nguyen and R. S. Ruoff, *J. Mater. Chem.*, 2006, **16**, 155.

19. H.-J. Shin, K. K. Kim, A. Benayad, S. M. Yoon, H. K. Park, I.-S. Yung, M. H. Jin, H.-K. Jeong, J. M. Kim, J.-Y. Choi and Y. H. Lee, *Adv. Funct. Mater.*, 2009, **19**, 1987.

20. L.-H. Liu and M. Yan, *Nano Lett.*, 2009, **9**, 3375.

21. C. Berger, Z. M. Song, X. B. Li, X. S. Wu, N. Brown, C. Naud, D. Mayou, T. B. Li, J. Hass, A. N. Marchenkov, E. H. Conrad, P. N. First and W. A. de-Heer, *Science*, 2006, **312**, 1191.

22. X. L. Li, X. R. Wang, L. Zhang, S. W. Lee and H. J. Dai, *Science*, 2008, **319**, 1229.

23. Y. Hernandez, V. Nicolosi, M. Lotya, F. M. Blighe, Z. Sun, S. De, I. T. McGovern, B. Holland, M. Byrne, Y. K. Gun'Ko, J. J. Boland, P. Niraj, G. Duesberg, S. Krishnamurthy, R. Goodhue, J. Hutchison, V. Scardaci, A. C. Ferrari and J. N. Coleman, *Nat. Nanotechnol.*, 2008, **3**, 563.

24. S. Stankovich, D. A. Dikin, G. H. B. Dommett, K. M. Kohlhaas, E. J. Zimney, E. A. Stach, R. D. Piner, S. T. Nguyen and R. S. Ruoff, *Nature*, 2006, **442**, 282.

25. J. S. Wu, W. Pisula and K. Mullen, *Chem. Rev.*, 2007, **107**, 718.

26. A. Dato, V. Radmilovic, Z. Lee, J. Phillips and M. Frenklach, *Nano Lett.*, 2008, **8**, 2012.

27. C. Valles, C. Drummond, H. Saadaoui, C. A. Furtado, M. He, O. Roubeau, L. Ortolani, M. Monthioux and A. Penicaud, *J. Am. Chem. Soc.*, 2008, **130**, 15802.

28. P. W. Sutter, J. I. Flege and E. A. Sutter, *Nat. Mater.*, 2008, **406**, 406.

29. D. A. C. Brownson and C. E. Banks, *Analyst*, 2010, **135**, 2768.

30. A. K. Geim and P. Kim, *Sci. Am.*, 2008, **298**, 90.

31. N. Mohanty, D. Moore, Z. Xu, T. S. Sreeprasad, A. Nagaraja, A. A. Rodriguez and V. Berry, *Nat. Commun.*, 2012, **3**, 844.

32. D. Yoon, H. Moon, H. Cheong, J. S. Choi, J. A. Choi and B. H. Park, *J. Korean Phys. Soc.*, 2009, **55**, 1299.

33. D. Graf, F. Molitor, K. Ensslin, C. Stampfer, A. Jungen, C. Hierold and L. Wirtz, *Nano Lett.*, 2007, **7**, 238.

34. A. C. Ferrari, *Solid State Commun.*, 2007, **143**, 47.

35. A. G. Guell, N. Ebejer, M. E. Snowden, J. V. Macpherson and P. R. Unwin, *J. Am. Chem. Soc.*, 2012, **134**, 7258.

36. D. A. C. Brownson, L. C. S. Figueiredo-Filho, X. Ji, M. Gomez-Mingot, J. Iniesta, O. Fatibello-Filho, D. K. Kampouris and C. E. Banks, *J. Mater. Chem. A*, 2013, **1**, 5962.

37. H.-L. Guo, X.-F. Wang, Q.-Y. Qian, F.-B. Wang and X.-H. Xia, *ACS Nano*, 2009, **3**, 2653.

38. S. Mao, H. Pu and J. Chen, *RSC Adv.*, 2012, **2**, 2643.

39. D. R. Dreyer, S. Park, C. W. Bielawski and R. S. Rouff, *Chem. Soc. Rev.*, 2010, **39**, 228.

40. Y. Zhu, S. Murali, W. Cai, X. Li, J. W. Suk, J. R. Potts and R. S. Ruoff, *Adv. Mater.*, 2010, **22**, 3906.

41. M. H. Rümmeli, C. G. Rocha, F. Ortmann, I. Ibrahim, H. Sevincli, F. Börrnert, J. Kunstmann, A. Bachmatiuk, M. Pötschke, M. Shiraishi, M. Meyyappan, B. Büchner, S. Roche and G. Cuniberti, *Adv. Mater.*, 2011, **23**, 4471.

42. C. Soldano, A. Mahmood and E. Dujardin, *Carbon*, 2010, **48**, 2127.

43. D. Chen, L. Tang and J. Li, *Chem. Soc. Rev.*, 2010, **39**, 3157.

44. D. A. C. Brownson and C. E. Banks, *Phys. Chem. Chem. Phys.*, 2012, **14**, 8264.

45. U. Khan, A. O'Neill, M. Lotya, S. De and J. N. Coleman, *Small*, 2010, **6**, 864.

46. M. Lotya, P. J. King, U. Khan, S. De and J. N. Coleman, *ACS Nano*, 2010, **4**, 3155.

47. X. Li, W. Cai, L. Colombo and R. S. Ruoff, *Nano Lett.*, 2009, **9**, 4268.

48. X.-M. Chen, G.-H. Wu, Y.-Q. Jiang, Y.-R. Wang and X. Chen, *Analyst*, 2011, **136**, 4631.

49. J. S. Park, A. Reina, R. Saito, J. Kong, G. Dresselhaus and M. S. Dresselhaus, *Carbon*, 2009, **47**, 1303.

50. D. R. Cooper, B. D'Anjou, N. Ghattamaneni, B. Harack, M. Hilke, A. Horth, N. Majlis, M. Massicotte, L. Vandsburger, E. Whiteway and V. Yu, *ISRN Condens. Matter Phys.*, 2012, **2012**, 501686.

51. A. A. Green and M. C. Hersam, *Nano Lett.*, 2009, **9**, 4031.

52. Internet-Resource, *Nano Integris Ltd.*, Accessed: 28/02/2012; http://www.nanointegris.com.

53. W. S. Hummers and R. E. Offeman, *J. Am. Chem. Soc.*, 1958, **80**, 1339.

54. Y. Shao, J. Wang, H. Wu, J. Liu, I. A. Aksay and Y. Lin, *Electroanalysis*, 2010, **22**, 1027.

55. Internet-Resource, *Graphene Supermarket Ltd.*, Accessed: 28/02/2012; http://www.graphene-supermarket.com.

56. A. Reina, X. Jia, J. Ho, D. Nezich, H. Son, V. Bulovic, M. S. Dresselhaus and J. Kong, *Nano Lett.*, 2009, **9**, 30.

57. X. Li, Y. Zhu, W. Cai, M. Borysiak, B. Han, D. Chen, R. D. Piner, L. Colombo and R. S. Ruoff, *Nano Lett.*, 2009, **9**, 4359.

58. C. Mattevi, H. Kim and M. Chhowalla, *J. Mater. Chem.*, 2011, **21**, 3324.

59. X. Li, C. W. Magnuson, A. Venugopal, R. M. Tromp, J. B. Hannon, E. M. Vogel, L. Colombo and R. S. Ruoff, *J. Am. Chem. Soc.*, 2011, **133**, 2816.

60. H. Kim, C. Mattevi, M. R. Calvo, J. C. Oberg, L. Artiglia, S. Agnoli, C. F. Hirjibehedin, M. Chhowalla and E. Saiz, *ACS Nano*, 2012, **6**, 3614.

61. K. S. Kim, Y. Zhao, H. Jang, S. Y. Lee, J. M. Kim, K. S. Kim, J.-H. Ahn, P. Kim, J.-Y. Choi and B. H. Hong, *Nature*, 2009, **457**, 706.

62. A. Reina, S. Thiele, X. Jia, S. Bhaviripudi, M. S. Dresselhaus, J. A. Schaefer and J. Kong, *Nano Res.*, 2009, **2**, 509.

63. Y.-H. Lee and J.-H. Lee, *Appl. Phys. Lett.*, 2010, **96**, 083101.

64. C. P. Jones, K. Jurkschat, A. Crossley and C. E. Banks, *J. Iran. Chem. Soc.*, 2008, **5**, 279.

65. L. J. Cote, J. Kim, V. C. Tung, J. Luo, F. Kim and J. Huang, *Pure Appl. Chem.*, 2011, **83**, 95.

66. D. A. C. Brownson, D. K. Kampouris and C. E. Banks, *J. Power Sources*, 2011, **196**, 4873.

67. R. L. McCreery, *Chem. Rev.*, 2008, **108**, 2646.

68. M. Pumera, *Chem. Rec.*, 2009, **9**, 211.

69. X. Wang, L. Zhi and K. Mullen, *Nano Lett.*, 2008, **8**, 323.

70. B. Soodchomshom, *Physica B*, 2010, **405**, 1383.

71. H. B. Heersche, P. Jarillo-Herrero, J. B. Oostinga, L. M. K. Vendersypen and A. F. Morpurgo, *Nature*, 2007, **446**, 56.

72. S. Sato, N. Harada, D. Kondo and M. Ohfuchi, *Fujitsu Sci. Tech. J.*, 2009, **46**, 103.

73. K. I. Bolotin, K. J. Sikes, Z. Jiang, M. Klima, G. Fudenberg, J. Hone, P. Kim and H. L. Stormer, *Solid State Commun.*, 2008, **146**, 351.

CHAPTER 4: A CRITICAL LITERATURE REVIEW OF GRAPHENE (ELECTROANALYTICAL APPLICATIONS)

This chapter provides a brief overview of the graphene literature (that being the use of graphene, as an electrode material, in electrochemical measurements) that was available prior to commencing this work in 2010. Of note is that, to the best of the author's knowledge, there were no fundamental studies published on the electrochemical properties of graphene at this early stage, *viz* attempts being made to understand its fundamental electron transfer properties. The majority of the literature available in 2010 was focused on the use of graphene as an electrode material for the fabrication of enhanced electrochemical sensors. As such a representative selection of academic papers is analysed in greater depth within this chapter, the aim of which is to draw attention to common experimental 'issues' that were apparent in the graphene literature in these early stages.

Note that the field of graphene electrochemistry is relatively 'fast paced' and that work within this thesis has been published in peer-reviewed journal articles. As such (given the availability of this work in the public domain) it has contributed to the knowledge base and influenced the direction of future work within the literature. Resultantly the literature presented within this chapter focuses on that published pre-2010 with further literature and key developments being introduced where relevant (and as they emerged) throughout later chapters so as not to pre-empt the novel work performed herein that has no doubt contributed to such developments in the understanding of *graphene electrochemistry*.

4.1. THE ELECTRO-CATALYSIS OF GRAPHENE

The 'electro-catalytic' behaviour and enhanced analytical performance of graphene and related structures has been widely reported. [1-14] For example, Wang *et al.* [3] have reported the electrochemical sensing of hydrazine, greatly significant in fuel cells, rocket

propellants, insecticides and explosives. [3] On graphite surfaces hydrazine usually exhibits irreversible kinetics, such that the electrochemical signal occurs at high potentials close to the end of the accessible voltammetric window, but is more electrochemically reversible on metallic surfaces. [15, 16] In Figure 4.1A it is evident that a graphene (synthesised *via* the reduction of graphene oxide) modified glassy carbon (GC) electrode was shown to possess excellent 'electro-catalytic' activity towards the sensing of hydrazine when compared to the unmodified underling GC substrate. [3] While the analytical utility was not examined in much depth, the smallest addition was 1 mM which was linear up to 25 mM. [3] In another notable example, Kang and co-workers [1] utilised graphene sheets (synthesised from graphite oxide and functionalised with both hydroxyl and carboxylic groups) for the sensing of acetaminophen. Figure 4.1B depicts the voltammetric profiles where a quasi-reversible redox process was obtained at a graphene-modified GC electrode, indicating that the over-potential at acetaminophen was significantly decreased when compared to that of the same analysis performed using an unmodified GC electrode. Thus the graphene-modified electrode was reported to exhibit excellent 'electro-catalytic' activity towards acetaminophen. [1] The graphene modified GC outperformed the unadulterated GC electrode consistently, where at low concentrations the graphene-modified GC electrode exhibited a pair of well-defined redox waves and in contrast the unadulterated GC showed irreversible behaviour with relatively weak redox (current) peaks. [1] The improvement in the observed electrochemical response of the graphene based electrode compared to the unadulterated GCE is claimed by the authors to be due to the nano-composite film of graphene 'accelerating' the electrochemical reaction. [1] Additionally, the large surface area of graphene can be attributed to the large background current exhibited by the graphene modified electrode in Figure 4.1B, however, besides from reporting these observations no further insights were divulged.

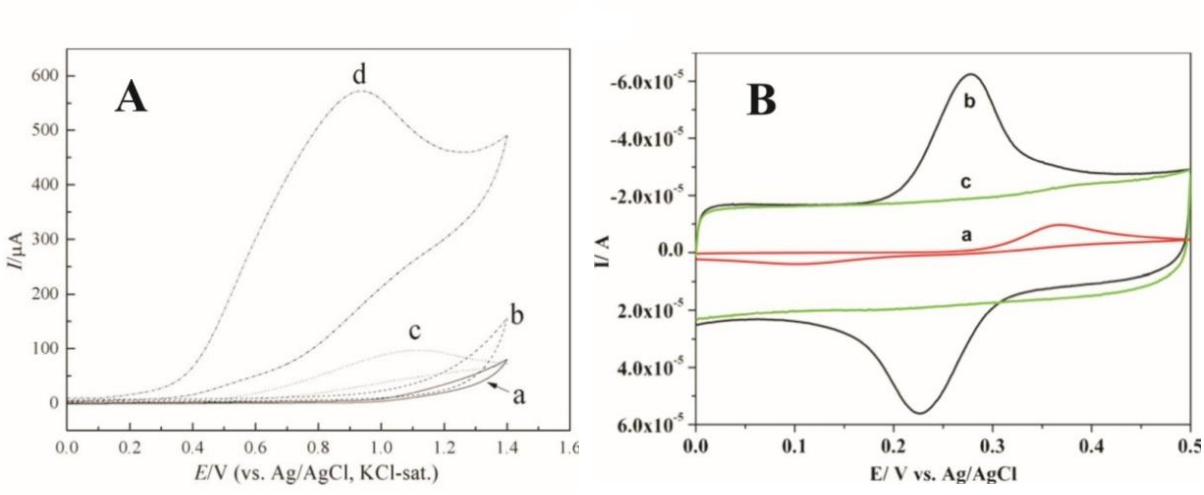

Figure 4.1 *(**A**) Cyclic voltammetric responses recorded at (a and c) the unmodified GC electrode and (b and d) the graphene modified GC electrode (a and b) in the absence and (c and d) in the presence of 10 mM hydrazine in 0.1 M KOH solution at a scan rate of 100 mV s^{-1}: Reproduced from Ref. [3]. (**B**) The electrochemical sensing of 100 μM acetaminophen at an unmodified GC electrode (a); and the sensing of 20 μM acetaminophen at a graphene modified GC electrode (b), and without acetaminophen (c) in the buffer of 0.1 M NH_3–NH_4Cl, pH 9.3, scan rate; 50 mV s^{-1}: Reproduced from Ref. [1].*

It is interesting to note that in the above examples (and in many others, see Table 4.1) [3-14] the electro-catalysis of graphene is compared *only* to the underlying electrode and not to other relevant carbon materials, such as graphite or graphene oxide, which could give a false sense of an improved electrochemical reactivity at graphene. A similar issue occurred when CNTs were first explored in electrochemistry and 'electro-catalysis' was claimed when compared only to the underlying substrates (usually GC electrodes), which was consequently proven to be false. [17]

In an attempt to gain insight into understanding the electro-catalytic performance of graphene, Lin *et al.* [18] compared graphene 'film' modified basal and edge plane pyrolytic graphite (BPPG and EPPG respectively) electrodes for the electro-catalytic oxidation of hydrogen peroxide and *β*-nicotinamide adenine dinucleotide (NADH) with that of unmodified BPPG and EPPG electrodes. They observed that the application of graphene to the electrode surface has the ability to lower the electro-oxidation potentials of hydrogen peroxide and

NADH in comparison with unmodified BPPG and EPPG electrodes, thus indicating that graphene appeared to exhibit an "electro-catalytic" activity towards both analytes. [18] However, a problem with their study [18] is that the graphene utilised contained on average four layers, and sometimes more than six graphene layers, which corresponds to the structural composition of *quasi*-graphene and is approaching that of graphite.

As is evident in Figure 4.2, Wang *et al*. [19] have shown a graphene (synthesised *via* the reduction of graphene oxide) modified GC electrode to possess excellent electro-catalytic activity towards the detection of kojic acid. The electro-catalytic activity was reported in terms of the graphene modified electrode exhibiting a reduced over-potential and a significantly increased peak current when compared to a graphite modified alternative and the unmodified GC electrode. [19] As is the case in the above reports, such data was inferred by the authors to indicate that graphene provides a greatly improved sensing capability at the given fabricated electrode. [19] However, although appropriate graphite controls were reported (unlike in the studies covered earlier), the authors failed to perform appropriate control experiments with graphene oxide and thus the role of oxygenated species that may reside on the reduced graphene oxide structure is not clear in this case and as such may contribute significantly to the observed electro-catalysis. [19] Thus, as is the case throughout the literature where graphene has been fabricated through the oxidation of graphite and the subsequent reduction of graphene oxide (see Chapter 3.2.3), due to the lack of diligent control experiments when using such graphene as an electrode material, [1, 3, 19] the true origin of the claimed 'electro-catalysis' is unclear given that contributions may arise from incomplete reduction of the graphene oxide or through graphitic impurities formed as a result of the fabrication process; which can also contribute to a highly disordered and porous graphene structure, in which case it is likely that the observed response is due to 'thin-layer' effects (see Chapter 1.4.5.1).

Table 4.1 *Depiction of the relative analytical parameters (limit of detection and linear range) of graphene based electrodes when utilised for the sensing of various analytes.*

Analyte	Analytical parameter		Electro-catalytic w.r.t (graphitic form)	Underlying electrode / complex	Comments	Ref.
	LOD	Linear range				
4-Aminophenol	0.057 µM	0.2 – 550 µM	G	GCE and CH/GCE	G synthesised *via* RGO	[4]
Adenine	0.75 µM	5 – 200 µM	G	G-NAF complex on a GCE	Explored DNA samples in milk powder, urine and herring sperm	[5]
Ascorbic Acid	0.12 mM	0.4 – 6.0 mM	G	PPFE	G synthesised *via* DMF exfoliation	[20]
Cadmium	0.18 nM	13.3 – 266 nM	G	G-NAF complex on a GCE and bare NAF/GCE	G synthesised *via* RGO	[6]
Caffeine	0.12 µM	0.4 – 40 µM	G	G-NAF complex on a GCE	N/A	[7]
Chlorpromazine	6 nM	0.01 – 9 µM	GPE	N/A	N/A	[21]
Dopamine	2.64 µM	4 – 100 µM	G	GCE	G synthesised *via* RGO. Tested in the presence of ascorbic acid	[8]
Ethanol	5 µM	5 – 200 µM	ADH/IL-functionalised G	GCE	G synthesised *via* RGO. Explored in diluted wine and beer samples	[9]
Glucose	0.02 mM	0.08 – 12 mM	GO	GCE and CH/GCE	GOD/GO/CH Nanocomposite film	[10]

Guanine	0.58 µM	2 – 200 µM	G	G-NAF complex on a GCE	Explored DNA samples in milk powder, urine and herring sperm	5
Guanosine	0.75 µM	2.0 µM – 0.35 mM	G	CH/GCE, nano-Fe_3O_4/GCE and G/CH/GCE	G synthesised *via* RGO	11
Hydrazine	1 mM	1 – 25 mM	G	GCE	G synthesised *via* RGO. 0.1 M KOH electrolyte	3
Hydrogen Peroxide	1.7 µM	5.0 µM – 5.13 mM	G	Au/HRP/GS/CH complex on a GCE	G synthesised *via* RGO	12
Lead	0.096 nM	7.2 – 14.5 nM	G	G-NAF complex on a GCE and bare NAF/GCE	G synthesised *via* RGO	6
NADH	0.25 mM	0.25 – 2 mM	ADH/IL-functionalised G	GCE and SWCNTs	G synthesised *via* RGO	9
NADH	1.9 µM	45 – 360 µM	G	PPFE	G synthesised *via* DMF exfoliation	22
Nitric Oxide	3.6 µM	3.6 – 43.2 µM	G	GCE	G synthesised *via* RGO	13
Paracetamol	0.032 µM	0.1 – 20 µM	G	GCE	G synthesised *via* RGO. Explored in real human blood, plasma, and pharmaceutical preparations	1
TNT	1 ppm	1 – 15 ppm	G	GCE	G synthesised *via* SC exfoliation	14

Abbreviations: ADH; alcohol dehydrogenase: Au; gold: CH; chitosan: DMF; dimethylformamide: G; graphene: GCE; glassy carbon electrode: GO; graphene oxide: GOD; glucose oxidase: GPE; graphene paste electrode: GS; graphene sheet: HRP; horseradish peroxidise: IL; ionic liquid: N/A; not applicable: NADH; β-nicotinamide adenine dinucleotide: NAF; nafion: PB; Prussian Blue: PPFE; pyrolysed photoresist film electrode: RGO; reduced graphene oxide: SC; sodium cholate: SWCNTs; single walled carbon nanotubes: TNT; 2,4,6-trinitrotoluene: w.r.t; with respect to.

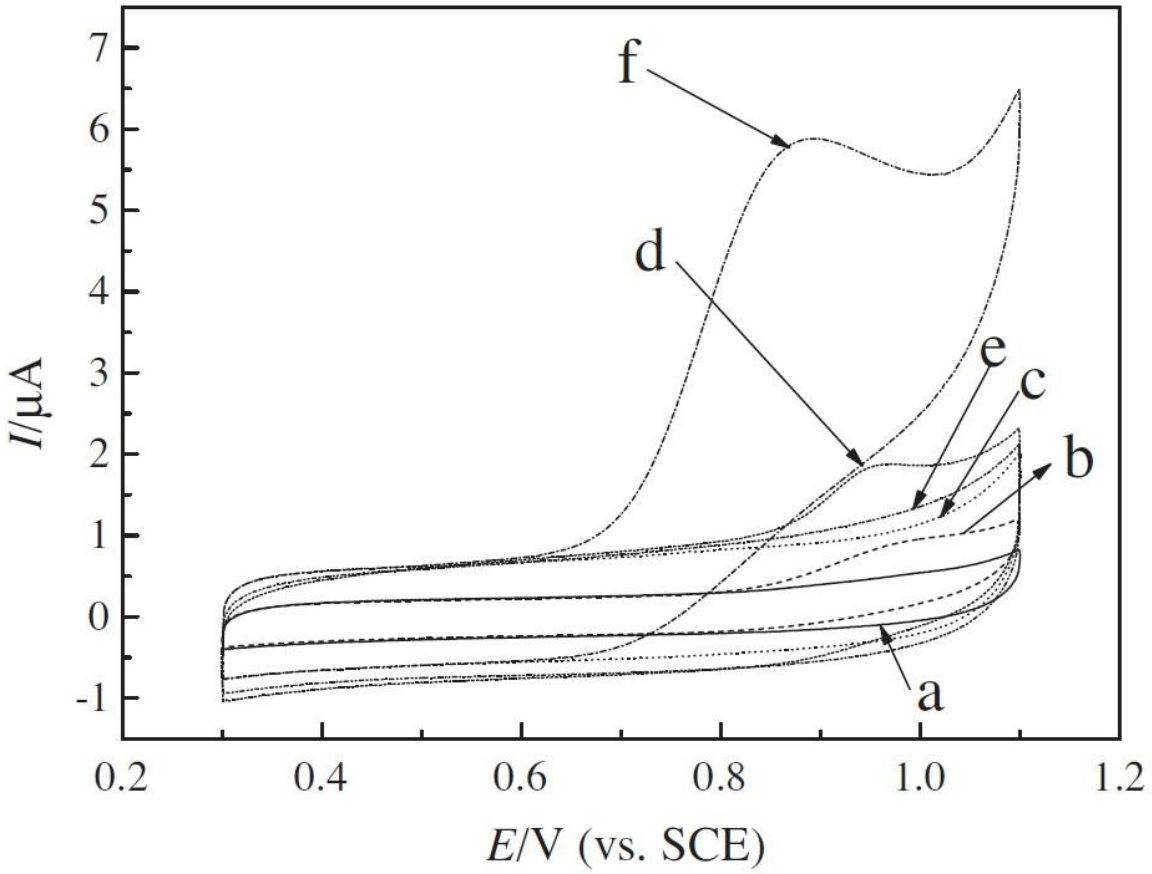

Figure 4.2 *Cyclic voltammograms at (a and b) the bare/unmodified GC electrode, (c and d) the graphite electrode, and (e and f) the graphene/GC electrode in 0.2 M acetic acid – sodium acetate solution (pH 6.0) (a, c, and e) in the absence and (b, d, and f) in the presence of 200 mM kojic acid. Scan rate: 100 mV* s^{-1}*. Reproduced from Ref. [*[19]*].*

Work by Keeley *et al.* [20, 22] has attempted to preclude the issues that have plagued earlier attempts at utilising graphene, where towards the sensing of *L*-ascorbic acid (AA) and NADH the authors used dimethylformamide (DMF) exfoliated graphene immobilised on pyrolysed photoresist film electrodes (PPFEs). The DMF fabrication was chosen in an attempt to avoid a high oxygen content (an issue with reduced graphene oxide fabrication methodologies) where for the stable and sensitive detection of NADH a low oxygen content is vital; PPFEs were chosen opposed to a GC electrode substrate as they are less electrochemically active and thus permit the de-convolution of kinetic data. Although the authors report favourable results, appropriate control experiments were not performed (with comparable graphitic electrodes and with the solvents utilised) and thus the electro-catalytic

influence of DMF is unclear. In addition to this, characterisation of the graphene utilised indicated an average thickness of five layers, which again is approaching that of graphite.

Finally, in an attempt to offer insight into the fundamental understandings of graphene and graphite alike, Pumera *et al.* [14] has utilised various graphitic forms towards the detection of 2,4,6-trinitrotoluene (TNT) in seawater. The authors compared the electrochemical responses of single-, few-, and multi-layer graphene nanoribbons to that of graphite microparticle based electrodes, where no significant difference in the performance was noted. [14] Note however, surfactants were used in the fabrication of the graphitic forms utilised and this factor was not taken into account when interpreting the experimental data (see Chapter 6). As a consequence it is unclear whether the surfactant present was partaking in the electrochemical reaction. If the latter is the case, and the surfactant contributes to an equal degree in each of the samples utilised, it would be the origin of the observed similar electrochemical responses. Thus this work [14] fails to offer conclusive insights into the fundamental understandings of graphene.

In summary, although still a relatively new material in the literature published pre-2010, owing to its reported advantageous properties graphene had already made a wide and diverse impact within electrochemistry. Literature at the time of commencing this work was depicting graphene as far-superior than its rival materials, thus there are many encouraging examples of the reported 'electro-catalysis' of graphene with improved sensitivity and detection limits being observed. [3-14] *However,* it is clear that a comprehensive understanding of the observed 'electro-catalysis' at graphene modified electrodes is somewhat lacking in the pre-2010 literature. It is obvious that the fundamental electrochemical mechanisms associated with graphene (for example its electron transfer properties) had yet to be fully addressed and the role of other interferents and impurities (such as surfactants and graphitic regions) had not been properly de-convoluted. There was a

clear lack of diligent control measures being reported; thus the '*true*' electrochemical response of graphene had yet to be fully observed. As a result of the aforementioned shortcomings in the graphene literature (pre-2010), the fundamental understanding of graphene electrodes was lacking and unfortunately such knowledge is generally required in order to impart improvements in the fabrication of enhanced carbon and graphitic based electrochemical sensors. It is with the acquisition of this 'fundamental' knowledge that the true potential of this revolutionary material, *graphene*, is to be uncovered and potentially utilised in the future.

4.2. REFERENCES

1. X. Kang, J. Wang, H. Wu, J. Liu, I. A. Aksay and Y. Lin, *Talanta*, 2010, **81**, 754.
2. M. Pumera, *Chem. Rec.*, 2009, **9**, 211.
3. Y. Wang, Y. Wan and D. Zhang, *Electrochem. Commun.*, 2010, **12**, 187.
4. H. Yin, Q. Ma, Y. Zhou, S. Ai and L. Zhu, *Electrochim. Acta*, 2010, **55**, 7102.
5. H. Yin, Y. Zhou, Q. Ma, S. Ai, P. Ju, L. Zhu and L. Lu, *Process Biochem.*, 2010, **45**, 1707.
6. J. Li, S. Guo, Y. Zhai and E. Wang, *Anal. Chim. Acta*, 2009, **649**, 196.
7. J.-Y. Sun, K.-J. Huang, S.-Y. Wei, Z.-W. Wu and F.-P. Ren, *Colloids Surf., B*, 2011, **84**, 421.
8. Y.-R. Kim, S. Bong, Y.-J. Kang, Y. Yang, R. K. Mahajan, J. S. Kim and H. Kim, *Biosens. Bioelectron.*, 2010, **25**, 2366.
9. C. Shan, H. Yang, D. Han, Q. Zhang, A. Ivaska and L. Niu, *Biosens. Bioelectron.*, 2010, **25**, 1504.
10. X. Kang, J. Wang, H. Wu, I. A. Aksay, J. Liu and Y. Lin, *Biosens. Bioelectron.*, 2009, **25**, 901.
11. H. Yin, Y. Zhou, Q. Ma, S. Ai, Q. Chen and L. Zhu, *Talanta*, 2010, **82**, 1193.
12. K. Zhou, Y. Zhu, X. Yang, J. Luo, C. Li and S. Luan, *Electrochim. Acta*, 2010, **55**, 3055.
13. J.-F. Wu, M.-Q. Xu and G.-C. Zhao, *Electrochem. Commun.*, 2010, **12**, 175.
14. M. S. Goh and M. Pumera, *Anal. Bioanal. Chem.*, 2011, **399**, 127.
15. C. E. Banks, A. Crossley, C. Salter, S. J. Wilkins and R. G. Compton, *Angew. Chem. Int. Ed.*, 2006, **45**, 2533.
16. X. Ji, C. E. Banks, W. Xi, S. J. Wilkins and R. G. Compton, *J. Phys. Chem. B*, 2006, **110**, 22306.

17. X. Ji, R. O. Kadara, J. Krussma, Q. Chen and C. E. Banks, *Electroanalysis*, 2010, **22**, 7.

18. W.-J. Lin, C.-S. Liao, J.-H. Jhang and Y.-C. Tsai, *Electrochem. Commun.*, 2009, **11**, 2153.

19. Y. Wang, D. Zhang and J. Wu, *J. Electroanal. Chem.*, 2012, **664**, 111.

20. G. P. Keeley, A. O'Neill, N. McEvoy, N. Peltekis, J. N. Coleman and G. S. Duesberg, *J. Mater. Chem.*, 2010, **20**, 7864.

21. M. H. Parvin, *Electrochem. Commun.*, 2011, **13**, 366.

22. G. P. Keeley, A. O'Neill, M. Holzinger, S. Cosnier, J. N. Coleman and G. S. Duesberg, *Phys. Chem. Chem. Phys.*, 2011, **13**, 7747.

This chapter details the general experimental conditions that are applicable to the work reported throughout this thesis unless specifically stated otherwise. Note that where deviation occurs from the reported conditions herein, 'chapter specific' experimental sections are concurrently reported within the given chapters. These individual experimental sections detail any amendments and/or additional experimental conditions that were utilised to complete the relevant work.

5.1. EXPERIMENTAL DETAILS

All chemicals used were of analytical grade (or higher) and were used as received from Sigma-Aldrich without any further purification. All solutions were prepared with deionised water of resistivity not less than 18.2 MΩ cm and (unless stated otherwise) were vigorously degassed with high purity, oxygen free, nitrogen prior to electrochemical measurements.

Voltammetric measurements were carried out using an 'Autolab PGSTAT 101' (Metrohm Autolab, The Netherlands) potentiostat which was controlled by Nova software version 1.6 for Windows XP. All electrochemical measurements were conducted using a three electrode system and were performed at a temperature of 297 K. The working electrode utilised was variable (*vide infra*, Chapters 5.2 and 5.4) and unless otherwise stated a platinum wire and a saturated calomel electrode (SCE) (Radiometer, Copenhagen, Denmark) were used to complete the circuit as auxiliary/counter and reference electrodes, respectively.

5.2.1. EPPG AND BPPG ELECTRODES CONSTRUCTED FROM HOPG

The edge plane pyrolytic graphite (EPPG) working electrode (Le Carbone, Ltd. Sussex, U.K.) was machined to possess a 4.9 mm diameter, with the disc face parallel to the edge plane, as required, from a slab of highly ordered pyrolytic graphite (HOPG) (highest grade available: SPI-1, which is equivalent to Union Carbide's ZYA grade, with a lateral grain size, L_a of 1–10 μm and 0.4 ± 0.1° mosaic spread). The basal plane pyrolytic graphite (BPPG) working electrode (4.9 mm diameter, Le Carbone, Ltd. Sussex, U.K.) was machined as above, however with the disc face was parallel to the basal plane as required.

5.2.2. SCREEN PRINTED ELECTRODES (SPES)

Basal plane like-screen printed electrodes (SPEs) were obtained commercially. [1] These sensor electrodes are on a flexible substrate consisting of a graphite working electrode (3.1 mm diameter) with a carbon counter and onboard silver/silver chloride (Ag/AgCl) reference electrode. [2] Note that these electrodes are basal plane-like in nature, with electron transfer rates of the order of *ca*. 10^{-5} cm s^{-1} as determined with potassium ferrocyanide in 1 M KCl. [1, 3] Alternatively, edge plane like-SPEs were obtained commercially and have been previously reported to exhibit a heterogeneous rate constant of *ca*. 1.7×10^{-3} cm s^{-1}, as measured using the ferro-/ferri-cyanide redox probe. [1, 3] Unless stated otherwise, where SPEs have been used within this work, it is to be assumed that the 'onboard' carbon and Ag/AgCl counter and reference electrodes were utilised for the employment electrochemical measurements.

Note that SPEs were utilised given that they are commercially available and thus allow worldwide repetition of this work. These electrodes mimic pyrolytic graphite

electrodes, yet they are cost effective, do not require extensive pre-treatment and provide a good electrode surface to ensure that the graphene modification is reproducible.

5.2.3. BDD AND GC WORKING ELECTRODES

Boron-doped diamond (BDD) (3 mm diameter, BAS, USA) and glassy carbon (GC) (3 mm diameter, BAS, USA) working electrodes were also utilised, which were obtained commercially.

5.2.4. ELECTRODE PREPARATION

SPEs were single-use only and thus were new when utilised and disposed of after use. EPPG, BPPG, GC and BDD electrodes however, were reused; prior to each experiment being performed the electrodes were first polished using diamond suspension in a spray format (Kemet international Ltd.). [4] The diamond particle size was decreased from 1 to 0.25 μm. Between each polishing step the electrode was washed to remove any adhered diamond microparticles.

5.2.5. ELECTRODE MODIFICATION

Where liquid suspensions of graphene (or appropriate control solutions) were utilised a drop-casting method was used to immobilise the given material onto the supporting electrode material of choice. For example, aliquots of the graphene were carefully pipetted onto the electrode surface using a micro-pipette and allowed to dry at room temperature under nitrogen flow in order to eliminate oxidation of the graphene by the presence of atmospheric oxygen. Following the evaporation of the solution/carrier liquid phase, the electrode could either be further modified, or was ready to use.

5.3.1. SCANNING ELECTRON MICROSCOPY (SEM) AND ENERGY-DISPERSIVE X-RAY (EDX) SPECTROSCOPY

Scanning electron microscope (SEM) images and surface element analysis were obtained with a JEOL JSM-840 model equipped with an X-ray detector for energy-dispersive X-ray spectroscopy (EDX) microanalysis. Furthermore, a transmission electron microscope (TEM) was utilised where appropriate with a JEOL JEM-2010 (Oxford, Inca Energy TEM 100).

Unless stated otherwise, SEM, TEM and EDX analysis performed by Dr. Maria Gómez-Mingot, University of Alicante, Spain.

5.3.2. ATOMIC FORCE MICROSCOPY (AFM)

Atomic Force Microscopy (AFM) data was collected in TappingModeTM using a Veeco Dimension 3100 scanning probe microscope with a NanoScope V controller; images were produced using NanoScope analysis v1.4.

Unless stated otherwise, AFM images were produced by Miss. Sarah A. Varey, University of Manchester, U.K.

5.3.3. RAMAN SPECTROSCOPY

Raman spectra were recorded using LabRam (Jobin-Ivon) with a confocal microscope ($\times$100 objective) spectrometer with a He-Ne laser at 488 nm excitation at a very low laser power level (0.9 mW) to avoid any heating effect (beam width *ca*. 100 μm).

Unless stated otherwise, Raman spectroscopy was performed by Miss. Sarah A. Varey, University of Manchester, U.K.

5.3.4. X-RAY PHOTOELECTRON SPECTROSCOPY (XPS)

X-ray photoelectron spectroscopy (XPS, K-Alpha, Thermo Scientific) was used to analyse the surface of various samples. All spectra were collected using Al-K radiation (1486.6 eV), monochromatised by a twin crystal monochromator, yielding a focused X-ray spot with a diameter of 400 µm, at 3 mA × 12 kV. The alpha hemispherical analyser was operated in the constant energy mode with survey scan pass energies of 200 eV to measure the whole energy band and 50 eV in a narrow scan to selectively measure the particular elements. Thus, XPS was used to provide the chemical bonding state as well as the elemental composition of the surface. Charge compensation was achieved with the system flood gun that provides low energy electrons and low energy argon ions from a single source.

Unless stated otherwise, XPS analysis was performed by Dr. Maria Gómez-Mingot, University of Alicante, Spain.

5.3.5. DENSITY-FUNCTIONAL THEORY (DFT)

Spin-polarised density-functional theory (DFT) calculations were performed using the ORCA program. [5] The geometries of all of the structures were optimised using the B3LYP hybrid exchange-correlation functional and a 6-31G** basis set, [6-8] where the optimisation was terminated when the magnitude of the force on each atom was less than 0.015 eV $Å^{-1}$.

DFT calculations were performed by Dr. Lindsey J. Munro, Manchester Metropolitan University, U.K.

5.4.1. S-GRAHENE: GRAPHENE WITH ADSORBED SURFACTANT

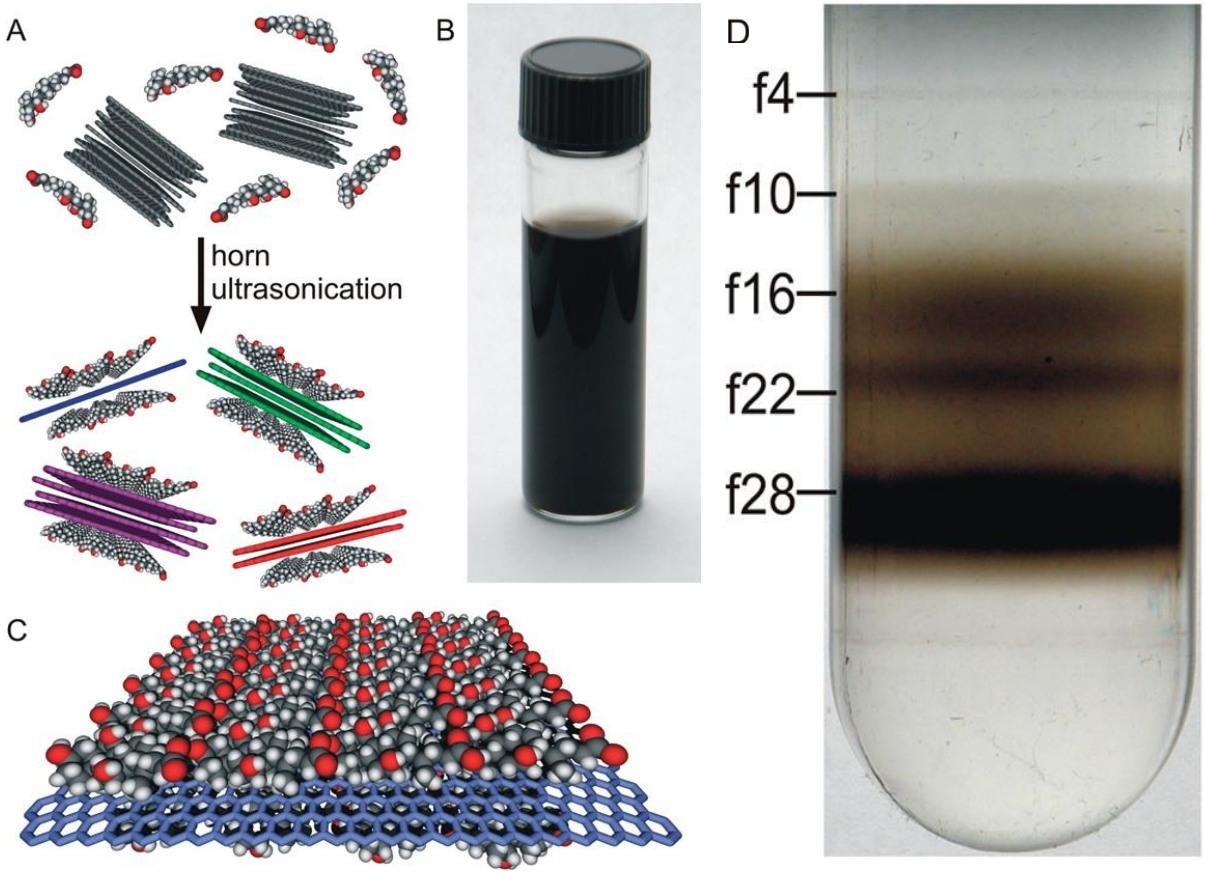

Figure 5.1 *(**A**) Schematic illustration of the graphene exfoliation process. Graphite flakes are combined with sodium cholate in aqueous solution. Horn ultrasonication exfoliates few-layer graphene flakes that are encapsulated by surfactant micelles. (**B**) Photograph of a 90 μg mL^{-1} graphene dispersion in sodium cholate six weeks after it was prepared. (**C**) Schematic illustrating an ordered surfactant(sodium cholate)-monolayer on graphene. (**D**) Photograph of a centrifuge tube following the first iteration of density gradient ultracentrifugation. Lines mark the positions of the sorted S-graphene fractions within the centrifuge tube. Reproduced from Ref. [*[9]*].*

S-graphene was commercially obtained from NanoIntegris, (Illinois, U.S.A.) [10] and is known as 'PureSheets^{TM}' (research grade). The graphene (*with surfactant* adsorbed on its surface) comprises entirely of pristine graphene platelets that have not been oxidised, reduced or chemically modified. The S-graphene is produced *via* density gradient ultracentrifugation and the methodology has been reported and characterised previously. [9] Figure 5.1 depicts a

schematic illustration of the surfactant based graphene exfoliation procedure. The process involves the bile salt 'sodium cholate' which promotes graphite exfoliation resulting in graphene-surfactant complexes having buoyant densities that vary with graphene thickness (*i.e.* the number of graphene sheets/layers making up the complexes). This results in a grading of the graphene and hence different fractions are observed, meaning that graphite and multi-layer graphene is not inadvertently incorporated into the graphene samples. [9, 10]

5.4.1.1. S-GRAPHENE CHARACTERISATION

The S-graphene is in an aqueous solution (0.5 µg per 10 µL) with an ionic surfactant (2 % w/v) and consists of a mean flake area of 10,000 nm^2. [9, 10] The graphene consists of: 27 % single layer, 48 % double layer, 20 % triple layer and 5 % ≥4 layers and due to the fabrication approach does not have any graphite impurities; given that only the upper-most 'top' layer of the solution indicated in Figure 5.1D is decanted and utilised. Figure 5.2 depicts a typical AFM image of several S-graphene flakes after deposition onto a SiO_2 substrate.

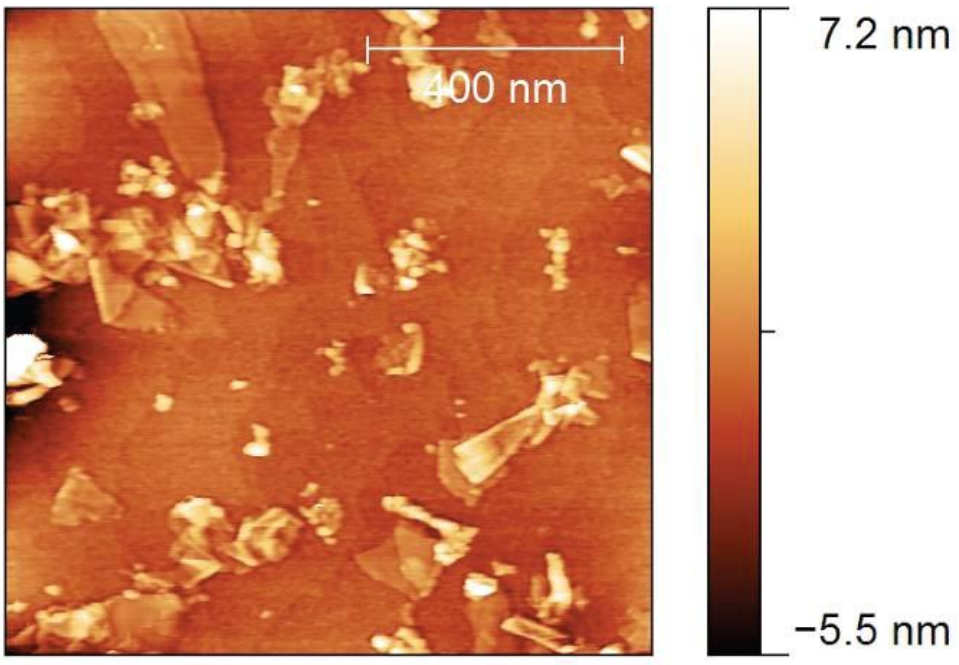

Figure 5.2 *A typical AFM image of several pristine S-graphene flakes deposited on a SiO_2 substrate, image provided by the manufacturer.* [10]

S-graphene flakes, deposited onto a SiO_2 substrate, have also been previously characterised by Raman spectroscopy. [9] Typical Raman spectra from each layer of the sorted S-graphene sample (as identified in Figure 5.1D) are depicted in Figure 5.3. Through analysis of the G band at *ca.* 1590 cm^{-1} and the 2D (or G') band at *ca*. 2700 cm^{-1}, for the case of fraction 'f4' Raman indicates the presence of single layer graphene, which is deduced through the ratio of the 2D/G bands where a G band of lower intensity than the 2D indicates single layer 'graphene' and additionally a symmetrical 2D peak supports the presence of few layer graphene (opposed to graphite, which, if present, would result in the said peak possessing a 'shoulder'). [9, 11] It is notable that the thickness (number of graphene layers) of the S-graphene flakes increases as a function of the fraction analysed, with more 'dense' fractions (thus those positioned lower down the centrifuge tube after centrifugation, *i.e.* f28) exhibiting Raman spectra constant with that expected for multi-layered graphene structures.

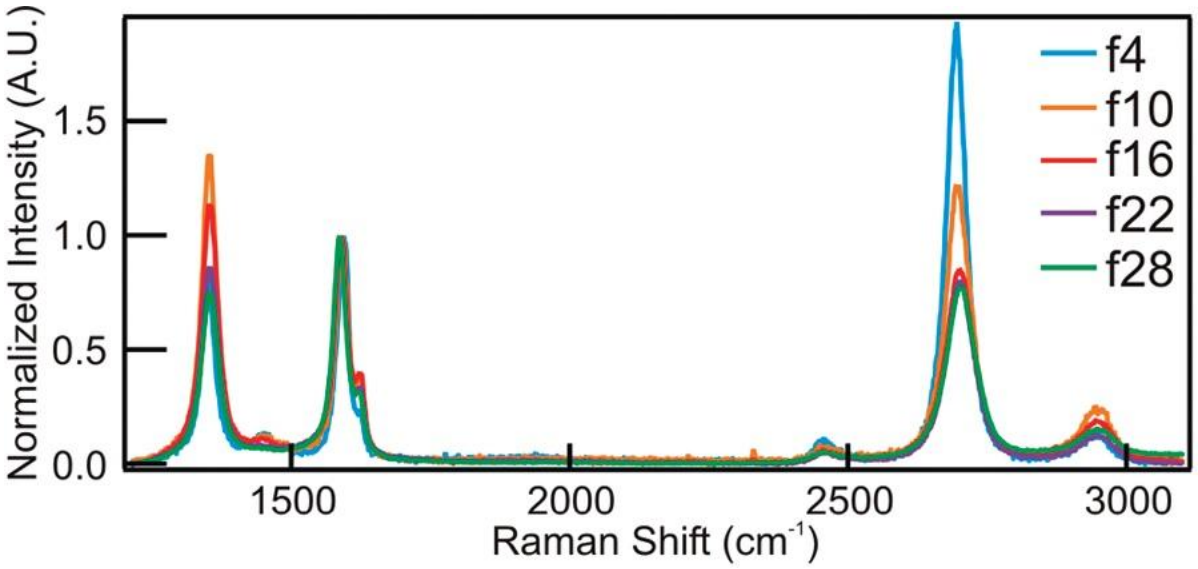

Figure 5.3 *Representative Raman spectra of sorted S-graphene flakes (as identified in Figure 5.1D) from fractions f4 (blue), f10 (orange), f16 (red), f22 (purple) and f28 (green) on SiO_2 with the G band (ca. 1590 cm^{-1}) intensity normalised to unity. Reproduced from Ref. [9].*

XPS analysis reveals the presence of 74.66 % atomic carbon, 16.43 % atomic oxygen, 4.12 % atomic nitrogen, 2.63 % atomic sodium and 2.13 % atomic sulphur. Interpretation of

the XPS spectra for the case of the oxygenated species reveals the presence of hydroxyl, carbonyl, epoxy, and ether functional groups. Identification of nitrogen *via* XPS indicates possible pyridone type functionalisation which is likely due to an acid treatment performed prior to the density gradient ultracentrifugation process. [9, 10] XPS indicates the presence of sulphur, sodium, and nitrogen which might suggest that both anionic (in addition to sodium cholate) and cationic surfactants are present, with the latter likely to be associated with post-processing by the company supplying the S-graphene. [10] However the company supplying the S-graphene is not willing to disclose this information. Furthermore, note that the assumed oxygen content of the graphene as revealed through XPS might actually result from a contribution of the sodium cholate present (Figure 5.4 depicts its structure); however de-convolution of this is not possible at this stage.

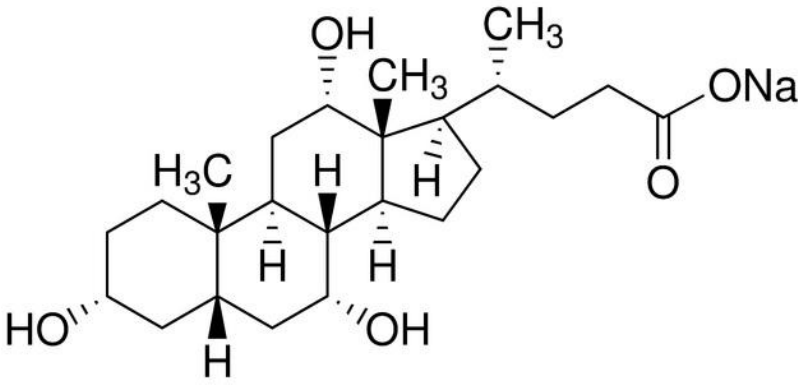

Figure 5.4 *The structure of sodium cholate.*

5.4.2. P-GRAHENE: PRISTINE (SURFACTANT FREE) GRAPHENE

P-graphene (*without surfactant*) was commercially obtained from 'Graphene Supermarket' (Reading, MA, USA) [12] and are known as 'Pristine Graphene Monolayer Flakes', comprising entirely of pristine graphene platelets dispersed in ethanol (solutions consisted of either 10 µg per 10 mL or 0.5 mg per 10 mL) that have not been oxidised, reduced, or chemically modified in anyway and are free from surfactants. The P-graphene was synthesised *via* the substrate-free gas-phase method, as previously reported and

characterised. [13-15] Figure 5.5 depicts a schematic illustration of the fabrication procedure. The single-step technique involves sending an aerosol consisting of liquid ethanol droplets and argon gas directly into a microwave-generated argon plasma (at atmospheric-pressure), where over a time scale in the order of 10^{-1} s, ethanol droplets evaporate and dissociate in the plasma forming solid matter that through characterisation by transmission electron microscopy (TEM) and Raman spectroscopy is confirmed to be graphene. [13-15] The fabricated graphene sheets are sonicated in ethanol to form a homogeneous suspension before being distributed by the supplier. [12, 15]

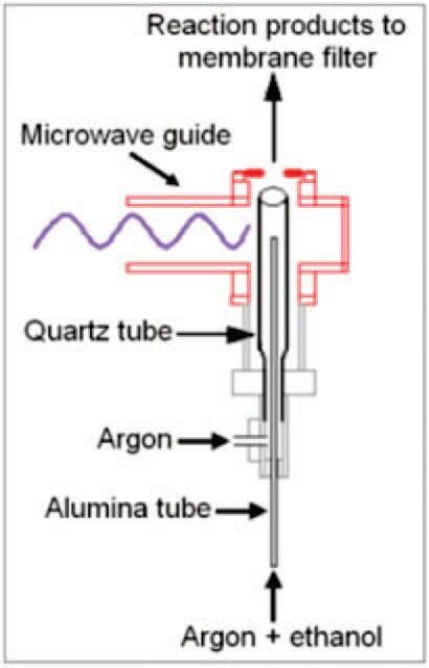

Figure 5.5 *Schematic of the atmospheric-pressure microwave plasma reactor used to synthesise P-graphene. Reproduced from Ref. [13].*

5.4.2.1. P-GRAPHENE CHARACTERISATION

The graphene has an average flake thickness of 0.35 nm (1 monolayer) with an average particle (lateral) size of 550 nm (150 – 3000 nm). [12, 15] Figure 5.6A depicts a typical TEM image of the commercially purchased graphene and Figure 5.6B shows a high-resolution TEM image, where a hexagonal arrangement of carbon atoms, which is characteristic of graphene, is clearly evident.

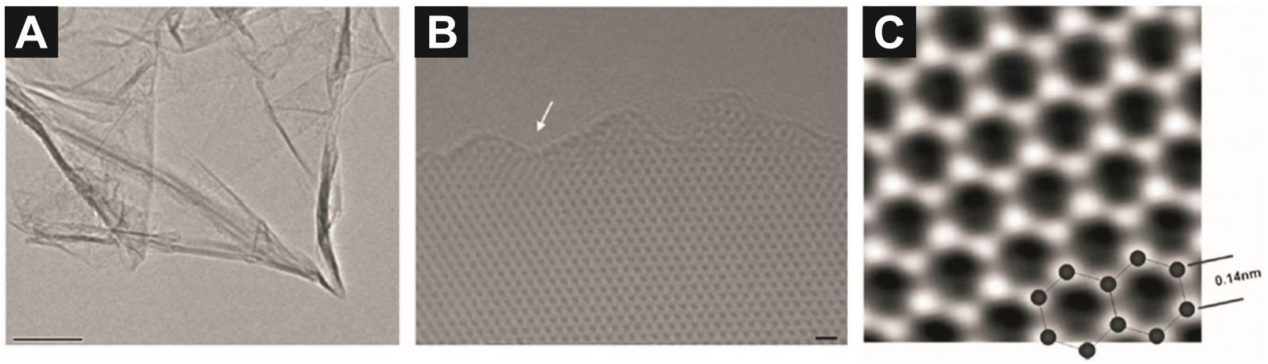

Figure 5.6 *(**A**) A typical low-magnification TEM image of the graphene sheets; the scale bar is 100 nm. (**B**) A high-resolution TEM image, where the white arrow indicates the edge of the graphene sheet; the scale bar is 4 Å. (**C**) An atomic-resolution image (TEAM 0.5) of a clean and structurally perfect synthesised graphene sheet. Individual carbon atoms appear white in the image. The image was obtained through the reconstruction of the electron exit wave function from 15 lattice images using MacTempas software. Reproduced from Ref. [14].*

This material has been characterised and reported previously by Dato and co-workers. [14] Figure 5.6C, from their work, shows an atomic-resolution image that reveals a highly ordered synthesized single-layer graphene sheet (captured with an aberration-corrected transmission electron microscope (TEAM 0.5), [14] capable of clearly resolving individual carbon atoms, adsorbates, and defects on graphene at an accelerating voltage of 80 kV). [14] Fourier Transform Infrared spectroscopy analysis was used to determine the presence of functional groups on the graphene, where it is evident that such groups were either absent or minimal. [14] XPS analysis was performed (using a PHI 5400 ESCA/XPS utilising an Al Ka radiation source – the spot size used was 1.1 mm in diameter) and reported to reveal that oxygen from the ethanol utilised during the synthesis process does not bond to the graphene sheets, and it was additionally reported that the clean and highly ordered free-standing graphene sheets are free from functional groups. [14]

P-graphene flakes, deposited a SiO_2 substrate, have also been previously characterised by Raman spectroscopy. [13] Raman spectra from a region on the substrate were obtained using a SPEX 1877 0.6 m triple spectrometer at 488 nm, with a 5 cm^{-1} spectral resolution.

Measurements were performed with an incident power of 40 mW using a spot size of 300 × 120 μm. [13] The most prominent feature in the Raman spectrum of graphene is the 2D peak; its position and shape can be used to clearly distinguish between single-layer, bi-layer, and few-layer graphene. [13] Single-layer graphene sheets have a single, sharp 2D peak below 2700 cm^{-1}, while bi-layer sheets have a broader and up shifted 2D peak located at *ca*. 2700 cm^{-1}. [13] The authors obtained a Raman spectrum from their (commercially available) synthesised graphene sheets (Figure 5.7), which exhibits a single, sharp 2D peak at *ca*. 2670 cm^{-1}, indicating that the analysed region consisted of single-layer graphene. [13]

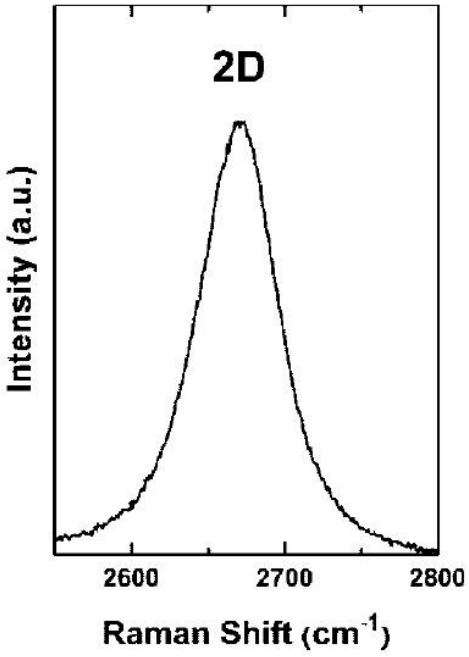

Figure 5.7 *Raman spectra of the commercially available P-graphene, focused on the 2D region. Reproduced from Ref. [13].*

Independent XPS chemical analysis was performed on the P-graphene and revealed the material to comprise of 95.04 % atomic carbon and 4.96 % atomic oxygen. Analysis of the spectra reveals a large peak at 284.6 eV associated to C-H bonding and analysis of the oxygen peak at 531.64 eV is associated to C=O moieties. The low O/C ratio is as expected for near true graphene.

5.4.3. GRAPHITE POWDER

Synthetic graphite powder was commercially obtained from 'Gwent Group' (Pontypool, UK) (P2010808P2, batch number: 2080512.05) [16] and as with the P-graphene, the powder was not oxidised, reduced or chemically modified in anyway prior to use.

5.4.3.1. GRAPHITE POWDER: CHARACTERISATION

Figures 5.8A and 5.8B depict the respective SEM and TEM images (Transmission Electron Microscopy (TEM) images were obtained using a JEOL JEM-2010 equipped with an EDX microanalysis (Oxford, Inca Energy TEM 100)) of the synthetic graphite powder where it is evident that the graphite possesses average L_a values similar to those observed for the P-graphene and for graphene powder (see Chapter 5.4.7), however, in this case it is clear that the material consists of multiple layers of stacked graphene sheets, resulting in a thick L_c ([2.72 nm (8 graphene-layers or larger)) consistent with that expected for graphite materials.

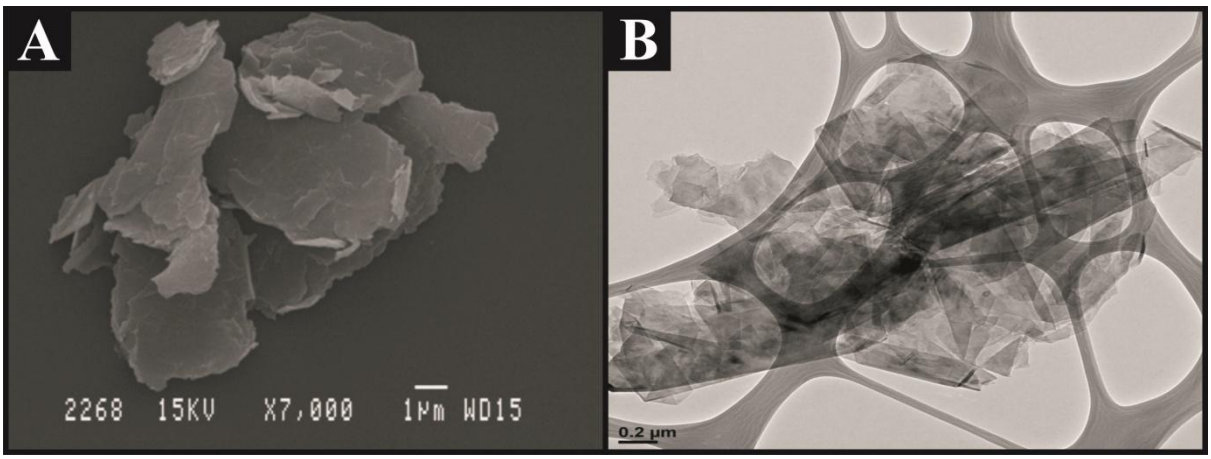

Figure 5.8 *SEM (**A**) and TEM (**B**) images of the synthetic graphite powder utilised. TEM image obtained by Maria Gómez-Mingot, University of Alicante, Spain.*

Figure 5.9 depicts the Raman spectrum of the graphite powder utilised, revealing the two characteristic peaks (G and 2D (G')) of graphitic materials at *ca*. 1579 and 2670 cm^{-1}. The asymmetrical nature of the 2D (G') band in this case (in addition to the 'shoulder' evident) is consistent with that expected at graphite samples of multiple graphene layers in

thickness, particularly that of HOPG. Furthermore, in this case the intensity ratio of the G and 2D bands also indicates the presence of multi-layered graphite, confirming the observations inferred through analysis of Figure 5.8. Note that the low/faint intensity of the D band (*ca*. 1335 cm^{-1}) suggests that the synthetic graphite is of high quality and possesses a low level of basal plane crystal defects across its lattice.

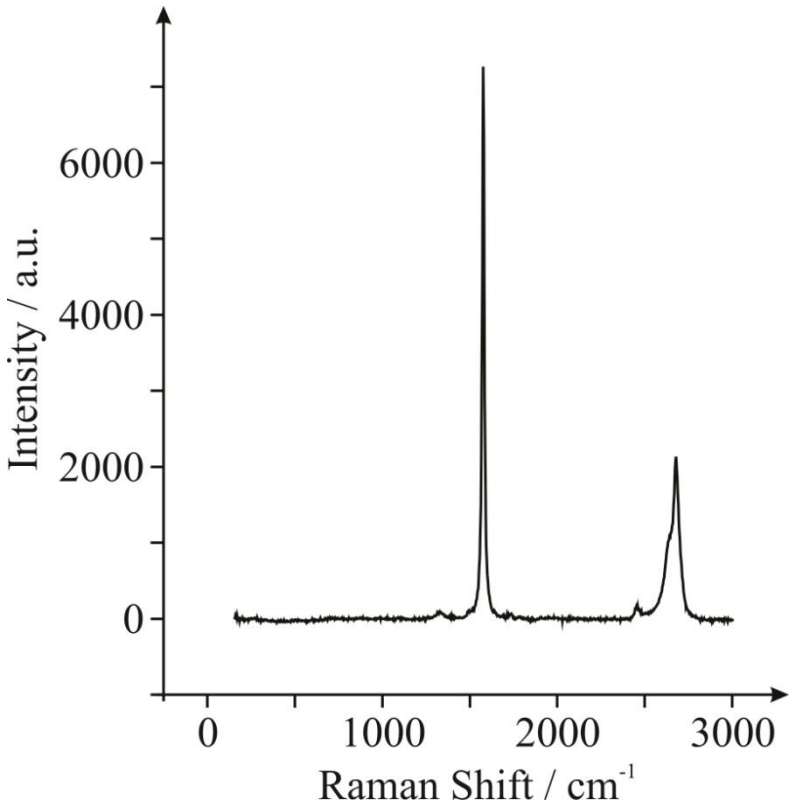

Figure 5.9 *Raman spectra of the graphite powder utilised.*

XPS analysis revealed the graphite material to comprise of 97.9 % atomic carbon and 2.1 % atomic oxygen. The carbon content comprises of 75.5 % corresponding to 284.5 eV which is characteristic of graphitic groups (with 15.4 % at 285.8 eV, relating to C–C, C=C and C–H graphitic groups), 3.8 % at 288.3 eV and 3.2% at 290.8 eV which both correspond to C–O and C=O bonds respectively. The oxygen content is 0.94 and 1.16 % at 531.7 and 533.1 eV, which corresponds to C–OH, C=O and C–O respectively.

5.4.4. CVD-GRAPHENE: CVD GROWN GRAPHENE ON NI SUBSTRATE

CVD-graphene was commercially obtained from 'Graphene Supermarket' (Reading, MA, USA) [12] and is known as 'CVD-Graphene^{TM}: Graphene Film on Nickel' where single- to few- layer continuous graphene films with low defect density are grown directly onto a Nickel (Ni) film deposited on an oxidised silicon wafer using a CVD process, as previously reported and characterised. [12, 17] Note that a schematic illustration of a CVD process is available in Figure 3.7.

5.4.4.1. CVD-GRAPHENE CHARACTERISATION

Figure 5.10 depicts a typical SEM image and Figure 5.11A shows Raman spectra for a single layer region of the commercially obtained CVD-graphene sample, provided by the manufacturer. [12] Observation of the Raman spectrum shows a symmetric single peak is observed for the 2D band, of which the intensity is significantly higher than the G peak, confirming that the graphene utilised in this study is of high quality single layers, which is in agreement with previous literature reports. [17-19]

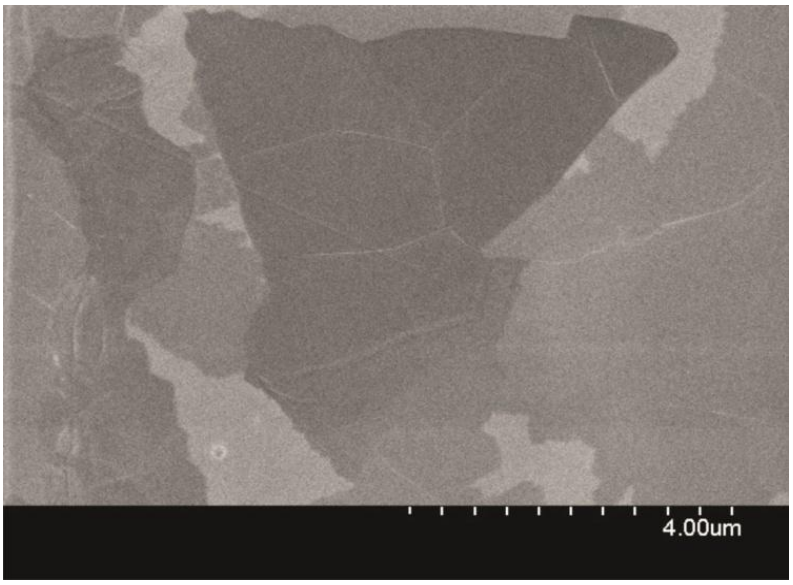

Figure 5.10 *SEM image of the commercially obtained CVD-graphene grown directly onto a Ni film on an oxidised silicon wafer. Image kindly provided by the manufacturer with the CVD-graphene sample, Ref. [12].*

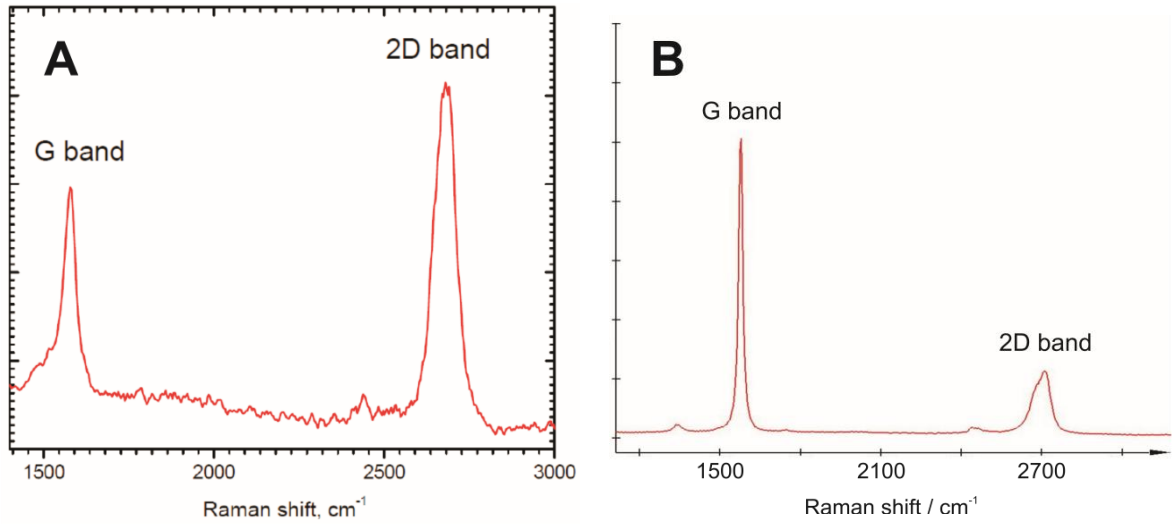

Figure 5.11 *Raman spectra of the commercially obtained CVD-graphene grown directly onto a Ni film on an oxidised silicon wafer, showing both graphene (**A**) and graphitic (**B**) regions. Images kindly provided by the manufacturer, Ref. [12].*

XPS analysis of the CVD-graphene surface revealed the presence of 81.74 % atomic carbon, 5.97 % atomic oxygen, 8.81 % atomic nickel and 3.47 % atomic silicon (note the last two components arise due to the probe depth of the XPS revealing the composition of the underlying supporting substrate – which also likely contributes to the % of atomic oxygen). Detailed analysis of the atomic carbon contribution revealed 63.2 % C1s at 284.6 eV which corresponds to C–H, C–C, $(CH_2)_n$ and C=C bonds that are characteristic of graphite/graphene, additionally 18.54 % of C1s occurred at 285.2 eV which is characteristic of C–C bonds. De-convolution of the atomic oxygen reveals O1s of 1.95 % (532.8 eV) and 0.45 % (533.7eV), corresponding to C=O, C-OH and C–O–C, and O from H2O adsorption. It is likely that the remaining oxygen originates from the presence of the underlying SiO_2.

Further insights were gained through the analysis of Raman spectra in Figure 5.11B, which shows that in certain areas, depending upon where the probe was aimed, a clear symmetrical 2D band was observed which is consistent with graphene (*e.g.* Figure 5.11A), while in other areas a broad peak for the 2D band is observed indicating the presence of multi-layered graphene. [17-19] Thus it is concluded that the CVD-graphene surface consists of

graphene with few- and multi- layered sections of graphene, *viz* effective graphitic islands, randomly distributed across the working surface. Hence, depending upon where is probed, researchers can readily gain false or misleading data indicating 'true graphene' when actually few- and multi- layered graphene is really evident.

Note, further characterisation of the CVD-graphene sample is provided in Chapters 8.1 and 8.2 (for example, optical and AFM images) given that in this case, the electrochemistry observed is used to support the understanding of the CVD-graphene surface topography. Hence, due to electrochemistry being utilised as a characterisation tool, the further understanding of the electrode surface is introduced throughout the aforementioned chapters.

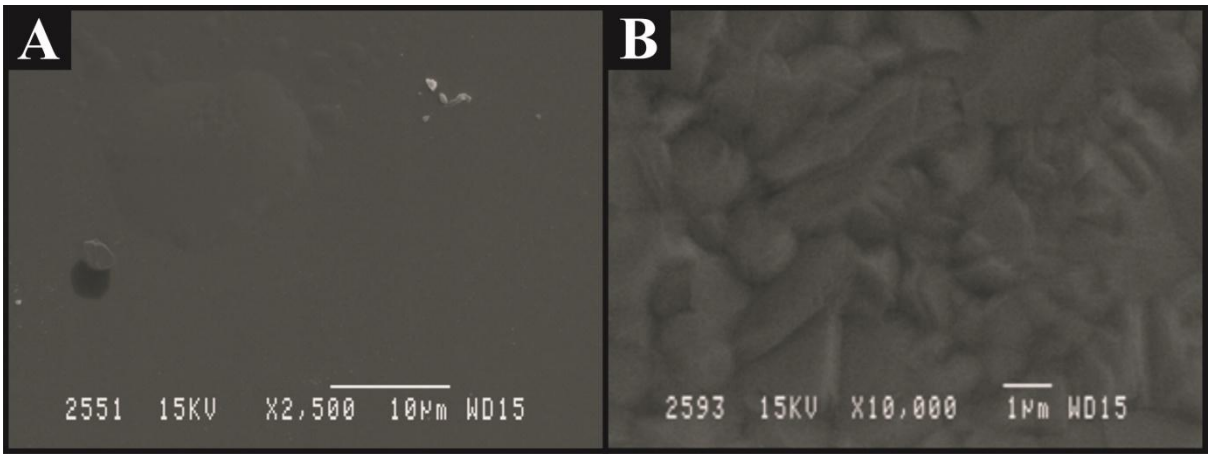

Figure 5.12 *SEM image of the bare (no graphene) Ni film on an oxidised silicon wafer (**A**) and of the commercially obtained CVD-graphene grown directly onto a Ni film on an oxidised silicon wafer support.*

A nickel film electrode was utilised as a control measure throughout work utilising the CVD-graphene. SEM images presented in Figure 5.12 show the underlying unmodified Ni film in comparison to that of CVD-graphene modified Ni film, revealing a modified surface at the latter.

M-graphene: the commercially available CVD synthesised monolayer graphene film (M-graphene) was obtained from 'Graphene Supermarket' (Reading, MA, USA) [12] and is known as 'Monolayer Graphene on 285 nm SiO_2 Wafer'. The single layer continuous graphene film (*ca*. 97 % graphene coverage (95 % monolayer) with occasional holes, cracks and small multi-layer islands) comprising graphene grains of different crystallographic orientations (polycrystalline in nature) is grown utilising a copper foil (25 µm thick) catalyst *via* a CVD synthesis method (*ca*. 1000 °C (cooling rate 40–300 °C min^{-1}) with H_2/CH_4 precursor (0.06 sccm and partial pressure 0.5 Torr) for less than three minutes growth time), [20-22] after which the graphene film is transferred onto an oxidised silicon wafer (electrochemically inert supporting substrate) *via* a poly-methyl methacrylate (PMMA) assisted transfer method, as previously reported and characterised; [20, 21, 23-25] note, the exact details are proprietary information. [12]

Q-graphene: the commercially available CVD synthesised *quasi*-graphene film (Q-graphene) was obtained from 'Graphene Supermarket' (Reading, MA, USA) [12] and is known as 'Multilayer Graphene on 285 nm SiO_2 Wafer'. The multi-layer (or few-layer) continuous graphene film (*ca*. 95 % graphene coverage with occasional holes and cracks) comprises graphene grains of polycrystalline nature. The multi-layer graphene film is not uniform, which is evident through observation of the optical microscopy image depicted in Figure 5.13B where a 'patchwork' like appearance indicates 'patches' of different thicknesses; the thickness varies from one to seven layers, with an average of four graphene layers (the graphene layers within the same 'patch' are aligned relative to each other (there is a graphitic AB-stacking order)). [12] The multi/few-layered continuous graphene film is grown utilising a nickel foil (500 nm thick) catalyst *via* a CVD synthesis method (*ca*. 1000 °C

(cooling rate 100 °C min^{-1}) with CH_4 precursor (10 sccm (H_2, 1400 sccm), ambient pressure) for *ca*. 5 minutes growth time), [20, 22, 26] after which the graphene film is transferred onto an oxidised silicon wafer *via* a poly-methyl methacrylate (PMMA) assisted transfer method; [20, 21, 24-26] the exact details are proprietary information. [12]

D-graphene: the commercially available CVD synthesised double-layer graphene film (D-graphene) was obtained from 'Graphene Supermarket' (Reading, MA, USA) [12] and is known as 'Single/Double Layer Graphene on 285 nm SiO_2 Wafer'. The mono-/bi-layer continuous graphene film (*ca*. 95% graphene coverage (up to *ca*. 30 % coverage is double-layer graphene islands) with occasional holes and cracks) comprising graphene grains of different crystallographic orientations (polycrystalline in nature) is grown utilising a modified method of the aforementioned CVD process. For example, a copper foil (206 nm thick) catalyst is utilised *via* a CVD synthesis method (*ca*. 800 °C (cooling rate 40–300 °C min^{-1}) with H_2/CH_4 precursor (5 sccm and partial pressure 0.39 Torr) for *ca*. 10 minutes growth time), [20-22] after which the graphene film is transferred onto an oxidised silicon wafer via the poly-methyl methacrylate (PMMA) assisted transfer method, as previously reported and characterised. [20, 21, 23-25] The exact details are proprietary information. [12]

5.4.5.1. M-GRAPHENE, Q-GRAPHENE AND D-GRAPHENE: PHYSICOCHEMICAL CHARACTERISATION

M-graphene and Q-graphene: monolayer graphene and *quasi*-graphene are the first materials to be considered in terms of their structural characterisation *via* optical spectroscopy and AFM analysis. Figures 5.13A and 5.14 depict the resultant optical and AFM images of the monolayer CVD grown graphene macrostructure (M-graphene). It is evident that the graphene domains comprising the material consist predominantly of single-layer graphene sheets, which appear to exhibit an intraplanar microcrystalline size, L_a of between 500 and

5000 nm and an average interplanar microcrystalline size, L_c of *ca*. 0.34 nm (one monolayer), which compares well to pristine graphene as reported theoretically in the literature. [27] The optical image in Figure 5.13A highlights occasional holes in the continuous graphene film and also reveals the presence of occasional small few-layer graphitic islands on the graphene surface. Closer inspection of the AFM images depicted in Figure 5.14 reveals the presence of ripples/wrinkles at the grain boundaries of the monolayer graphene domains, which are an inherent property of CVD grown graphene. [28, 29] Note that these structural features, present at the 'edge sites' of these graphene flakes/domains (*i.e.* grain boundaries), are likely to be the origin of the electron transfer properties observed at the graphene electrode and thus influence the observed electrochemical response, potentially giving rise to beneficial HET kinetics. [20, 27] Figures 5.13B and 5.15 depict the respective optical and AFM images of the CVD grown *quasi*-graphene macrostructure (Q-graphene). It is evident that the graphene domains comprising the surface possess average L_a values similar to those observed for the monolayer graphene alternative (M-graphene, *vide supra*); however, in this case it is clear that the graphene material consists of a single-/few- layer graphene support film (which as above is continuous, with occasional holes, cracks and ripples occurring at grain boundaries) over which large few-layer graphitic domains (graphitic islands) are distributed across the surface. These multiple layers of stacked graphene sheets, so-called graphitic islands, [30] result in the few-layer graphene domains/islands possessing large L_c values (L_c ranges from *ca*. 0.34 to 2.38 nm, *i.e.* 1–7 layers with an average of 4 graphene layers); however, such values do not correspond to the structural characteristics of graphite [28, 29, 31] and thus the composition of the CVD grown few-/multi- layer graphene electrode (Q-graphene) is consistent with that expected for *quasi*-graphene. [32]

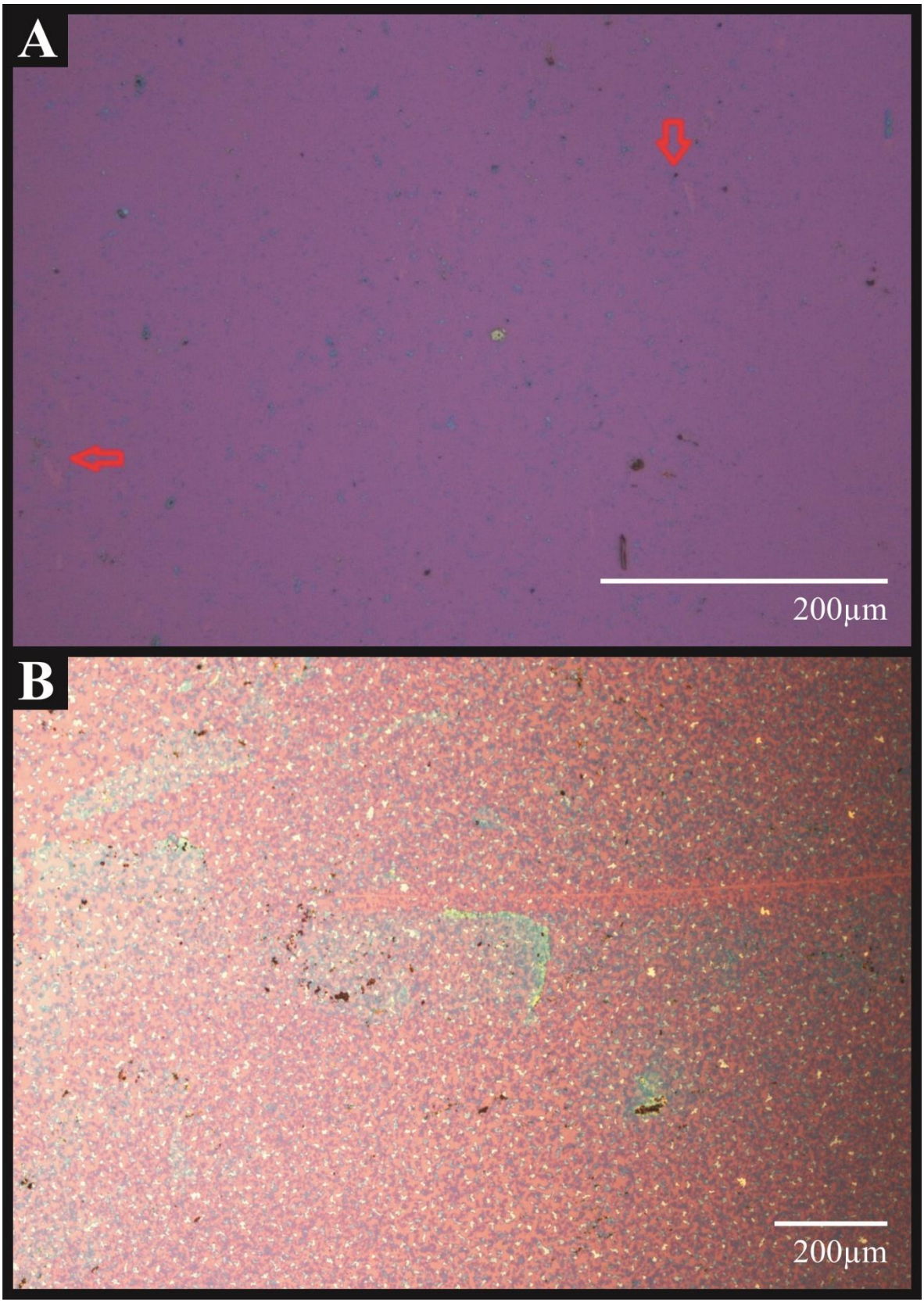

Figure 5.13 *Optical micrographs of the monolayer graphene (**A**, M-graphene) and quasi-graphene (**B**, Q-graphene) samples. Note that the red arrows in (**A**) indicate the occasional occurrence of holes in the M-graphene film.*

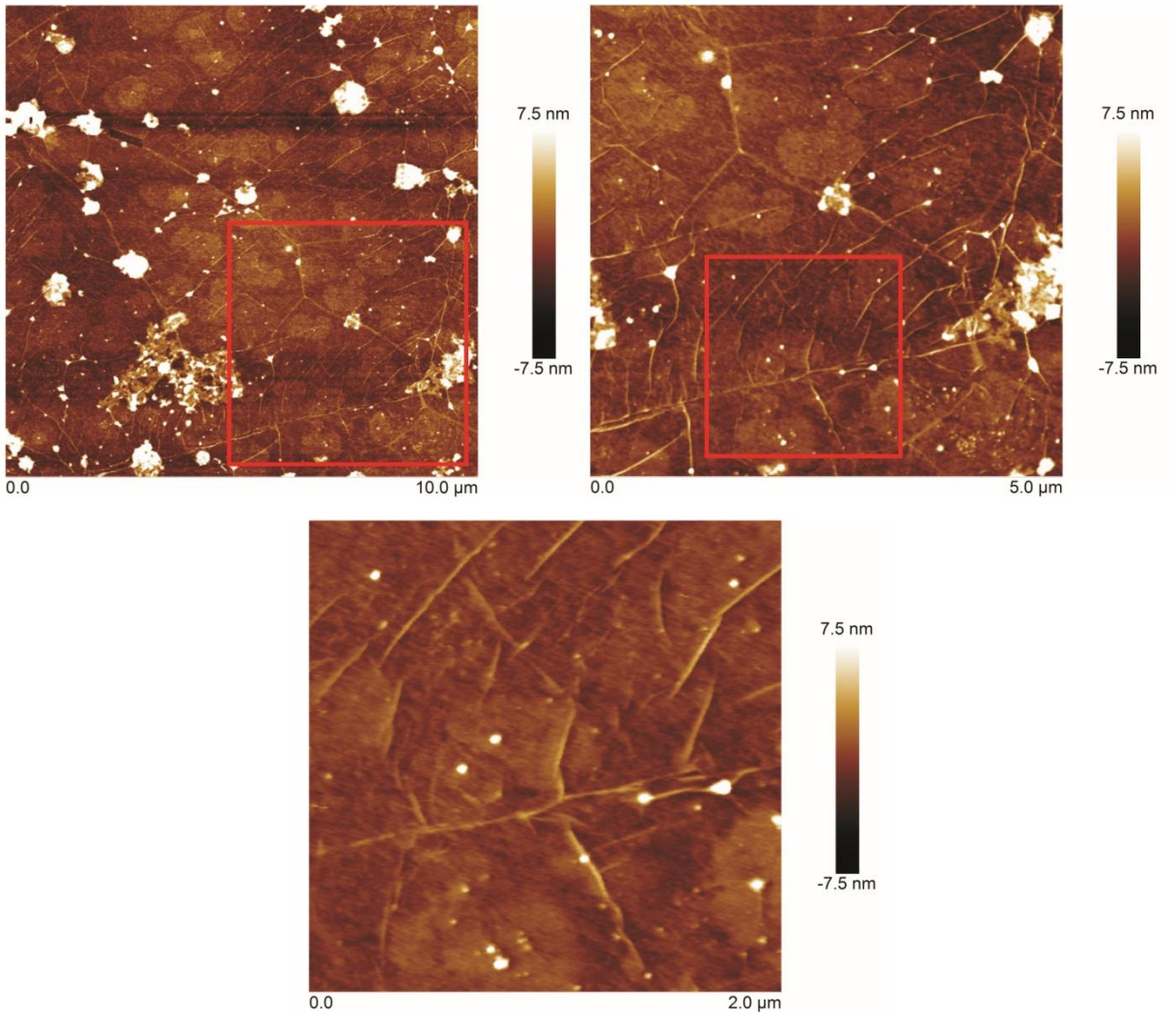

Figure 5.14 *AFM images of the monolayer graphene (M-graphene), successive images are progressively focused into the sample.*

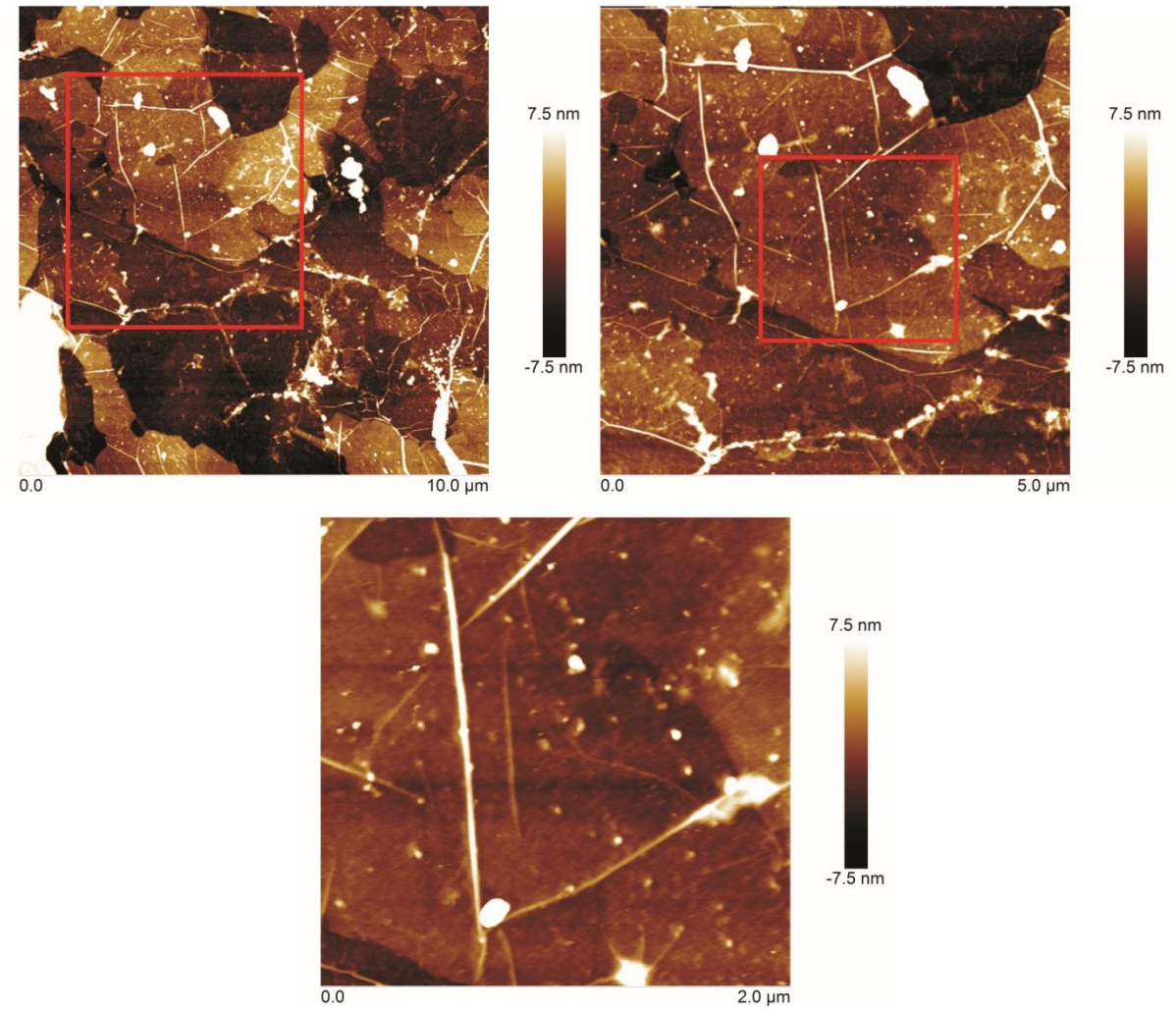

Figure 5.15 *AFM characterisation of the quasi-graphene (Q-graphene), with consecutive images arising from being progressively focused upon the sample.*

To gain further insight into the above observations, Raman spectroscopy was next performed on the graphene macrostructures of M-graphene and Q-graphene. Figure 5.16A depicts the Raman spectrum of the 'monolayer' graphene film (M-graphene) in addition to an optical micrograph of the probe position upon the domain surface. The Raman spectrum reveals two characteristic peaks at *ca*. 1550 and 2680 cm^{-1}, which are due to the G and 2D (G') bands respectively. Note that the highly symmetrical 2D (G') peak indicates that the surface is comprised of single-layer graphene (consistent with AFM and optical images, *vide supra*, Figures 5.13A and 5.14). [11, 28, 29] Additionally, the intensity ratio of the G and 2D bands (G/2D = 0.37) indicates that the graphene electrode is indeed comprised principally of

single-layer graphene domains, where the low intensity of the G band in relation to the 2D peak is characteristic of monolayer graphene. [11, 28, 29] The presence of a small D band (*ca*. 1330 cm^{-1}) indicates a small number of structural defects on the graphene surface (limited basal plane crystal defects), however the relatively low intensity of the D band, which is not easily distinguishable from the 'base line', suggests that an ordered graphene structure is present which is of high quality and thus represents that of pristine graphene in nature. [11, 28, 29]

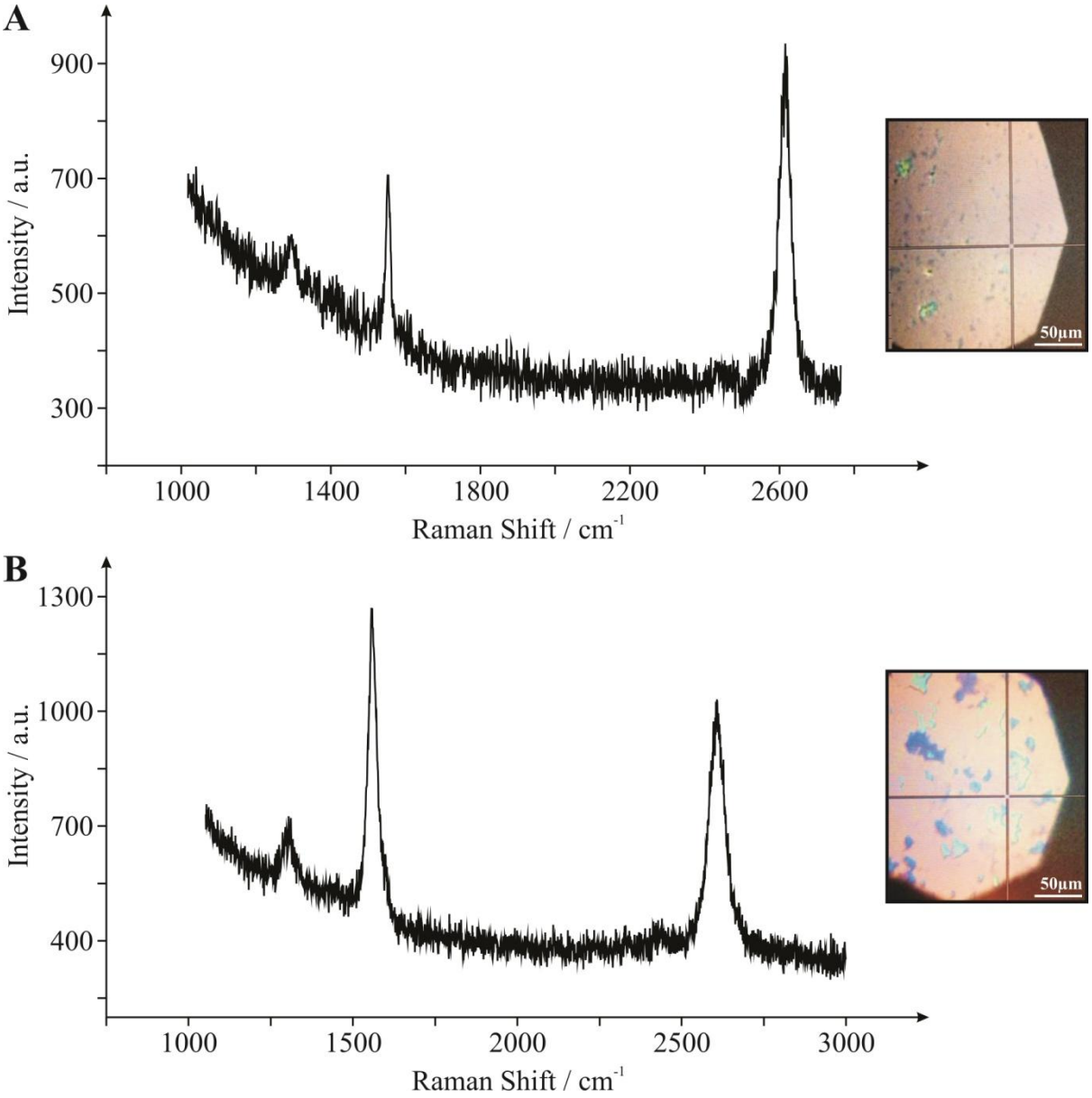

Figure 5.16 *Raman spectroscopy characterisation of monolayer graphene (**A**, M-graphene) and quasi-graphene (**B**, Q-graphene). Also shown are optical micrographs indicating the probe position utilised. Note that the dark spots indicate few- stacked graphene layers/islands.*

Figure 5.16B depicts the respective optical micrograph and Raman spectrum of the 'few-/multi- layered' (*quasi*-) graphene film (Q-graphene). The Raman spectrum reveals the two characteristic peaks (G and 2D (G')) of graphene/graphitic materials at *ca*. 1550 and 2680 cm^{-1}. [11, 28, 29] The high symmetry of the 2D (G') band peak, indicates that the surface comprises single- to few- layer graphene sheets (the slightly broader peak signifies the presence few-layer graphene, which is consistent with AFM and optical images, *vide supra*, Figures 5.13B and 5.15). Note that the 2D peak does not indicate the presence of graphite, which is characterised by a non-symmetrical, broad peak with distortion evident in the form of a 'shoulder'. [11, 28, 29] In this case the intensity ratio of the G and 2D bands (G/2D = 1.22) also indicates the presence of few-layered graphene domains, with the relatively equal intensities of the G and 2D peaks coinciding with the presence of *ca*. 3 or 4 graphene layers (for this probe position), [11, 28, 29] which again is consistent with that expected for the structural configuration of *quasi*-graphene. [32] The low/faint intensity of the D band (*ca*. 1315 cm^{-1}) again suggests that in this case the quasi-graphene is of high quality and pristine in nature, possessing a low level of basal plane crystal defects across its lattice. [11, 28, 29] Note that increasing the number of graphene layers towards the structural composition of graphite would result in evolution of the G peak intensity such that it would significantly surpass that of the 2D peak, characterised by G/2D ratios exceeding 3.75 (in addition to the emergence of the 'shoulder' effect noted above); thus it is clear that the graphene samples M-graphene and Q-graphene *do not* display similar structural characteristics relating to graphite.

Close inspection of the optical micrographs presented in Figure 5.16 reveals the presence of thicker graphene islands distributed predominately across the *quasi*-graphene domain (Q-graphene). These multi-layered/defect site domains were probed *via* Raman spectroscopy and the resultant spectrums are presented in the Figure 5.17). Surprisingly, analysis of the Raman spectra in these cases at both the mono- and *quasi*- graphene materials

(M-graphene and Q-graphene respectively) indicate no significant alterations in the reported G/2D band ratios from the values reported above and thus indicate that the number of graphene layers remain unaltered. However, what is evident (again predominately in the case of the *quasi*-graphene) is an increment in the intensity of the D band (*ca*. 1330 cm^{-1}) at such sites. This is as expected due to the D band relating directly to the degree of edge plane defects across the graphene surface, where the visible graphitic islands depicted in Figure 5.16B give rise to a larger coverage of edge plane like- sites/defects on the *quasi*-graphene surface (Q-graphene), resulting from the exposed 'edges' of these few-/multi- layered graphene domains.

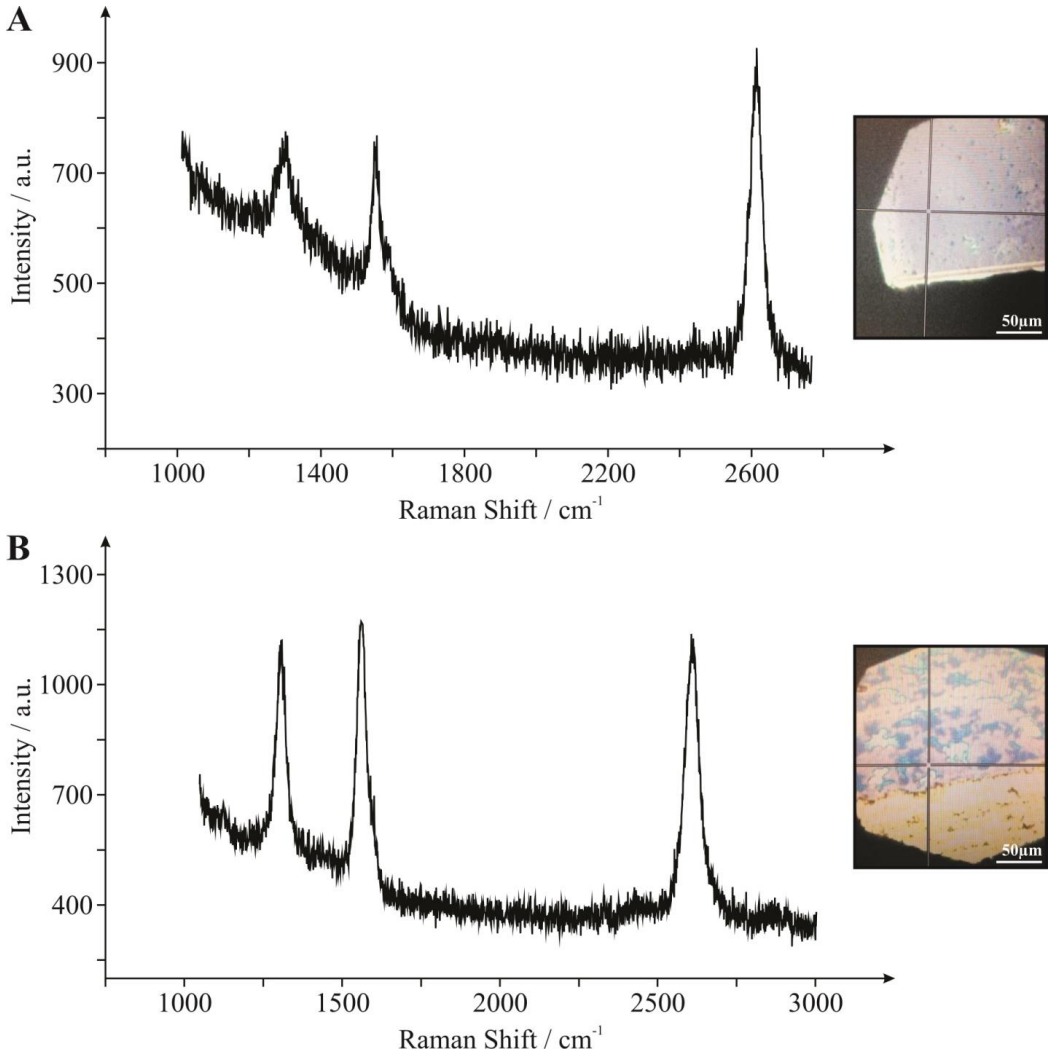

Figure 5.17 *Raman spectroscopy characterisation of the edge regions (comprising multi-layered/edge plane defect sites) of the monolayer graphene (**A**, M-graphene) and quasi-graphene (**B**, Q-graphene) materials. Also shown are optical micrographs indicating the probe position utilised.*

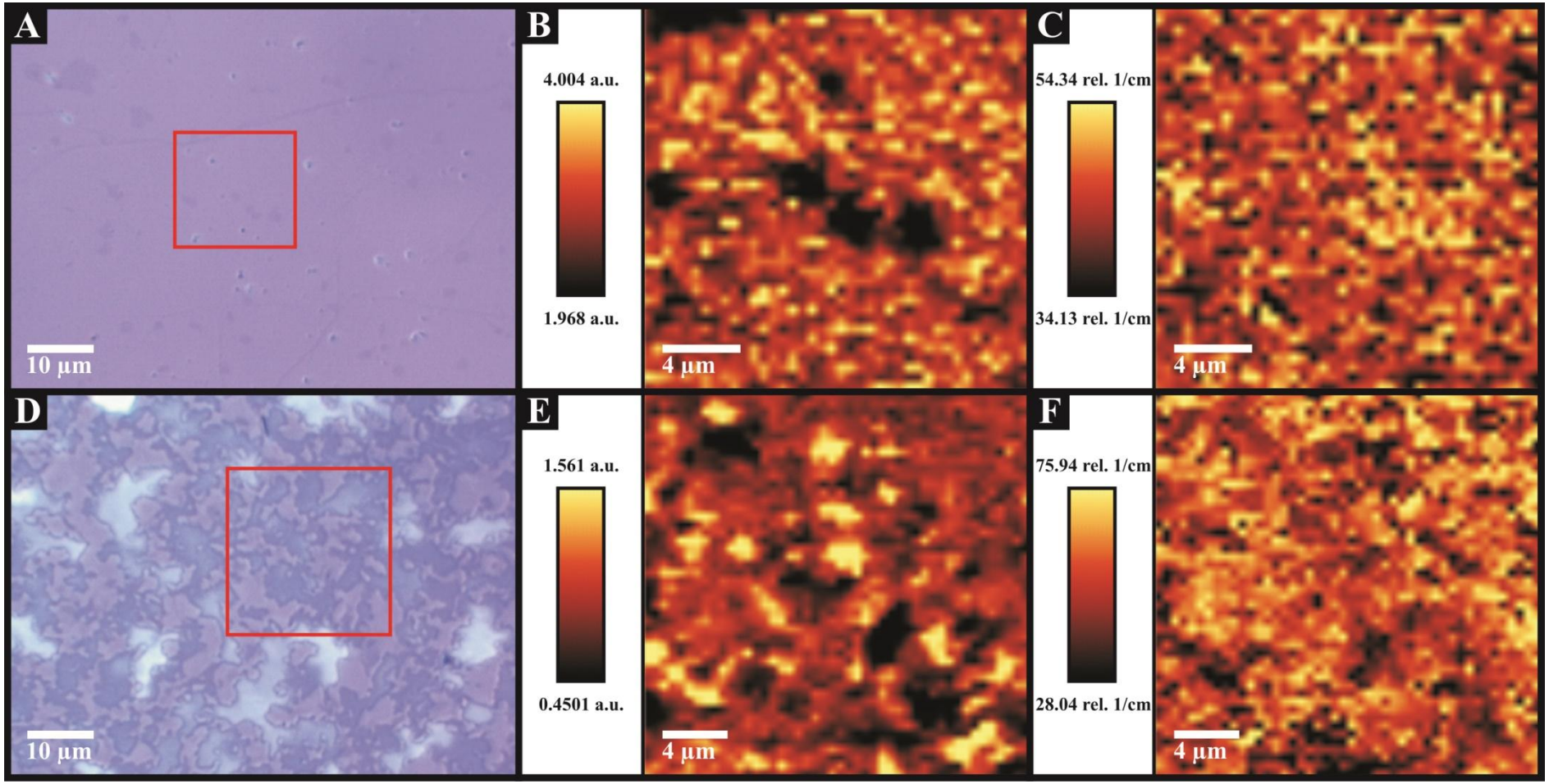

Figure 5.18 *Raman maps and supporting optical micrographs indicating the sample area utilised. Samples were (M-graphene) monolayer graphene (**A**, **B** and **C**) and (Q-graphene) quasi-graphene (**D**, **E** and **F**). Raman maps show: (**B** and **E**) 2D/G band ratio, where darker areas represent increased graphene layer numbers; and (**C** and **F**) the FWHM of the 2D peak, with lighter areas indicative of thicker graphene domains.*

Figure 5.18 depicts Raman maps that were obtained over a relatively large central area of the graphene surfaces (M-graphene and Q-graphene) in order to ascertain the overall quality of the graphene present on the monolayer graphene (Figures 5.18B and 5.18C) and *quasi*-graphene (Figures 5.18E and 5.18F) materials. The Raman maps are in excellent agreement with analysis obtained *via* the individual Raman probe positions and with the AFM images (see Figures 5.14 and 5.15). Figures 5.18B and 5.18E represent variations in the intensity of the 2D/G peak ratios over the area analysed on the monolayer and *quasi*-graphene samples respectively (M-graphene and Q-graphene), with the darker spots (relative to the scale provided) indicating thicker graphene regions. It is evident that the 'monolayer graphene' (M-graphene) indeed comprises a single-layer continuous graphene film (indicated by the uniform distribution of 'lighter pixels') with occasional defects or islands present (*i.e.* the darker spots in Figure 5.18B). In contrast the *quasi*-graphene (Q-graphene) possesses a large number of apparent multi-layered islands distributed across the surface, each with varying thickness as indicated by the severe contrast observed between multiple 'light' and 'dark' patches. Figures 5.18C and 5.18F represent variations in the Full Width at Half Maximum (FWHM) of the 2D peak over the areas analysed on the monolayer and *quasi*-graphene surfaces respectively. The width of the 2D peak is related to the quality of the graphene present, where 'thinner' peak widths (darker pixels) indicate pristine single layer graphene and 'thicker' (more perturbed) peak widths (lighter pixels) are indicative of thicker graphene layers (as discussed earlier). The even distribution of colour in both maps (Figures 5.18C and 5.18F) indicates pristine graphene is present on both samples, however relative to the scale provided, the 'darker' colouring of the map representing the monolayer graphene (Figure 5.18C, M-graphene) is indicative of single-layer graphene relative to the 'lighter' colouring of the *quasi*-graphene (Figure 5.18F, Q-graphene) indicating the presence of multi-layered graphene.

Finally, XPS was conducted on the two graphene materials (M-graphene and Q-graphene). De-convolution of the spectra relating to the monolayer graphene domain (M-graphene) reveals it to be composed of 42.73 % carbon, 27.72 % oxygen and 29.55 % silicon. The carbon content comprises of 32.15 % corresponding to 284.8 eV which is characteristic of graphitic groups, and 10.27 % at 286.6 eV which corresponds to C–O and C=O bonds. Of the oxygen content, 2.1 % is comprised from contributions at 287.9 and 533.15 eV, which correspond to C=O and C–O groups. Note that contributions from the silicon (29.55 %) and remaining oxygen content (25.62 %) are a result of the probe depth (*ca*. 2–3 nm) given that the thin graphene film is supported on top of an oxidised silicon wafer. In considering only the carbon and oxygen contributions arising from the graphene material (which are exposed only to the solution when used in electrochemistry), XPS reveals the monolayer graphene (M-graphene) to comprise a O/C ratio of *ca*. 0.05, which is consistent with that of a low oxygen content of the graphene domain and thus is pristine in nature. De-convolution of the spectra relating to *quasi*-graphene (Q-graphene) reveals it to be composed of 61.50 % carbon, 20.06 % oxygen and 18.44 % silicon (note that due to the probe depth (*vide supra*) and the increased thickness of the multi-layered graphene surface, in this case the % contribution of carbon has increased and the respective % contribution of silicon has decreased; as expected). The carbon content comprises of 45.62 % corresponding to 284.6 eV which is characteristic of graphitic groups, and 8.05 and 6.64 % at 285.7 and 286.9 eV respectively which correspond to C–H, C=C, C–O and C=O bonds. In this case, of the oxygen content, 4.4 % is comprised from contributions at 287.9 and 533.15 eV. As above, the silicon (18.44 %) and the remaining oxygen content (15.66 %) contributions are a result of the probe depth utilised (which penetrates the support surface). For the case of the *quasi*-graphene (Q-graphene), considering only the carbon and oxygen contributions arising from the graphene material XPS reveals a O/C ratio of *ca*. 0.07, which is consistent

with inferences gained through Raman spectroscopy and indicates that the *quasi*-graphene structure is comprised of pristine graphene domains.

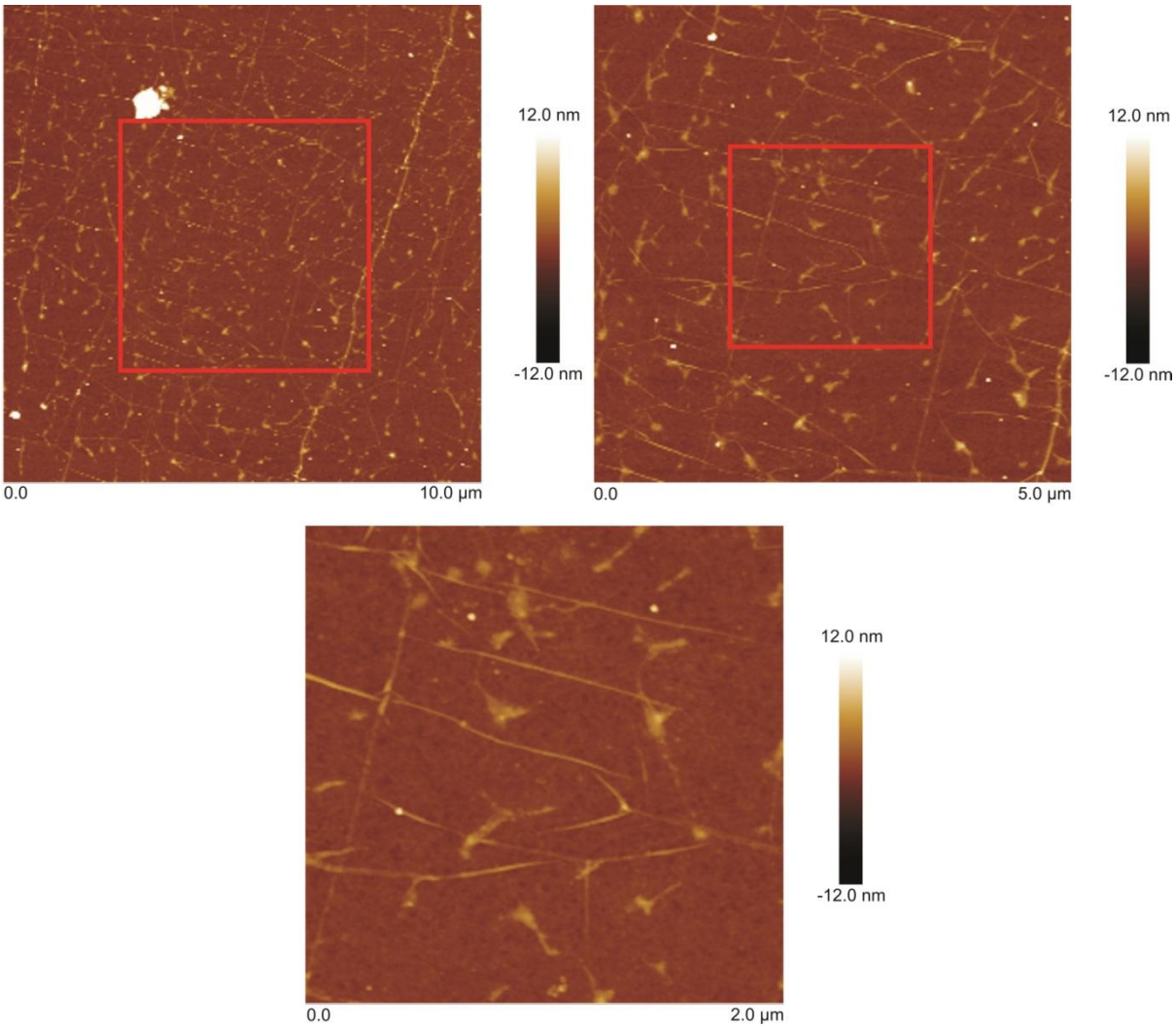

Figure 5.19 *AFM images of the double-layer defect-graphene (D-graphene), successive images are progressively focused into the sample.*

<u>*D-graphene:*</u> Figure 5.19 depicts AFM images of a double-layer CVD grown graphene macrostructure (an optical image of the graphene macrostructure is shown in Figure 5.20). It is evident that the graphene domains comprising the material possess a large number of surface defect sites, where 'cracks' are observable between/throughout the double-layer graphene domains. Also evident is the distinction between the AFM images of the monolayer graphene (M-graphene, Figure 5.14) and this two-layer sample (D-graphene, Figure 5.19),

with the latter possessing a 'bulky' topography (*i.e.* wrinkles and ripples characteristic of single-layer graphene are absent in the double-layer graphene).

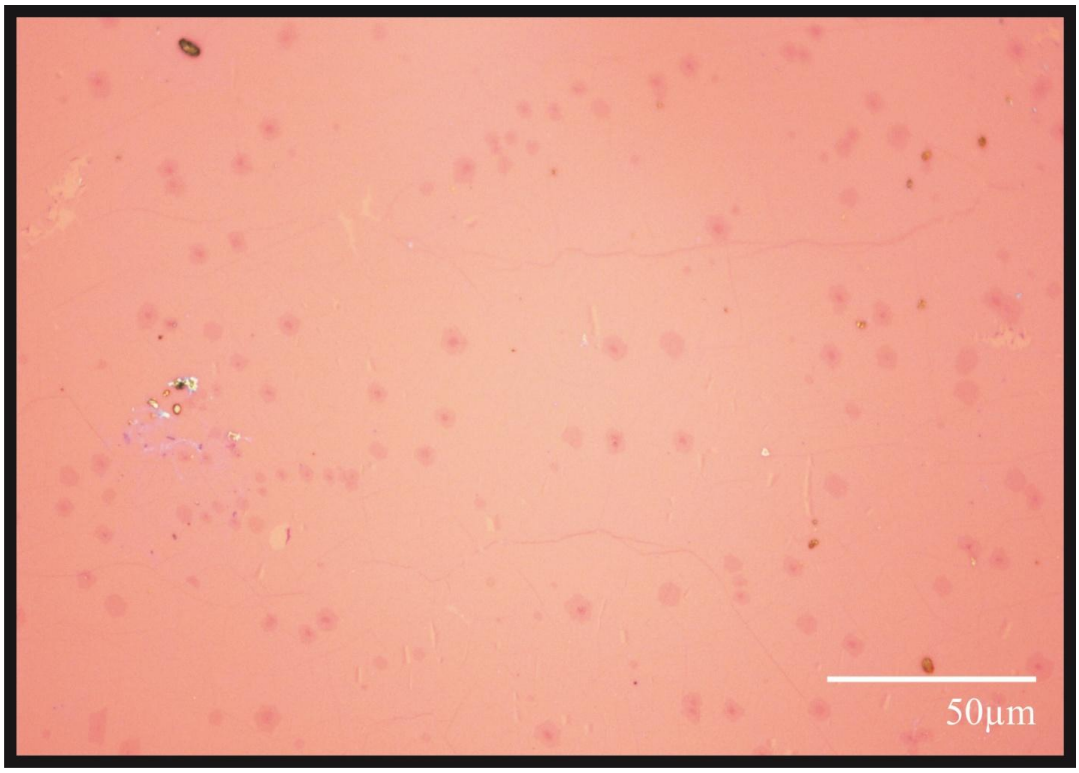

Figure 5.20 *An optical micrograph of the double-layer defect-graphene (D-graphene) macrostructure.*

Raman spectroscopy of the double-layer graphene (D-graphene) is shown in Figure 5.21A, revealing the two characteristic G and 2D peaks of graphitic materials at *ca*. 1580 and 2800 cm^{-1} respectively. As with the previous two graphene materials characterised (M-graphene and Q-graphene, *vide supra*), the high symmetry of the 2D peak indicates the presence of pristine graphene. The intensity ratio of the G and 2D bands (G/2D = 0.86) evident in Figure 5.21A indicates the presence of double-layered graphene domains given that the relatively equal intensities (with only a minimal reduction in the G peak relative to the 2D peak) coinciding with previous reports for two-layer graphene.

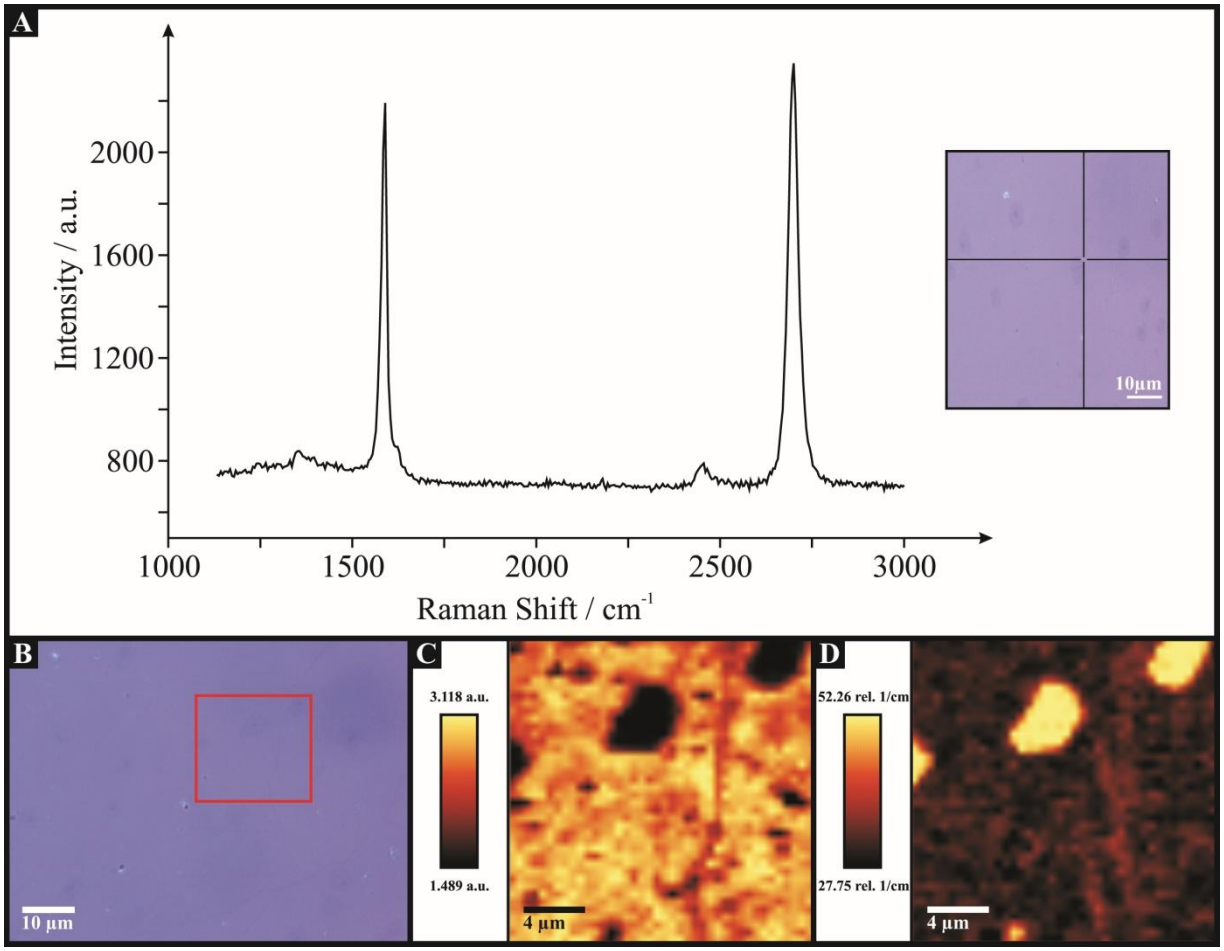

Figure 5.21 *Characterisation of the double-layer defect-graphene (D-graphene) macrostructure. (A) Raman spectroscopy, with an optical micrograph (inset) indicating the single probe position utilised. Raman maps and a supporting optical micrographs indicating the sample area utilised are reported in B, C and D. (C) 2D/G band ratio, where darker areas represent increased graphene layer numbers. (D) FWHM of the 2D peak, with lighter areas indicative of thicker graphene domains.*

Raman mapping (which is presented in Figures 5.21C and 5.21D) was again utilised to validate the overall quality of the graphene sample (D-graphene), which indeed confirmed the inferences gained *via* AFM and Raman analysis using a single probe position. Figures 5.21C and 5.21D confirm that the double-layer graphene macrostructure (D-graphene) is comprised of a uniform two-layer graphene domain, on top of which occasional graphitic islands exist. Also evident in Figure 5.21C is an observable 'crack', which indicates the presence of an edge plane like- site/defect (*i.e.* a grain boundary).

XPS was next conducted on the double-layer graphene material (D-graphene). De-convolution of the spectra reveals a composition of 29.21 % carbon, 30.12 % oxygen and 39.06 % silicon. The carbon content comprises of 18.7 % corresponding to 284.5 eV which is characteristic of graphitic groups, and 8.73 and 1.78 % at 286.1 and 288.9 eV respectively which correspond to C–H, C=C, C–O and C=O bonds. Of the oxygen content, 0.82 % is comprised from contributions at 535.4 eV. The silicon (39.1 %) and the remaining oxygen content (29.3 %) contributions are a result of the probe depth utilised (which penetrates the support surface, see earlier). For the case of the double-layer defect-graphene (D-graphene), considering only the carbon and oxygen contributions arising from the graphene material, XPS reveals a O/C ratio of *ca*. 0.03.

5.4.6. FREESTANDING 3D GRAPHENE AND CARBON FOAMS

The freestanding 3D graphene foam electrode was commercially obtained from 'Graphene Supermarket' (Reading, MA, USA). [12] The 3D graphene foam was fabricated as reported and described previously, [33] which involves using a nickel skeleton (that will define the resulting 3D graphene macrostructure, *i.e.* pore size *etc*). Carbon atoms are introduced *via* decomposition of methane (*ca*. 1 % volume) at *ca*. 1000 °C under ambient pressure where graphene films become precipitated upon the nickel surface (a CVD process). The underlying nickel skeleton/scaffold is then coated with PMMA to reduce the likelihood of the structure collapsing whilst the nickel is etched in 3 M HCl at 80 °C for 12 hours. The PMMA is then removed *via* washing the sample with hot acetone; note that if the PMMA is not used the resulting structure is significantly deformed. [33] To confirm that both the PMMA and nickel are removed, EDX and XPS are conducted. Note that due to the etching, that is, a continuous film of graphene completely encapsulating the nickel surface, some of the macrostructure needs to be broken to allow the etching solution to penetrate; this is evident in the presented

SEM images (Figure 5.22), which appears not to be substantially extrusive to dramatically change the resulting freestanding 3D graphene macrostructure.

After receiving the 3D graphene foam from the suppliers, it was carefully cut/shaped (average dimensions: 0.8 cm × 1.0 cm × 0.12 cm) appropriately for use as an electrode material prior to it being characterised and subsequently utilised without any further modification.

For comparison, a freestanding 3D reticulated vitreous carbon (RVC) – a micro-porous, glassy carbon material – foam was employed (The Electrosynthesis Company Inc., Lancaster, N.Y., U.S.A.) which has been characterised and extensively utilised in electrochemistry (essentially a glassy carbon foam electrode), [34] particularly industrial scale-up. [35] Other than preparation for use as an electrode (average dimensions: 1.0 cm × 1.0 cm × 0.5 cm) this foam was utilised as received from the supplier without any further modification.

5.4.6.1. FREESTANDING 3D GRAPHENE AND CARBON (RVC) FOAMS: PHYSICOCHEMICAL CHARACTERISATION

First the structural characterisation of the freestanding 3D graphene foam is considered *via* SEM as depicted in Figure 5.22 which reveals the graphene foam to exhibit a well-defined 3D macro-porous structure with an average pore diameter of *ca*. 200 μm. Closer inspection reveals a smooth surface at the thin graphene skeleton which appears to assume a similar surface topology and architecture of the nickel substrate utilised during synthesis owing to conformal CVD growth. Also evident from the SEM images are ripples/wrinkles at the grain boundaries of the graphene flakes which are an inherent property of the interconnected 3D scaffold structure and CVD grown graphene; [20] it is the differing thermal expansion coefficients of nickel and graphene that give rise to these ripples and wrinkles. As shown previously, these structural features can potentially influence the electrochemical

response and could give rise to beneficial electron transfer properties. [20] Also shown in Figure 5.22 is the breakage of the 3D graphene macrostructure which is unavoidable due to the fabrication process where the nickel skeleton used as the template for the growth of graphene is completely covered, and as such breakage occurs as the etching solution needs to access the underlying nickel. The severity of this is observed better in Figure 5.22A; however, the process still leaves a freestanding 3D graphene macrostructure. Such defects (Figure 5.22B) will give rise to improvements in the electron transfer properties at the 3D graphene macrostructure as these "edge sites" will reveal the edge plane of the grown graphene.

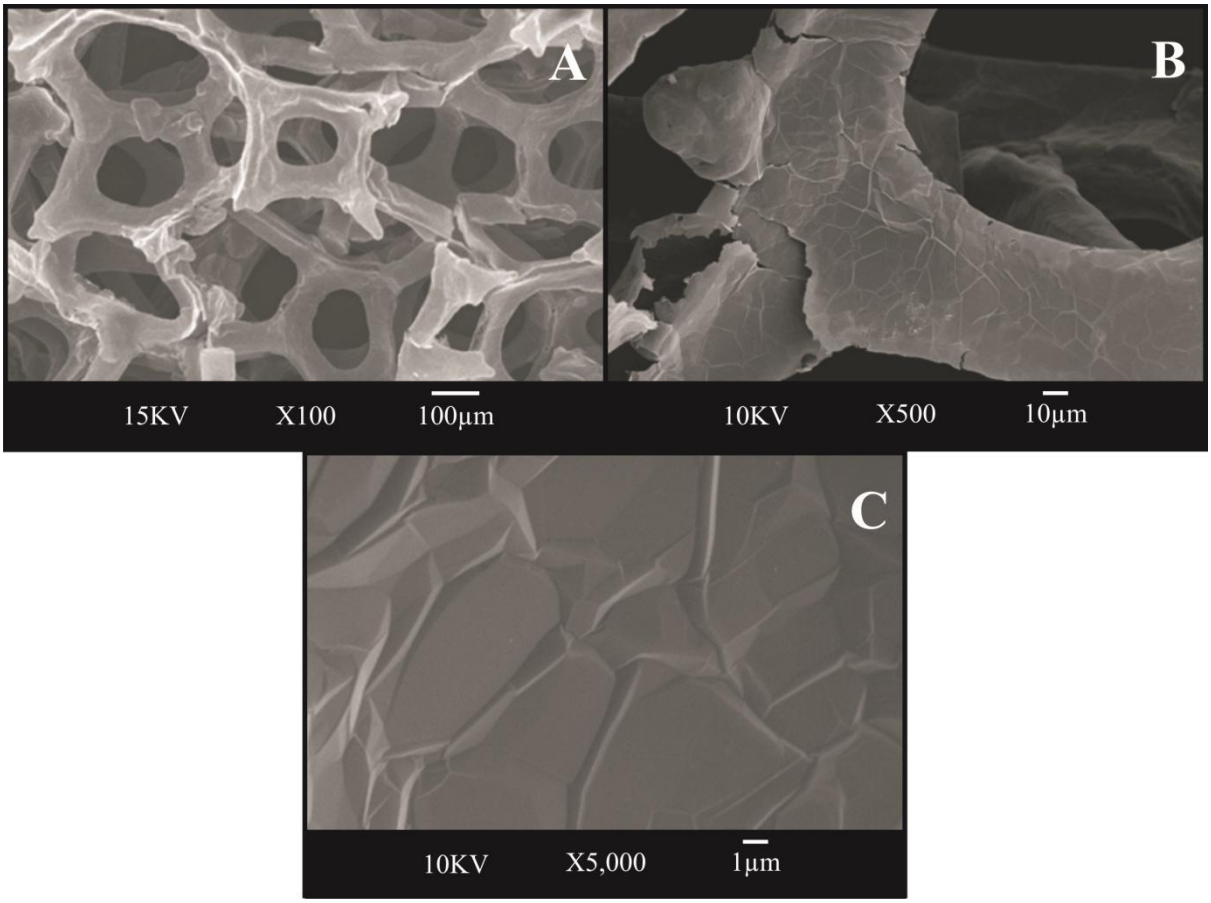

Figure 5.22 *SEM image of the freestanding 3D graphene foam (**A**), and at increasingly higher magnifications (**B** and **C**).*

Further characterisation of the freestanding 3D graphene foam is presented in Figure 5.23 where the Raman spectrum reveals two characteristic peaks at *ca*. 1581 and 2684 cm^{-1} which are due to the G and 2D (G') bands respectively. Note that the highly symmetrical 2D (G') band peak indicates that the surface is comprised of mono- to few- layer graphene sheets (consistent with SEM images, Figure 5.22). Furthermore, the intensity ratio of the G and 2D bands also indicates that the graphene foam is comprised of single and few layer graphene domains.

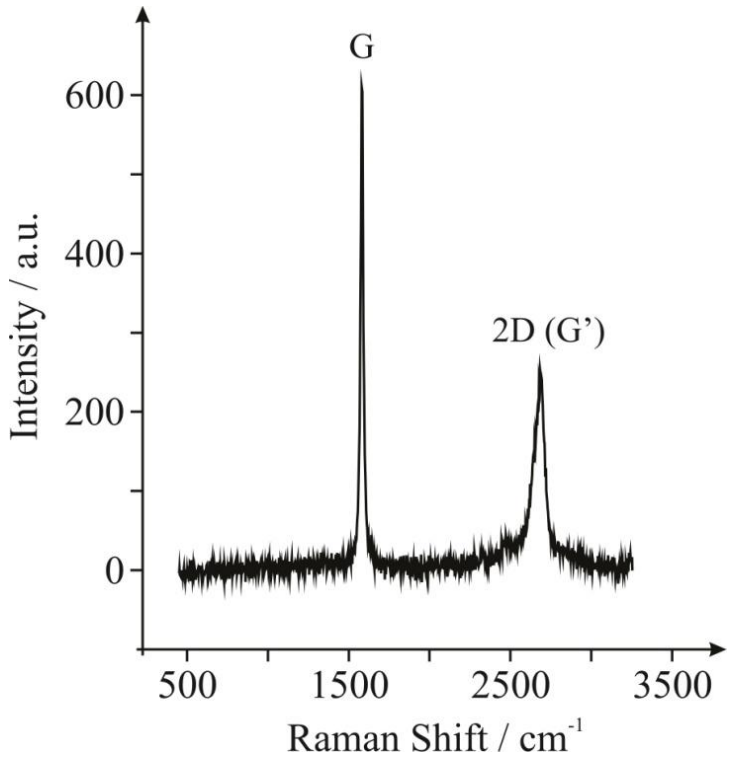

Figure 5.23 *Raman spectra of the freestanding 3D graphene foam.*

As is the case with planar CVD grown graphene, depending upon where one focuses the probe, different layer numbers (mono and in other areas few layer graphene) are present, [20, 30] and as such the freestanding 3D macrostructure is heterogeneous in-nature. The lack of a D band suggests that the graphene is of high quality and is defect free (no basal crystal defects), thus is near pristine in nature. Such observations/characterisation of this commercially obtained freestanding 3D graphene foam is in agreement with previous

reports. [33, 36] As such the fabricated freestanding 3D graphene foam can be termed *quasi*-graphene as it deviates from true pristine graphene (monolayer) but is not that of a bulk graphene crystal (*viz* graphite).

Next, given that the freestanding 3D graphene foam is initially grown upon a nickel template, EDX analysis was performed to establish the elemental composition of the freestanding foam, where it was indicated to be comprised of 90.11 % atomic carbon and 9.89 % atomic oxygen. Thus no nickel impurities were detected after the etching of the underlying support and hence are not considered to contribute towards the electro-catalytic activities of the graphene electrode. [20] Furthermore, XPS was conducted on the 3D graphene foam. De-convolution of the spectra reveals the foam to be composed of 95 % carbon and 5 % oxygen. The carbon content comprises of 80 % corresponding to 284.6 eV which is characteristic of graphitic groups, 14 % at 286 eV and 1 % at 289 eV which both correspond to C–O and C=O bonds respectively. The oxygen content is comprised from 3 % at 531.7 eV which corresponds to C–OH bonds and 2 % at 533.3 eV which corresponds to groups such as C=O, O=C–O, and C–O. Note, again traces of nickel could not be identified at 710 eV. Additionally, whilst the XPS shows oxygenation in the carbon structure Raman does not exhibit any D band, this is most probably due to the higher/larger surface area analysed in XPS (400 μm) in comparison with the laser spot of Raman. It is clear that the low O/C ratio for the graphene foam is near that of true pristine graphene, [27] which in conjunction with the pristine *quasi*-graphene present and its unique 3D and freestanding structure makes this a fascinating material to study.

Throughout the experimental (electrochemical) use of the freestanding 3D graphene foam electrode (see Chapter 9.1). An alternative (commercially available) freestanding 3D RVC ‘carbon’ foam is utilised for comparative purposes to allow the electronic properties

and applicability of the new and intriguing 3D graphene material to be correctly 'benchmarked'.

The alternative 3D foam is comprised of RVC, essentially meaning that it is a micro-porous glassy carbon electrode material and as such the characterisation in addition to the electrochemistry of glassy carbon materials are well known and widely reported throughout the literature. [35] The RVC foam structure is generally achieved by polymerisation of a resin combined with foaming agents, followed by carbonisation. The result is a low volume disordered glassy porous carbon with some crystallographic order, low electrical resistance and a continuous skeletal structure. [35]

SEM images of the freestanding 3D RVC foam are depicted in Figure 5.24 where it is evident that the foam exhibits a similar architecture to the 3D graphene alternative, revealing a well-defined 3D macro-porous structure with an average pore diameter of *ca*. 400 μm (note that a correction factor is employed between the two foams to allow direct comparison of the voltammetry given that they exhibit different pore sizes – see Chapter 9.1.2). [35] At a higher magnification it is evident that unlike at the 3D graphene, where wrinkles and ripples are evident from the synthesis process, the 3D carbon foam does not exhibit such micro-structural characteristics and instead exhibits a smooth continuous surface with less structural defects.

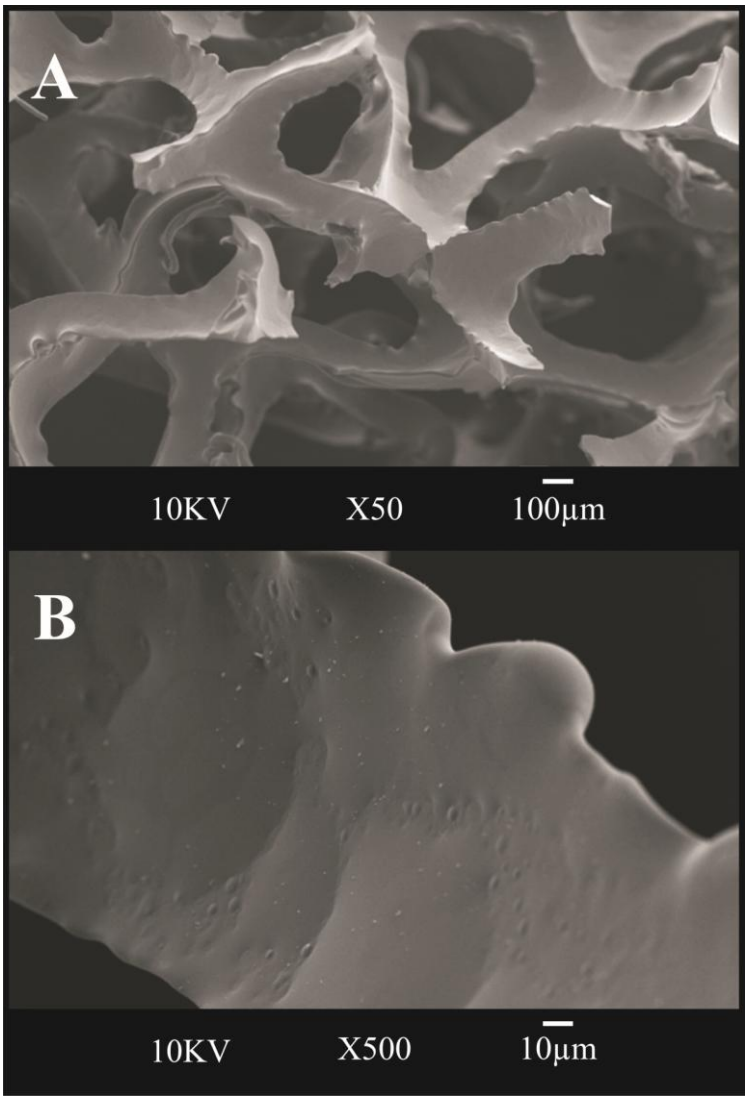

Figure 5.24 *SEM image of the freestanding 3D Reticulated Vitreous Carbon (RVC) foam (**A**); and at a higher magnification (**B**).*

Raman spectroscopy of the 3D carbon foam (Figure 5.25) reveals two characteristic bands: D (1321 cm^{-1}) and G (1593 cm^{-1}) and a wide G' band at *ca*. 2800 cm^{-1}; which as reported widely in the literature is consistent with glassy carbon (RVC). [37]

XPS was conducted on the 3D carbon foam which revealed it to exhibit a similar structural composition to graphene however with different percentage compositions in terms of the carbon and oxygen content. Analysis of the XPS de-convoluted spectra for the RVC foam reveals that of the 88.8 % composition of carbon (C1s), 69.2 % corresponded to 284.6 eV which is characteristic of graphitic groups from –C-C- and –C-H- bonds, whereas

15.6 % was at 286 eV and 4 % at 289 eV which correspond to –C=O and O=C-O respectively. The oxygen content (9.6 %) resulted from 7.2 % of O1s at 531.7 eV which correspond to C–OH groups, and 2.4 % at 533.3 eV which corresponds to groups such as, C=O, O=C-O or -C-O bonds. Unlike at the 3D graphene foam, impurities (sulphide) were present, making up a 1.6 % composition at 170 eV (corresponding to CS2 bonds presumably) and of further note is that traces of N could occasionally/rarely be seen at 396 eV. Note that while the 3D graphene foam exhibits an oxygen composition of *ca*. 5.0 %, the 3D carbon (RVC) alternative comprises of *ca*. 9.6 %, of which the highly oxygenated species of O=C are 4 % for the 3D carbon foam and 1 % for the 3D graphene.

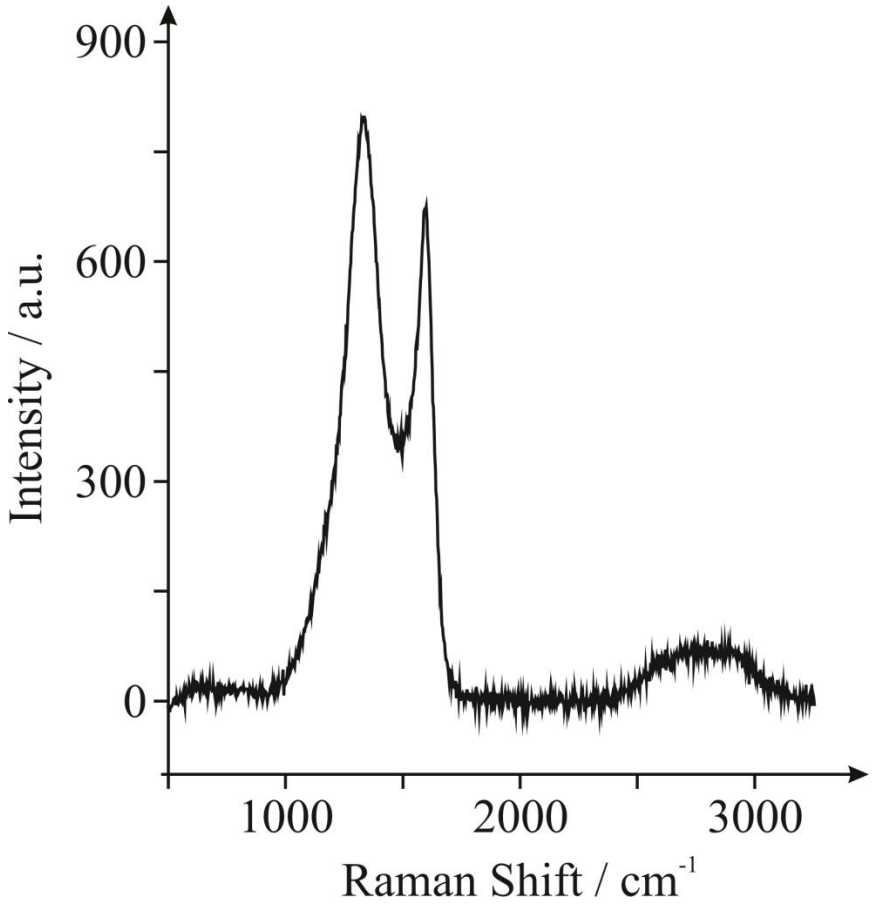

Figure 5.25 *Raman spectra of the freestanding 3D carbon (RVC) foam.*

5.4.7. GRAPHENE POWDER

Graphene powder was commercially obtained from 'Graphene Supermarket' (Reading, MA, USA) [12] and is known as 'Graphene Nanopowder: 12 nm Flakes' comprising entirely of graphene platelets that have not been oxidised, reduced or chemically modified in anyway. The graphene nano-platelets were synthesised *via* the mechanical/thermal splitting of graphite, [27] however the exact details are proprietary information. [12]

5.4.7.1. GRAPHENE POWDER: CHARACTERISATION

Figures 5.26A and 5.26B depict the respective SEM and TEM images of the graphene powder where it is evident that the graphitic material consists of a mixture of single- and few-layer graphene sheets, which appear to exhibit an intraplanar microcrystalline size, L_a, of between 1400 and 3000 nm and an interplanar microcrystalline size, L_c, of *ca*. 0.34 nm and larger, indicating the combined presence of single layer graphene and *quasi*-graphene. [32] This analysis compares well with pristine graphene, which has an L_a value ranging from 50 up to 3000 nm (or larger) and an L_c value of 0.34 nm respectively. [27]

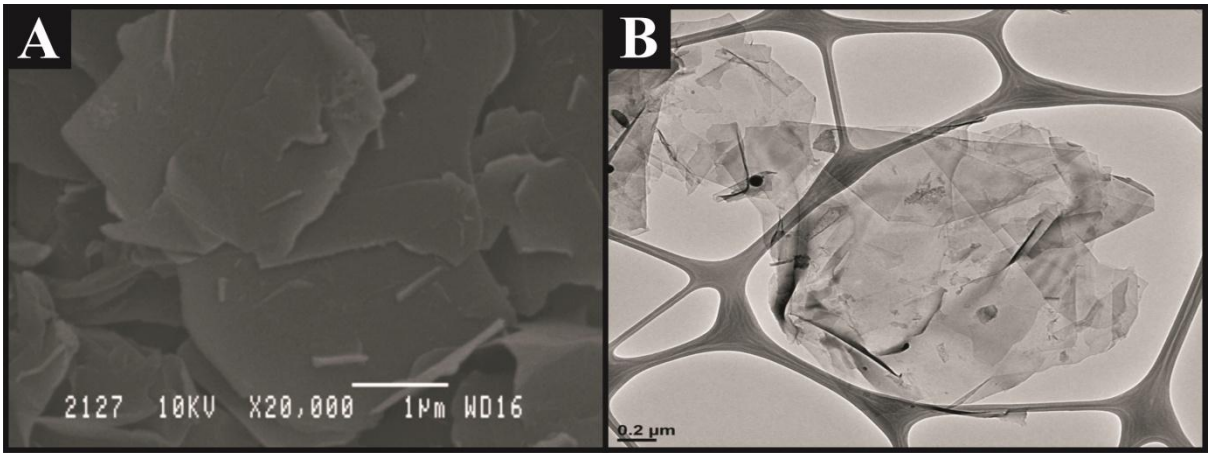

Figure 5.26 *SEM (**A**) and TEM (**B**) images of the graphene powder utilised.*

Figure 5.27 depicts the Raman spectrum of the graphene powder which reveals two characteristic peaks at *ca*. 1579 and 2687 cm^{-1} which are due to the G and 2D (G') bands

respectively. The highly symmetrical 2D (G') band peak indicates that the surface is comprised of single- to few-layer graphene sheets (consistent with SEM and TEM images, Figure 5.26). [28] Furthermore, the intensity ratio of the G and 2D bands also indicates that the graphene powder is comprised of single- and few- layered graphene domains. [11] The presence of a small D band (1335 cm^{-1}) indicates that there are a small number of structural defects on the graphene surface (limited basal crystal defects), however the relatively low intensity of the D band suggests that generally an ordered graphene structure is present which is of high quality and thus near pristine in nature. [11, 28]

XPS analysis revealed the graphene material to be composed of 96.75 % carbon and 3.25 % oxygen. The carbon content comprises of 71.8 % corresponding to 284.5 eV which is characteristic of graphitic groups (with 16.9 % at 285.6 eV, relating to C–C, C=C and C–H graphitic groups), 4.6 % at 287.9 eV and 3.4 % at 290.7 eV which both correspond to C–O and C=O bonds respectively. The oxygen content is comprised from 1.97 % at 531.8 eV which corresponds to C–OH, C=O and C–O bonds and 1.28 % at 533.4 eV which corresponds to groups such as O=C–O and C–O.

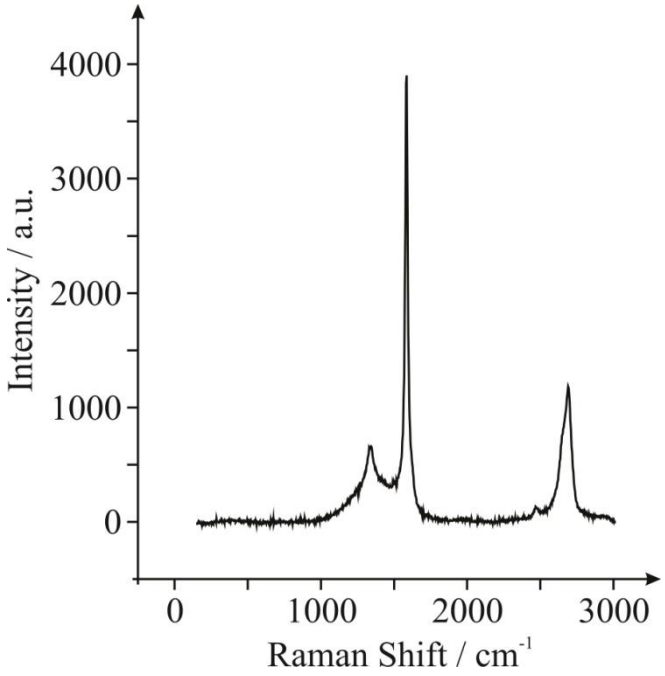

Figure 5.27 *Raman spectra of the graphene powder utilised.*

5.4.8. GO: GRAPHENE/GRAPHITIC OXIDE

Commercially available graphene oxide (GO) was purchased from 'Graphene Supermarket' (Reading, MA, USA) [12] and consists of 'single layered graphene oxide dispersed in water' at a concentration of 275 mg L^{-1}. The GO was synthesised using a modified Hummers oxidation method, which has been reported and characterised previously. [38, 39]

5.4.8.1. GO: CHARACTERISATION

The GO has an average flake size of between 0.5 and 5.0 μm and a thickness of 1 atomic layer with at least 80 % of the sample being single layer GO. [12] A typical SEM image of the GO, supplied by the manufacturer, is presented in Figure 5.28.

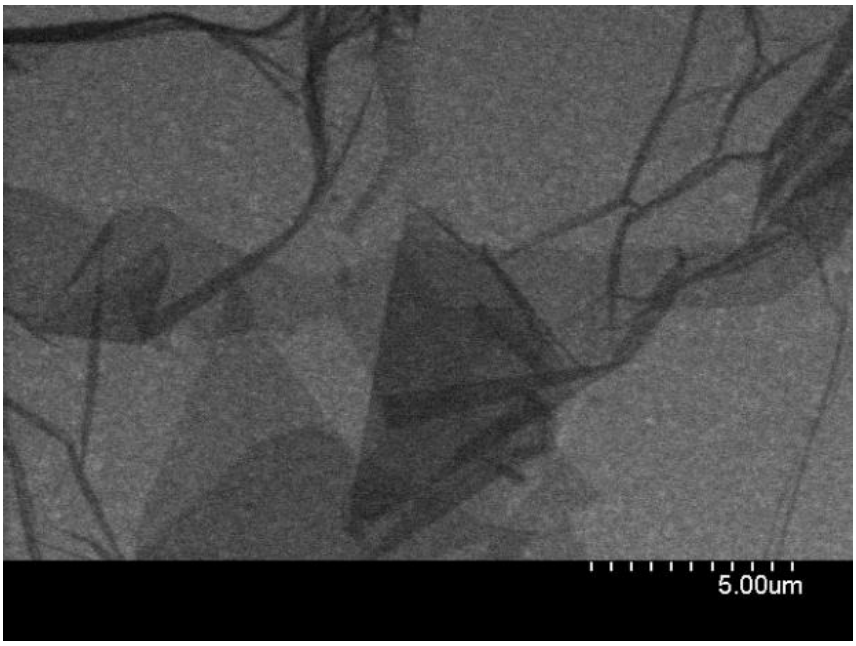

Figure 5.28 *A typical SEM image of the commercially available graphene oxide. Provided by the manufacturer.* [12]

XPS analysis was performed on the sample: de-convolution of the XPS spectra reveals 59 % (284.6 eV) to correspond to graphitic groups, with 29 % (286.8 eV) characteristic of C–O bonds and 11.5 % (288.2 eV) corresponding to C=O bonds, which is in

excellent agreement with previous literature reports regarding GO. [40, 41] The overall composition of the GO was 79 % carbon and 20 % oxygen.

5.5. CONTROL EXPERIMENTS AND SOLUTIONS

All control measurements were conducted in an identical manner to when graphene was being utilised (*vide supra*) other than varying the modification material in liquid suspensions.

Surfactant Control: where surfactant control experiments were utilised, a 2 % w/v aqueous solution of sodium cholate was prepared. Surfactant deposits (aliquots) of 10 µL were utilised to duplicate the content present in the S-graphene samples.

S-graphite Control: comparison measurements (with respect to S-graphene) involving graphite (0.5 µg per 10 µL) utilised the same ionic surfactant content (2 % w/v sodium cholate). For details of the graphite utilised please see Chapter 5.4.3.

Pristine Graphite Control: comparison experiments (with respect to P-graphene) utilised the graphite detailed in Chapter 5.4.3 in a dilute (1 µg per 2 µL) and concentrated (100 µg per 1 µL) ethanol dispersions.

Ethanol Controls: control experiments were performed using ethanol modified electrodes (with respect to P-graphene) for the purpose of de-convoluting the origin of the electro-activity and ensuring that electrochemical responses observed were not a result of the solvents utilised; such control experiments revealed that ethanol has no effect upon electro-activity.

5.6. CVD ELECTROCHEMICAL CELL: UTILISING CVD GROWN GRAPHENE

For the employment of the CVD chip working electrodes (*i.e.* CVD-graphene, D-graphene, M-graphene and Q-graphene) an electrochemical cell was utilised in order to connect to and 'electrically wire' the CVD grown graphene. Essentially the CVD chip was secured into a polytetrafluoroethylene (PTFE) housing unit with a silicone O-ring defining the working surface (diameter, 4.9 mm) and a steel contact making connection to the back of the chip, which *via* the use of silver conductive paint (applied to cover the back and sides of the chip in their entirety) ensures electrical conductivity from the front 'working surface' of the electrode to the electrode connector, to which a lead for the working electrode can be attached. Figure 5.29 details the experimental set-up, adapted specifically for electrochemical measurements utilising CVD grown graphene. This unique cell design ensures that the *graphene surface* is the *only electrochemically active surface* that is in contact with the solution during electrochemical measurements and allows the direct electrical wiring of the graphene – but without worry that the connecting silver conductive paint might be exposed to the solution, which would give rise to false voltammetry.

Using this electrochemical cell, the exposed working electrode area is consistently 0.189 cm^2 for all graphene samples studied (CVD-graphene, D-graphene, M-graphene and Q-graphene), which is consistent with the HOPG electrodes utilised. Note that other than securely 'housing' the CVD grown graphene chips/electrodes into the appropriate 'housing' unit prior to electrochemical measurements, the graphene films were used as received from the supplier without any further modification. The graphene 'wafer' macrostructures, before being adapted using the electrode housing cell into electrodes, are 1×1 cm^2 in size.

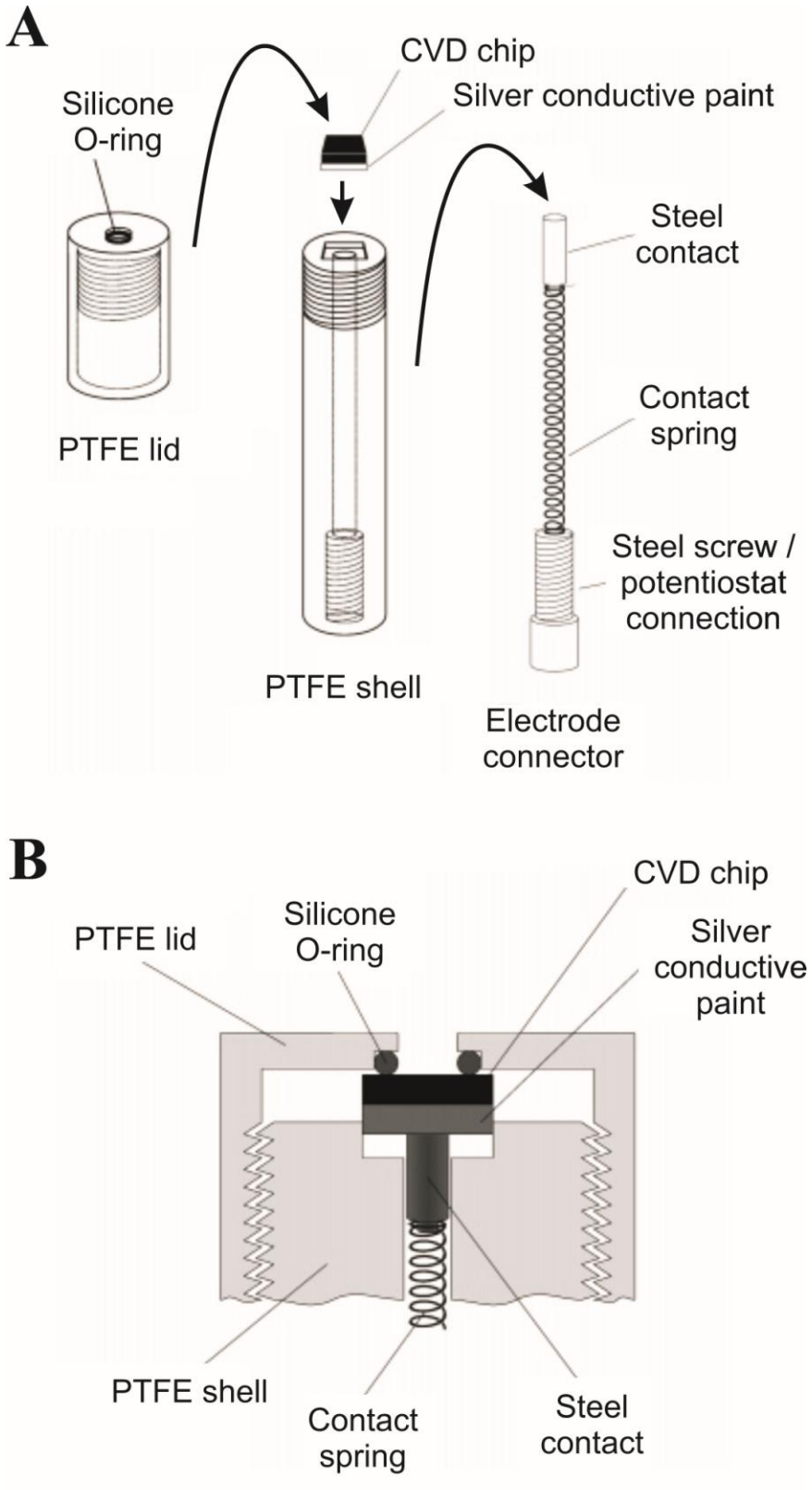

Figure 5.29 *Schematic diagram of the CVD graphene chip 'housing' unit (**A**). Cross-sectional view of the assembled CVD grown graphene working electrode when fully incorporated (**B**) for exclusive use with the CVD grown graphene chips/substrates.*

1. Internet-Resource, *Kanichi Research Ltd.*, Accessed: 29/11/2011; http://www.kanichi-research.com.
2. J. P. Metters, R. O. Kadara and C. E. Banks, *Analyst*, 2011, **136**, 1067.
3. R. O. Kadara, N. Jenkinson and C. E. Banks, *Sens. Actuators B*, 2009, **138**, 556.
4. Internet-Resource, *Kemet Ltd.*, Accessed: 29/11/2011; http://www.kemet.co.uk.
5. F. Neese, *An ab initio, density functional and semi-empirical program package-Version 2.8*, (1999-2011) ORCA, University of Bonn.
6. A. D. Becke, *J. Chem. Phys.*, 1993, **98**, 5648.
7. C. Lee, W. Yang and R. G. Parr, *Phys. Rev. B*, 1988, **37**, 785.
8. P. J. Stephens, F. J. Devlin, C. F. Chabalowski and M. J. Frisch, *J. Phys. Chem. C*, 1994, **98**, 11623.
9. A. A. Green and M. C. Hersam, *Nano Lett.*, 2009, **9**, 4031.
10. Internet-Resource, *Nano Integris Ltd.*, Accessed: 29/11/2011; http://www.nanointegris.com.
11. Y. Y. Wang, Z. H. Ni, T. Yu, Z. X. Shen, H. M. Wang, Y. H. Wu, W. Chen and A. T. S. Wee, *J. Phys. Chem. C*, 2008, **112**, 10637.
12. Internet-Resource, *Graphene Supermarket Ltd.*, Accessed: 29/11/2011; http://www.graphene-supermarket.com.
13. A. Dato, V. Radmilovic, Z. Lee, J. Phillips and M. Frenklach, *Nano Lett.*, 2008, **8**, 2012.
14. A. Dato, Z. Lee, K.-J. Jeon, R. Erni, V. Radmilovic, T. J. Richardson and M. Frenklach, *Chem. Commun.*, 2009, 6095.
15. Z. Lee, K.-J. Jeon, A. Dato, R. Erni, T. J. Richardson, M. Frenklach and V. Radmilovic, *Nano Lett.*, 2009, **9**, 3365.
16. Internet-Resource, *Gwent Ltd.*, Accessed: 18/04/2013; http://www.gwent.org.
17. L. Gomez-Du-Arco, Y. Zhang, A. Kumar and C. Zhou, *IEEE Trans. Nanotechnol.*, 2009, **8**, 135.
18. A. Reina, X. Jia, J. Ho, D. Nezich, H. Son, V. Bulovic, M. S. Dresselhaus and J. Kong, *Nano Lett.*, 2009, **9**, 30.
19. W. Li, C. Tan, M. A. Lowe, H. D. Abruna and D. C. Ralph, *ACS Nano*, 2011, **5**, 2264.
20. D. A. C. Brownson and C. E. Banks, *Phys. Chem. Chem. Phys.*, 2012, **14**, 8264.
21. X. Li, W. Cai, J. An, S. Kim, J. Nah, D. Yang, R. Piner, A. Velamakanni, I. Jung, E. Tutuc, S. K. Banerjee, L. Colombo and R. S. Ruoff, *Science*, 2009, **324**, 1312.
22. X. Li, W. Cai, L. Colombo and R. S. Ruoff, *Nano Lett.*, 2009, **9**, 4268.
23. X. Li, Y. Zhu, W. Cai, M. Borysiak, B. Han, D. Chen, R. D. Piner, L. Colombo and R. S. Ruoff, *Nano Lett.*, 2009, **9**, 4359.

24. X. Liang, B. A. Sperling, I. Calizo, G. Cheng, C. A. Hacker, Q. Zhang, Y. Obeng, K. Yan, H. Peng, Q. Li, X. Zhu, H. Yuan, A. R. H. Walker, Z. Liu, L.-M. Peng and C. A. Richter, *ACS Nano*, 2011, **5**, 9144.

25. M. Her, R. Beams and L. Novotny, *Phys. Lett. A*, 2013, **377**, 1455.

26. A. Reina, S. Thiele, X. Jia, S. Bhaviripudi, M. S. Dresselhaus, J. A. Schaefer and J. Kong, *Nano Res.*, 2009, **2**, 509.

27. D. A. C. Brownson, D. K. Kampouris and C. E. Banks, *Chem. Soc. Rev.*, 2012, **41**, 6944.

28. D. Graf, F. Molitor, K. Ensslin, C. Stampfer, A. Jungen, C. Hierold and L. Wirt, *Nano Lett.*, 2007, **7**, 238.

29. A. C. Ferrari, *Solid State Commun.*, 2007, **143**, 47.

30. D. A. C. Brownson and C. E. Banks, *Phys. Chem. Chem. Phys.*, 2011, **13**, 15825.

31. A. G. Guell, N. Ebejer, M. E. Snowden, J. V. Macpherson and P. R. Unwin, *J. Am. Chem. Soc.*, 2012, **134**, 7258.

32. D. A. C. Brownson, L. C. S. Figueiredo-Filho, X. Ji, M. Gómez-Mingot, J. Iniesta, O. Fatibello-Filho, D. K. Kampouris and C. E. Banks, *J. Mater. Chem. A*, 2013, **1**, 5962.

33. Z. Chen, W. Ren, L. Gao, B. Liu, S. Pei and H.-M. Cheng, *Nat. Mater.*, 2011, **10**, 424.

34. R. L. McCreery, *Chem. Rev.*, 2008, **108**, 2646.

35. J. M. Friedrich, C. Ponce-de-Leon, G. W. Reade and F. C. Walsh, *J. Electroanal. Chem.*, 2004, **561**, 203.

36. E. Singh, Z. Chen, F. Houshmand, W. Ren, Y. Peles, H.-M. Cheng and N. Koratkar, *Small*, 2013, **9**, 75.

37. Y. Wang, D. C. Alsmeyer and R. L. McCreery, *Chem. Mater.*, 1990, **2**, 557.

38. W. S. Hummers and R. E. Offeman, *J. Am. Chem. Soc.*, 1958, **80**, 1339.

39. D. R. Dreyer, S. Park, C. W. Bielawski and R. S. Ruoff, *Chem. Soc. Rev.*, 2010, **39**, 228.

40. J.-L. Chang, K.-H. Chang, C.-C. Hu, W.-L. Cheng and J.-M. Zen, *Electrochem. Commun.*, 2010, **12**, 596.

41. T. Szabo, O. Berkesi, P. Forgo, K. Josepovits, Y. Sanakis, D. Petridis and I. Dekany, *Chem. Mater.*, 2006, **18**, 2740.

CHAPTER 6: ELECTROCHEMISTRY OF SURFACTANT EXFOLIATED GRAPHENE (EXPLORING TOP-DOWN FABRICATION)

This chapter considers the use of graphene fabricated *via* a 'top-down' surfactant exfoliation method (see Chapters 3.2.2 and 5.4.1) in order to investigate and evaluate the fundamental electrochemical properties of graphene as a novel electrode material. As highlighted in Chapter 3.2.6 this solution-based approach towards the fabrication of graphene is favoured for electrochemical applications in order to electrically wire and 'connect to' the graphene. Connection is achieved through a drop-coating method, in which specific volumes of a graphene liquid suspension are pipetted and immobilised onto the surface of a suitable electrode support.

In addition to being used routinely in the production of graphene, surfactants are used in the solubilisation and stabilisation of graphene solutions with the aim of reducing the aggregation of graphene sheets back to their lowest energy conformation, that is, graphite, due to the strong π–π interactions between the graphene sheets. It is apparent from inspection of Chapter 4.1 that surfactant adsorbed graphene has been used within the literature without consideration to the presence of surfactants when interpreting the data. This chapter investigates, for the first time, the impact and effects that surfactants have on the electrochemical performance of graphene.

Experimental Overview: this chapter utilises cyclic voltammetry, chronoamperometry and SWV experiments using a three electrode system as detailed in Chapter 5.1. Graphene modified electrodes are studied and thus the underlying working electrodes employed were EPPG (Chapter 5.2.1), edge plane like- and basal plane like-SPEs (Chapter 5.2.2), with carbon and Ag/AgCl comprising the auxiliary and reference electrodes respectively. The graphene utilised herein (S-graphene) is described as 'graphene sheets with adsorbed

surfactant (sodium cholate) suspended in aqueous solution' and is fully characterised in Chapter 5.4.1. Where necessary control/comparison experiments were performed utilising surfactant and S-graphite modified electrodes as detailed in Chapter 5.5.

6.1. EFFECT OF THE PRESENCE OF SURFACTANTS ON GRAPHENE RELATED ELECTROCHEMICAL PROCESSES

Chapter 6.1 contains published work [1] which considers the contribution of the surfactant, sodium cholate, on the electrochemical performance of graphene modified electrodes where the graphene used has been fabricated through the intercalation of said surfactant; forming surfactant-graphene complexes. The effect of the surfactant is considered towards the electrochemical oxidation of NADH, used prolifically as the basis of over 300 biosensors and is therefore of great significance, [1] and in the electrochemical oxidation of acetaminophen, an analgesic and antipyretic drug which requires routine monitoring in a plethora of areas. [2] The use of control experiments in the form of surfactant modified carbon electrodes are performed, which are lacking in the literature, in order to de-convolute the origin of the electrochemical response of said graphene modified electrodes.

6.1.1. INTRODUCTION

As highlighted in Chapter 4.1, there is a plethora of literature reports in which the authors claim to have fabricated enhanced electroanalytical sensing platforms *via* the incorporation of graphene as an electrode material. For example the reported electro-catalytic properties of graphene in relation to other graphitic electrodes has been demonstrated towards cadmium, [3] dopamine [4] and hydrogen peroxide. [5] In these cases, electron transfer at graphene has been assumed to originate at edge plane 'like' sites, similar to that reported at CNTs. [6, 7] However, in reality (for CNTs) in some instances this is due to the presence of metallic impurities. [8-10] For graphene however, one of the most popular fabrication routes involves the incorporation of surfactants, [11] which are used due to the high cohesive van der Waals energy (*ca*. 5.9 kJ mol^{-1}) of

[1] D. A. C. Brownson, J. P. Metters, D. K. Kampouris and C. E. Banks, *Electroanalysis*, 2011, **23**, 894.

carbon, [12] since graphenes would adhere/coalesce into multi-layer graphene (*viz* graphite) in the absence of surfactants. It is evident that the effect of these surfactants on the electrochemical response has been overlooked and resultantly this chapter investigates the influence of said surfactants on the observed electrochemistry.

6.1.2. RESULTS AND DISCUSSION

First the electrochemical oxidation of 1 mM NADH in a phosphate buffer solution (PBS, pH 7) is considered. As depicted in Figure 6.1A the resultant cyclic voltammogram exhibits a voltammetric peak at *ca*. 0.26 V (*vs*. Ag/AgCl) using an EPPG electrode whilst the basal plane like- screen printed electrode (SPE) exhibits a wave at *ca*. 0.47 V (*vs*. Ag/AgCl). Both responses are as expected and in agreement with literature reports [1, 13, 14] where it is well known that increasing the proportion of edge plane like- sites/defects results in an increase in the electrochemical reversibility of the analyte under investigation at graphite based electrodes (see Chapter 2). [13, 14] For comparative purposes graphite (S-graphite) was immobilised onto the basal plane like- SPE. Figure 6.1A shows that the voltammetric peak shifts towards a less positive potential of *ca*. 0.34 V (*vs*. Ag/AgCl) indicating an increase in the electrochemical reversibility, which is due to the graphite having a larger proportion of edge plane like- sites/defects than that of the underlying basal plane like- SPE, but not as many as that of the EPPG electrode. [13] In the case of graphene (S-graphene), a voltammetric response occurring at *ca*. 0.46 V (*vs*. Ag/AgCl) is observed, which is quantitatively similar to that of the underlying basal plane like- electrode. Note that the most important parameter is the position of the voltammetric peak rather than the magnitude of the wave and in this case the larger peak current is likely due to a slightly larger surface area at the graphene modified electrode (due to increased roughness) than that of the underlying electrode. [15, 16]

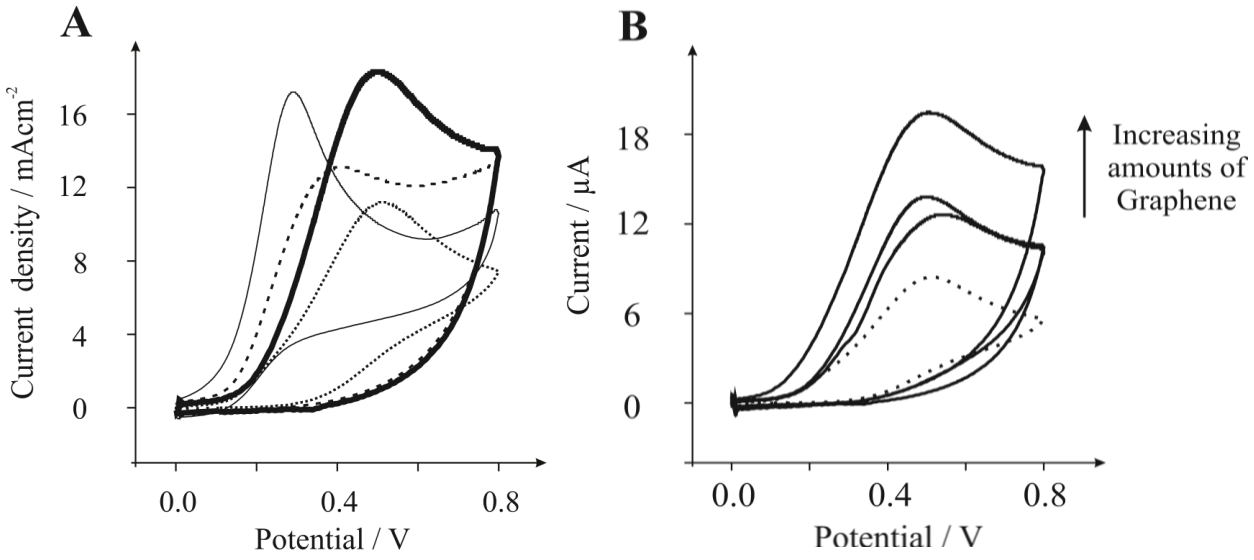

Figure 6.1 *(**A**) Cyclic voltammetric profiles recorded for 1 mM NADH in a pH 7 PBS using an EPPG electrode (thin line), basal plane like- SPE (dotted line), 0.5 µg S-graphene (thick line) and 0.5 µg S-graphite (dashed line) modified SPEs. Note that the current is normalised by the underlying electrode area. (**B**) Cyclic voltammetric profiles obtained using a SPE (dotted line) and resulting from the addition of increasing amounts of 0.25, 0.5 and 0.75 µg S-graphene (new electrode each time). Scan rate: 50 mVs^{-1} (vs. Ag/AgCl).*

The effect of adding increasing amounts of S-graphene onto the electrode surface, with respect to the electrochemical oxidation of NADH, is depicted in Figure 6.1B where an increase in the voltammetric peak height is evident. This is accompanied however by only a modest increase in the electrochemical reversibility, as is manifested in the slight reduction in the electrochemical over-potential relative to the bare (unmodified) underlying electrode. This response is unexpected as the introduction of graphene, with a larger proportion of edge plane sites (as reported in the literature where electro-catalysis was claimed towards other analytes/electrochemical-probes, see Chapter 4.1), [5, 17, 18] should improve the electrochemical reversibility of NADH. Note that work by Pumera *et al*. has shown unambiguous proof that the adsorption of NADH is due to the presence of carboxylic groups formed at the edges and

edge-like defects of graphene sheets. [19] XPS analysis of the commercially obtained S-graphene (see Chapter 5.4.1.1) indicates the distinct lack of carboxylic groups which is due, in part, to the fabrication method while other approaches explore extensive acid treatments to exfoliate graphite forming graphene. [20, 21] Thus the response observed in Figure 6.1 derives from other sources; this unexpected response is now further explored by considering the role of the surfactant, which is adsorbed on the apparent S-graphene.

A 2 % w/v solution of sodium cholate hydrate was prepared to mimic the surfactant content of the S-graphene solution from which aliquots, of course without any graphene, were taken and immobilised onto the basal plane like- SPE. The effect of the surfactant on the electrochemical oxidation of NADH is depicted in Figure 6.2, where a large voltammetric peak is observed at *ca*. 0.34 V (*vs*. Ag/AgCl) which in comparison to the bare (graphene free) basal plane like- SPE exhibits a more electrochemically reversible signal. It is also apparent that a voltammetric signal is observed in the absence of NADH (see later). Note that increasing the amount of surfactant immobilised onto the electrode surface results in an increase to the voltammetric peak height but has no effect on the peak potential. It is inferred that the observation in Figure 6.1B, where increasing amounts of S-graphene did not result in any improvement in the electrochemical reversibility towards the electrochemical oxidation of NADH, is due to the surfactant (adsorbed/intercalated with the graphene in S-graphene) 'masking' the role of the edge plane sites of graphene, which are well known (and demonstrated above, see Chapter 2) to dictate the electrochemical performance. The response of "graphene" (S-graphene) in this case is significantly affected by the surfactant; the graphene apparently makes a relatively small contribution to the overall response. It is therefore potentially incorrect to assign the total response only to the 'graphene' for the case of S-graphene.

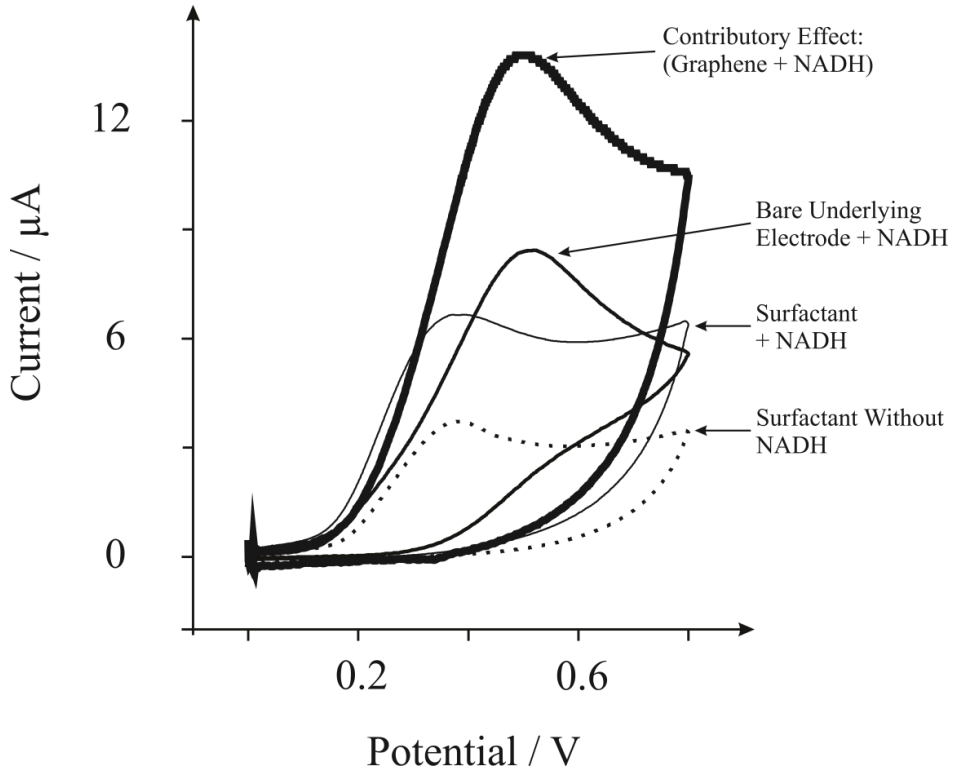

Figure 6.2 *Cyclic voltammetric profiles recorded for 1 mM NADH in a pH 7 PBS using a bare SPE (solid line) following modification with 0.5 µg S-graphene (thick line) and equivalent surfactant (thin line, no graphene). Also shown is the response of the SPE modified with surfactant (dotted line) in the absence of NADH. Scan rate: 50 mVs^{-1} (vs. Ag/AgCl).*

Considering the electrochemistry of the surfactant (sodium cholate hydrate) further, Figure 6.3 depicts the voltammetric responses observed using a surfactant modified SPE (in the absence of NADH) over a range of solution pHs. It is clear that a large voltammetric profile is observed at pH 7. The latter is the physiological pH that is widely used for NADH and acetaminophen sensing (*vide infra*). The optimal conditions for the surfactant appear to be basic with it displaying least electrochemical activity under acidic conditions. Therefore acidic conditions appear to partially alleviate interference issues associated with the surfactant; it is therefore advisable, where possible, to perform analysis under acidic conditions. As far as the author has investigated, the electrochemistry of the surfactant sodium cholate hydrate is yet to be

reported. However, based on the chemical structure it is surmised that the electrochemical response at sodium cholate hydrate is due to the oxidation of cyclohexanol (hydroxyl groups), *via* an equal proton/electron transfer which is likely to be 2. The effect of surfactants on electrochemical processes are not completely understood [22, 23] and more work is needed to elucidate the exact mechanism, but in the case of the electrochemical oxidation of NADH it is likely there is no favourable interaction between the electrochemical product formed with that of the surfactant.

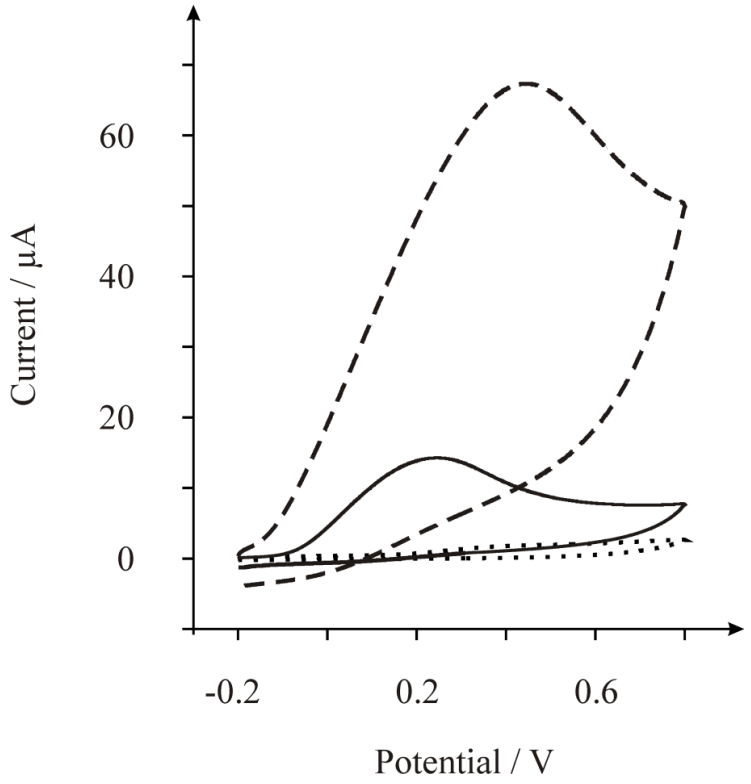

Figure 6.3 *Cyclic voltammetric profiles recorded using a surfactant modified SPE in pH 3 buffer solution (dotted line), pH 7 PBS (solid line) and pH 13 buffer solution (dashed line).*
Scan rate: 50 mVs^{-1} (vs. Ag/AgCl).

The electrochemical oxidation of 1 mM acetaminophen in a pH 7 PBS at a basal plane like SPE will now be considered. A typical cyclic voltammetric profile is depicted in Figure 6.4

exhibiting an oxidation peak at *ca*. 0.45 V and a reduction wave at *ca*. –0.25 V (*vs*. Ag/AgCl). The effect of scan rate on the voltammetric response was explored using a plot of peak height (I_P) against square root of scan rate. This was found to be linear (I_P (A) = 2.41 x 10^{-6} A/$(Vs^{-1})^{1/2}$ + 2.68 x 10^{-6} A; R^2 = 0.99, N = 10), indicating a diffusion process as opposed to a surface confined process which has been reported recently for MWCNTs [24] and graphene. [25] Next attention was turned to exploring the electrochemical oxidation of the acetaminophen over the pH range of 1.5 to 12. The peak potential (E_P) corresponding to the electrochemical oxidation of acetaminophen was observed to shift to less negative potentials as the solution pH was increased. A linear response was observed over the pH range of 1.5 to 9, beyond which a non-linear response is observed due to the *pKa* of the phenolic proton of the acetaminophen being 9.5. [26] The linear response of the peak potential as a function of pH (E_P (V) = 0.76 – 0.0485 *pH*) indicates a gradient of 48.5 mV/pH which shows deviation from the typical Nernstian response for a two-electron, two-proton process (59 mV/pH) as observed on a glassy carbon electrode, [27] yet is in agreement with 45 mV/pH reported by Fanjul-Bolado *et al.* [28] using commercially available SPEs and also agrees with other previously reported results of 37, 46.5, and 42 mV/pH, [26, 29, 30] indicating a complex oxidation mechanism for acetaminophen.

Next, the exploration of the voltammetric response of S-graphene modified electrodes for the electrochemical sensing of acetaminophen is explored. Figure 6.4 shows a typical voltammetric response obtained after S-graphene modification, which is distinctively different to that observed at the underlying electrode substrate. It is interesting to note that in comparison to the underlying basal plane like- SPE, the oxidation peak has shifted to a higher potential at *ca*. 0.69 V (*vs*. Ag/AgCl) and also exhibits a large increase in the magnitude of the voltammetric

peak due to the increase in the electrode surface area; additionally the reduction wave is significantly reduced in magnitude and has shifted to *ca*. –0.52 V (*vs*. Ag/AgCl).

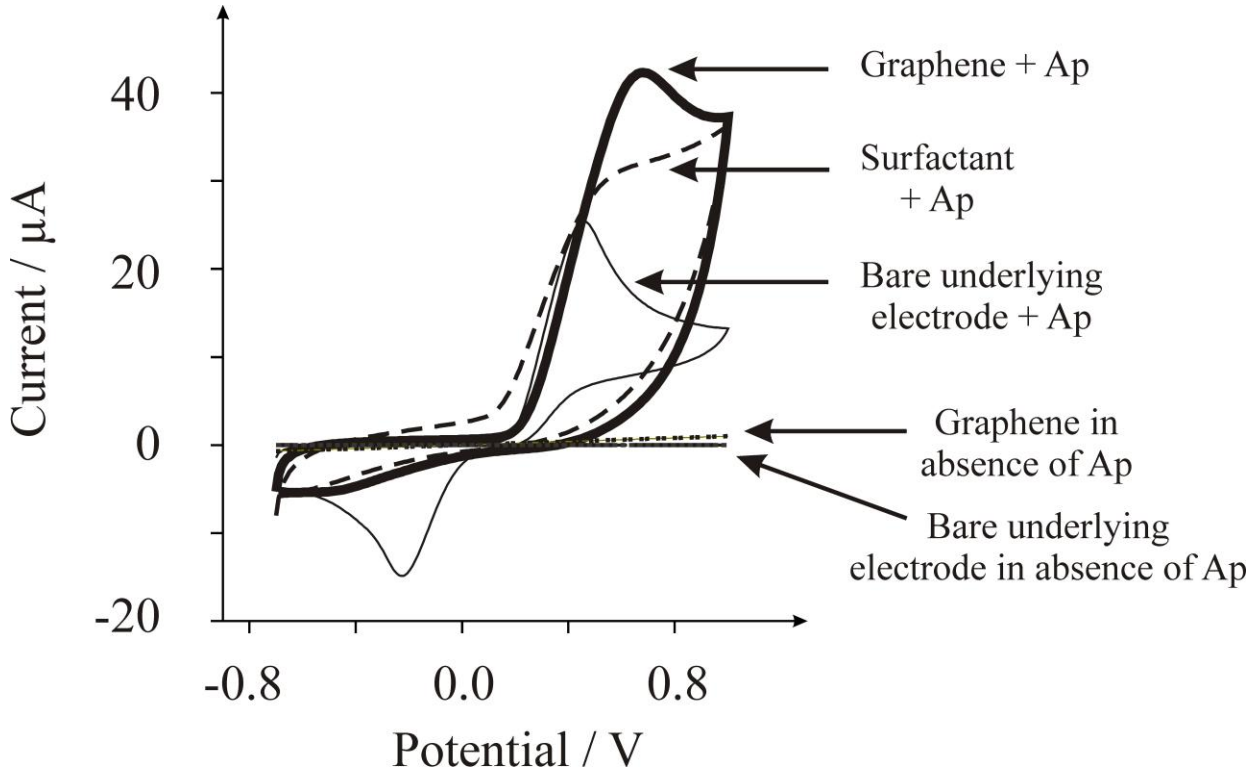

Figure 6.4 *Cyclic voltammetric profiles recorded for 1 mM acetaminophen (Ap) in a pH 7 PBS using a 0.5 µg S-graphene modified electrode (thick line) and in the absence of acetaminophen (dotted line) and the response of an unmodified basal plane like- SPE in the presence (thin line) and absence (solid line) of acetaminophen. Also shown is the response of a surfactant modified (dashed line) electrode in the presence of acetaminophen. Scan rate: 200 mV* s^{-1} *(vs. Ag/AgCl).*

The effect of pH on the electrochemical oxidation of acetaminophen at the S-graphene modified electrode was explored over the same pH range explored above (1.5 to 12). Again deviation from linearity is observed beyond pH 9 due to the *pKa* (*vide supra*) with a linear response for E_P as a function of pH observed over the range 1.5 to 9 (E_P (V) = 0.63 – 0.026 *pH*). The gradient of 26 mV/pH agrees well with 29.5 mV/pH (at 298K) for an electrochemical process involving two-electrons and one-proton. Note that this is in distinct

contrast to that observed above for the underlying electrode and with that reported previously for the electrochemical detection of acetaminophen using graphene. The latter was found to exhibit a surface confined process rather than a diffusional one as observed here, and additionally a gradient of 59 mV/pH was observed indicating a two-proton, two-electron electrochemical process. [25]

A surfactant modified electrode was consequently explored in relation to the sensing of acetaminophen (Figure 6.4). An electrochemical peak is observed at *ca*. 0.56 V (*vs*. Ag/AgCl), and when comparison between the surfactant and S-graphene response is sought, it is clear that a similar electrochemical response is observed. This is most likely to be attributed to the surfactant and not the graphene, usually assumed in the absence of appropriate control experiments. Note that increasing the amount of surfactant immobilised onto the electrode surface results in an increase to the magnitude of the voltammetric peak height but has no effect on the peak potential. Next the effect of pH was explored as above (1.5 to 12) where again deviation from linearity is observed beyond pH 9 with a linear response of E_P as a function of pH observed over the range 1.5 to 9 (E_P (V) = 0.705 – 0.0355 pH). The gradient of 35 mV/pH agrees well with 29.5 mV/pH (at 298K) as observed above for the S-graphene and once more indicates an electrochemical process involving two-electrons and one-proton. It is clear that the electrochemical process occurring (at the surface of S-graphene) is significantly different to that of the underlying electrode and additionally is distinctly different from that of recent literature reports utilising graphene. [25]

The agreement between the S-graphene (graphene with adsorbed surfactant) and that of the surfactant modified electrode undoubtedly demonstrates that the surfactant dramatically

affects the electrochemical process for the sensing of acetaminophen. A tentative mechanism for the electrochemical oxidation of acetaminophen at S-graphene may be described as:

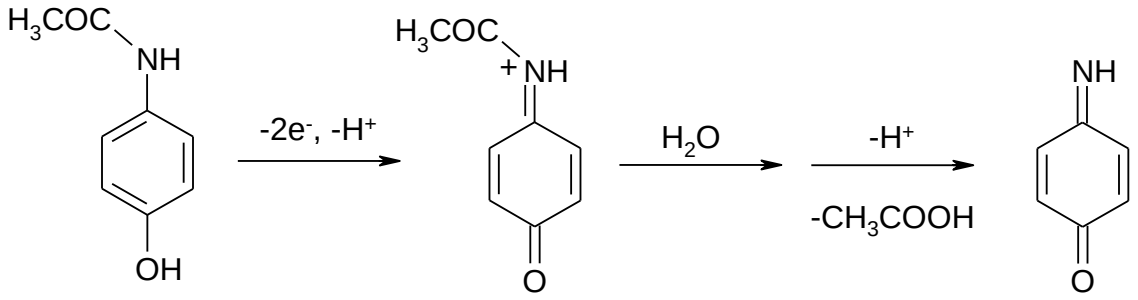

Scheme 6.1 *A possible mechanism for the electrochemical oxidation of acetaminophen at surfactant and surfactant-graphene modified electrodes.*

It is well known that this end product (as described in Scheme 6.1) is unstable and undergoes, at this pH, a slow hydrolysis reaction chemically forming benzoquinone [31] which is electrochemically active, but unfortunately no new voltammetric waves are observed. Note that a common observation for acetaminophen is the two-electron and two-proton process that directly yields *p*-benzoquinoneimine, which then consequently undergoes hydrolysis to benzoquinone. [31] Thus it is likely that the surfactant stabilises the intermediate following the two-electron and one-proton step which then produces *p*-benzoquinoneimine. It is possible that the surfactant attracts the starting reagent through hydrogen bonding and also stabilises the intermediate species leaving the amino end in the bulk solution in order to allow the transformation to the product; the hydrophobic part of the surfactant is interacting with the hydrophobic graphene and thus the hydrophilic polar end faces the solution. Note that the presence of surfactants can alter electrochemical processes, for example, it was shown that the dimerisation behaviour of an electro-generated species is remarkably affected, [33] but the effect of surfactants adsorbed onto graphene, is yet to be reported according to literature surveys carried out by the author.

It should be noted that not all surfactants are electrochemically active, and they are not always used in the fabrication of graphene. However, where surfactants *are* incorporated it is thus recommend that sufficient and appropriate control experiments be performed and reported. This will allow the true origin of the electrochemical response to be established and will reduced the possibility of the response being wrongly attributed to graphene itself.

6.1.3. CONCLUSIONS

This chapter highlights, for the first time, that the electro-catalytic response of graphene (S-graphene) should not be assumed to be solely due to the graphene itself, *viz* edge plane like sites, but rather the surfactant (when present), which is routinely used in the production of graphene and can contribute significantly to the observed electrochemical performance. It was demonstrated in this chapter (for the case of NADH and acetaminophen) that the surfactant, sodium cholate, is detrimental to electrochemical processes.

Given the wide variety of ionic and non-ionic surfactants that are utilised in the manufacture of graphene, and other compounds such as polyvinylpyrrolidone, [34] and N-methyl-pyrrolidone, [35] the use of control experiments in the form of surfactant modified carbon electrodes must be performed when claims of electro-catalysis for graphene are made, as such control measures are particularly effects at de-convoluting the origin of the electrochemical response at graphene modified electrodes, which is usually (wrongly) attributed to the graphene.

6.1.4. REFERENCES

1. C. E. Banks and R. G. Compton, *Analyst*, 2005, **130**, 1232.
2. M. E. Bosch, A.J.R. Sanchez, F. S. Rojas and C. B. Ojeda, *J. Pharm. Biomed. Anal.*, 2006, **42**, 291.
3. J. Li, S. Guo, Y. Zhai and E. Wang, *Anal. Chim. Acta*, 2009, **649**, 196.

4. Y.-R. Lim, S. Bong, Y.-J. Kong, Y. Yang, R. K. Mahajan, J. S. Kim and H. Kim, *Biosens. Bioelectron.*, 2010, **25**, 2366.

5. K. Zhou, Y. Zhu, X. Yang, J. Luo, C. Li and S. Luan, *Electrochim. Acta*, 2010, **55**, 3055.

6. T. J. Davies, M. E. Hyde, R. G. Compton, *Angew. Chem. Int. Ed.*, 2005, **44**, 5121.

7. C. E. Banks, R. R. Moore, T. J. Davies, and R. G. Compton, *Chem. Commun.*, 2004, **16**, 1804.

8. B. Sljukic, C. E. Banks and R. G. Compton, *Nano Letters*, 2006, **6**, 1556.

9. C. E. Banks, A. Crossley, C. Salter, S. J. Wilkins and R. G. Compton, *Angewandte Chemie-International Edition*, 2006, **45**, 2533.

10. G. G. Wildgoose, C. E. Banks and R. G. Compton, *Small*, 2006, **2**, 182.

11. C. Shan, H. Yang, J. Song, D. Han, A. Ivaska and L. Niu, *Anal. Chem.*, 2009, **81**, 2378.

12. J.-F. Wu, M.-Q. Xu and G.-C. Zhao, *Electrochem. Commun.*, 2010, **12**, 175.

13. C. E. Banks, T. J. Davies, G. G. Wildgoose and R. G. Compton, *Chem. Commun.*, 2005, **7**, 829.

14. N. A. Choudry, D. K. Kampouris, R. O. Kadara and C. E. Banks, *Electrochem. Commun.*, 2010, **12**, 6.

15. R. G. Compton and C. E. Banks, *Understanding Voltammetry*, World Scientific, London, 2007.

16. B. Šljukić, C. E. Banks and R. G. Compton, *Nano Lett.*, 2006, **6**, 1556.

17. X. Kang, J. Wang, H. Wu, J. Liu, I. A. Aksay and Y. Lin, *Talanta*, 2010, **81**, 754.

18. W.-J. Lin, C.-S. Liao, J.-H. Jhang and Y.-C. Tsai, *Electrochem. Commun.*, 2009, **11**, 2153.

19. M. Pumera, R. Scipioni, H. Iwai, T. Ohno, Y. Miyahara and M. Boero, *Chem. Eur. J.*, 2009, **15**, 10851.

20. H.-L. Guo, X.-F. Wang, Q.-Y. Qian, F.-B. Wang and X.-H. Xia, *ACS Nano*, 2009, **3**, 2653.

21. X. Li, Y. Zhu, W. Cai, M. Borysiak, B. Han, D. Chen, R. D. Piner, L. Colombo and R. S. Ruoff, *Nano Lett.*, 2009, **9**, 4359.

22. D. S. Shishmarev, N. V. Rees and R. G. Compton, *Electroanalysis*, 2010, **22**, 31.

23. J. F. Rusling, *Colloids and Surfaces*, 1997, **123**, 81.

24. R. T. Kachoosangi, G. G. Wildgoose and R. G. Compton, *Analytica Chimica Acta*, 2008, **618**, 55.

25. X. Kang, J. Wang, H. Wu, J. Liu, I. A. Aksay and Y. Lin, *Talanta*, 2010, **81**, 754.

26. D. J. Miner, J. R. Rice, R. M. Riggin and P. T. Kissinger, *Anal. Chem.*, 1981, **53**, 2258.

27. I. Baranowska, M. Koper, *Electroanalysis*, 2009, **21**, 1194.

28. P. Fanjul-Bolado, P. J. Lamas-Ardisana, D. Hernandez-Santos and A. Costa-Garcia, *Analytica Chimica Acta*, 2009, **638**, 133.

29. M. A. T. Gilmartin and J. P. Hart, *Analyst*, 1994, **119**, 2431.

30. F. S. Felix, C. M. A. Brett and L. Angnes, *J. Pharm. Biomed. Anal.*, 2007, **43**, 1622.

31. Z. Wang, X. Li, Y. Wu, Y. Tang and S. Ma, *J. Electroanal. Chem.*, 1999, **464**, 181.

32. H. J. Salavagione, J. Arias, P. Garces, E. Morallon, C. Barbero and J. L. Vazquez, *J Electroanal Chem*, 2004, **565**, 375.

33. P. A. Quintela, A. Diaz and A. E. Kaifer, *Langmuir*, 1988, **4**, 663.

34. T. T. Baby, S. S. J. Aravind, T. Arockiadoss, R. B. Rakhi, and S. Ramaprabhu, *Sens. Actuators, B*, 2010, **145**, 71.

35. M. Lotya, Y. Hernandez, P. J. King, R. J. Smith, V. Nicolosi, L. S. Karlsson, F. M. Blighe, S. De, Z. Wang, I. T. McGovern, G. S. Duesberg and J. N. Coleman, *J. Am. Chem. Soc.*, 2009, **131**, 3611.

6.2. EFFECT OF GRAPHENE ADSORBED SURFACTANTS ON METAL ANALYSIS

Continuing with the observations and conclusions from Chapter 6.1 where the effect of the surfactant 'sodium cholate' was explored towards the electrochemical oxidation of NADH and acetaminophen, this chapter explores the effect of the same surfactant towards the electro-analytical sensing of cadmium (II) ions *via* anodic stripping voltammetry in order to assess the wider implications of surfactant adsorbed graphenes. This chapter contains work that has been published. [2]

6.2.1. INTRODUCTION

It is well known that heavy metals pose a severe health risk to humans and thus exploration of fast, sensitive and reliable analysis is urgently needed. [1] Given the widespread exploration of graphene in many electrochemical areas, the use of graphene for sensing heavy metals is surprisingly limited (pre-2010). In one paper available, Li *et al.* have reported the trace level detection limit of 0.02 μgL^{-1} for cadmium (II) using a graphene-Nafion modified *in-situ* plated bismuth film glassy carbon (GC) electrode. The analytical performance of this sensor is reported to be superior over both a Nafion film and a Nafion/carbon nanotube coated bismuth film GC electrode, which exhibited limits of detection of 0.1 and 0.04 μgL^{-1} respectively. [1] Li *et al.* have also explored using this sensor modified *in-situ* with a mercury film allowing the detection limit to be significantly reduced. [2] However, to the best of the author's knowledge, in 2010, there were no literature reports focusing on the detection of heavy metal ions using solely a graphene modified electrode.

[2] D. A. C. Brownson and C. E. Banks, *Electrochem. Commun.*, 2011, **13**, 111.

6.2.2. RESULTS AND DISCUSSION

First the nucleation of the target metal cadmium (II) is considered *via* chronoamperometry. Using a deposition potential of −1.5 V (*vs*. SCE) for 120 s in a pH 2.5 buffer solution containing 200 μgL^{-1} (1.78 μM) cadmium (II), the chronoamperometric response was explored at a bare (unmodified) edge plane like-SPE: note, within Chapter 6.2 all experimental analysis was performed using the aforementioned SPE, a carbon counter and a SCE reference electrode. As depicted in Figure 6.5 a charge of –0.78 mC is passed. In comparison, the response of a commercially available graphene (with adsorbed surfactant, S-graphene) modified SPE was explored which as shown in Figure 6.5 is distinctly different to that observed at the bare SPE, with a charge passed of –1.61 mC. This increment in the charge passed has likely resulted from increasing the global coverage of edge plane sites through the introduction of the graphene.

As depicted above (Chapter 6.1) this work has highlighted that the surfactant needs to be considered, [3, 4] since surfactants are readily employed in the fabrication of graphene to reduce coalescing of graphenes into multi-layer graphene *viz* graphite. [5] Consequently a control experiment was performed in which a surfactant (sodium cholate in this case) modified SPE was explored. As can be observed in Figure 6.5 the response was noticeably different to that observed for the bare SPE, and remarkably similar to that obtained using the S-graphene modified SPE. With a charge passed of –1.48 mC, the surfactant modified electrode passes more charge than the bare SPE and it can be readily observed that a similar charge is passed to that perceived when using S-graphene. The effect of reducing the applied potential and the charge passed was explored where log-log plots reveal linear dependences, as depicted in Figure 6.5B.

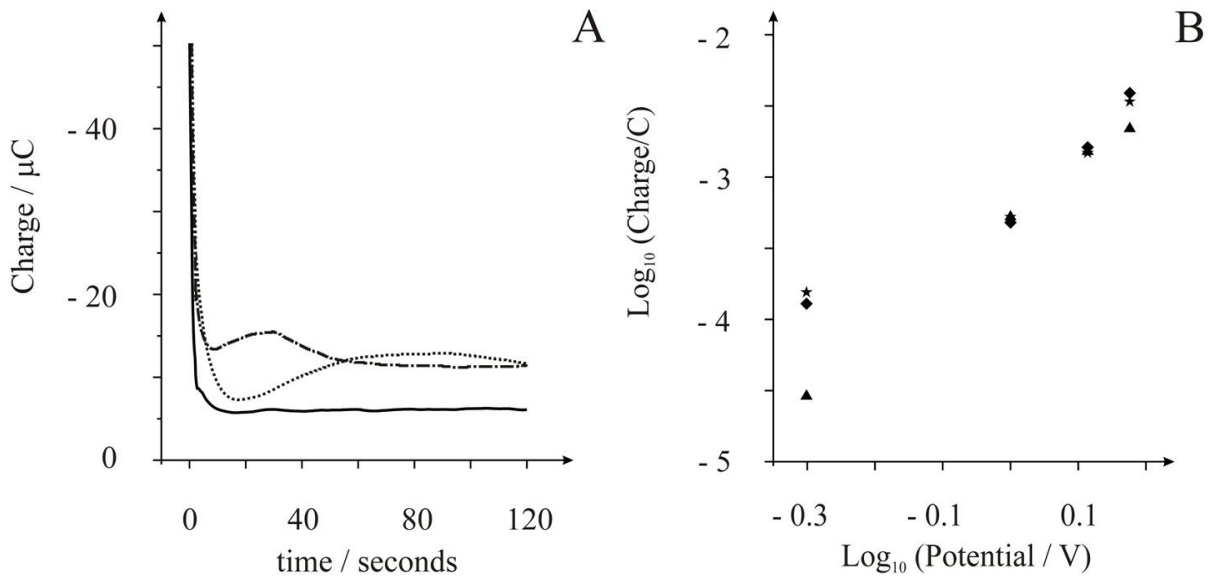

Figure 6.5 *Chronoamperometric curves (**A**) obtained for the deposition of 200 µgL^{-1} cadmium in a pH 2.5 buffer solution obtained at a bare SPE (solid line), a 0.5 µg S-graphene modified SPE (dotted line) and a surfactant modified SPE (dot-dashed line). A potential of –1.5 V (vs. SCE) was utilised. (**B**) Relationship between log$_{10}$ charge and log$_{10}$ potential for bare (triangles, ▲), S-graphene (diamonds, ♦) and surfactant (stars, *) modified SPEs.*

The transients depicted in Figure 6.5 exhibit steady state currents at long times indicating the smooth deposition of cadmium metal with high current and under interfacial control. SEM was attempted in order to try and observe the possible difference in the number of cadmium nuclei on the bare, S-graphene and surfactant modified SPEs, but was inconclusive and non-illuminating. Based on the chronoamperometric profiles observed in Figure 6.5 it is clear that differing nucleation dynamics are likely to be occurring and a full detailed study is required with *in-situ* AFM [6] to confirm this. The difference in charge suggests more nucleated material, [7] which in the case of S-graphene as compared to the underlying (bare) electrode is likely due to the unique structure of graphene but also due to a contribution from the adsorbed surfactant.

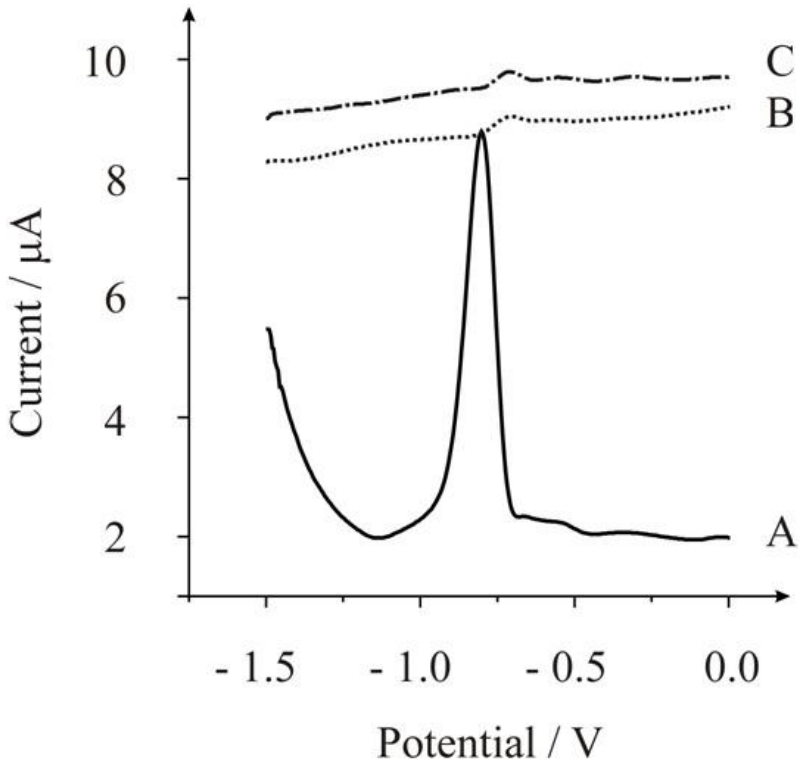

Figure 6.6 *Typical square-wave voltammetric profiles for detection of 200 µgL^{-1} cadmium in pH 2.5 buffer solution obtained at a bare SPE (**A**), a 0.5 µg S-graphene modified SPE (**B**) and a surfactant modified SPE (**C**). A deposition potential of –1.5 V (vs. SCE) for 120 s was utilised; SWV was performed using a frequency of 25 Hz and amplitude of 20 mV.*

We the stripping voltammetry of 200 µgL^{-1} (1.78 µM) cadmium (II) in a pH 2.5 buffer solution is explored by employing a deposition time and potential of 120 s and –1.5 V respectively. Figure 6.6 depicts the voltammetric signatures of the target metal at a bare SPE which is due to the voltammetric stripping of the *in-situ* formed metal to its corresponding ion. It is readily evident that a large and easily quantifiable signal is observed, which is in agreement with the literature. [8] The effect of the applied deposition time on the voltammetric signature was explored, where a log-log plot of peak area *vs*. time demonstrated that more material is deposited and consequently stripped as a result of increased deposition time (data not shown). Next the response of S-graphene, which was immobilised onto a SPE is explored. Using the same conditions as described above, the response of the S-graphene is depicted in Figure 6.6, which clearly exhibits a poor voltammetric signature in comparison to

the bare SPE. This is contrary to recent literature reports where the incorporation of graphene has lead to an increase in sensitivity. [1, 2] Finally the response of a surfactant modified SPE is explored as a control experiment. Again, Figure 6.6 depicts the voltammetric response and it is clear that the introduction of the surfactant exhibits a similar response as that of the S-graphene, indicating that the surfactant is detrimental to the anodic stripping voltammetry of the target metal.

It is noted that the voltammetric profiles observed in Figure 6.6 display a large capacitance when S-graphene is utilised, which has been reported by Pumera *et al.* to be due to multi-layer graphene on the electrode surface rather than single layer graphene. [9] However, a similar response is observed in the presence of the surfactant (no graphene), suggesting that this might rather derive from the presence of the surfactant (sodium cholate) in this system. Additionally, more information was attempted to be deduced using microscopy but again was inconclusive. However, the voltammetric profiles in Figure 6.6 are illuminating.

Previous work using carbon based electrode substrates has demonstrated that the presence of the surfactant Triton X-100 inhibits the electro-deposition of cadmium(II) [10] whilst in the case of sodium dodecyl sulphate and Triton X-100, a detrimental effect is observed on the electro-analysis of copper, albeit at differing severities. This is thought to be due to the differing hydrophilicities of the electrode surfaces employed, where a more hydrophobic GC electrode is more prone to surfactant adsorption than a hydrophilic edge plane pyrolytic graphite electrode. [11] Thus if similar surfactants were to be incorporated into graphene's manufacturing process it may be likely that similar inhibiting effects would be observed.

6.2.3. CONCLUSIONS

This chapter has built upon the knowledge established in Chapter 6.1 and in doing so, has demonstrated the wide-spread implications of surfactants utilised in the production of graphene. It has been shown that such surfactants (sodium cholate in this case) inhibit the electro-analytical sensing of cadmium (II) *via* anodic stripping voltammetry. Inspection of the deposition and stripping steps reveals that the surfactant inhibits the latter corresponding to the transition of cadmium metal to cadmium ions. This observation is in distinct contrast to the electrochemical literature of graphene for metal analysis. Chapter 6 has highlighted the importance of surfactant control experiments when de-convoluting the origin of electrochemical responses. Effectively, all cases where the electrocatalysis of graphene is claimed with surfactant modified/fabricated graphene should be re-examined.

6.2.4. REFERENCES

1. J. Li, S. Guo, Y. Zhai and E. Wang, *Anal. Chim. Acta*, 2009, **649**, 196.
2. J. Li, S. Guo, Y. Zhai and E. Wang, *Electrochem. Commun.*, 2009, **11**, 1085.
3. D. A. C. Brownson and C. E. Banks, *Analyst*, 2010, **135**, 2768.
4. D. K. Kampouris and C. E. Banks, *Chem. Commun.*, 2010, **46**, 8986.
5. J.-F. Wu, M.-Q. Xu and G. C. Zhao, *Electrochem. Commun.*, 2010, **12**, 175.
6. M. E. Hyde, R. Jacobs and R. G. Compton, *J. Phys. Chem. B*, 2002, **106**, 11075.
7. A. O. Simm, X. Ji, C. E. Banks, M. E. Hyde and R. G. Compton, *ChemPhysChem*, 2006, **7**, 704.
8. M. F. Noh, R. O. Kadara and I. E. Tothill, *Anal. Bioanal. Chem.*, 2005, **382**, 1175.
9. M. S. Goh and M. Pumera, *Electrochem. Commun.*, 2010, **12**, 1375.
10. C. E. Banks, M. E. Hyde, P. Tomčík, R. Jacobs and R. G. Compton, *Talanta*, 2004, **62**, 279.
11. D. S. Shishmarev, N. V. Rees and R. G. Compton, *Electroanalysis*, 2010, **22**, 31.

CHAPTER 7: ELECTROCHEMISTRY OF SURFACTANT FREE PRISTINE GRAPHENE (EXPLORING TOP-DOWN ELECTRODE MODIFICATION)

The previous chapter has shown that surfactants, commonly adsorbed onto graphene's surface when employed as part of the fabrication process, can significantly affect the observed electrochemical response. It is clear that such surfactants (when present) have led to erroneous assignments related to the electrochemical properties of graphenes produced in such a manner and resultantly have inhibited the 'true' investigation of graphene's electrochemistry.

This chapter considers the use of pristine graphene that, due to its fabrication methodology (see Chapter 5.4.2), is completely *free from surfactants* and has not been purposely oxidised or pre-treated. The graphene exhibits an oxygen content of *ca*. 4.96 %; indicating near-true graphene, which will enable the 'true' electronic properties of graphene to be explored and de-convoluted *for the first time.*

The chapter first explores the fundamental electrochemical properties of the solution-based graphene through the utilisation of 'graphene modified electrodes' (using a drop-casting method in order to immobilise and 'connect to' the graphene, as is favoured for electrochemical applications) prior to investigating the implications of the knowledge gained in earlier sections towards the implementation of these graphene modified electrodes for electroanalytical applications.

Experimental Overview: this chapter utilises cyclic voltammetry, chronoamperometry and SWV experiments using a three electrode system as detailed in Chapter 5.1. Graphene modified electrodes are studied and thus the underlying working electrodes employed were EPPG (Chapter 5.2.1), BPPG (Chapter 5.2.1), edge plane like-SPEs (Chapter 5.2.2),

BDD and GC (Chapter 5.2.3), with a platinum wire and a SCE comprising the auxiliary and reference electrodes respectively. The graphene utilised herein (P-graphene) is described as 'pristine (surfactant free) graphene sheets suspended in ethanol' and is fully characterised in Chapter 5.4.2. Graphene oxide (GO) is also utilised and is described as 'graphene oxide sheets suspended in aqueous solution', with full characterisation depicted in Chapter 5.4.8. Where necessary, control/comparison experiments were performed utilising ethanol and pristine graphite modified electrodes as detailed in Chapter 5.5.

7.1. THE ELECTROCHEMICAL PROPERTIES OF (SURFACTANT FREE) GRAPHENE MODIFIED ELECTRODES

Chapter 7.1 contains published work [3] which critically evaluates the reported electro-catalysis of graphene (through exploration of its electron transfer properties and through the utilisation of various electrode 'coverages' of the graphene material) using inner-sphere and outer-sphere electrochemical redox probes, namely potassium ferrocyanide (II) and hexaammine-ruthenium (III) chloride, in addition to *L*-ascorbic acid and *β*-nicotinamide adenine dinucleotide (NADH). The effect of varying the supporting substrate is also considered.

7.1.1. INTRODUCTION

There are many optimistic reports of where graphene has been used as an electrode material within a variety of sensing and energy related devices. With claims of superior electrochemical performances being reported when compared to traditional noble metals and various fullerene based electrode materials (such as graphite and CNTs). [1-3] While these reports do exist, reports have emerged demonstrating that graphene might not provide a significant advantage over existing electrode materials. [4-7] For example, Pumera *et al.* [4] have shown that single-, few- and multi-layer graphene does not exhibit a significant advantage over graphite micro-particles in terms of sensitivity, linearity and repeatability towards the electro-analytical detection of uric acid. However, as shown in Chapter 6, surfactants routinely used in the production of commercially available graphene both detrimentally and beneficially interfere towards the observed electrochemical response at different analytes and are a major contribution. The presence of said surfactants can potentially lead to false claims of the electro-catalysis of graphene, [5, 6] given that their 'contribution' towards the electrochemical response prevents the

[3] D. A. C. Brownson, L. J. Munro, D. K. Kampouris and C. E. Banks, *RSC Adv.*, 2011, **1**, 978.

true heterogeneous electron transfer properties of graphene from being observed. Resultantly, this chapter explores, for the first time, the electronic structure of graphene (P-graphene) which is commercially available and well characterised (produced *via* a substrate-free gas-phase synthesis method) [8-10] and completely *free from surfactants*; with the effect of coverage also explored when utilising the drop-casting method to explore the use of graphene as an electrode material.

7.1.2. RESULTS AND DISCUSSION

7.1.2.1. RESULTS

First the electron transfer properties of EPPG and BPPG electrodes, constructed from HOPG, are evaluated with the inner-sphere electron transfer redox probe, [11] 1 mM potassium ferrocyanide (II) in 1 M KCl. Figure 7.1B depicts characteristic voltammetric profiles obtained at EPPG and BPPG electrodes where the former exhibits a peak-to-peak potential separation, ΔE_P, of 60 mV whilst the latter exhibits a ΔE_P of 242 mV. Both responses are in excellent agreement with previous studies [11-14] since the edge plane electrode has a high global coverage of edge plane sites, which exhibit anomalously fast electron transfer rates over that of basal plane sites. [15] Conversely, the BPPG electrode, due to its structure, has a low global coverage of edge plane sites and hence a poor voltammetric activity is exhibited. [15] Attention was next turned to exploring the cyclic voltammetric performance of an EPPG electrode following modification with 40 ng of graphene (P-graphene, containing no surfactant). As depicted in Figure 7.2A the introduction of graphene results in a change to the peak-to-peak separation from 60 to 192 mV, which is similar to that observed for the unmodified BPPG electrode (242 mV, see Figure 7.1B). Note that this approach, where an electrode material exhibiting fast electron transfer rates is modified with graphene, is commonly utilised in the literature. [16, 17]

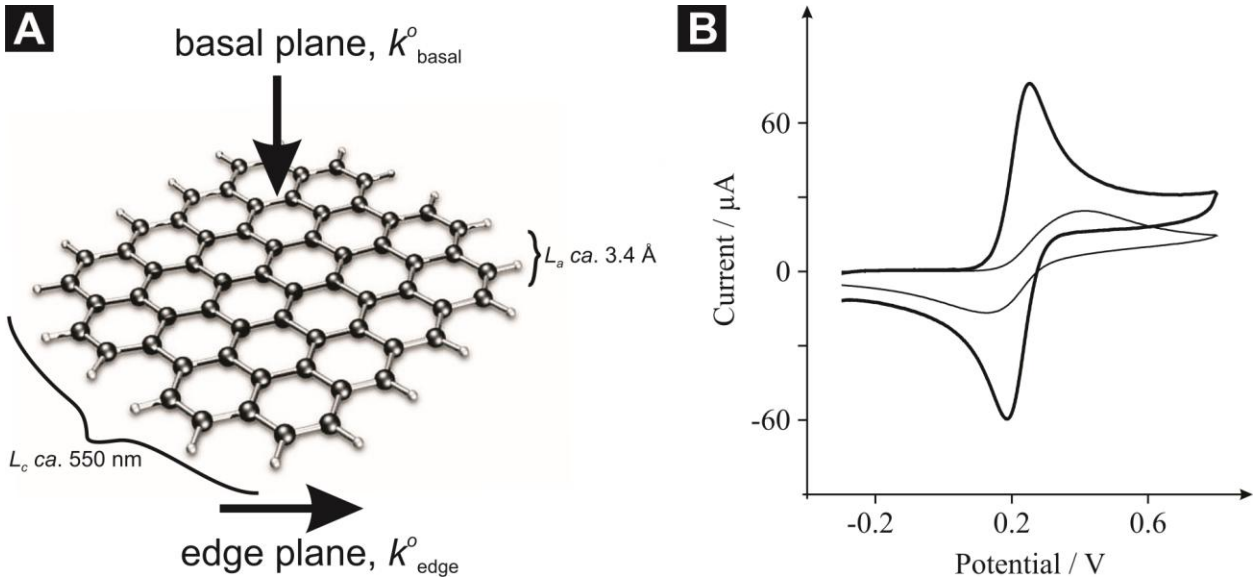

Figure 7.1 *(**A**) Schematic representation of graphene indicating its edge and basal sites, where the heterogeneous electron transfer rate of the former (k^o edge) is anomalously faster over that of the latter (k^o basal), which constitutes the largest contribution to its surface area. (**B**) Cyclic voltammetric profiles recorded for 1 mM potassium ferrocyanide (II) in 1 M KCl using an EPPG electrode (thick line) and a BPPG electrode (thin line). Scan rate: 100 mVs^{-1} (vs. SCE).*

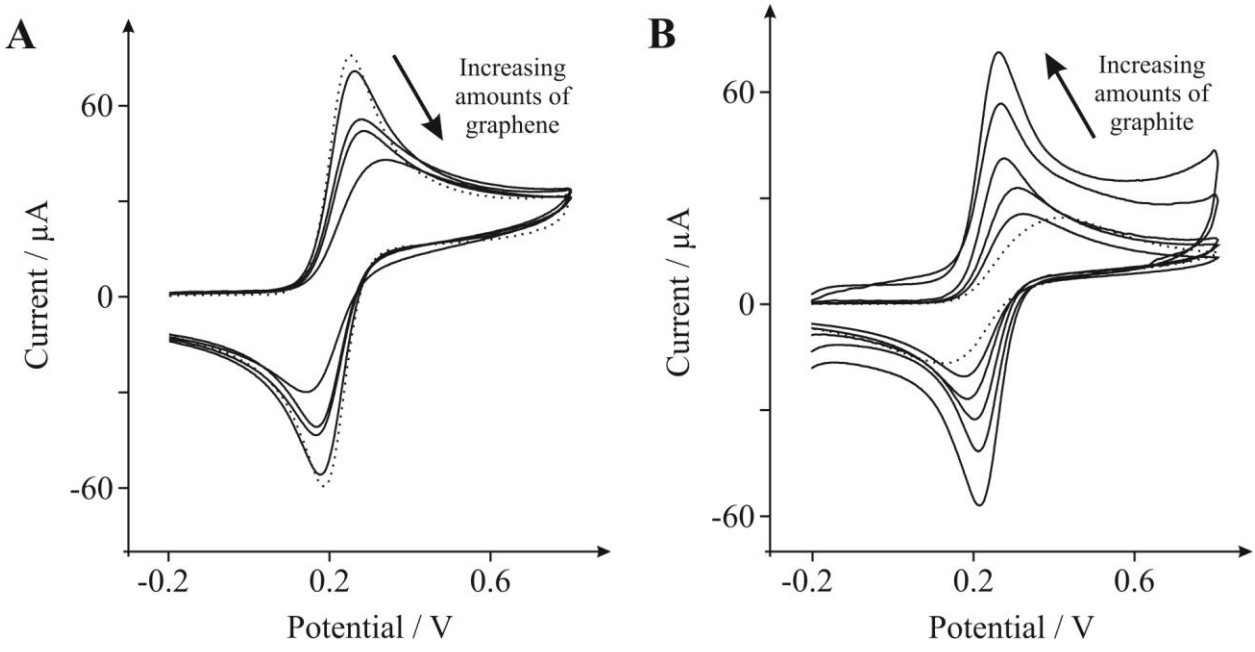

Figure 7.2 *Cyclic voltammetric profiles recorded utilising 1 mM potassium ferrocyanide (II) in 1 M KCl. **A:** Cyclic voltammetric profiles obtained using an EPPG electrode (dotted line) with the addition of increasing amounts of 10, 20, 30, and 40 ng P-graphene (solid lines). **B:** Cyclic voltammetric profiles obtained using a BPPG electrode (dotted line) with the addition of increasing amounts of 2, 4, 50, 100, and 200 µg graphite (solid lines). Scan rate: 100 mVs^{-1} (vs. SCE).*

Next the effects of graphene coverage on the electrochemical response are considered. Figure 7.2A depicts the increasing mass deposition of P-graphene onto an underlying EPPG electrode surface where it is clear that with increasing graphene coverage, a decrease in the voltammetric peak height is evident together with a significant decrease in the electrochemical reversibility of the redox probe, as evident by the increasing ΔE_P. Note that this response is distinctly different to all current literature regarding graphene.

For comparative purposes exploration of the cyclic voltammetric performance of a BPPG electrode following modification with 50 μg of graphite (as above, see Chapter 5.5) was subsequently conducted. As evident in Figure 7.2B, the graphite modified electrode exhibits a ΔE_P of 66 mV, which is similar to that observed at an EPPG electrode (60 mV, see Figure 7.1B) and significantly smaller than that observed at both the P-graphene modified EPPG and the underlying BPPG electrodes (192 and 242 mV respectively). Note that this response is as commonly observed in the literature. [18] Through comparison of the peak-to-peak separations it is clear that modification with graphite leads to an increased proportion of edge plane sites (electron transfer sites). This results in an enhanced electrochemical response with increased reaction kinetics, reversibility and electro-catalytic relative to that of the underlying BPPG electrode and a P-graphene modified EPPG electrode (*vide supra*). [15, 18-21]

Next the electronic properties of an EPPG electrode is characterised using the outer-sphere electron transfer redox probe, [11] 1 mM hexaammine-ruthenium (III) chloride in 1 M KCl. Figure 7.3A shows the typical cyclic voltammetric profile obtained at an EPPG electrode where a ΔE_P of 60 mV is observed, which is in excellent agreement with previous literature. [22] Figure 7.3A also shows the cyclic voltammetric response obtained as a result of the modification of the underlying EPPG electrode with 200 ng P-graphene, where an increase in the ΔE_P occurs

from 60 (EPPG) to 115 mV (after modification with 200 ng P-graphene), which is characteristically similar to that reported for a BPPG electrode. [22] The effect of increasing the mass deposition of P-graphene on the underlying EPPG electrode is also depicted in Figure 7.3A. An increased coverage of graphene causes the electron transfer kinetics (*viz* reversibility of the redox probe) to be significantly reduced. Thus after modifying an EPPG electrode with 400 ng of P-graphene a ΔE_P of 141 mV is observed. Figure 7.3B depicts a plot of 'ΔE_P' *versus* 'mass of P-graphene deposited', which reveals a positive correlation where an increase in the mass of graphene results in an increase in the ΔE_P; again such a response has never been reported in the literature, with respect to graphene, before this work.

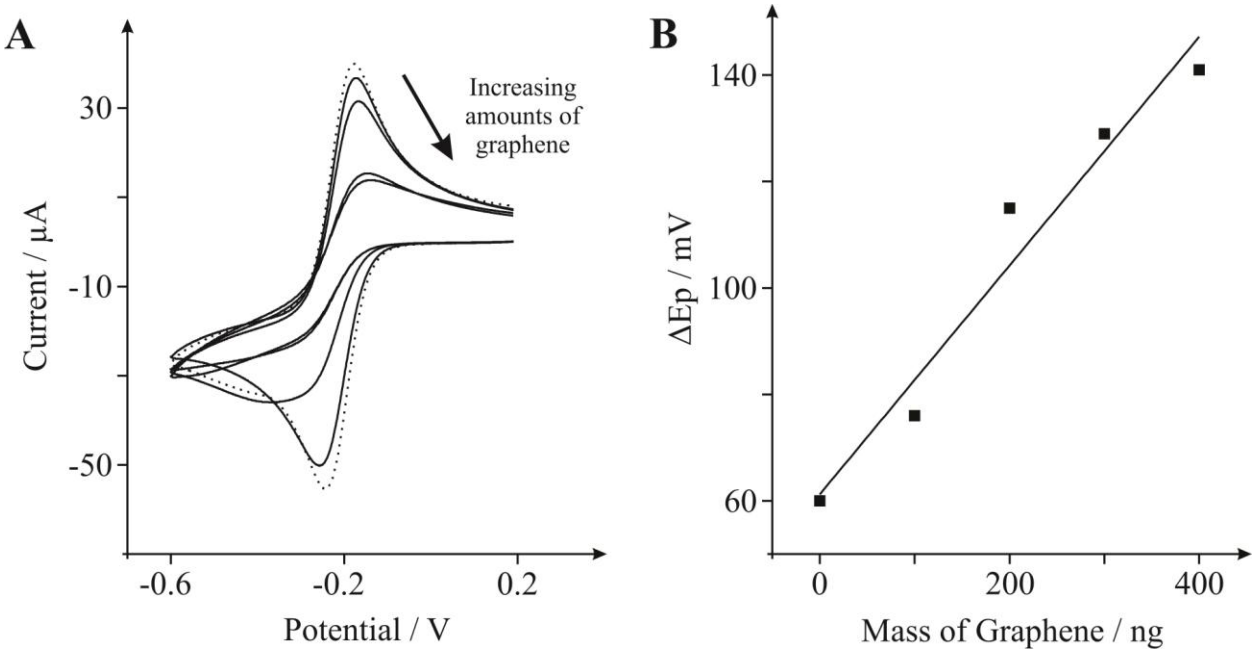

Figure 7.3 *(**A**) Cyclic voltammetric profiles recorded utilising 1 mM hexaammine-ruthenium (III) chloride in 1 M KCl, obtained using an EPPG electrode (dotted line) with the addition of increasing amounts of 100, 200, 300, and 400 ng P-graphene (solid lines). Scan rate: 100 mVs^{-1} (vs. SCE). (**B**) Relationship between the 'mass of P-graphene deposited' upon the electrode surface and the resultant 'peak-to-peak separation'.*

The electrochemical properties of graphene modified electrodes are now explored within bio-sensing applications. First the effect of various electrode modifications towards the electrochemical oxidation of 1 mM NADH in pH 7 PBS is considered using both EPPG and BPPG electrodes. Figure 7.4 shows a typical voltammetric response towards NADH utilising both EPPG and BPPG electrodes where the oxidation peak potentials occur at *ca*. 490 and 660 mV respectively and are in excellent agreement with a previous literature report. [18] In the former, a voltammetric signature is observed at a lower (positive) over-potential than that observed for the latter. Thus is indicative of a greater reactivity on the EPPG over that of the BPPG electrode due to a larger global coverage of edge plane sites, [15] which represents increased heterogeneous electron transfer kinetics at the EPPG electrode.

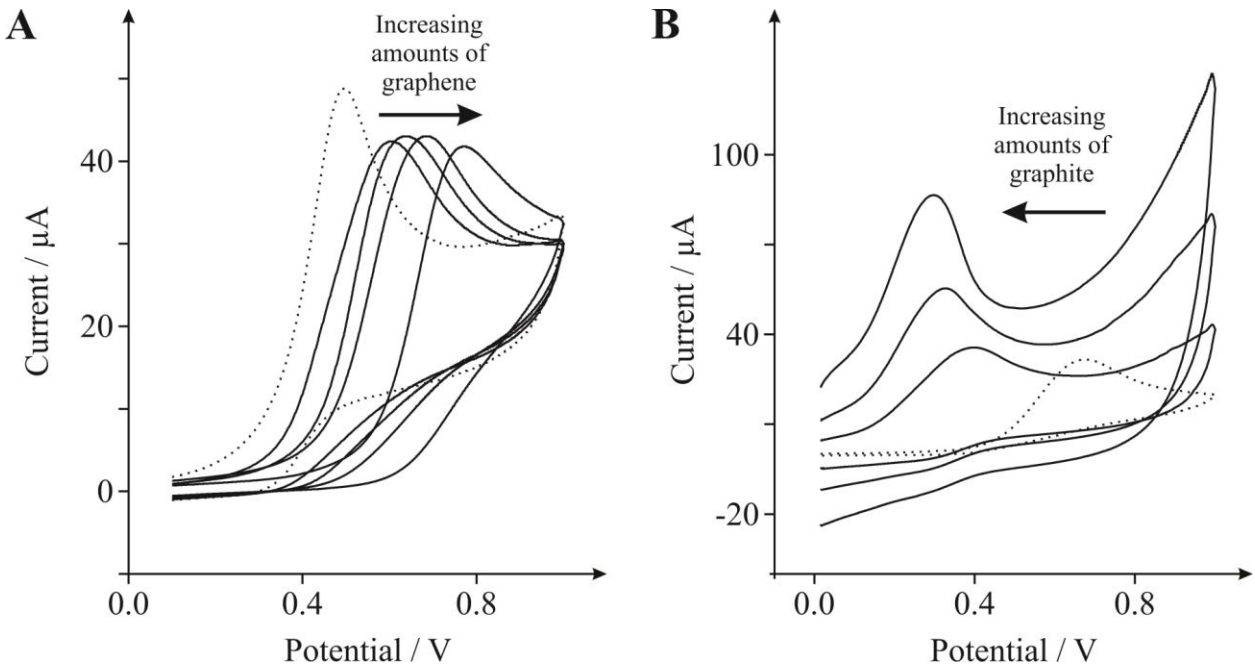

Figure 7.4 *Cyclic voltammetric profiles recorded utilising 1 mM NADH in PBS (pH 7).* ***A:*** *Cyclic voltammetric profiles obtained using an EPPG electrode (dotted line) with the addition of increasing amounts of 2.5, 5.0, 10.0, and 40.0 ng P-graphene (solid lines).* ***B:*** *Cyclic voltammetric profiles obtained using a BPPG electrode (dotted line) with the addition of increasing amounts of 50, 100, and 200 µg graphite (solid lines). Scan rate: 100 mVs^{-1} (vs. SCE).*

Attention was next turned to exploring the cyclic voltammetric performance of an EPPG electrode following modification with 10 ng of P-graphene, again, common practice in the current graphene literature. As depicted in Figure 7.4A the introduction of graphene results in a positive shift in the oxidative peak potential from *ca*. 490 (EPPG) to 665 mV (10 ng graphene), which is characteristic of an unmodified BPPG electrode (*ca*. 660 mV, see Figure 7.4B). When considering the effect of graphene coverage on the voltammetric response (shown in Figure 7.4A) it is evident that increasing the mass of graphene deposited results in a clear shift in the voltammetric over-potential (oxidation peak) of NADH towards more electropositive regions, where at 40 ng of P-graphene the oxidation peak occurs at *ca*. 772 mV, indicating slow heterogeneous electron transfer at graphene.

Now exploration of the effect of graphite upon a BPPG electrode is again considered as a control measure. In Figure 7.4B it is evident that the addition of 50 µg of graphite onto the BPPG electrode surface results in a negative shift in the oxidative peak potential from *ca*. 660 (BPPG) to 380 mV (50 µg graphite). The response, after modification with graphite, is characteristically similar to that of an unmodified EPPG electrode (*ca*. 490 mV). Addition of increasing quantities of graphite onto the BPPG electrode leads to a further shift of the NADH oxidation peak which displays continuous movement towards less electropositive over-potentials. Addition of 200 µg graphite onto the underlying BPPG electrode surface gives rise to an oxidation peak at *ca*. 292 mV, indicating fast heterogeneous electron transfer at graphite; such a response is routinely reported in the literature. [18]

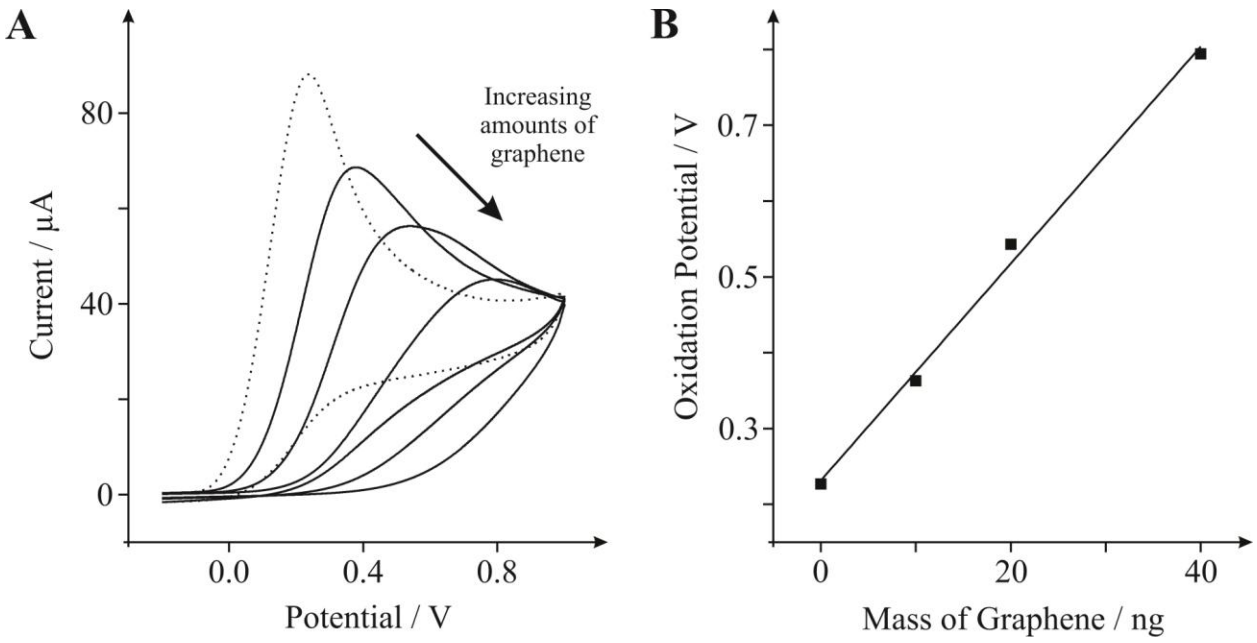

Figure 7.5 *(**A**) Cyclic voltammetric profiles recorded utilising 1 mM L-ascorbic acid in PBS (pH 7) obtained using an EPPG electrode (dotted line) with the addition of increasing amounts of 10, 20 and 40 ng P-graphene (solid lines). Scan rate: 100 mVs^{-1} (vs. SCE). (**B**) Relationship between the 'mass of P-graphene deposited' upon the electrode surface and the 'resultant oxidation peak potential'.*

To further explore the effects of graphene upon various biologically relevant compounds, the electronic properties of P-graphene are next considered using 1 mM *L*-ascorbic acid (AA) in PBS (pH 7). Figure 7.5A depicts the standard cyclic voltammetric response observed at an EPPG electrode where an oxidation peak is evident at *ca*. 227 mV. Upon modification of the EPPG electrode with 20 ng of graphene there is a positive shift in the oxidative peak potential (over-potential) from *ca*. 227 (EPPG) to 543 mV (20 ng graphene), which is characteristic of a BPPG electrode. [23] Figure 7.5B shows the effect of increasing P-graphene coverage on the position of the oxidation peak for AA. The positive correlation indicates that an increased mass of P-graphene deposited upon the underlying electrode surface results in a further shift in the oxidative over-potential towards electropositive regions. After the addition of 10, 20 and 40 ng of P-graphene the oxidation potential shifts to *ca*. 363, 543 and 794 mV respectively; for

comparative purposes, note that the oxidation potential was *ca*. 386 mV for an unmodified BPPG electrode.

7.1.2.2. DISCUSSION

If the response (Figure 7.3) where the addition of P-graphene results in greater peak-to-peak separations is assumed to be akin to that of a partially blocked electrode (as identified by Amatore and co-workers), [24] the observed heterogeneous electron transfer rate kinetics, k^0_{obs}, are related to the electron transfer rate of the unmodified electrode, k^0_{UE}, and the fractional coverage of graphene, θ, by:

$$k^0_{obs} = k^0_{UE}(1-\theta) \tag{7.1}$$

Note that for an overlapping random distribution, the real coverage, θ_R, is given by: [25]

$$\theta_R = 1 - e^{-\theta} \tag{7.2}$$

To determine k^0_{obs} and k^0_{UE} from the relevant cyclic voltammetric profiles the Nicholson method is invoked (see equation (1.44)), [26] where the diffusion coefficient of the outer-sphere redox probe, hexaammine-ruthenium (III) chloride, is 9.1×10^{-6} cm^2 s^{-1} (0.1 M KCl). [27, 28] Consequently a value for k^0_{UE} (unmodified EPPG electrode) was found to correspond to 106×10^{-3} cm s^{-1}, which is in excellent agreement with previous studies. [21] Following the modification of the underlying electrode surface with 100 and 400 ng of P-graphene, the determined k^0_{obs} values are 8.86×10^{-3} and 1.33×10^{-3} cm s^{-1} respectively, from which a real coverage (θ_R) of 0.60 and 0.63 is deduced *via* equations (7.1) and (7.2). In the case where quasi-reversible voltammetric profiles are obtained in the accessible range of scan rates, as found here, data relating to diffusion domain sites and their sizes would not be assigned. [24]

Comparison of the standard heterogeneous electron transfer rates indicate that the addition of P-graphene onto the EPPG electrode results in the reduction of the observed electron transfer kinetics. It is well documented that the voltammetric response of graphitic electrodes depends on the proportion of edge plane sites (see Chapter 2), where a low and high proportion result in slow and fast electron transfer respectively; [19, 29] which has also recently been shown to be the case for graphene (although the graphene used in the study [12] contained the surfactant, sodium cholate, and thus in line with Chapter 6 the 'true' response of 'graphene' is not easily de-convoluted from their data). Nonetheless, consequently where graphene was utilised earlier the deterioration in the electrochemical responses observed are likely due to the reduced proportion of available edge plane sites and an increased basal plane contribution arising from the addition of graphene (which is basal plane abundant by nature, see Figure 7.1A). Note that the range of electro-active species studied here allow the contribution from the oxygenated species residing on the edge plane of the graphene to be neglected since the observed trend is the same for all compounds studied which range from simple outer-sphere electron transfer probes to surface sensitive inner-sphere species (see Appendix A.1). [45]

To further understand and highlight the contribution of edge and basal plane sites, which are an inherent property of graphene and graphite alike, the surface area ratio of basal plane, S_{basal}, to edge plane (perimetrical boundary carbon atoms), S_{edge}, is now considered for the case of increasing layers of graphene. The mean surface area of the basal contribution for a single piece of graphene may be deduced using $S_{basal} = \pi r^2$, where for the P-graphene utilised in this study the radius, *r*, is *ca*. 275 nm. The surface area of the edge plane for a single piece of graphene is deduced using $S_{edge} = 2\pi rh$, where the S_{edge} is considered be a round strip or band consisting of the boundary of carbon atoms of the graphene layer, the same as the length of the

perimeter of a circular disk, whereas the width is the height of this stripe (*h*) – thus for a single layer of graphene the height of the strip is equal to the thickness of the monolayer sheet, which is 3.35 Å, and each layer of graphene added contributes to an increase in the S_{edge} by 604.76 nm^2. [7, 19, 29] Note, the assumption that graphene sheets are circular is an approximation (for exemplification) and is not likely to be exactly the case in true graphene (see Figure 7.1A). Figure 7.6 compares the ratio of S_{basal}/S_{edge} on increasing the number of graphene layers, where it is evident that as more layers are introduced, the amount of edge, *viz* edge plane sites is increased. Additionally, this is related to the theoretical current that would be expected as the amount of edge plane is increased, assuming the S_{edge} to be a 'band type' electrode, where the edge of the graphene is effectively the surface area of the electrode and as a consequence of increasing the amount of edge plane an increase in the current is expected. [7]

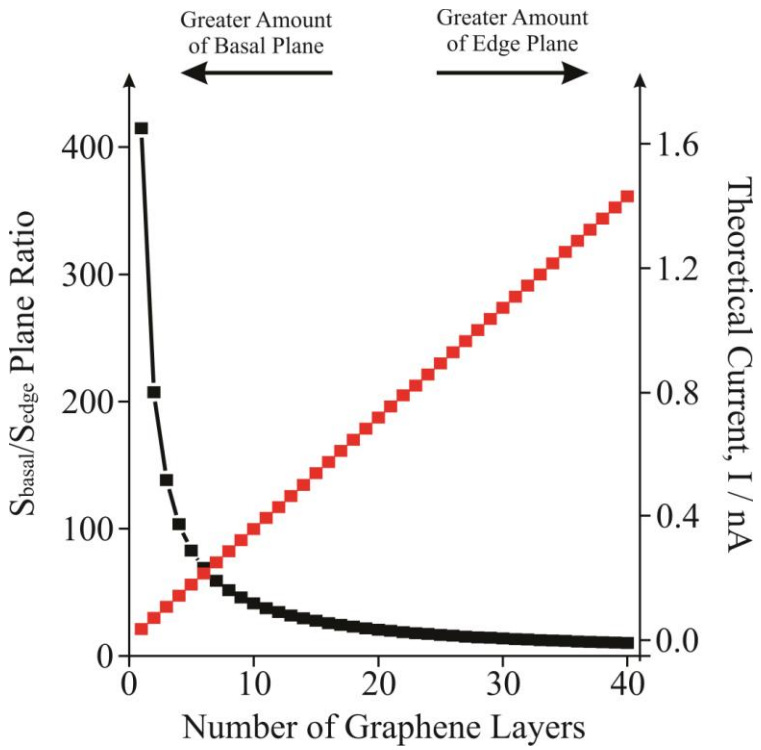

Figure 7.6 *The effect of increasing the number of graphene layers upon the ratio of basal/edge plane sites for a single piece of graphene (black squares) and the effect on the theoretical observed current (red squares). Note that this is for a single piece of graphene.*

Thus as one moves from single-layer graphene to multi-layer graphene, which is approaching that of graphite, the observed voltammetric responses will 'theoretically' surpass that of graphene. Note that this representation considers a single piece of graphene for simplicity, but nevertheless offers important insights into the effects observed. However in a real experimental case the graphene is likely to be immobilised onto an underlying electrode surface. Assuming that graphene exhibits fast electron transfer kinetics relative to that of the underlying electrode, the response of the electrode would be akin to that of an electrode array. The current response would therefore need to be multiplied according to the total number of graphene particles/sheets comprising the electrode. The latter assumes that there is no physical interaction of the graphene domains and that they are sufficiently separated from their nearest neighbour, therefore meeting the voltammetric requirements for diffusional independence. [30, 31] Note that in reality there will be some degree of overlap and the diffusion domain approach pioneered by Compton [30, 32] would ideally be suited and could be adapted to include the variance in the graphene from true graphene, *viz* single layer graphene, to graphene consisting of several layers.

It is evident that modification of an electrode surface with nanogram quantities of P-graphene leads to incomplete 'monolayer' coverage of the underlying electrode surface. The remaining 'uncovered' underlying electrode material remains electrochemically active (*viz* EPPG electrode) or relatively inactive (*viz* BPPG electrode) depending on the material utilised. In this case the high global coverage of edge plane sites on the underlying EPPG electrode exhibit improved heterogeneous electron transfer kinetics relative to that of the large basal plane surface contribution at graphene, which is effectively electrochemically inert in contrast to the edge plane sites. Thus with increased coverage of graphene up to one 'complete single layer' (a monolayer) the underlying material is increasingly inhibited. Consequently slower

heterogeneous electron transfer occurs, which is induced from the basal plane sites of graphene now dominating the electrochemical reactivity and 'blocking' the underlying edge plane sites of the host material. This is manifested as the continual increase in the observed ΔE_P values in the case of potassium ferrocyanide (II) (Figure 7.2A).

Interestingly, when larger quantities of graphene are utilised (micrograms opposed to nanograms) (Figure 7.7A) it is clear that the electrochemical reversibility and respective heterogeneous electron transfer rate begins to increase with increased mass deposition of graphene (ΔE_P of *ca*. 155, 128 and 123 mV for the addition of 0.5, 1.0 and 2.0 µg of P-graphene respectively). This is additionally confirmed utilising the biologically relevant compound (1 mM AA in PBS (pH 7)). In Figure 7.7B the modification of an EPPG electrode with 20 and 100 ng of P-graphene leads to the continual reduction in electrode rate kinetics and consequently a shift in the over-potential to higher electropositive regions. The oxidation peak potentials for an unmodified EPPG electrode and EPPG electrodes modified with 20 and 100 ng of P-graphene reside at *ca*. 195, 441 and 776 mV, respectively. However, when larger quantities of P-graphene are added (1.0 and 1.5 µg) the over-potential is significantly reduced, resulting in a shift towards lower electropositive regions. Thus the peak potential is observed at *ca*. 422 and 383 mV respectively. This trend is also exemplified in Figure 7.7C where with large microgram masses of P-graphene, the oxidation potential shifts beneficially to less positive potentials.

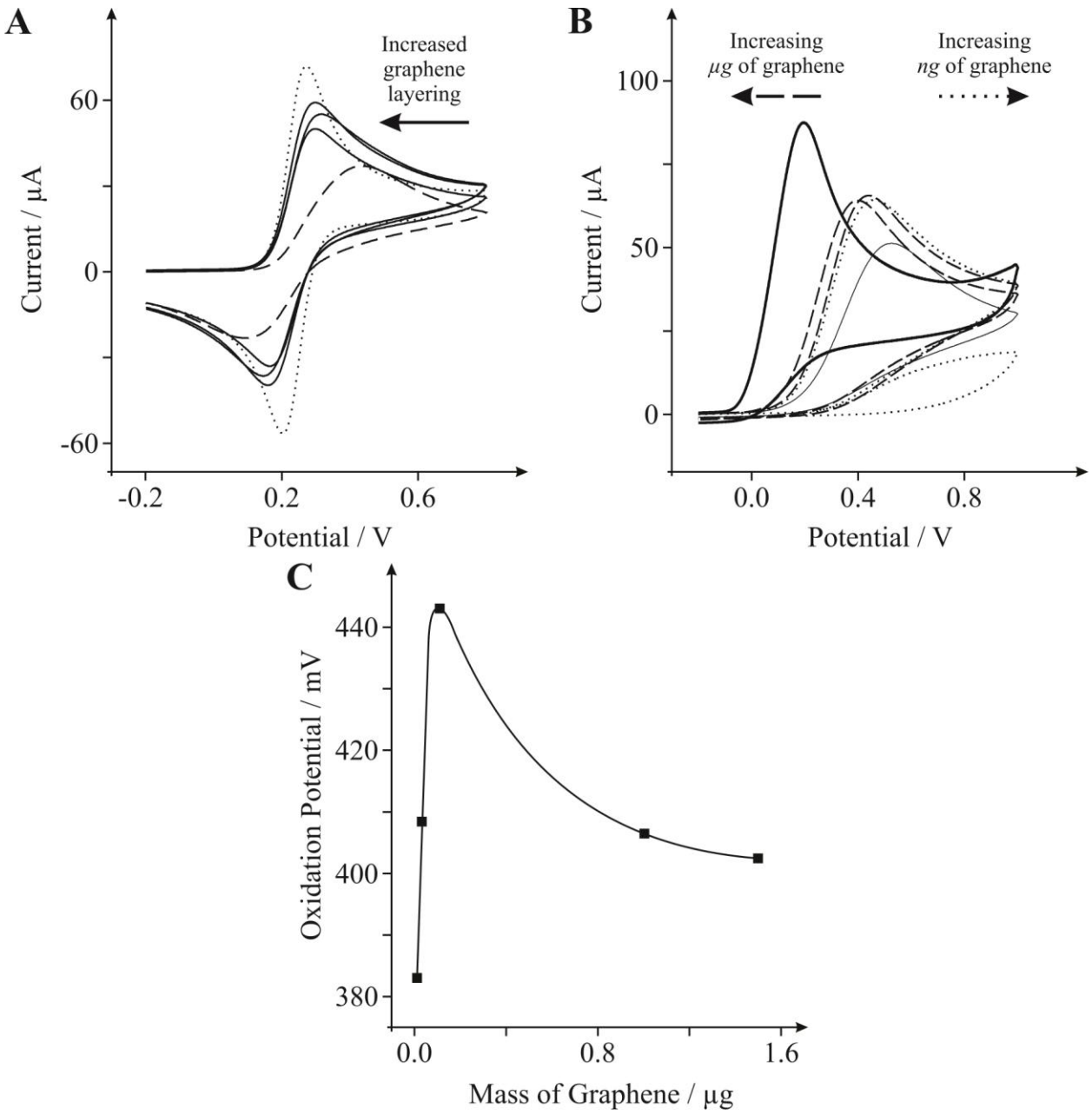

Figure 7.7 *(**A**) Cyclic voltammetric profiles recorded utilising 1 mM potassium ferrocyanide (II) in 1 M KCl, obtained using an EPPG electrode (dotted line) with the addition of increasing amounts of 0.5, 1.0 and 2.0 µg P-graphene (solid lines), and using a BPPG electrode (dashed line). (**B**) Cyclic voltammetric profiles recorded for 1 mM L-ascorbic acid in PBS (pH 7) utilising a BPPG electrode (thin solid line), and an EPPG electrode (thick solid line) with the addition of increasing amounts of; 20 and 100 ng P-graphene (dotted lines), and 1.0 and 1.5 µg P-graphene (dashed lines). (**C**) Relationship between; the mass of P-graphene deposited upon the EPPG electrode surface (from Figure 7.7B) and the resultant oxidation peak potential of 1 mM L-ascorbic acid in PBS (pH 7). Scan rates: 100 mVs^{-1} (vs. SCE).*

From the above observations this work is able to define differentiating coverage-based working regions for the electrochemical utilisation of graphene:

- '*Zone I*': where graphene additions do not result in complete coverage of the underlying electrode surface and thus an increasing basal plane contribution from the graphene modification leads to increasingly reduced electron transfer kinetics and electrochemical reactivity.
- '*Zone II*': once complete single-layer coverage is achieved, layered graphene *viz* graphite materialises with an increased global coverage of edge plane content and thus an increase in the heterogeneous electron transfer kinetics is observed with increased layering. This is manifested in an improvement in the electrochemical response (as evident where microgram quantities of P-graphene are deposited onto the electrode surface in the case of this work).

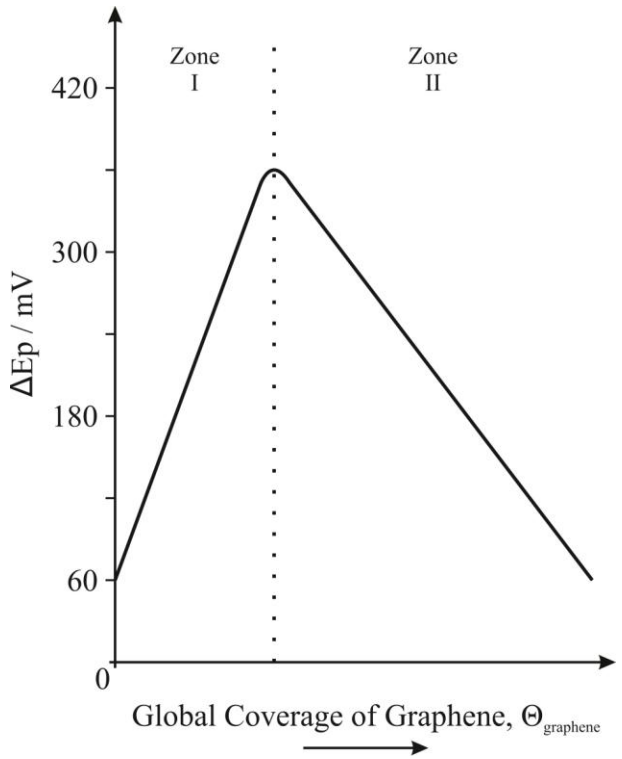

Figure 7.8 *The effect of the global coverage of graphene, $\Theta_{graphene}$, on the heterogeneous electron transfer rate/kinetics, indicating two distinctive regions that are commonly encountered (versus peak-to-peak separation, ΔE_P, in this case to simulate a standard redox probe where large ΔE_P values are indicative of slow electron transfer): note that in this case the underlying electrode substrate is assumed to possess fast electron transfer rate kinetics and the redox probe is a simple outer-sphere species.*

A schematic representation of the transition between these two extremes, where the basal dominant single layered graphene materialises into the edge dominated graphite response, is depicted in Figure 7.8. Note that the exact shape of Figure 7.8 depends on the electrochemical process under investigation. The latter is representative of the modification of a fast electron transfer underlying electrode towards a typical outer-sphere redox probe. In addition to this, Figure 7.9 depicts the observable change in the composition of the electrode surface and the resultant electrochemical responses expected. Where Figure 7.9A is that of a HOPG electrode that is assumed to possess fast electron transfer kinetics and Figure 7.9B represents the situation after incomplete coverage of single-layered graphene. Figure 7.9C represents complete single-layer coverage of graphene (represented *via* the dotted line in Figure 7.8 at the interface between the two working zones). Figure 7.9D illustrates the effect of increased graphene content which leads to the coalescence of graphene sheets into double-, few- and multi- layered graphene (*viz* graphite). Note that until layering begins, there is a continual decrease in the electrochemical response due to graphene platelets blocking electron transfer at the underlying electrode surface (*Zone I* in Figure 7.8). Conversely, when multiple layers materialise, an improvement in the electrochemical response is observed which is due to increased electron transfer at the electrochemically active edge plane sites (*Zone II* in Figure 7.8). Furthermore, note that a '*Zone III*' is likely to exist if the graphene exhibits 'thin-layer' behaviour in which the peak-to-peak separation will become less than 60 mV. However recent studies have shown that for the type of commercially available graphene utilised and the analytes studies within, graphene does not suffer from this thin-layer behaviour, [33] however, there may be exceptions.

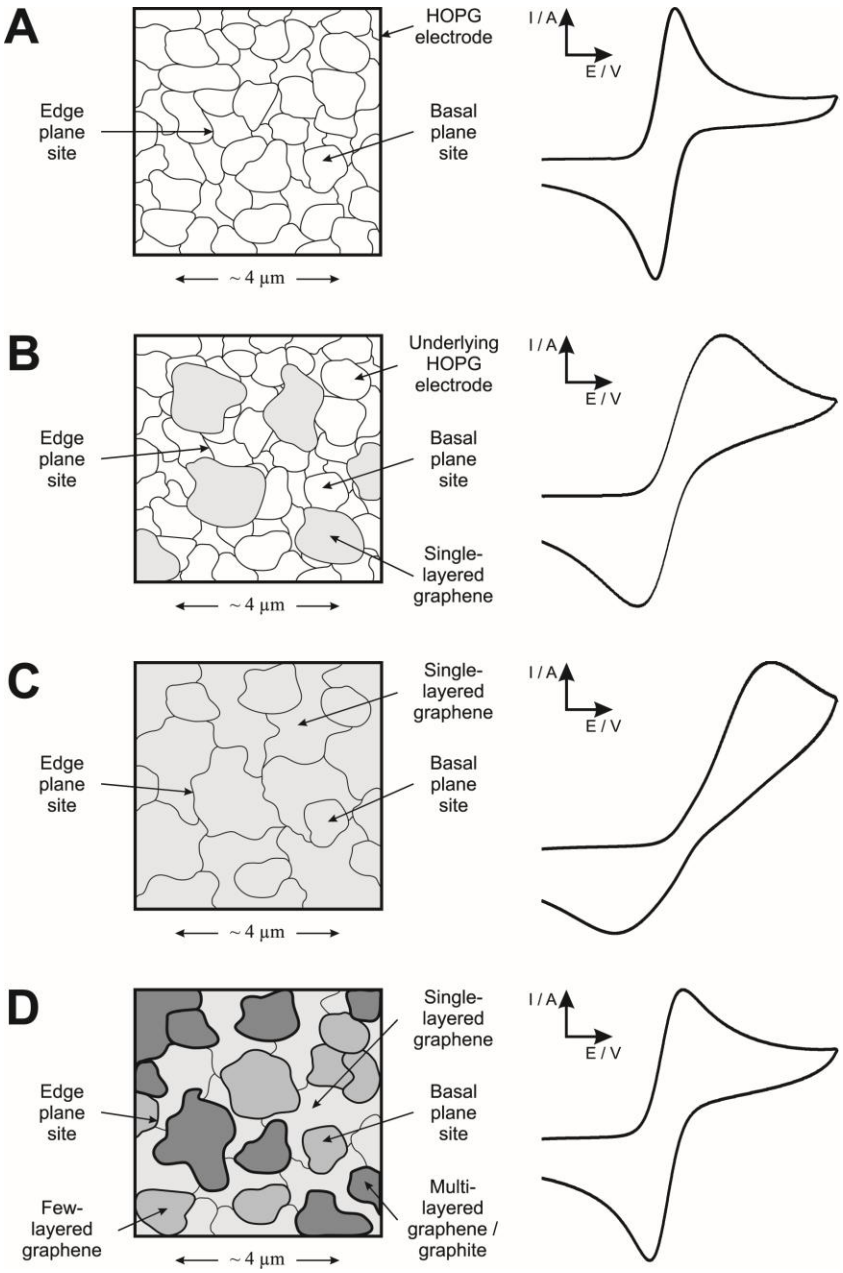

Figure 7.9 *Schematic representation of the effect on the voltammetric performance resulting from differing coverages of graphene using a simple outer-sphere electron transfer redox probe.* ***(A)*** *represents an unmodified HOPG electrode surface where fast electron transfer kinetics are observable,* ***(B)*** *after modification with graphene leading to incomplete coverage where reduced electron transfer rates occur,* ***(C)*** *after modification with graphene leading to complete single layer coverage where due to the large basal content of graphene (in contrast to edge plane) poor electrochemical activity is observed where electron transfer is effectively blocked, and* ***(D)*** *after continual modification with graphene leading to layered structures with increased edge plane sites available (origin of fast electron transfer) and thus an improvement in the electrochemical response is observed.*

In the above case an underlying electrode with fast electron transfer is modified with graphene (*viz* EPPG electrode). To explore this further the effect of modification of a BPPG electrode with nanogram quantities of P-graphene on the response towards an inner-sphere redox probe (1 mM potassium ferrocyanide (II)) is considered. Figure 7.10 explores the addition of 5 and 40 ng of P-graphene on the BPPG electrode surface. This modification results in increased peak-to-peak separations at the redox probe, indicating slower heterogeneous electron transfer at P-graphene with respect to the unmodified BPPG electrode, indicating a partially blocked electrode (*Zone I – vide supra*). Interestingly however, with further additions of P-graphene (0.5, 3.0 and 5.0 μg) the voltammetric response continues to exhibit increasing peak-to-peak separations, before eventually complete blockage of the surface occurs. This response is distinct to that observed in Figure 7.7A. It is thus abundantly clear that graphene modification on an EPPG and BPPG results in highly contrasting electrochemical behaviour.

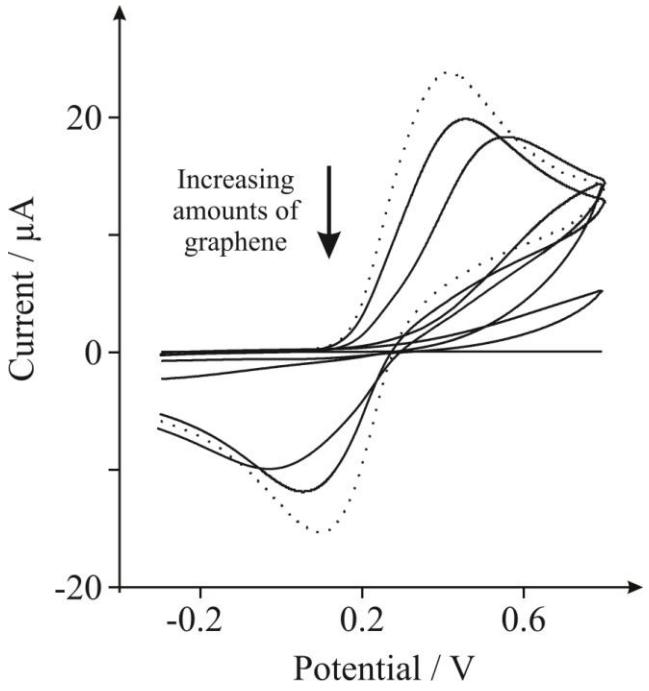

Figure 7.10 *Cyclic voltammetric profiles recorded utilising 1 mM potassium ferrocyanide (II) in 1 M KCl, obtained using a BPPG electrode (dotted line) with the addition of 5 and 40 ng, and 0.5, 3.0 and 5.0 μg of P-graphene (solid lines). Scan rate: 100 mVs^{-1} (vs. SCE).*

The next step is to explore the effect of orientation of the immobilised graphene on both EPPG and BPPG surfaces *via* SEM. Figure 7.11A/B/C depicts SEM images of the EPPG surface before and after modification with P-graphene, which exhibits coalesced graphene folding over edge plane sites; this potentially explains the blocking effect observed in Figures 7.2A, 7.3, 7.4A and 7.5 as discussed above. When further graphene is immobilised onto the electrode surface this then realigns in orientation with the edge plane sites of the underlying electrode, resulting in vertically aligned graphene and hence a beneficial increase in the electrochemical response is observed due to the increment in the proportion of edge plane sites accessible for electron transfer; this response is reported schematically in Figure 7.12. In this model it is assumed that the graphene will adopt a similar architecture to that of the underlying electrode. As graphene has a distributed electron density of the planar 'basal site' ($\pi - \pi$) which will be disturbed by the high electron density of the underlying edge sites of graphene (in the case of EPPG), this results in alignment with the underlying electrode surface as this arrangement reflects the lowest energy settlement. Though due to the high number of graphene sheets on the surface of the EPPG, the graphene sheets will be forced to stack (as a continuation of the edge planes) in parallel to each other in order to fit the limited space available on the EPPG.

Figure 7.11D/E/F depicts SEM images of a basal plane surface before and after modification with P-graphene, which are distinct to those observed above, indicating a different orientation of graphene on the electrode surface. In this case, the immobilised graphene follows the same architecture presented on the BPPG sheets, meaning that the graphene will stack basal face down on the BPPG due to $\pi - \pi$ stacking. This explains the experimental result observed in Figure 7.10 (and is shown schematically in Figure 7.12B). Note however, further deposition of graphene may lead to an improvement in the electrochemical response. Extremely high levels of

graphene coverage are likely to give a highly porous and rough surface with poor reproducibility, which is effectively approaches that of a graphite modified electrode. In such a case the electrochemical response is expected to reach that of *Zone II*.

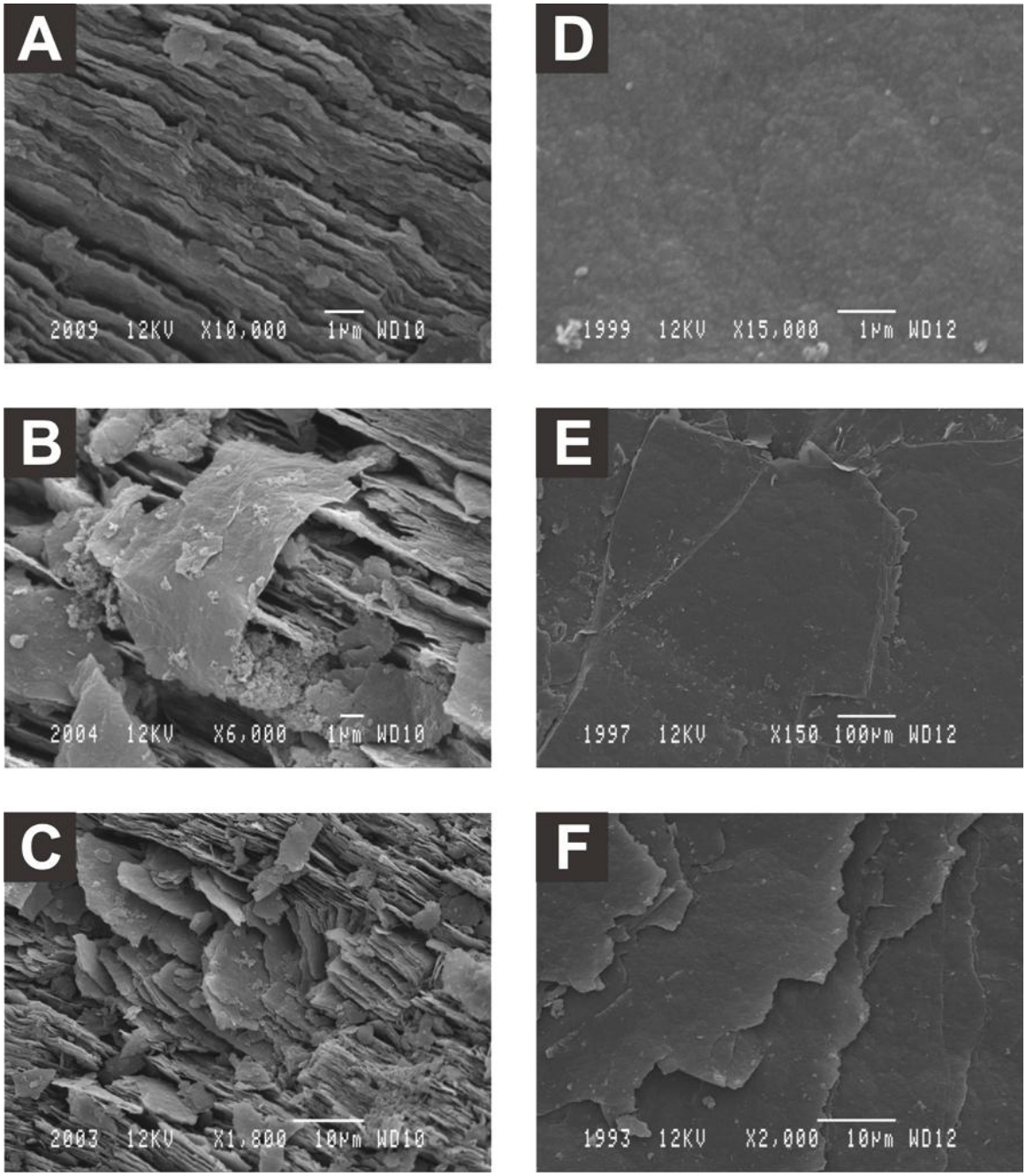

Figure 7.11 *SEM images of: an unpolished EPPG electrode before (**A**) and after modification with low (**B**) and high (**C**) coverages of P-graphene; an unpolished BPPG electrode before (**D**) and after modification with low (**E**) and high (**F**) coverages of P-graphene.*

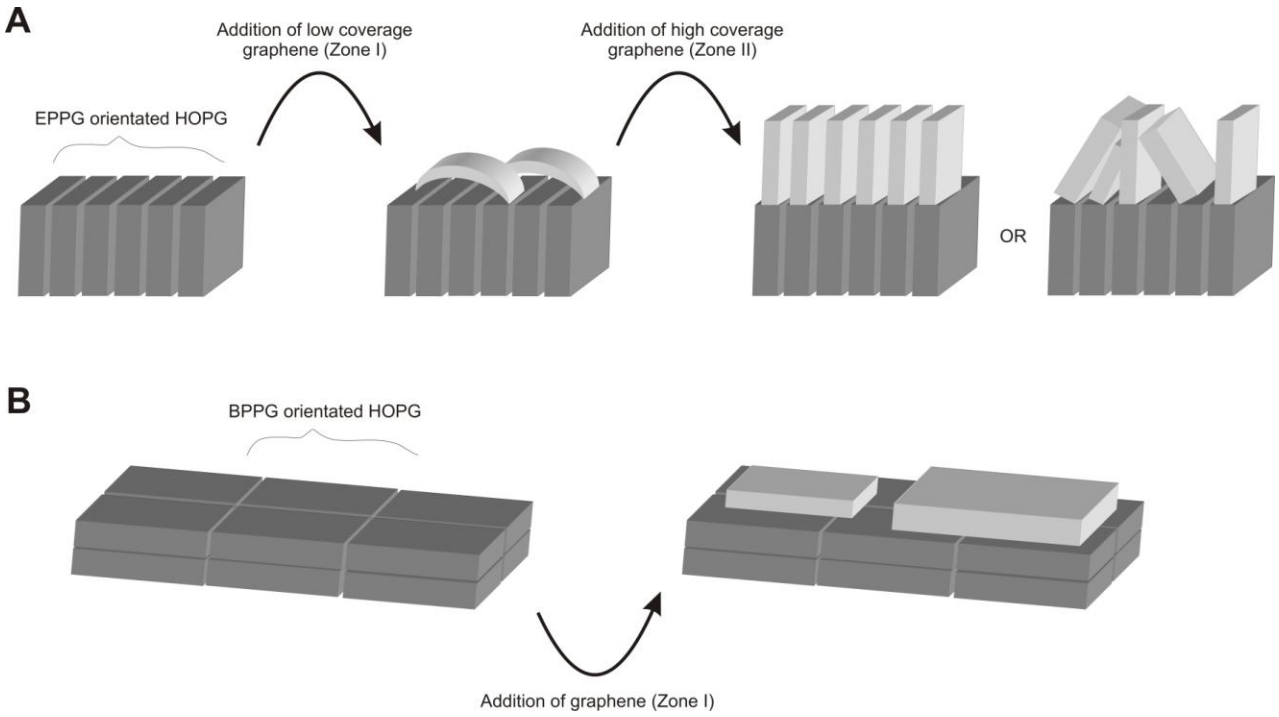

Figure 7.12 *Schematic representation of the differentiating orientations of graphene sheets encountered depending on the architecture of the underlying substrate. Note that variations occur between low and high coverages in the case of modifying an EPPG electrode (**A**), whereas the modification of a BPPG electrode (**B**) results in a singular orientation.*

Last, the electron distribution in graphene was probed utilising computational spin-polarised DFT calculations. Five models were used to represent increasingly large symmetric flakes of graphene which have *m* rings in the top row and *n* rows of rings along each diagonal edge to give an $m \times n$ sheet: 2×2 sheet (coronene), 3×3 sheet, 4×4 sheet, 5×5 sheet and 6×6 sheet. The surface-area ratio of the basal plane to the edge plane increases from 1.34 (for coronene) to 3.96 for the 6×6 sheet of graphene. Although these surface-area ratios are significantly lower than those found in the experimental samples, this series of models still provides valuable insights. Figure 7.13 depicts the electron density in both the HOMOs and LUMOs, which is found to be concentrated around the edge of the graphene sheets, even in flakes as small as the 3×3 sheet (see Figure 7.13B). The side view shows that any electron

density concentrated in the basal region is less than that concentrated at the edges. The probability that the electrons will be concentrated around the edge of the graphene flake increases as the size of the sheet increases. Thus, in graphene, the electrons that have the highest energies and are therefore the most likely to transfer, have a higher probability of being concentrated in the edge plane than in the central basal plane region. This is consistent with the experimental results within this chapter and with fundamental theory associated with the electron transfer sites of graphitic materials.

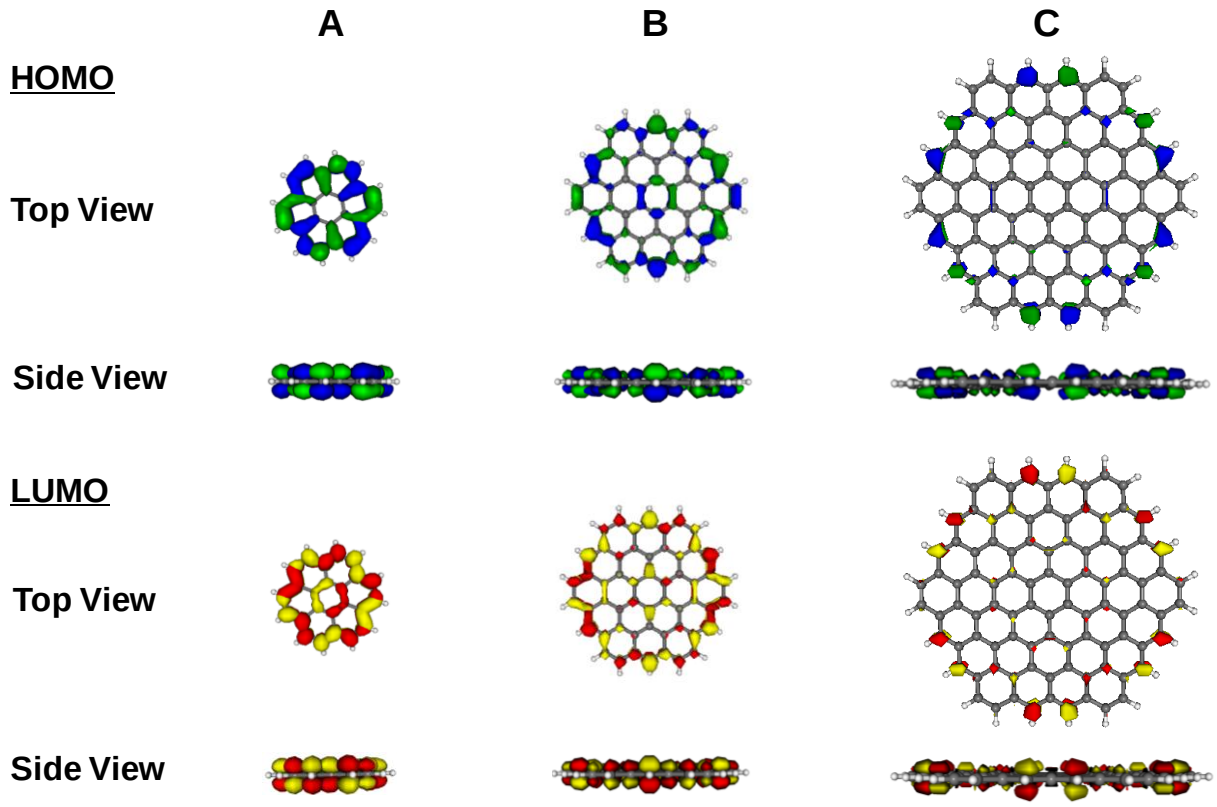

Figure 7.13 *Electron density distribution of electrons in the HOMO (shown in blue and green) and the LUMO (shown in red and yellow) of a (**A**) 2 × 2 sheet (coronene), (**B**) 3 × 3 sheet and (**C**) 4 × 4 sheet of graphene. Due to the symmetry of the sheets, the HOMO and HOMO–1 are degenerate in energy and both are displayed simultaneously. Similarly, the LUMO and LUMO+1 are degenerate in energy and both are displayed simultaneously in these figures. In each case, the 0.035 a.u. surface is shown. All molecular orbital diagrams were visualised using MOLEKEL 4.2.* [34, 35]

7.1.3. CONCLUSIONS

This chapter has shown, for the first time, the effect of coverage when utilising graphene (P-graphene) as an electrode material. The physicoelectrochemical electron transfer nature/properties of P-graphene modified electrodes were compared to that of graphite alternatives utilising a range of electrochemically well characterised analytes. It was shown that the use of graphene in electrochemical sensing applications is questionable, where interestingly in the cases studied herein the graphene utilised was found to block the underlying electrochemical reactivity of the supporting electrode. Due to the poor electrochemical responses observed at graphene (towards various analytes) in contrast to those observed at graphite alternatives, it is proposed that graphene possesses slow heterogeneous electron transfer kinetics owing to its large basal and low edge plane content (see Figure 7.1A). Insights from DFT calculations confirmed that the electron density is concentrated around the edge of the graphene, indicating that the edge to basal ratio is critical for graphene (and graphitic materials alike).

It is demonstrated that there are two essential coverage regions for graphene (for the case where the underlying electrode exhibits fast electron transfer, such as in the case of an EPPG electrode). Where in '*Zone I*' a low global coverage of graphene, $\Theta_{graphene}$, immobilised onto an electrode substrate exhibits slow heterogeneous electron transfer owing to a large basal plane content. Conversely in '*Zone II*', equating to a high coverage of graphene, fast heterogeneous electron transfer is observed as layering leads to increased edge plane content. Interestingly, these Zones are not observed when the underlying electrode is switched from an EPPG to a BPPG electrode and complementary SEM analysis provided insights into this differing behaviour indicating that the *orientation* of the graphene and the underlying supporting electrode is of key importance.

This work is the first to show, *via* the quantification of heterogeneous electron transfer, that the use of graphene is not so beneficial, as commonly (mis)reported in the literature, as an "electro-catalytic" electrode material. Graphene possesses a low proportion of electron transfer sites (edge plane content) resulting in slow electrode kinetics and consequently (for these select analytes) it is clear that graphite is ultimately far superior in terms of electrochemical activity and electron transfer kinetics. It must be considered, that in the fabrication of sensing devices, utilisation of graphite needs to be considered over that of graphene, or at least control experiments need to be diligently performed and reported. Note however, that this work is based purely from the perspective of electrode kinetics. One must bear in mind that fast heterogeneous electron transfer is not the only criteria for a good electrode material and inversely in some cases slow electron transfer may be considered an advantage, thus in such select sensing applications where this is the case, graphene still has huge potential to revolutionise said fields. [3]

7.1.4. REFERENCES

1. D. A. C. Brownson and C. E. Banks, *Analyst*, 2010, **135**, 2768.
2. M. Pumera, *Chem. Rec.*, 2009, **9**, 211.
3. D. A. C. Brownson, D. K. Kampouris and C. E. Banks, *J. Power Sources*, 2011, **196**, 4873.
4. M. S. Goh and M. Pumera, *Anal. Chem.*, 2010, **82**, 8367.
5. D. A. C. Brownson and C. E. Banks, *Electrochem. Commun.*, 2011, **13**, 111.
6. D. A. C. Brownson, J. P. Metters, D. K. Kampouris and C. E. Banks, *Electroanalysis*, 2011, **23**, 894.
7. D. A. C. Brownson and C. E. Banks, *Analyst*, 2011, **136**, 2084.
8. A. Dato, V. Radmilovic, Z. Lee, J. Phillips and M. Frenklach, *Nano Lett.*, 2008, **8**, 2012.
9. A. Dato, Z. Lee, K.-J. Jeon, R. Erni, V. Radmilovic, T. J. Richardson and M. Frenklach, *Chem. Commun.*, 2009, 6095.
10. Z. Lee, K.-J. Jeon, A. Dato, R. Erni, T. J. Richardson, M. Frenklach and V. Radmilovic, *Nano Lett.*, 2009, **9**, 3365.
11. X. Ji, C. E. Banks, A. Crossley and R. G. Compton, *ChemPhysChem*, 2006, **7**, 1337.

12. D. K. Kampouris and C. E. Banks, *Chem. Commun.*, 2010, **46**, 8986.

13. C. E. Banks, R. R. Moore, T. J. Davies and R. G. Compton, *Chem. Commun.*, 2004, **16**, 1804.

14. A. S. Adekunle and K. I. Ozoemena, *Electrochim. Acta*, 2008, **53**, 5774.

15. T. J. Davies, M. E. Hyde and R. G. Compton, *Angew. Chem. Int. Ed.*, 2005, **44**, 5121.

16. X. Kang, J. Wang, H. Wu, J. Liu, I. A. Aksay and Y. Lin, *Talanta*, 2010, **81**, 754.

17. W.-J. Lin, C.-S. Liao, J.-H. Jhang and Y.-C. Tsai, *Electrochem. Commun.*, 2009, **11**, 2153.

18. C. E. Banks and R. G. Compton, *Analyst*, 2005, **130**, 1232.

19. C. E. Banks, T. J. Davies, G. G. Wildgoose and R. G. Compton, *Chem. Commun.*, 2005, **7**, 829.

20. C. E. Banks and R. G. Compton, *Analyst*, 2006, **131**, 15.

21. T. J. Davies, R. R. Moore, C. E. Banks and R. G. Compton, *J. Electroanal. Chem.*, 2004, **574**, 123.

22. M. C. Henstridge, L. Shao, G. G. Wildgoose, R. G. Compton, G. Tobias and M. L. H. Green, *Electroanalysis*, 2008, **20**, 498.

23. F. Wantz, C. E. Banks and R. G. Compton, *Electroanalysis*, 2005, **17**, 1529.

24. C. Amatore, J. M. Saveant and D. Tessier, *J. Electroanal. Chem.*, 1983, **147**, 39.

25. T. J. Davies, E. R. Lowe, S. J. Wilkins and R. G. Compton, *ChemPhysChem*, 2005, **6**, 1340.

26. R. S. Nicholson, *Anal. Chem.*, 1965, **37**, 1351.

27. C. E. Banks, R. G. Compton, A. C. Fisher and I. E. Henley, *PCCP*, 2004, **6**, 3147.

28. Y. Wang, J. G. Limon-Petersen and R. G. Compton, *J. Electroanal. Chem.*, 2011, **652**, 13.

29. R. L. McCreery, *Chem. Rev.*, 2008, **108**, 2646.

30. T. J. Davies and R. G. Compton, *J. Electroanal. Chem.*, 2005, **585**, 63.

31. T. J. Davies, S. Ward-Jones, C. E. Banks, J. Del Campo, R. Mas, F. X. Muñoz and R. G. Compton, *J. Electroanal. Chem.*, 2005, **585**, 51.

32. T. J. Davies, C. E. Banks and R. G. Compton, *J. Solid State Electrochem.*, 2005, **9**, 797.

33. P. M. Hallam and C. E. Banks, *Electrochem. Commun.*, 2011, **13**, 8.

34. P. Flukiger, H. P. Luthi, S. Portmann and J. Weber, *Swiss Center for Scientific Computing*, (2000-2009), Manno (Switzerland).

35. S. Portmann and H. P. Lüthi, *CHIMIA*, 2000, **54**, 766.

7.2. THE ELECTROCHEMICAL PERFORMANCE OF (SURFACTANT FREE) GRAPHENE MODIFIED ELECTRODES: AN ANALYTICAL PERSPECTIVE

Continuing with the observations and conclusions from the previous section, where graphene modified electrodes were shown to exhibit unfavourable heterogeneous electron transfer kinetics relative to graphite modified (and unmodified) alternative electrodes. This chapter, which contains published work, [4] considers the implications of this knowledge when using graphene modified electrodes in electroanalysis.

Graphene modified electrodes are explored towards the electroanalytical sensing of dopamine hydrochloride (DA), uric acid (UA), acetaminophen (AP) and *p*-benzoquinone (BQ) *via* cyclic voltammetry, the monitoring of which has considerable importance in a plethora of areas where electrochemistry is conveniently and beneficially utilised. In line with literature methodologies and to investigate the full implications of employing graphene in this electrochemical context, modification is performed on electrode substrates that exhibit either fast or slow electron transfer kinetics (EPPG or BPPG electrodes respectively), which allows the true electroanalytical applicability of graphene to de-convoluted and determined.

7.2.1. INTRODUCTION

The employment of graphene has been reported, most notably, as an enhanced sensor substrate in terms of the improved electroanalytical monitoring of various substances. The fabrication of graphene based sensors is of substantial interest and importance depending upon the variable toxicity and nature of the analyte studied (see Chapter 4.1). [1-3] Considering such reports, future electrochemical prospects for graphene appear promising. However, as

[4] D. A. C. Brownson, C. W. Foster and C. E. Banks, *Analyst*, 2012, **137**, 1815.

highlighted in Chapter 4.1, such claims of the electro-catalysis of graphene electrodes are made only when the performance is compared to that of the underlying supporting electrode (usually a GC electrode, that is not directly comparable to the graphene structure, unlike, for example HOPG electrodes). As highlighted in Chapters 6 and 7.1, a tentative approach must be employed when utilising graphene and when such an approach is employed, it appears that graphene may not be such a beneficial electrode material as widely reported in the literature. [4-6]

In this chapter the analytical perspectives of P-graphene modified electrodes are determined through critical comparisons in the electroanalytical performance of said P-graphene modified EPPG and BPPG electrodes (constructed from HOPG) with that of unmodified EPPG and BPPG electrodes towards various analytes. It is the aim of this chapter, through the utilisation of both 'fast' and 'slow' supporting electrodes (in terms of the heterogeneous electron transfer kinetics), to sufficiently de-convolute and observe the true analytical performance of graphene.

7.2.2. RESULTS AND DISCUSSION

7.2.2.1. RESULTS

Prior to the electrochemical investigation of target analytes, a 'blank run' (see Appendix A.3) was explored in order to ensure that the buffer solution and electrode materials of use were free from contaminants and that the electrode materials did not give rise to electrochemical signatures that could be mistaken for the electrochemical response of the analyte in question. Figure 7.14 depicts typical cyclic voltammetric responses obtained in a pH 7 PBS at unmodified EPPG and BPPG electrodes in addition to EPPG and BPPG electrodes following modification with P-graphene. It is clear that within both the anodic and cathodic

potential regions of interest, there are no evident voltammetric peaks prior to the addition of the analytes studied herein.

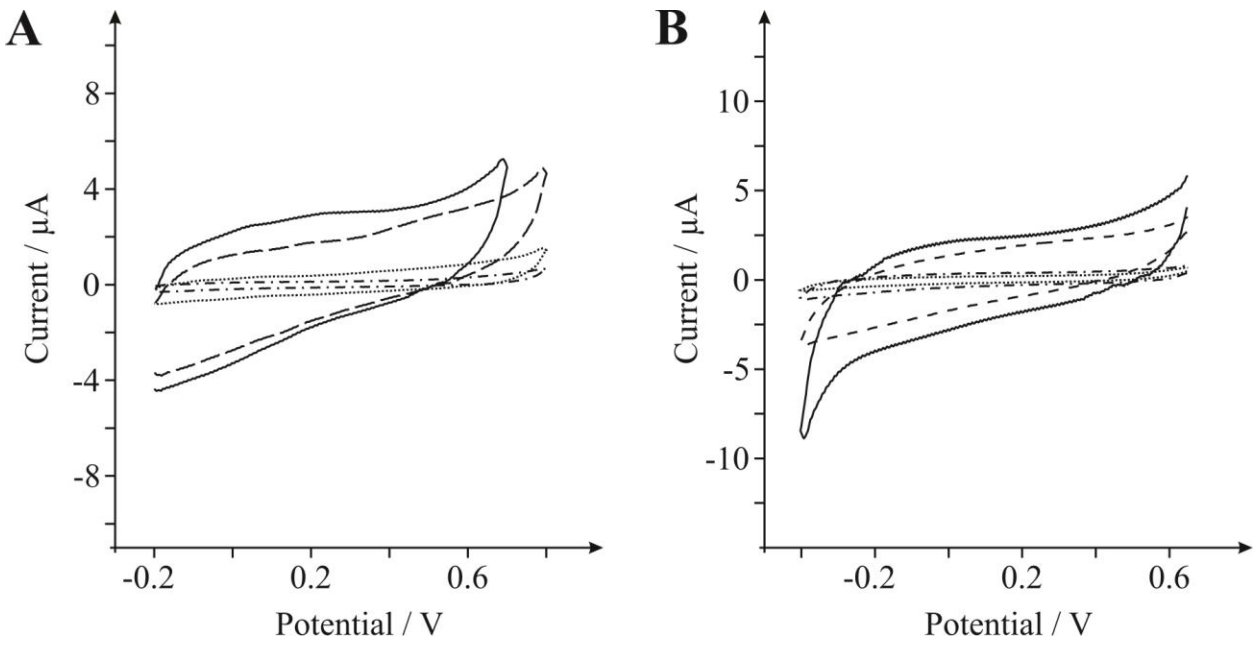

Figure 7.14 *Cyclic voltammetric profiles recorded in a PBS (pH 7) using unmodified EPPG (solid line) and BPPG (dot-dashed line) electrodes, and P-graphene modified EPPG (dashed line) and BPPG (dotted line) electrodes. Within the anodic (**A**) (20 ng P-graphene) and cathodic (**B**) (40 ng P-graphene) potential regions. Scan rate: 100 mVs^{-1} (vs. SCE).*

First, the electrochemical properties of the EPPG and BPPG electrodes are characterised towards 50 µM DA in pH 7 PBS. Note that DA is of great significance given that it is an important neurotransmitter that plays a pivotal role in the function of the hormonal, renal and central nervous systems. [7] Figure 7.15 depicts typical cyclic voltammetric responses obtained using EPPG and BPPG electrodes, which exhibit voltammetric peaks ($E_P{}^{ox}$) at *ca.* 0.19 and 0.32 V respectively and are in agreement with previous literature reports. [8] Next the effect of immobilising P-graphene upon the electrode materials of interest was explored. As depicted in Figure 7.15, modification of the HOPG electrodes with 20 ng of P-graphene results in the voltammetric peaks ($E_P{}^{ox}$) shifting to more positive potentials (compared to the underlying

supporting electrodes) at *ca.* 0.29 and 0.41 V respectively, which is in agreement with previous work utilising graphene (see Chapter 7.1). [7, 9, 10]

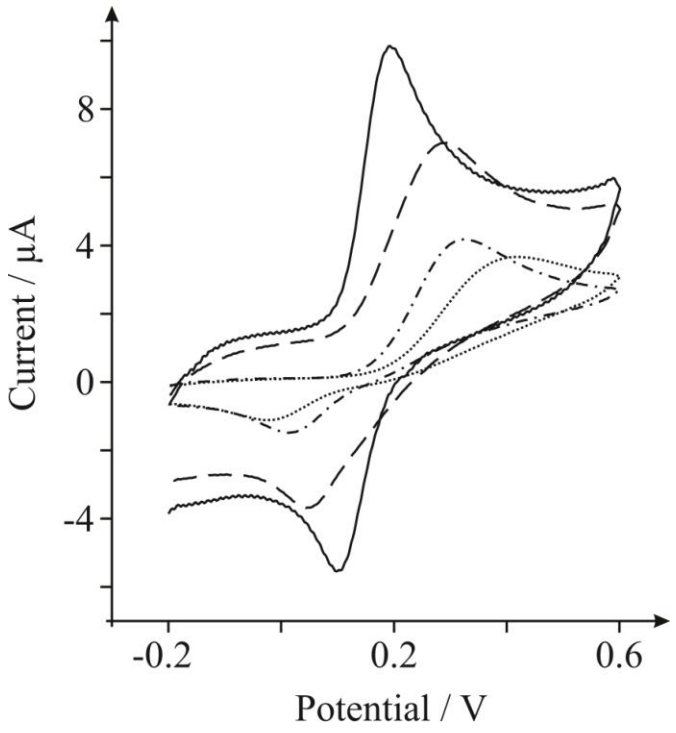

Figure 7.15 *Cyclic voltammetric profiles recorded for 50 µM DA in pH 7 PBS using unmodified EPPG (solid line) and BPPG (dot-dashed line) electrodes, and 20 ng P-graphene modified EPPG (dashed line) and BPPG (dotted line) electrodes. Scan rate: 100 mVs^{-1} (vs. SCE).*

Attention was next turned to exploring the electroanalytical response arising from successive additions of DA into a pH 7 PBS. Cyclic voltammograms for the case of a 20 ng P-graphene modified EPPG electrode are shown in Figure 7.16A, whereas Figure 7.16B depicts the response observed using a 20 ng P-graphene modified BPPG electrode. It is clear that successive additions of DA resulted in an increment in the observed voltammetric peak height. Figure 7.16C depicts the response of the peak height ($I_P{}^{ox}$) as a function of DA concentration at each of the electrode materials of interest. It is readily evident that linear responses are observed over the concentration range studied (5 to 50 µM), however most striking, is that when compared

to the bare (unmodified) EPPG and BPPG electrodes, the respective P-graphene modified electrodes exhibit reduced and inferior analytical sensitivities (Figure 7.16C). This observation is contradictory of that currently reported in the literature concerning DA (see Chapter 4.1). [7, 10, 11] Table 7.1 details the observed analytical sensitivities and limits of detection (LODs, based on three-sigma) for the electrode materials studied. See Appendix A.3 for an overview of useful concepts in Analytical Chemistry. Note, the concentration range utilised is of analytical relevance and the values obtained using EPPG and BPPG electrodes are in favourable agreement with previous studies at other carbon materials towards the electrochemical sensing of DA. [7, 10]

The electrochemical performance of P-graphene towards UAis next explored, which is a neurochemical commonly encountered in biological samples and it is the primary end product of purine metabolism. [12] Unusual levels of UA can be indicative of several illnesses such as hyperuricaemia, gout and Lesch-Nyhan disease, [13] thus making its detection and quantification an important issue in clinical medicine. [12] First, as above, the electrochemical properties of the electrode materials of interest are characterised with regards to the analyte (160 μM UA in pH 7 PBS) where *via* cyclic voltammetric analysis oxidation peaks are observed at *ca.* 0.32, 0.86, 0.53 and 1.10 V when utilising unmodified EPPG and BPPG electrodes and EPPG and BPPG electrodes following modification with 20 ng of P-graphene respectively (see Figure 7.17). The responses obtained at EPPG and BPPG electrodes are in excellent agreement with previous literature reports, [14, 15] furthermore those observed at the graphene modified electrodes are in accordance with the work presented in Chapter 7.1. [16, 17]

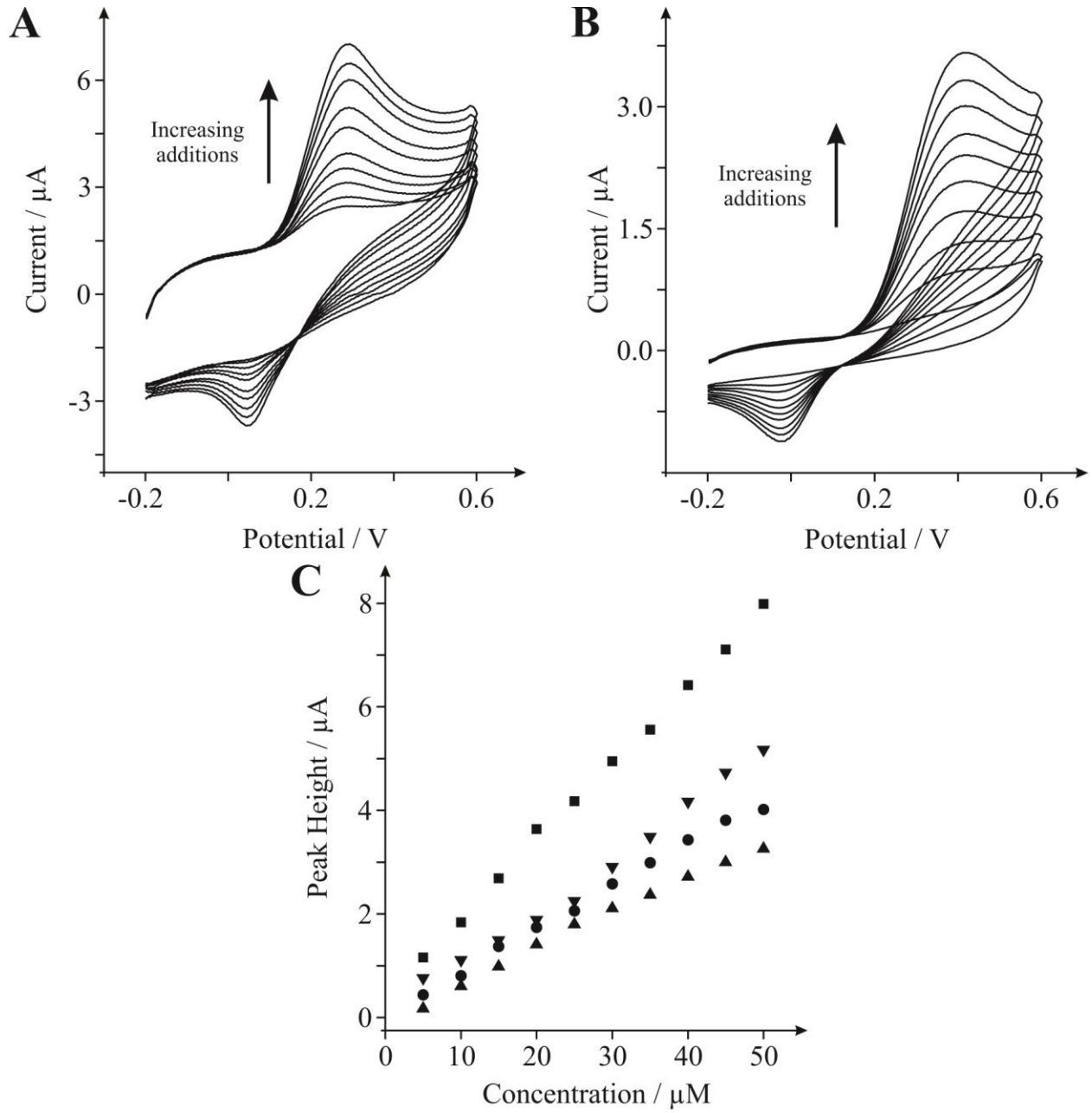

Figure 7.16 *Cyclic voltammetric profiles recorded towards successive additions of 5 µM DA into a pH 7 PBS (range: 5 to 50 µM) utilising EPPG (**A**) and BPPG (**B**) electrodes following modification with 20 ng P-graphene.* ***C:*** *Calibration plots towards the detection of DA depicting the peak height as a function of concentration, obtained via cyclic voltammetric measurements performed using unmodified EPPG (squares) and BPPG (circles) electrodes in addition to EPPG (inverted triangles) and BPPG (triangles) electrodes following modification with 20 ng P-graphene.*

Data obtained at a scan rate of 100 mVs^{-1} (vs. SCE).

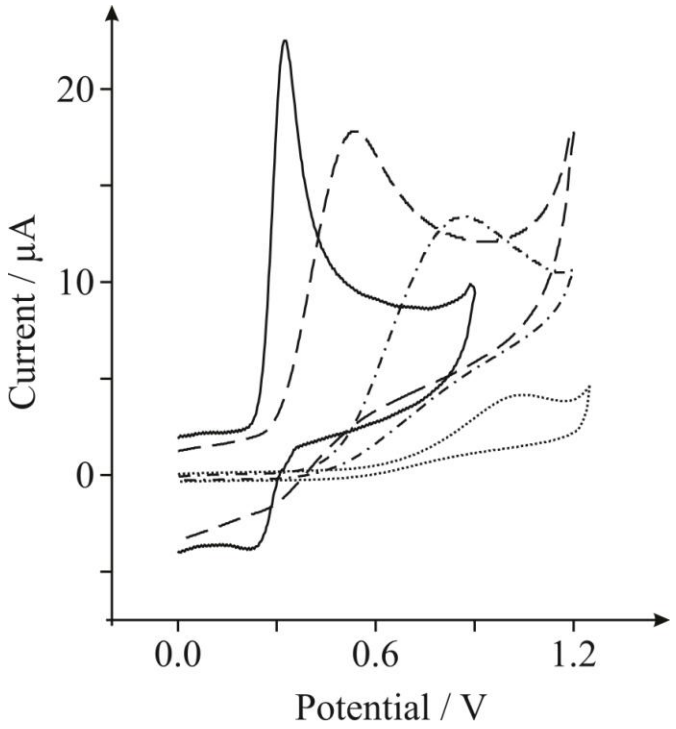

Figure 7.17 *Cyclic voltammetric profiles recorded for 160 µM UA in pH 7 PBS using unmodified EPPG (solid line) and BPPG (dot-dashed line) electrodes, and 20 ng P-graphene modified EPPG (dashed line) and BPPG (dotted line) electrodes. Scan rate: 100 mVs^{-1} (vs. SCE).*

Attention was next turned to exploring the electroanalytical response of the electrode materials of interest towards the sensing of UA arising from successive additions of the analyte into a pH 7 PBS. As expected additions of UA lead to an increment in the observed voltammetric peak height of the respective oxidation wave. The cyclic voltammetric responses obtained at P-graphene modified (20 ng) EPPG and BPPG electrodes are depicted in Figures 7.18A and 7.18B respectively. Figure 7.18C depicts the resultant calibration plots for each of the electrode materials, detailing the voltammetric peak height ($I_P{}^{ox}$) as a function of UA concentration. It is clear that linear responses are observed over the concentration range studied (20 to 160 µM) and surprisingly (as is also the case for DA) relative to the unmodified EPPG and BPPG electrodes it is apparent that the corresponding P-graphene modified electrodes exhibit poor analytical

performances (Figure 7.18C), which is again contradictory of that currently reported in the electrochemical literature concerning the sensing of UA at graphene. [16-18] Note that the concentration range utilised is also of analytical relevance and that the values obtained at the EPPG and BPPG electrodes are in favourable agreement with previous studies on carbonaceous materials towards the electrochemical sensing of UA. [14, 19] Table 7.1 depicts the resultant analytical sensitivities and LODs (three-sigma).

Next the electrochemical characteristics and performance of the electrode materials of interest are explored towards AP, an analgesic and antipyretic drug which requires routine monitoring in many bio-fluids and also in quality assurance. [20] Figure 7.19 depicts typical cyclic voltammetric responses obtained using the EPPG and BPPG electrodes which exhibit voltammetric peaks ($E_P{}^{ox}$) at *ca.* 0.42 and 0.58 V respectively and are in agreement with a previous literature report. [21, 22] Also shown in Figure 7.19 are the responses observed through the utilisation of P-graphene modified (20 ng) EPPG and BPPG electrodes, which exhibit voltammetric peaks ($E_P{}^{ox}$) at *ca.* 0.50 and 0.53 V respectively. The response of graphene is again in favourable agreement with Chapter 7.1. It is important to note for this analyte that there appears to be no significant change in the electrochemical mechanism (as was observed for the case of S-graphene *which has surfactant residues present* on the basal (side) face of the graphene, see Chapter 6.1) [4] and rather the voltammetric peaks are shifted due to a change in the global coverage of edge plane sites (see Chapters 7.1 and 7.2.2.2).

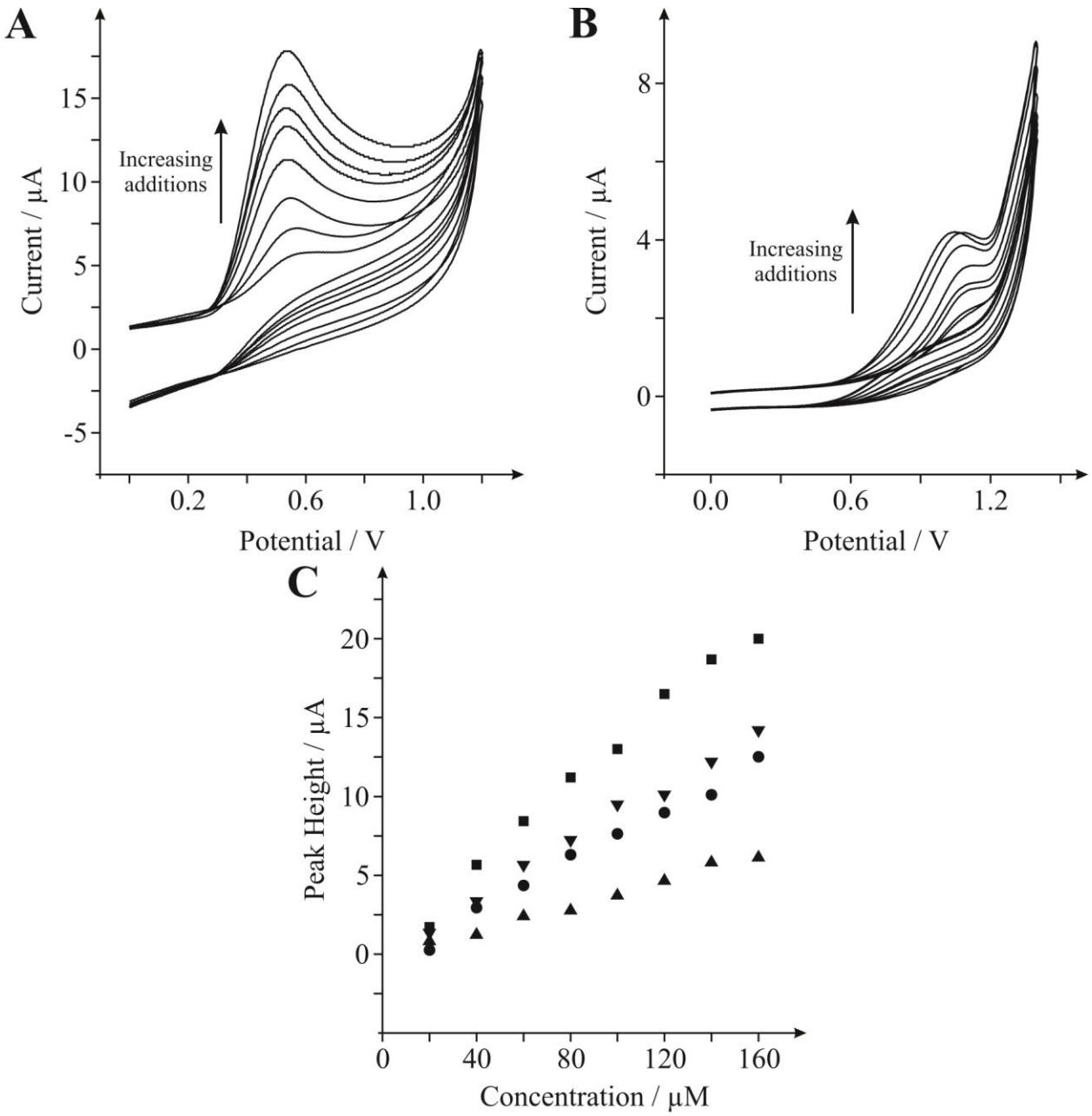

Figure 7.18 *Cyclic voltammetric profiles recorded towards successive additions of 20 µM UA into a pH 7 PBS (range: 20 to 160 µM) utilising EPPG (**A**) and BPPG (**B**) electrodes following modification with 20 ng P-graphene.* ***C:*** *Calibration plots towards the detection of UA depicting the peak height as a function of concentration, obtained via cyclic voltammetric measurements performed using unmodified EPPG (squares) and BPPG (circles) electrodes in addition to EPPG (inverted triangles) and BPPG (triangles) electrodes following modification with 20 ng P-graphene.*
Data obtained at a scan rate of 100 mVs^{-1} (vs. SCE).

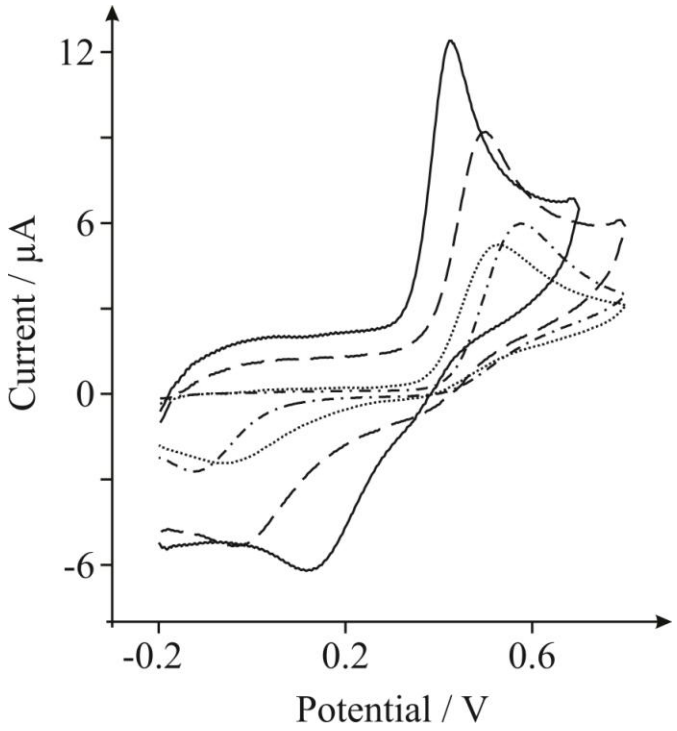

Figure 7.19 *Cyclic voltammetric profiles recorded for 50 µM AP in pH 7 PBS using unmodified EPPG (solid line) and BPPG (dot-dashed line) electrodes, and 20 ng P-graphene modified EPPG (dashed line) and BPPG (dotted line) electrodes. Scan rate: 100 mVs^{-1} (vs. SCE).*

The electroanalytical performance (with respect to AP) of the electrode materials of interest is next considered. Figures 7.20A and 7.20B depict the cyclic voltammetric responses observed as a result of consecutive additions of AP into a pH 7 PBS at 20 ng P-graphene modified EPPG and BPPG electrodes respectively. As expected increasing the concentration of AP results in a respective increment in the observed peak height ($I_P{}^{ox}$). Calibration plots depicting the correlation between the concentration of AP and the resultant peak height ($I_P{}^{ox}$) are shown in Figure 7.20C where linear responses are readily observed at each of the electrodes over the concentration range studied (5 to 50 µM). The analytical sensitivities and LODs (three-sigma) are detailed in Table 7.1, where over the concentration range utilised (which is of analytical relevance) [21-24] the P-graphene modified electrodes exhibit inferior electroanalytical performances relative to the unmodified alternatives.

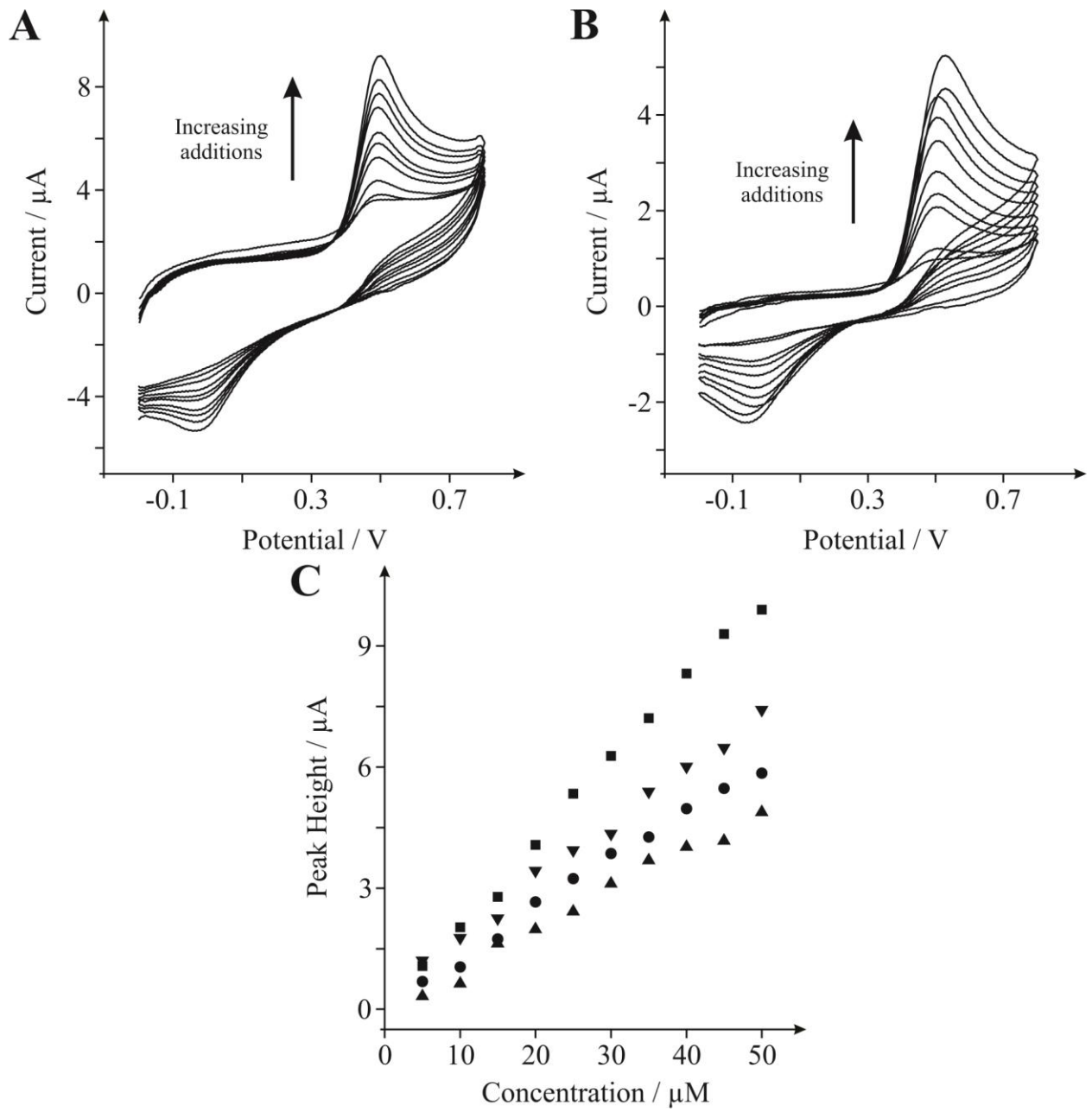

Figure 7.20 *Cyclic voltammetric profiles recorded towards successive additions of 5 µM AP into a pH 7 PBS (range: 5 to 50 µM) utilising EPPG (**A**) and BPPG (**B**) electrodes following modification with 20 ng P-graphene.* ***C:*** *Calibration plots towards the detection of AP depicting the peak height as a function of concentration, obtained via cyclic voltammetric measurements performed using unmodified EPPG (squares) and BPPG (circles) electrodes in addition to EPPG (inverted triangles) and BPPG (triangles) electrodes following modification with 20 ng P-graphene.*
Data obtained at a scan rate of 100 mVs^{-1} (vs. SCE).

To further investigate the electroanalytical outcome of utilising graphene modified electrodes, BQ is next considered. BQ is a toxic metabolite of benzene that is readily found in human blood and can thus be utilised to monitor exposure to compounds containing benzene, [25, 26] where elevated exposure has been linked to an increased risk of developing haematological cancer. [26] Additionally, note that BQ plays an important role in various biological redox processes and owing to its large electron affinity it is commonly employed as a redox mediator within electrochemistry. [27, 28] Figure 7.21 shows the typical cyclic voltammetric responses obtained towards 50 µM BQ in pH 7 PBS when utilising unmodified EPPG and BPPG electrodes and EPPG and BPPG electrodes following modification with 40 ng of P-graphene. Voltammetric peaks ($E_P{}^{red}$) are evident at *ca.* –0.01, –0.12, –0.14 and –0.23 V respectively. The redox couple observed is as reported previously in the literature at carbonaceous electrodes. [29, 30]

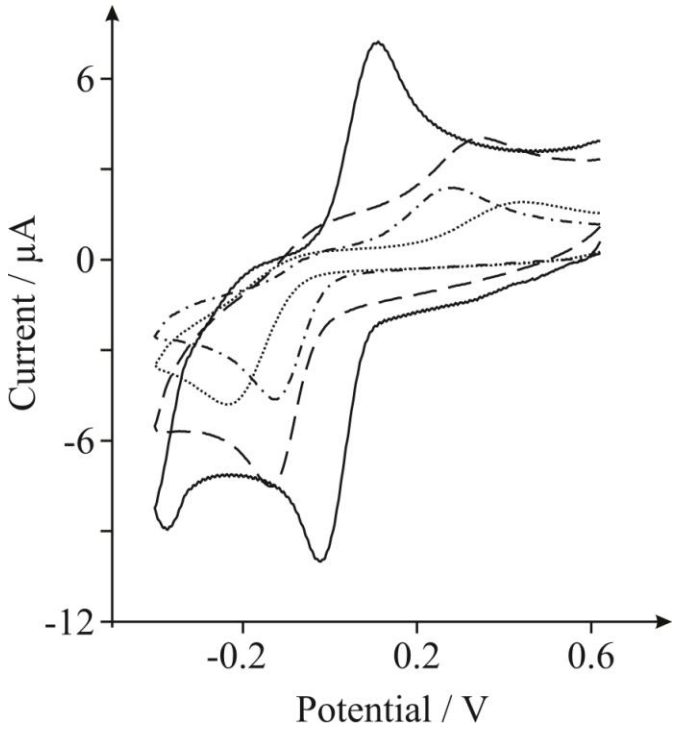

Figure 7.21 *Cyclic voltammetric profiles recorded for 50 µM BQ in pH 7 PBS using unmodified EPPG (solid line) and BPPG (dot-dashed line) electrodes, and 40 ng P-graphene modified EPPG (dashed line) and BPPG (dotted line) electrodes. Scan rate: 100 mVs^{-1} (vs. SCE).*

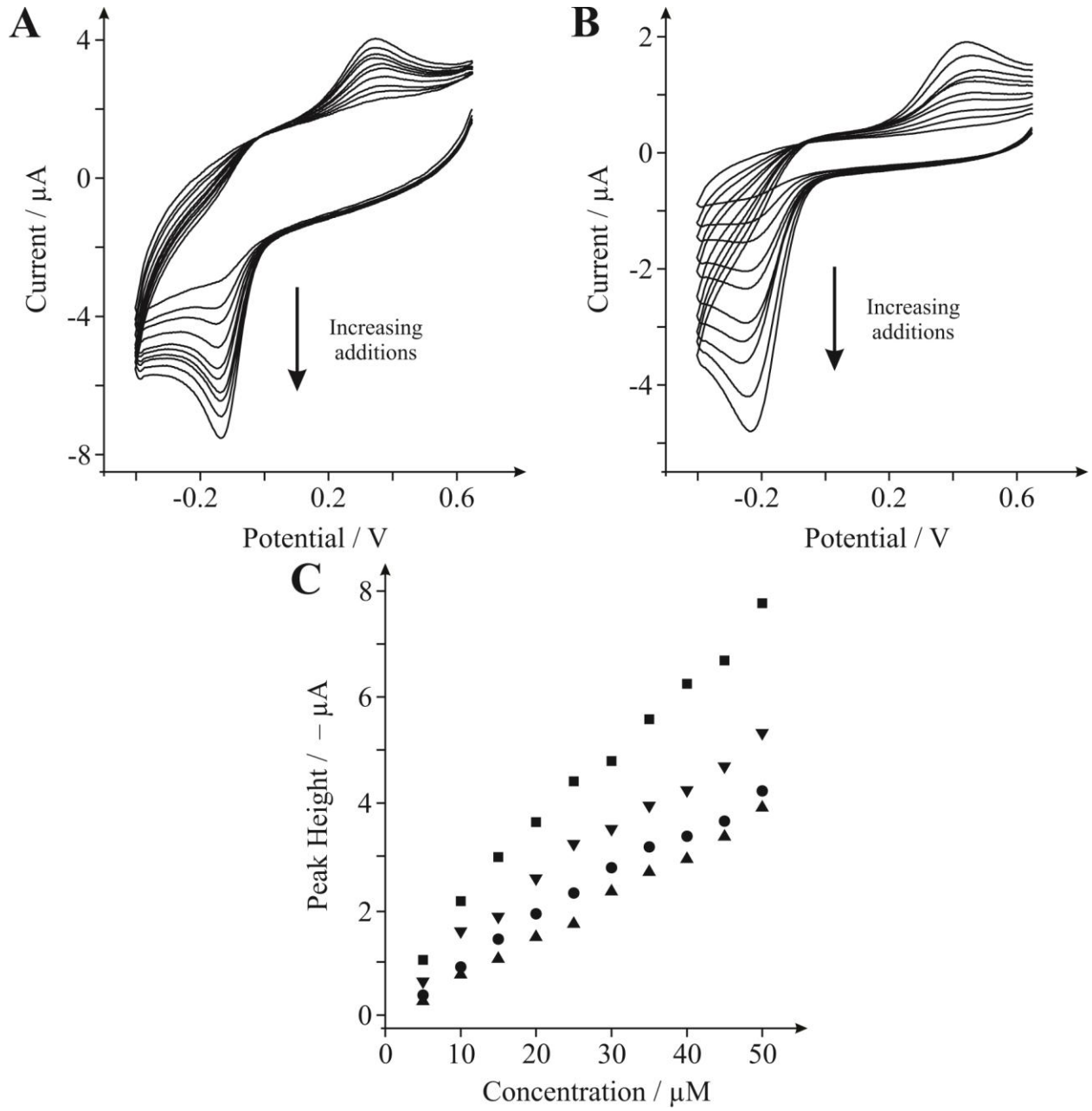

Figure 7.22 *Cyclic voltammetric profiles recorded towards successive additions of 5 µM BQ into a pH 7 PBS (range: 5 to 50 µM) utilising EPPG (**A**) and BPPG (**B**) electrodes following modification with 40 ng P-graphene.* ***C:*** *Calibration plots towards the detection of BQ depicting the peak height as a function of concentration, obtained via cyclic voltammetric measurements performed using unmodified EPPG (squares) and BPPG (circles) electrodes in addition to EPPG (inverted triangles) and BPPG (triangles) electrodes following modification with 40 ng P-graphene.*
Data obtained at a scan rate of 100 mVs^{-1} (vs. SCE).

Again, the electroanalytical response of the electrode materials of interest was next explored. The electrochemical response resulting from subsequent additions of BQ into a pH 7 PBS are presented in Figures 7.22A and 7.22B for the case of the 40 ng P-graphene modified EPPG and BPPG electrodes respectively. Figure 7.22C depicts the relevant calibration plots, detailing the voltammetric peak height (I_P ^{red}) as a function of BQ concentration. Linear responses are evident for each of the electrode materials studied over the concentration range utilised (5 to 50 μM) and once more (as is the case with each of the analytes studied above) the analytical performance of the graphene modified electrodes are poor in comparison to the equivalent unmodified electrodes (*i.e.* a reduced sensitivity is apparent at the 40 ng P-graphene electrodes. This observation is, again, largely deviated from that reported in the electrochemical literature concerning the utilisation of graphene towards the sensing of various analytes. [18, 31-34]

It has been shown that for the type of commercially available graphene utilised and the analytes studied herein, the electrochemical response at graphene is of diffusional control and thus graphene does not exhibit 'thin-layer' behaviour. [35] However, there may be exceptions to this finding. Consequently a scan rate study was performed for AP and BQ, utilising a 20 ng P-graphene modified EPPG electrode and a fixed concentration of 50 μM for the respective analytes. The voltammetric peak height (I_P) was monitored as a function of scan rate (v) with plots of peak height *versus* square-root of the scan rate revealing linear responses (I_P ^{ox} (A) = 1.25×10^{-4} A/$(Vs^{-1})^{0.5}$ + 3.92×10^{-6} A, R^2 = 0.99 and I_P ^{red} (A) = 3.79×10^{-5} A/$(Vs^{-1})^{0.5}$ + 2.84×10^{-7} A, R^2 = 0.99, for AP and BQ respectively) which indicates a diffusional process at P-graphene. Furthermore, as is expected for the case of the semi-infinite diffusion model as governed by the Randles–Ševćik equation, analysis of

log I_P *versus* log *v* revealed gradients of 0.42 and 0.48 for AP and BQ respectively, indicating the absence of thin-layer effects for the P-graphene modified electrodes. [35]

As a further control measure the respective electrochemical mechanisms present at both the unmodified and P-graphene modified graphitic electrodes were next explored to ensure that the P-graphene did not give rise to differing mechanistic pathways. The electrochemical oxidation of 50 μM DA was considered using an EPPG electrode over the pH range of 3.0 to 8.0 in order to determine the reaction mechanism present and hence the number of electrons and protons involved in the voltammetric oxidation of DA. Cyclic voltammograms at different pH values were explored over the voltammetric range with the effect of solution pH explored as a function of the voltammetric peak potential, $E_P{}^{ox}$. A plot of $E_P{}^{ox}$ *versus* pH yielded a linear response over the pH range studied with a gradient of 55 mV per pH unit observed. This gradient suggests an equal electron and proton electrochemical process, which is in agreement with literature reports for a process involving two electrons and two protons. [36, 37] Next attention was turned to exploring the effect of the P-graphene (20 ng) modified EPPG electrode. Analysis of the $E_P{}^{ox}$ *versus* pH was found, in this case, to produce a linear response with a gradient of 52 mV per pH unit, which is in agreement with that observed above and suggests that similar electrochemical mechanisms are operating at a both P-graphene modified and unmodified EPPG electrodes. Note that the effect of peak current is explored in Chapter 7.2.2.2. Furthermore, note that the above process was performed with regards to the reduction of 50 μM BQ. In this case plots of $E_P{}^{ox}$ *versus* pH yielded linear responses over the pH range studied and gradients of 60 and 62 mV per pH unit were observed the unmodified and P-graphene (40 ng) modified EPPG electrodes respectively. The gradients observed indicate a two electron and two proton process as indicated in previous literature. [44, 45] Again the electrochemical mechanisms evident at

both the unmodified and the P-graphene modified graphitic electrodes are in agreement, suggesting no changes due to the presence of graphene.

A key factor in terms of an excellent analytical performance is the inherent reproducibility of the response. [38] The inter-repeatability of the electrode materials of interest were thus explored towards the oxidation of 160 μM UA in pH7 PBS. A % Relative Standard Deviation (% RSD) in the analytical signal of 4.57 (unmodified EPPG, N = 3), 3.58 (20 ng P-graphene modified EPPG, N = 3), 3.24 (unmodified BPPG, N = 3) and 3.25 % (20 ng P-graphene modified BPPG, N = 3) was observed. Furthermore, inter-repeatability was also explored towards the reduction of 50 μM BQ in pH 7 PBS where a % RSD in the analytical response of 2.20 (unmodified EPPG, N = 3), 1.29 (40 ng P-graphene modified EPPG, N = 3), 4.35 (unmodified BPPG, N = 3) and 4.06 % (40 ng P-graphene modified BPPG, N = 3) was observed at the respective electrodes. Notably the values obtained at each of the electrode materials of interest are within the typically accepted analytical RSD of 5 %. [38]

7.2.2.2. DISCUSSION

Table 7.1 summarises the analytical performance in terms of the sensitivity (A M^{-1}) and LODs towards the target analytes at the EPPG and BPPG electrodes and as a result of immobilising P-graphene on the electrode surfaces. Note that electrodes with both fast and slow heterogeneous electron transfer kinetics (EPPG and BPPG respectively) were purposely studied, as is common practice throughout the literature. [9, 39] It is clear from inspection of Table 7.1 that in all cases, the addition of P-graphene results in a reduction in the sensitivity and LOD relative to that observed at the unmodified HOPG electrode. This observation is contradictory to current literature, which reports (as of 2011, see Chapter 4.1) the application of graphene modified electrodes to lead to an enhancement in the electroanalytical response. [18, 31-34]

Table 7.1 *Comparison of the analytical sensitivities and resultant LODs (based on three-sigma) obtained at the various electrode materials/modifications towards the electroanalysis of DA, UA, AP and BQ (20 ng P-graphene modification for DA, UA and AP, 40 ng modification for BQ) (N = 3).*

Electrode Material	Sensitivity/A M^{-1}	LOD (3σ)/μM
DA:		
EPPG	0.15	1.73 (±0.03)
Graphene/EPPG	0.10	3.78 (±0.08)
BPPG	0.08	2.44 (±0.05)
Graphene/BPPG	0.07	4.18 (±0.11)
UA:		
EPPG	0.13	10.40 (±0.48)
Graphene/EPPG	0.09	11.25 (±0.40)
BPPG	0.08	11.18 (±0.36)
Graphene/BPPG	0.04	14.02 (±0.46)
AP:		
EPPG	0.21	2.41 (±0.06)
Graphene/EPPG	0.14	2.77 (±0.08)
BPPG	0.12	3.33 (±0.11)
Graphene/BPPG	0.10	4.11 (±0.14)
BQ:		
EPPG	−0.14	2.14 (±0.05)
Graphene/EPPG	−0.10	3.05 (±0.04)
BPPG	−0.08	3.40 (±0.15)
Graphene/BPPG	−0.08	2.31 (±0.09)

Note that Chapter 7.1 showed, *via* electrochemical analysis and DFT, that in terms of electrode kinetics, graphene has a high electron density around its edge as opposed to its centre. Resultantly, owing to graphene's low portion of edge surface area (see Figure 7.1A) it exhibits slow heterogeneous electron transfer kinetics. [9] Graphene's slow electron transfer rates are evidently observed above (for the analytes studied in this chapter) where two cases have been presented. The first is for the EPPG electrode, which exhibits relatively fast electron transfer kinetics due to its surface having a high global coverage of edge plane like– sites/defects (which

are well known to be the origin of electron transfer in such materials). [40-46] The second case is for that of a BPPG electrode, which due to the low percentage coverage of edge plane sites populating its surface, it exhibits slow electron transfer to most analytes under diffusional control. Interestingly, (in both cases) when the electrode substrate is modified with a material that has a lower global coverage of edge plane sites (P-graphene) a reduced electrochemical performance is observed. This effect is due to one ultimately modifying an electrode surface which has relatively fast electron transfer with a slower electron transfer material (P-graphene) which, as observed here, exhibits inferior electrochemical performances relative to the HOPG electrodes, *viz* decreased electrochemical reversibility of the analyte being studied which is evident through the shift of the over-potential to higher electropositive (or electronegative) regions (see Figures 7.15, 7.17, 7.19 and 7.21). What is interesting is that a reduced performance is even observed in the case of modifying a BPPG electrode (a 'slow' electron transfer substrate) with P-graphene, where graphene exhibits inferior electron transfer rates owing to the respective global coverages of edge plane sites.

As established in Chapter 7.1, the coverage and orientation of graphene immobilised upon a supporting electrode is highly important. [9] Based on this understanding a coverage of *ca.* 20 ng was utilised throughout, corresponding to the boundary of the two zones (defined in Chapter 7.1), [9] since one wants to mimic that of near-true graphene coverage (rather than multi-layer graphene, which would be akin to graphite). In the above experiments it is found that a decrease in the analytical signal is observed, which is due to the decline in the global coverage of edge plane like– sites/defects of the EPPG/BPPG electrode with the introduction of P-graphene given that graphene is predominantly basal plane in nature and thus when immobilised upon an electrode surface these basal plane sites effectively block the underlying edge plane sites

resulting in suppressed electron transfer. For the purpose of this chapter (electroanalysis), one needs to consider why, when P-graphene is immobilised upon an electrode surface, a reduction in the analytical performance would ensue.

From an analytical perspective, it is the peak current (I_P) that is of analytical use. For a fully reversible electron transfer process, the peak current is governed by the Randles–Ševćik equation (equation (1.40)), which at 298 K is defined as:

$$I_{P,\,Rev} = (2.69 \times 10^5) n^{3/2} A C D^{1/2} v^{1/2} \qquad (7.3)$$

where *n* is the number of electrons participating in the electrochemical process, *A* is the working electrode area, *D* is the diffusion coefficient and *C* is the concentration of the target analyte. Alternatively, for the case of a fully irreversible electron transfer process, the peak current is described by equation (1.48), which at 298 K is defined as:

$$I_{P,\,Irrev} = (2.99 \times 10^5) \alpha^{1/2} n^{3/2} A C D^{1/2} v^{1/2} \qquad (7.4)$$

Thus, assuming the charge transfer coefficient, α, to be 0.5, $I_{P,\,Obs} = I_{P,\,Rev} / I_{P,\,Irrev} = 1.27$ indicating that peak currents, which are of analytical importance, for the fully reversible and fully irreversible limit differ by a factor of 1.27. [47] This means that when changing electrode kinetics from irreversible to reversible, a significant change, only a small increment in the voltammetric peak current (I_P) will be observed. Conversely, using the same analogy, a change from quasi-reversible to that of fully reversible kinetics, where $I_{P,\,Quasi}$ is described by equation (1.46), would correspond to a change in the peak current of *ca.* 1.01. Such a response has been observed previously by Kozub *et al.* [47] when utilising the above approach, where changes in the voltammetric response obtained at an EPPG electrode relative to that of a

GC electrode for the electrochemical oxidation of nitrite indicated that the peak current for the EPPG was 1.3 times larger than that at the GC electrode, where the former electrode substrate exhibits a more electrochemically reversible response towards the target analyte than that of the latter (as evidenced by a lower over-potential required for oxidation). It is important to note that graphitic electrodes are electrochemically heterogeneous with their response clearly dependant on the population of edge plane sites/defects and an 'effective electron transfer rate constant', k^0_{eff} is used to describe the electrochemical response. Graphitic electrodes have two contributions, the response of edge plane which exhibits anomalously fast electron transfer over that of basal plane, thus the contribution of basal plane can be ignored such that k^0_{eff} is equal to the coverage Θ of edge plane sites and the electron transfer rate of edge plane for the same system. [41] Such an approach has been shown to be applicable to CNTs and graphene. [35, 48] Note that it has been shown [9] that imaging (TEM/SEM *etc*.) is not such an effective way to determine the coverage of graphene and rather an electrochemical approach, which determines the electrochemical activity, is superior. Using the approach identified in Ref. [[48]] (and Chapter 8.3.3) the coverage of edge plane sites is found to correspond to 0.58.

Thus in the case considered here, if an EPPG electrode is utilised, which exhibits reversible electrode kinetics, and its surface modified with P-graphene, which exhibits irreversible electrode kinetics, due to its large contribution of basal relative to edge plane sites, [9] a reduction in the observed peak current should be observed by a factor of 1.27 (*vide supra*). Equally, if the P-graphene exhibits quasi-reversible electrode kinetics, a "reduction" of 1.01 would be evident, which is relatively negligible. If modification of the electrode surface with P-graphene results in a reduction of the peak current by a factor greater than 1.27, a physical reason other than a change in electrode kinetics must arise. [47] Note that such analysis assumes

identical geometric areas, but it is the coverage/proportion of edge plane sites upon this geometric area that is of key importance, as discussed above. P-graphene was observed to block the underlying electrode surface in Chapter 7.1. Thus, modification with P-graphene results in a new surface with a low portion of edge plane sites and hence may result in a reduced electroactive surface area.

Firstly the response of the EPPG electrode is considered towards the electrochemical oxidation of AP. Upon the immobilisation of P-graphene on the electrode surface a reduction in the voltammetric peak height (I_P) occurs where $I_{P,\,Obs} = 1.33$. This value is close to the theoretically predicted value of 1.27, suggesting that diffusion controlled reversible and irreversible peaks are being observed. In the cases of UA and BQ, modification of the electrode surface with P-graphene results in a reduced analytical response where $I_{P,\,Obs}$ is 1.40 and 1.44 respectively, which is slightly deviated from the theoretically predicted $I_{P,\,Obs}$. Hence factors other than electrode kinetics are likely in operation. Note that the graphene utilised in this study (P-graphene) is largely free from oxygenated species relative to the EPPG electrode surface. In the case of electroactive species that are sensitive to particular surface conditions and functionalities that are present at carbonaceous electrodes (for example UA), it is well known that the voltammetric response is strongly dependent on the pre-treatment of the electrode surface and ultimately the carbon-oxygen content, [49, 50] as is the case for BQ, [51] and thus it might be that in these cases the deviation from that theoretically predicated is due to the change in oxygenated species. On the contrary, the near perfect match observed for $I_{P,\,Obs}$ with theory in the case of AP is supported/confirmed from the knowledge that AP is relatively insensitive to surface oxygenated species. [52]

The largest deviation (reduced I_P resulting from the introduction of P-graphene) is that observed for DA where $I_{P,\,Obs} = 1.60$, which (as stated above) indicates that deviation from theory must originate from other factors. It has been reported that slow electrode kinetics towards DA are primarily observed due to a lack of adsorption sites, as observed on boron-doped diamond (BDD). [53] It is inferred that this is likely the case for graphene.

Thus in terms of the analytical response, a 1.27 change in voltammetric peak height when going from fully reversible to fully irreversible electrode kinetics, which is a significant change, does not result in a large *analytical* deviation, which is clearly observed from inspection of Table 7.1 for EPPG electrodes when modified with P-graphene. Given that such responses, although indicative of a reduced analytical performance, are not substantially different, it is concluded that in the analytical context studied here there appears to be no advantages of modifying a graphite electrode surface with graphene towards the target analytes studied.

7.2.3. CONCLUSIONS

This chapter has demonstrated that, in the case of the target analytes studied DA, UA, AP and BQ, the modification of graphite electrodes with graphene (P-graphene) has no significant analytical advantage. It was shown that the EPPG electrode (constructed from HOPG) exhibits the best *analytical* performance, which questions the need to modify electrodes with graphene for the electroanalysis of target analyte; such an observation and proposition has not been questioned before in the literature.

7.2.4. REFERENCES

1. D. A. C. Brownson and C. E. Banks, *Analyst*, 2010, **135**, 2768.
2. T. Gan and S. Hu, *Microchim. Acta*, 2011, **175**, 1.

3. K. R. Ratinac, W. Yang, J. J. Gooding, P. Thordarson and F. Braet, *Electroanalysis*, 2011, **23**, 803.

4. D. A. C. Brownson, J. P. Metters, D. K. Kampouris and C. E. Banks, *Electroanalysis*, 2011, **23**, 894.

5. D. A. C. Brownson and C. E. Banks, *Electrochem. Commun.*, 2011, **13**, 111.

6. D. A. C. Brownson and C. E. Banks, *Chem. Commun.*, 2012, **48**, 1425.

7. Y. Wang, Y. Li, L. Tang, J. Lu and J. Li, *Electrochem. Commun.*, 2009, **11**, 889.

8. D. A. C. Brownson, M. Gomez-Mingot and C. E. Banks, *Phys. Chem. Chem. Phys.*, 2011, **13**, 20284.

9. D. A. C. Brownson, L. J. Munro, D. K. Kampouris and C. E. Banks, *RSC Adv.*, 2011, **1**, 978.

10. Y.-R. Kim, S. Bong, Y.-J. Kang, Y. Yang, R. K. Mahajan, J. S. Kim and H. Kim, *Biosens. Bioelectron.*, 2010, **25**, 2366.

11. Y. Wang, W. Peng, L. Liu, M. Tang, F. Gao and M. Li, *Microchim. Acta*, 2011, **174**, 41.

12. S.-H. Huang, H.-H. Liao and D.-H. Chen, *Biosens. Bioelectron.*, 2010, **25**, 2351.

13. V. V. S. Eswara-Dutt and H. A. Mottola, *Anal. Chem.*, 1974, **46**, 1777.

14. R. T. Kachoosangi, C. E. Banks and R. G. Compton, *Electroanalysis*, 2006, **18**, 741.

15. F. Wantz, C. E. Banks and R. G. Compton, *Electroanalysis*, 2005, **17**, 1529.

16. D. Han, T. Han, C. Shan, A. Ivaska and L. Niu, *Electroanalysis*, 2010, **22**, 2001.

17. C.-L. Sun, H.-H. Lee, J.-M. Yang and C.-C. Wu, *Biosens. Bioelectron.*, 2011, **26**, 3450.

18. N. G. Shang, P. Papakonstantinou, M. McMullan, M. Chu, A. Stamboulis, A. Potenza, S. S. Dhesi and H. Marchetto, *Adv. Funct. Mater.*, 2008, **18**, 3506.

19. H. R. Zare, N. Nasirzadeh and M. M. Ardakani, *J. Electroanal. Chem.*, 2005, **577**, 25.

20. M. E. Bosch, A. J. R. Sanchez, F. S. Rojas and C. B. Ojeda, *J. Pharm. Biomed. Anal.*, 2006, **42**, 291.

21. R. T. Kachoosangi, G. G. Wildgoose and R. G. Compton, *Anal. Chim. Acta*, 2008, **618**, 54.

22. Y. Fan, J.-H. Liu, H.-T. Lu and Q. Zhang, *Colloids Surf., B*, 2011, **85**, 289.

23. X. Kang, J. Wang, H. Wu, J. Liu, I. A. Aksay and Y. Lin, *Talanta*, 2010, **81**, 754.

24. C. Radovan, C. Cofan and D. Cinghita, *Electroanalysis*, 2008, **20**, 1346.

25. Y. S. Lin, W. McKelvey, S. Waidvanatha and S. M. Rappaport, *Biomarkers*, 2006, **11**, 14.

26. E. S. Johnson, S. Langard and Y.-S. Lin, *Sci. Total Environ.*, 2007, **374**, 183.

27. D. Bao, S. Ramu, A. Contreras, S. Upadhyayula, J. M. Vasquez, G. Beran and V. I. Vullev, *J. Phys. Chem. B*, 2010, **114**, 14467.

28. A. S. N. Murthy and J. Sharma, *Electroanalysis*, 1997, **9**, 726.

29. R. O. Kadara, N. Jenkinson and C. E. Banks, *Sens. Actuators, B*, 2009, **138**, 556.

30. M. Aklilu, M. Tessema and M. Redi-Abshiro, *Talanta*, 2008, **76**, 742.

31. X. Kang, J. Wang, H. Wu, I. A. Aksay, J. Liu and Y. Lin, *Biosens. Bioelectron.*, 2009, **25**, 901.

32. C. Wang, L. Zhang, Z. Guo, J. Xu, H. Wang, K. Zhai and X. Zhuo, *Microchim. Acta*, 2010, **169**, 1.

33. M. Zhou, Y. Zhai and S. Dong, *Anal. Chem.*, 2009, **81**, 5603.

34. J.-F. Wu, M. Q. Xu and G. C. Zhao, *Electrochem. Commun.*, 2010, **12**, 175.

35. P. M. Hallam and C. E. Banks, *Electrochem. Commun.*, 2011, **13**, 8.

36. G.-P. Jin, X.-Q. Lin and J.-M. Gong, *J. Electroanal. Chem.*, 2004, **569**, 135.

37. R. T. Kachoosangi and R. G. Compton, *Anal. Bioanal.Chem.*, 2007, **387**, 2793.

38. C. M. A. Brett and A. M. O. Brett, *Electroanalysis*, Oxford University Press Inc., New York, 1998.

39. W.-J. Lin, C. S. Liao, J. H. Jhang and Y.-C. Tsai, *Electrochem. Commun.*, 2009, **11**, 2153.

40. R. L. McCreery, *Chem. Rev.*, 2008, **108**, 2646.

41. T. J. Davies, M. E. Hyde and R. G. Compton, *Angew. Chem. Int. Ed.*, 2005, **117**, 5251.

42. T. J. Davies, C. E. Banks and R. G. Compton, *J. Solid State Electrochem.*, 2005, **9**, 797.

43. T. J. Davies, R. R. Moore, C. E. Banks and R. G. Compton, *J. Electroanal. Chem.*, 2004, **574**, 123.

44. C. E. Banks, T. J. Davies, G. G. Wildgoose and R. G. Compton, *Chem. Commun.*, 2005, 829.

45. C. E. Banks and R. G. Compton, *Analyst*, 2005, **130**, 1232.

46. C. E. Banks and R. G. Compton, *Analyst*, 2006, **131**, 15.

47. B. R. Kozub, N. V. Rees and R. G. Compton, *Sens. Actuators, B*, 2010, **143**, 539.

48. P. M. Hallam and C. E. Banks, *Phys. Chem. Chem. Phys.*, 2011, **13**, 1210.

49. S. Hason, V. Vetterl, F. Jelen and M. Fojta, *Electrochim. Acta*, 2009, **54**, 1864.

50. J.-L. Chang, K.-H. Chang, C.-C. Hu, W.-L. Cheng and J.-M. Zen, *Electrochem. Commun.*, 2010, **12**, 596.

51. T.-W. Hui, K.-Y. Wong and K.-K. Shiu, *Electroanalysis*, 1996, **8**, 597.

52. P. Fanjul-Bolado, P. J. Lamas-Ardisana, D. Hernandez-Santos and A. Costa-Garcia, *Anal. Chim. Acta*, 2009, **638**, 133.

53. M. C. Granger, M. Witek, J. Xu, J. Wang, M. Hupert, A. Hanks, M. D. Koppang, J. E. Butler, G. Lucazeau, M. Mermoux, J. W. Strojek and G. M. Swain, *Anal. Chem.*, 2000, **72**, 3793.

7.3. GRAPHENE ELECTROANALYSIS: THE STRIPPING VOLTAMMETRY OF CADMIUM WITH (SURFACTANT FREE) GRAPHENE MODIFIED ELECTRODES

Continuing with the observations and conclusions from Chapters 7.1 and 7.2, this chapter further explores the electroanalytical performance of *surfactant free* graphene modified electrodes. In this chapter the implications of employing graphene (P-graphene) towards the sensing of heavy metals is considered, namely the ASV of cadmium. Note that this chapter contains published work. [5]

7.3.1. INTRODUCTION

As highlighted in Chapter 6.2, the utilisation of graphene in the sensing of heavy metal ions (such as lead and cadmium, which are well known to exhibit toxic effects on living organisms) is of particular importance and relevance. [1] Chapter 6.2 explored the sensing of cadmium (II) ions in aqueous solution *via* ASV using commercially available graphene, which, due to its fabrication has the surfactant sodium cholate adsorbed onto the surface of the graphene sheets/flakes (S-graphene). [2] It was shown that while the deposition of cadmium metal at an S-graphene modified electrode is possible, the stripping of the *in situ* formed cadmium metal back to cadmium (II) ions was significantly inhibited. [2] Control experiments revealed that the surfactants used in the fabrication of the S-graphene significantly contributed to the electrochemical processes and in this particular case, were detrimental. [2] This chapter revisits the ASV of cadmium (II) ions using commercially available graphene which is completely *free from surfactants* (P-graphene) and consequently will allow the de-convoluted implications of utilising graphene modified electrodes in the electroanalysis of heavy metals to be realised.

[5] D. A. C. Brownson, A. C. Lacombe, D. K. Kampouris and C. E. Banks, *Analyst*, 2012, **137**, 420.

First voltammetric response of cadmium (II) ions in aqueous solution is explored *via* ASV at a bare (unmodified) edge plane like-SPE. Figure 7.23 depicts the response arising through utilisation of a deposition potential of –1.2 V for a duration of 120 s, with a fixed cadmium (II) concentration of 400 μgL^{-1} in pH 1.5 HCl solution. The voltammetric response corresponds to the transition of *in situ* formed cadmium metal back to cadmium (II) ions and provides a characteristic stripping peak that is evidently large and quantifiable, in excellent agreement with previous reports at edge plane like-graphite-SPEs. [2, 3]

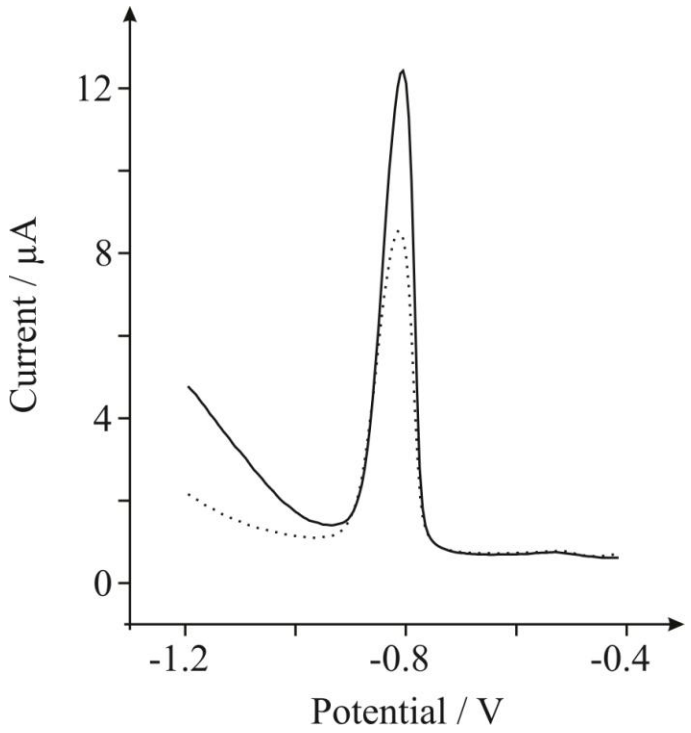

Figure 7.23 *Typical square-wave voltammetric responses for the detection of 400 μgL^{-1} cadmium (II) ions in pH 1.5 aqueous HCl solution at an unmodified edge plane like-SPE (solid line) and a SPE after modification with 35 ng P-graphene (dotted line). A deposition potential of –1.2 V (vs. SCE) for 120 s was utilised. An amplitude of 25 mV and a frequency of 25 Hz were utilised for ASV experiments.*

Figure 7.23 also shows the voltammetric response corresponding to the addition of 35 ng of P-graphene onto the underlying SPE surface. It is important to note that this approach,

where a carbon electrode with relatively fast electrochemical rate kinetics is modified with graphene, is usually absent from the literature (see Chapter 4.1, where usually an electrode with slow kinetics is utilised), however it was as identified for the first time in Chapter 7.1 and after the introduction said work into the literature, this approach is now commonly used to study the electrochemistry of graphene. [4, 5] Interestingly, it is readily observed that the addition of P-graphene onto the SPE's surface results in a reduction in the magnitude of the stripping peak relative to underlying (unmodified) SPE.

Figure 7.24A explores the effect of varying the mass (coverage) of P-graphene immobilised onto the SPE surface where it is evident that as the coverage of graphene is increased, the voltammetric stripping peak exhibits a further reduction in magnitude. This trend indicates that the P-graphene modified electrode exhibits a poor electroanalytical response (voltammetric signature) when contrasted to that of the underlying SPE. Note that this is distinctly different to recent literature reports where the incorporation of graphene has resulted in an improved electrochemical response (see Chapter 4.1). [1, 6, 7]

Next the analytical utility of the P-graphene modified SPE is considered towards the sensing of cadmium (II). Figure 7.24B depicts the response of cadmium (II) additions over the range of 100 to 1000 μgL^{-1} at a 20 and 35 ng P-graphene modified SPE. Additionally, a control experiment was performed where the response of a graphene free (unmodified) SPE was explored towards the sensing of cadmium (II) ions over the same concentration range. These experiments are highly informative, showing that there is no improvement in the electrochemical response from utilising P-graphene. It is clear in Figure 7.24B that the utilisation of graphene induces a reduction in the observed voltammetric signal, leading to decreased sensitivity towards the detection of cadmium (II) ions at graphene modified SPEs. Note that modification with

graphene also resulted in the reduced inter-repeatability of the analytical signal, where the % RSD of the observed peak height/area at an unmodified SPE and a SPE following modification with 20 and 35 ng of P-graphene were 0.7/4.4, 5.2/2.8 and 16.3/15.8 % (N = 4) respectively towards the detection of 400 μgL^{-1} cadmium (II) ions.

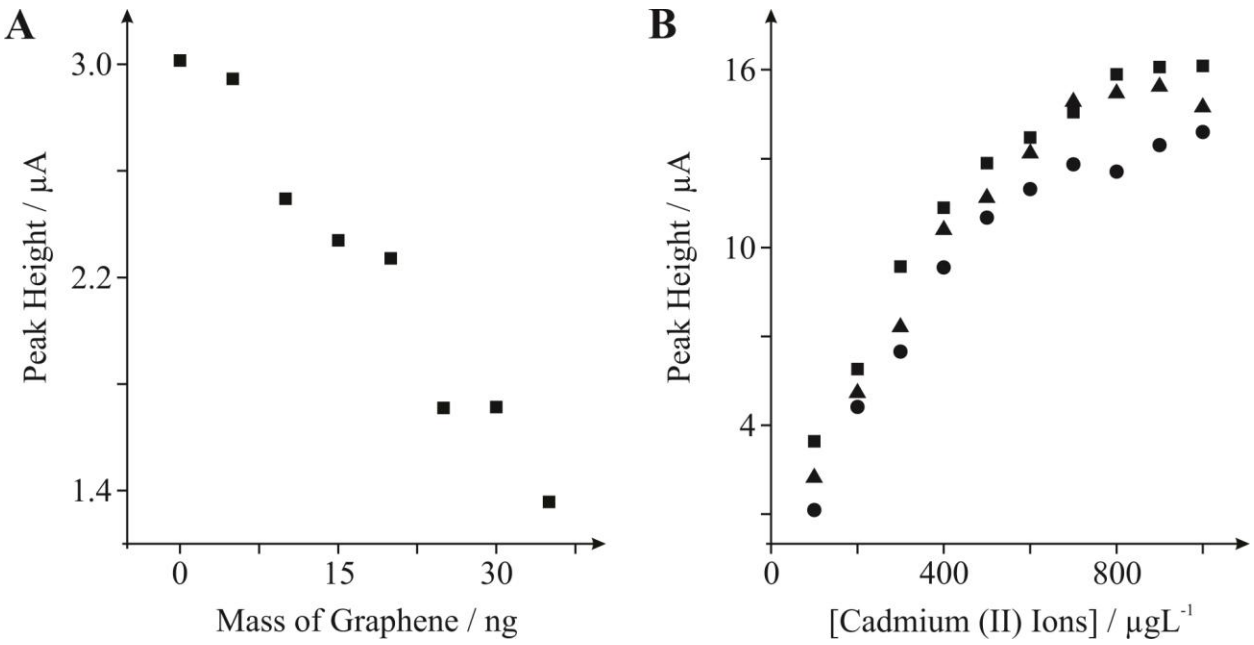

Figure 7.24 *(**A**) Relationship between the mass of P-graphene coverage on the electrode surface and the resultant peak height, viz analytical signal, towards the detection of 400 μgL^{-1} cadmium (II) ions in pH 1.5 HCl aqueous solution. (**B**) Calibration plots indicating the relationship between the concentration of cadmium (II) ions and the observed peak height at an unmodified SPE (squares) and at SPEs following modification with 20 (triangles) and 35 ng (circles) of P-graphene. **A** and **B** were both obtained via square-wave ASV, utilising a deposition potential of –1.2 V (vs. SCE) for 120 s, an amplitude of 25 mV and a frequency of 25 Hz.*

Note it is likely that that the voltammetric peak corresponding to the electrochemical stripping of nucleated cadmium metal to cadmium (II) ions is not inhibited in this case as reported in Chapter 6.2, which was identified to be due to surfactants present within the S-graphene, [2] since no surfactants are used in any part of the fabrication or post-production processing of the P-graphene utilised. The poor voltammetric response, as observed in

Figure 7.23, is somewhat surprising when comparison to the literature is sought. It has been established in Chapters 7.1 and 7.2 that the edge of graphene is the origin of electron transfer and consequently graphene has a low edge to basal surface ratio such that when applied in sensing, the response is not beneficial (Chapter 7.2). [8, 9] In the case of ASV, it is well known that metals nucleate exclusively on the edge plane sites at graphite based electrodes. [10, 11] Hence it is logical to assume this is also the case for graphene and due to the low edge to basal surface area ratio of the graphene relative to the underlying graphite-SPE, the poor voltammetric response when P-graphene is introduced can be understood to be due to graphene's low edge plane content and resultantly slow electron transfer kinetics. [8]

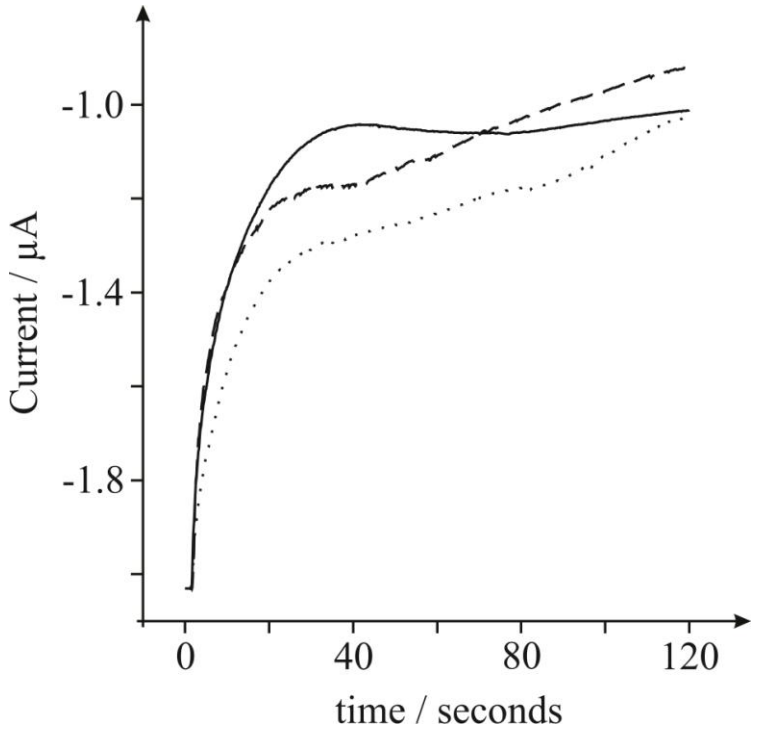

Figure 7.25 *Chronoamperometric curves obtained for the deposition of 400 µgL^{-1} cadmium (II) in pH 1.5 HCl aqueous solution. Obtained at an unmodified SPE (solid line) and at a 20 ng (dashed line) and 35 ng (dotted line) P-graphene modified SPE. A potential of −1.2 V (vs. SCE) was utilised.*

Consequently, in order to try and gain insight into the analytical process observed above, the nucleation of the target metal (cadmium) was explored *via* chronoamperometry. The

chronoamperometric response was explored at an unmodified (graphene free) SPE in addition to SPEs following modification with 20 and 35 ng of P-graphene. Figure 7.25 shows the corresponding charges passed, which were found to be –134.7, –136.1 and –152.1 μC respectively. Note that at 40 seconds there is a clear decrease in charge resulting from the addition of P-graphene, after which it appears that natural convection causes problems, resulting in the apparent increment in charged passed (in which case the issue at the modified electrode would be the kinetics of its stripping, which is shown in Figure 7.24 to be slower at P-graphene-coated electrodes). A further influence may be changes in the macroscopic surface structure from the addition of P-graphene, which might improve mass transport of the target analyte (see Chapter 1.4.2). However, considering the charged passed at 40 seconds, it can be inferred that the nucleation process, resulting from the electrochemical deposition of cadmium ions to metal, is suppressed from the introduction of P-graphene, which can be attributed to graphene's low edge plane content [8] resulting in a reduced number of available nucleation sites when compared to that of the unmodified SPE. This consequently results in reduced metal deposition and hence a reduction in the magnitude of the stripping peak (see Figure 7.23). Note that the structural model of graphene is likely that of re-assembly, such that upon modification with increasing amounts of P-graphene, deviation from single layer is observed, likely towards double and few layered graphene.

Thus the overall outcome, shown in this work for the first time, is that when P-graphene is introduced onto the electrode surface, not such a beneficial response is observed (*viz* Figure 7.23) which, as identified above, is not completely understood. Additionally, one needs to consider that the slow stripping kinetics at graphene might be accountable, hence producing an analytical signal as observed in Figure 7.23, *i.e.* not so beneficial. Note however, a

further problem could possibly be the disconnection of graphene layers during the course of the experiment (*i.e.* instability of the P-graphene modified layer on the electrode surface) which could be reflective of the greater % RSDs observed and would result in a reduced stripping current.

An attempted was made to gain further insights *via* surface characterisation with microscopy; however such analysis was inconclusive and were unable to provide supporting information. Here, given that nucleated cadmium metal is relatively unstable and possibly due to re-assembly issues, visualisation was not achieved. In support of this fact note that to the best of the author's knowledge within the current literature, there is a distinct lack of SEM images in support of the electroanalytical detection of cadmium. [12, 13] However, insights gained from voltammetry are clear and allow one to confirm that nucleation is inhibited. Thus it is evident that owing to graphene's structure, differing nucleation dynamics are likely occurring coupled with different stripping kinetics, which is highly fascinating, and a full detailed study is likely required with *in situ* AFM [14] to provide insights into this process (which is beyond the scope of this thesis).

7.3.3. CONCLUSIONS

This chapter has explored, *for the first time*, commercially available P-graphene which is *free from surfactants* towards the sensing of cadmium (II) ions in model aqueous solutions. It was found that graphene, in this example, is not beneficial as an electroanalytical electrode material as it reduces the analytical performance towards the detection of cadmium (II) at modified SPEs relative to the unmodified SPE. Furthermore, reproducibility at P-graphene modified electrodes is above the typically accepted RSD of 5 %, which is analytically

unacceptable and hence the use of graphene in electroanalysis, in-particular this application, is not beneficial.

7.3.4. REFERENCES

1. J. Li, S. Guo, Y. Zhai and E. Wang, *Anal. Chim. Acta*, 2009, **649**, 196.
2. D. A. C. Brownson and C. E. Banks, *Electrochem. Commun.*, 2011, **13**, 111.
3. M. Khairy, R. O. Kadara, D. K. Kampouris and C. E. Banks, *Anal. Methods*, 2010, **2**, 645.
4. W.-J. Lin, C.-S. Liao, J.-H. Jhang and Y.-C. Tsai, *Electrochem. Commun.*, 2009, **11**, 2153.
5. G. P. Keeley, A. O'Neill, N. McEvoy, N. Peltekis, J. N. Coleman and G. S. Duesberg, *J. Mater. Chem.*, 2010, **20**, 7864.
6. C. M. Willemse, K. Tlhomelang, N. Jahed, P. G. Baker and E. I. Iwuoha, *Sensors*, 2011, **11**, 3970.
7. J. Li, S. Guo, Y. Zhai and E. Wang, *Electrochem. Commun.*, 2009, **11**, 1085.
8. D. A. C. Brownson, L. J. Munro, D. K. Kampouris and C. E. Banks, *RSC Adv.*, 2011, **1**, 978.
9. D. A. C. Brownson and C. E. Banks, *Analyst*, 2011, **136**, 2084.
10. J. V. Zoval, R. M. Stiger, P. R. Biernacki and R. M. J. Penner, *J. Phys. Chem.*, 1996, **100**, 837.
11. C. E. Banks and R. G. Compton, *Analyst*, 2006, **131**, 15.
12. J. Kruusma, L. Nei, J. L. Hardcastle, R. G. Compton, E. Lust and H. Keis, *Electroanalysis*, 2004, **16**, 399.
13. L. M. D. Carvalho, P. C. D. Nascimento, A. Koschinsky, M. Bau, R. F. Stefanello, C. Spengler, D. Bohrer and C. Jost, *Electroanalysis*, 2007, **19**, 1719.
14. M. E. Hyde, R. Jacobs and R. G. Compton, *J. Phys. Chem. B*, 2002, **106**, 11075.

7.4. EXPLORING THE ORIGINS OF THE APPARENT "ELECTROCATALYTIC" OXIDATION OF KOJIC ACID AT GRAPHENE MODIFIED ELECTRODES

The previous sections of Chapter 7 have shown, for the first time, that P-graphene modified electrodes exhibit poor electro-catalytic behaviour. However, intrigued by literature reports (see Chapter 4.1) where beneficial electroanalytical responses are observed when utilising graphene (*without the presence of surfactants*); this chapter explores, through the employment of diligent control experiments, the possible origins of said *catalytic* effects. This chapter, which contains published work, [6] considers reports that the use of graphene modified electrodes gives rise to the electrocatalytic oxidation of kojic acid.

7.4.1. INTRODUCTION

The design, synthesis and fabrication of analytical sensors and sensing systems is a highly diverse field and a global pursuit. [1, 2] Many sensors have been continuously developed for a number of years, such as optical, thermal, mass-based and electrochemical devices, which have a vast range of important applications in the fields of clinical, industrial, environmental and agricultural analysis. [3-6] Electrochemical derived sensors attract attention due to their ability to convert chemical information into an electrical signal and through careful design can give rise to sensitive, selective, experimentally simple and low cost sensors. [1, 2, 7] The output of an electrochemical sensor is a variable current, of which the peak height (maxima) is proportional to the concentration of the electroactive species of interest (analyte), which arises from applying electrode potentials at suitable values to give rise to electron transfer to or from the target analyte (as established in Chapter 1). [2] In this area of research, electrochemists are constantly searching

[6] L. C. S. Figueiredo-Filho, D. A. C. Brownson, O. Fatibello-Filho and C. E. Banks, *Analyst*, 2013, **138**, 4436.

for new electrode materials that can give rise to improvements in the analytical signal (peak height) through the application of more facile electrode potentials (*i.e.* lower over-potentials), with the former potentially giving rise to lower detection levels. [2] As such, electrochemists typically modify electrode surfaces with materials such as micro- and nano-particles, mediators and catalysts. [8-12] Other approaches involve the modification of electrode surfaces with carbon nanomaterials, [13] such as carbon nanotubes, which have been reported to give rise to improvements in electrochemical processes when compared to the underlying electrode surface which is used to support the modifier and allow electrical connection. [14, 15]

Following such approaches, graphene has been used for the modification of electrode surfaces with the aim of improving electrochemical processes (see Chapter 4.1). [2] For example, it has been reported that graphene modified electrodes give rise to beneficial improvements for the sensing of acetaminophen, hydroquinone and dopamine. [16-18] In these cases, and in many more, the modification of electrode surfaces has been shown to provide improvements in the analytical signal when compared to the previously unmodified/bare electrode surfaces. [16-21] Intrigued by the report that graphene modified electrodes gives rise to an apparent 'electrocatalytic' response towards the electrochemical oxidation of kojic acid, [22] this chapter explores the electrochemical detection of this analyte at graphitic electrodes and critically compares the responses to that of *P-graphene* modified electrodes.

7.4.2. RESULTS AND DISCUSSION

It has been reported that chemically reduced graphene oxide (*producing reduced graphene sheets* (RGSs)) immobilised upon a GC electrode can be beneficial for the sensing of kojic acid. [22] Cyclic voltammetric responses were reported to be optimal when using the RGS

modified GC electrode and comparing the response to that of a bare (unmodified) GC electrode and a graphite electrode towards the electrochemical oxidation of kojic acid. [22] The authors noted that the peak current was 'faint' and 'not well identified' in the latter two cases (see Figure 4.2). Given that the presence of RGSs on the GC electrode greatly increased the peak current compared with the inverse case (when the RGSs are absent), the authors attributed this to indicate that the RGSs have a high electrocatalytic activity towards the electrochemical oxidation of kojic acid. [22] Interested by this report, which is contradictory to the work reported in Chapters 7.1, 7.2 and 7.3 of this thesis, this chapter considers the electrochemical oxidation of kojic acid at various unmodified carbon based and graphitic electrodes.

Figure 7.26 shows the electrochemical oxidation of kojic acid at BDD, GC, BPPG and EPPG electrodes. Surprisingly, it is clear that large 'well-defined' voltammetric signatures are observed at all of the electrodes studied. Of note is the voltammetric potential at which the electrochemical oxidation peak appears, where peak potentials of *ca.* 1.21, 1.13, 0.91 and 0.86 V are evident for the BDD, GC, BPPG and EPPG electrodes respectively. Clearly there is a dependence on the electronic structure of the graphite electrodes where the electrochemical oxidation is observed to occur at the lowest potential (most beneficial electrochemical response) using the EPPG electrode, which is due to its large coverage of edge plane like- sites/defects giving rise to fast electron transfer properties/kinetics in comparison to the alternative electrodes. [2, 23, 24] Additionally, the EPPG electrode gives rise to the largest electrochemical signature (peak current), which is optimal when compared to the other graphitic/carbon electrodes studied. Insights can be derived from Tafel analysis which involves analysis of the voltammograms corresponding to the electrochemical oxidation of kojic acid, plotted as potential *versus* $\log_{10}$(current). Such analysis was constructed for the EPPG electrode, resulting in a value

of 95 mV per decade being obtained. Using the following equation: $b = 2.303RT / \alpha n' F$, where b is the slope of potential (measured in V) against $\log_{10}$(current), α is the electron transfer coefficient and n' is the number of electrons transferred in the rate determining step; a value of 0.44 for $\alpha n'$ was deduced. This value suggests that it is the transfer of the first electron which is electrochemically irreversible, so that n' = 1 and α = 0.44.

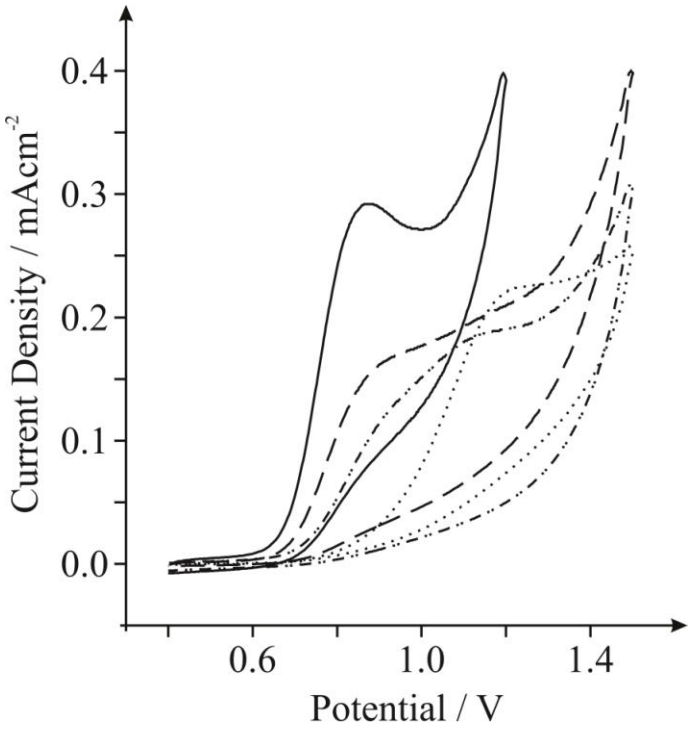

Figure 7.26 *Cyclic voltammetric profiles recorded for 1 mM kojic acid in PBS (pH 6, with 0.1 M KCl) at EPPG (solid line), BPPG (dashed line), GC (dot-dot-dashed line) and BDD (dotted line) electrodes. Scan rate: 50 mVs^{-1} (vs. SCE).*

The voltammetric signature at the EPPG electrode was monitored as a function of pH in terms of both peak height and potential. A plot of peak potential (*V*) *versus* pH was found to be linear (*E/V* = 0.0525 (*V/pH*) + 1.14 V; R^2 = 0.98; *N* = 6) over the pH range of 2 to 8, where beyond this pH range up to more alkaline values deviation from linearity was observed, which is due to the *pKa* of kojic acid being 7.9. The gradient of 52.5 mV pH^{-1} suggests an equal number

of protons and electrons are involved in the electrochemical oxidation of kojic acid. Indeed, recent work has suggested that this value is 1. [22]

An approximate diffusion coefficient value was calculated (using the EPPG electrode) based on experimental data for the diffusion controlled electrochemically irreversible reaction (*vide infra*), in which the first electron transfer is rate-determining, using the Randles–Ševćik relationship in equation (1.48). Using a value of 0.44 deduced above for $\alpha n'$ and a value of 1 for n' (the number of electrons involved in the charge-transfer step), the diffusion coefficient was estimated (from equation (1.48)) to correspond to 6.1 x 10^{-5} cm^2 s^{-1}, which is in agreement with the reported value of $D = 1.5 \times 10^{-5}$ cm^2 s^{-1} for RGS modified GC electrodes. [22]

Next, this chapter turns to exploring whether the introduction of P-graphene onto the EPPG surface improves the electrochemical oxidation of kojic acid as suggested by Wang and co-workers. [22] Figure 7.27A depicts the typical cyclic voltammetric response observed at an EPPG electrode, where upon the immobilisation of increasing masses of P-graphene onto the supporting surface the voltammetric potential corresponding to the oxidation of kojic acid is observed to shift to higher over-potentials resulting in the following peak potential values: *ca*. 0.84, 0.91, 0.94 and 1.00 V for the EPPG electrode after modification with 0, 10, 20 and 30 ng of P-graphene respectively. Note that there is no observable peak present in the case of the immobilisation of 40 ng of P-graphene onto the EPPG electrode. In addition to the observable shift in the peak potential, a reduction in the I_P is also evident when immobilising increasing masses of P-graphene (as depicted in Figure 7.28). It is clear from the above results that the introduction of graphene (that being P-graphene) onto the EPPG electrode serves to simply block the electrochemical process at the underlying substrate rather than giving rise to any 'electrocatalysis'. The above observation is as expected and in agreement with Chapters 7.1,

7.2 and 7.3 given that graphene's geometry results in an electrode material with a low coverage of edge plane like- sites/defects (see Figure 7.1A), [2, 23, 25] which are well known to be the origin of fast heterogeneous electron transfer kinetics at graphitic materials and thus a larger coverage of such sites gives rise to an electrode material with a beneficial electronic structure (density of states) and improved electrochemical properties/performance. [26, 27]

Note that undeniably the electrochemical oxidation of kojic acid can be readily observed at the bare/unmodified EPPG electrode, prior to the addition of P-graphene (in addition to the unmodified GC and BPPG, see Figure 7.26), suggesting that in these cases the coverage of edge plane like- sites/defects is adequate for the electrochemical process to occur (and indeed for electrochemical sensing, *vide infra*) rather than attributing this to the 'electrocatalytic' nature of graphene.

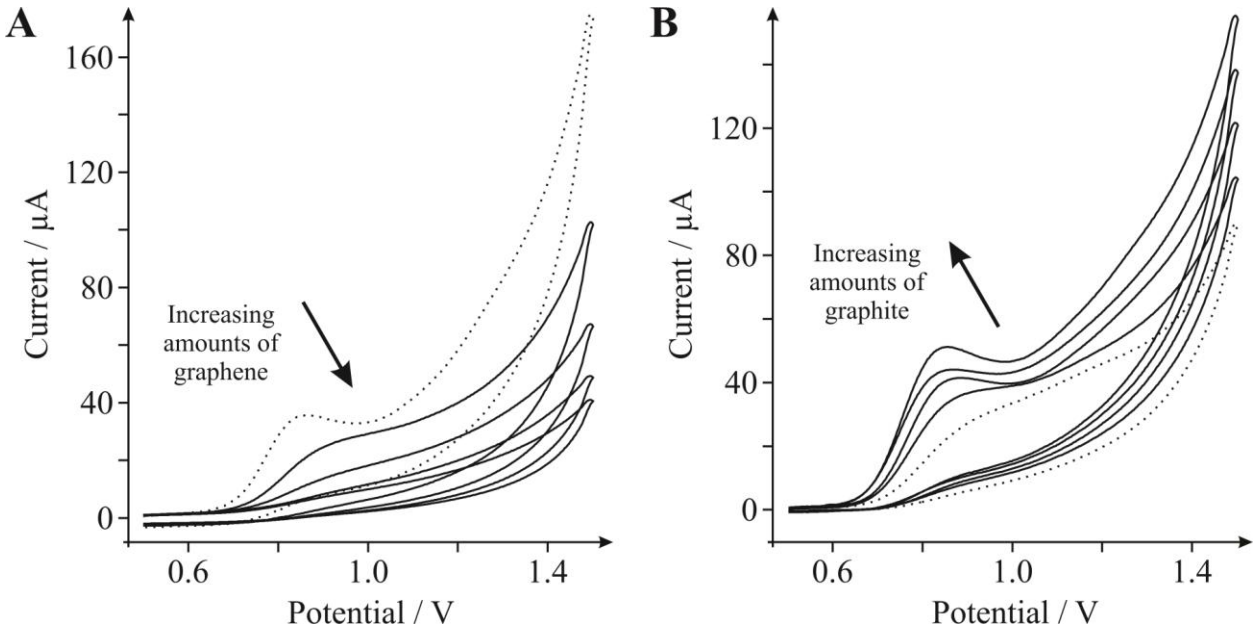

Figure 7.27 *Cyclic voltammetric profiles recorded for 1 mM kojic acid in PBS (pH 6, with 0.1 M KCl) at a scan rate of 100 mVs^{-1} (vs. SCE).* ***A:*** *using an EPPG electrode (dotted line) with the addition/immobilisation of increasing masses/amounts of 10, 20, 30 and 40 ng P-graphene (solid lines).* ***B:*** *using a BPPG electrode (dotted line) with the addition/immobilisation of increasing masses/amounts of 4, 10, 15 and 20 µg graphite (solid lines).*

Given the contrasting report by Wang (and indeed by many others with regard to other possible analytes, see Chapter 4.1) [16-21] *one must question where this 'electrocatalysis' originates from in such cases*. Thus next, the possible source of the commonly reported 'electrocatalytic' effect of graphene is considered *via* the implementation of further control experiments. Note that Chapter 7.1 has established that the coverage and orientation of graphene immobilised on a supporting electrode substrate is highly important and influences the observed electrochemistry. [23] Based on this understanding, in the above experiments the mass of graphene utilised was selected such that it corresponded to *Zone I* coverages [23] since one wants to create an electrode with near-true single layer graphene coverage (rather than multi-layer graphene which would be akin to graphite, *Zone II*). It is clear therefore that if a graphene experimentalist was to immobilise too large a quantity of graphene onto an electrode surface, the resultant coverage would correspond to that of *Zone II* [23] where the graphene is likely to stack and coalesce into multi-layered graphite, aided by the high cohesive van der Waals forces.

Given the above insight, this chapter next explores whether the introduction of graphite onto a BPPG surface improves the electrochemical oxidation of kojic acid. Figure 7.27B depicts the typical cyclic voltammetric response observed at a BPPG electrode, where upon the immobilisation of increasing masses of graphite the voltammetric potential corresponding to the oxidation of kojic acid is observed to shift to lower (more beneficial) over-potentials, resulting in the following peak potential values: *ca*. 0.90, 0.88, 0.86, 0.84 and 0.83 V for the BPPG electrode after modification with 0, 4, 10, 15 and 20 μg of graphite respectively. Furthermore, increments in the I_P are evident with the addition of graphite (as depicted in Figure 7.28). It is clear that the introduction of graphite onto the BPPG electrode (an underlying electrode material that possesses a low coverage of edge plane sites and hence slow electron transfer rates) serves to

improve the electrochemical properties and the observed performance, which can be attributed to graphite's geometry in terms of its large global coverage of edge plane sites. Resultantly, introducing graphite onto a supporting substrate that possesses a low coverage of such sites gives rise to beneficial voltammetry *via* incurring fast heterogeneous electron transfer kinetics. Returning to the case of the 'electrocatalysis' reported at graphene, it is evident that if experimentalists use an electrode coverage of graphene that corresponds to *Zone II* as defined in Chapter 7.1 then the 'electrocatalytic' nature of the 'graphene' likely arises from the formation of multi-layered graphene structures and indeed deviation from the structural conformation of true single layer graphene. Furthermore, note that given the said improvements arise due to an increment in the available edge plane like- sites/defects (graphite>>graphene, in terms of edge plane sites contributing to their geometry) [28] such improvements can also originate when using defect abundant graphene and therefore one should utilise as near pristine graphene as possible (and stay within *Zone I* coverage) to avoid misinterpretation of experimental data when studying the electrochemistry of graphene modified electrodes. [2]

In electrochemistry the vast majority of studies reporting the use of graphene fabricate their 'graphene' *via* the reduction of GO (as was the case for Wang *et al*. [22]). Thus it is appropriate to investigate the electrochemical response of GO towards the oxidation of kojic acid to determine the effect of any oxygenated species remaining on the graphene (such as due to its incomplete reduction). It was found that the immobilisation of GO onto the surface of a BPPG electrode resulted in a shift in the electrochemical oxidation potential towards lower over-potentials, corresponding to *ca*. 0.92, 0.88, 0.87, 0.85, 0.83 and 0.81 V for the BPPG electrode after modification with 0, 2, 4, 10, 15 and 20 μg of GO respectively. The improved electrochemical response likely arises due to the level of edge plane like- sites/defects on the

structure of GO, where the defects give rise to improvements in electron transfer kinetics. [2] As depicted in Figure 7.28, note that in addition to the improved electron transfer rates at GO, alterations occur in the observed I_P. It is evident that the addition of 2 µg of GO onto the BPPG surface results in an increased voltammetric peak height. However, notably, extending coverage of the GO beyond 2 µg impedes the electrochemical process and a decreased I_P is evident with further additions. It is likely that in the initial case the contribution of the oxygenated species is beneficial towards the electrochemical process (or that the quantity of said species is small such that it has little influence/contribution to the observed voltammetry) and in conjunction with the high degree of edge plane defect sites across the basal plane surface of the functionalised graphene sheet, this gives rise to favourable electrochemistry. In the latter case however, it is apparent that larger coverages of GO lead to higher levels of oxygenated species across the electrode surface, which are likely detrimental to the electrochemical process in terms of disrupting favourable interaction and thus electron transfer across the electrode | solution interface: it is only when large quantities of oxygenated species are present that their combined effect are encountered and observable in the voltammetry. From the above observations, it is evident that in the case of a partially reduced graphene electrode, the reported 'electrocatalytic' effects most likely result from the presence of a large number of edge plane like- sites/defects present on the basal plane of the graphene surface, which would not be present if using *pristine graphene*. It is also clear that the presence of oxygenated species plays a part in contributing to the observed electrochemistry, either beneficially or detrimentally. [2, 29]

Tafel and pH analysis was performed on all of the modified electrodes in addition to each of the unmodified electrode substrates, where as expected, no mechanistic changes were observed in the electrochemical oxidative process of kojic acid at the various graphitic/carbon

materials explored. Furthermore, scan rate studies were performed on all of the (modified)electrodes utilised, which indicated there to be no contributions in the observed voltammetry arising from thin-layer effects, [30] in which case all electrodes were governed by diffusional processes: as expected and as previously reported for the graphitic materials utilised. [23, 29]

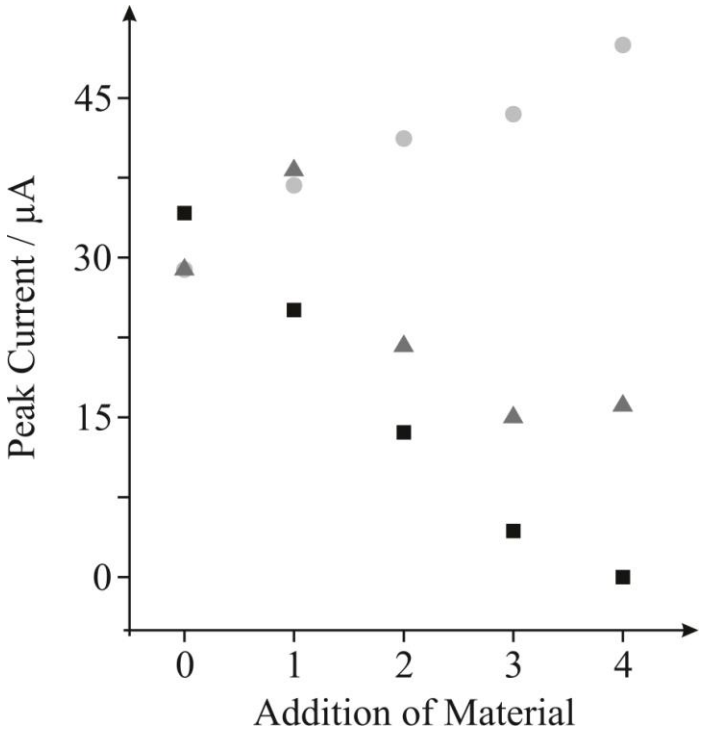

Figure 7.28 *A plot depicting the relationship between 'the mass of a given graphitic material immobilised on a supporting electrode substrate' and 'the voltammetric peak current recorded due to the oxidation of 1 mM kojic acid' in PBS (pH 6, with 0.1 M KCl). Cyclic voltammograms utilised a scan rate of 100 mVs^{-1} (vs. SCE).* ***Squares:*** *additions of 10, 20, 30 and 40 ng P-graphene onto an EPPG electrode,* ***Circles:*** *additions of 4, 10, 15 and 20 µg graphite onto a BPPG electrode, and* ***Triangles:*** *additions of 2, 4, 10 and 15 µg GO onto a BPPG electrode. Note that increasing additions relate to their respective 'addition number' on the x-axis, where '0' (addition of material) represents the voltammetry observed at the bare/unmodified supporting electrode in each case.*

Figure 7.28 provides a summary of the effect of different graphitic and graphene modifiers. It is clear that the electroanalytical detection of kojic acid using a bare/unmodified

EPPG electrode provides a beneficial electrochemical signature. As such, this questions the need to modify graphitic electrodes with graphene (see Figure 7.28).

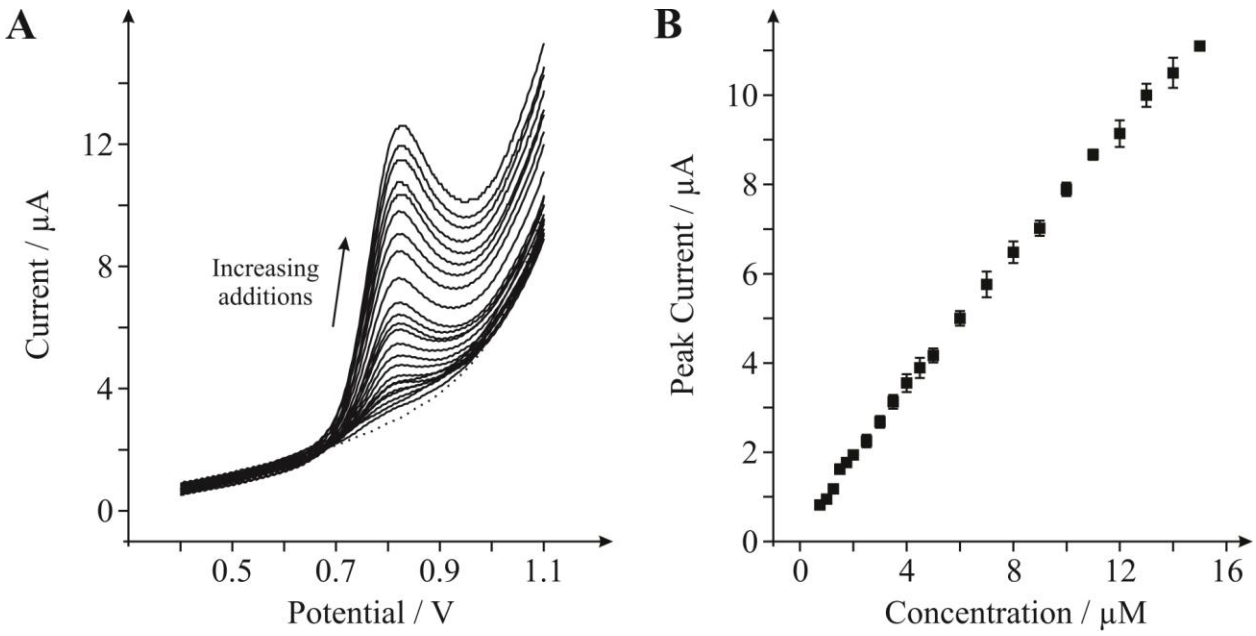

Figure 7.29 *(**A**) Linear sweep voltammograms recorded utilising an EPPG electrode in a PBS (pH 6, with 0.1 M KCl), 'blank' (dotted line) and following the successive addition of kojic acid into the buffer solution to give the following concentration range: 0.75, 1.00, 1.25, 1.50, 1.75, 2.00, 2.50, 3.00, 3.50, 4.00, 4.50, 5.00, 6.00, 7.00, 8.00, 9.00, 10.00, 11.00, 12.00, 13.00, 14.00 and 15.00 µM (solid lines).* ***(B)*** *A calibration plot of kojic acid concentration versus the voltammetric peak current obtained at the EPPG electrode. All data obtained at a scan rate of 100 mVs^{-1} (vs. SCE).*

Next the analytical performance of the bare EPPG electrode is explored, where the responses arising from successive additions of kojic acid into a PBS are shown in Figure 7.29, in which a large linear range from 0.75 to 15 µM is clearly evident with a limit of detection (LOD, based on 3σ) found to correspond to 0.23 µM. The inter-repeatability of the electroanalytical measurement is evident from inspection of Figure 7.29B where error bars are shown (with the largest % RSD found to be 6.6 %). Such a response is comparable, superior even, to that of the RGS modified GC electrode described in Ref. [22], where a linear

range from 0.01 to 0.14 mM was reported (with an analytical sensitivity of 42.9 µA mM^{-1}) and an inter-reproducibility of 7.5 % (note that whilst the LOD was not strictly reported, the lowest concentration utilised corresponded to 10 µM). [22] Table 7.2 depicts the sensitivities and LODs of various electrode materials and modifications utilised throughout this study. Comparison of the EPPG response to that of the other electrode materials reveals that the choice of EPPG gives rise to a beneficial electrochemical performance, which is clearly analytically useful. [24] Note that poor LODs and analytical sensitivities are observed in the case of the P-graphene modified electrodes questioning the need, in analytical terms and a practicability (and cost) point of view, to modify electrodes with graphene. Evidently, the immobilisation of P-graphene onto the EPPG results in a reduced analytical performance, which is supported by the fact that the unmodified EPPG electrode out-performs the RGS modified GC electrode reported by Wang *et al*. [22]

Table 7.2 *Comparison of the analytical sensitivities and resultant LODs (based on three-sigma) obtained at various electrode materials and modifications as utilised throughout this study towards the (electro) analytical detection of kojic acid in PBS (pH 6, 0.1 M KCl) (N = 3). Note that P-graphene is denoted as 'graphene' for the purpose of this table.*

Electrode substrate/ modification	Sensitivity/A M^{-1}	LOD (3σ)/µM
GC	0.10	0.28 (±0.02)
EPPG	0.73	0.23 (±0.02)
EPPG/10 ng graphene	0.11	1.03 (±0.07)
EPPG/10 µg graphite	0.72	0.31 (±0.02)
EPPG/10 µg GO	0.49	0.56 (±0.04)

In summary, throughout the literature graphene is reported to be a beneficial sensor substrate with electrocatalytic effects widely claimed. [16-21] It is evident that the vast majority of

said work claims such ‘electrocatalysis’ when only comparing the response of the graphene modified electrode to that of the underlying electrode substrate, which is usually a poor electron transfer mediator in terms of exhibiting unfavourable electrochemical characteristics (GC or BPPG for example). This chapter has demonstrated, utilising kojic acid as a representative example of the literature, that graphene is not so beneficial if compared and contrasted sufficiently to graphitic alternatives which possess favourable electrochemical properties; allowing one to confirm the origins (or lack thereof) of the ‘catalytic’ response at *pristine graphene*.

7.4.3. CONCLUSIONS

This work has shown that adequate control experiments (in the form of a range of graphitic electrodes and additionally graphite and graphene coverage studies) need to be performed when “electrocatalysis” is conferred at graphene modified electrodes. It was demonstrated that the electrochemical sensing of kojic acid is not beneficial at P-graphene modified electrodes, which is in contrast to recent literature claims. [22] Graphene’s poor electrochemical performance is likely due to its low edge plane content [2, 23, 25] and rather bare/unmodified graphitic electrodes give rise to analytically superior and useful responses.

7.4.4. REFERENCES

1. J. P. Metters, R. O. Kadara and C. E. Banks, *Analyst*, 2011, **136**, 1067.
2. D. A. C. Brownson, D. K. Kampouris and C. E. Banks, *Chem. Soc. Rev.*, 2012, **41**, 6944.
3. J. N. Anker, W. P. Hall, O. Lyandres, N. C. Shah, J. Zhao and R. P. Van-Duyne, *Nat. Mater.*, 2008, **7**, 442.
4. F. Yi and D. A. La-Van, *WIREs Nanomed. Nanobiotechnol.*, 2012, **4**, 31.
5. P. S. Waggoner and H. G. Craighead, *Lab Chip*, 2007, **7**, 1238.
6. G. Hanrahan, D. G. Patil and J. Wang, *J. Environ. Monit.*, 2004, **6**, 657.

7. J. P. Metters, R. O. Kadara and C. E. Banks, *Sens. Actuators, B*, 2012, **169**, 136.
8. J. Wang, *Electroanalysis*, 1991, **3**, 255.
9. H. Cui, W. Yang, X. Li, H. Zhao and Z. Yuan, *Anal. Methods*, 2012, **4**, 4176.
10. S. A. Wring, J. P. Hart and B. J. Birch, *Analyst*, 1991, **116**, 123.
11. N. A. Choudhry, D. K. Kampouris, R. O. Kadara, N. Jenkinson and C. E. Banks, *Anal. Methods*, 2009, **1**, 183.
12. C. Huang, C. Li and G. Shi, *Energy Environ. Sci.*, 2012, **5**, 8848.
13. R. R. Moore, C. E. Banks and R. G. Compton, *Anal. Chem.*, 2004, **76**, 2677.
14. Q. Zhao, Z. Gan and Q. Zhuang, *Electroanalysis*, 2002, **14**, 1609.
15. G. G. Wildgoose, C. E. Banks, H. C. Leventis and R. G. Compton, *Microchim. Acta*, 2006, **152**, 187.
16. M. Zhou, Y. Zhai and S. Dong, *Anal. Chem.*, 2009, **81**, 5603.
17. L. Chen, Y. Tang, K. Wang, C. Liu and S. Luo, *Electrochem. Commun.*, 2011, **13**, 133.
18. L. Tan, K.-G. Zhou, Y.-H. Zhang, H.-X. Wang, X.-D. Wang, Y.-F. Guo and H.-L. Zhang, *Electrochem. Commun.*, 2010, **12**, 557.
19. D. A. C. Brownson and C. E. Banks, *Analyst*, 2010, **135**, 2768.
20. K. R. Ratinac, W. Yang, J. J. Gooding, P. Thordarson and F. Braet, *Electroanalysis*, 2011, **23**, 803.
21. T. Kuila, S. Bose, P. Khanra, A. K. Mishra, N. H. Kim and J. H. Lee, *Biosens. Bioelectron.*, 2011, **26**, 4637.
22. Y. Wang, D. Zhang and J. Wu, *J. Electroanal. Chem.*, 2012, **664**, 111.
23. D. A. C. Brownson, L. J. Munro, D. K. Kampouris and C. E. Banks, *RSC Adv.*, 2011, **1**, 978.
24. C. E. Banks and R. G. Compton, *Analyst*, 2006, **131**, 15.
25. D. A. C. Brownson, C. W. Foster and C. E. Banks, *Analyst*, 2012, **137**, 1815.
26. T. J. Davies, M. E. Hyde and R. G. Compton, *Angew. Chem., Int. Ed.*, 2005, **44**, 5121.
27. T. J. Davies, R. R. Moore, C. E. Banks and R. G. Compton, *J. Electroanal. Chem.*, 2004, **574**, 123.
28. D. A. C. Brownson and C. E. Banks, *Analyst*, 2011, **136**, 2084.
29. D. A. C. Brownson, A. C. Lacombe, M. Gómez-Mingot and C. E. Banks, *RSC Adv.*, 2012, **2**, 665.
30. P. M. Hallam and C. E. Banks, *Electrochem. Commun.*, 2011, **13**, 8.

CHAPTER 8: ELECTROCHEMISTRY OF CVD GROWN GRAPHENES (EXPLORING BOTTOM-UP FABRICATION)

Previous chapters have explored the electrochemical properties of graphenes that have been fabricated *via* various 'top-down' routes. Such top-down methods generally result in the said graphene being made available in solution phase, aliquots of which are then modified onto existing electrodes through a drop-casting method in order to 'connect to' and electrically wire the 'graphene'. Although this method is widely (and favourably) implemented within the electrochemical literature (and has allowed for electrochemical investigation of graphene thus far in this work – leading to significant knowledge on the electrochemical properties/performance of graphene to be uncovered), there are various limitations with this approach. For example, it was shown in previous chapters that the coverage of the graphene is crucial with respect to the observed response, and controlling this factor is difficult, furthermore the surface stability of the graphene once immobilised onto an electrode surface has also been highlighted in previous chapters where graphene modified electrodes exhibited increased RSD values relative to the unmodified alternatives. Most importantly though, is that it is difficult to characterise the graphene 'once immobilised' on the electrode surface and thus one does not 'truly' know the exact coverage/state of the 'graphene' surface is that they are utilising. Further issues (and one of the most crucial problems thus far) include the effect of the underlying surface which may/may-not contribute to the observed electrochemistry – thus if incomplete coverage of a modified graphene film is obtained, then depending on the electrochemical reactivity of the underlying support material, this can possibly influence (and dominate the 'graphene' response). Given these insights, it is clear that one should 'ideally' explore graphene that is supported on an inert substrate.

Various methods exist for fabricating graphene, of which CVD appears ideally suited to explore the 'true' electrochemical characteristics of graphene due to the prevalence of

volume-produced, large surface area, uniform graphene sheets which possess extremely low defect densities and thus exhibit 'outstanding' electrical conductivity (see Chapter 3.2.5). A major advantage of CVD synthesised graphene is that following growth onto a catalytic metal surface, the resultant high quality graphene films are readily transferable onto a multitude of substrates for electrochemical investigation. Furthermore, through employment of the electrochemical cell depicted in Figure 5.29, the graphene film electrodes can effectively be characterised *in-situ* so that one is able to determine exactly what is being utilised (see Chapter 8.3). Although this method gives rise to pristine graphene, note that tailoring of the graphene films (in terms of layer numbers, orientation and impurity levels) is possible through variation of the procedural parameters (see later, Chapter 8.3).

This chapter first considers the electrochemical response arising from the implementation of a CVD grown graphene electrode that remains supported on top of the Nickel catalyst utilised for its growth (denoted, CVD-graphene), this is utilised to demonstrate the ability of employing electrochemistry as a characterisation technique to effectively determine the topography of graphene surfaces. Thereafter CVD grown graphenes are utilised that have been transferred (post-production) onto an insulating support substrate, where through comparisons of a fully 'in-situ' characterised single-layer graphene electrode (M-graphene) to that of *quasi*-graphene electrodes (Q-graphene) fabricated *via* the same method and further towards HOPG electrodes, the *true* and unambiguous electrochemical properties of graphene films are divulged, *for the first time*.

Experimental Overview: this chapter utilises cyclic voltammetric experiments using a three electrode system as detailed in Chapter 5.1. Variable working electrodes are employed throughout; however, a platinum wire and a SCE consistently comprise the auxiliary and reference electrodes respectively. Where CVD grown graphene based working electrodes are utilised, the electrochemical cell depicted in Figure 5.29 was employed. Chapters 8.1 and 8.2

use CVD-graphene as the working electrode, which is described as ‘CVD grown graphene on a nickel substrate/underlying-support’ (see Chapter 5.4.4 for full characterisation). In such chapters a nickel film electrode (Chapter 5.4.4) in addition to EPPG and BPPG electrodes (Chapter 5.2.1) were utilised where appropriate for control and comparison experiments. Chapter 8.3 utilises various CVD grown graphene samples as the working electrode (all deposited on top of an insulating SiO_2 wafer). These graphene samples are denoted as M-graphene, D-graphene and Q-graphene and relate to ‘monolayer’, ‘double-layered defect-abundant’ and ‘few-/multi-layered (*quasi*-)’ graphene samples respectively, which are ‘on a silicon dioxide (electrochemically inert) supporting substrate’ where the respective graphene is ‘grown *via* a CVD process and transferred onto the supporting substrate using a PMMA method’. Full characterisation of the M-graphene, D-graphene and Q-graphene can be found in Chapter 5.4.5. Comparison experiments performed in Chapter 8.3 consisted of utilising EPPG and BPPG electrodes, *vide supra*.

8.1. THE ELECTROCHEMICAL CHARACTERISATION OF CVD GROWN GRAPHENE ELECTRODES (SUPPORTED ON NICKEL SUBSTRATES): THE ROLE OF GRAPHITIC ISLANDS

Chapter 8.1 contains published work [7] which utilises electrochemistry to characterise the surface state and topography of CVD grown graphene electrodes. The role of graphitic islands, resulting as part of the fabrication process, is considered towards the electrochemistry observed at common redox probes, namely the inner-sphere and outer-sphere electrochemical redox probes potassium ferrocyanide (II) and hexaammine-ruthenium (III) chloride.

8.1.1. INTRODUCTION

As stated in Chapter 3.2.5, Chemical Vapour Deposition (CVD) appears the most promising fabrication approach for graphene that is suitable for exploration within electrochemistry. However, given the widespread exploration of graphene in many electrochemical areas the use of CVD grown graphene is surprisingly limited. At the time of conducting the work within this chapter (early 2011), there was only one report, to the best of the author's knowledge, concerning the electrochemical utilisation of CVD grown graphene, in which Li *et al.* reported the electron transfer rates of ferrocenemethanol at a CVD fabricated graphene electrode to be more than ten-fold faster than at the basal plane of bulk graphite. [1]

Inspired by the limited literature available, and of course by the initial aims and objectives of this thesis, this chapter consequently explores and electrochemically characterises commercially available CVD grown graphene (see Chapter 5.4.4) [2] with the aim of studying electron transfer. However, it is found that graphitic islands exist in the form of

[7] D. A. C. Brownson and C. E. Banks, *Phys. Chem. Chem. Phys.*, 2011, **13**, 15825.

few- and multi- layer graphene flakes distributed across the electrode surface and consequently their role on the electrochemical activity of CVD-graphene is investigated.

8.1.2. RESULTS AND DISCUSSION

The electrochemical properties of the CVD-graphene electrode are first explored with the 'outer-sphere' redox probe, [3] 1 mM hexaammine-ruthenium (III) chloride in 1 M KCl. Figure 8.1 depicts a typical cyclic voltammetric profile of the CVD-graphene which exhibits a well defined pair of redox peaks with a peak-to-peak separation (ΔE_P) of *ca*. 108 ± 2 mV. The effect of varying the scan rate results in the voltammetric peak potentials gently shifting to larger values, indicating a quasi-reversible electron transfer system (see Chapter 1.4.1), with the magnitude of the voltammetric peak height dependant on the square-root of the scan rate. Using the Nicholson method (equation (1.44)) [4] the heterogeneous electron transfer rate constant (k^0) is found to correspond to 2.51 x 10^{-3} cm s^{-1}, which is in good agreement with a previous literature report utilising CVD-graphene. [1]

A control experiment was performed utilising a bare Ni electrode (no graphene), [5] which was explored towards the ruthenium redox probe (as above). The cyclic voltammetric response can be observed in Figure 8.1 where a pair of well defined redox peaks exhibit a ΔE_P of *ca*. 62 ± 1 mV and a k^0 of 71.8 x 10^{-3} cm s^{-1}. On comparison, it is clear that the Ni electrode exhibits faster electron transfer kinetics relative to the CVD-graphene modified Ni electrode, thus it can be inferred that the material deposited (*i.e.* graphene) upon the Ni film in the CVD-graphene is in fact a continuous film, and consequently blocks the electro-catalytic activity of the underlying Ni. Conversely, if discrete islands of graphene existed rather than a continuous film then the observed electrochemical response would be dominated by the material exhibiting faster electron transfer kinetics.

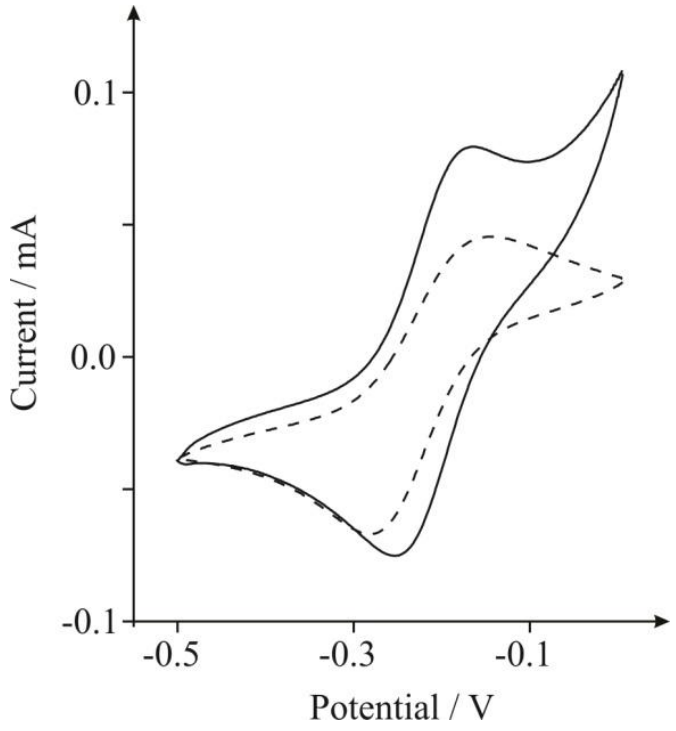

Figure 8.1 *Cyclic voltammetric profiles recorded utilising 1 mM hexaammine-ruthenium (III) chloride in 1 M KCl, obtained using a bare (no graphene) Ni film electrode (solid line) and a CVD-graphene electrode (dashed line). Scan rate: 100 mVs^{-1} (vs. SCE).*

Next the 'inner-sphere' redox probe, [3, 6] 1 mM potassium ferrocyanide (II) in 1 M KCl, is considered utilising the given electrodes. As observed in Figure 8.2A the voltammetric response of the CVD-graphene is distinctly different to that observed in Figure 8.1. Note that Figure 8.2A was only obtained after continually cycling the potential across the electrochemical window.

Again a control experiment was performed where the response of the CVD-graphene electrode was compared with that of a bare Ni electrode (no graphene). [5] As evident in Figure 8.2B no voltammetric peaks are observed, which is as expected given the lack of literature on Ni electrodes towards this target analyte. It is clear that electron transfer is dominating on the graphene and that the underlying Ni film, which the graphene is supported/grown upon, is not contributing to the electrochemical response. It is important to contrast the differing behaviours observed using the outer-sphere (see Figure 8.1) and

inner-sphere (see Figure 8.2) electron transfer redox probes, where in the former the voltammetric behaviour is characteristic of a macro-electrode [7] while the latter exhibits a response associated with that of a micro-electrode (see Chapter 1.4.2). [7]

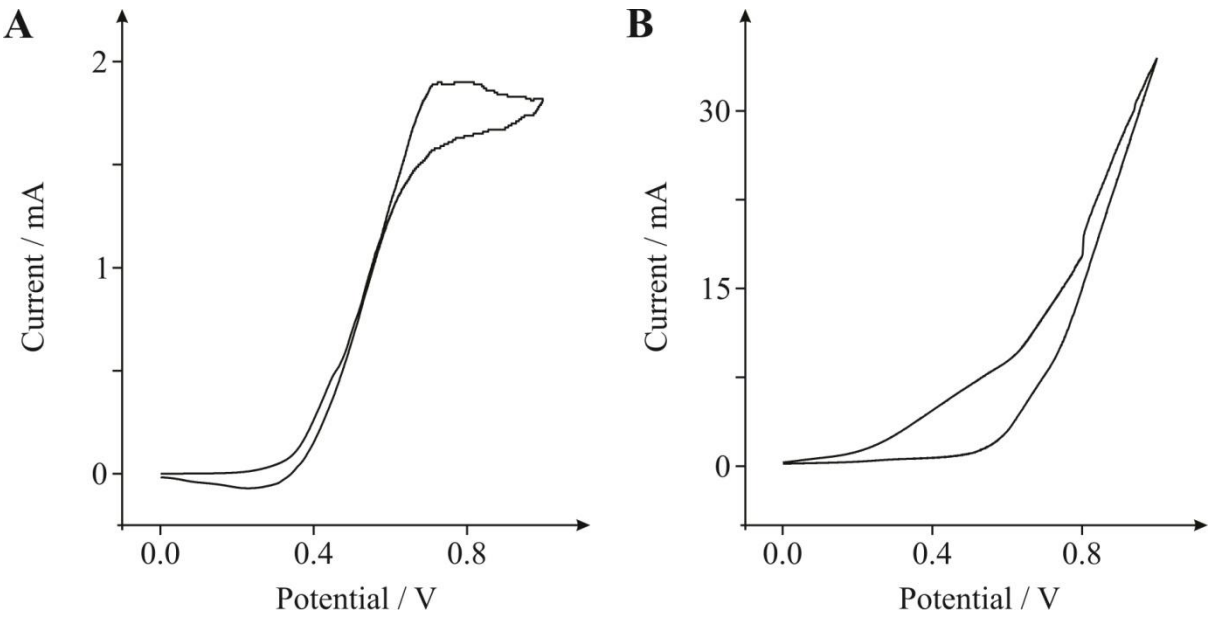

Figure 8.2 *Cyclic voltammetric profiles recorded for 1 mM potassium ferrocyanide (II) in 1 M KCl using a CVD-graphene electrode (**A**) and a bare (no graphene) Ni film electrode (**B**).*
*Scan rate: 100 mVs^{-1} (vs. SCE). Note, the respective $E_{1/2}$ value in **A** is ca. 0.54 ± 0.02 V.*

In order to try and gain further insights, energy-dispersive X-ray spectroscopy (EDX) was utilised on a SEM and an area within the centre of the bare nickel and CVD-graphene electrodes was mapped. Analysis of the bare Ni electrode exhibited a uniform EDX signature indicating the presence of 100 % atomic nickel throughout the sample, as expected. In contrast, when analysing the CVD-graphene electrode, areas were observed where EDX signatures indicated the presence of 100 % nickel atomic composition and other areas where the atomic composition consisted of on average 18.4 % carbon and 81.6 % nickel respectively. At first sight this analysis can be interpreted to infer that the CVD-graphene electrode consists of an underlying nickel film compromised of discrete graphene islands. However since EDX is a relatively deep probe (*ca*. micrometres)

the carbonaceous signatures likely originate from relatively thick graphene layers, *i.e.* few- and multi-layered graphene. Further insights are gained utilising Raman spectroscopy (provided by the manufacturer) [2] on the CVD-graphene, which shows that depending on the location that is probed, a continuous single layer graphene film is observed over the entire area, see Figure 5.11A, while in other areas, few- and multi-layered graphene is observed as depicted in Figure 5.11B where a broad peak for the 2D band is clearly observed, the intensity of which is significantly smaller than the G peak, confirming the presence of multiple layer graphene, [1, 8, 9] *i.e.* graphite is present. This analysis indicates that the CVD-graphene electrode consists of graphitic islands on a continuous film of graphene which are both grown upon a nickel film. Note that the observation of varying layer numbers in CVD grown graphene is in agreement with a previous literature report. [10]

Additionally, important morphological features on the CVD-graphene surface can be readily derived from optical images. [8] Figure 8.3 depicts the variations in the film thickness, which are easily identifiable by the distinct change in colour in the optical image, where the darker regions are resultant of few and multiple layers of graphene due to the increased optical absorption over the surrounding 'single layered graphene' lighter region. [8] Thus the optical image in Figure 8.3 clearly depicts graphitic islands residing on an underlying continuous single layer graphene film, where analysis of the optical image shows that on average these graphitic islands are *ca*. 11.4 μm in diameter (range: 6.3 – 16.3 μm). It is assumed, through inspection of Figure 8.3, that these graphitic islands to be approximately circular in shape and randomly distributed over the graphene film, with an average centre-to-centre separation distance towards each graphitic islands nearest neighbour of *ca*. 19.1 μm (range: 15.0 – 26.3 μm); with a coverage of 1.4 % over the observable optical window.

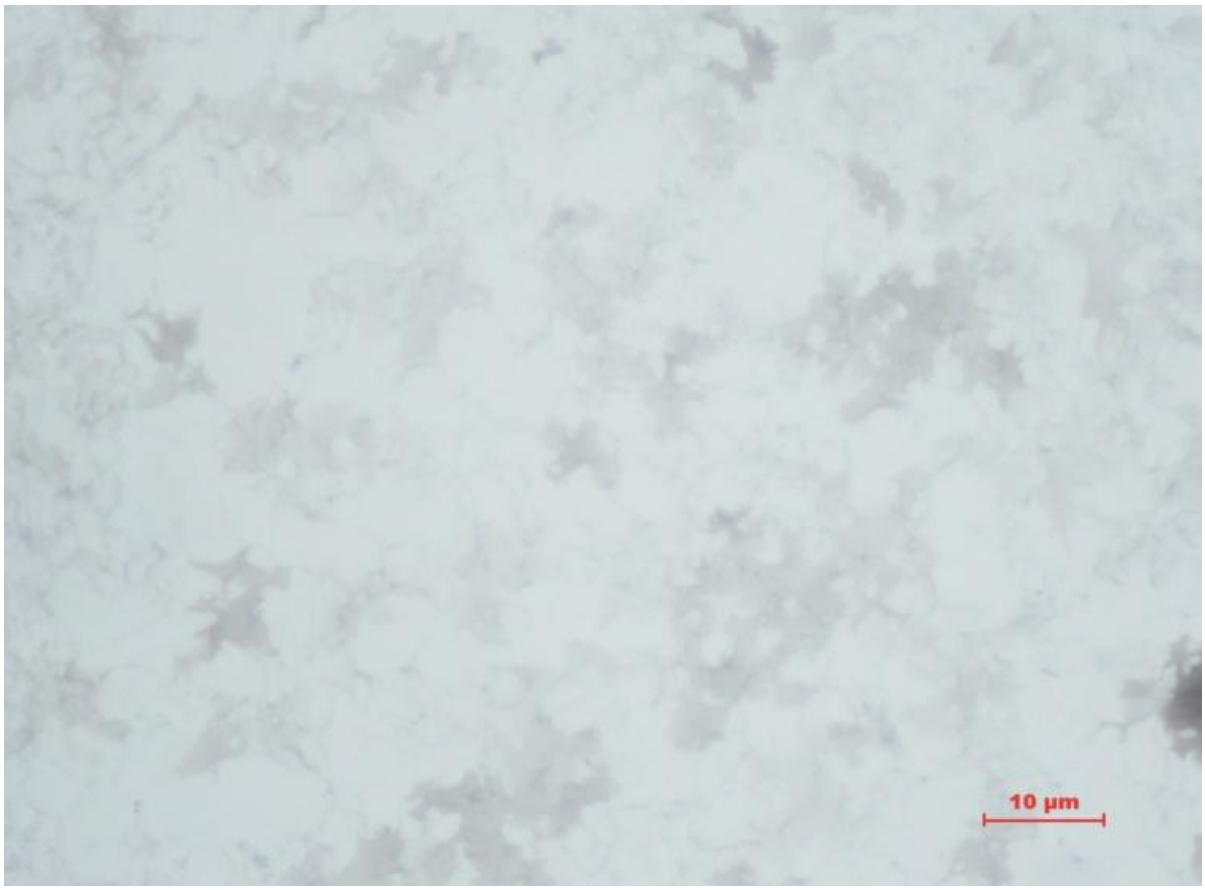

Figure 8.3 *An optical image of the graphitic regions of the CVD-graphene electrode. Image provided by the manufacturer with the CVD-graphene sample.* [2]

Next, the differing electrochemical responses observed using the outer-sphere (Figure 8.1) and inner-sphere (Figure 8.2) redox probes is explored. Firstly, in terms of the former, macro-electrode behaviour is evident where a peak shaped voltammetric response is observed. This can be interpreted in-light of the characterisation of the CVD-graphene (*vide supra*) to be due to the heterogeneity of the surface, where graphitic domains are randomly distributed over that of graphene, which are akin to that of a random microelectrode array; a schematic representation is shown in Figure 8.4. Note that (through knowledge gained in previous chapters) it is inferred that electron transfer dominates at the edge of graphene, such that in terms of a single piece of graphene the edge is highly electro-active while the side (it's basal plane) is effectively electrochemically inert; where the former acts electrochemically akin to that of edge plane- and the latter to that of basal plane-

like sites/defects of HOPG. [11-14] Thus the electro-active sites will be the peripheral edge of the graphene (the origin of electron transfer), and on a continuous film of graphene the main surface area, its side (basal plane), is electrochemically inert. [11-14] Additionally, electro-active sites likely reside at graphene grain boundaries and folded edges, and also where deviation from true graphene exists. As shown in Figure 8.4, in essence, the CVD-graphene mimics the response of a basal plane pyrolytic graphite electrode!

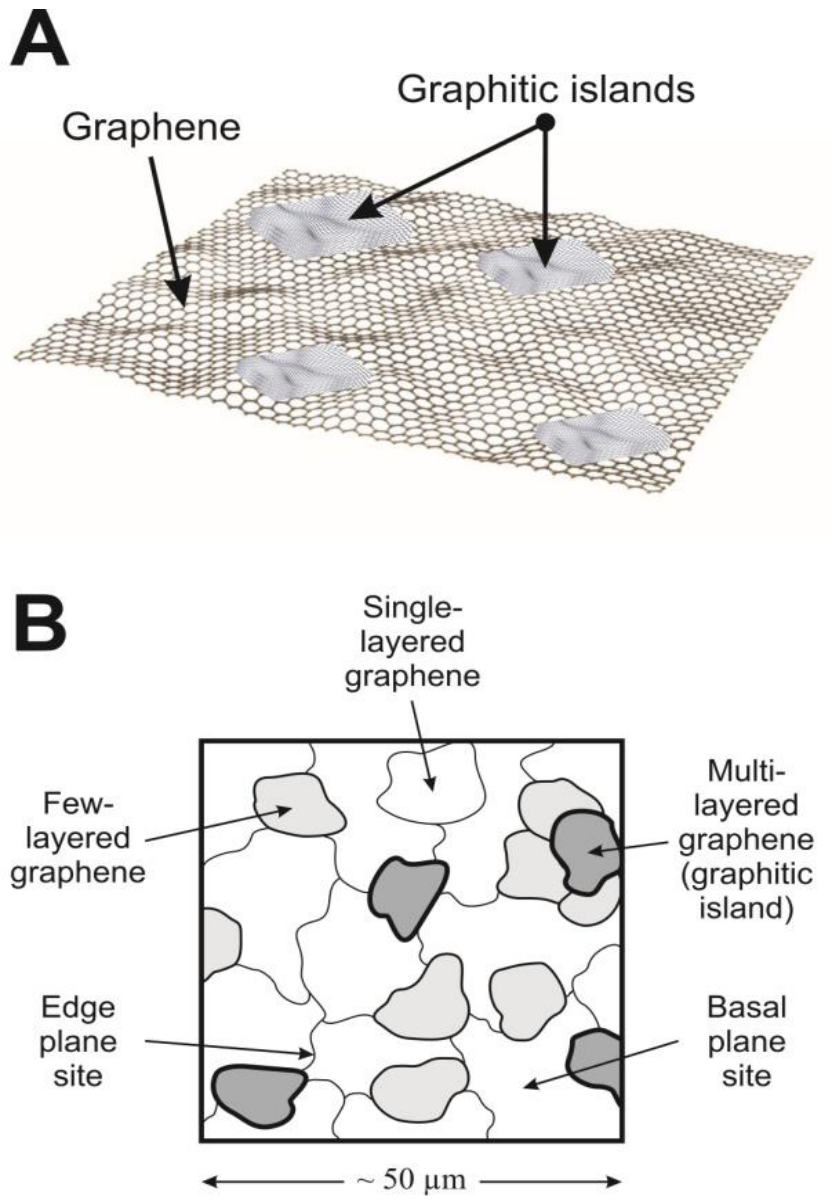

Figure 8.4 *A schematic representation of: (**A**) layered graphitic regions on a graphene film, and (**B**) an underlying graphene surface with few- and multi- layered graphitic islands, indicating the basal and edge plane electron transfer sites. Notice the electrode surface is akin to a HOPG surface.*

The diffusion layer thickness at each graphitic island can be readily estimated from the following equation (adapted from equation (1.32)): [15]

$$\delta = \sqrt{2D\ (\Delta E/v)} \qquad (8.1)$$

where δ is the diffusion layer, D is the diffusion coefficient, ΔE is the potential range over which Faradaic processes occur, and v is the applied voltammetric scan rate. Using the centre-to-centre separation distance and the diameter of the graphitic islands, for adjacent diffusion zones to overlap, δ must be greater than [(19.1 / 2) — (11.4 / 2)] *ca*. 3.9 μm. Thus at the scan rate employed in Figure 8.1 a diffusion layer size of *ca*. 230 μm is evident at each graphitic domain. This results in heavily overlapping diffusion layers and hence the voltammetric response is observed to be that of a macro-electrode of diffusional processes being planar in nature, and a clear reversible/quasi-reversible peak shaped response is observed. This is also verified by the observational dependence of the magnitude of the peak height on the square-root of the scan rate.

In terms of the inner-sphere electron transfer redox probe, differing voltammetric behaviour at the graphitic islands is evident (*vide supra*). This is due to the lack of oxygenated species residing at the graphene edges. The ferro/ferri-cyanide redox probe is classed as a inner-sphere redox probe and is sensitive to the state of the carbon surface, [6] where the presence of oxygenated species can be both detrimental and beneficial towards the electrochemical response of the redox probe; [3, 16] the redox reaction strongly depends on the presence of surface oxides on graphite and is significantly inhibited if they are absent. [6] This is the case seen above in Figure 8.2A, where on initial scans no voltammetric waves are observed using the CVD-graphene unless the potential was swept back and forth across the potential window to create surface oxygenated species; such approaches are common in the literature, observed at many other carbon based electrode surfaces. [17, 18] As the changes in

surface functional groups occur from the potential cycle, the surface now becomes favourable for the redox probe to interact with the CVD-graphene surface. Such approaches have been readily observed for graphite prior to this work, [6] where the outer-sphere electron transfer probe is surface insensitive, thus the edge of graphene and graphitic islands act as a source (or sink) of electrons, while the potassium ferrocyanide redox (inner-sphere) probe is surface sensitive with electron transfer kinetics that are greatly influenced by an electro-catalytic interaction. Since the potential cycling only actives certain parts of the graphitic islands, the overlap of diffusion zones does not occur and consequently the voltammetric response observed is that of a micro-electrode where a steady-state voltammetric profile is evident; a schematic representation of differing diffusion patterns is shown in Figure 8.5.

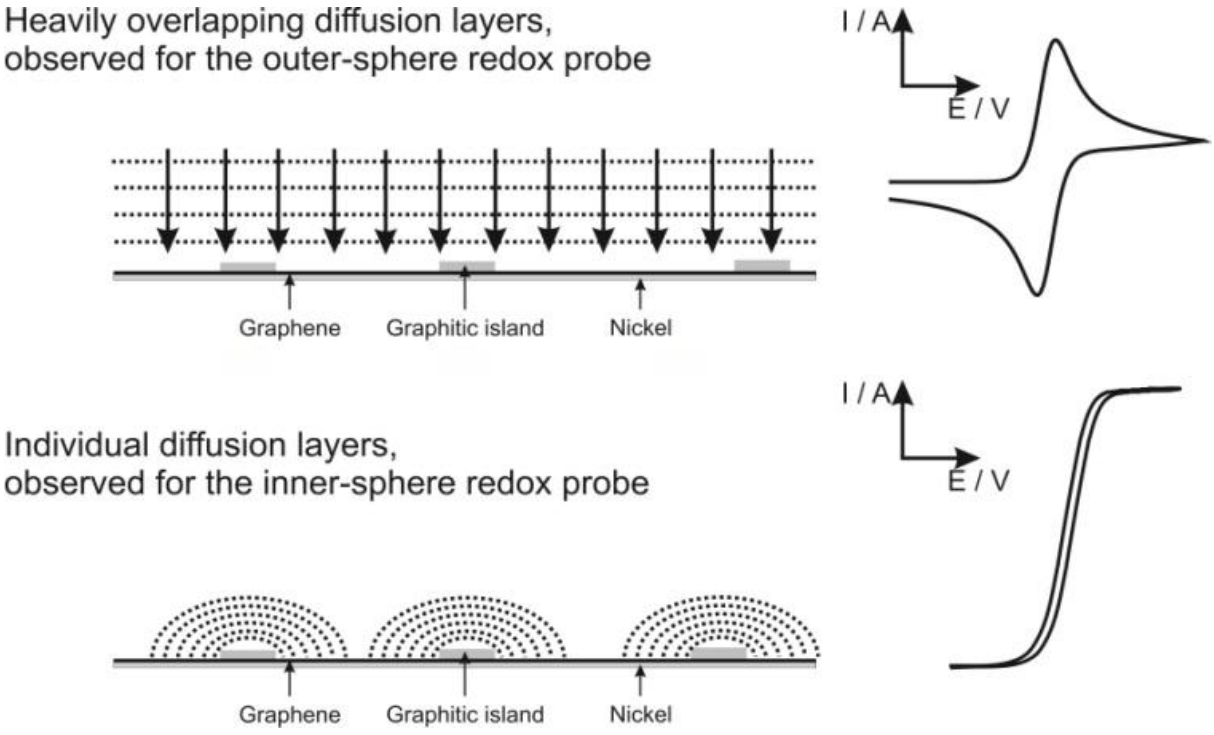

Figure 8.5 *A schematic representation of differing diffusion zones observable towards graphitic islands present upon CVD-graphene.*

Since the graphitic islands are distributed randomly across the CVD-graphene surface, which arise from the fabrication methodology. When using surface sensitive analytes a

steady-state voltammetric response will likely be observed, quite different to that when a non-surface sensitive analyte is utilised, since not many graphitic islands will be potential-cycle activated. However exceptions to this are expected to occur when extensive potential cycling is employed.

8.1.3. CONCLUSIONS

This chapter has demonstrated, with inner-sphere and outer-sphere redox probes, that graphitic islands dominate the electrochemical response of CVD-graphene. This is inferred due to graphene's relative inactivity in comparison to these graphitic regions. One should also be alerted to the reverse case where a non-discrete graphene (and graphitic) covered nickel surface could result in the underlying nickel dominating the electrochemical response towards target analytes, which would of course depend on the electron transfer kinetics of the heterogeneous electrode towards the target analyte. Note that these findings are of great importance on a broader scale and are of general interest for redox reactions on graphene, not only for electrochemistry and sensors. It is clear from the work presented in this chapter that electrochemistry can be implemented as a characterisation tool for a greater understanding of the surface topography of 'graphene' materials under investigation.

8.1.4. REFERENCES

1. W. Li, C. Tan, M. A. Lowe, H. D. Abruna and D. C. Ralph, *ACS Nano*, 2011, **5**, 2264.
2. Internet-Resource, *Graphene Supermarket Ltd.*, Accessed: 04/02/2011; http://www.graphene-supermarket.com.
3. X. Ji, C. E. Banks, A. Crossley and R. G. Compton, *ChemPhysChem*, 2006, **7**, 1337.
4. R. S. Nicholson, *Anal. Chem.*, 1965, **37**, 1351.
5. D. A. C. Brownson and C. E. Banks, *Analyst*, 2010, **135**, 2768.
6. R. L. McCreery, *Chem. Rev.*, 2008, **108**, 2646.
7. R. G. Compton and C. E. Banks, *Understanding Voltammetry*, World Scientific, Singapore, 2007.

8. A. Reina, X. Jia, J. Ho, D. Nezich, H. Son, V. Bulovic, M. S. Dresselhaus and J. Kong, *Nano Lett.*, 2009, **9**, 30.

9. A. C. Ferrari, J. C. Meyer, V. Scardaci, C. Casiraghi, M. Lazzeri, F. Mauri, S. Piscanec, D. Jiang, K. S. Novoselov, S. Roth and A. K. Geim, *Phys. Rev. Lett.*, 2006, **97**, 187401.

10. A. Dato, Z. Lee, K.-J. Jeon, R. Erni, V. Radmilovic, T. J. Richardson and M. Frenklach, *Chem. Commun.*, 2009, 6095.

11. D. K. Kampouris and C. E. Banks, *Chem. Commun.*, 2010, **46**, 8986.

12. P. M. Hallam and C. E. Banks, *Electrochem. Commun.*, 2011, **13**, 8.

13. D. A. C. Brownson and C. E. Banks, *Electrochem. Commun.*, 2011, **13**, 111.

14. A. Ambrosi and M. Pumera, *Phys. Chem. Chem. Phys.*, 2010, **12**, 8943.

15. T. J. Davies, R. R. Moore, C. E. Banks and R. G. Compton, *J. Electroanal. Chem.*, 2004, **574**, 123.

16. I. Yagi, H. Notsu, T. Kondo, D. A. Tryk and A. Fujishima, *J. Electroanal. Chem.*, 1999, **473**, 173.

17. M. C. Granger, M. Witek, J. Xu, J. Wang, M. Hupert, A. Hanks, M. D. Koppang, J. E. Butler, G. Lucazeau, M. Mermoux, J. W. Strojek and G. M. Swain, *Anal. Chem.*, 2000, **72**, 3793.

18. F. Marken, C. A. Paddon and D. Asogan, *Electrochem. Commun.*, 2002, **4**, 62.

8.2. CVD GROWN GRAPHENE *VS*. HIGHLY ORDERED PYROLYTIC GRAPHITE FOR USE IN ELECTROANALYTICAL SENSING

This chapter explores and contrasts the electroanalytical performance of a commercially available CVD grown graphene electrode (CVD-graphene) with that of edge- and basal- plane pyrolytic graphite electrodes constructed from HOPG for the sensing of biologically important analytes, namely *β*-nicotinamide adenine dinucleotide (NADH) and uric acid (UA). Note that this chapter contains published work. [8]

8.2.1. INTRODUCTION

As highlighted in Chapter 8.1, CVD fabricated graphene has been utilised by Ralph *et al.* [1] whom report electron transfer rates towards ferrocenemethanol to be more than ten-fold faster at CVD-graphene over the basal plane of bulk graphite. Since said reports emerged, Dai *et al.* [2] have reported improved electro-catalytic activity and long-term operational stability towards the reduction of oxygen at a nitrogen doped graphene electrode formed *via* CVD when compared to commercially available platinum loaded carbon, furthermore, Loh *et al.* [3] have beneficially utilised an anodised epitaxial graphene electrode towards the improved sensing of DNA.

Chapter 8.1 showed proof-of-concept that CVD grown graphene (CVD-graphene) is not a continuous layer of graphene, but rather is heterogeneous in nature and has few- and multi-layered graphitic domains which can dominate the electrochemical response; an insight which is only evident when differing redox probes, *viz* inner- and outer- sphere redox probes are employed. [4] This was further explored towards biologically prevalent molecules where again

[8] D. A. C. Brownson, R. V. Gorbachev, S. J. Haigh and C. E. Banks, *Analyst*, 2012, **137**, 833.

these graphitic islands were shown to dominate the observed electrochemical response, see Ref. [5]. Given these insights, one must therefore question the initial literature regarding the beneficial implementation of CVD-graphene (given the knowledge gained in earlier chapters), [1-3] where it is likely the electrochemical response observed is originating from these 'graphitic islands' and other graphite-like impurities comprising the electrode surface. Furthermore, one ponders the electroanalytical implications of said impurities (and consequential beneficial response), with respect to the performance of CVD-graphene *versus* HOPG.

This chapter now explores the analytical utility of commercially available CVD grown graphene (CVD-graphene). The electroanalytical performance of the CVD-graphene is compared against that of widely used EPPG and BPPG electrodes of HOPG towards NADH and UA, the monitoring of which is of considerable importance in a plethora of areas where electrochemistry is conveniently utilised.

8.2.2. RESULTS AND DISCUSSION

8.2.2.1. RESULTS

First, the electrochemical properties of the electrode materials of interest are recorded towards 100 μM NADH in pH 7 PBS: note that NADH is of great significance since it is utilised in a diverse range of over 300 dehydrogenase-based biosensors which are dependent on the coenzyme (NADH) and its oxidised form (NAD^+). [6] Figure 8.6A depicts typical cyclic voltammetric responses obtained where it is evident the EPPG electrode exhibits an oxidation wave at *ca.* 0.45 V which is in excellent agreement with *ca.* 0.47 V as reported in the literature. [5-7] In contrast, at the BPPG electrode a peak is observed at *ca.* 0.81 V, which is also in good agreement with previous reports of *ca.* 0.82 V. [5-7] The CVD-graphene electrode exhibits an

oxidation peak towards NADH at *ca.* 0.41 V which is in agreement with previous work (*ca.* 0.48 V). [5]

Next the electroanalytical performance of the electrode materials of interest is considered towards the electrochemical sensing of NADH. Figure 8.6B depicts the cyclic voltammetric response of the CVD-graphene electrode showing successive additions (10 μM increments) of NADH into a pH 7 PBS where it is evident that subsequent additions of NADH lead to an increment in the voltammetric peak height. Analysis of the peak height (I_P) as a function of concentration is depicted in Figure 8.6C, which reveals a linear response over the range of 10 to 100 μM (I_P (Acm^{-2}) = 2.61 x 10^{-1} Acm^{-2}/M – 1.20 x 10^{-6} Acm^{-2}; R^2 = 0.988, N = 3) where based on three-sigma, a LOD was determined to be 7.21 μM. The electroanalytical performance of an EPPG electrode was also explored, which is depicted in Figure 8.6C, where again a linear response is observed over the range of 10 to 100 μM (I_P (Acm^{-2}) = 2.18 x 10^{-1} Acm^{-2}/M + 7.35 x 10^{-7} Acm^{-2}; R^2 = 0.995, N = 3) with a LOD of 4.82 μM (three-sigma). Furthermore, use of a BPPG electrode over the range of 10 to 100 μM was linear (I_P (Acm^{-2}) = 1.45 x 10^{-1} Acm^{-2}/M + 7.08 x 10^{-7} Acm^{-2}; R^2 = 0.989, N = 3) and the resultant LOD (three-sigma) was determined to be 7.03 μM. Note that both responses using the EPPG and BPPG electrodes are in favourable agreement with previous studies, [6, 8-10] and that the concentration range utilised is of analytical relevance. [11] The LOD values obtained are clearly comparable to those found at other carbon materials towards the electrochemical sensing of NADH; a LOD range of between 0.15 and 8 μM is readily observed within the literature, analysis *via* cyclic voltammetry. [6, 8-10]

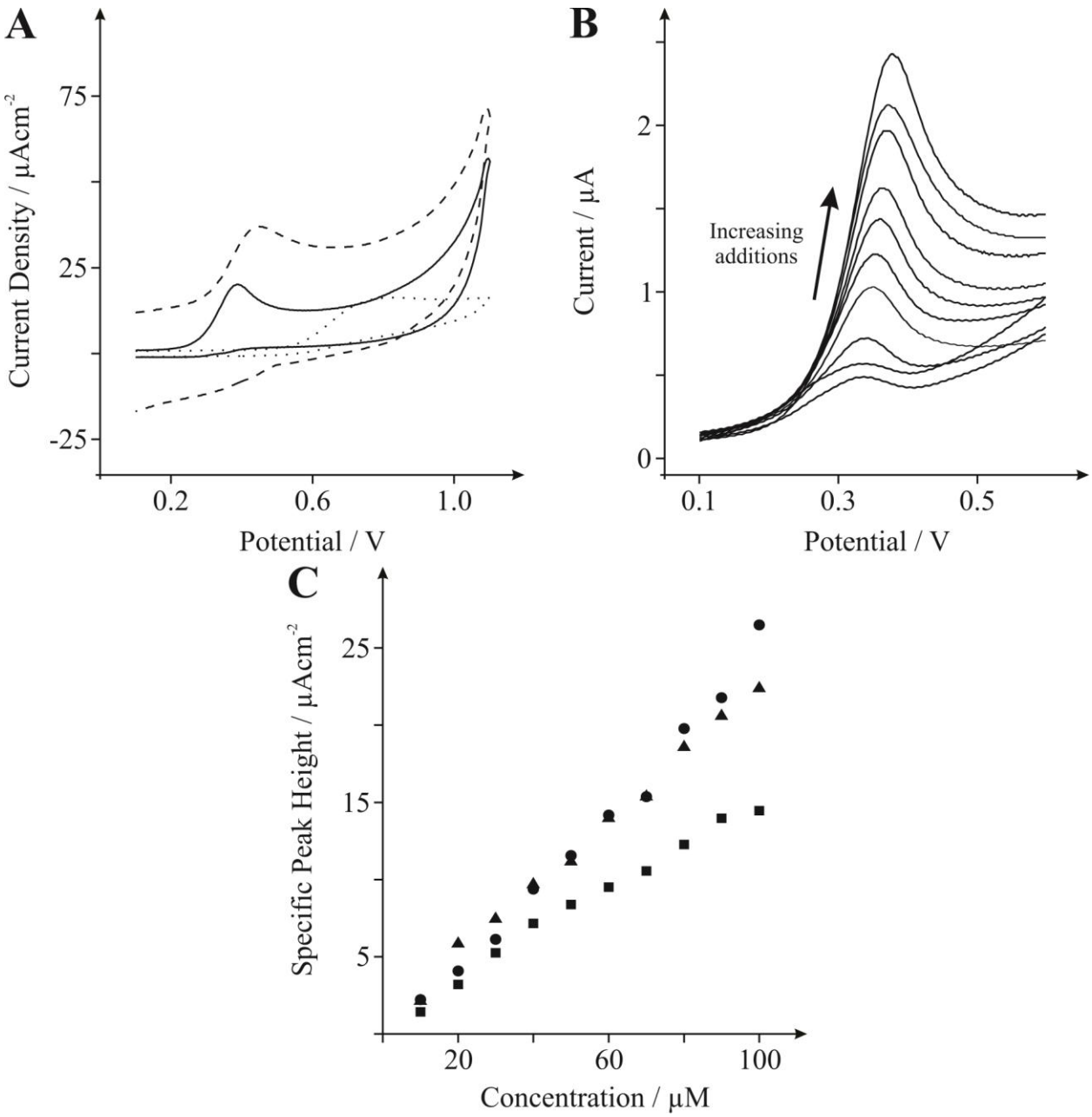

Figure 8.6 *(**A**) Cyclic voltammetric profiles recorded towards 100 µM NADH in pH 7 PBS utilising an EPPG (dashed line), a BPPG (dotted line) and a CVD-graphene (solid line) electrode. (**B**) Cyclic voltammetric profiles recorded towards successive additions of 10 µM NADH into a pH 7 PBS (10 to 100 µM) at a CVD-graphene electrode. Note, as the concentration of NADH is increased the peak potential can be observed to shift to more positive potentials, this reflects the electrochemical irreversibility of the electrochemical reaction.* [6] *(**C**) Calibration plots depicting the peak height as a function of concentration, obtained via cyclic voltammetric measurements performed using an EPPG (triangles), a BPPG (squares) and a CVD-graphene (circles) electrode towards the detection of NADH. All data obtained at a scan rate of 100 mVs^{-1} (vs. SCE).*

The electroanalysis of UA is now considered. UA is a neurochemical which is commonly encountered in biological samples and is the primary end product of purine metabolism, [12] unusual levels of UA can be indicative of several illnesses such as hyperuricaemia, gout and Lesch-Nyhan disease, [13] thus making its detection and quantification an important issue in clinical medicine. [12] First, as above, the electrochemical properties of the electrode materials of interest were characterised with regards to the analyte (100 µM UA in pH 7 PBS) where *via* cyclic voltammetric analysis (data not shown) oxidation peaks were present at *ca.* 0.32, 0.29 and 0.54 V when utilising CVD-graphene, EPPG and BPPG electrodes respectively. The responses obtained at EPPG and BPPG electrodes are in excellent agreement with previous literature, [5, 14] furthermore, the oxidative peak potential observed using the CVD grown graphene electrode (CVD-graphene) is in strong agreement with previous work (*ca.* 0.41 V). [5]

Finally, as per above, the electroanalytical performance of the electrode materials of interest were explored towards the electrochemical sensing of UA. Figure 8.7A depicts the cyclic voltammetric response observed through successive additions (10 µM increments) of UA into a pH 7 PBS at the CVD-graphene electrode. As depicted in Figure 8.7B a linear response is obtained at the CVD-graphene electrode over the range of 10 to 100 µM (I_P (Acm^{-2}) = 4.79 x 10^{-1} Acm^{-2}/M + 7.11 x 10^{-7} Acm^{-2}; R^2 = 0.971, N = 3) where again based on three-sigma a LOD was determined to be 8.84 µM. Also depicted in Figure 8.7B are the linear responses (over the range of 10 to 100 µM) of the EPPG (I_P (Acm^{-2}) = 6.11 x 10^{-1} Acm^{-2}/M + 5.08 x 10^{-7} Acm^{-2}; R^2 = 0.998, N = 3) and BPPG (I_P (Acm^{-2}) = 3.32 x 10^{-1} Acm^{-2}/M + 1.78 x 10^{-6} Acm^{-2}; R^2 = 0.994, N = 3) electrodes, which result in the respective LOD values of 2.65 and 5.03 µM (three-sigma). Again, note that the range utilised is of significant analytical

relevance and that the responses obtained are clearly comparable to those found at other carbon materials towards the electrochemical sensing of UA. [15-18]

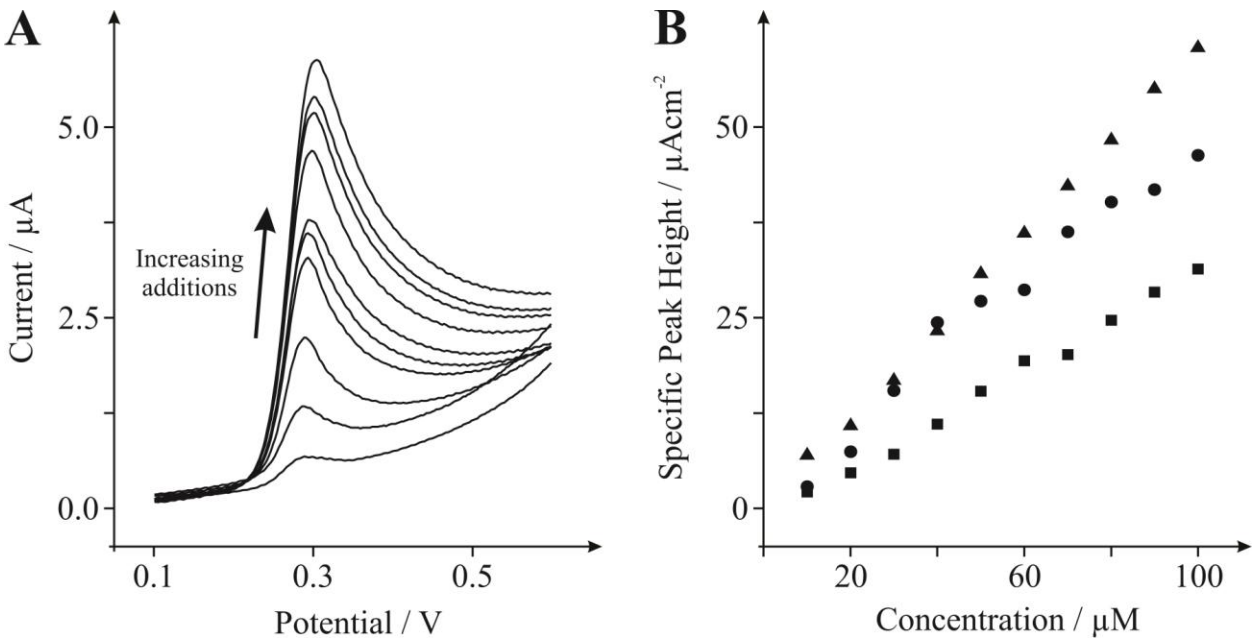

Figure 8.7 *(**A**) Cyclic voltammetric profiles recorded towards successive additions of 10 µM UA into a pH 7 PBS (10 to 100 µM) at a CVD-graphene electrode. (**B**) Calibration plots depicting the peak height as a function of concentration, obtained via cyclic voltammetric measurements performed using an EPPG (triangles), a BPPG (squares) and a CVD-graphene (circles) electrode towards the detection of UA. Scan rate 100 mVs^{-1} (vs. SCE).*

Note that the inter-reproducibility of the CVD-graphene substrate was explored towards the oxidation of 50 µM UA where a % RSD in the analytical signal of 22.3 % (N = 3) was obtained, which is somewhat higher than that reported in the literature at EPPG (8 %) [19] and is notably above the typically accepted analytical RSD of 5 %.

8.2.2.2. DISCUSSION

Table 8.1 depicts the electroanalytical responses observed towards the target analytes where there appears to be no significant difference between the sensitivity (Acm^{-2}M^{-1}) observed at EPPG towards the target analyte compared with that at CVD-graphene. In fact, for the case of

NADH, the CVD-graphene appears to mimic that of the EPPG (*viz* Table 8.1), while for UA the EPPG electrode has a marginal advantage in terms of analytical performance.

Table 8.1 *Comparison of the analytical sensitivities and resultant LODs (based on three-sigma) obtained at the various electrode materials towards the electroanalysis of NADH and UA.*

Electrode Material	Sensitivity/$Acm^{-2}M^{-1}$	LOD (3σ)/μM
NADH:		
CVD-graphene	0.26	7.21
EPPG	0.22	4.82
BPPG	0.15	7.03
UA:		
CVD-graphene	0.48	8.84
EPPG	0.61	2.65
BPPG	0.33	5.03

In the case of NADH, its electrochemical oxidation at carbonaceous surfaces is relatively insensitive to surface oxygenated species (see later) and the most important parameter is the electronic properties of the respective electrode material, specifically the density of states (DOS). [6, 20] The characteristic oxidation responses observed at the electrode materials of interest (detailed in Figure 8.6A) are thus as expected, given that the improved electrochemical response (lower over-potential) observed at EPPG relative to that of BPPG is widely reported and well known to be due to a high global coverage of edge plane sites on the former over the latter; which consequently leads to an improved DOS and fast heterogeneous electron transfer kinetics. [21, 22] Interestingly, the response observed at CVD-graphene mimics that of the EPPG electrode, which owing to the relative insensitivity of NADH (predominantly dependent on DOS) is most likely attributed to similar electronic structures of the electrode surfaces, in which case the greater sensitivity observed at the CVD-graphene over that of the BPPG can (as with EPPG) be inferred to be due to an improved electronic structure (greater global coverage of edge

plane sites) at the former over that of the latter. To gain further insight and to allow the influence of the lack of oxygenated species possessed by the CVD-graphene electrode (low O/C ratio of 0.073) to be de-convoluted, oxygenated species were introduced onto the surface of the CVD-graphene electrode *via* repeatedly cycling throughout the voltammetric window. Such an approach is commonly employed in the literature, observed at many other carbon based electrode surfaces. [23, 24] Figure 8.8 depicts the response where it is evident that with successive cycles (thus the introduction of surface oxygenated species) there is no improvement in the electrochemical response (*viz* reduction in the over-potential) and alternatively fouling of the electrode is apparent, which is commonly reported in the literature to be due to the presence of polar oxygen-containing functionalities on the electrode surface that allow adsorption of the oxidised form of NADH on the surface, hindering heterogeneous charge transfer, which results in a sensor that lacks sensitivity due to it becoming inactive as the analysis proceeds. [6, 25] Thus in this case, the oxygenated species introduced are detrimental towards the electrochemical oxidation of NADH. Note that the type of carbon oxygenated species that reside is of key importance given that literature reports [26] have shown specific oxygenated species to be problematic and detrimental towards the electrochemical performance, whilst other work [20] has shown that the inclusion of specific surface oxygenated species can catalyse the electrochemical oxidation.

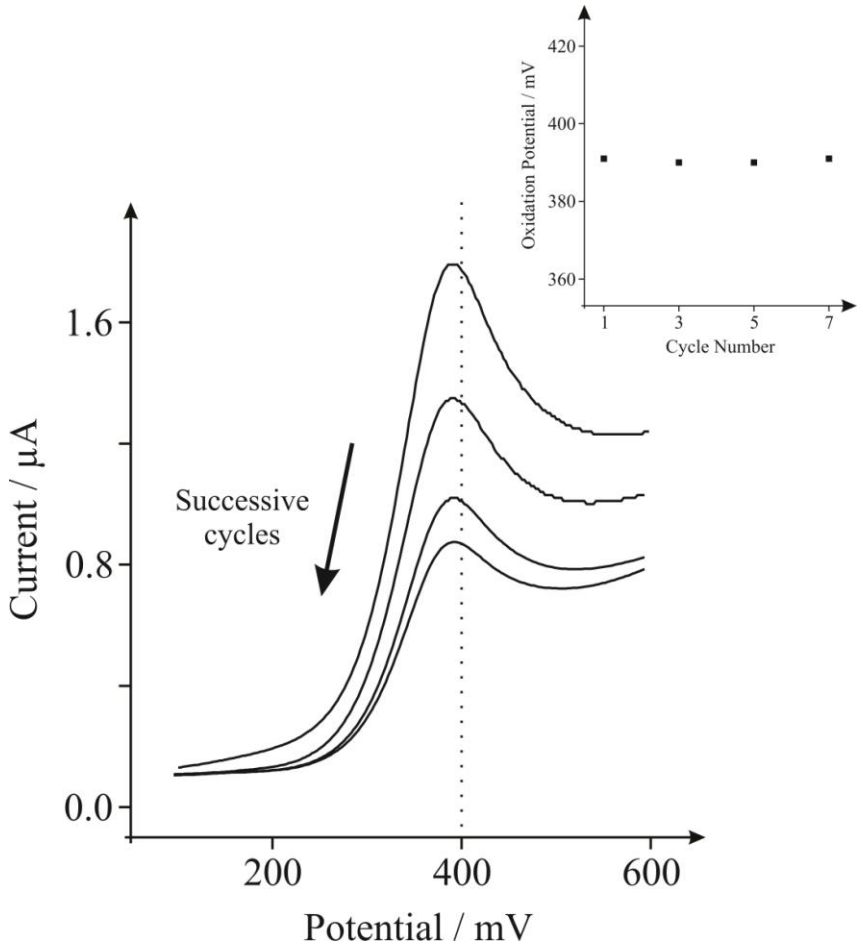

Figure 8.8 *Cyclic voltammetric profiles recorded towards 100 µM NADH in pH 7 PBS utilising a CVD-graphene electrode, showing the effect of continually cycling across the potential window (between – 0.2 V and + 1.1 V). Scan rate 100 mVs^{-1} (vs. SCE). Inset: relationship between the oxidation peak potential and the respective cycle number.*

Insights can be gained through measuring the heterogeneous electron transfer rate constant (k^0) of the CVD-graphene substrate, which was found in Chapter 8.1.2 to correspond to *ca.* 2.51 x 10^{-3} cm s^{-1}. Such a value initially indicates a quasi-reversible electrochemical process, but to fully determine if this is the case one turns to the classic work of Matsuda and Ayabe [27] which considers the rate of mass transport of the electroactive species to a macro-electrode surface. The parameter, ζ, is related to the electron transfer rate, k^0, the diffusion coefficient of the electroactive species, D, and the applied voltammetric scan rate, v, by equation (1.43) where

the reversible limit corresponds to $\zeta \geq 15$ and the quasi-reversible limit is $15 > \zeta > 10^{-3}$. Thus in this case the electrochemical process has quasi-reversible electrode kinetic behaviour. Based on the method outlined in Ref. [28, 29] the global % coverage of edge-plane defects, Θ, on the electrode surface may be approximated from:

$$\% \Theta edge = \left(k_{eff}/k_{edge}\right) \times 100 \qquad (8.2)$$

which provides a value of *ca.* 0.6 % on the CVD-graphene surface, which is slightly less than that reported at a HOPG surface (1 – 10 %). [28]

Further insights are gained *via* AFM of the CVD-graphene, where as depicted in Figure 8.9 a highly fractal surface is observed where multilayer planes of graphene are orientated vertically on the surface with AFM software indicating an average RMS surface roughness of 16 nm with an arithmetic average roughness, R_a, of 12.1 nm. The RMS value observed at the CVD-graphene surface is somewhat deviated from that reported at HOPG electrodes (*ca.* 0.6 nm) indicating that the former has a rougher electrode surface. [30, 31] Note, in Chapter 8.1 it was inferred that the CVD-graphene surface was a continuous layer of graphene upon which few- and multi- layered graphene resided (*viz* graphitic islands) which were electrochemically activated, giving rise to unique voltammetry (see Figure 8.2A). AFM images (see Figure 8.9) reveal that actually a highly disordered graphene surface is evident with graphene orientated both parallel and perpendicular to the surface. Note that prior chapters have *indicated* that the basal like sites of graphene are relatively inert under standard voltammetric conditions while the edge of the graphene is highly electrochemically reactive, thus a truly heterogeneous surface is evident. Furthermore, in the case of graphene orientated perpendicular to the surface these sites are highly electrochemically active [4] and when electrochemically activated *via* potential cycling

(see Chapter 8.1 for further details) these represent the main electroactive domains, which due to their few- and multi- layer composition act akin to that of graphitic islands as previously inferred. Note that the potential cycling will only activate *some* and not all of the graphitic islands.

Overall, it is clear that the similar electroanalytical performance (analytical sensitivity) observed at EPPG and CVD-graphene electrodes is most likely due to the similar DOS present at both electrodes: which for the CVD-graphene is as expected given the prevalence of graphitic islands across its surface, [4, 5] which contribute to a large global coverage of edge plane sites (an abundance of electron transfer sites, leading to fast heterogeneous electron transfer) that will closely replicate the composition of a HOPG electrode. [4, 5] Note that from inspection of Table 8.1 the sensitivity of the response for the EPPG and CVD-graphene is similar but there is a difference in the observed LOD, which is due to the high % RSD observed on the latter (*vide supra*). Thus in the case of sensing NADH, there is no significant benefit of utilising a CVD-graphene substrate in terms of analytical performance given the availability of the CVD grown graphene, its cost and high % RSD.

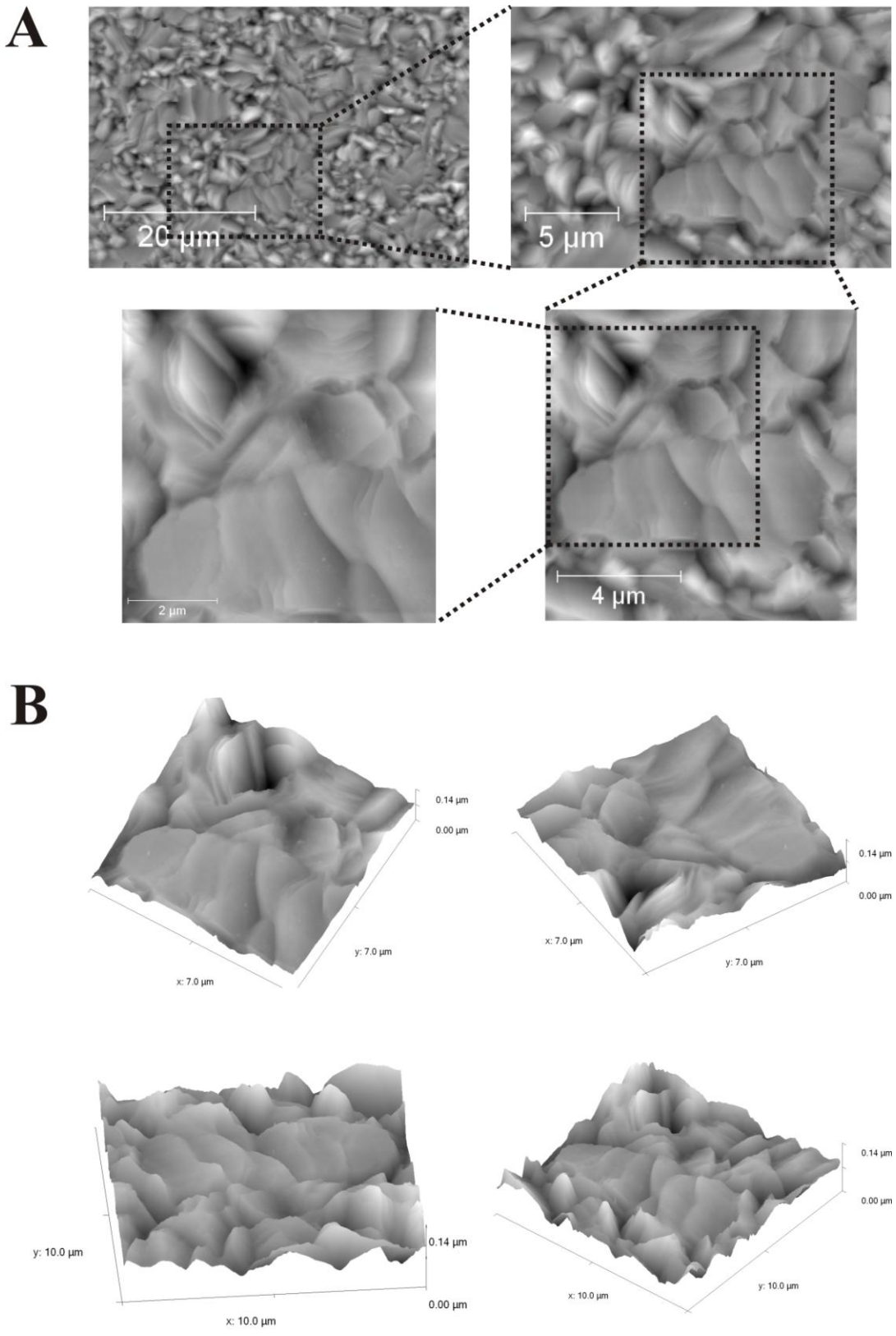

Figure 8.9 *AFM images of the 'as received' commercially available CVD-graphene surface. Observed from various top-down (**A**) and three-dimensional (**B**) perspectives.*

This chapter next considers the electroanalysis of UA at the given electrodes. Note that it is widely reported in the literature that the electrochemical oxidation of UA is highly sensitive to oxygenated species, [5, 32, 33] where improved voltammetry can be observed at electrochemically activated electrodes [32] and at electrode surfaces with large O/C ratios where the oxygenated species residing at the surface would usually act as adsorption/mediation sites. [33] The improved electrochemical performance of the EPPG relative to the BPPG electrode can be attributed to the DOS present, where the EPPG possesses a larger number of electron transfer sites. Thus the improved analytical sensitivity of the CVD-graphene over that of the BPPG can again (as is the case for NADH) be attributed to its improved electronic structure; where, as identified earlier, the CVD-graphene exhibits a similar electronic structure to that of the EPPG. However, through observation of the electroanalytical performances observed above, it is evident that the CVD-graphene exhibits a poor response (in terms of a reduced analytical sensitivity and a higher LOD) relative to the EPPG. Owing to the similar electronic structures of the two materials (*vide supra*) this reduced performance is likely due to the low O/C ratio of the CVD-graphene. [33] To gain further insight, oxygenated species were introduced onto the surface of the CVD-graphene electrode *via* repeatedly cycling around the voltammetric window, as is common practice in the literature. [23, 24] As depicted in Figure 8.10 an improvement in the electrochemical response, *viz* reduction in the over-potential towards less electro-positive potentials (increased electron transfer kinetics), is observed through successive cycling which is likely due to the introduction of oxygenated species on the CVD-graphene surface and thus a greater electro-catalytic activity towards the analyte. It is clear that over a period of 7 cycles there is a reduction in the oxidative peak potential from *ca.* 302 to 290 mV. It is evident that the reduced sensitivity at the CVD-graphene electrode over that of the EPPG electrode, towards the detection

of UA, is likely due to their respective O/C ratios, where favourable interaction is resultantly predominant at the EPPG electrode owing to an increased proportion of oxygenated species relative to that of the CVD-graphene. [34]

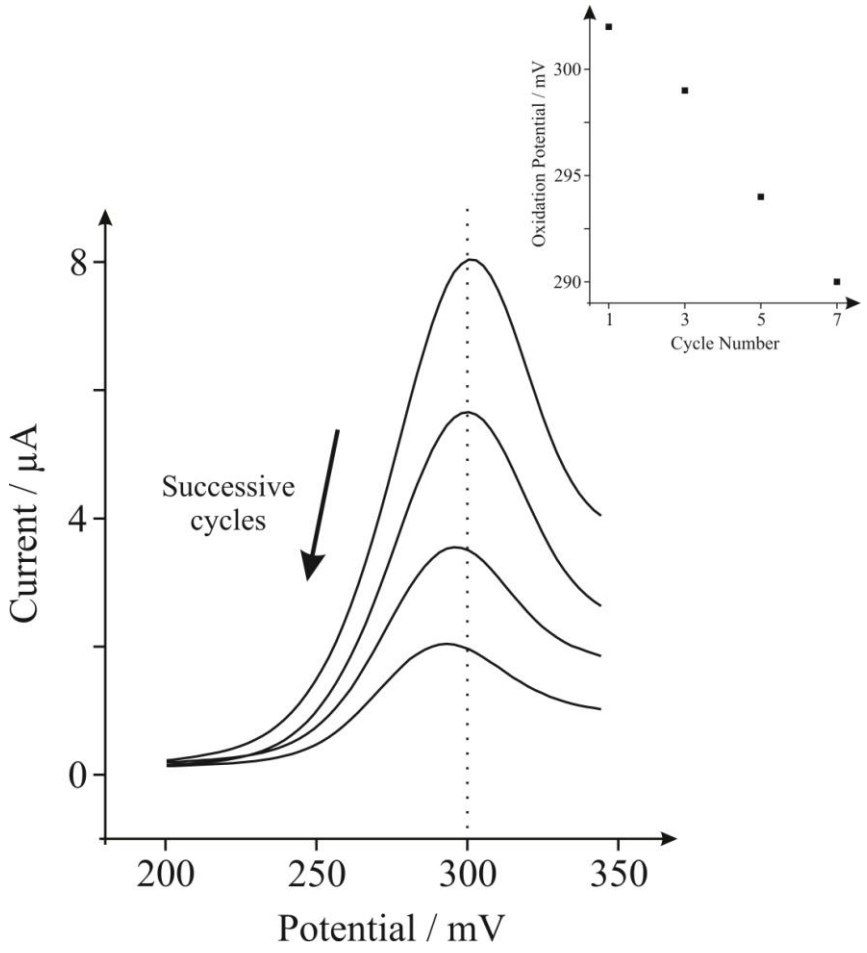

Figure 8.10 *Cyclic voltammetric profiles recorded towards 100 µM UA in pH 7 PBS utilising a CVD-graphene electrode, showing the effect of continually cycling across the potential window (between – 0.2 V and + 1.1 V). Scan rate 100 mVs^{-1} (vs. SCE). Inset: Relationship between the oxidation peak potential and the respective cycle number.*

8.2.3. CONCLUSIONS

This chapter has explored the electroanalytical performance of a commercially available CVD grown graphene electrode (CVD-graphene), and compared the response to EPPG and

BPPG electrodes constructed from HOPG, towards a selection of electrochemically active analytes. It was found that for the analytes studied herein, there appears to be no significant advantage of using CVD-graphene within electroanalysis, which likely arises due to the absence of oxygenated species where it appears that the control of such oxygenated species (either their absence or presence) is of high importance in electroanalysis. It can thus be suggested, that for electrochemical sensing applications, EPPG could be utilised preferably over that of CVD-graphene to obtain enhanced analytical performances owing to its favourable electronic structure, beneficial content of oxygenated species, relative cost and respective % RSD; control experiments utilising EPPG and BPPG of HOPG are clearly a requirement when advantageous responses are reported using CVD-graphene.

8.2.4. REFERENCES

1. W. Li, C. Tan, M. A. Lowe, H. D. Abruna and D. C. Ralph, *ACS Nano*, 2011, **5**, 2264.
2. L. Qu, Y. Liu, J.-B. Baek and L. Dai, *ACS Nano*, 2010, **4**, 1321.
3. E. Dubuisson, Z. Yang and K. P. Loh, *Anal. Chem.*, 2011, **83**, 2452.
4. D. A. C. Brownson and C. E. Banks, *Phys. Chem. Chem. Phys.*, 2011, **13**, 15825.
5. D. A. C. Brownson, M. Gómez-Mingot and C. E. Banks, *Phys. Chem. Chem. Phys.*, 2011, **13**, 20284.
6. C. E. Banks and R. G. Compton, *Analyst*, 2005, **130**, 1232.
7. P. M. Hallam, B. L. Riehl, B. D. Riehl and C. E. Banks, *RSC Adv.*, 2011, **1**, 93.
8. K. S. Prasad, J.-C. Chen, C. Ay and J.-M. Zen, *Sens. Actuators, B*, 2007, **123**, 715.
9. M. G. Zhang, A. Smith and W. Gorski, *Anal. Chem.*, 2004, **76**, 5045.
10. C. M. Maroneze, L. T. Arenas, R. C. S. Luz, E. V. Benvenutti, R. Landers and Y. Gushikem, *Electrochim. Acta*, 2008, **53**, 4167.
11. S. A. Kumar and S.-M. Chen, *Sensors*, 2008, **8**, 739.
12. S.-H. Huang, H.-H. Liao and D.-H. Chen, *Biosens. Bioelectron.*, 2010, **25**, 2351.
13. V. V. S. E. Dutt and H. A. Mottola, *Anal. Chem.*, 1974, **46**, 1777.
14. F. Wantz, C. E. Banks and R. G. Compton, *Electroanalysis*, 2005, **17**, 1529.
15. Z. Wang, Y. Wang and G. Luo, *Analyst*, 2002, **127**, 1353.

16. A. Ozcan and Y. Sahin, *Biosens. Bioelectron.*, 2010, **25**, 2497.
17. P. R. Roy, T. Okajima and T. Ohsaka, *J. Electroanal. Chem.*, 2004, **561**, 75.
18. D. Lakshmi, M. J. Whitcombe, F. Davis, P. S. Sharma and B. B. Prasad, *Electroanalysis*, 2011, **23**, 305.
19. M. S. Goh and M. Pumera, *Anal. Chem.*, 2010, **82**, 8367.
20. M. Wooten and W. Gorski, *Anal. Chem.*, 2010, **82**, 1299.
21. D. A. C. Brownson, L. J. Munro, D. K. Kampouris and C. E. Banks, *RSC Adv.*, 2011, **1**, 978.
22. T. J. Davies, M. E. Hyde and R. G. Compton, *Angew. Chem. Int. Ed.*, 2005, **44**, 5121.
23. M. C. Granger, M. Witek, J. Xu, J. Wang, M. Hupert, A. Hanks, M. D. Koppang, J. E. Butler, G. Lucazeau, M. Mermoux, J. W. Strojek and G. M. Swain, *Anal. Chem.*, 2000, **72**, 3793.
24. F. Marken, C. A. Paddon and D. Asogan, *Electrochem. Commun.*, 2002, **4**, 62.
25. G. P. Keeley, A. O'Neill, M. Holzinger, S. Cosnier, J. N. Coleman and G. S. Duesberg, *Phys. Chem. Chem. Phys.*, 2011, **13**, 7747.
26. M. Pumera, R. Scipioni, H. Iwai, T. Ohno, Y. Miyahara and M. Boero, *Chem. Eur. J.*, 2009, **15**, 10851.
27. H. Matsuda and Y. Ayabe, *Z. Elektrochem.*, 1955, **59**, 494.
28. T. J. Davies, R. R. Moore, C. E. Banks and R. G. Compton, *J. Electroanal. Chem.*, 2004, **574**, 123.
29. P. M. Hallam and C. E. Banks, *Electrochem. Commun.*, 2011, **13**, 8.
30. M. Miranda-Hernandez, I. Gonzalez and N. Batina, *J. Phys. Chem. B*, 2001, **105**, 4214.
31. M. T. McDermott, C. A. McDermott and R. L. McCreery, *Anal. Chem.*, 1993, **65**, 937.
32. J. X. Qiaoa, H. Q. Luoa and N. B. Li, *Colloids Surf., B*, 2008, **62**, 31.
33. J.-L. Chang, K.-H. Chang, C.-C. Hub, W.-L. Cheng and J.-M. Zen, *Electrochem. Commun.*, 2010, **12**, 596.
34. C. E. Banks and R. G. Compton, *Anal. Sci.*, 2005, **21**, 1263.

8.3. ELECTROCHEMICAL PROPERTIES OF CVD GROWN PRISTINE GRAPHENE (ON INERT SUBSTRATE): MONOLAYER- *VS.* QUASI- GRAPHENE

The main aim of this thesis has been to electrochemically characterise the electron transfer properties of graphene based electrodes. Previous chapters have established a strong foundation towards establishing a fundamental understanding of the electrochemistry of various graphene modified electrodes and at graphene films supported on nickel supports. However, although effective control measures have been performed to ensure the de-convoluted electrochemical properties of graphene are reported, contributions from the underlying surface (towards the observed electrochemical response) have hindered a '*true*' and unambiguous understanding of the electrochemistry at graphene. Ideally, to gain such insights one would study the electrochemical response arising from a *pristine single-layer graphene film* that is supported on an *(electrochemically) inert substrate*.

This chapter, which contains published work, [9] reports the electrochemical properties of pristine monolayer and few-layer (termed *quasi*-) graphene grown *via* CVD and transferred using PMMA onto an insulating substrate (silicon dioxide wafers). Characterisation has been performed by Raman spectroscopy, optical spectroscopy, Atomic Force Microscopy and X-ray Photoelectron Spectroscopy, revealing 'true' pristine single-layer graphene (O/C of 0.05) at the former (M-graphene) and pristine *quasi*-graphene (Q-graphene) at the latter (O/C of 0.07); the term "*quasi*-graphene" is coined due to the surface comprising on average 4-graphene-layers (see Chapter 3.1.2). As per Chapters 8.1 and 8.2, a specially designed graphene electrochemical cell is utilised (see Chapter 5.6) to perform electrochemical characterisation of the graphene

[9] D. A. C. Brownson, S. A. Varey, F. Hussain, S. J. Haigh and C. E. Banks, Nanoscale, 2014, *Accepted Manuscript "Electrochemical properties of CVD grown pristine graphene: monolayer- vs. quasi-graphene",* In Press.

surfaces in order to correlate the macroscopic responses of the graphenes, *which has not yet been fully reported within the literature*.

The graphene electrodes are electrochemically characterised using both inner-sphere and outer-sphere redox probes, namely potassium ferrocyanide (II), hexaammine-ruthenium (III) chloride and N,N,N',N'-tetramethyl-*para*-phenylenediamine (TMPD). The electrochemical performances of the graphene electrodes are compared to other available graphitic electrodes, namely that of basal- and edge- plane pyrolytic graphite electrodes constructed from HOPG, with information on heterogeneous rate constants (k^o) obtained. Last, the response of the said electrodes are compared to a double-layered defect abundant graphene film electrode (D-graphene) in order to further establish the influence of 'edge plane like- sites/defects' on the electrochemical performance and properties of *graphene*.

8.3.1. INTRODUCTION

One should be aware through deliberation of the previous chapters within this thesis that 'graphene', a monolayer lattice comprising hexagonally configured sp^2 bonded carbon atoms, [1, 2] is one of the world's thinnest electrode materials. Graphene attracts widespread interest from a plethora of scientific and technological fields due to its reported outstanding and unique array of properties, [2-4] which has resulted in the emergence of a diverse range of graphene based new-generation-devices. [3, 4] The area that is of focus in this thesis is the implementation of graphene for electrochemical applications, where benefits have been extensively reported in energy storage and generation, sensor fabrication and for various electrical nano-devices. [5-7]

However, in order for future enhancements in graphene-based electrochemical applications to emerge, a greater understanding of the fundamental electrochemical properties of

graphene is first required, which will also lead to an improved comprehension of electrochemistry at other carbon-based materials; an invaluable element for the future progression of electrode design. [1] As one should be aware from previous chapters, the main limitations of using graphene are experimental in nature: [8] the first problem (i) is how to 'electrically wire' and connect to such a material as to explore its individual electrochemical properties without interference from undesired contributing factors (such as impurities, alterations in mass transport, or the electrochemical reactivity of underlying surfaces); and the second issue (ii) is how to reduce aggregation of graphene sheets back to their lowest energy confirmation, that is, graphite, due to the strong π-π interactions between the graphene sheets.

A limited number of fundamental studies on the electrochemical properties of graphene exist at the time of writing this thesis (2013); however, such reports generally fall-foul to the above noted experimental limitations or researchers fail to perform the appropriate control experiments with comparable graphitic materials prior to reporting the 'true' electrochemical behaviour of 'graphene'. [1, 9] As such, the key literature is critically summarised below.

The electrochemistry of an individual monolayer graphene crystal (prepared *via* mechanical exfoliation) has been reported by Ralph *et al.* [10] The authors reported a favourable standard heterogeneous electrochemical rate constant, k^o, at a graphene ultra-microelectrode (*ca*. 0.5 cm s^{-1}, as deduced for ferrocenemethanol), indicating that the electrode material exhibited fast heterogeneous electron transfer (HET) kinetics. Comparisons were made to an alternative graphene electrode (fabricated *via* Chemical Vapour Deposition, CVD) and to the basal plane of highly ordered pyrolytic graphite (HOPG) using similar experimental methods, where k^o values were reported as *ca*. 1 and 2 orders of magnitude smaller than that at the exfoliated 'individual graphene sheet' respectively. [10] However, issues in the experimental set-up

are apparent, for example comparison of the graphene ultra-microelectrode (*ca*. 117 μm^2, geometric area) was made to that of larger macro-sized electrodes (the CVD graphene possessed a geometric area of *ca*. 0.19 mm^2, and although the value for HOPG is not reported this is assumed to be 'larger') and thus with respect to point (i) above the origin of the improved k^o is unclear, with changes in mass transport evident and likely to dominate over the electron transfer activity. [1] In another key study the electrochemical characteristics of micrometer sized graphene electrodes, consisting of single- and double- layer mechanically exfoliated graphene flakes, have been reported to exhibit *quasi*-reversible behaviour during voltammetric measurements in potassium ferrocyanide: [11] note that samples were masked with an epoxy resin to leave an electroactive window/area in the order of 50 μm in diameter. The authors demonstrated that while their graphene surface had a low level of defects (broken/dangling/missing bonds *etc*.), fast electron transfer was observed due to the defects that *were* present on the graphene surface (most likely introduced due to the mechanical stresses involved when obtaining graphene from graphite using the exfoliation method) [12] and resultantly similar voltammetric responses were observed at both the single- and double- layer graphene due to only the top layer of the graphenes being exposed. Through further critical analysis of this work it must be noted that the Raman spectrums provided do not indicate the presence of single-layer graphene, rather that of multi-layered graphene samples. [11] Moreover, as was the case with the previous report (and in conflict of point (i) above) [10] mass transport effects likely dominate over the electron transfer activity in this case as a result of setting the graphene in epoxy resin, which likely gives rise to a recessed electrode where the mass transport characteristics will be quantitatively changed. [1, 13]

Fundamental electrochemical studies on large area graphene domains have also been reported. Key insights into the electrochemical reactivity of pristine graphene have been

provided (through work presented in this thesis, see Chapter 7) through the modification of graphene onto basal plane- and edge plane- pyrolytic graphite (BPPG and EPPG respectively) electrodes, as is common place in the literature in order to 'electrically connect' to the graphene under investigation. [9] When utilising a plethora of electroactive probes that are well characterised on graphitic materials, it was found that (in Chapter 7.1) at each of the probes studied pristine graphene exhibited slow HET behaviour, effectively blocking electron transfer at the underlying support substrates; which exhibited either slow (BPPG) or fast (EPPG) HET characteristics in order to fully de-convolute the 'true' graphene contribution. [9] Although the above study diligently reports appropriate control experiments involving unmodified graphite electrodes and varies the electrochemical reactivity of the underlying substrate for greater clarity, [9] in-line with point (i) above, critical analysis suggests that the use of an electrochemically active substrate gives rise to contributing factors affecting the observed response at graphene, which must be de-convoluted. Furthermore, conflicting with issue (ii) above, due to the drop-casting method utilised to immobilise the graphene onto a suitable electrode substrate, it is likely that the pristine graphene sheets coalesce *in-situ* on the substrate surface giving rise to *quasi*-graphene and graphite structures. [1]

Note that *quasi*-graphene (see Chapter 3.1.2) is defined as an intermediate phase between graphene and graphite, [8] generally comprising stacked graphene sheets consisting of ≥ 2 and ≤ 7 layers, [8] where 1 layer implies graphene and ≥ 8 layers implies the structure of graphite (as determined by scanning electrochemical cell microscopy (SECM) and Raman spectroscopy in terms of evolution of the electronic structure). [14, 15-17]

A major advantage of CVD synthesised graphene is that following growth onto a catalytic metal surface, the resultant high quality single layer graphene films are readily

transferable onto a multitude of substrates for electrochemical investigation. [12, 18-20] After transfer onto an insulating substrate the graphene maintains its high quality and subsequently can be characterised *in-situ* prior to electrochemical measurements; overcoming both points (i) and (ii) from earlier once effectively 'housed' in order to connect to the graphene and define the geometric 'working surface area' (see Chapter 5.6). For example, Pumera *et al*. [21] have explored the electron transfer properties of a CVD grown multi-layer graphene film after transfer onto an insulating flexible substrate, demonstrating that it is possible to retain the electrochemical properties of graphene following transfer. [21]

From the above reports it is noted that currently (at the time of writing this thesis, 2013), to the best of the author's knowledge, there are no literature reports concerning the evaluation of graphene's fundamental electrochemical properties through the utilisation of a single layer CVD fabricated macroscopic graphene film that has been subsequently transferred onto an electrochemically inert substrate and through its comparison with multi-layer graphene and graphitic electrodes in order to provide a thorough overview.

Inspired by the limited number of fundamental reports and the benefits of utilising CVD grown graphene after transfer onto a suitable insulating substrate, this chapter investigates the electrochemical characteristics of pristine graphene electrodes; *ensuring the elimination of other contributing factors*. This chapter reports the electron transfer properties of pristine monolayer graphene, grown *via* CVD and transferred onto SiO_2, which is fully characterised *in-situ* prior to experimental use. For the first time, the electrochemical performance of monolayer graphene (M-graphene) is compared to that of a *quasi*-graphene alternative (Q-graphene, comprising *ca*. 4 graphene layers, prepared *via* the same process) and further to that of BPPG and EPPG electrodes constructed from HOPG (all experiments are performed under identical conditions).

This allows the electrochemical activity to be correlated as a function of the number of graphene layers over the macroscopic response. Through the diligent use of appropriate control experimentation and through the determination of HET kinetics at each material, vital insights into the fundamental electrochemistry of graphene and graphitic electrodes are revealed, providing acuity for the future design of carbon based electrodes for both fundamental exploration and the continued development of enhanced electrochemical devices/applications.

8.3.2. CHAPTER SPECIFIC EXPERIMENTAL DETAILS

Test solutions (potassium ferrocyanide (II), hexaammine-ruthenium (III) chloride and N,N,N',N'-tetramethyl-*para*-phenylenediamine (TMPD)) were utilised at a concentration of 1 mM separately in solution, with each containing 0.1 M potassium chloride as the supporting electrolyte.

The diffusion coefficients used for calculations of the k^o_{eff} values were as follows: $Fe(CN)_6^{3-/4-}$, $D = 6.5 \times 10^{-6}$ cm^2 s^{-1}; [22, 23] $Ru(NH_3)_6^{2+/3+}$, $D = 9.1 \times 10^{-6}$ cm^2 s^{-1}; [22, 23] TMPD, $D = 6.6 \times 10^{-6}$ cm^2 s^{-1}. [24] Note, all D values are reported in the presence of 0.1 M KCl supporting electrolyte and k^o_{eff} values are deduced over the entire scan rate range of 5–500 mVs^{-1} unless stated otherwise. A commercial simulation package (Digisim^{TM}) was utilised where appropriate to support the Nicholson analysis (see Chapter 1.4.1) and additionally when this was not suitable to determine k^o_{eff} values.

Prior to utilising the graphenes within this chapter, note that they were fully characterised in-situ, see Chapter 5.4.5. In summary, the fully characterised graphene samples, which have been fabricated *via* CVD and transferred onto an inert SiO_2 substrate utilising a PMMA transfer

process comprise the following. The monolayer graphene film (M-graphene) comprises 97 % single-layer graphene domains with occasional small multi-layered graphene islands and possesses a O/C ratio of *ca*. 0.05, indicating the presence of pristine monolayer graphene. The *quasi*-graphene film (Q-graphene) comprises 95 % graphene coverage with the thickness of individual graphene domains varying from 1 to 7 layers, with an average of 4 graphene layers (on top of which the multi/few-layered graphene islands are situated) and possesses a O/C ratio of *ca*. 0.07, indeed indicating the presence of *quasi*-graphene. Finally, the double-layer graphene film (D-graphene) is comprised of 95% graphene coverage, with an average thickness of two-layers across the graphene domains (O/C ratio of *ca*. 0.03), however with a large number of structural defects/islands giving rise to a high global coverage of edge plane like- sites/defects.

8.3.3. RESULTS AND DISCUSSION

8.3.3.1. ELECTROCHEMISTRY AT MONOLAYER- AND QUASI- GRAPHENE (*VS.* HOPG)

Prior to the electrochemical utilisation of the fully characterised graphene materials (*vide supra*, see Chapter 5.4.5) it was first necessary to incorporate the CVD grown graphene chips into a specially designed graphene electrochemical cell connector, giving rise to the respective graphene electrodes. Figure 5.29 depicts the experimental set-up of the graphene electrochemical cell utilised to fabricate the graphene electrodes and further details are available in Chapter 5.6. The main benefits of this approach is that one is actually electrically wiring to the graphene and thus achieving an efficient electrical connection, but also such that the working electrode area is consistently defined for all the graphene samples being interrogated. Once securely ‘housed’ the design of the electrochemical cell ensures that the graphene material is the only electrochemically active surface that is in contact with the solution during electrochemical measurements. Note that prior work has not fully achieved this, for example, the

connection methodology used to connect/wire to the graphene has been exposed to the solution in some cases, which dominates the electrochemical response and gives rise to false indications of electrochemistry at graphene.

8.3.3.1.2. INNER-SPHERE ELECTROCHEMICAL CHARACTERISATION

This chapter first turns to electrochemically characterising the CVD grown graphene electrodes (M-graphene and Q-graphene) towards the widely used inner-sphere electrochemical redox probe, potassium ferrocyanide (II). Figure 8.11 depicts typical cyclic voltammograms obtained at well-known and widely characterised EPPG and BPPG electrodes (constructed from HOPG). It is evident that the EPPG and BPPG electrodes both exhibit a pair of well-defined redox peaks, with peak-to-peak separations (ΔE_P) of *ca*. 97.7 and 190.4 mV respectively; such values are in excellent agreement with prior literature. [9] Note that the ΔE_P is an important factor to consider in terms of the performance of an electrode material and is used to determine the HET rate, where smaller ΔE_P values represent an increased reversibility in the electrochemistry at the redox probe utilised and thus faster HET kinetics at the given electrode material, which is generally beneficial in numerous instances. The electrochemical response observed at a carbon based electrode material utilising an inner-sphere redox probe is influenced by the density of electronic states (DOS) near the Fermi level of the said material and more significantly by the surface microstructure, for example in terms of the presence of oxygenated species (which are either beneficial or detrimental) or the surface cleanliness. [1, 25] In particular, it is known that the presence of edge plane like- sites/defects on graphitic materials significantly accelerates the observed electron transfer processes (see Chapter 2.1), leading to improved HET at electrodes with a large surface coverage of edge plane like sites. [26, 27]

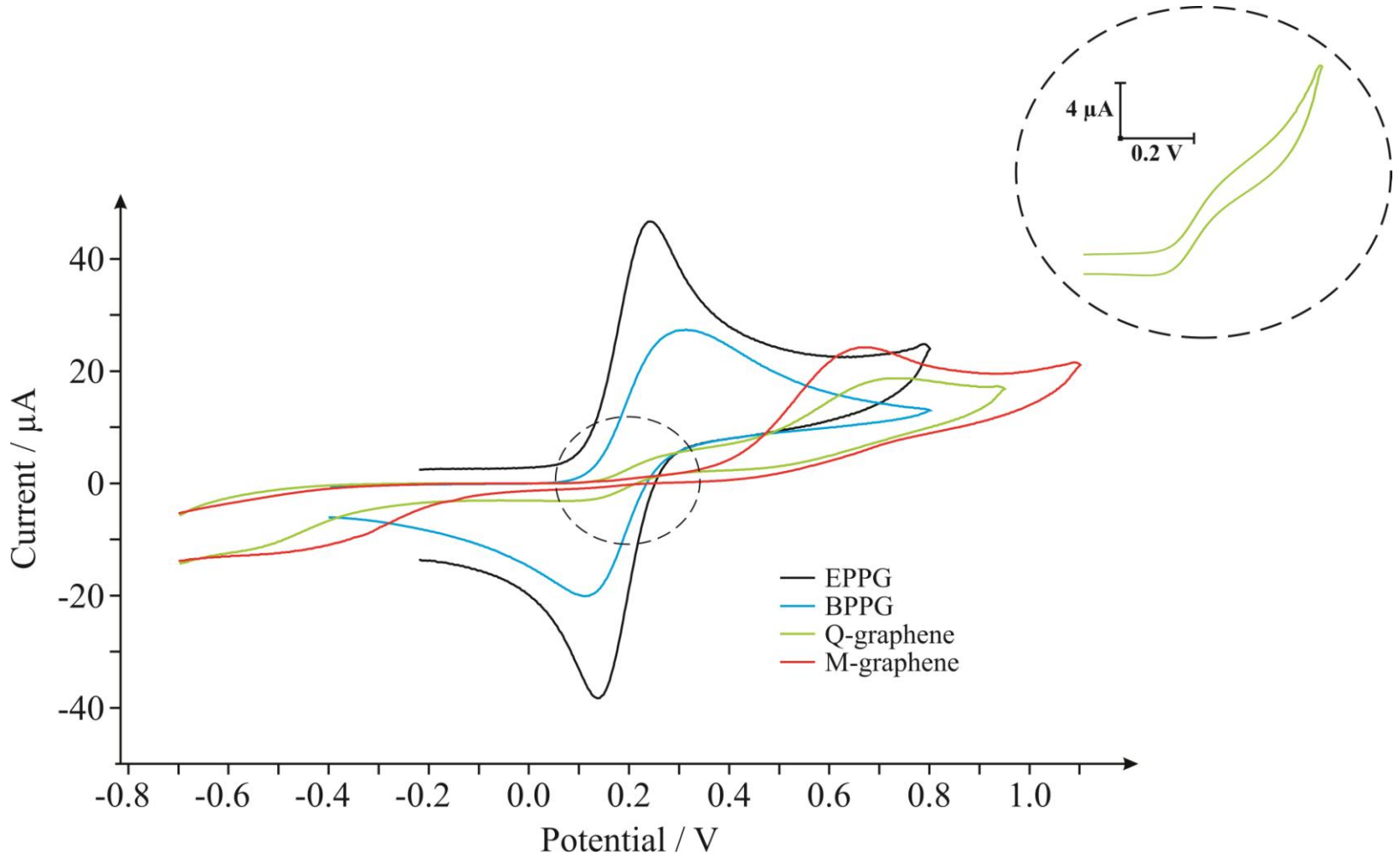

Figure 8.11 *Cyclic voltammetric signatures obtained using potassium ferrocyanide(II) at EPPG (black), BPPG (blue), quasi-graphene (Q-graphene, green) and monolayer graphene (M-graphene, red) electrodes. Scan rate: 100 mVs^{-1} (vs. SCE). The dotted circle shows a zoomed in portion of the voltammetric window, highlighting the heterogeneous electrode response of the Q-graphene, giving rise to two distinctive voltammetric signatures. Shown is a separate scan of the region indicated with Q-graphene, using the same parameters except with limiting the potential window.*

Returning to the response observed at the EPPG and BPPG electrodes in Figure 8.11, the former exhibits superior electrochemical properties over that of the later since the EPPG electrode has a high global coverage of edge plane sites (which exhibit anomalously fast electron transfer rates over that of basal plane sites). [26, 27] Conversely, the BPPG electrode, due to its structure, has a low global coverage of edge plane sites and hence a poor voltammetric activity is exhibited, in terms of a larger ΔE_P, when contrasted to the EPPG. [1, 9]

The electrochemical response of the monolayer graphene (M-graphene) was next explored towards the $Fe(CN)_6^{3-/4-}$ probe. A typical cyclic voltammetric profile is depicted in Figure 8.11, which exhibits a large ΔE_P value of *ca*. 1147.5 mV. This response is unique in terms of the extent of the irreversibility of the redox probe observed at the single-layer graphene electrode, with such a large ΔE_P value indicating slow HET kinetics. The electrochemical response of the *quasi*-graphene (Q-graphene) is also presented in Figure 8.11 which reveals an interesting occurrence. In addition to a large ΔE_P of *ca*. 1242.7 mV, again with the large ΔE_P indicating slow and unfavourable HET kinetics, closer inspection reveals the presence of an additional voltammetric process, which is shown for clarity as an insert within Figure 8.11. This unique latter response indicates changes in the mass transport of the electroactive analyte which is akin to that of a microelectrode, indicating a change from linear (expected for macroelectrodes) to non-linear diffusion (observed at micro/nanoelectrodes), see Chapter 1.4.2. Since the response is only evident when utilising the *quasi*-graphene electrode it is highly likely that the response originates from the multi-layer islands that are comprised of *ca*. 4 graphene layers (see characterisation for Q-graphene) which are supported upon a single underlying layer of graphene. Note that the effect of scan rate was explored upon the voltammetric response where a plot of 'peak height' against 'Log_{10} scan rate' was found to be non-linear over the

experimentally chosen scan rate range, which is due to the mass transport being dominated by non-linear diffusion, as has been observed for nano-band type geometric electrodes (deviation from this is observed when linear diffusion becomes dominant, usually following the application of very fast voltammetric scan rates or if the geometric size is micron-sized). [25] As shown in the insert of Figure 8.11, the response is distinctively and quantitatively different from that observed in the case of the EPPG and BPPG despite comprising the same electrode area. If one assumes that such a graphene island is comprised of (on average) four graphene layers, where only the edge plane sites are active and neglect any defects upon the basal sheets, [26, 27] one has an electrode which is nanoscopic in width and microscopic in length, akin to a nanoband type electrode. As such, the Faradaic current can be predicted by the following equation for the current at a hemi-cylinder of equivalent area: [28]

$$i = 2\pi nFDCl\left[1/(Ln4\Theta)\right] \qquad (8.3)$$

where n is the number of electrons involved in the reaction, F is the Faraday constant, D is the diffusion coefficient of the electroactive species, C the concentration of the redox probe, l (cm) is the length of the micro/nanoband, and $\Theta = Dt/(w/\pi)^2$, where w (cm) is the width of the band and $t = RT/Fv$, where v is the voltammetric scan rate. From inputting the typical geometric features of the graphene island exhibited in this case (8.64 μm length (based on an average island diameter of 2.75 μm), 4 layers thick (1.36 nm)) into equation (8.3) the current predicted is 213.0 nA for one *quasi*-graphene island. Hence, the response observed in Figure 8.11 (insert) is a multiple of equation (8.3), since there is more than one such graphene island comprising the electrode surface. As such, equation (8.3) can be adapted to be $i_{graphene} = i \times N$, where $i_{graphene}$ is the current observed for the graphene surface, i is defined by a graphene island (equation (8.3))

and N is the number of graphene islands comprising the electrode surface. Such an arrangement is similar to that of a micro/nano electrode array where the main consideration is the diffusional zones and their interaction between neighbouring micro/nano electrodes. Since the observed voltammetric profile (insert of Figure 8.11) is clearly sigmoidal shaped, it is highly likely that the diffusional zones do not interact. [25]

It is important to note that in the case of inner-sphere redox probes the electrochemical response obtained is dependent on both the electronic structure and the content of oxygenated species comprising carbonaceous electrode materials (see Appendix A.1). In the case of *quasi*-graphene (Q-graphene), the structural composition satisfies both these conditions and as such one can observe two voltammetric profiles due to the heterogeneous nature of the graphene surface; the response of the graphene islands with adequate carbon-oxygen content and also the response of the underlying supporting graphene (which exhibits a similar voltammetric characteristic to that observed at the pristine monolayer graphene electrode, M-graphene) which has a very low proportion of edge plane defects across its surface and a level of suitable surface oxygen groups residing at these sites, thus overall exhibits large/unfavourable ΔE_P values and electrochemical properties.

8.3.3.1.3. OUTER-SPHERE ELECTROCHEMICAL CHARACTERISATION

Next, the electrochemical characterisation of the graphene electrodes is considered using the outer-sphere redox probes TMPD and hexaammine-ruthenium(III) chloride. This work utilises these well-known and widely characterised outer-sphere electrochemical redox systems due to the outer-sphere system being dependent only on the electronic structure (DOS) of carbon based electrode materials and thus the degree of edge plane sites, which offers useful insights.

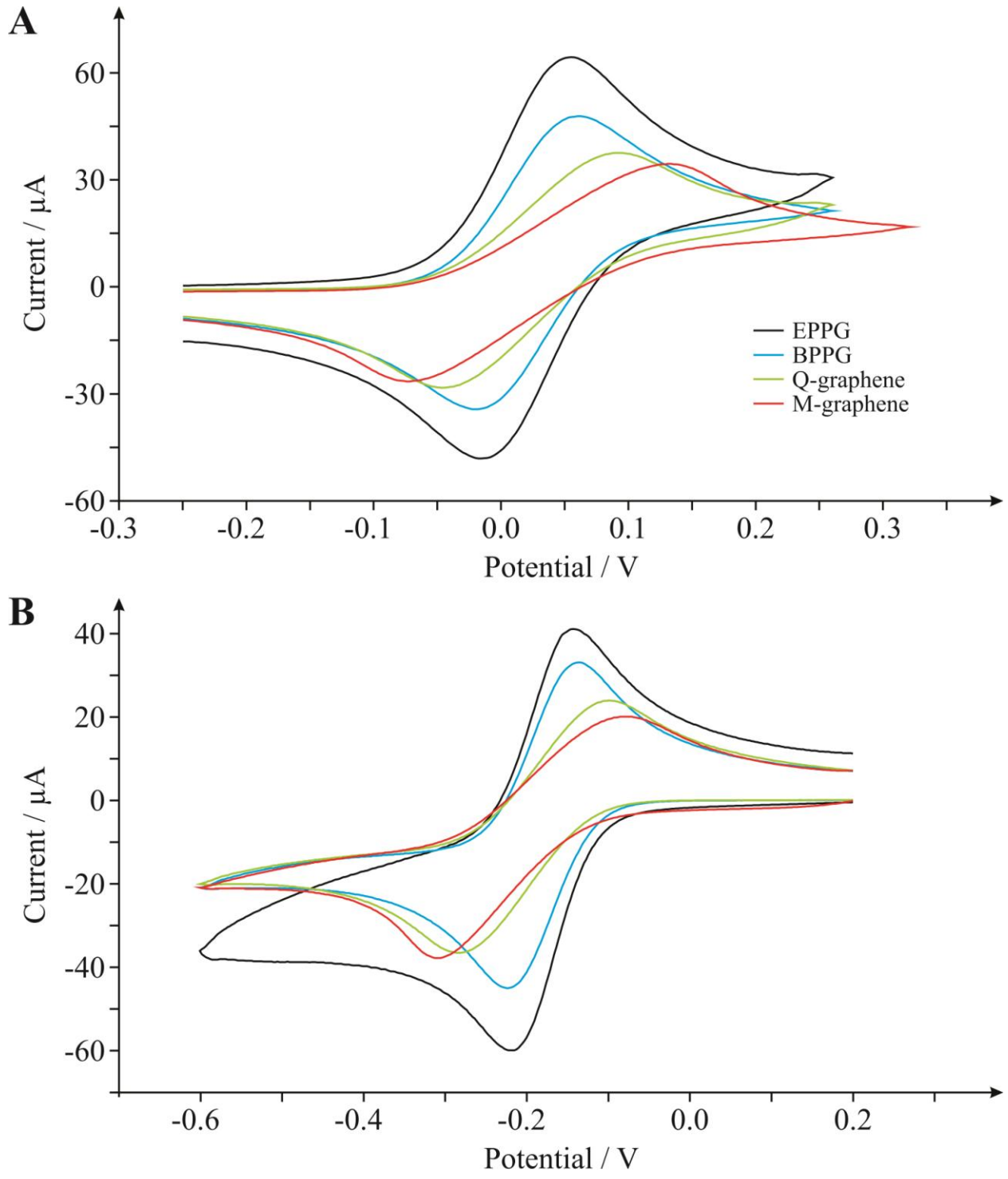

Figure 8.12 *Cyclic voltammetric signatures obtained using (**A**) N,N,N',N'-tetramethyl-para-phenylenediamine (TMPD) and (**B**) hexaammine-ruthenium(III) chloride at EPPG (black), BPPG (blue), quasi-graphene (Q-graphene, green) and monolayer graphene (M-graphene, red) electrodes. Scan rate: 100 mVs^{-1} (vs. SCE).*

Figure 8.12A depicts the cyclic voltammetric signatures recorded using the TMPD electrochemical redox probe, where ΔE_P values of *ca*. 63.5, 78.1, 136.7 and 205.1 mV are evident at the EPPG, BPPG, *quasi*-graphene (Q-graphene) and monolayer graphene (M-graphene) electrodes respectively. Similarly, shown in Figure 8.12B are the cyclic voltammograms recorded at each of the electrodes of interest towards the $Ru(NH_3)_6^{2+/3+}$ redox probe where the trend in ΔE_P values (HET properties) and the electrochemical responses agree well with those observed for TMPD.

It is clear that in both cases the voltammetric signatures are distinctively different according to a function of the different surface morphologies. For example in the case of $Ru(NH_3)_6^{2+/3+}$, in the first instance the EPPG and BPPG electrodes give rise to ΔE_P values of *ca*. 68.4 and 83.0 mV respectively. Such values are in excellent agreement with literature reports where it is well documented that an electrode surface with a large global coverage of edge plane like- sites/defects gives rise to fast heterogeneous electron transfer. [9, 26, 27] What is insightful, *and never before reported in the literature*, is that the *quasi*- and monolayer graphene electrodes (Q-graphene and M-graphene) give rise to dramatically larger ΔE_P separations over that of the graphite electrodes, namely values of *ca*. 183.1 and 227.1 mV respectively. Such a response has, to the best of the author's knowledge, never been reported for graphite/graphene electrodes using this redox probe since the most important factor affecting the rate of reaction is the electronic properties of the electrode, explicitly the potential-dependent electronic DOS near the formal potential of the redox system. [29] In terms of graphitic electrodes this is usually observed to a limit where an electrode with a relatively low edge plane coverage (1–10 %) gives rise to a near-reversible electrode response. [26, 27] In terms of semi- conducting/metallic diamond, the DOS is important and HET becomes worse/slow at diamond with decreasing boron doping levels. [29]

Thus in this case, in terms of the response of graphene, one can observe a clear dependence on the surface morphology with HET, which has never before been reported.

$Ru(NH_3)_6^{3+/2+}$ is classed as outer-sphere electrochemical redox probe (see Appendix A.1), involving a simple electron transfer on most graphitic electrodes and thus the electrode kinetics are relatively insensitive to the surface microstructure, surface oxides and adsorbed monolayers on sp^2 carbon electrodes. [1] The rate of reaction is insensitive to surface modification, indicating that electron transfer does not depend on interaction with a surface site or functional group. The most important factor affecting the rate of reaction is the density of electronic states (DOS) near the formal potential of the redox system: as noted above in the case of metallic and graphite electrodes, usually there is not a low DOS and this is seldom an issue, and is only seen at boron-doped diamond electrodes (semi-conducting/semi-metallic diamond) where the ΔE_P increases at diamond with decreasing boron-doping level (*vide supra*). [25] In the experiments performed within this chapter (*vide supra*) one is able to observe, for the first time, a clear dependence of the effects of electronic structure of graphene (density of states, DOS) upon the electrochemical response of the TMPD and $Ru(NH_3)_6^{3+/2+}$ probes, as evidenced by the dramatic changes in the ΔE_P values, which increase significantly as we utilise fewer graphene layer numbers. Such results indicate that there is a reduction in the HET kinetics at graphene electrodes as the surface composition/morphology comprises fewer layers and thus comprise less edge plane content than those structures comprising of multiple graphene layers *viz* graphite.

The effective heterogeneous electron transfer rate constant, k_{eff}^o, was estimated using the Nicholson method (see equation (1.44)) which is applicable for quasi-reversible systems. Consequently k_{eff}^o is determined to correspond to 1.81 x 10^{-3}, 3.25 x 10^{-3}, 19.3 x 10^{-3} and

53.2 x 10^{-3} cm s^{-1} for monolayer-graphene (M-graphene), *quasi*-graphene (Q-graphene), BPPG and EPPG respectively at the TMPD redox probe and to 1.11 x 10^{-3}, 1.58 x 10^{-3}, 3.80 x 10^{-3} and 8.77 x 10^{-3} cm s^{-1} for the monolayer-graphene, *quasi*-graphene, BPPG and EPPG electrodes respectively utilising $Ru(NH_3)_6^{3+/2+}$. As expected the two data sets support the inferences made earlier where the monolayer graphene electrode possesses the smallest/slowest k_{eff}^{o} when contrasted to the *quasi*-graphene and HOPG alternatives, indicating unfavourable electrochemical properties and a poor electronic structure (DOS) at true single-layer pristine graphene (M-graphene). It is apparent however, that increasing the number of graphene layers from mono- to *quasi*-graphene (*ca*. 4 layers) and graphite (≥ 8, however utilising BPPG in this case) results in an average improvement of *ca*. 1.7 and 7.5 times faster k_{eff}^{o} kinetics generally for when one is utilising the same geometry and only increasing the number of graphene layers (*i.e.* BPPG possesses same 'flat' geometry), and interestingly for EPPG (which has favourable orientation allowing a larger portion of its edge plane sites to be accessible to the solution) this exhibits HET rates on average 21.2 times faster than that of monolayer graphene. [1, 25]

The term "*effective electron transfer rate constant*" is used since the graphene surfaces are electrochemically heterogeneous, and the response is clearly dependent on the population of edge plane like- sites/defects. Using the k_{eff}^{o} values determined for the $Ru(NH_3)_6^{3+/2+}$ redox probe and a value of 0.4 cm s^{-1} for k_{edge}^{o} for $Ru(NH_3)_6^{3+/2+}$, [26, 27] the global coverage of edge plane sites can be readily deduced from $k_{eff}^{o}\left(graphene\right) = k_{edge}^{o}\left(\theta_{edge}\right)$ where the global coverage is given by: $\theta_{edge}\left(graphene\right) \approx \Theta_{edge}\left(graphene\right)$. [26, 27] From analysis of the data presented here (see Figure 8.12B) one can deduce the edge plane coverages ($\Theta_{edge}\left(graphene\right)$) of

2.2 and 0.95 % for the EPPG and BPPG electrodes respectively, which is well within the 1–10 % edge plane defect range expected and reported. [26, 27] This benchmarks the system, giving confidence that the approach will be valid for analysis of the graphene surfaces.

Using the same approach edge plane coverages ($\Theta_{edge}\left(graphene\right)$) of 0.39 and 0.28 % are deduced for the *quasi*- and monolayer- graphene electrodes respectively (Q-graphene and M-graphene). This analysis clearly highlights that the % of edge plane coverage is extremely low on the graphene materials, hence explaining the observed voltammetric profiles. Thus the surface of the pristine single-layer graphene consists of low coverage of edge-plane site/defects, which given that they are the predominant source of electron transfer, [26, 27] results in poor electrochemical performances. However, as the number of graphene layers is increased from monolayer (M-graphene), to *quasi*- (Q-graphene) and finally to BPPG, there is an increment in the % coverage of edge plane sites at each of the electrode materials, which is as expected, and resultantly improvements in the electrochemical responses can be observed. Note also that whilst BPPG is that of graphite (HOPG), EPPG has favourable orientation of the edge plane sites and thus exhibits the largest coverage of reactive edge plane sites, and hence the most reversible electrochemistry and superior HET rates are observed at this electrode configuration.

Above, this work has shown, for the first time, the 'true' electronic properties of electrodes comprising single-layer and *quasi*-layer pristine graphene films (M-graphene and Q-graphene respectively). It is evident from the range of electrochemical redox probes utilised (from simple outer-sphere to more complex inner-sphere electron transfer mechanisms) that pristine monolayer graphene exhibits unfavourable HET kinetics in terms of possessing small/low k^o values relative to the other graphitic materials utilised with an increased number of

graphene layers comprising their structure. Through analysis of the % coverage of edge plane contribution at the various graphitic electrodes, the response of graphene correlates to a low coverage of said sites, which is as expected given its geometry (where its pristine structure comprises predominantly of basal plane contribution, see Figure 7.1A). [1] Unsurprisingly the graphitic structures utilised with geometries comprising stacked/thicker graphene/graphite structures are shown to possess larger % coverages of electrochemically reactive edge plane sites, where resultantly a correlation between greater edge plane coverage and faster HET rates (improved electrochemical properties) is evident at the graphitic electrodes. In terms of the current literature, never before has monolayer graphene and *quasi*-graphene been directly compared and contrasted with graphitic electrodes (HOPG). It is satisfying to note that work by Unwin *et al*., [14] utilising SECM to study the relationship between the structure and properties of micro-graphene domains, supports the observations and inferences drawn in this work, where it was shown that HET rates at graphene increased as the structure evolved into multi-layered graphene.

It is next insightful to consider the electrochemical response arising from utilising a graphene electrode that possesses a high global coverage of edge plane like- sites/defects (D-graphene). The electrochemical response of the (edge plane abundant) double-layer defect-graphene electrode (D-graphene, see Chapter 5.4.5 for full characterisation) is shown in Figure 8.13 towards the outer-sphere redox probes TMPD and $Ru(NH_3)_6^{3+/2+}$, with ΔE_P values of ca. 112.3 and 128.5 mV respectively. Through employment of the appropriate scan rate studies the k_{eff}^{o} was estimated, corresponding to 6.53×10^{-3} and 3.12×10^{-3} cm s^{-1} at the TMPD and $Ru(NH_3)_6^{3+/2+}$ redox probes respectively; with the latter value relating to an edge plane coverage ($\Theta_{edge}\left(graphene\right)$) of 0.78 % for the double-layer defect-graphene electrode (D-grpahene).

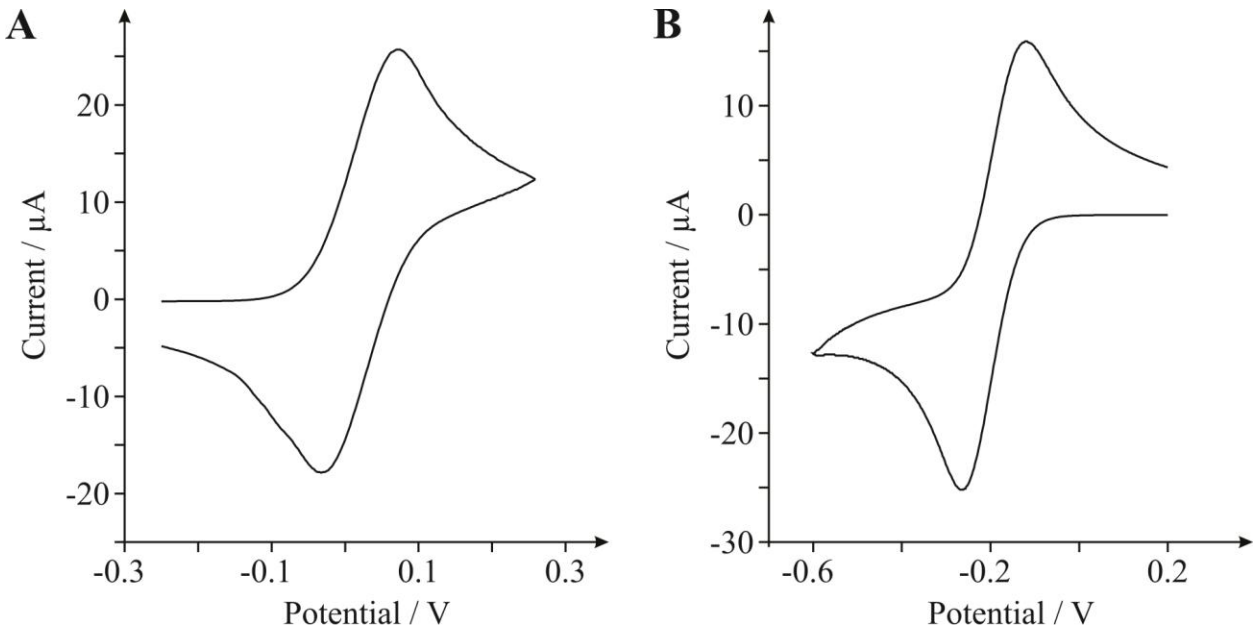

Figure 8.13 *Cyclic voltammetric signatures obtained using the double-layer defect-graphene electrode (D-graphene) at (**A**) TMPD and (**B**) hexaammine-ruthenium(III) chloride.*
Scan rate: 100 mVs^{-1} (vs. SCE).

Through comparison of the respective values, it is clear that the double-layer defect-graphene (D-graphene) exhibits favourable HET rates relative to the pristine monolayer and quasi-graphene electrodes (M-graphene and Q-graphene). Also evident is that the performance of the double-layer graphene does not surpass that observed at the HOPG electrodes. Considering that the domain edges are somewhat sealed in monolayer graphene, while the edge of basal planes are exposed in HOPG, it is the response at double-layer defect-graphene that is interesting and of critical importance here, because it is neither bulk nor monolayer. Given that favourable k^o values are observed at the double-layer defect-graphene relative to the monolayer graphene (with few double-layered islands distributed across its surface, see Chapter 5.4.5), it is apparent that simply introducing an increased number of edge plane defect sites across the surface of a graphene macrostructure (opposed to increasing the number of graphene layers in order to give rise to increased edge plane coverage) results in

improvements in the electrochemical behaviour of said electrode material. Hence, in support of earlier inferences, there is a clear correlation relating observed improvements in the electrochemical performance of the given graphitic electrode to increased global coverages of edge plane like- sites/defects comprising the electrode surface.

Last, it is illuminating to consider the further potential implications of graphene's geometry and thus unfavourable HET properties on its electroanalytical performance (the peak height, I_P). Re-inspection of Figures 8.11 and 8.12 reveal that in terms of the voltammetric I_P, monolayer graphene (M-graphene) exhibits reduced magnitudes in the current passed at each of the redox probes utilised when its performance is contrasted to that of the other graphitic materials. Again (as observed above in the case of considering the HET rates) there is a distinct correlation evident between the % coverage of edge plane sites and the magnitude of the electroanalytical signal (I_P) produced. This work has shown that increasing the number of graphene layers comprising an electrode material (evolution from monolayer to *quasi*-graphene and to BPPG) results in improved electrochemical responses, with further improvements evident when altering the geometry to exhibit higher degrees of edge plane sites (such as the distinct BPPG and EPPG responses). As the monolayer graphene has the lowest proportion of edge plane like/sites- defects it will give rise to the smallest peak current since the peak current is proportional to the 'active area', the analytical response will be far from optimal with the best and most favourable responses originating from multi-layer graphene, which is structurally similar to graphite; hence an edge plane pyrolytic graphite electrode is the obvious choice for electroanalysis since it can additionally be mechanically polished between voltammetric experiments (this inference is supported by work presented in Chapters 7.2, 7.3 and 7.4). [30]

8.3.4. CONCLUSIONS

In summary, this chapter has, for the first time, directly shown a correlation of the structure of graphene, in terms of its number of layers directly upon its electrochemical performance. Critically contrasting the performance of monolayer graphene to *quasi*-graphene and HOPG electrodes revealed that increasing the number of graphene layers results in improved electrochemical properties, where in terms of the electrochemical reversibility of the probes studied: monolayer-graphene < *quasi*-graphene < HOPG, as governed by the respective HET electrochemical rate constants. Thus it was shown that the macroscopic electrochemical response of graphene is highly dependent on the number of graphene layers which determines its electrochemical behaviour, which in turn corresponds to the density of edge plane like-site/defects comprising its structure. This work is an important and fundamental contribution to those studying the electron transfer properties of graphene since it provides the first comparison of true mono- *vs*. *quasi*- graphene on the macro-scale.

Given pristine monolayer graphene (M-graphene) has a low degree of edge plane coverage compared to the multi-layered structures of *quasi*-graphene (Q-graphene) and HOPG, in comparison it possesses poor/slow electrochemical properties in terms of HET kinetics. In scenarios when favourable/fast HET rates are required, recourse to *quasi*-graphene and edge plane of HOPG is suggested. Note that manipulation of the graphene structure in terms of orientation (such as exposing more edge) or through the introduction of surface edge plane like- sites/defects will result in beneficial alterations in the observed electrochemical properties; [31] which was shown herein utilising a defect abundant double-layer graphene electrode (D-graphene). The ability to tailor graphene's electrochemical response through surface composition/control makes this a fascinating area of study.

1. D. A. C. Brownson, D. K. Kampouris and C. E. Banks, *Chem. Soc. Rev.*, 2012, **41**, 6944.
2. K. S. Novoselov, D. Jiang, F. Schedin, T. J. Booth, V. V. Khotkevich, S. V. Morozov and A. K. Geim, *Proc. Natl. Acad. Sci. U.S.A.*, 2005, **102**, 10451.
3. A. K. Geim and K. S. Novoselov, *Nat. Mater.*, 2007, **6**, 183.
4. Y. Zhu, S. Murali, W. Cai, X. Li, J. W. Suk, J. R. Potts and R. S. Ruoff, *Adv. Mater.*, 2010, **22**, 3906.
5. D. A. C. Brownson, D. K. Kampouris and C. E. Banks, *J. Power Sources*, 2011, **196**, 4873.
6. T. Gan and S. Hu, *Microchim. Acta*, 2011, **175**, 1.
7. X. Huang, Z. Zeng, Z. Fan, J. Liu and H. Zhang, *Adv. Mater.*, 2012, **24**, 5979.
8. D. A. C. Brownson, L. C. S. Figueiredo-Filho, X. Ji, M. Gómez-Mingot, J. Iniesta, O. Fatibello-Filho, D. K. Kampouris and C. E. Banks, *J. Mater. Chem. A*, 2013, **1**, 5962.
9. D. A. C. Brownson, L. J. Munro, D. K. Kampouris and C. E. Banks, *RSC. Adv.*, 2011, **1**, 978.
10. W. Li, C. Tan, M. A. Lowe, H. D. Abruna and D. C. Ralph, *ACS Nano*, 2011, **5**, 2264.
11. A. T. Valota, I. A. Kinloch, K. S. Novoselov, C. Casiraghi, A. Eckmann, E. W. Hill and R. A. W. Dryfe, *ACS Nano*, 2011, **5**, 8809.
12. D. A. C. Brownson and C. E. Banks, *Phys. Chem. Chem. Phys.*, 2012, **14**, 8264.
13. A. M. Bond, D. Luscombe, K. B. Oldham and C. G. Zoski, *J. Electroanal. Chem. Interfacial Electrochem.*, 1988, **249**, 1.
14. A. G. Guell, N. Ebejer, M. E. Snowden, J. V. Macpherson and P. R. Unwin, *J. Am. Chem. Soc.*, 2012, **134**, 7258.
15. D. Graf, F. Molitor, K. Ensslin, C. Stampfer, A. Jungen, C. Hierold and L. Wirt, *Nano Lett.*, 2007, **7**, 238.
16. A. C. Ferrari, *Solid State Commun.*, 2007, **143**, 47.
17. Y. Y. Wang, Z. H. Ni, T. Yu, Z. X. Shen, H. M. Wang, Y. H. Wu, W. Chen and A. T. S. Wee, *J. Phys. Chem. C*, 2008, **112**, 10637.
18. X. Li, Y. Zhu, W. Cai, M. Borysiak, B. Han, D. Chen, R. D. Piner, L. Colombo and R. S. Ruoff, *Nano Lett.*, 2009, **9**, 4359.
19. C. Mattevi, H. Kim and M. Chhowalla, *J. Mater. Chem.*, 2011, **21**, 3324.
20. J. Kang, D. Shin, S. Bae and B. H. Hong, *Nanoscale*, 2012, **4**, 5527.
21. A. Ambrosi and M. Pumera, *J. Phys. Chem. C*, 2013, **117**, 2053.
22. R. N. Adams, *Electrochemistry at solid electrodes*, Marcel Dekker, Inc., New York, U.S.A., 1969.

23. C. E. Banks, R. G. Compton, A. C. Fisher and I. E. Henley, *Phys. Chem. Chem. Phys.*, 2004, **6**, 3147.

24. M. J. Moorcroft, N. S. Lawrence, B. A. Coles, R. G. Compton and L. N. Trevani, *J. Electroanal. Chem.*, 2001, **506**, 28.

25. D. A. C. Brownson and C. E. Banks, *The handbook of graphene electrochemistry*, Springer Publishing, London, U.K., 2013.

26. T. J. Davies, M. E. Hyde and R. G. Compton, *Angew. Chem. Int. Ed.*, 2005, **44**, 5121.

27. T. J. Davies, R. R. Moore, C. E. Banks and R. G. Compton, *J. Electroanal. Chem.*, 2004, **574**, 123.

28. K. R. Wehmeyer, M. R. Deakin and R. M. Wightman, *Anal. Chem.*, 1985, **57**, 1913.

29. M. C. Granger, M. Witek, J. Xu, J. Wang, M. Hupert, A. Hanks, M. D. Koppang, J. E. Butler, G. Lucazeau, M. Mermoux, J. W. Strojek and G. M. Swain, *Anal. Chem.*, 2000, **72**, 3793.

30. C. E. Banks and R. G. Compton, *Analyst*, 2006, **131**, 15.

31. C. X. Lim, H. Y. Hoh, P. K. Ang and K. P. Loh, *Anal. Chem.*, 2010, **82**, 7387.

CHAPTER 9: ELECTROCHEMISTRY AT MODIFIED GRAPHENE STRUCTURES

The aim of this thesis thus far has been to explore and characterise the fundamental electrochemical properties of *pristine single-layer graphene* and to evaluate the implications of utilising said graphene based electrodes for electroanalysis. It was shown in Chapters 6 – 8, for the first time, that the electrochemical response of graphene corresponds to the density of edge plane like- site/defects comprising its structure. Given that *pristine single-layer graphene* possesses a low density of edge plane coverage, it was then shown to exhibit slow heterogeneous electron transfer kinetics and resultantly, when compared to, for example graphite, it is *not so beneficial* when employed as a state-of-art sensor substrate.

This chapter explores the electrochemical response/properties of modified graphene structures when utilised as electrode materials. Chapter 9.1 considers the implications of altering graphene's *physical structure* in terms of utilising a novel three-dimensional graphene foam electrode. Thereafter, Chapter 9.2 explores the implementation of a graphene paste electrode with consideration towards a reproducible method of connecting to 'graphene' based electrodes and with potential for scale-up, with responses contrasted and compared to a graphite based alternative. Last, Chapter 9.3 investigates the effects of changing graphene's *chemical structure* in terms of introducing oxygenated functionalities onto the graphene lattice (*i.e.* the use of *graphene oxide*, GO). The aim of this chapter is to evaluate if modifying the graphene structure (beyond that of the introduction of edge plane like- sites/defects) can impart improvements on the fundamental electrochemical properties/applicability of graphene based electrodes.

Experimental Overview: this chapter utilises cyclic voltammetric experiments to explore the various graphene structures using a three electrode system as detailed in Chapter 5.1. Variable working electrodes are employed throughout; however, a platinum wire and a SCE comprise the auxiliary and reference electrodes respectively (expect for in Chapter 9.1 where a silver wire reference electrode is utilised for non-aqueous experiments). Chapter 9.1 uses a 3D graphene foam working electrode that is described as a 'freestanding, three-dimensional graphene foam' and is fully characterised in Chapter 5.4.6. For comparison purposes a 3D carbon foam alternative is studied, which is described as a 'freestanding, three-dimensional RVC foam' and is also fully characterised in Chapter 5.4.6. Chapter 9.2 uses graphene and graphite paste electrodes which are fabricated as described in Chapter 9.2.2.1, with graphene powder (full characterisation available in Chapter 5.4.7) and graphite powder (full characterisation available in Chapter 5.4.3) utilised for the respective paste electrodes. Finally, GO modified electrodes are studied in Chapter 9.3 and thus the underlying working electrodes employed were EPPG and BPPG (Chapter 5.2.1). The GO is described as 'graphene oxide sheets suspended in aqueous solution', with full characterisation available in Chapter 5.4.8.

9.1. EXPLORING THE ELECTROCHEMICAL PROPERTIES OF A FREESTANDING THREE-DIMENSIONAL GRAPHENE FOAM ELECTRODE

This chapter, containing published work, [10] considers whether a novel three-dimensional (3D) graphene foam can, due to its unique macroscopic/microscopic structure, provide a promising and beneficial architecture relative to that of two-dimensional (2D) pristine graphene with respect to possessing beneficial electrochemical properties.

The freestanding 3D graphene foam has a macroscopic structure with microscopic (graphene) features and through characterisation (see Chapter 5.4.6) is found to comprise pristine graphene (O/C of 0.05) which is in the range of mono- to few- layered graphene sheets and is thus termed *quasi*-graphene. Thus a *physical change* in the graphene structure, to that of a unique '3D graphene foam', is electrochemically explored in this chapter towards both aqueous and non-aqueous electrochemistry. The response of the 3D graphene foam is compared to a freestanding 3D reticulated vitreous carbon (RVC) foam alternative in order to evaluate its electrochemical properties.

9.1.1. INTRODUCTION

As is realised through consideration of previous chapters, the world's thinnest electrode material, *graphene*, has been extensively explored in a plethora of applications, such as in energy storage and generation, sensor fabrication and in various electrical nano-devices due to its reported beneficial electronic properties (amongst others). [1-4]

The main limitations of using graphene, which are experimental in nature, were introduced in earlier chapters. Essentially two 'problems' exist. The first problem is how to electrically wire/connect to such a material so as to obtain the reported benefits, and secondly is how to reduce aggregation of graphene sheets back to their lowest energy conformation,

[10] D. A. C. Brownson, L. C. S. Figueiredo-Filho, X. Ji, M. Gómez-Mingo, J. Iniesta, O. Fatibello-Filho, D. K. Kampouris and C. E. Banks, *J. Mater. Chem. A*, 2013, **1**, 5962.

that is, graphite, due to the strong π–π interactions between the graphene sheets. The latter reduces true graphene (single layer) into *quasi*-graphene consisting of double-, few- and multi-layers which typically occurs when one is trying to immobilise graphene onto an electrode surface, such as trying to overcome the former problem (see Chapters 7.1 and 7.4 for related examples). The problem of graphene aggregation can significantly limit the performance of graphene based electrochemical devices, for example, in graphene derived supercapacitors and batteries where it reduces the accessible surface area and d-spacing between individual graphene sheets which decreases as the number of aggregated layers increase and greatly reduces Li intercalation capabilities (and hence the performance of the fabricated device). [5] An approach to alleviate such problems is to use 3D graphene foams for electrochemical applications, where graphene is incorporated into a macroscopic geometric structure such that the reported beneficial electronic properties of graphene may be realised without encountering the issues highlighted above.

Cheng and co-workers [6] presented 3D graphene foams fabricated by using a nickel skeleton upon which graphene was grown *via* CVD; the underlying skeleton was then etched away to leave a free-standing graphene structure. The unique graphene structure was demonstrated to give rise to high quality graphene with outstanding electrical conductivity, superior to macroscopic graphene structures from chemically derived graphene sheets. [6] The same authors went on to report that the 3D graphene foam coated with Teflon exhibits super-hydrophobicity; [7] a contact angle of 129.95° was observed at the 3D graphene foam, which increased to 150.21° following Teflon treatment. In a similar approach Chen *et al.* [8] reported on 3D graphene foams coated with CNTs, which exhibited super-hydrophobic and super-oleophilic properties; a contact angle of 89.4° was measured for a CVD grown graphene film while this was 108.5° for the 3D graphene foam, which was increased to 152.3° when modified with CNTs.

In terms of electrochemical performance, which corresponds to the key aims of this thesis, Chen *et al.* have utilised a 3D graphene foam structure as a support for cobalt oxide [9] and separately for zinc oxide, [10] exhibiting useful specific capacitances of *ca*. 1100 F g^{-1} (at a current density of 10 A g^{-1}) and *ca*. 400 F g^{-1} (at a current density of 6.7 A g^{-1}) respectively. This research group have also utilised these hybrid structures for electrochemical sensing applications; using the zinc oxide modified 3D graphene foam towards the detection of $[Fe(CN)_6]^{3+}$ and dopamine, [10] whilst the cobalt oxide modification was shown to be useful for sensing glucose. [9] Furthermore, the unmodified/bare 3D graphene foam was reported to be useful for dopamine sensing. [11] Note that in all these literature reports, no comparisons are made with a similar structure, that is, a 3D carbon foam. This key comparison is performed in this chapter.

Interestingly, in all these exciting examples, the freestanding 3D graphene foam is attached to a glass side (or equivalent) for ease of experimentation – where effectively the unique freestanding 3D structure is turned, detrimentally, into a *quasi*-2D graphene structure! The reasons for the researchers doing this become evident later in this chapter.

Inspired by the limited amount of literature available on these highly fascinating 3D graphene macroscopic structures within electrochemistry, this chapter explores, for the first time, a freestanding 3D graphene foam as a novel electrode material towards commonly encountered redox probes in both aqueous and non-aqueous (namely, ionic liquids (RTILs)) solutions. The response is contrasted to a freestanding 3D carbon (RVC) foam alternative, providing information on the electronic properties and applicability of this intriguing material.

9.1.2. CHAPTER SPECIFIC EXPERIMENTAL DETAILS

Non-aqueous solutions were prepared using one of three Room Temperature Ionic Liquids (RTILs): 1-butyl-3-methylimidazolium tetrafluoroborate, $[C_4MIM][BF_4]$; 1-butyl-3-methylimidazolium hexafluorophosphate, $[C_4MIM][PF_6]$; and 1-butyl-3-methylimidazolium bis(trifluoromethylsulfonyl)imide, $[C_4MIM][NTf_2]$.

For aqueous solution voltammetry a platinum wire and a SCE were used as counter and reference electrodes respectively. Alternatively, for non-aqueous solution voltammetry a platinum wire counter electrode and a silver wire reference electrode were utilised as counter and reference electrodes respectively.

Current density is presented in all of the figures in this chapter, that is, the 3D graphene and carbon foams are normalised (current density, A cm^{-3}) in terms of their volume to allow direct comparison. Additionally, since the average pore size of the 3D graphene is found to correspond to *ca*. 200 μm and that of the 3D carbon is *ca*. 400 μm (see Chapter 5.4.6), a correction factor is applied by dividing the current density of the 3D graphene foam by a factor of two to allow direct comparison of the alternative foams. [12]

A digital goniometer equipped with a dispensing needle and respective software (DSA II Version 2.4; Kruss GmbH, Hamburg) was used for contact angle measurements, which were estimated/calculated using the 'Young-Laplace Fit' method.

9.1.3. RESULTS AND DISCUSSION

9.1.3.1. ELECTROCHEMISTRY IN AQUEOUS SOLUTIONS

The electrochemical characterisation of the freestanding 3D graphene foam is first considered in aqueous solutions, where its performance is contrasted to that of a commonly employed and readily commercially available 3D carbon (RVC) foam alternative.

First to be considered is the voltammetric response of both the 3D foams using the ferrocyanide(II) redox probe in 0.1 M KCl electrolyte. Figure 9.1A depicts typical voltammetric profiles obtained utilising the 3D carbon foam electrode at varying voltammetric scan rates. At a scan rate of 100 mVs^{-1} a well defined pair of redox peaks is observed with a peak-to-peak separation (ΔE_P) of *ca.* 194.5 mV, which is in good agreement with previous literature reports. [13, 14] In the case of the 3D graphene foam, Figure 9.1B shows the voltammetric profiles observed under identical conditions. Interestingly the response observed at the 3D graphene foam electrode differs significantly from that obtained in Figure 9.1A for the case of the carbon foam, where the former appears to exhibit two oxidative (anodic) peaks when one such peak is usually expected for the analyte utilised (as per the latter).

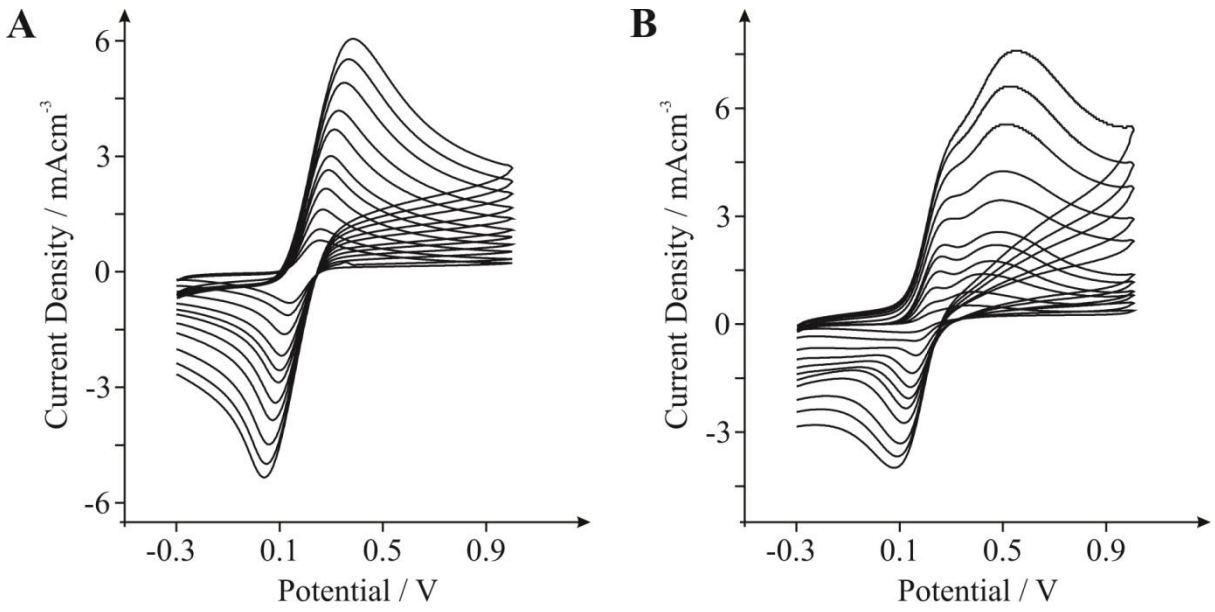

Figure 9.1 *Typical cyclic voltammetric profiles recorded towards 1 mM potassium ferrocyanide (II) in 0.1M KCl utilising increasing scan rates over the range 5–500 mVs^{-1}, vs. SCE. Obtained at the freestanding 3D carbon (**A**) and graphene (**B**) foam electrodes respectively.*

Scan rate studies were performed on both the 3D carbon and graphene foams where the voltammetric peak height (I_P) was monitored as a function of scan rate (υ) with a plot of

peak height *versus* square-root of the scan rate revealing the following trends: 3D carbon foam, I_P (A) = 4.25 x 10^{-3} A/$(Vs^{-1})^{0.5}$ + 1.97 x 10^{-4} A (R^2 = 0.99); 3D graphene foam (first peak), I_P (A) = 4.23 x 10^{-4} A/$(Vs^{-1})^{0.5}$ + 5.17 x 10^{-6} A (R^2 = 0.99); 3D graphene foam (second peak), I_P (A) = 5.67 x 10^{-4} A/$(Vs^{-1})^{0.5}$ + 1.78 x 10^{-5} A (R^2 = 0.99). It is clear that in each of the cases noted a linear response is evident, indicating diffusional processes. Furthermore, as is expected for the case of the semi-infinite diffusion model as governed by the Randles–Ševćik equation, analysis of log I_P *versus* log υ revealed the gradients of 0.44 (3D carbon foam), 0.54 (3D graphene foam, first peak) and 0.53 (3D graphene foam, second peak), indicating the absence of thin-layer effects (such that the redox probe is not trapped within the 3D network of the foam electrode) and representing a response that is purely diffusional in each case. [1] Given the above insights (that contributions *via* adsorption and/or thin-layer effects can be neglected) one has to conclude that the 'double peak' observed in Figure 9.1B likely arises from other factors.

Returning to the electrochemical comparison of the 3D graphene and carbon foams, although specific/reliable contrasts cannot be drawn owing to the 'double peak phenomenon' observed for the 3D graphene foam, generalised observations are highly enlightening. In terms of the ΔE_P values obtained for the first and second peaks at the freestanding 3D graphene foam electrode (*ca.* 127.0 and 256.9 mV respectively at 100 mVs^{-1}), it appears that in the case of the first peak (which is related to the reverse peak/redox couple) the 3D graphene foam gives rise to a smaller ΔE_P value than that exhibited by the 3D carbon foam alternative (see earlier), which is indicative of a more favourable electrochemical interaction at the electrode surface and thus enhanced electron transfer kinetics are likely to reside at the graphene foam. [1]

To support this observation, that is, a general improvement in the electrochemical signatures of the redox probe is apparent at the 3D graphene electrode relative to the

3D carbon foam, upon comparison of the magnitude of the oxidative currents passed at each electrode one would expect the voltammetric peak height to be larger at the graphene foam over that of the carbon alternative. However, this is not the case here, with the currents passed appearing to exhibit similar magnitudes; suggesting similar electrochemical sensing capabilities at the two electrodes in this instance. Note that electron transfer at the ferro-/ferri-cyanide redox probe is known to be complex on carbon surfaces, influenced by specific surface sites, and is consequently termed as an 'inner-sphere' redox probe (see Appendix A.1); [1, 15] thus the voltammetric responses observed in Figure 9.1 can be attributed to both a combination of electronic factors and specific surface interactions arising from two differing contributions, which are not easily de-convoluted. In order to greater understand the responses observed above, voltammetric characteristics of the freestanding 3D foam electrodes are next explored towards an 'outer-sphere' redox probe which does not have any surface sensitivity and depends exclusively on electronic factors. [1, 15]

The voltammetric response of the freestanding 3D foam electrodes was next sought towards 1 mM hexaammine-ruthenium(III) chloride in 0.1 M KCl, which has been shown to exhibit reversible voltammetry (involving an 'outer-sphere' one electron transfer process) on carbon surfaces. [1] The voltammetric profiles obtained utilising the freestanding 3D carbon and graphene foams at various scan rates are presented in Figures 9.2A and 9.2B respectively. Note that as expected given the analysis performed at the ferro/ferri redox probe, employment of the appropriate scan rate studies indicated that neither of the two 3D foam electrodes exhibited thin-layer behaviour when utilised in aqueous solution towards the ruthenium redox probe and thus the voltammetry observed originates from a diffusion controlled process in both instances.

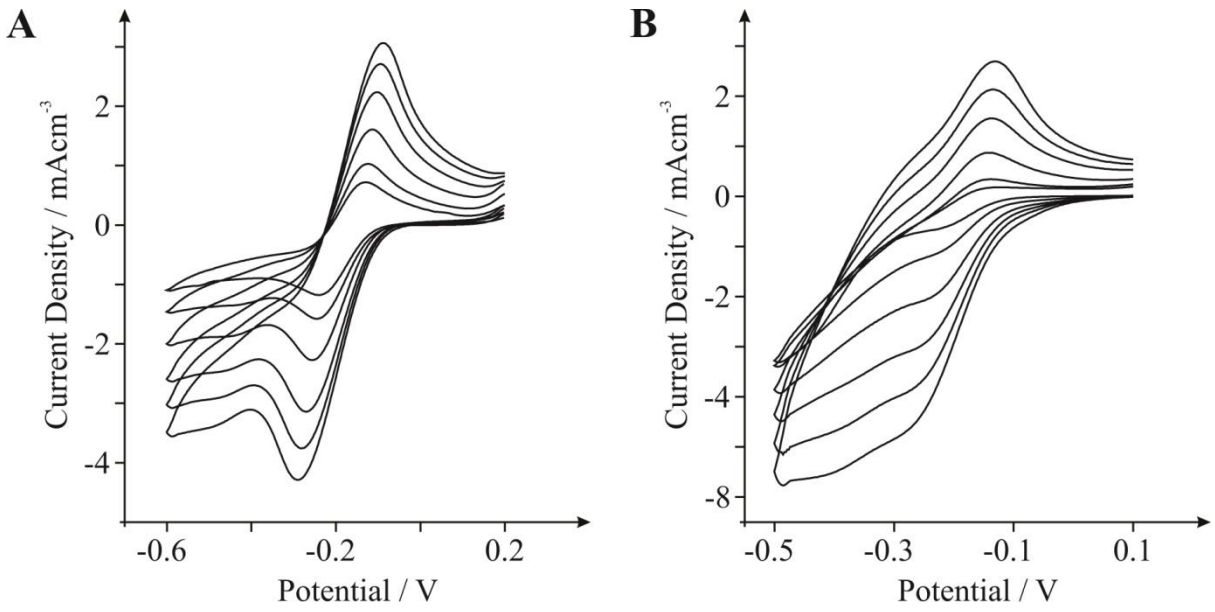

Figure 9.2 *Typical cyclic voltammetric profiles recorded towards 1 mM hexaammine-ruthenium (III) chloride in 0.1M KCl utilising increasing scan rates over the range 5–100 mVs^{-1}, vs. SCE. Obtained at the freestanding 3D carbon (**A**) and graphene (**B**) foam electrodes respectively.*

An important factor to consider is the heterogeneous electron transfer (HET) rates of the respective electrode materials, which is indicated *via* the ΔE_P values obtained. As highlighted in Chapter 1.4.1, a smaller ΔE_P value represents an increased reversibility of the redox probe utilised and thus faster electron transfer kinetics at the given electrode material (which is beneficial in numerous instances) relative to an alternative with larger ΔE_P values. [1] In the case of Figure 9.2 analysis of the ΔE_P for the 3D carbon (*ca*. 192.9 mV) and 3D graphene foams (*ca*. 134.3 mV) at a scan rate of 100 mVs^{-1} reveals that the latter exhibits an enhanced electrochemical response in terms of increased heterogeneous electron transfer kinetics and exhibits an improvement in electrochemical reversibility over that of the former. Thus in terms of HET, the freestanding 3D graphene foam appears beneficial over that of the commonly utilised alternative foam.

Comparisons of the cyclic voltammograms obtained at 100 mVs^{-1} indicate that in terms of the electroanalytical signal produced (the peak height, I_P) the graphene and carbon foams again (as was the case in Figure 9.1) exhibit currents with similar magnitudes –

although the current passed at the graphene foam is generally, slightly (but not significantly), improved. This lack of a greatly enhanced analytical related performance at the 3D graphene foam (over that of the RVC carbon alternative) is unexpected given the improved electron transfer kinetics observed at the macro-porous 3D graphene electrode in both of the cases studied thus far.

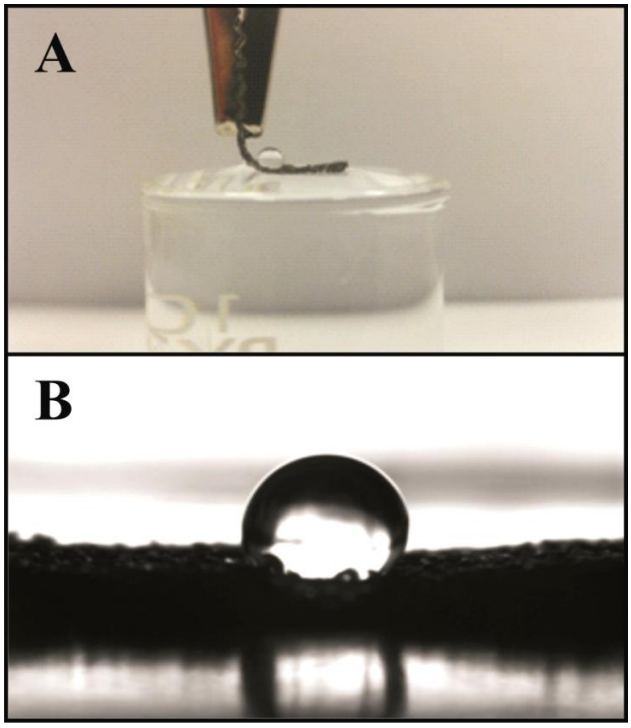

Figure 9.3 *Optical images of: the freestanding 3D graphene foam being introduced to the surface of an aqueous solution (water) (**A**); and a water droplet placed on top of the respective foam (**B**), which exhibits a contact angle of ca. 120° showing quasi-super-hydrophobicity. The inherent hydrophobicity of the graphene foam is clear from both images.*

The poor aqueous voltammetry was explored further. Figure 9.3 depicts an image of the freestanding 3D graphene foam being introduced to an aqueous solution. The response is extremely fascinating given that as the macroscopic structure of the graphene foam is introduced to the aqueous (water) solution it (the foam) is observed to physically bend/repel away from the surface (water). [16] This is only evident due to the very thin, freestanding 3D graphene foam that is being utilising. The hydrophobicity of the 3D graphene foam is

exemplified in Figure 9.3A where it (the foam) is lying upon a beaker containing the aqueous (water) solution and on top a droplet of water has been placed. Also shown (see Figure 9.4) are the oleophilic properties of the freestanding 3D graphene foam macrostructure as exemplified with the absorption of 3-octanol (with added iodine to produce a colour contrast) floating on the surface of water; where the 3-octanol is immediately and completely absorbed into the freestanding 3D graphene foam. Other work reporting a CNT modified 3D graphene foam has extensively explored the absorption capabilities towards oils; [8] the focus here is the electrochemistry of this unique freestanding 3D graphene foam.

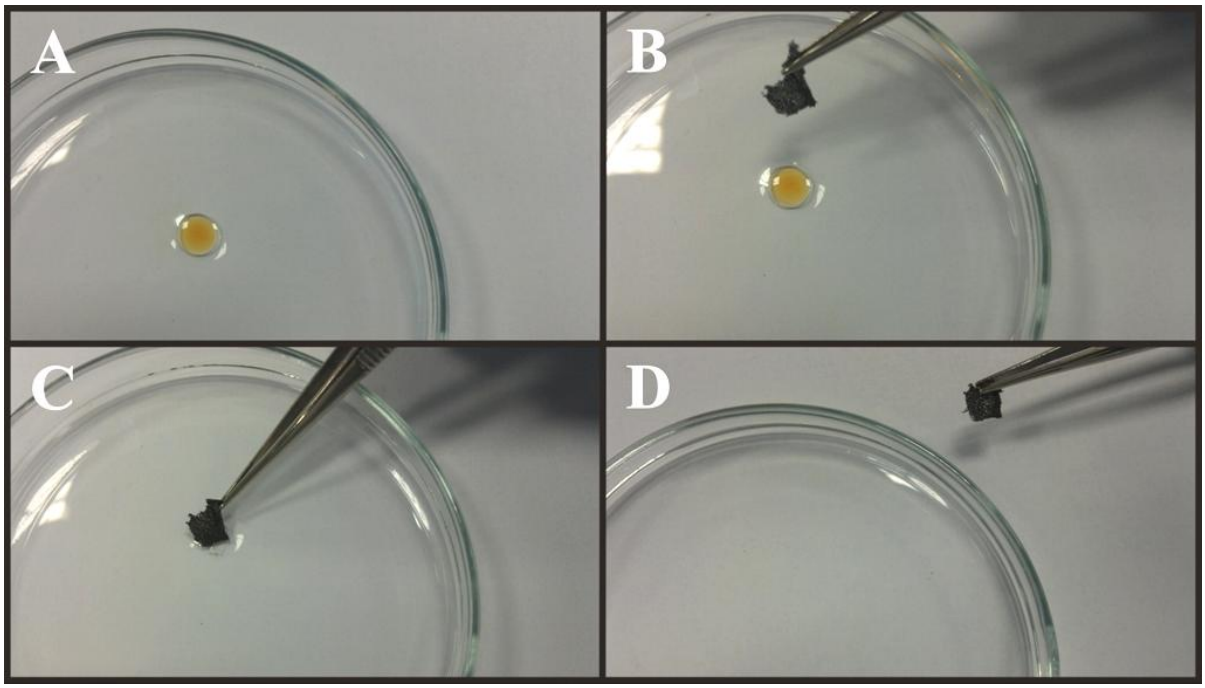

Figure 9.4 *Optical images depicting the oleophilic capabilities of the freestanding 3D graphene foam: (**A**) a drop of 3-octanol (with added iodine to produce a colour contrast) is placed onto the surface of water; (**B**) the 3D graphene foam is positioned; (**C**) the 3D graphene is introduced to the 3-octanol/water where the 3-octanol is immediately and completely absorbed into the freestanding 3D graphene foam; (**D**) removal of the foam from the water surface, and with it, the complete removal of 3-octanol.*

As shown in Figure 9.3B the contact angle of the '3D graphene foam' material was found to correspond to 120° (±1°). It is well reported that graphene is hydrophobic. [17, 18]

Benchmarking this value against other graphenes and related structures, it is found from the literature that HOPG (multiple layers of graphene) exhibits a value of *ca*. 91° and single-layer pristine graphene is reported to possess a value of *ca*. 92.5°, [18] with 2D CVD grown graphene being reported at *ca*. 89.4°. [8] Other work has shown that graphene sheets (*ca*. 3 layers, thus *quasi*-graphene) can give rise to super-hydrophobicity (*ca*. 160^{o}). [17] Of particular comparison, the measured contact angle here (120^{o}) is greater than that reported at other bare/unmodified 3D graphene structures (108.5°) [8] and is slightly less than *ca*. 134.86° which was reported at a Teflon^{TM} coated 3D graphene foam. [7]

Indeed, there is some discrepancy in the literature, perhaps not surprising given the various approaches that are available to fabricate graphene. [19] Marmur [20] gives an excellent overview of the wetting upon rough hydrophobic surfaces which is not pure Cassie and Baxter or Wenzel models, where the former relates to heterogeneous wetting while the latter is that of a homogeneous wetting regime. In the case studied here, as reported by Singh *et al*., [7] who explored hydrophobicity at 3D graphene foams (with the same porosity as that utilised in this chapter) alongside that of Teflon treated/covered 3D graphene, a mixed wetting state is observed such that *quasi*-super-hydrophobicity is evident as a combination of a mixed wetting state where the water penetrates to some extent into the pores of the 3D graphene structure, leaving air pockets below it coupled with influences from the surface roughness (deviation from monolayer graphene). The concept of surface roughness effects upon hydrophobicity is a widely pursued area and in the case of the freestanding 3D graphene foam, other work [7] suggests that the exact origin is on-going.

Returning to the focus of this chapter, which is the electrochemical performance, the *quasi*-super-hydrophobicity accounts for the poor voltammetric signatures observed (Figure 9.1B and 9.2B), which is due to poor surface wetting and thus a reduced accessibility and utilisation of the available surface area.

As a result of the above insights, this chapter next explores the use of non-aqueous media, *viz* Room Temperature Ionic Liquids (RTILs), due to their reported archetypical properties of high intrinsic conductivity, low volatility, high polarity, high thermal stability and wide electrochemical windows, [21] giving rise to their beneficial use in gas sensors, [22] Li-ion batteries, [23] supercapacitors [24] and as electrode composites. [25]

9.1.3.2. ELECTROCHEMISTRY IN NON-AQUEOUS MEDIA

First the electrochemical behaviour of the two 3D foam electrodes is considered towards the well characterised outer-sphere redox probe ferrocene, [26-28] using $[C_4MIM][NTf_2]$ as the electrolyte. Figure 9.5 depicts the typical cyclic voltammetric profiles obtained utilising the freestanding 3D carbon and graphene foams. As with the aqueous studies, scan rate analysis was performed on both of the electrode materials, with a plot of I_P *versus* $\upsilon^{0.5}$ revealing the following trends: 3D carbon foam, I_P (A) = 1.50 x 10^{-3} A/$(Vs^{-1})^{0.5}$ + 1.19 x 10^{-4} A (R^2 = 0.99); 3D graphene foam, I_P (A) = 6.25 x 10^{-3} A/$(Vs^{-1})^{0.5}$ + 3.66 x 10^{-6} A (R^2 = 0.99). Again it is clear that in both instances a linear response is evident, indicating diffusional processes, which is supported by the analysis of log I_P *versus* log υ revealing gradients of 0.41 (3D carbon foam) and 0.46 (3D graphene foam) confirming that the observed voltammetry is governed by diffusion limited processes and thus contributions from possible thin-layer behaviour can be excluded. [1]

As stated earlier, an important indicator of an electrode materials quality is its HET rate; often indicated *via* the ΔE_P values, which in this case are *ca*. 119.6 and 163.5 mV for the graphene and carbon foams respectively at 100 mVs^{-1}. The heterogeneous electrochemical rate constant, k^o, was estimated at the 3D carbon and graphene foams over the scan rate range employed. Such values are deduced using the well-known Nicholson method (see equation (1.44)). [29] The k^o values of the 3D graphene and carbon foams were

estimated to correspond to *ca*. 8.2×10^{-4} and 5.3×10^{-4} cm s^{-1} respectively (utilising a diffusion coefficient of 3.77×10^{-7} cm^2 s^{-1} for ferrocene in [C_4MIM][NTf2]). [30] Thus, although not substantially different, since ferrocene is an outer-sphere redox probe and consequently needs a general 'sink/source' of electrons to obtain fast reversible voltammetry (such electron sources are determined *via* the % global coverage of edge plane like-sites/defects at carbon materials: *vide infra*), [1, 15] there is a slight noticeable improvement in the k^o values obtained at the 3D graphene foam over that of the carbon alternative, however values in these instances are usually similar.

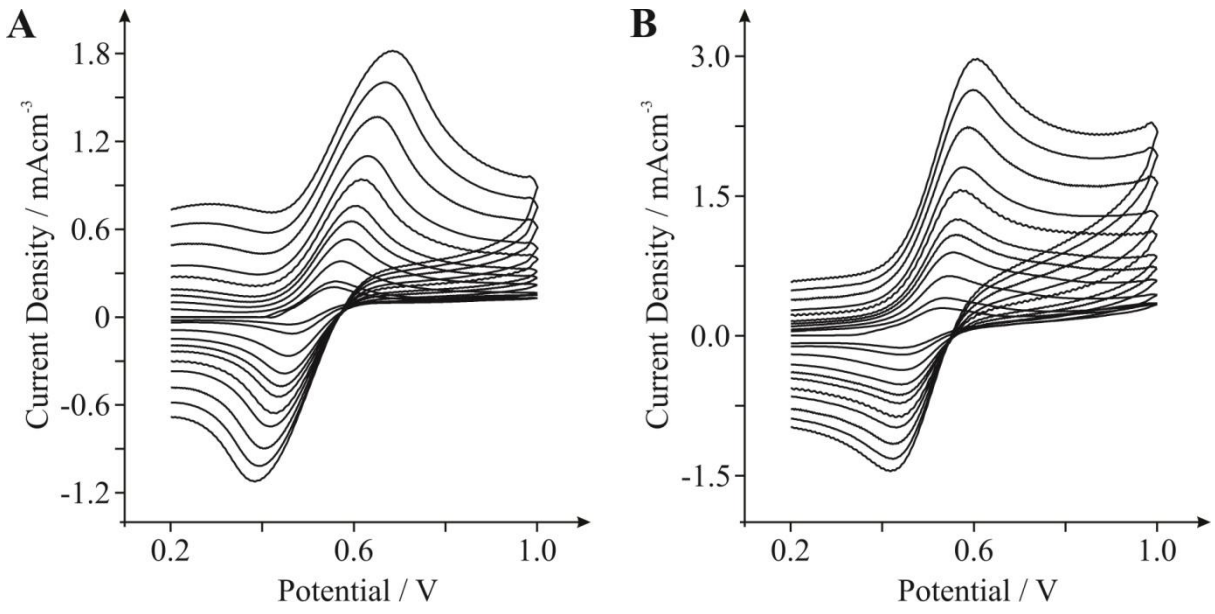

Figure 9.5 *Typical cyclic voltammetric profiles recorded towards 1 mM ferrocene in [C_4MIM][NTf_2] utilising increasing scan rates over the range 5–500 mVs^{-1}, vs. Ag. Obtained at the freestanding 3D carbon foam (**A**) and graphene (**B**) foam electrodes respectively.*

Contrary to the above, significant differences between the freestanding 3D graphene foam and the 3D carbon alternative are observed when considering the magnitude of the analytically valuable peak currents. Comparison of the voltammograms obtained at 100 mVs^{-1} clearly indicates that the current density passed at the 3D carbon (0.62 $mAcm^{-3}$) and graphene (0.98 $mAcm^{-3}$) foams differ considerably. In fact, the peak height, I_P, of the

3D graphene foam is over 50 % larger than that of the 3D carbon foam, indicating its potential for future use as an enhanced electrochemical sensor substrate. The reasons as to why this improved electrochemical response is observed at the freestanding 3D graphene electrode over that of the carbon alternative are discussed later in this section (*vide infra*).

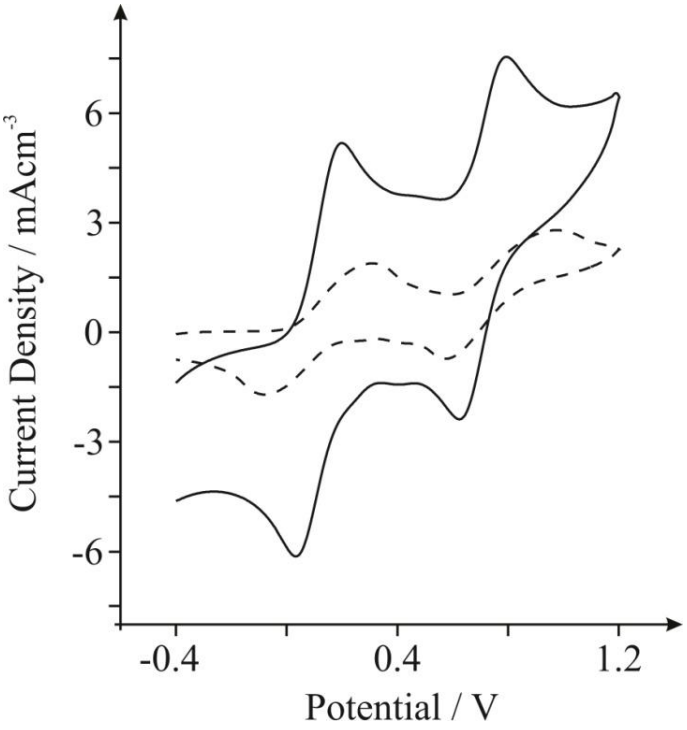

Figure 9.6 *Typical cyclic voltammetric profiles recorded towards 1 mM TMPD [C_4MIM][NTf_2] utilising a scan rate of 100 mVs^{-1}, vs. Ag. Obtained at the freestanding 3D graphene foam (solid line) and carbon (dashed line) foam electrodes respectively.*

Next the voltammetry of N,N,N',N'-tetramethyl-*para*-phenylenediamine (TMPD) is explored in the chosen RTILs. Figure 9.6 shows the observed voltammetric profiles for the electrochemical oxidation of TMPD in [C_4MIM][NTf_2]. First, it is evident from the cyclic voltammograms (CVs) that in terms of HET kinetics, as deduced through the ΔE_P values for the first and second redox peak-couples (*ca*. 134.3 and 119.6 (at 3D graphene) and 302.7 and 312.5 mV (at 3D carbon (RVC)) respectively, at 100 mVs^{-1}) the 3D graphene foam exhibits a large improvement in its electrochemical reversibility over that of the RVC alternative. In support of this observation, the k^o was estimated (with respect to the first redox couple, over the scan rate range employed) [29] and found to correspond to *ca*. 31.7×10^{-5} and

9.17×10^{-5} cm^2 s^{-1} for the 3D graphene and carbon foams respectively (utilising a diffusion coefficient of 3.32×10^{-9} cm^2 s^{-1} for TMPD in $[C_4MIM][NTf_2]$). [31] Such values indicate that enhanced HET kinetics and a beneficial electrochemical response are evident at the 3D graphene foam relative to the 3D carbon foam alternative. The second noticeable characteristic of the CVs presented in Figure 9.6, that is clearly evident, is that there is a significant improvement in the magnitude of the voltammetric peak height observed at the freestanding 3D graphene foam over that of the 3D carbon electrode.

Figure 9.7 *Analysis of voltammetric peak height against square-root of the applied scan rate for 1 mM TMPD in* ***A****: $[C_4MIM][NTf_2]$;* ***B****: $[C_4MIM][BF_4]$; and* ***C****: $[C_4MIM][PF_6]$, using the freestanding 3D graphene (circles) and carbon (RVC) foam (squares) electrodes.*

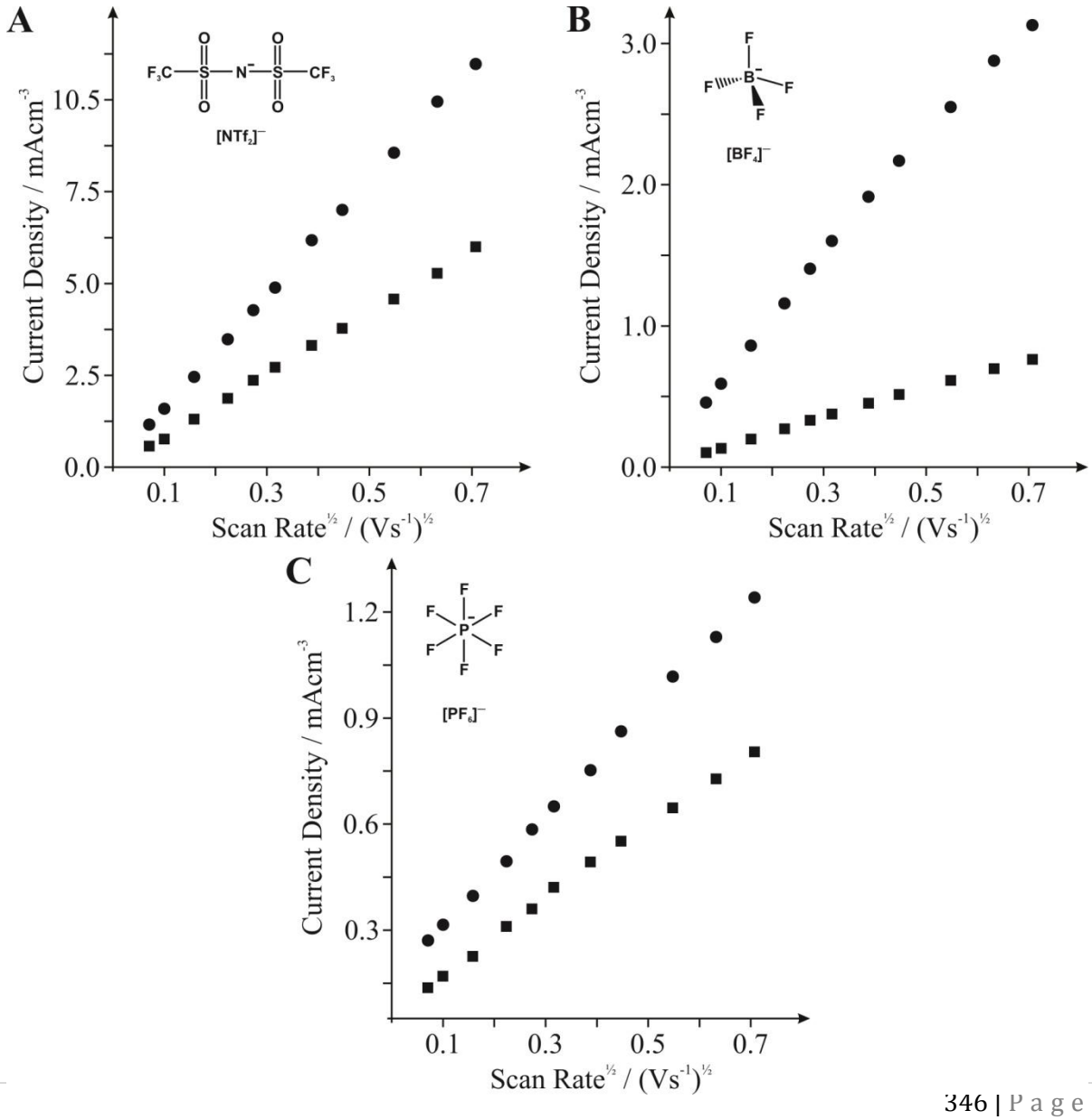

The electrochemical process at TMPD is due to two one-electron oxidations (and corresponding reductions on the reverse scan) which has been well established in aprotic solvents and various ionic liquids, [32] described by equation (1.53). Figure 9.7 shows the analysis of the voltammetric peak height (first redox couple) *versus* square root of the scan rate obtained with both the freestanding 3D graphene and carbon (RVC) foam macrostructures. Note that (as discussed earlier) in both cases, diffusional processes are in operation. Of interest is that in all the RTILs studied, that is $[C_4MIM][NTf_2]$, $[C_4MIM][BF_4]$ and $[C_4MIM][PF_6]$, the response of the 3D graphene foam gives rise to significant improvements when contrasted to that of the 3D carbon alternative. Additionally however, note that as the anion is changed (Figure 9.8) the magnitude of the voltammetric response decreases as a function of the anion, which could be due to a change in the stability (through solvent-solute interactions) of the electro-generated species: *i.e.* $TMPD^{\bullet+}X^-$ where X^- is: NTf_2, BF_4 or PF_6. However, due to no observed peak potential shifts, a more plausible explanation is that the different ionic liquids have substantially different viscosities, with the following values independently reported: $[C_4MIM][NTf_2]$ = 52 mPa.s; $[C_4MIM][BF_4]$ = 112 mPa.s; and $[C_4MIM][PF_6]$ = 371 mPa.s (all at T = 293K). [33] The diffusion coefficient of the species under investigation (D) is inversely related to the viscosity (η) as given by the classic Stokes-Einstein equation:

$$D = \frac{k_B T}{6\pi\eta r} \qquad (9.1)$$

where k_B is the Boltzmann constant and r is the molecular radius of the diffusing species (assuming the molecule is spherical). Such that a change in the diffusion coefficient at the diffusing species $(TMPD / TMPD^{\bullet+})$ occurs due to the ionic liquid's viscosity; becoming slower. Thus as the peak current is related to the diffusion coefficient *via* the Randles–Ševćik equation (see equation (1.40) for example), as a result, the peak current decreases as the viscosity of the ionic liquid is increased. Since it is well known that the diffusion coefficients

of species in ionic liquids are highly dependent on the viscosity of the ionic liquid, it is likely that this is the case for the response observed in Figure 9.8; the reduction in the magnitude of the voltammetric peak height is due to this, coupled with the differing hydrophobicity of the electrode materials.

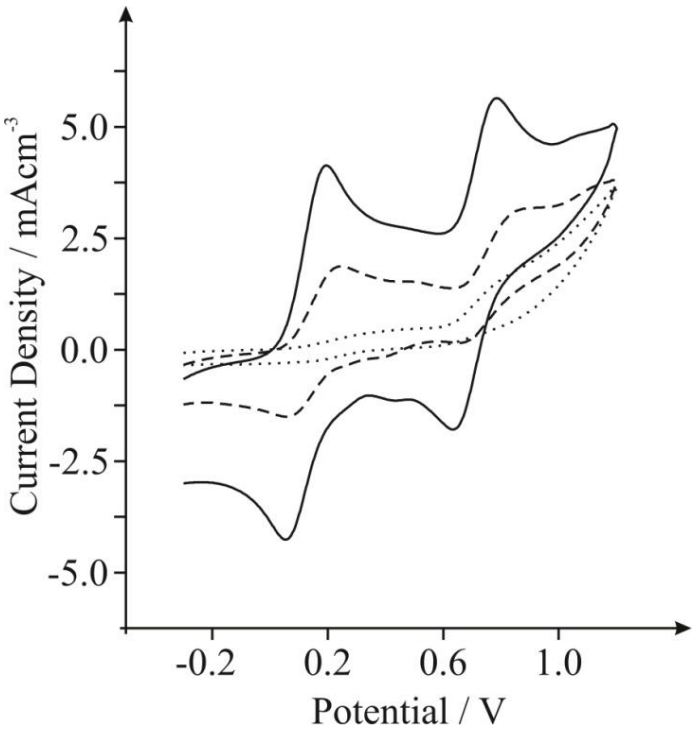

Figure 9.8 *Typical cyclic voltammetric profiles recorded using a freestanding 3D graphene foam towards 1 mM TMPD in: [C_4MIM][NTf_2] (solid line); [C_4MIM][BF_4] (dashed line); and [C_4MIM][PF_6] (dotted line). Scan rate: 100 mVs^{-1} (vs. Ag).*

In summary, in terms of the HET rates observed at the freestanding 3D graphene and carbon foams, which are inferred towards with respect to the given ΔE_P values (which are highly indicative/informative), [1] within each of the examples studied herein it is evident that the 3D graphene foam out-performs the 3D carbon alternative to some degree. In order to better understand this observation one first refers back to the case of ferrocene (Figure 9.5). For the case of this simple outer-sphere redox probe it is well known that the response obtained for carbonaceous materials is dependent on the relative coverage of edge plane sites/defects: which have been shown to be the origin of fast electron transfer kinetics – in

contrast to the other geometric contribution to the structure of carbon materials, basal plane sites, which have been shown to be relatively 'electrochemically' inert. [1, 34] In the case of utilising planar EPPG and BPPG electrodes towards the oxidation of ferrocene, the EPPG electrode has a higher global coverage of edge plane sites over that of basal plane sites and conversely the BPPG electrode (due to its structure) has a low global coverage of edge plane sites: hence poor voltammetric activity is exhibited at the BPPG when contrasted to that of the EPPG, with the ΔE_P (decreasing) and consequent HET kinetics increasing with increments in the coverage of edge plane sites – which is well known behaviour at numerous electrochemical redox probes. [1, 34, 35] Given these insights, it is clear that the freestanding 3D graphene foam exhibits a greater coverage of edge plane like- sites/defects over that of the 3D carbon (RVC) foam alternative. This is expected given that the carbon foam is constructed of glassy carbon, GC, like material and thus would agree with literature reports and the SEM images provided (see Figure 5.24). [15, 36] Note however that the k^o obtained at the EPPG electrode was estimated to be *ca*. 1.1×10^{-2} cm s^{-1} which is in good agreement with literature reports (see k^o's reported above for comparison with the respective foams). [37] As such it is clear that the degree of edge plane coverage at the 3D graphene foam is significantly less than that of the EPPG and thus dramatically improved HET rates are observed at the latter over that of the former. However, one must additionally note that in terms of improving the response obtained at the 3D graphene foam further, the introduction of a larger number of structural defects or the act of increasing the number of graphene layers (or manipulating their orientation) is likely to result in improvements in the HET rate (k^o) (see for example Chapter 8.3). [1, 19, 38] Also of importance is the differing degrees of oxygenated species present on the two foams (*ca*. 5.0 and 9.6 % oxygen content at the 3D graphene and 3D carbon foams respectively) which have been shown to strongly influence the voltammetry observed when not utilising an outer-sphere redox probe, [39, 40] and

thus due to the convolution of the responses of edge plane sites and oxygenated species, it is likely these factors contribute to the variations observed in the sensitivity (in terms of the varying degree of differences between the HET rates (ΔE_P values) observed at the different electrodes) evident at different probes, but this cannot be easily de-convoluted.

In relation to the performance of 2D planar pristine graphene, [34] of which the 3D graphene foam is of similar 'pristine' nature (see Chapter 5.4.6.1) other than possessing a different architecture. It is clear that the novel 3D architecture of this graphene foam gives rise to beneficial electrochemistry over that of the former, which was shown in previous chapters to exhibit poor electrochemical behaviour owing to its geometry (low edge plane and high basal plane content). [34] Thus the wrinkles and structural defects induced through the unique structure of the 3D graphene foam (and its *quasi*-graphene composition) likely give rise to increased coverage and accessibility of edge plane sites on the foam structure.

In terms of the electroanalytical potential of the 3D graphene and carbon foams, it is evident that the freestanding 3D macro-porous graphene foam gives rise to poor voltammetric responses in aqueous solutions due to its hydrophobicity inhibiting the solution accessibility to active surface area. However, the graphene foam consequently gives rise to improved electrochemical signatures in non-aqueous media due to enhanced wettability and thus improved accessibility of its larger portion of reactive edge plane sites (as inferred above) and surface area available. The beneficial response observed herein at the novel 3D graphene network is in direct contrast to that of its 2D planar counterpart, where detrimental sensing capabilities have been noted at the latter owing to factors discussed earlier. [41, 42]

On a final note, the average % RSD, in terms of inter-repeatability of the analytical I_P was determined to correspond to *ca*. 2.3 and 3.8 % (N = 4) when calculated as an average across all of the probes utilised to characterise the 3D graphene and carbon foams

respectively. Given the general improvements known of 3D architectures over the planar alternatives (standard electrodes) [43] coupled with these % RSD values, the freestanding 3D graphene foam clearly has the potential to exhibit superior performance in terms of its application as an enhanced electrochemical sensor substrate. From inspection of Figures 9.5 and 9.6 and in terms of the analysis of k^o's and I_P's, the 3D graphene structure is superior to that of the commonly utilised and commercially available 3D carbon network alternative.

9.1.4. CONCLUSIONS

This chapter has explored, for the first time, the electrochemistry of a true freestanding 3D graphene foam electrode. This has allowed one to demonstrate that due to the hydrophobic nature of the freestanding 3D graphene foam, its application is inhibited in aqueous solutions. Conversely, such 3D graphene foams demonstrate favourable electrochemical characteristics when utilised as an electrode material in RTILs (non-aqueous media) towards some commonly employed redox probes. Interestingly, when the performance of a commercially available and commonly utilised 3D carbon (RVC) foam alternative is contrasted to that of the novel 3D graphene foam electrode, the graphene foam consistently out-performs the alternative in terms of both electron transfer kinetics (HET rates) and the magnitude of the analytically important current passed. Furthermore, with the added improvements of the 3D macro-porous structure over that of the standard 2D planar electrodes commonly employed within electrochemistry, freestanding 3D graphene foams provide a promising platform from which the development of next generation electrochemical sensors can potentially originate. This chapter has demonstrated a novel and useful structural configuration of graphene that holds great promise for future use/advancements in electrochemistry.

9.1.5. REFERENCES

1. D. A. C. Brownson, D. K. Kampouris and C. E. Banks, *Chem. Soc. Rev.*, 2012, **41**, 6944.
2. D. A. C. Brownson, D. K. Kampouris and C. E. Banks, *J. Power Sources*, 2011, **196**, 4873.
3. T. Gan and S. Hu, *Microchim. Acta*, 2011, **175**, 1.
4. X. Huang, Z. Zeng, Z. Fan, J. Liu and H. Zhang, *Adv. Mater.*, 2012, **24**, 5979.
5. E.-J. Yoo, J. Kim, E. Hosono, H.-S. Zhou, T. Kudo and I. Honma, *Nano Lett.*, 2008, **8**, 2277.
6. Z. Chen, W. Ren, L. Gao, B. Liu, S. Pei and H.-M. Cheng, *Nat. Mater.*, 2011, **10**, 424.
7. E. Singh, Z. Chen, F. Houshmand, W. Ren, Y. Peles, H.-M. Cheng and N. Koratkar, *Small*, 2013, **9**, 75.
8. X. Dong, J. Chen, Y. Ma, J. Wang, M. B. Chan-Park, X. Liu, L. Wang, W. Huang and P. Chen, *Chem. Commun.*, 2012, **48**, 10660.
9. X.-C. Dong, H. Xu, X.-W. Wang, Y.-X. Huang, M. B. Chan-Park, H. Zhang, L.-H. Wang, W. Huang and P. Chen, *ACS Nano*, 2012, **6**, 3206.
10. X. Dong, Y. Cao, J. Wang, M. B. Chan-Park, L. Wang, W. Huang and P. Chen, *RSC Adv.*, 2012, **2**, 4364.
11. X. Dong, X. Wang, L. Wang, H. Song, H. Zhang, W. Huang and P. Chen, *ACS Appl. Mater. Interfaces*, 2012, **4**, 3129.
12. J. M. Friedrich, C. Ponce-de-Leon, G. W. Reade and F. C. Walsh, *J. Electroanal. Chem.*, 2004, **561**, 203.
13. E. S. Gonçalves, M. C. Rezende, M. F. K. Takahashi and N. G. Ferreira, *Mater. Res.*, 2006, **9**, 147.
14. E. Nossol and A. J. G. Zarbin, *Electrochim. Acta*, 2008, **54**, 582.
15. R. L. McCreery, *Chem. Rev.*, 2008, **108**, 2646.
16. *Note that in all of the above experiments (i.e. in aqueous solutions only viz Figures 9.1 and 9.2), the 3D graphene foam was forcefully inserted/submerged into the aqueous solution and held/secured in position during electrochemical measurements*.
17. J. Rafiee, M. A. Rafiee, Z. Z. Yu and N. Koratkar, *Adv. Mater.*, 2010, **22**, 2151.
18. Y. J. Shin, Y. Y. Wang, H. Huang, G. Kalon, A. T. S. Wee, Z. X. Shen, C. S. Bhatia and H. Yang, *Langmuir*, 2010, **26**, 3798.
19. D. A. C. Brownson and C. E. Banks, *Phys. Chem. Chem. Phys.*, 2012, **14**, 8264.
20. A. Marmur, *Langmuir*, 2003, **19**, 8343.
21. M. C. Buzzeo, R. G. Evans and R. G. Compton, *ChemPhysChem*, 2004, **5**, 1106.
22. M. C. Buzzeo, C. Hardacre and R. G. Compton, *Anal. Chem.*, 2004, **76**, 4583.
23. A. Lewandowski and A. Świderska-Mocek, *J. Power Sources*, 2009, **194**, 601.

24. Y. Shim, H. J. Kim and Y.-J. Jung, *Faraday Discuss.*, 2012, **154**, 249.

25. W. Sun, X. Qi, Y. Chen, S. Liu and H. Gao, *Talanta*, 2011, **87**, 106.

26. V. Balland, S. Lecomte and B. Limoges, *Langmuir*, 2009, **25**, 6532.

27. J. F. Smalley, S. W. Feldberg, C. E. D. Chidsey, M. R. Linford, M. D. Newton and Y.-P. Liu, *J. Phys. Chem.*, 1995, **99**, 13141.

28. W. Park and H.-G. Hong, *Bull. Korean Chem. Soc.*, 2006, **27**, 381.

29. R. S. Nicholson, *Anal. Chem.*, 1965, **37**, 1351.

30. E. I. Rogers, D. S. Silvester, D. L. Poole, L. Aldous, C. Hardacre and R. G. Compton, *J. Phys. Chem. C*, 2008, **112**, 2729.

31. J. S. Long, D. S. Silvester, A. S. Barnes, N. V. Rees, L. Aldous, C. Hardacre and R. G. Compton, *J. Phys. Chem. C*, 2008, **112**, 6993.

32. R. G. Evans, O. V. Klymenko, P. D. Price, S. G. Davies, C. Hardacre and R. G. Compton, *ChemPhysChem*, 2005, **6**, 526.

33. A. M. O'Mahony, D. S. Silvester, L. Aldous, C. Hardacre and R. G. Compton, *J. Chem. Eng. Data*, 2008, **53**, 2884.

34. D. A. C. Brownson, L. J. Munro, D. K. Kampouris and C. E. Banks, *RSC Adv.*, 2011, **1**, 978.

35. T. J. Davies, M. E. Hyde and R. G. Compton, *Angew. Chem. Int. Ed.*, 2005, **44**, 5121.

36. C. E. Banks and R. G. Compton, *Analyst*, 2006, **131**, 15.

37. K.-Q. Ding, Q.-F. Wang and M. Zhao, *J. Chin. Chem. Soc.*, 2007, **54**, 723.

38. D. A. C. Brownson, R. V. Gorbachev, S. J. Haigh and C. E. Banks, *Analyst*, 2012, **137**, 833.

39. E. P. Randviir, D. A. C. Brownson, M. Gómez-Mingot, D. K. Kampouris, J. Iniesta and C. E. Banks, *Nanoscale*, 2012, **4**, 6470.

40. D. A. C. Brownson, A. C. Lacombe, M. Gómez-Mingot and C. E. Banks, *RSC Adv.*, 2012, **2**, 665.

41. D. A. C. Brownson, C. W. Foster and C. E. Banks, *Analyst*, 2012, **137**, 1815.

42. D. A. C. Brownson, A. C. Lacombe, D. K. Kampouris and C. E. Banks, *Analyst*, 2012, **137**, 420.

43. S. Nardecchia, D. Carriazo, M. L. Ferrer, M. C. Guiérrez and F. del-Monte, *Chem. Soc. Rev.*, 2013, **42**, 794.

9.2. EXPLORING THE ELECTROCHEMICAL PERFORMANCE OF GRAPHITIC PASTE ELECTRODES: GRAPHENE *VS*. GRAPHITE

This chapter reports the fabrication, characterisation (SEM, TEM, XPS and Raman spectroscopy) and electrochemical implementation of a graphene paste electrode. The paste electrodes utilised are constructed by simply mixing graphene with mineral oil (which acts as a binder) prior to loading the resultant paste into a piston-driven polymeric-tubing electrode-shell, where this electrode configuration allows for rapid renewal of the electrode surface. Note that this chapter contains published work. [11]

The fabricated paste electrode is electrochemically characterised using both inner-sphere and outer-sphere redox probes, namely potassium ferrocyanide (II), hexaammine-ruthenium (III) chloride and hexachloroiridate (III), in addition to the biologically relevant and electroactive analytes, *L*-ascorbic acid (AA) and uric acid (UA). Comparisons are made with a graphite paste alternative and the benefits of graphene implementation as a paste electrode within electrochemistry are explored, as well as the characterisation of their electroanalytical performances. Such work is highly important and informative for those working in the field of electroanalysis where electrochemistry can provide portable, rapid, reliable and accurate sensing protocols (bringing the laboratory into the field), with particular relevance to those searching for new electrode materials.

[11] L. C. S. Figueiredo-Filho, D. A. C. Brownson, M. Gómez-Mingo, J. Iniesta, O. Fatibello-Filho and C. E. Banks, *Analyst*, 2013, **138**, 6354.

9.2.1. INTRODUCTION

To reiterate a statement that has been highlighted many times throughout this thesis, a major issue in graphene research, particularly in electrochemistry, is 'how to connect to (and electrically wire) graphene as to obtain the reported benefits. [1-3] The most common approach when utilising graphene is to immobilise it upon a suitable electrode surface, such that one is effectively averaging a response over that of the graphene domains. [1] However, modifying such surfaces has potential to leave underlying 'reactive' surfaces exposed, which can influence and in certain cases dominate the observed electrochemistry. [1, 4-6] Thus to overcome the earlier issue, researchers have recently turned to fabricating three-dimensional graphene architectures [2, 3] (such as the work presented in Chapter 9.1) or have utilised 'bulk' graphene in order to connect directly to it; for example, fabricating and utilising paste electrodes comprised primarily of the material in question. [7, 8]

Carbon based paste electrodes have been widely used and explored in electrochemistry since 1958 and generally offer beneficial attributes over the more traditional electrodes, such as exhibiting low background currents, large potential domains and their ease of modification. [9-11] As such it is evident that the fabrication of graphene paste electrodes should have widespread appeal, where the reported beneficial properties of graphene can be combined with the significant benefits of paste electrodes (for example, the ease and rapid nature of their fabrication and the ability to readily renew the electrode surface, alleviating the need for extensive surface pre-treatment) giving rise to improved electrode performances. However, given the widespread electrochemical exploration of both graphene and paste electrodes alike, reports concerning the fabrication and use of graphene paste electrodes are surprisingly limited. One of the first reports of a graphene paste electrode emerged in 2011, [7, 8] in which Parvin demonstrated its applicability

(although utilising functionalised graphene) towards the improved electroanalytical detection of chlorpromazine when contrasted to a carbon alternative (with later efforts focusing on acetazolamide detection). [7, 12] Interestingly, a report by Li *et al.* [8] emerged at around the same time as the former work, which concerned the fabrication of a graphene doped carbon paste electrode and demonstrated its superior electrochemical performance over that of the standard/unmodified carbon paste, particularly towards sensing AA. Following these pioneering reports, further work emerged reporting the analytical detection of β-nicotinamide adenine dinucleotide (NADH), [13] paracetamol, [14] cadmium/lead, [15] and the simultaneous determination of hydroquinone, catechol and resorcinol [16] at graphene doped carbon paste electrodes. Moreover, modified graphene based paste electrodes have recently been reported with constituents such as Prussian blue, platinum and organic solvents. [17-20] Note that to the best of the author's knowledge there is no current literature on solely a graphene paste electrode (that has not been functionalised or is not present as part of a hybrid mixture).

Given the limited examples above, it appears that graphene has the potential to be beneficially implemented as a paste electrode within electrochemistry. It is important to note however, that attempting to preclude the earlier issue (electrically connecting to the graphene) in this manner (fabricating a paste electrode) gives rise to a further issue: due to the high cohesive van der Waals energy graphene has a tendency to coalesce into few- and multi-layered structures (*viz quasi*-graphene [2] and graphite). [21] Such eventualities must be borne in mind when utilising graphene and adequate control measures must be performed in terms of directly comparing the response of said graphene devices to that of a graphitic (graphite) alternative of comparable chemical composition (same level of functionalisation), which is seldom seen throughout the literature.

In this chapter, inspired by the recent reports of graphene based carbon paste electrodes, the fabrication, characterisation and electrochemical implementation of a graphene paste electrode is reported. Comparisons of the electrochemical performances are made with respect to a graphite paste alternative and the benefits of utilising graphene are critically explored.

9.2.2. CHAPTER SPECIFIC EXPERIMETNAL DETAILS

Test solutions were utilised as follows (unless stated otherwise): potassium ferrocyanide (II), hexaammine-ruthenium (III) chloride and hexachloroiridate (III) were prepared separately at a concentration of 1 mM in 0.1 M KCl supporting electrolyte; AA and UA were prepared separately at a concentration of 1 mM in a PBS at a pH of *ca*. 7 (which was prepared utilising 50 mM KH_2PO_4, 50 mM K_2HPO_4 and 0.1 M KCl supporting electrolyte).

The graphene powder (see Chapter 5.4.7) and graphite powder (see Chapter 5.4.3) utilised in this chapter, to fabricate the respective graphitic paste electrodes, have been fully characterised prior to use within the paste mediums. Note that the graphitic materials possess similar oxygen compositions and thus in terms of the electrochemical performance of the two materials, comparisons can be drawn with the confidence that electronic configuration and physical differences (in terms of graphene *vs*. graphite) are the only contributing factors in the differences observed. It is clear that the low O/C ratio for the graphene powder is near that of true pristine graphene, [1, 4] which in conjunction with the Raman spectroscopy and SEM/TEM analysis (see Chapter 5.4.7.1) confirms that the graphene used is of high quality (in addition to the use of high quality synthetic graphite, see Chapter 5.4.3.1).

The relevant (either graphene or graphite) paste mixtures were prepared by hand-mixing *ca*. 850 mg of the respective powder with *ca*. 365 mg of mineral oil (Nujol) in a 70:30 (% weight) composition; note that this composition was optimal, which was determined through varying the composition of the electrode constituents and monitoring the analytical peak height/peak-to-peak separation/reversibility of the ferro-/ferri-cyanide redox probe such that 70:30 gave rise to the most favourable characteristics. Mixtures were homogenised (30 min) and then packed into a polymeric piston-driven paste electrode shell, where the polymeric cylindrical tube possessed an inner diameter (5 mm) defining the planar disk electrode working surface. An electrical contact point was situated at the piston end of the tube ensuring electrical conductivity from the front 'working surface' of the paste electrode to an electrical wire at the rear, to which a lead for the working electrode can be attached. [11, 12] Prior to use within electrochemical measurements a fresh electrode surface was obtained by squeezing out a small portion of paste and polishing the electrode surface on soft clean filter paper until a smooth working surface was obtained, after which the surface was washed with deionised water and the electrode was ready to be used.

Typical cyclic voltammetric responses obtained at each of the fabricated paste electrodes (graphene and graphite) in a pH 7 PBS with 0.1 M KCl electrolyte are depicted in Figure 9.9. Within both the anodic and cathodic potential regions of interest in this work there are no evident voltammetric peaks prior to the addition of the analytes studied herein.

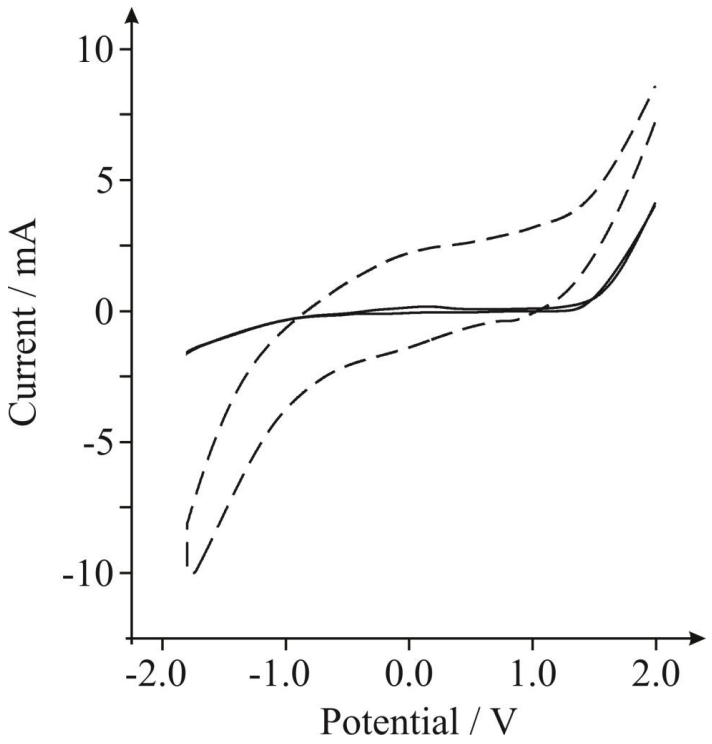

Figure 9.9 *Cyclic voltammetric profiles recorded in a pH 7 PBS (with 0.1 M KCl electrolyte) using the fabricated graphene (dashed line) and graphite (solid line) paste electrodes.*
Scan rate: 100 mV s^{-1} *(vs. SCE).*

9.2.3. RESULTS AND DISCUSSION

9.2.3.1. RESULTS

First the fabricated graphitic paste electrodes are electrochemically characterised towards well-known and widely characterised inner- and outer-sphere electrochemical redox probes, namely potassium ferrocyanide (II), hexaammine-ruthenium (III) chloride and hexachloroiridate (III). [1, 22, 23] Figure 9.10A depicts typical cyclic voltammograms obtained at each of the respective paste electrodes towards the inner-sphere electron transfer redox probe, potassium ferrocyanide (II). It is evident that the graphene and graphite paste electrodes both exhibit a pair of well defined redox peaks, with peak-to-peak separations (ΔE_P) of *ca*. 153.8 and 393.1 mV respectively. Note that the ΔE_P values observed are in good agreement with a previous

literature report and are discussed in detail below. [8] Interestingly, comparisons of the voltammograms indicate that in terms of the electroanalytical signal produced (*i.e.* the voltammetric peak height (I_P) or current passed), similar magnitudes are evident at both of the graphitic paste electrodes (see Figure 9.10B) although a capacitative current is present in the case of the graphene electrode. Using the Randles–Ševćik equation (for a quasi-reversible redox system and utilising a D of 6.3×10^{-6} cm^2 s^{-1} for ferrocyanide (II)) the electrochemical area of the graphene and graphite paste electrodes were deduced to correspond to *ca*. 0.212 and 0.195 cm^2 respectively and thus correspond well with the physical geometric area of 0.196 cm^2; clearly they are not porous.

In order to ensure that the voltammetric responses obtained are diffusional in nature and not due to 'thin-layer' type behaviour, as has been seen before for porous structures such as carbon nanotubes, [1] scan rate studies were performed using both the graphene and graphite paste electrodes. The I_P was monitored as a function of scan rate (υ), with a plot of I_P *versus* square-root of υ revealing the following trends: graphene paste, I_P (A) = 1.24 x 10^{-4} A/$(Vs^{-1})^{0.5}$ + 4.46 x 10^{-6} A (R^2 = 0.99); graphite paste, I_P (A) = 1.16 x 10^{-4} A/$(Vs^{-1})^{0.5}$ + 5.10 x 10^{-6} A (R^2 = 0.99). In both cases it is clear that a linear response is evident, indicating diffusional electrochemical processes. Furthermore, as is expected for the case of the semi-infinite diffusion model as governed by the Randles–Ševćik equation, analysis of log I_P *versus* log υ revealed the gradients of 0.43 (graphene paste) and 0.41 (graphite paste), indicating the absence of thin-layer effects (which if present can give rise to a false impression of 'electrocatalysis' at the material under investigation, when actually a change in mass transport is responsible, see Chapter 1.4.5.1) and representing a response that is purely diffusional in each case. [1, 24]

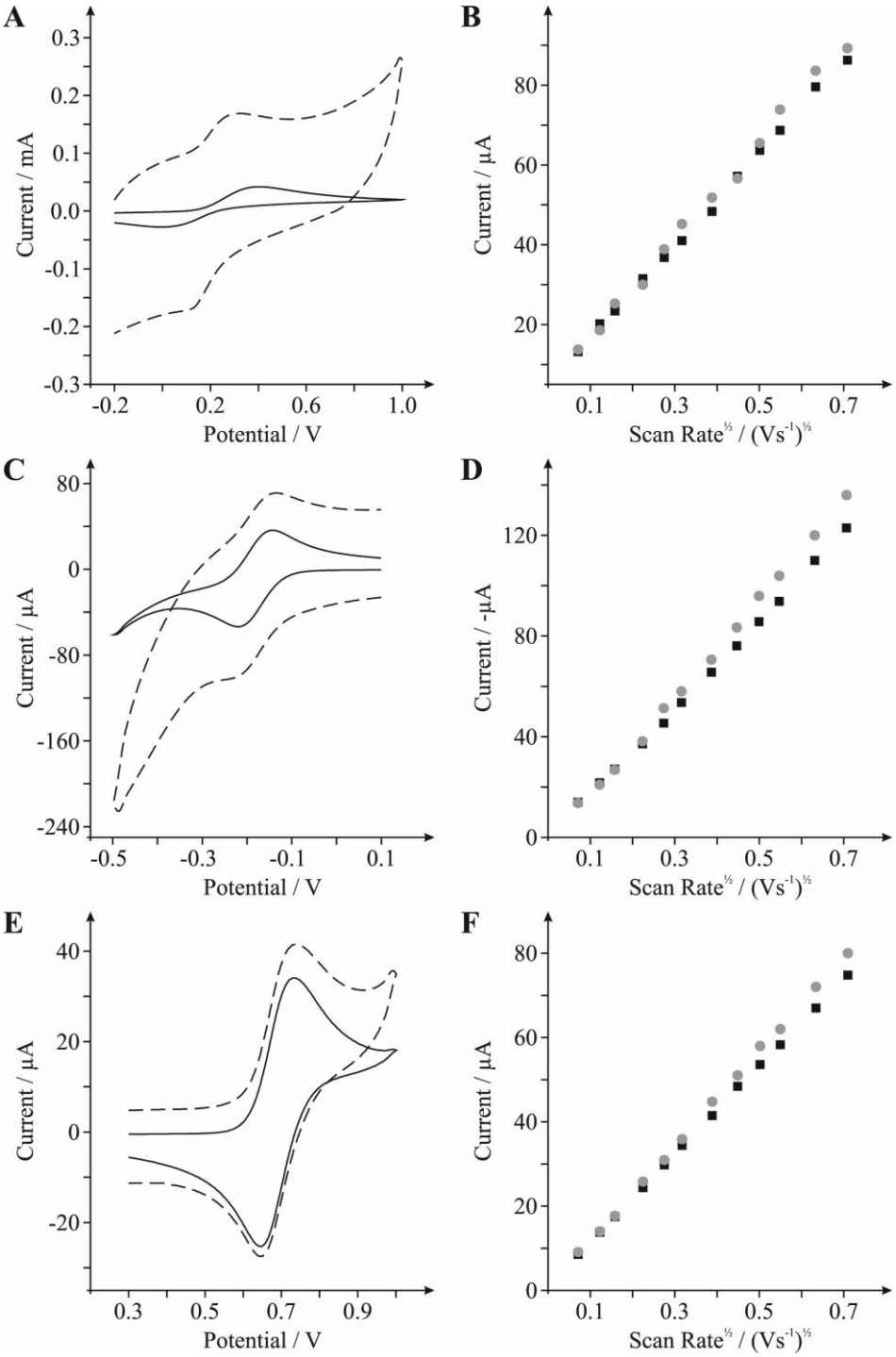

Figure 9.10 *Cyclic voltammetric profiles recorded for: (**A**) 1 mM potassium ferrocyanide (II) in 0.1 M KCl; (**C**) 1 mM hexaammine-ruthenium (III) chloride in 0.1 M KCl; and (**E**) 1 mM hexachloroiridate (III) in 0.1 M KCl, utilising the fabricated graphene (dashed lines) and graphite (solid lines) paste electrodes at a scan rate of 100 mV s^{-1}, vs. SCE. (**B**), (**D**) and (**F**) depict the analysis of voltammetric peak height against square-root of the applied scan rate for each of the redox probes (**A**, **C** and **E**) respectively, using the graphene (grey-circles) and graphite (black-squares) paste electrodes.*

The voltammetric responses of the paste electrodes are next explored towards the outer-sphere electron transfer redox probes, hexaammine-ruthenium (III) chloride and hexachloroiridate (III). As is evident in Figures 9.10C and 9.10E, typical cyclic voltammograms obtained at a υ of 100 mVs^{-1} (*vs.* SCE) exhibited well defined pairs of reversible redox peaks with a ΔE_P for graphene and graphite of *ca*. 61.7 and 63.1 mV (hexaammine-ruthenium (III) chloride) and *ca*. 90.3 and 87.9 mV (hexachloroiridate (III)) respectively; both sets of values agree well with the literature available on graphite electrodes. [23, 25] As was the case in the earlier example, in terms of the voltammetric I_P observed at each of the outer-sphere probes, both of the graphitic paste electrodes exhibited similar magnitudes (see Figure 9.10D and 9.10F) and again a capacitative current was evident at the graphene electrode in both instances. Note that, as expected given the analysis performed at the ferro/ferri redox probe above, employment of the appropriate scan rate studies indicated that neither of the paste electrodes exhibited thin-layer behaviour when utilised with the outer-sphere redox probes and thus diffusion controlled electrochemical processes are dominant in both instances.

Finally, the biologically relevant analytes AA and UA are utilised separately in solution. These electroactive probes are commonly explored in electrochemistry and that due to their biological importance they are often the target analyte for electroanalytical sensors. [14, 32] Furthermore, note that in terms of responses observed when utilising these analytes, their 'surface sensitivity' has been widely characterised and it is known that the response of AA is relatively insensitive to the surface state of the electrode and thus depends predominantly on its electronic structure, whereas UA is in fact surface sensitive (see *discussion* for further details). [1, 23, 26] Figures 9.11A and 9.11C depict the typical cyclic voltammograms observed at the respective graphene and graphite paste electrodes, where the oxidation peaks of AA and UA

occur at *ca*. 0.303 and 0.374 V for graphene and at *ca*. 0.345 and 0.403 V for graphite respectively; relating to a inter-solution peak-to-peak resolution (AA and UA) of *ca*. 71 and 58 mV at the graphene and graphite paste electrodes respectively.

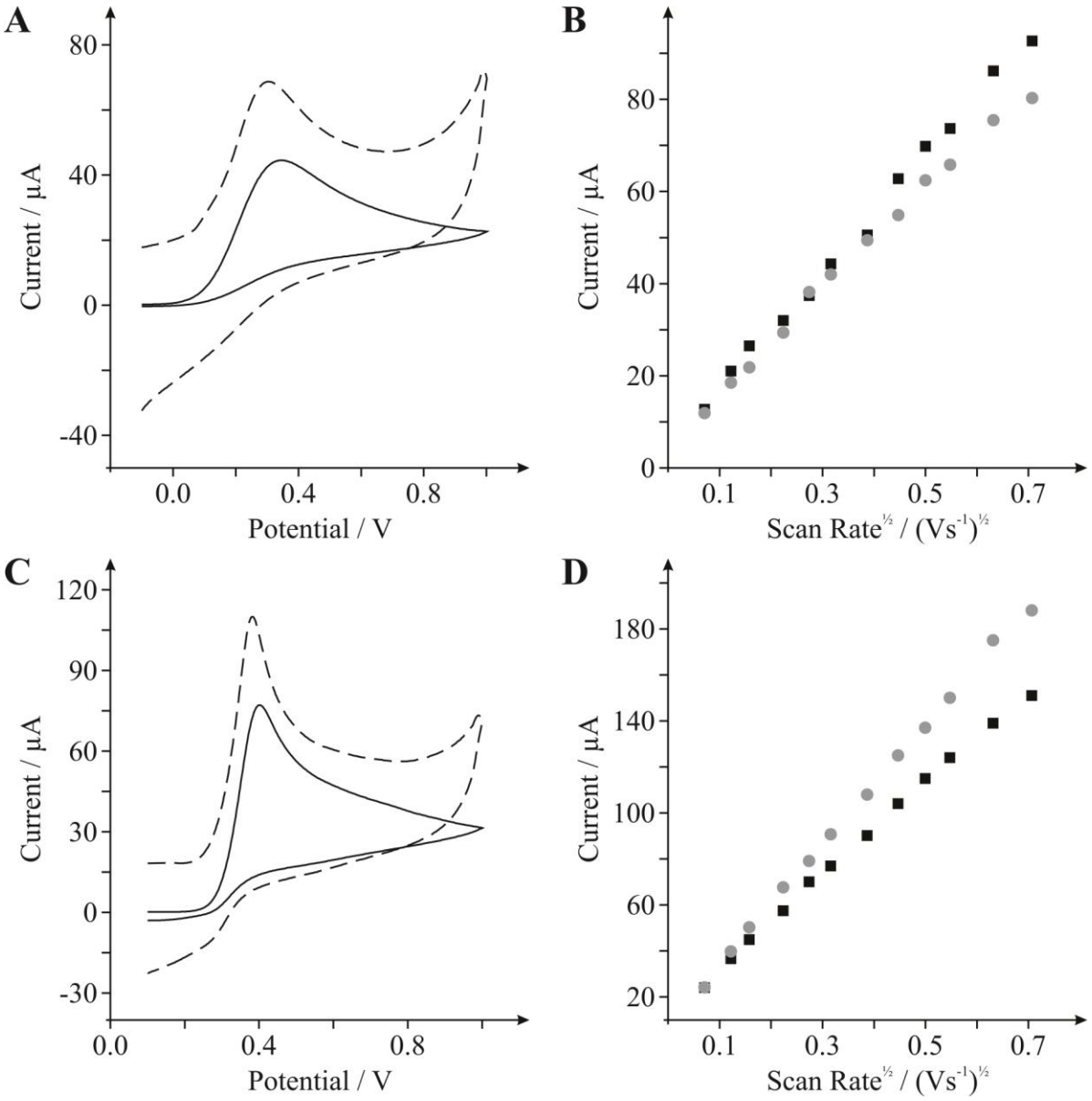

Figure 9.11 *Cyclic voltammetric profiles recorded for: (**A**) 1 mM AA in pH 7 PBS (0.1 M KCl) and (**C**) 1 mM UA in pH 7 PBS (0.1 M KCl), utilising the fabricated graphene (dashed lines) and graphite (solid lines) paste electrodes at a scan rate of 100 mV s^{-1}, vs. SCE. (**B**) and (**D**) depict the analysis of voltammetric peak height against square-root of the applied scan rate for both of the analytes (**A** and **C**) respectively, using the graphene (grey-circles) and graphite (black-squares) paste electrodes.*

In both instances (AA and UA) analysis of the I_P revealed similar magnitudes in the voltammetric currents passed at each of the electrodes studied (see Figures 9.11B and 9.11D respectively) where once more a larger background (capacitative) current was evident at the graphene paste electrode over that of the graphite alternative. Employment and analysis of the relevant scan rate studies revealed that neither of the paste electrodes exhibited thin-layer behaviour with respect to these analytes, with results indicating diffusion controlled electrochemical processes.

9.2.3.2. DISCUSSION

In terms of evaluating the quality of an electrode material the most important parameter to consider is its heterogeneous electron transfer (HET) rate, of which the ΔE_P values obtained at both inner- and outer-sphere redox probes are generally indicative, where a smaller ΔE_P value represents an increased reversibility of the redox probe utilised and thus faster HET kinetics at a given electrode material (when contrasted to an alternative with larger ΔE_P values), which is a beneficial characteristic in numerous electrochemical areas. [1]

In the case of the outer-sphere redox probes utilised there were no significant changes observed in the reversibility of the probes at both the graphene and graphite paste electrodes, which exhibited similar ΔE_P values. Note that the electrochemical response of an outer-sphere system is sensitive primarily to the electronic structure of the electrode material (electronic density of states, DOS, and thus the respective coverage of 'reactive' edge plane sites (opposed to the relatively 'un-reactive' basal plane sites) [27] for the case of graphitic materials), [1, 28] where the electrode acts merely as a source (or sink) of electrons and electron transfer is not influenced by the surface state (absence/presence of specific oxygen containing functionalities, or the surface cleanliness in terms of the presence of uncharged adsorbates). [1, 28] The insights gained

above indicate that the two graphitic paste electrodes exhibit similar electronic structures, *i.e.* edge plane content. Furthermore, this inference is supported when considering the case of AA. As noted earlier AA is relatively insensitive to the electrode surface (such as the presence of oxides terminating the edge plane sites) and thus as with outer-sphere systems the response observed depends predominantly on the electrode's electronic structure (DOS), where the oxidation potential will shift to less positive over-potentials (indicative of improved HET kinetics) with increasing global coverage of edge plane like- sites/defects at a graphitic electrode material given that these 'edge plane' sites are the origin of fast electron transfer. [1, 27] For the case of the graphene and graphite paste electrodes there is little change in the electrochemical response observed, with both electrodes exhibiting AA oxidation peaks at similar over-potentials, suggesting that comparable electronic structures (edge plane compositions) reside at the two electrode materials.

In the case of the inner-sphere redox system utilised there is a small reduction evident in the ΔE_P value observed at the graphene over that of the graphite paste electrode, indicative of an improved electrochemical response (faster HET rates) at the graphene electrode. Note that inner-sphere redox mediators are termed *surface sensitive*, where electron transfer (and in turn the electrochemical response observed) is strongly influenced by the state of the electrode surface (surface chemistry and micro-structure; for example an improvement (or inhibition) may be observed *via* particular electro-catalytic interactions with specific surface oxygenated species (or the lack of said surface groups/presence of impurities may give rise to the inverse case)) with surface effects strongly influencing either beneficial or detrimental responses. [1, 28] Given the above insights, one would suggest that although the two paste electrodes have a similar physicochemical composition in terms of their electronic structure and low levels of oxygenated

species (*ca*. 3.3 and 2.1 % for graphene and graphite respectively), in this instance the graphene and graphite paste electrodes possess a varied surface-oxygenated functional group that is responsible for either the favourable surface interaction at the graphene electrode or unfavourable interaction at the graphite paste electrode, resulting in distinct electrochemical performances being observed. Contrary to the response observed above, for the case of UA similar electrochemical responses were observed at both the graphene and graphite paste electrodes. As indicated earlier, UA is a surface sensitive probe with the electrochemical response observed highly sensitive to/dependent on oxygenated species, where improved voltammetry has been observed at electrochemically activated electrodes and at electrode surfaces with large O/C ratios. [29, 30] For the case of the graphene and graphite paste electrodes there is little change in the electrochemical response observed, with both electrodes exhibiting UA oxidation peaks at similar over-potentials, suggesting that in addition to their comparable electronic structures (edge plane compositions), the two electrode materials possess a similar % of oxygen content. This inference confirms XPS analysis provided in Chapters 5.4.7.1 and 5.4.3.1 where similar and low O/C ratios were observed.

The heterogeneous electron transfer rate constant, k^o, was estimated at both the graphene and graphite paste electrodes using the outer-sphere electron transfer probe hexaammine-ruthenium (III) chloride. The Nicholson method was invoked to estimate the observed standard HET rate constant (k^o) for a quasi-reversible system as depicted in equation (1.44). Using this approach the k^o values of 0.19 (± 0.02) and 0.18 (± 0.02) cm s^{-1} were estimated for the graphene and graphite paste electrodes respectively (utilising a D of 9.1 x 10^{-6} cm^2 s^{-1} for hexaammine-ruthenium (III) chloride in 0.1 M KCl and deduced over the scan rate range of 5–500 mV s^{-1}, N = 3). [4, 31] It is clear that the similarity in the estimated k^o

values supports the above inferences and evidently both the graphene and graphite paste electrodes exhibit similar electronic properties, which give rise to similar electrochemical performances.

Thus it is apparent that in terms of the electronic structure of the graphene and graphite paste electrodes, when graphene powder is utilised in such circumstance as to fabricate a paste electrode, it is likely that the graphene sheets coalesce which results in the formation of multi-layered graphene structures (*viz quasi*-graphene [2] and graphite) – *vide infra* for characterisation of the coalesced paste mediums. As a result of the coalesced graphene sheets the fabricated 'graphene' paste electrode possesses a similar structural signature to that of the alternative graphite paste electrode, resulting in similar electrochemical characteristics/performance and thus no advantages of using graphene over graphite are evident when fabricating such electrodes. It is important to note that care was taken to utilise graphene and graphite powders of similar chemical composition (level of functionalisation) as to allow direct and accurate comparisons to be drawn. However, although it is apparent from the characterisation that the graphene and graphite paste electrodes possessed similar levels of surface-oxygenated functional groups, a distinct oxygenated functional group was likely present on the surface of the graphene paste electrode which resulted in an improved electrochemical response at the graphene paste electrode in the case of the ferro-/ferri-cyanide redox probe. Note also that the distinct oxygen group that is likely present on the graphene paste electrode is expected to give rise to the capacitance that is evident at this electrode, given that it is well known that specific oxygenated functionalities on graphitic structures can result in larger capacitance values, [32, 33] for example in this case there is a modestly larger % of C–O groups on the graphene paste electrode than on the graphite alternative.

From an electroanalytical perspective it is the voltammetric I_P observed that is of analytical use. In terms of the results presented above it is evident that in all cases the respective graphene and graphite paste electrodes exhibited similar I_P values and therefore one would expect this to relate to similar electroanalytical performances at the two electrodes; it is this that is now explored within this chapter, utilising the biologically important analytes AA and UA. [23, 34]

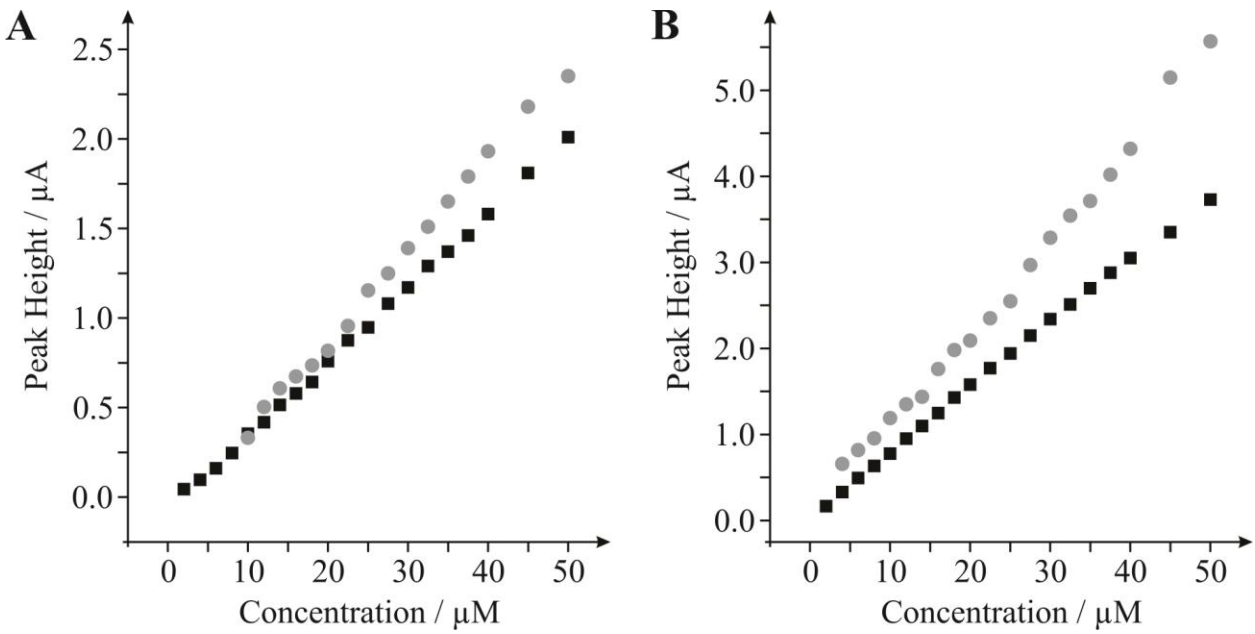

Figure 9.12 *Calibration plots towards the detection of AA (**A**) and UA (**B**) depicting the I_P as a function of concentration, obtained via cyclic voltammetric measurements performed using either a graphene (grey-circles) or graphite (black-squares) paste electrode.*
All data was obtained at a scan rate of 100 mVs^{-1}, vs. SCE.

Figures 9.12A and 9.12B depict the electroanalytical performance of both the graphene and graphite paste electrodes towards the sensing of AA and UA respectively, where the I_P relating to the electro-oxidation of the given analyte was monitored in relation to successive additions of the analyte of interest into a pH 7 PBS (0.1 M KCl). Table 9.1 depicts a summary of the electroanalytical responses observed towards the target analytes where there appears to be no

significant difference between the analytical sensitivity (A M^{-1}) observed at the graphene and graphite paste electrodes towards either of the target analytes utilised. Also presented in Table 9.1 are the calculated limit of detection (LOD, based on three-sigma) values for the respective electrodes, where it is evident that the graphite paste exhibits an improved LOD relative to the graphene paste electrode towards both of the analytes of interest.

Table 9.1 *Comparison of the analytical sensitivities and resultant LODs (based on three-sigma) obtained at the fabricated paste electrodes towards the electroanalytical detection of AA and UA (N = 3).*

Electrode material	Sensitivity/A M^{-1}	LOD (3σ)/μM
AA		
Graphene paste	0.052	1.67 (±0.04)
Graphite paste	0.041	0.51 (±0.01)
UA		
Graphene paste	0.109	1.68 (±0.04)
Graphite paste	0.075	0.58 (±0.02)

Although the two electrodes (as established above) exhibit similar electrochemical properties and thus have similar analytical sensitivities towards the given analytes, it is clear that the capacitative response evident at the graphene paste electrode causes an interference in terms of its electroanalytical performance, where this 'capacitance' inhibits the detection of the target analytes at lower concentrations. In both instances it is apparent that the graphite paste electrode is superior in terms of its electroanalytical performance. With respect to the sensitivities and LOD values reported above, note that the purpose of this thesis is to depict a proof of concept regarding the fabrication (and limitations) of graphitic paste electrodes and thus 'state of the art' sensing at low levels is not within the intended scope. It is expected that the performances of the

electrodes reported herein are less sensitive to others reported within the literature, for example, in comparison the performance of an EPPG electrode has been reported to achieve a lower detection limit of 30 nM, with three linear ranges observed from 100 nM to 3400 µM for UA. [35]

Of further interest is the performance of the two paste electrodes in terms of the relative resolution of the AA and UA oxidation peaks (if they were to be presented in the same sample). Note that these two analytes are often found together, for example in biological samples, where resolution of the peaks is an important parameter. Based on the separation data calculated above (*ca*. 71 and 58 mV for graphene and graphite respectively) it is clear that there are no significant advantages of employing a graphene paste electrode over a graphite alternative in such instances.

In terms of the average Relative Standard Deviation (RSD) of the fabricated graphitic paste electrodes, the inter-repeatability of the analytical I_P was determined to correspond to *ca*. 2.44 and 2.66 % (N = 3, graphene and graphite respectively) when calculated as an average across all of the probes utilised in this work. Furthermore, in terms of fabricating the said electrode for commercial use the 'cost per gram' of electrode material is an important factor to consider. Currently, at the time of writing this thesis, graphite is *ca*. 1.48 USD (*ca*. 0.97 GBP) and graphene is *ca*. 4.95 USD (*ca*. 3.25 GBP) per gram of material. Thus it is more economical to fabricate the graphite electrode, with lower fabrication costs per electrode. Given the similar electrochemical properties, analytical sensitivity and % RSD of both the graphitic paste electrodes and the improved electroanalytical LOD of the graphite paste electrode, when combined with the economical insights stated above; it is apparent that there is no significant advantage of using graphene (to replace graphite) in the fabrication of a paste electrode.

This work has highlighted the need for rigorous control experimentation (as conducted within this study), where if one refers back to the previous literature highlighted in the Chapter 9.2.1, given the overwhelming incorporation of functionalised graphene (produced from reduced graphene oxide) into the fabricated paste electrodes the reported 'improvements' likely originate from the oxygenated species present rather than the graphene itself. [25]

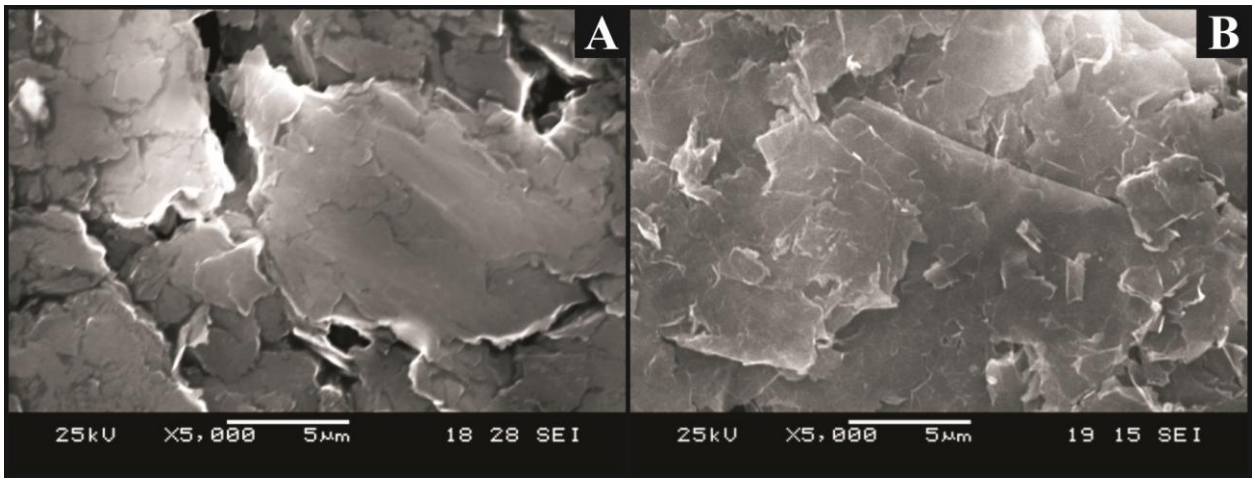

Figure 9.13 *SEM images of the surface of the fabricated graphene (A) and graphite (B) paste electrodes.*

Last this chapter considers the surface morphology of the graphene and graphite paste electrodes, as shown in Figure 9.13 *via* SEM, where no discernible differences are evident between the two materials. Raman analysis of the graphene and graphite paste mediums is presented in Figure 9.14. Interpretation of the Raman spectrums obtained reveals the pastes to exhibit striking similarities in terms of both the intensity ratio of the G and 2D (G') bands and the presence of asymmetrical 2D bands (which exhibit 'shoulders'), characteristics that are consistent with that expected at graphite samples of multiple graphene layers in thickness. The SEM and Raman data presented above clearly support (and are physical evidence for) the inference gained through the electrochemical performances with respect to the coalescence of graphene sheets during the synthesis of paste electrodes and indeed the presence of graphite in

the ‘graphene paste’ medium. Thus it is clear that when utilised in this electrode formation the graphene powder coalesces into graphite and that the appropriate control experiments must be employed to ensure this is not the case in other work concerning graphene in this manner, for example the graphene experimentalist should compare the response of their ‘graphene’ electrode to that of a graphite alternative.

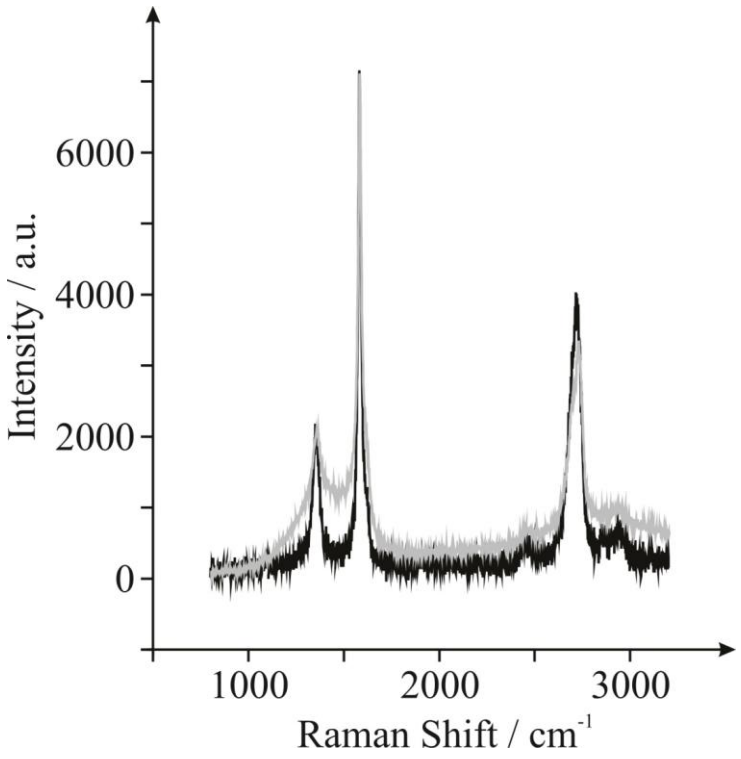

Figure 9.14 *Raman spectrums of the graphene (grey-line) and graphite (black-line) paste mediums as utilised within the graphitic paste electrodes. Note that variation in the D band (1335 cm^{-1}) simply reflects the presence of distinct oxygenated species (defect sites) as identified within the chapter.*

It is insightful to consider how one might keep the graphene sheets separated whilst in the paste medium. Insights can be obtained from work on supercapacitors where carbon nanotubes (CNTs) are used in order to separate graphene sheets to allow greater accessibility and utilisation of graphene’s large surface area. [36] For the fabrication of graphene paste electrodes, CNTs or other nano/micro sized particles (such as metallic nanoparticles) could be used as spacers to

reduce the coalescence of graphene into graphite structures within the paste medium, also advantageously increasing the available surface area of the graphene sheets. It is important to note however, that where such hybrid materials are utilised one needs to carefully consider the electrochemical reactivity of the individual component materials. For example, in the case of utilising CNTs as graphene spacers (see Figure 9.15) the CNTs will be electroactive and thus will act like an electrode and if the CNTs have favourable electrochemical properties (k^o) towards the analyte in contrast to graphene ($k^0_{graphene} << k^0_{CNT}$) the CNTs can potentially dominate (depending on each respective global % coverage of edge plane like- sites/defects) and dictate the electrochemical response such that the contribution from graphene will not be observed or could be misinterpreted as graphene exhibiting excellent electrochemical activity if control experiments are not diligently undertaken (alternatively, electrochemically inert spacers could be utilised). [1]

In terms of future work with regard to graphitic/carbon materials (with the aim of improving the electrochemical and electroanalytical response of such paste electrodes, whilst disregarding cost implications or the functionalisation of the material with beneficial oxygenated species) it is evident that increasing the global coverage of edge plane like- sites/defects across the electrode surface is key. [1, 27] Insights gained above indicate that utilising graphitic materials with smaller L_c values (graphene) does not result in an improved response owing to the re-formation of stacked structures. However, given insights gained from Density Functional Theory (see Chapter 7.1), [4] if one could vary the lateral grain size (L_a) of the graphitic material towards structures with smaller basal plane contributions (a smaller flake size, for example towards the structural configuration of coronene) then the effective coverage of edge plane sites

within the material (and resultant paste electrode) would be increased, which in turn is expected to result in the increased electrochemical reactivity of the electrode material. [4]

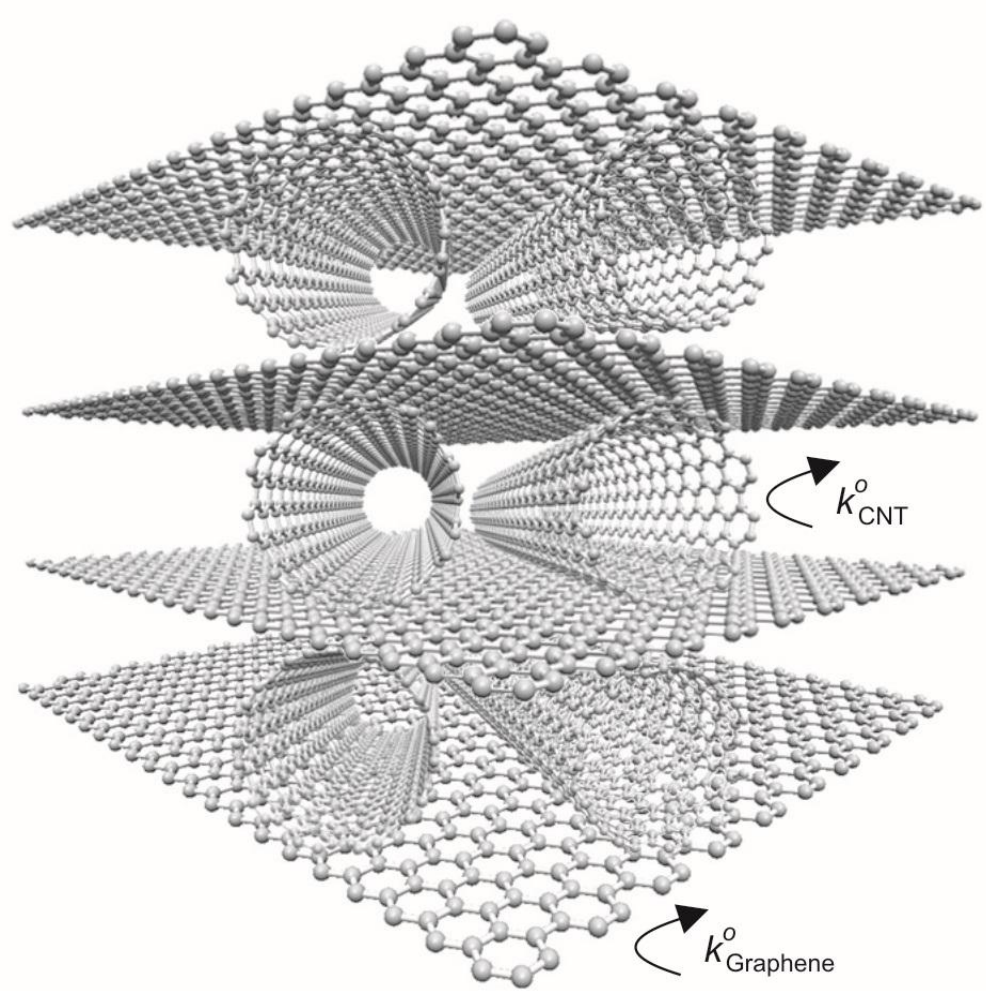

Figure 9.15 *A schematic representation of how CNTs may be utilised as spacers between separate layers of graphene sheets, also indicated is the possibility of each 'component material' possessing distinct electrochemical properties (electron transfer kinetics, k^o).*

9.2.4. CONCLUSIONS

This chapter has explored the use of a graphene paste electrode within electrochemistry and electroanalysis. Through the implementation of careful control and comparison experiments with a graphite paste alternative it has been possible to fully assess the benefits of employing a

graphene paste electrode in this context, for the first time. It has been demonstrated that there appears to be no advantages or benefits of using graphene as a paste electrode (in place of graphite), with both materials/electrodes exhibiting similar electrochemical responses and electron transfer kinetics towards a variety of redox probes. In terms of electroanalysis the graphite paste alternative was superior to the graphene electrode given that capacitative currents at the graphene paste preclude low level sensing of target analytes, with the graphite electrode additionally possessing economical benefits. This work highlights the importance of control experimentation and the need for such measures to be performed consistently throughout the literature, with the aim of reducing the likelihood of erroneous claims with regard to beneficial performances 'observed' at the new electrode materials of the future.

9.2.5. REFERENCES

1. D. A. C. Brownson, D. K. Kampouris and C. E. Banks, *Chem. Soc. Rev.*, 2012, **41**, 6944.
2. D. A. C. Brownson, L. C. S. Figueiredo-Filho, X. Ji, M. Gómez-Mingot, J. Iniesta, O. Fatibello-Filho, D. K. Kampouris and C. E. Banks, *J. Mater. Chem. A*, 2013, **1**, 5962.
3. C. Li and G. Shi, *Nanoscale*, 2012, **4**, 5549.
4. D. A. C. Brownson, L. J. Munro, D. K. Kampouris and C. E. Banks, *RSC Adv.*, 2011, **1**, 978.
5. D. A. C. Brownson and C. E. Banks, *Phys. Chem. Chem. Phys.*, 2011, **13**, 15825.
6. D. A. C. Brownson and C. E. Banks, *RSC Adv.*, 2012, **2**, 5385.
7. M. H. Parvin, *Electrochem. Commun.*, 2011, **13**, 366.
8. F. Li, J. Li, Y. Feng, L. Yang and Z. Du, *Sens. Actuators, B*, 2011, **157**, 110.
9. R. N. Adams, *Anal. Chem.*, 1958, **30**, 1576.
10. M. E. Rice, Z. Galus and R. N. Adams, *J. Electroanal. Chem. Interfacial Electrochem.*, 1983, **143**, 89.
11. K. Kalcher, J.-M. Kauffmann, J. Wang, I. Švancara, K. Vytřas, C. Neuhold and Z. Yang, *Electroanalysis*, 1995, **7**, 5.
12. V. Shakibaian and M. H. Parvin, *J. Electroanal. Chem.*, 2012, **683**, 119.
13. A. Gasnier, M. L. Pedano, M. D. Rubianes and G. A. Rivas, *Sens. Actuators, B*, 2013, **176**, 921.

14. H. Bahramipur and F. Jalali, *J. Pharm. Pharmacol.*, 2012, **6**, 1298.

15. W. Wonsawat, S. Chuanuwatanakul, W. Dungchai, E. Punrat, S. Motomizu and O. Chailapakul, *Talanta*, 2012, **100**, 282.

16. L. Ma and G.-C. Zhao, *Int. J. Electrochem.*, 2012, **2012**, 243031.

17. Y. Bo, W. Wang, J. Qi and S. Huang, *Analyst*, 2011, **136**, 1946.

18. X. Yuan, Y. Chai, R. Yuan, Q. Zhao and C. Yang, *Anal. Methods*, 2012, **4**, 3332.

19. M. Saber-Tehrani, A. Pourhabib, S. W. Husain and M. Arvand, *Electroanalysis*, 2012, **24**, 2395.

20. R. Ojani, J.-B. Raoof and R. Valiollahi, *J. Solid State Electrochem.*, 2013, **17**, 217.

21. D. A. C. Brownson and C. E. Banks, *Electrochem. Commun.*, 2011, **13**, 111.

22. R. L. McCreery, *Chem. Rev.*, 2008, **108**, 2646.

23. E. P. Randviir, D. A. C. Brownson, M. Gómez-Mingot, D. K. Kampouris, J. Iniesta and C. E. Banks, *Nanoscale*, 2012, **4**, 6470.

24. I. Streeter, G. G. Wildgoose, L. Shao and R. G. Compton, *Sens. Actuators, B*, 2008, **133**, 462.

25. D. A. C. Brownson, A. C. Lacombe, M. Gómez-Mingot and C. E. Banks, *RSC Adv.*, 2012, **2**, 665.

26. D. A. C. Brownson, R. V. Gorbachev, S. J. Haigh and C. E. Banks, *Analyst*, 2012, **137**, 833.

27. T. J. Davies, M. E. Hyde and R. G. Compton, *Angew. Chem. Int. Ed.*, 2005, **44**, 5121.

28. D. A. C. Brownson and C. E. Banks, *The handbook of graphene electrochemistry*, Springer Publishing, UK, London, 2013.

29. D. A. C. Brownson, M. Gómez-Mingot and C. E. Banks, *Phys. Chem. Chem. Phys.*, 2011, **13**, 20284.

30. J.-L. Chang, K.-H. Chang, C.-C. Hub, W.-L. Cheng and J.-M. Zen, *Electrochem. Commun.*, 2010, **12**, 596.

31. C. E. Banks, R. G. Compton, A. C. Fisher and I. E. Henley, *Phys. Chem. Chem. Phys.*, 2004, **6**, 3147.

32. W. Deng, X. Ji, M. Gómez-Mingot, F. Lu, Q. Chen and C. E. Banks, *Chem. Commun.*, 2012, **48**, 2770.

33. W. Song, X. Ji, W. Deng, Q. Chen, C. Shen and C. E. Banks, *Phys. Chem. Chem. Phys.*, 2013, **15**, 4799.

34. D. A. C. Brownson, C. W. Foster and C. E. Banks, *Analyst*, 2012, **137**, 1815.

35. R. T. Kachoosangi, C. E. Banks and R. G. Compton, *Electroanalysis*, 2006, **18**, 741.

36. Q. Cheng, J. Tang, J. Ma, H. Zhang, N. Shinya and L.-C. Qin, *Phys. Chem. Chem. Phys.*, 2011, **13**, 17615.

9.3. ELECTROCHEMISTRY AT GRAPHENE OXIDE MODIFIED ELECTRODES: UNIQUE AND INTRIGUING VOLTAMMETRY?

Following the observations of Chapter 9.1 where *physical* alterations in the graphene structure were shown to give rise to beneficial electrochemical properties. This chapter considers the electrochemical implications of altering the *chemical* composition of graphene.

In this chapter, which contains published work, [12] the electrochemical properties of *graphene oxide* modified electrodes are explored relative to the electrochemical response of *pristine graphene* modified electrodes (as previously characterised in Chapter 7.1).

9.3.1. INTRODUCTION

Graphene oxide (GO), while not a new material, [1, 2] has been reported to be beneficial in a number of technological areas within electrochemistry, such as in the fabrication of microbial fuel cells, [3] supercapacitors, [4] vanadium redox flow batteries, [5] and as the foundation in a tyrosinase biosensor. [6] Additionally, GO has been employed in the monitoring of nucleic acids, [7] sensing of adenine and guanine, [8] and decoration with platinum to simultaneously characterise ascorbic acid, dopamine and uric acid levels. [9] There is a vast array of literature where GO is electrochemically [10] or chemically [11] reduced to graphene prior to its implementation into a cornucopia of potential applications. [12] It is apparent from the literature that the basic voltammetric understanding of GO before and after being reduced to graphene is clearly lacking, where researchers fail to perform diligent control experiments, such as the electrochemical probing of the supporting (underlying) electrode substrate before modification and following reduction to graphene.

[12] D. A. C. Brownson, A. C. Lacombe, M Gómez-Mingo and C. E. Banks, *RSC Adv.*, 2012, **2**, 665.

Consequently, this chapter explores GO as an electrode material towards the electrochemistry of commonly encountered/explored redox probes, which can provide information on the electronic properties of this intriguing material.

9.3.2. RESULTS AND DISCUSSION

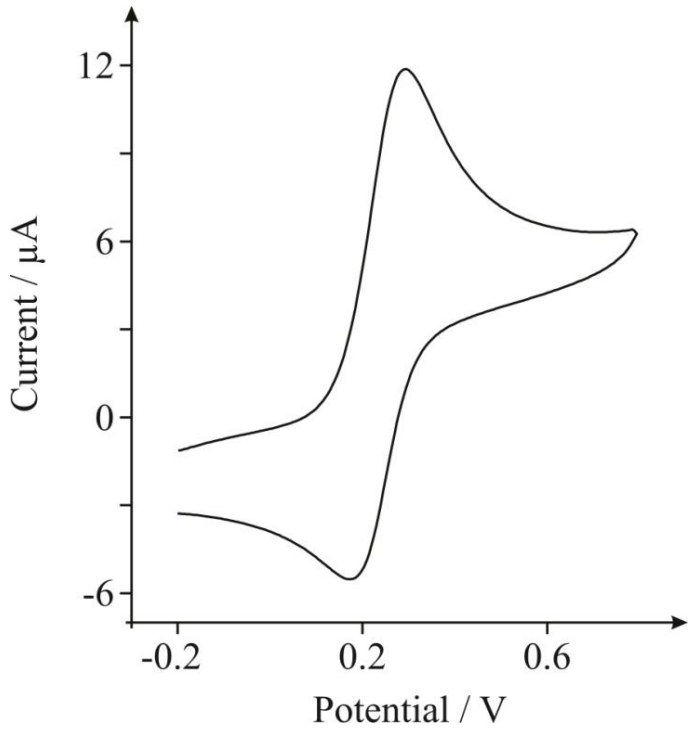

Figure 9.16 *A typical cyclic voltammetric profile recorded towards 1 mM potassium ferrocyanide (II) in 1 M KCl, obtained using a BPPG electrode after modification with 13.75 µg of GO. Scan rate: 100 mVs^{-1} (vs. SCE).*

First, the voltammetric response of GO is considered using the ferro-/ferri- cyanide redox probe in 1 M potassium chloride. Figure 9.16 depicts a typical voltammetric profile obtained at a BPPG electrode following modification with 13.75 µg of GO, which exhibits a well defined pair of redox peaks with a peak-to-peak separation of *ca.* 90 mV. In comparison to widely reported literature values for an unmodified BPPG electrode (*ca.* 240 at 100 mVs^{-1}) [13, 14] an improvement in the electrochemical reversibility of the redox probe at GO is evident over that of the underlying electrode. A scan rate study was performed where the voltammetric peak height (I_P) was monitored as a function of scan rate (v), with a plot of

peak height *versus* square-root of the scan rate revealing a linear response (I_P (A) = 3.16 × 10^{-5} A/$(Vs^{-1})^{0.5}$ + 1.32 × 10^{-6} A; R^2 = 0.99) indicating a diffusional process; furthermore, as is expected for the case of the semi-infinite diffusion model as governed by the Randles–Ševćik equation (see equation (1.40)), analysis of log I_P *versus* log v revealed a gradient of 0.41, indicating the absence of thin-layer effects. [15]

The ferro-/ferri- cyanide redox probe is known to be complex on carbon surfaces, influenced by specific surface sites, and is consequently termed as an 'inner-sphere' redox probe (see Appendix A.1); [16, 17] thus the voltammetric response observed at GO in Figure 9.16 can likely be attributed to both electronic factors and specific surface interactions, which are not easily de-convoluted. Interestingly there is a clear lack of literature reports regarding the utilisation of GO towards this redox probe. Thus, this chapter next turns to exploring the voltammetric characteristics of GO towards 'outer-sphere' redox probes which do not have any surface sensitivity. [16]

The voltammetric response of GO in 1 mM hexaammine-ruthenium (III) chloride (1 M KCl supporting electrolyte) was next sought. Figure 9.17A depicts the typically observed voltammetric profiles, where upon increasing the amount of immobilised GO, a unique voltammetric response is observed. Note that such a response, to the best of the author's knowledge, has never been reported before on graphitic surfaces and consequently derives entirely from the introduction of the GO.

To further explore this unique response, the 'outer-sphere' redox probe, potassium hexachloroiridate (III) in 1 M KCl – which has been shown to exhibit reversible voltammetric responses on graphitic surfaces, [17] is next explored. The voltammetric response observed using GO is presented in Figure 9.17B, which again yields unique voltammetry.

Surprisingly, neither of these redox probes have been previously explored in the literature when utilising GO as an electrode material.

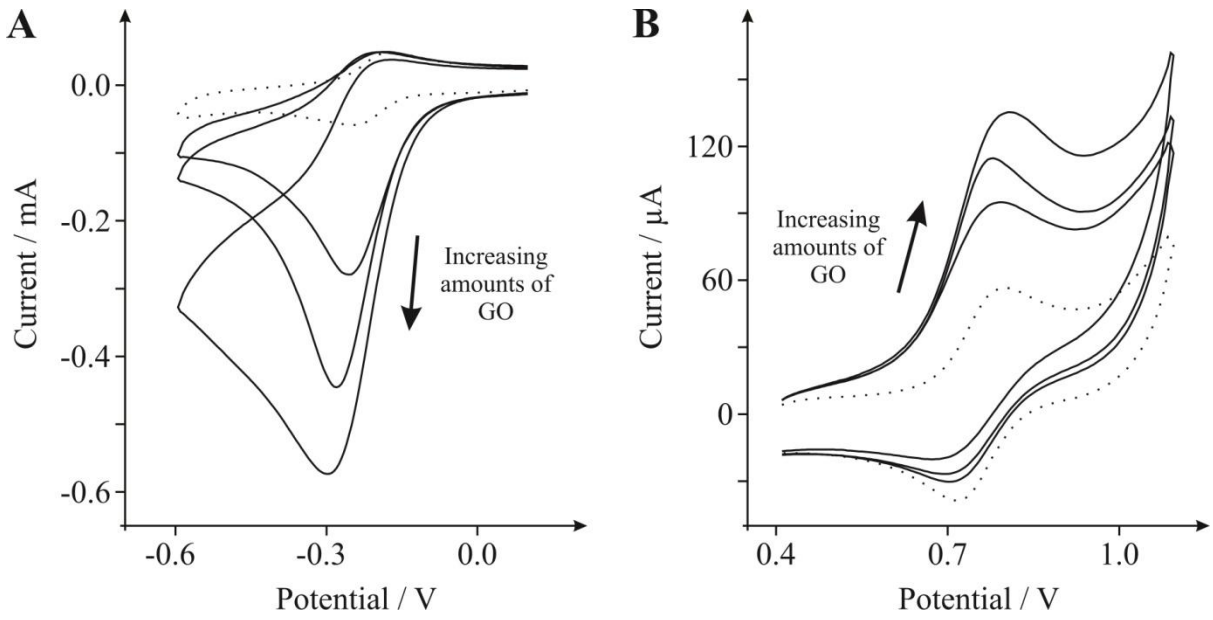

Figure 9.17 *Cyclic voltammetric profiles recorded towards: (**A**) 1 mM hexaammine-ruthenium (III) chloride in 1 M KCl, obtained using an EPPG electrode (dotted line) after modification with increasing depositions of 1.38, 2.75 and 8.25 µg GO (solid lines). (**B**) 1 mM potassium hexachloroiridate (III) in 1 M KCl, obtained using an EPPG electrode (dotted line) after modification with increasing depositions of 1.38, 2.75 and 5.50 µg GO (solid lines). Note that both **A** and **B** utilised a scan rate of 100 mVs^{-1} (vs. SCE).*

The observed voltammetric profiles presented in Figure 9.17 appear characteristic of a catalytic process, the *EC'* reaction, where a first 'electron transfer process' (E process), as described generally as:

$$A + e^- \rightleftharpoons B \qquad \text{(E Step)}$$

is then followed by a 'chemical process' (C process) involving the electro-generated product, which regenerates the starting material *A*, as described by:

$$B + C \overset{k}{\rightarrow} A + Products \qquad \text{(C Step)}$$

It is evident from Figure 9.17, that as the amount of graphene oxide is increased, the observed cyclic voltammetric profile is perturbed such that in Figure 9.17A the reduction peak increases with a decrease in the magnitude of the oxidation peak, which is characteristic of the above *EC'* reaction where *B* (the electro-generated product, reduced hexaammine-ruthenium (III) chloride) is consumed and regenerates *A* (hexaammine-ruthenium (III) chloride) (for further information see Chapter 1.4.3). The voltammetric response arises as the amount of *C* is increased (the oxygenated species in this case, GO). The effect of the voltammetric scan rate is shown in Figure 9.18, where on applying faster scan rates a respective increase in the magnitude of the back (oxidation) peak is evident, as well as a reduction in the forward (reduction) peak, since the reversible *A*/*B* process is unperturbed by the catalytic chemical *C* step; where at higher scan rates the rate of reaction of the reversible *E* step is prevalent over that of the rate of reaction, *k*, of the *C* step which resultantly partakes to a lesser extent and thus there is a reduction in the observed unique feature (*EC'* reaction). Such a response highly suggests that as the GO coverage is increased, which has a large proportion of oxygenated species, the amount of oxygenated species catalyse the chemical reaction of transforming the electrochemically generated species *B* back into *A*, hence a catalytic-type voltammetric signal is observed.

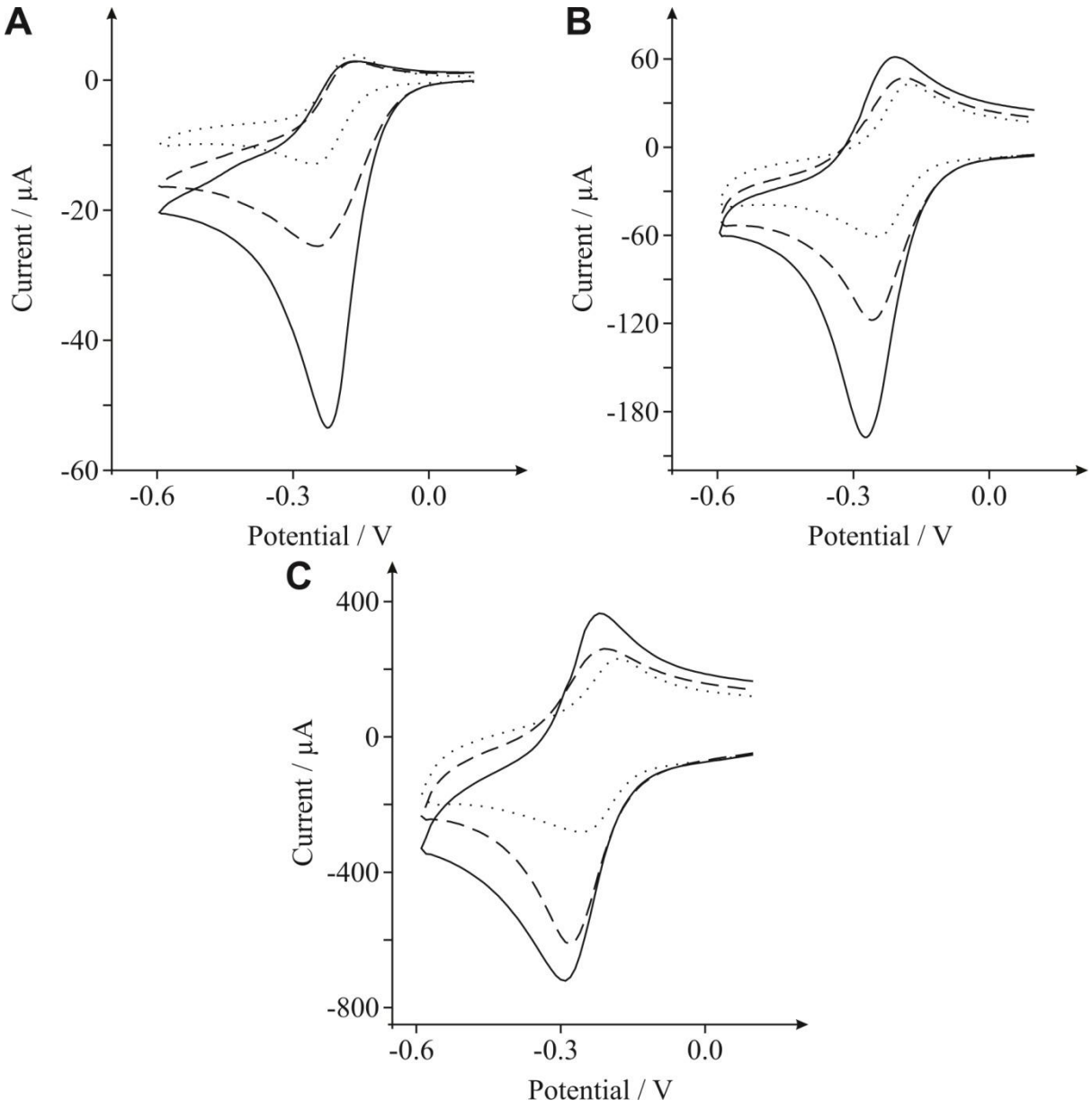

Figure 9.18 *Cyclic voltammetric profiles recorded towards 1 mM hexaammine-ruthenium (III) chloride in 1 M KCl, obtained using an EPPG electrode (dotted line) after modification with 1.4 µg (dashed line) and 5.5 µg GO (solid line). Scan rates: 5 (**A**), 100 (**B**) and 1000 (**C**) mVs^{-1} (vs. SCE).*

Further insights can be gained through consecutive scan analysis of the GO modified electrode, where as evident in Figure 9.19 the second-cycle voltammetric scan exhibits a clear reduction in the magnitude of the unique feature (*i.e.* the reduction peak exhibits a significantly decreased I_P in this case), such that it is evident that the oxygenated species are 'exhausted' in the first reductive cycle. Interestingly, when scanning the potential anodically

to induce the re-introduction of surface oxygenated species, an approach commonly employed in the literature, [18-20] it is evident that this 'anodic activation' regenerates the surface oxygenated species, where the magnitude of the reduction peak at further cycles is thus returned to that of the first initial cycle at the GO modified electrode. This response is *self-sustaining* upon successive scans, where the unique voltammetric profile remains stable owing to the anodic activation and thus re-introduction of surface oxygenated species between each successive scan. This key experimental observation supports the theory as described above, *viz* the *EC'* reaction, that the oxygenated species give rise to this unique and exciting voltammetry.

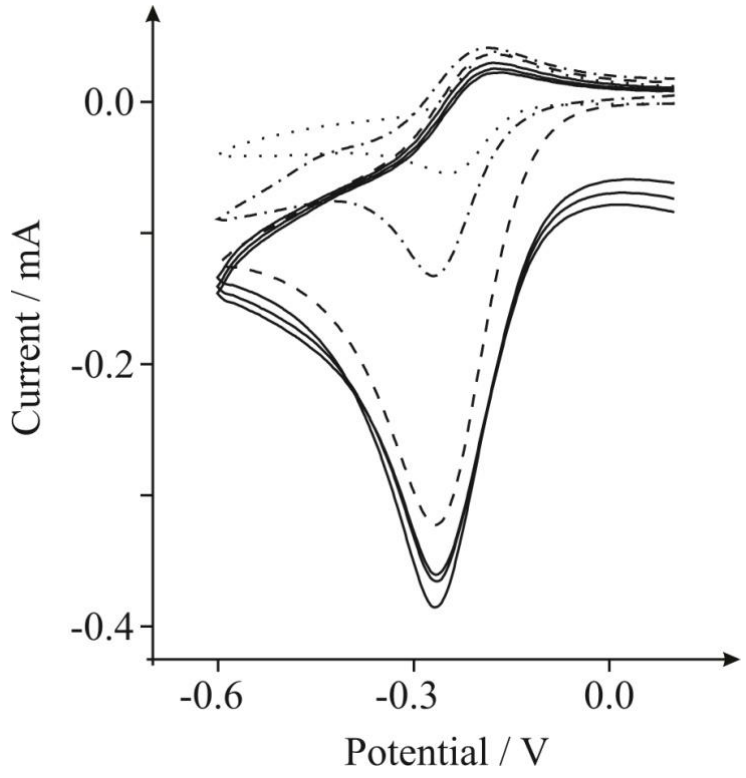

Figure 9.19 *Cyclic voltammetric profiles recorded towards 1 mM hexaammine-ruthenium (III) chloride in 1 M KCl, obtained using an unmodified EPPG electrode (dotted line) and an EPPG electrode following modification with 2.75 µg GO (first-cycle: dashed line / second-cycle: dot-dashed line). Solid lines represent further consecutive cycles (third – fifth) at the GO modified EPPG electrode following anodic activation via scanning the potential up to + 1.6 V. Scan rate: 100 mVs^{-1} (vs. SCE).*

Note that such responses at GO have never been observed before in the literature, and this work highlights that the large proportion of oxygenated species present on GO could be beneficially utilised in electrochemistry where oxygenated electro-catalytic reactions are employed.

Note that since the electrochemical response of *pristine graphene* (P-graphene) towards such redox probes does *not* exhibit this unique behaviour, [13] these observations can be utilised to test for the presence of 'true' graphene and as a means of characterisation to ensure the completion of a successful reduction reaction of GO to graphene (when fabricating graphene *via* the oxidation and subsequent reduction of graphite, which is a commonly utilised approach to prepare graphene for electrochemical testing (see Chapter 4.1)). Furthermore, note the difference in voltammetric characteristics of the explored redox probes, where a catalytic response of greater intensity is evident for the hexaammine-ruthenium (III) chloride over that of the hexachloroiridate (III) complex, which likely arises due to differing structures of the transition complexes where the two reactions are chemically distinct.

It is noted that a similar response has been reported for the utilisation of nanodiamond towards the $IrCl_6$ redox probe, where the mechanism inferred surface states; [21] while the mechanism in this case (for GO) is not completely determined, this may also be a potential possibility. However, it is also benevolently noted that Kovach *et al.* [22] found nearly identical voltammetric responses at a heavily electrochemically oxidised carbon-fibre electrode towards the $Ru(NH_3)_6$ redox probe, which was attributed to the large degree of oxygenated species. Hence, this adds weight to the inference of this chapter, that the reaction mechanism at GO is due to surface oxygenated species.

9.3.3. CONCLUSIONS

This chapter demonstrates, for the first time, that *unique and intriguing voltammetry* can be observed at GO modified electrodes. The fascinating nature of this remarkable material has been highlighted, revealing that GO can be utilised beneficially where oxygenated electro-catalytic reactions are employed. Note that the voltammetric responses reported in this work can be used by researchers to confirm that GO has been reduced to graphene, *via* chemical or electrochemical means, owing to the contrasting behaviours of these materials. Thus Chapters 7.1 and 9.3 can be combined to reveal a simple methodology for the *electrochemical characterisation of graphene and graphene oxide* prior to their application in a plethora of areas.

9.3.4. REFERENCES

1. B. C. Brodie, *Proc. R. Soc. London, Ser.*, 1859, **10**, 249.
2. W. S. Hummers and R. E. Offeman, *J. Am. Chem. Soc.*, 1958, **80**, 1339.
3. Y.-X. Huang, X.-W. Liu, J.-F. Xie, G.-P. Sheng, G.-Y. Wang, Y.-Y. Zhang, A.-W. Xu and H.-Q. Yu, *Chem. Commun.*, 2011, **47**, 5795.
4. S. H. Aboutalebi, A. T. Chidembo, M. Salari, K. Konstantinov, D. Wexler, H. K. Liu and S. X. Dou, *Energy Environ. Sci.*, 2011, **4**, 1855.
5. P. X. Han, H. B. Wang, Z. H. Liu, X. A. Chen, W. Ma, J. H. Yao, Y. W. Zhu and G. L. Cui, *Carbon*, 2011, **49**, 693.
6. W. Song, D.-W. Li, Y.-T. Li, Y. Li and Y.-T. Long, *Biosens. Bioelectron.*, 2011, **26**, 3181.
7. M. Muti, S. Sharma, A. Erdem and P. Papakonstantinou, *Electroanalysis*, 2011, **23**, 272.
8. Y. Fan, K.-J. Huang, D.-J. Niu, C.-P. Yang and Q.-S. Jing, *Electrochim. Acta*, 2011, **56**, 4685.
9. C.-L. Sun, H.-H. Lee, J.-M. Yang and C.-C. Wu, *Biosens. Bioelectron.*, 2011, **26**, 3450.
10. M. Zhou, Y. Wang, Y. Zhai, J. Zhai, W. Ren, F. Wang and S. Dong, *Chem. Eur. J.*, 2009, **15**, 6116.
11. D. Li, M. B. Müller, S. Gilje, R. B. Kaner and G. G. Wallace, *Nat. Nanotechnol.*, 2008, **3**, 101.

12. J. Wang, S. Yang, D. Guo, P. Yu, D. Li, J. Ye and L. Mao, *Electrochem. Commun.*, 2009, **11**, 1892.

13. D. A. C. Brownson, L. J. Munro, D. K. Kampouris and C. E. Banks, *RSC Adv.*, 2011, **1**, 978.

14. D. K. Kampouris and C. E. Banks, *Chem. Commun.*, 2010, **46**, 8986.

15. P. M. Hallam and C. E. Banks, *Electrochem. Commun.*, 2011, **13**, 8.

16. R. L. McCreery, *Chem. Rev.*, 2008, **108**, 2646.

17. X. Ji, C. E. Banks, A. Crossley and R. G. Compton, *ChemPhysChem*, 2006, **7**, 1337.

18. F. G. Gonon, C. M. Fombarlet, M. J. Buda and J. F. Pujol, *Anal. Chem.*, 1981, **53**, 1386.

19. J.-X. Feng, M. Brazell, K. Renner, R. Kasser and R. N. Adams, *Anal. Chem.*, 1987, **59**, 1863.

20. J. Wang and P. Tuzhi, *Anal. Chem.*, 1986, **58**, 1787.

21. K. B. Holt, D. J. Caruana and E. J. Millan-Barrios, *J. Am. Chem. Soc.*, 2009, **131**, 11272.

22. P. M. Kovach, M. R. Deakin and R. M. Wightman, *J. Phys. Chem.*, 1986, **90**, 4612.

CHAPTER 10: CONCLUSIONS AND FUTURE WORK

10.1. OVERALL CONCLUSIONS

This thesis has significantly contributed to the fundamental understanding of graphene electrochemistry and its application as an electrode material. Consequently, the aims and objectives of this thesis have been met.

A key oversight within the current graphene literature is the implementation of control experiments (such as comparing the response of graphene to other graphitic forms and other materials as identified in this thesis), that through their implementation, for the first time as reported within this thesis, have allowed the true performance/properties of graphene as an electrode material to be fully evaluated. Initial chapters considered the application of graphene modified electrodes *via* top-down modification, where aliquots of graphene solutions were immobilised onto a variety of electrode substrates. This thesis demonstrated that the type of graphene utilised is key, in that graphene utilised with surfactant adsorbed onto its surface (where the surfactant is used in the fabrication of graphene and to reduce coalescence) prevents the fundamental study of graphene being realised due to the fact that the surfactant contributes (detrimentally or beneficially) to the observed electrochemistry. Moving on from this, pristine graphene (graphene suspended in solution, *without* surfactants present) has also been studied, for the first time, allowing graphene modified electrodes to be realised and the fundamental electrochemistry to be explored. This has allowed this thesis to demonstrate that pristine graphene is not such a beneficial material for use in electrochemistry due to its low % coverage of edge plane sites, virtually no C–O groups and also that the underlying electrode substrate critically affects the graphene modified electrodes response, as well as the coverage (amount immobilised) being equally critical.

Building on the above insights, bottom-up fabricated graphene electrodes were explored (which are produced *via* chemical vapour deposition (CVD)) allowing, for the first time, the structural composition of the graphene to be correlated with its electrochemical response. It was demonstrated, without doubt, that the edge plane like-sites/defects are the origin of electron transfer at graphene electrodes; it has generally been assumed that this is the case, but never unambiguously demonstrated.

Moving forward from the fundamental studies identified above, graphene macrostructures were explored. A freestanding 3D graphene foam electrode was compared to a freestanding 3D carbon foam electrode, which allows one to demonstrate that beneficial voltammetric signatures are observed at the former in non-aqueous solutions *viz* ionic liquids. Such an electrode configuration allows the beneficial properties of graphene to be utilised due to the foam electrode being macroscopic in nature with microscopic graphene domains; and this additionally allows one to electrically connect to the graphene with ease and with controlled graphene coverage. Next in this chapter, the fundamental concept of a graphene paste electrode was explored and critically contrasted to a graphite paste electrode for the first time, demonstrating that there are no advantages of the former relative to the latter due to the structural configuration of the 'end' paste product. Last, the electrochemical response of graphene/graphitic oxide modified electrodes was considered. It is shown that such electrodes give rise to a coverage dependent unique electrochemical response, which once combined with the newly realised fundamental electrochemical response arising from graphene, reveals a simple methodology for the electrochemical characterisation of graphene and graphene/graphitic oxide prior to their utilisation in an vast array of research fields.

Given the numerous different approaches that have been reported to fabricate graphene, each giving rise to different graphene structures (edge plane site coverage, difference L_c and L_a sizes, C/O ratios, composites/macro-/micro-structures and so on) which give rise to differing electrochemical properties, the area is truly fascinating!

Now that the work within this thesis has allowed a greater understanding of graphene as an electrode material, future work can be directed to exploring the beneficial properties of graphene in the field of electrochemistry. Chapter 10.2 considers future suggested work.

Future work continuing the work in this thesis is suggested as follows:

1) As reported in Chapter 8.3, monolayer, *quasi*-graphene and defects abundant graphene were studied fundamentally. Such future work should consider the electroanalytical application of these graphene electrodes to evaluate their usefulness and the need to critically compare the response obtained to HOPG and other graphitic electrodes is essential.
2) Since graphene can be fabricated *via* CVD (see Chapter 8), different modifications could be explored fundamentally and in electroanalysis, such as boron-doped CVD grown graphene (differing boron doping levels) and nitrogen-doped CVD grown graphene. Additionally, the fundamental role of catalytic surfaces (usually nickel and copper) should be explored, such as alloys for example.
3) Since edge plane sites are the key to electron transfer, the introduction of defects onto graphene and related structures should be explored further/fully, which allow graphene to be beneficially utilised.
4) Graphene foam structures should be decorated with metals for use in supercapacitors as reported preliminary (see Chapter 9.1.1); only limited reports have appeared so far.
5) Graphene paste electrodes, as discussed in Chapter 9.2, could be explored and fabricated to include spacers between the graphene sheets, such as the insertion of inert (alumina) or electroactive (gold, CNTs, *etc*.) components to reduce coalescence to graphite and to increase the active area of the graphene; hopefully allowing the unique properties of graphene to be realised.
6) Last, the mass production of graphene electrodes is lacking. Graphene screen-printed electrodes should be developed with graphene ink utilised and fully explored.

Surface sensitivity at inner- and outer- sphere redox probes

A common approach within electrochemical studies in order to greater understand the material under investigation, is the utilisation of inner-sphere and outer-sphere redox mediators/probes. Such electron transfer processes differ significantly according to the 'sensitivity' of their electron transfer kinetics to the surface chemistry of the carbon electrode/material under investigation in terms of the surface structure/cleanliness (defects, impurities or adsorption sites) and the absence/presence of specific oxygen containing functionalities, that is, variations in k^o with the condition of the electrode surface. [1, 2]

Outer-sphere redox mediators (see Figure A1.1 for examples) are termed *surface insensitive* such that k^o is not influenced by the surface oxygen-carbon ratio, surface state/cleanliness in terms of a surface coating of a monolayer film of uncharged adsorbates, or specific adsorption to surface groups/sites. [2] There is no chemical interaction or catalytic mechanism involving interaction (*i.e.* an adsorption step) with the surface or a surface group – such systems often have low reorganisation energies; [1, 2] in this case the electrode merely serves as a source (or sink) of electrons and as such outer-sphere systems are sensitive primarily to the electronic structure due to the electronic DOS of the electrode material. [1, 2]

Inner-sphere redox mediators (see Figure A1.1 for examples) are termed *surface sensitive* in that the k^o is strongly influenced by the state of the electrode surface (surface chemistry and microstructure) *via* specific electro-catalytic interactions that are inhibited significantly if the surface is obscured by adsorbates (or impurities). Such interactions can also depend strongly on the presence (or absence) of specific oxygenated species which give rise to either beneficial or

detrimental effects. [1, 2] In this case systems are more largely affected by surface state/structure and/or require a specific surface interaction, being catalysed (or inhibited) by specific interactions with surface functional groups (adsorption sites) rather than the DOS as such systems generally have high reorganisation energies. [1, 2]

The observation of differing responses when using varied inner- and outer- sphere redox probes allows insights to be deduced regarding the state of the surface structure of the electrode material in question. McCreery [62, 87] has provided a "road map" for commonly utilised redox probes, as shown in Figure A1.1, which allows researchers to clarify from experimental observations the redox systems and how they are affected.

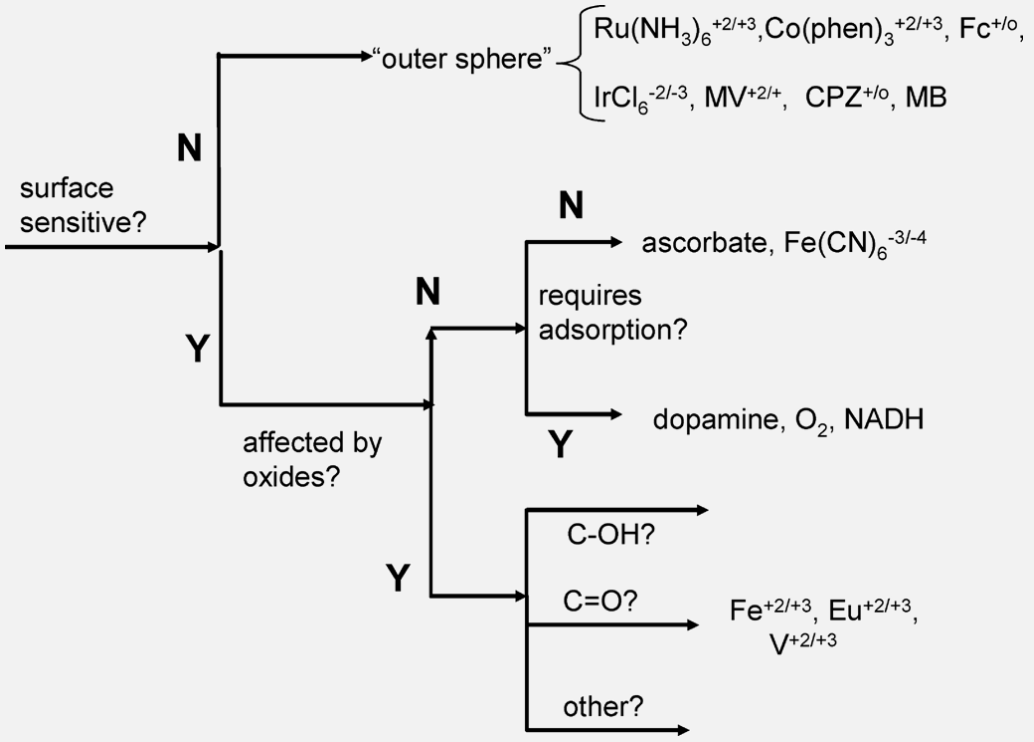

Figure A1.1 *Classification of redox systems according to their kinetic sensitivity to particular surface modifications on carbon electrodes. Reproduced from Ref. [3].*

1. P. Chen and R. L. McCreery, *Anal. Chem.*, 1996, **68**, 3958.
2. R. L. McCreery, *Chem. Rev.*, 2008, **108**, 2646.
3. P. Chen, M. A. Fryling and R. L. McCreery, *Anal. Chem.*, 1995, **67**, 3115.

The letter to the Nobel Committee below was written in response to the 'Scientific Background' document issued by the Nobel Committee in support of the 2010 Nobel Prize in Physics being awarded jointly to Geim and Novoselov "for groundbreaking experiments regarding the two-dimensional material graphene" (an updated version of the 'Scientific Background' document can be found at Ref. [A1]). The letter has been reproduced in full from Ref. [A2] for scientific clarity [sic].

Letter from Walt de Heer

November 17, 2010

To: The Nobel Committee,

Class for Physics of the Royal Swedish Academy of Sciences

The Nobel Prize in Physics is the most prestigious scientific achievement award and it is expected that the award be based on diligent and independent investigations. The scientific background document published by the Class for Physics of the Royal Swedish Academy of Sciences that accompanies the 2010 Nobel Prize in Physics is considered to reflect this process and it is therefore presumed to be accurate. I am recognized to be an authoritative source in the research area of the 2010 Nobel Prize in Physics. I can attest to the fact that this document contains serious inaccuracies and inconsistencies, so that the document presents a distorted picture that will be echoed in the community at large if the errors remain uncorrected. I list below several of the more serious errors with suggested changes.

1. Figure 3 is a reproduction of a figure in Novoselov et al's 2004 paper [1]. The figure caption incorrectly states the measurements were made on *graphene* (a single layer of carbon). The 2004 caption states that the measurement was performed on a FLG sample (i.e. ultrathin graphite composed of several graphene layers). In fact Noveoselov's 2004 paper does *not report any electronic transport measurements on graphene*. The band-structure figure accompanying this figure represents graphite and not graphene and

the magnetoresistance measurements are explicitly graphitic. The Manchester group published graphene transport measurements in 2005 [2]. Please note also, that the right panel of Fig. 4 is incorrectly labelled and ambiguously credited.

2. Page 2 states: "*It should be mentioned that graphene-like structures were already known of in the 1960's but there were experimental difficulties [13-16] and there were doubts that this was practically possible.*" The references all relate to graphene under various conditions. None of the references discuss experimental difficulties nor do they express doubts about the practical possibility (to produce) graphene. For example the respected graphite scientist, H-P Boehm, who later coined the name "graphene", published his 1962 observations of graphene in a most highly regarded journal (Ref. 13) and demonstrated beyond reasonable doubt the existence of freestanding graphene. He certainly showed that the existence of graphene was practically possible. The Nobel committee cites this work and then contradicts its main conclusion without explanation. Boehm's work has stood the test of time and has been reproduced by others. Refs. 14-16 demonstrate that besides freestanding graphene, other forms of graphene are also practically possible. The document must explain how it arrives at the opposite conclusion or replace the sentence with, for example: "*It should be mentioned that graphene structures were already known of before 2004[13-16]*".

3. Page 1 states: "*It was well known that graphite consists of hexagonal carbon sheets that are stacked on top of each other, but it was believed that a single such sheet could not be produced in isolated form. It, therefore, came as a surprise to the physics community when in 2004, Konstantin Novoselov, Andre Geim and their collaborators [1] showed that such a single layer could be isolated and that it was stable.*" This critically important assertion is repeated several times in the document without justification. In fact, the (chemical) stability of graphene did not come as a surprise, even for those who were unaware of Boehm's experiments. Despite Novoselov et al's claim in Ref.1, the chemical stability of graphene did not violate any physical principle and its existence was not doubted in any research paper. Graphene had previously been observed and characterized as a two-dimensional crystal by several research groups [4]. Careful reading of Ref. 1 suggests

that Novoselov et al. had confused highly stable covalently bonded two-dimensional macromolecules (like micron-sized graphene flakes), with chemically unstable freestanding two dimensional metal crystals, causing them to presume that theoretically graphene should also be chemically unstable. None of the references cited in Ref. 1 questions the existence of graphene in any circumstance, contradicting the statement in the document that its observation 'came as a complete surprise'. On the contrary, several references cited in Ref. 1 actually show images of graphene under various conditions. Had graphene's existence in any form truly violated accepted physical principles, then its observation would have resulted in a flurry of activity to explain the discrepancy. In reality, Ref.1 did not give rise to a single paper re-examining the chemical stability of isolated graphene.

The document must satisfactorily justify the controversial statement quoted above which certainly does not reflect the consensus opinion of experts in the field and it is overwhelmingly contradicted by facts as pointed out in item 2, above. The sentence might be replaced with "*It was well known that graphite consists of hexagonal carbon sheets that are stacked on top of each other and researchers were developing methods to deposit single sheets on substrates. In 2005, Konstantin Novoselov, Andre Geim and their collaborators demonstrated a simple method to deposit and to identify a single graphene sheet on an oxidized silicon carbide wafer [2]*." with a reference to their 2005 PNAS article[2], and not their 2004 Science article Ref[1], as explained in item 5.

4. Page 7 states: *The mobility of graphene is very high which makes the material very interesting for electronic high frequency applications [37]. Recently it has become possible to fabricate large sheets of graphene. Using near-industrial methods, sheets with a width of 70 cm have been produced.[38,39]*

Geim and Novoselov's method obviously cannot be used for electronic applications; for such purposes, other, previously established graphene production methods are used. The large graphene sheets were made by a CVD method (first described in the 1990's) developed by Ruoff et al. The first actual high frequency transistors were made with epitaxial graphene on silicon carbide at Hughes Research Laboratories in 2009 and at IBM in 2010 using concepts and methods (first described in the 1970's) developed by

de Heer et al. [3] Earlier in the document, epitaxial graphene is referred to as "carbon layers" on silicon carbide as if it were somehow different than graphene. Well before 2004, epitaxial graphene on silicon carbide had been described as a 2-dimensional crystal that is free floating above the substrate (cf Ref. 15 of the document). It has been shown to exhibit every essential graphene property and photoemission measurements have become icons for graphene's band structure. De Heer's research preceded, and, most importantly, developed entirely independently from Geim and Novoselov's research. (In 2004 he performed the first graphene transport measurements: the incorrect thickness measurement in Ref. 3a was corrected in Ref. 3b.) The document gives the impression that de Heer's research on graphene based electronics (initiated in 2001) was contingent, stimulated or in some other way motivated by Geim and Novoselov. This is not the case, and the document should clarify this.

5. The Summary paragraph, page 7 states: *The development of this new material opens new exiting possibilities. It is the first crystalline 2D-material and it has unique properties, which makes it interesting both for fundamental science and for future applications. The breakthrough was done by Geim, Novoselov and their co-workers; it was their paper from 2004 which ignited the development. For this they are awarded the Nobel Prize in Physics 2010.*

Geim and Novoselov developed a very simple method to produce and observe microscopic graphene slivers on oxidized, degenerately doped silicon wafers. This method was copied by many and provides an ideal method to produce graphene samples for two-dimensional transport studies. The development of this experimental technique was very important for the field of mesoscopic physics, and as pointed out in the document, this was Geim and Novoselov's most important contribution.

However this method and its application to graphene by Novoselov et al. was *not* reported in 2004 [1] but in 2005 [2]. In Ref. 1 the ultrathin graphite flakes (FLG) whose transport properties were measured, were produced by a more cumbersome method that certainly would not have attracted so much attention [cf supporting on-line material for Ref. 1]. In fact Ref. 1 does not report measurements nor characterization of graphene: instead, it

presents evidence of a microscopic sliver of graphene protruding from an ultrathin graphitic flake, not unlike those observed earlier by others (i.e. Shioyama op cit. Ref. 1). It is relevant that Ref. 1 is often wrongly cited for "the discovery of graphene" and for the "Scotch tape method", even by the authors of Ref.1. This misrepresentation of Ref. 1 should be corrected in the document.

Further note that de facto isolated graphene had been identified and characterized as a 2D-crystalline material in many reports prior to 2004 (see for example [4] for a review). The characterization of graphene as a *new* 2D material is incorrect. This might be corrected in the document along the lines of the second paragraph in this item.

The authors of the Scientific Background document misquoted essential facts pertaining to Ref. 1. An independent review of this document would be helpful to assure that the statements are clear, unambiguous, and factually correct.

We hope that the committee reviews these facts, corrects and publishes an erratum to the scientific background document so that it rises to the exacting standards expected of it.

Sincerely yours,

Walt de Heer

Regents Professor of Physics

Georgia Institute of Technology

1. K. Novoselov et al., "Electric Field Effect in Atomically Thin Carbon Films" *Science* **306**, 666 (2004).

2. K. Novoselov et al., "Two-dimensional atomic crystals", *Proc. Nat. Acc. Sci.* **102**, 10451 (2005).

3. *a.* C. Berger et al., "Ultrathin Epitaxial Graphite: 2D Electron Gas Properties and a Route toward Graphene-based Nanoelectronics" *J. Phys. Chem.* **108**, 19912 (2004). *b.* W.A. de Heer "Epitaxial graphene", *Sol. St. Comm.* **43**, 92 (2007).

4. N.R. Gall et al, "Two dimensional graphite films on metals and their intercalation", *Int. J. Mod. Phys. B* **11**, 1865 (1997).

A.2.1. REFERENCES

A1. Internet-Resource, *The 2010 Nobel Prize in Physics - Press Release - Nobelprize.org*, Accessed: 28/02/2012; http://www.nobelprize.org/nobel_prizes/physics/laureates/2010/press.html.

A2. Internet-Resource, *Graphene - Letter from Walt de Heer - Georgia Institute of Technology*, Accessed: 30/07/2012; http://www.gatech.edu/graphene/.

The main thrust of this thesis is to explore the electrochemical properties and resultant analytical performance of novel graphene based electrodes. In order to evaluate graphene in this manner, fabricated graphene based electrodes are studied towards target analytes within an electroanalytical context in order to benchmark the electrochemical performance/properties with the current literature (and indeed in comparison to alternative, well known and understood, electrodes) in order to discover the potential benefits and/or limitations of the given graphene 'sensor'. Note that target analytes which have been well-characterised and studied in relation to not only their electrochemical determination, but also generic analytical monitoring have been purposely chosen to allow such benchmarking and in turn evaluation of the proposed graphene based electrochemical devices.

The two key parameters that are utilised extensively and routinely within the literature to benchmark and evaluate electrochemical devices (electrode materials) in terms of their electroanalytical merits are: the analytical linear range and the statistical limit of detection (LOD). Consequently these two tools of evaluation are used extensively within Chapters 6 – 9. Note that it is not the thrust of this thesis to extensively explore the electroanalytical performance/merits of the graphene based devices described herein, but rather to demonstrate that such novel graphene based electrodes are feasible and to consider their merit in terms of the current state-of-the-art (and relative to other pre-existing electrode materials of similar structure in order to deduce an understanding of the electrochemical properties of graphene).

In Analytical Chemistry, and indeed electroanalysis, a calibration curve is produced so that analysts can determine how their system responds towards the target analyte under

investigation. In-particular the calibration curve gives the electrochemist a benchmark of their electroanalytical system, such as a graphene modified electrode towards sensing analyte X.

Shown in Figure A3.1 is a typical calibration curve which is made by recording the signal output of a piece of apparatus after presenting different concentrations of the target analyte X to the system, which is electrochemical in this case. This is usually achieved by preparing a solution and running the response in absence of analyte X (termed "blank"), after which additions of analyte X are made into the solution to produce a final concentration of analyte X (carefully taking into account the dilution factor) from a concentrated stock solution. Additions are made in order to deduce the response (or sensitivity) of the system/electrode configuration.

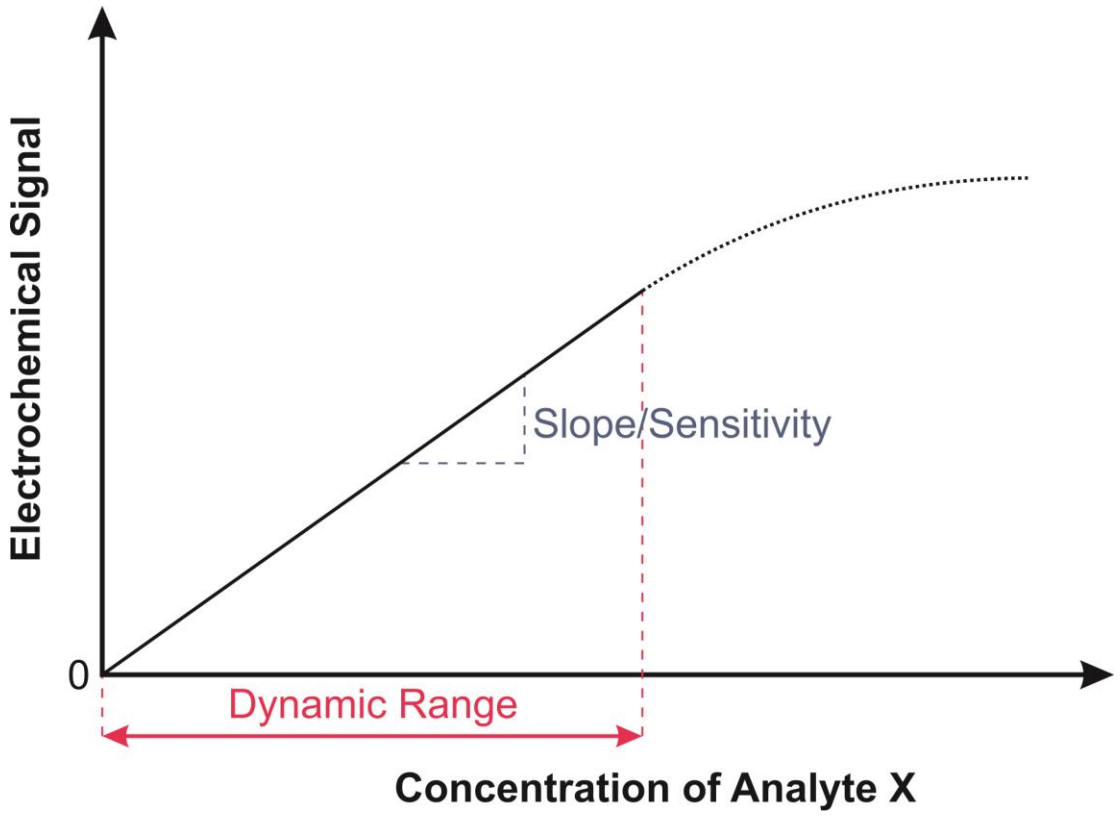

Figure A3.1 *Typical calibration plot highlighting the dynamic range and other pertinent analytical useful parameters that are used to benchmark (electro)analytical systems.*

As noted above Figure A3.1 shows a typical calibration curve, however it also highlights upon this calibration curve the dynamic linear range. The data – the increasing concentrations of the analyte and the instrument response – can be fit to a line of best fit (using the linear portion only) using linear regression analysis. This yields a model described by the equation $y = q_1 x + q_0$, where y is the electrochemical response, q_1 represents the sensitivity (gradient of the slope), and q_0 is a constant that describes the background/blank response which has a contribution from non-Faradaic processes.

For clarity the linear range is defined as the concentration range over which an increase in the analyte concentration present within a given solution results in a proportional increase in the electrochemical signal recorded. Linearity is measured and rationalised through the monitoring of the coefficient of determination, commonly denoted at R^2. In statistics, the R^2 value indicates how well data points *fit* a line or curve. The extent of linearity is determined through the value determined for the R^2 value, which can range from 0 to 1, with 1 describing complete linearity over the entire data range. When considering the coefficient of determination in relation to experimental data, as is the case within this thesis, it would be unexpected to achieve an R^2 value of 1, but rather one in the range of 0.96 to 0.99, which would be sufficient to support the conclusion that the analytical performance of a given 'sensor' was linear over the range studied for a particular analyte.

When constructing the calibration plot, the approach should be repeated to obtain statistically meaningful data. However, the approach employed determines whether the *intra*-electrochemical or the *inter*-electrochemical (ideal) response is observed: definitions are as follows.

Intra–electrochemical response:

This is also known as repeatability. *I.e.* the ability to repeat the same procedure with the same analyst, using the same reagent and equipment in a short interval of time, *e.g*. using the same electrode with measurements made within a day and obtaining similar results.

Inter–electrochemical response:

The ability to repeat the same method under different conditions, *e.g.* change of analyst, reagent, or equipment; or on subsequent occasions, *e.g.* change of electrode, measurements recorded over several weeks or months, this is covered by the between batch precision or reproducibility, also known as inter–assay precision.

A.3.1. LIMIT OF DETECTION (LOD)

The limit of detection (LOD) is defined as the minimum value of the signal from the species being measured that is significantly different from the blank signal. Although there is some discussion on this point, the vast majority of the electroanalytical literature available utilises this concept to benchmark proposed electrochemical systems/sensors. Here the LOD is determined based upon its calculation from calibration plots on *three times* the standard deviation of the *y*-residuals. Thus, the intercept of the linear plot, $y = a + bx$, is the blank value of the response y_B (= a), and the LOD for x corresponds to the y-value for $y = y_B + 3s_B$, where s_B is the standard deviation of the y-residuals from the line of best fit. The LOD is then ($3s_B/b$) as shown in Figure A3.2.

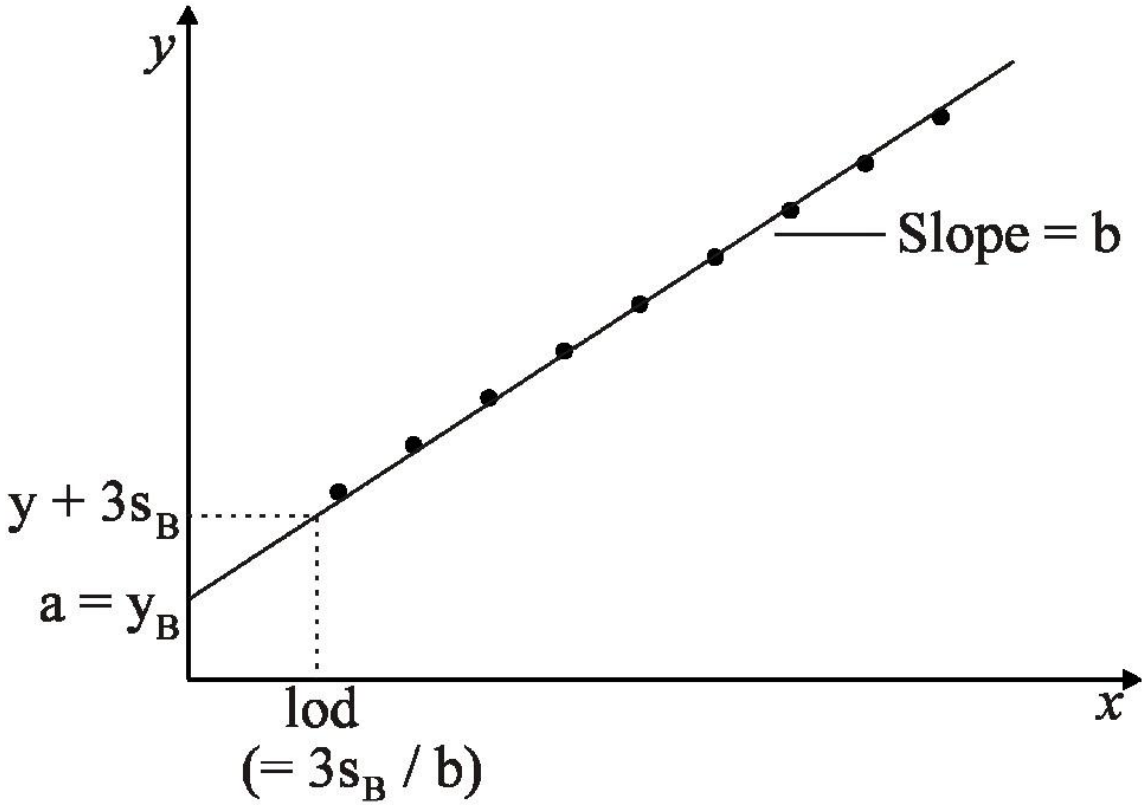

Figure A3.2 *A typical calibration plot constructed to determine the theoretical LOD using experimental data.*

It is important to note that the LOD is a theoretical value and as such, not always a definitive value, however such a determination is required to allow the benchmarking of electrochemical systems (such as graphene modified electrodes) against the current literature and indeed other various 'systems' (such as to that of a graphite electrode, in this case).

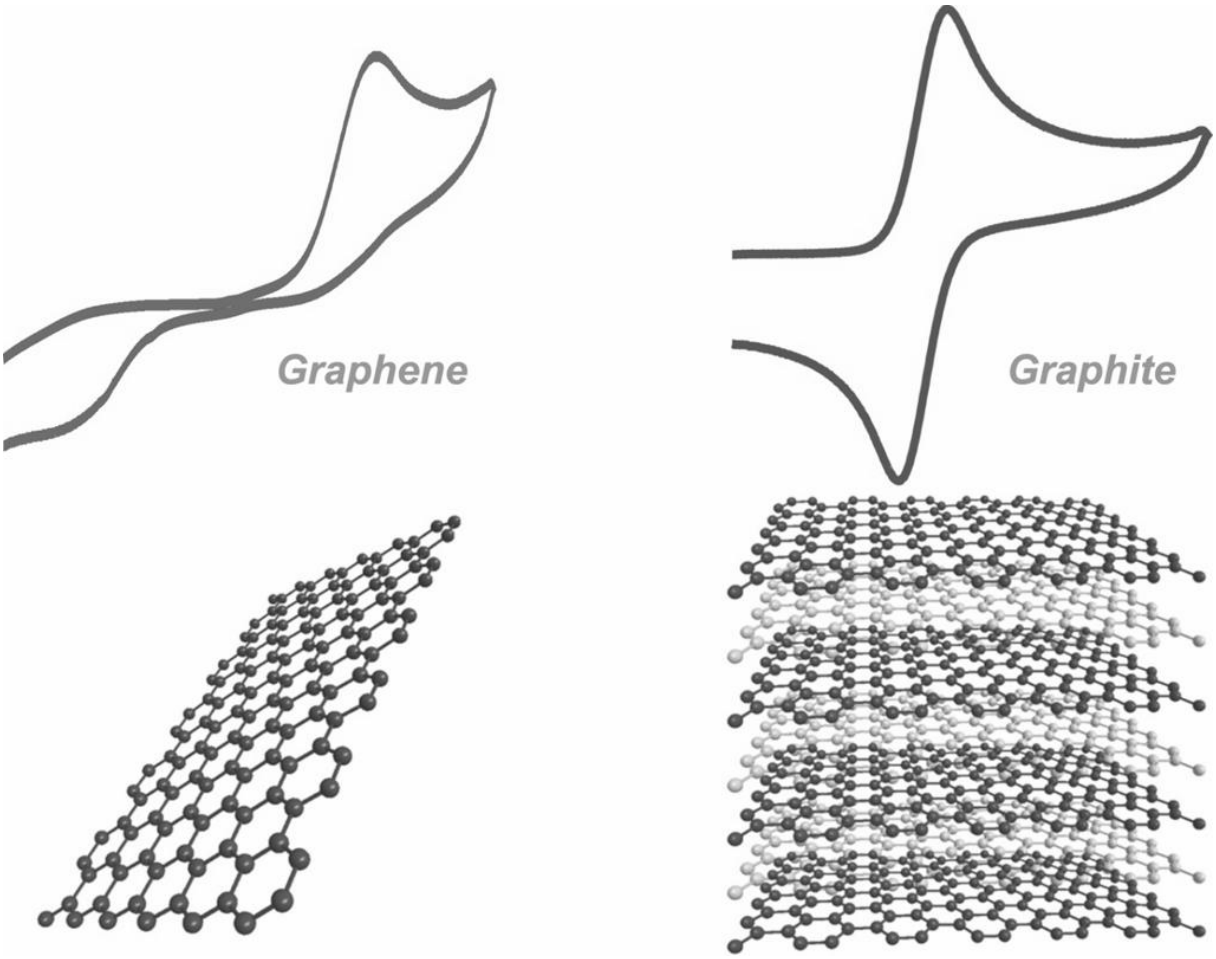

"*The important thing is not to stop questioning. Curiosity has its own reason for existing. One cannot help but be in awe when he contemplates the mysteries of eternity, of life, of the marvelous structure of reality. It is enough if one tries merely to comprehend a little of this mystery every day. Never lose a holy curiosity.*"

Albert Einstein, 1879–1955